Enhancing the performance of low concentrating photovoltaics via spectral conversion

Submitted by Joseph Day to the University of Exeter as a thesis for the degree of

Doctor of Philosophy in Renewable Energy

in November 2019.

I certify that all material in this thesis which is not my own work has been identified and that no material has previously been submitted and approved for the award of a degree by this or any other University.

Abstract

The spectral mismatch between the incoming solar spectrum and photovoltaic cells is a fundamental factor which curtails their efficiencies. Through luminescent processes, known as spectral conversion, the wavelengths of the incident sunlight may be changed to better match the optimal values for charge carrier generation by the solar cell. There are three means by which this can occur: upconversion, downconversion and luminescent downshifting, whereby two low energy photons can combine into one of a higher energy, one high energy photon can split its energy into two lower energy ones and a single high energy photon can reduce its energy, respectively. Collectively, these processes have attracted interest as an area of research for their application to solar cells as a method to enhance PV device performance, an important technological challenge to aid in the transition to a decarbonised economy.

In this thesis, particles with spectral conversion properties are incorporated into two kinds of novel solar PV devices of relevance to the emerging and building integrated photovoltaic technology sectors, 3D static SEH concentrator photovoltaic modules with potential for building integration and high stability dye sensitized solar cells. Following an introduction to the topic, concisely discussing the underlying mechanisms of each spectral conversion process, and conducting a literature review which catalogues the evolution of state-of-the-art results from the field, experiments are designed to test two candidate spectral conversion materials ($Sr_4Al_{14}O_{25}$: Eu^{2+}, Dy^{3+} and $NaYF_4$: Er^{3+}, Yb^{3+}) on silicon PV and dye sensitized solar cells, both with and without SEH concentrators. Under an A+A+A+ solar simulator at 1000 W/m^2, the power conversion efficiency of silicon PV devices improved up to 11.1% relative to controls through the addition of these materials. At lower irradiances and compared to cells without concentrators, the relative efficiency gains were more pronounced and external quantum efficiency (EQE) measurements suggested spectral conversion was potentially responsible for these enhancements. For a large scale BICPV system, a simple analysis showed cost per watt could fall by up to 8.1% and power output increase from 19.3 to 21.4 W/m^2 through this approach. For the dye sensitized solar cells a 53.4% efficiency enhancement (relative to un-doped controls) was

achieved with a potential cost reduction of 39.6%. Finally, simple optical models (including one developed in-house) and a statistical analysis are used to justify the findings and develop understanding of the physical processes behind the results, while conclusions are drawn with regards to the future outlook of this approach and its impact on the drive towards lower cost sources of clean electricity.

Acknowledgments

I would first and foremost like to thank my supervisors Prof. Tapas Mallick and Dr. Senthil Sundaram for the opportunity to undertake this PhD and their guidance throughout. In addition, I'd like to thank the solar group and all the Environment and Sustainability Institute staff for being a pleasure to work with and always helpful. Especially, Drs. Shivangi Sharma, Katie Shanks, Prabhu Selveraj, Anurag Roy, Hasan Baig and Mr. James Yule for taking the time to explain miscellaneous things in the lab over the last few years. A big thanks also to Dr. Lingamallu Giribabu, Dr. Nanaji Islavath and the other kind people from the research group at IICT, Hyderabad for the collaborative work on porphyrin based DSSCs and hosting me in their lab. Moving back to the UK, I'd like to thank Mr. Malcolm Spence and Dr. Joe Pickles for support here on campus with XRD and SEM, as well as Dr. Matthew Davies and Mr. Adam Salter from the University of Swansea for helping facilitate photoluminescent spectroscopy. Finally, a big shout out to all my other friends and family in Cornwall, Devon and elsewhere who supported me through this journey!

List of Contents

Abstract **3**
Acknowledgments **5**
List of Contents **6**
List of Tables **10**
List of Figures **16**
List of Abbreviations **26**
List of Publications **31**
Chapter 1. Introduction **33**
1.1 Background 33
1.2 Solar PV 35
1.2.1 Solar PV Technologies 36
1.2.2 CPV 39
1.2.3 BIPV 42
1.3 Fundamental Limits of Solar Cell Efficiency 44
1.4 Spectral Conversion 53
1.4.1 Upconversion 55
1.4.2 Downconversion 60
1.4.3 Luminescent Downshifting 62
1.5 Chapter Overviews and Aims 64
1.5.1 Chapter 2 64
1.5.2 Chapter 3 65
1.5.3 Chapter 4 65
1.5.4 Chapter 5 65
1.5.5 Chapter 6 65
1.5.6 Chapter 7 66
1.5.7 Expectations 66
Chapter 2. Literature Review **67**
2.1 Introduction 67
2.2 Rare Earth Ions and Early Spectral Conversion Experiments 67
2.3 Spectral Conversion Efficiency Limitations and Optimisation Parameters 73
2.4 State-of-the-art Upconversion Materials 80
2.4.1 Upconversion for Silicon PV 80
2.4.2 Upconversion for Emerging PV 85
2.5 State-of-the-art Downconversion Materials 91
2.5.1 Downconversion for Silicon PV 92

2.5.2 Downconversion for Emerging PV 92
2.6 State-of-the-art Luminescent Downshifting Materials 94
2.6.1 Luminescent Downshifting for Silicon PV 94
2.6.2 Luminescent Downshifting for Thin-film PV 95
2.7 Luminescent Solar Concentrators 97
2.7.1 Luminescent Solar Concentrator Efficiency 98
2.7.2 Luminescent Solar Concentrator Materials 99
2.7.3 Luminescent Solar Concentrator Designs 100
2.7.4 Luminescent Solar Concentrators for BIPV 102
2.8 Nanoscale Phenomena to Enhance Spectral Conversion 107
2.8.1 Quantum Dots as Rare Earth Ion Sensitizers 107
2.8.2 Photonic Crystals 108
2.8.3 Core-Shell Nanostructures 108
2.8.4 Plasmon Resonance 110
2.9 Challenges and Opportunities 111
2.9.1 Solar Cells Designed for Upconversion 112
2.9.2 Simultaneous Up and Downconversion or Luminescent Downshifting 113
2.9.3 Costs of Spectral Conversion Materials 115
2.9.4 Future Outlook for Spectral Conversion Materials 116
2.10 Relation of Knowledge Gaps to Thesis 119
Chapter 3. Material Properties, Characterisation Methods and Application to Silicon PV 123
3.1 Introduction 123
3.2 Choice of Materials 123
3.2.1 $Sr_4Al_{14}O_{25}$: Eu^{2+}, Dy^{3+} 123
3.2.2 $NaYF_4$: Er^{3+}, Yb^{3+} 125
3.3 Initial Characterisation 125
3.3.1 X-ray Diffraction 126
3.3.2 Scanning Electron Microscopy 129
3.3.3 Photoluminescent Spectroscopy 130
3.4 Thin Film Preparation and Characterisation 135
3.4.1 Spin Coating 135
3.4.2 UV-Vis Spectroscopy 137
3.4.3 Sylgard 139
3.4.4 TiO_2 141
3.4.5 Ball Milling in Ethanol Solvent 144
3.5 Silicon PV Device Preparation 146

3.5.1 Silicon Solar Cells 146
3.5.2 Application of Thin Film 147
3.6 Electrical Performance Characterisation Methods 148
3.6.1 Solar Simulator 148
3.6.2 Incident Photon-to-electron Conversion Efficiency 150
3.7 Results 152
3.7.1 Sylgard Static Spin Coated 152
3.7.2 TiO_2 Dynamic Spin Coated ..... **Error! Bookmark not defined.**
3.7.3. Sylgard drop casted 158
3.8 Conclusion 171
Chapter 4. Application to Low Concentrator Photovoltaic Modules 172
4.1 Introduction 172
4.2 Square Elliptical Hyperboloid Concentrators 172
4.3 Concentrator Photovoltaic Module Fabrication 175
4.4 Results 180
4.5 Comparing the Effect of Concentrator vs. No Concentrator 197
4.6 Effect of the Angle of Incidence 203
4.7 Conclusion 213
Chapter 5. Application to Dye Sensitized Solar Cells 215
5.1 Introduction 215
5.2 Dye Sensitized Solar Cells 215
5.2.1 Dye Sensitized Solar Cell Operating Principles 216
5.2.2 Dye Sensitized Solar Cell Limitations 218
5.3 Dye Sensitized Solar Cell Fabrication 222
5.4 Incorporation of Spectral Conversion Materials 226
5.5 Results 231
5.5.1 Indoor Characterisation under the Solar Simulator 231
5.5.2 Incident Photon-to-electron Conversion Efficiency 236
5.5.3 Discussion 237
5.6 SEH Concentrators on DSSCs 240
5.7 Y_2O_3: Yb^{3+}, Tm^{3+}, Ho^{3+} and Y_2O_3: Yb^{3+}, Ho^{3+} in Porphyrin-Carbon Counter Electrode Based DSSCs 245
5.8 Conclusion 250
Chapter 6. Financial, Statistical and Optical Models 251
6.1 Introduction 251
6.2 Cost Analysis 251
6.2.1 Silicon PV and LCPV devices 252

6.2.2 DSSC devices 254
6.2.3 Commercialisation Opportunities 257
6.3 Sensitivity Analysis 260
6.3.1 Pure Statistical Analysis of Results 261
6.3.2 Analysis via Propagated Sources of Error 267
6.3.3 DSSC variation in device efficiency 274
6.4 Optical Models 276
6.4.1 Thin Film Layer 276
6.4.2 Concentrator 2-D Ray Trace 289
6.5 Conclusion 316
Chapter 7. Conclusions and Future Outlook 318
7.1 Chapter Summaries 318
7.2 Future Outlook 320
7.3 Concluding Remarks 323
Bibliography 326

List of Tables

Table 1: Maximum cell efficiency and cost per W_p for various solar technologies [25, 26]. 39
Table 2: The letters used to represent the respective total orbital angular momentum quantum numbers in the term symbol notation. 68
Table 3: Summary of the UC materials used, and PV device performance enhancements noted in recent studies on various solar cell technologies. 91
Table 4: Summary of the DC materials used, and PV device performance enhancements noted in recent studies on various solar cell technologies. 94
Table 5: Summary of the LDS materials used, and PV device performance enhancements noted in recent studies on various solar cell technologies. 97
Table 6: Estimates for the maximum mass of rare earth ion that can be added per Wp of solar cell power output to still reduce the cost per Wp, using ΔPCE data from state-of-the-art studies presented in this chapter. 116
Table 7: The reference cell I_{SC} required for the light intensity to be calibrated to the appropriate level and corresponding HelioCon value. 149
Table 8: PCE measurements and relative PCE changes for the solar cells when bare and then when spin coated with Sylgard or $Sr_4Al_{14}O_{25}$: Eu^{2+}, Dy^{3+} doped Sylgard. 152
Table 9: J_{SC} measurements and relative J_{SC} changes for the solar cells when bare and then when spin coated with Sylgard or $Sr_4Al_{14}O_{25}$: Eu^{2+}, Dy^{3+} doped Sylgard. 152
Table 10: PCE measurements and relative PCE changes for the solar cells when bare and then when spin coated with TiO_2 or $Sr_4Al_{14}O_{25}$: Eu^{2+}, Dy^{3+} doped TiO_2. 155
Table 11: J_{SC} measurements and relative J_{SC} changes for the solar cells when bare and then when spin coated with TiO_2 or $Sr_4Al_{14}O_{25}$: Eu^{2+}, Dy^{3+} doped TiO_2. 156
Table 12: PCE and J_{SC} data for drop casted $Sr_4Al_{14}O_{25}$: Eu^{2+}, Dy^{3+} doped Sylgard devices at 1 sun irradiance. 161
Table 13: PCE and J_{SC} data for drop casted $Sr_4Al_{14}O_{25}$: Eu^{2+}, Dy^{3+} doped Sylgard devices at 0.8 suns irradiance. 161
Table 14: PCE and J_{SC} data for drop casted $Sr_4Al_{14}O_{25}$: Eu^{2+}, Dy^{3+} doped Sylgard devices at 0.6 suns irradiance. 161
Table 15: PCE and J_{SC} data for drop casted $Sr_4Al_{14}O_{25}$: Eu^{2+}, Dy^{3+} doped Sylgard devices at 0.4 suns irradiance. 161
Table 16: PCE and J_{SC} data for drop casted $NaYF_4$: Er^{3+}, Yb^{3+} doped Sylgard devices at 1 sun irradiance. 162
Table 17: PCE and J_{SC} data for drop casted $NaYF_4$: Er^{3+}, Yb^{3+} doped Sylgard devices at 0.8 suns irradiance. 162
Table 18: PCE and J_{SC} data for drop casted $NaYF_4$: Er^{3+}, Yb^{3+} doped Sylgard devices at 0.6 suns irradiance. 162
Table 19: PCE and J_{SC} data for drop casted $NaYF_4$: Er^{3+}, Yb^{3+} doped Sylgard devices at 0.4 suns irradiance. 162
Table 20: V_{OC} and FF data for drop casted $Sr_4Al_{14}O_{25}$: Eu^{2+}, Dy^{3+} doped Sylgard devices at 1 sun irradiance. 170
Table 21: V_{OC} and FF data for drop casted $Sr_4Al_{14}O_{25}$: Eu^{2+}, Dy^{3+} doped Sylgard devices at 0.8 suns irradiance. 170
Table 22: V_{OC} and FF data for drop casted $Sr_4Al_{14}O_{25}$: Eu^{2+}, Dy^{3+} doped Sylgard devices at 0.6 suns irradiance. 170

Table 23: V_{OC} and FF data for drop casted $Sr_4Al_{14}O_{25}$: Eu^{2+}, Dy^{3+} doped Sylgard devices at 0.4 suns irradiance. 170
Table 24: V_{OC} and FF data for drop casted $NaYF_4$: Er^{3+}, Yb^{3+} doped Sylgard devices at 1 sun irradiance. 170
Table 25: V_{OC} and FF data for drop casted $NaYF_4$: Er^{3+}, Yb^{3+} doped Sylgard devices at 0.8 suns irradiance. 170
Table 26: V_{OC} and FF data for drop casted $NaYF_4$: Er^{3+}, Yb^{3+} doped Sylgard devices at 0.6 suns irradiance. 171
Table 27: V_{OC} and FF data for drop casted $NaYF_4$: Er^{3+}, Yb^{3+} doped Sylgard devices at 0.4 suns irradiance. 171
Table 28: J_{SC} and PCE data for $Sr_4Al_{14}O_{25}$: Eu^{2+}, Dy^{3+} doped LCPV devices at 1 sun irradiance. 184
Table 29: J_{SC} and PCE data for $Sr_4Al_{14}O_{25}$: Eu^{2+}, Dy^{3+} doped LCPV devices at 0.8 suns irradiance. 185
Table 30: J_{SC} and PCE data for $Sr_4Al_{14}O_{25}$: Eu^{2+}, Dy^{3+} doped LCPV devices at 0.6 suns irradiance. 185
Table 31: J_{SC} and PCE data for $Sr_4Al_{14}O_{25}$: Eu^{2+}, Dy^{3+} doped LCPV devices at 0.4 suns irradiance. 185
Table 32: J_{SC} and PCE data for $NaYF_4$: Er^{3+}, Yb^{3+} doped LCPV devices at 1 sun irradiance. 185
Table 33: J_{SC} and PCE data for $NaYF_4$: Er^{3+}, Yb^{3+} doped LCPV devices at 0.8 suns irradiance. 186
Table 34: J_{SC} and PCE data for $NaYF_4$: Er^{3+}, Yb^{3+} doped LCPV devices at 0.6 suns irradiance. 186
Table 35: J_{SC} and PCE data for $NaYF_4$: Er^{3+}, Yb^{3+} doped LCPV devices at 0.4 suns irradiance. 186
Table 36: Difference in the relative PCE and J_{SC} gains between the LCPV and non-LCPV devices containing $Sr_4Al_{14}O_{25}$: Eu^{2+}, Dy^{3+} at 1 sun irradiance. 199
Table 37: Difference in the relative PCE and J_{SC} gains between the LCPV and non-LCPV devices containing $Sr_4Al_{14}O_{25}$: Eu^{2+}, Dy^{3+} at 0.8 suns irradiance. 199
Table 38: Difference in the relative PCE and J_{SC} gains between the LCPV and non-LCPV devices containing $Sr_4Al_{14}O_{25}$: Eu^{2+}, Dy^{3+} at 0.6 suns irradiance. 200
Table 39: Difference in the relative PCE and J_{SC} gains between the LCPV and non-LCPV devices containing $Sr_4Al_{14}O_{25}$: Eu^{2+}, Dy^{3+} at 0.4 suns irradiance. 200
Table 40: Difference in the relative PCE and J_{SC} gains between the LCPV and non-LCPV devices containing $NaYF_4$: Er^{3+}, Yb^{3+} at 1 sun irradiance. 200
Table 41: Difference in the relative PCE and J_{SC} gains between the LCPV and non-LCPV devices containing $NaYF_4$: Er^{3+}, Yb^{3+} at 0.8 suns irradiance. 200
Table 42: Difference in the relative PCE and J_{SC} gains between the LCPV and non-LCPV devices containing $NaYF_4$: Er^{3+}, Yb^{3+} at 0.6 suns irradiance. 200
Table 43: Difference in the relative PCE and J_{SC} gains between the LCPV and non-LCPV devices containing $NaYF_4$: Er^{3+}, Yb^{3+} at 0.4 suns irradiance. 200
Table 44: PCE and J_{SC} data for $Sr_4Al_{14}O_{25}$: Eu^{2+}, Dy^{3+} doped LCPV devices at 10° angle of incidence. 205
Table 45: PCE and J_{SC} data for $Sr_4Al_{14}O_{25}$: Eu^{2+}, Dy^{3+} doped LCPV devices at 20° angle of incidence. 206
Table 46: PCE and J_{SC} data for $Sr_4Al_{14}O_{25}$: Eu^{2+}, Dy^{3+} doped LCPV devices at 30° angle of incidence. 206

Table 47: PCE and J_{SC} data for $Sr_4Al_{14}O_{25}$: Eu^{2+}, Dy^{3+} doped LCPV devices at 40° angle of incidence. *206*
Table 48: PCE and J_{SC} data for $Sr_4Al_{14}O_{25}$: Eu^{2+}, Dy^{3+} doped LCPV devices at 50° angle of incidence. *206*
Table 49: PCE and J_{SC} data for $Sr_4Al_{14}O_{25}$: Eu^{2+}, Dy^{3+} doped LCPV devices at 60° angle of incidence. *207*
Table 50: PCE and J_{SC} data for $Sr_4Al_{14}O_{25}$: Eu^{2+}, Dy^{3+} doped LCPV devices at 70° angle of incidence. *207*
Table 51: PCE and J_{SC} data for $Sr_4Al_{14}O_{25}$: Eu^{2+}, Dy^{3+} doped LCPV devices at 80° angle of incidence. *207*
Table 52: PCE and J_{SC} data for $NaYF_4$: Er^{3+}, Yb^{3+} doped LCPV devices at 10° angle of incidence. *207*
Table 53: PCE and J_{SC} data for $NaYF_4$: Er^{3+}, Yb^{3+} doped LCPV devices at 20° angle of incidence. *208*
Table 54: PCE and J_{SC} data for $NaYF_4$: Er^{3+}, Yb^{3+} doped LCPV devices at 30° angle of incidence. *208*
Table 55: PCE and J_{SC} data for $NaYF_4$: Er^{3+}, Yb^{3+} doped LCPV devices at 40° angle of incidence. *208*
Table 56: PCE and J_{SC} data for $NaYF_4$: Er^{3+}, Yb^{3+} doped LCPV devices at 50° angle of incidence. *208*
Table 57: PCE and J_{SC} data for $NaYF_4$: Er^{3+}, Yb^{3+} doped LCPV devices at 60° angle of incidence. *209*
Table 58: PCE and J_{SC} data for $NaYF_4$: Er^{3+}, Yb^{3+} doped LCPV devices at 70° angle of incidence. *209*
Table 59: PCE and J_{SC} data for $NaYF_4$: Er^{3+}, Yb^{3+} doped LCPV devices at 80° angle of incidence. *209*
Table 60: PCE and J_{SC} data for $NaYF_4$: Er^{3+}, Yb^{3+} doped spin coated DSSCs at 1 sun. *231*
Table 61: V_{OC} and FF data for $NaYF_4$: Er^{3+}, Yb^{3+} doped spin coated DSSCs at 1 sun. *231*
Table 62: PCE and J_{SC} data for $Sr_4Al_{14}O_{25}$: Eu^{2+}, Dy^{3+} doped screen printed DSSCs at 1 sun. *233*
Table 63: V_{OC} and FF data for $Sr_4Al_{14}O_{25}$: Eu^{2+}, Dy^{3+} doped screen printed DSSCs at 1 sun. *233*
Table 64: PCE and J_{SC} data for $NaYF_4$: Er^{3+}, Yb^{3+} doped screen printed DSSCs at 1 sun. *233*
Table 65: V_{OC} and FF data for $NaYF_4$: Er^{3+}, Yb^{3+} doped screen printed DSSCs at 1 sun. *233*
Table 66: P_{max} and J_{SC} data for control and rare earth doped screen printed DSSCs with SEH concentrators under 1 sun. *241*
Table 67: P_{max} and J_{SC} data for control and rare earth doped screen printed DSSCs with SEH concentrators under 0.8 suns. *242*
Table 68: P_{max} and J_{SC} data for control and rare earth doped screen printed DSSCs with SEH concentrators under 0.6 suns. *242*
Table 69: P_{max} and J_{SC} data for control and rare earth doped screen printed DSSCs with SEH concentrators under 0.4 suns. *242*
Table 70: PCE and J_{SC} data for control and rare earth doped porphyrin-carbon counter electrode DSSCs under 1 sun. *248*

Table 71: V_{OC} and FF data for control and rare earth doped porphyrin-carbon counter electrode DSSCs under 1 sun. 249
Table 72: Costs of the materials required for fabrication of the silicon PV and LCPV devices. 252
Table 73: Cost analysis for the $Sr_4Al_{14}O_{25}$: Eu^{2+}, Dy^{3+} doped coated PV devices. 252
Table 74: Cost analysis for the $NaYF_4$: Er^{3+}, Yb^{3+} doped coated PV devices. 252
Table 75: Cost analysis for the $Sr_4Al_{14}O_{25}$: Eu^{2+}, Dy^{3+} doped LCPV devices. 253
Table 76: Cost analysis for the $NaYF_4$: Er^{3+}, Yb^{3+} doped LCPV devices. 253
Table 77: Costs of the materials required for fabrication of the silicon PV and LCPV devices. 254
Table 78: Cost analysis for the $Sr_4Al_{14}O_{25}$: Eu^{2+}, Dy^{3+} doped screen printed DSSC devices. 256
Table 79: Cost analysis for the $NaYF_4$: Er^{3+}, Yb^{3+} doped screen printed DSSC devices. 256
Table 80: Cost analysis for the control and rare earth doped screen printed DSSC devices with SEH concentrators. 256
Table 81: Power and cost per area of different BIPV technologies presented in this work compared with that of a commercial standard mono-c-Si PV module. 260
Table 82: Results of t-test for $Sr_4Al_{14}O_{25}$: Eu^{2+}, Dy^{3+} doped LCPV devices at 1 sun. . 263
Table 83: Results of t-test for $Sr_4Al_{14}O_{25}$: Eu^{2+}, Dy^{3+} doped LCPV devices at 0.8 suns. 263
Table 84: Results of t-test for $Sr_4Al_{14}O_{25}$: Eu^{2+}, Dy^{3+} doped LCPV devices at 0.6 suns. 263
Table 85: Results of t-test for $Sr_4Al_{14}O_{25}$: Eu^{2+}, Dy^{3+} doped LCPV devices at 0.4 suns. 264
Table 86: Results of t-test for $NaYF_4$: Er^{3+}, Yb^{3+} doped LCPV devices at 1 sun. 264
Table 87: Results of t-test for $NaYF_4$: Er^{3+}, Yb^{3+} doped LCPV devices at 0.8 suns. ... 264
Table 88: Results of t-test for $NaYF_4$: Er^{3+}, Yb^{3+} doped LCPV devices at 0.6 suns. ... 264
Table 89: Results of t-test for $NaYF_4$: Er^{3+}, Yb^{3+} doped LCPV devices at 0.4 suns. ... 265
Table 90: Results of t-test for $Sr_4Al_{14}O_{25}$: Eu^{2+}, Dy^{3+} doped Sylgard PV cells at 1 sun. 265
Table 91: Results of t-test for $Sr_4Al_{14}O_{25}$: Eu^{2+}, Dy^{3+} doped Sylgard PV cells at 0.8 suns. 265
Table 92: Results of t-test for $Sr_4Al_{14}O_{25}$: Eu^{2+}, Dy^{3+} doped Sylgard PV cells at 0.6 suns. 265
Table 93: Results of t-test for $Sr_4Al_{14}O_{25}$: Eu^{2+}, Dy^{3+} doped Sylgard PV cells at 0.4 suns. 265
Table 94: Results of t-test for $NaYF_4$: Er^{3+}, Yb^{3+} doped Sylgard PV cells at 1 sun. 265
Table 95: Results of t-test for $NaYF_4$: Er^{3+}, Yb^{3+} doped Sylgard PV cells at 0.8 suns. 266
Table 96: Results of t-test for $NaYF_4$: Er^{3+}, Yb^{3+} doped Sylgard PV cells at 0.6 suns. 266
Table 97: Results of t-test for $NaYF_4$: Er^{3+}, Yb^{3+} doped Sylgard PV cells at 0.4 suns. 266
Table 98: Results of z-test for $Sr_4Al_{14}O_{25}$: Eu^{2+}, Dy^{3+} doped LCPV devices at 1 sun. 270
Table 99: Results of z-test for $Sr_4Al_{14}O_{25}$: Eu^{2+}, Dy^{3+} doped LCPV devices at 0.8 suns. 270
Table 100: Results of z-test for $Sr_4Al_{14}O_{25}$: Eu^{2+}, Dy^{3+} doped LCPV devices at 0.6 suns. 270
Table 101: Results of z-test for $Sr_4Al_{14}O_{25}$: Eu^{2+}, Dy^{3+} doped LCPV devices at 0.4 suns. 271
Table 102: Results of z-test for $NaYF_4$: Er^{3+}, Yb^{3+} doped LCPV devices at 1 sun. 271

Table 103: Results of z-test for $NaYF_4$: Er^{3+}, Yb^{3+} doped LCPV devices at 0.8 suns. 271
Table 104: Results of z-test for $NaYF_4$: Er^{3+}, Yb^{3+} doped LCPV devices at 0.6 suns. 271
Table 105: Results of z-test for $NaYF_4$: Er^{3+}, Yb^{3+} doped LCPV devices at 0.4 suns. 272
Table 106: Results of z-test for $Sr_4Al_{14}O_{25}$: Eu^{2+}, Dy^{3+} doped Sylgard PV cells at 1 sun. 272
Table 107: Results of z-test for $Sr_4Al_{14}O_{25}$: Eu^{2+}, Dy^{3+} doped Sylgard PV cells at 0.8 suns. 272
Table 108: Results of z-test for $Sr_4Al_{14}O_{25}$: Eu^{2+}, Dy^{3+} doped Sylgard PV cells at 0.6 suns. 272
Table 109: Results of z-test for $Sr_4Al_{14}O_{25}$: Eu^{2+}, Dy^{3+} doped Sylgard PV cells at 0.4 suns. 272
Table 110: Results of z-test for $NaYF_4$: Er^{3+}, Yb^{3+} doped Sylgard PV cells at 1 sun. . 273
Table 111: Results of z-test for $NaYF_4$: Er^{3+}, Yb^{3+} doped Sylgard PV cells at 0.8 suns. 273
Table 112: Results of z-test for $NaYF_4$: Er^{3+}, Yb^{3+} doped Sylgard PV cells at 0.6 suns. 273
Table 113: Results of z-test for $NaYF_4$: Er^{3+}, Yb^{3+} doped Sylgard PV cells at 0.4 suns. 273
Table 114: Variation in the PCE of the $Sr_4Al_{14}O_{25}$: Eu^{2+}, Dy^{3+} doped screen printed DSSCs. 274
Table 115: Variation in the PCE of the $NaYF_4$: Er^{3+}, Yb^{3+} doped screen printed DSSCs. 274
Table 116: The derived model parameters and goodness of fit for each concentration of rare earth compound for $Sr_4Al_{14}O_{25}$: Eu^{2+}, $Dy^{3+}$and $NaYF_4$: Er^{3+}, Yb^{3+} doped Sylgard devices. 285
Table 117: Predicted J_{SC} data for the $Sr_4Al_{14}O_{25}$: Eu^{2+}, Dy^{3+} doped Sylgard layers on PV cells (from the optical model and IPCE measurements) compared to that observed under the solar simulator. 288
Table 118: Predicted J_{SC} data for the $NaYF_4$: Er^{3+}, Yb^{3+} doped Sylgard layers on PV cells (from the optical model and IPCE measurements) compared to that observed under the solar simulator. 288
Table 119: Refracted angle of incidence (θ_r) for a ray entering the concentrator at angle of incidence (θ_i) to the normal. 290
Table 120: Optical efficiency for the SEH concentrator from the 2D model at different angles of incidence compared to earlier work by Sellami et al. 297
Table 121: The J_{SC} predicted by the ray trace model and as measured experimentally for the un-doped LCPV modules under 1 sun of light at varying angles of incidence. 298
Table 122: Probability of emission that originates at the co-ordinate in the table directly reaching the solar cell at the exit aperture of the SEH concentrator. 301
Table 123: Probability of emission that originates at the co-ordinate in the table indirectly reaching the solar cell at the exit aperture of the SEH concentrator via one TIR event. 301
Table 124: Total probability of emission that originates at the co-ordinate in the table reaching the solar cell at the exit aperture of the SEH concentrator directly or via one TIR event. 302
Table 125: Predicted optical efficiencies of the control (un-doped), homogenously doped, top doped and bottom doped SEH concentrators. 303

Table 126: Calculated absorption coefficients for the un-doped concentrator, $Sr_4Al_{14}O_{25}$: Eu^{2+}, Dy^{3+} doped concentrator and $NaYF_4$: Er^{3+}, Yb^{3+} doped concentrator at 400 and 410 nm. 305

Table 127: Optical efficiency components and effect on J_{SC} for the control (un-doped), bottom doped, top doped and homogenously doped $Sr_4Al_{14}O_{25}$: Eu^{2+}, Dy^{3+} concentrators at 400 nm irradiance. 312

Table 128: Optical efficiency components and effect on J_{SC} for the control (un-doped), bottom doped, top doped and homogenously doped $Sr_4Al_{14}O_{25}$: Eu^{2+}, Dy^{3+} concentrators at 410 nm irradiance. 312

Table 129: Optical efficiency components and effect on J_{SC} for the control (un-doped), bottom doped, top doped and homogenously doped $NaYF_4$: Er^{3+}, Yb^{3+} concentrators at 400 nm irradiance. 312

Table 130: Optical efficiency components and effect on J_{SC} for the control (un-doped), bottom doped, top doped and homogenously doped $NaYF_4$: Er^{3+}, Yb^{3+} concentrators at 410 nm irradiance. 312

Table 131: Total predicted effect on J_{SC} for the bottom doped, top doped and homogeneously doped $Sr_4Al_{14}O_{25}$: Eu^{2+}, Dy^{3+} concentrators compared to the control alongside the experimentally observed J_{SC} data. 312

Table 132: Total predicted effect on J_{SC} for the bottom doped, top doped and homogeneously doped $NaYF_4$: Er^{3+}, Yb^{3+} concentrators compared to the control alongside the experimentally observed J_{SC} data. 313

List of Figures

Figure 1: The global energy potential of various renewable and non-renewable sources. It can clearly be seen that solar is by far the energy source with the largest potential instantaneous power output at 23000 TW. Figure taken from [8]. ... 34

Figure 2: The cumulative solar PV generation capacity from 2005-2018. An exponential growth is observed with the total amount installed approximately doubling every 3 years in the last decade. Data from [12], [13] and [14]..... 36

Figure 3: The contemporary maximum efficiency achieved by PV devices of different solar technologies since the 1970s as verified by the National Renewable Energy Laboratory [22]..... 38

Figure 4: The working principles and designs of two types of optical concentrator used in HCPV systems: a) Fresnel lens and b) Parabolic reflecting mirror..... 40

Figure 5: The designs of six types of optical concentrator used in LCPV systems that all operate via TIR: a) Luminescent solar concentrator, b) 3D static square elliptical hyperboloid (SEH) concentrator, c) 3D crossed V-trough, d) 3D polygonal compound parabolic concentrator (CPC), e) 3D crossed CPC and f) lens walled CPC. 41

Figure 6: Images of BIPV systems: a) PV modules integrated as roof tiles for a slate effect [45], b) roof and ceiling made from PV modules for sky lighting effect [46], c) LCPV module based on SEH concentrators that could form part of a window due to high transparency [47] and d) flexible PV modules attached to the surface of a curved building [48]. 43

Figure 7: The solar irradiance spectrum here at Earth in terms of: that derived from the black body spectrum of the sun (black line), the actual radiation received at the top of the Earth's atmosphere, AM0 (shaded yellow) and the actual radiation received at the Earth's surface after absorption by the atmosphere, AM 1.5 (shaded red) [50]..... 45

Figure 8: A simple diagram of the band structure in three types of material. In insulators the valence bands are full and there is a large energy gap between this band and the conduction band. Conversely for conductors, the electrons can move freely between the two bands. Finally, in semiconductors the energy gap between the valence and conduction band is smaller such that a photon can promote an electron to the conduction band and create a hole. This process is known as the photovoltaic effect [51]..... 46

Figure 9: The structure and working principle of a typical single junction silicon solar cell. Electron-hole pairs are generated by photons in the p-type base and the charges travel in opposite directions; electrons across the p-n junction to the emitter and front contact, and holes to the rear contact. When the front and rear contacts are connected via an external load a light generated current flows [55]. 47

Figure 10: Graph to show the useable electrical power and sources of efficiency loss for single junction solar cells of varying band gap under the Shockley-Queisser model. The maximum theoretical efficiency is approximately 30% for a 1.1 eV band gap device [58]..... 49

Figure 11: A typical I-V profile of a solar cell (the red curve) in which the y-intercept is the I_{SC} and x-intercept V_{OC}. The blue curve is the power generated by the cell which reaches a maximum at point V_{MP} and I_{MP} [59]..... 49

Figure 12: The basic concept of spectral conversion is to harness more energy from the parts of the spectrum that are not fully utilised. The green shaded area represents the energy that can be used by a silicon solar cell, the red that which may be captured via UC of low energy photons and the blue that which can be utilised by DC of high energy photons. 54

Figure 13: Examples of three spectral conversion processes: a) UC where two low energy photons are combined to make a single higher energy photon, b) DC where the energy of one high energy photon is split between two lower energy photons and c) LDS where the energy of a single high energy photon is reduced. The generalised energy level picture is also shown for each process..... 54

Figure 14: Design of a UC-PV system in which transmitted sub-band gap radiation is absorbed by the UC layer and converted to wavelengths that can be used to generate current upon being re-directed to the bifacial solar cell above. 55

Figure 15: Energy level diagram representation for the proposed UC mechanisms within rare earth ions: a) excited state absorption (ESA), b) energy transfer upconversion (ETU), c) photon avalanche (PA), d) co-operative energy transfer (CET) and e) energy migration upconversion (EMU). Modified from [75]..... 57

Figure 16: Energy level diagram for the states and steps involved in UC via TTA. The numbered processes are referred to in the text. Modified from [77]..... 58

Figure 17: Diagram of the potential UC processes within QD nanostructures. The overall process for QDs 1 and 2 which are connected by a semiconductor rod is shown at the top of the figure. This can occur in two ways: a) direct intraband hole absorption and b) an Auger mediated process. Modified from [79]..... 59

Figure 18: The concept of UC via thermal radiation. Infrared photons are absorbed by a material and, by multi-phonon relaxation, raise the material's temperature. This in turn shifts the peak of the emitted black body radiation towards the visible and UV part of the spectrum, meaning UC of photons has taken place. Taken from [80]..... 60

Figure 19: Design of a DC-PV system in which incoming short wavelength light is absorbed by the DC layer placed above the solar cell. The photons are then re-emitted at wavelengths which cause less thermalisation losses, increasing the overall efficiency of the PV. 61

Figure 20: Energy level diagram of the proposed DC mechanisms within rare earth ions: a) ESA in reverse, b), c), and d) resonant energy transfer between two ions and e) CET. Modified from [75]. 62

Figure 21: Energy level diagram of one proposed simple mechanism for LDS in which an absorbed high energy photon decays non-radiatively to an intermediate state, before emitting a single lower energy photon..... 63

Figure 22: A Dieke style diagram which shows the energy levels of trivalent rare earth ions. The red highlighted states are able to undergo UC when excited. 68

Figure 23: Electron configuration for the 4f subshell of Er^{3+} derived via Hund's rules with m_s = +½ denoted by upward arrows and m_s = -½ denoted by downward arrows. 69

Figure 24: Energy level diagram which shows the potential emissions from the Yb^{3+}- Er^{3+} ion pair. In this representation the dashed arrows correspond to energy transfer between ions, the curly arrows non-radiative decay and the solid arrows radiative decay of that colour. Modified from [92]. 70

Figure 25: Energy level diagram which shows the potential emissions from the Eu^{2+}-Dy^{3+}ion pair. Modified from [100] and [101]. 71

Figure 26: Two ways concentrating optics can be integrated with UC: a) cross-section of a single cell UC-CPV module in which a CPC is placed between the PV cell and UC layer in order to increase the intensity of the light that reaches it, b) the schematic of a modelled CPV system in which the parameters α (acceptance angle) and f/D (focal ratio) are varied [89] and c) simulations show high concentrations of 1000 suns can be achieved at the UC layer in this set up.. 83
Figure 27: Designs of potential UC via thermal radiation systems: a) angular selectivity by surface nano-patterning, b) enclosing the upconverter into a reflective cavity with small aperture, c) geometrical and spectral splitting of sunlight onto a cell and d) same concept as c) but with two cells. Modified from [150]. 85
Figure 28: The paths through which the major sources of optical loss occur in an LSC: reflection, reabsorption, escape cone losses and surface scattering. Taken from [194]..... 98
Figure 29: Potential BIPV applications of LSCs: (a) Façade of the Palais du Congrès in Montréal; these windows are only decorative but LSC-PV systems of a similar appearance could one day be widespread, (b) LSC could function as a roadside noise barrier or (c) a canopy for parked vehicles. Taken from [227]. 104
Figure 30: Examples of real LSC-PV modules for applications in BIPV: (a) Roof Leaf module design [237], (b) smart window powered by yellow LSC-PV [236] and (c) greenhouse made from red LSC-PV [238]. 106
Figure 31: Unit cell of the synergistic plasmonic and photon crystal structure, containing perfectly matched layers which are labelled PML. Taken from [244]. 109
Figure 32: 2D cross-section of the core-shell nanostructure with separate rare earth ions in each active layer. The ions absorb at different wavelengths and are kept apart by an inert layer that prevents them from interacting with each other which would lead to energy losses. By using three ions, a wider region of the spectrum can be harnessed as shown on the diagram. Modified from [247]..... 110
Figure 33: Representation of the promising prospect of simultaneous UC and LDS which shifts light from both short and long wavelength parts of the spectrum, along with the design of the prepared layers which can achieve this for a PV cell. Modified from [263]. 114
Figure 34: Nexus of issues and research themes addressed in this thesis based on the web of current PV technology and knowledge. Topics within green boxes fall within the scope of this work and white boxes are beyond that which is considered. 122
Figure 35: $Sr_4Al_{14}O_{25}$: Eu^{2+}, Dy^{3+} powder in vessels: a) ground and b) unground. Persistent phosphorescence was observed after exposure to simulated sunlight in both samples: c) ground and d) unground. 124
Figure 36: $NaYF_4$: Er^{3+}, Yb^{3+} powder in a vessel. Unlike the $Sr_4Al_{14}O_{25}$: Eu^{2+}, Dy^{3+} sample, it did not exhibit phosphorescence once the lights had been turned off after exposure to sunlight, so the lifetimes of its photoexcited states are much shorter. 125
Figure 37: Representation of the derivation of Bragg's law of x-ray diffraction. Lattice ions separated by a distance, d, and subject to an x-ray beam of angle θ to the horizontal, will result in constructive interference when integer multiples of the wavelength are equal to 2dsin θ. Taken from [286]. 126
Figure 38: The simple layout of an x-ray diffractometer. The x-ray tube and detector can move along the circumference of the circle so that θ and 2θ can be varied to produce a profile. Taken from [287]..... 127

Figure 39: XRD profiles obtained for: a) the ground $Sr_4Al_{14}O_{25}$: Eu^{2+}, Dy^{3+} and b) $NaYF_4$: Er^{3+}, Yb^{3+} powder. 128
Figure 40: ICDD profile for $Sr_4Al_{14}O_{25}$ from the powder diffraction profile database... 129
Figure 41: ICDD profile for $NaYF_4$: Er^{3+}, Yb^{3+} from the powder diffraction profile database. 129
Figure 42: SEM images obtained for the $Sr_4Al_{14}O_{25}$: Eu^{2+}, Dy^{3+} powder samples: a) unground and b) ground. 130
Figure 43: Photoluminescence spectra for 1% $Sr_4Al_{14}O_{25}$: Eu^{2+}, Dy^{3+} doped thin film. 132
Figure 44: First photoluminescence spectra for 1% $NaYF_4$: Er^{3+}, Yb^{3+} doped thin film. 133
Figure 45: Second photoluminescence spectra for 1% $NaYF_4$: Er^{3+}, Yb^{3+} doped thin film. 133
Figure 46: Emission spectrum for 1% $NaYF_4$: Er^{3+}, Yb^{3+} doped thin film under 979 nm excitation. 133
Figure 47: Relative emission spectra for 0.25, 0.5, 1 and 2% doped $Sr_4Al_{14}O_{25}$: Eu^{2+}, Dy^{3+} doped thin films under 360 nm excitation. 134
Figure 48: Relative emission spectra for 0.25, 0.5, 1 and 2% doped $NaYF_4$: Er^{3+}, Yb^{3+} doped thin films under 380 nm excitation. 134
Figure 49: Relative emission spectra for the 1% $Sr_4Al_{14}O_{25}$: Eu^{2+}, Dy^{3+} doped thin films under 400, 410, 420, 430 and 440 nm excitation. 135
Figure 50: Relative emission spectra for the 1% $NaYF_4$: Er^{3+}, Yb^{3+} doped thin films under 400, 410, 420, 430 and 440 nm excitation. 135
Figure 51: Common spin coating error patterns: a) air bubbles on wafer surface, b) comets, streaks or flares, c) swirl pattern, d) centre circle chuck mark, e) uncoated areas and f) pinholes. Taken from [294]. 137
Figure 52: Transmittance of the $Sr_4Al_{14}O_{25}$: Eu^{2+}, Dy^{3+} doped Sylgard layers, in concentrations by weight from 0-2%, drop casted on acrylic. 140
Figure 53: Transmittance of the $NaYF_4$: Er^{3+}, Yb^{3+} doped Sylgard layers, in concentrations by weight from 0-2%, drop casted on acrylic. 141
Figure 54: Transmittance spectrum of TiO_2 (Greatcell 18NR-T) containing 10% $Sr_4Al_{14}O_{25}$: Eu^{2+}, Dy^{3+} by weight and spin coated at 6000 RPM on a glass substrate. 142
Figure 55: a) Picture of two films of TiO_2 synthesised via the $TiCl_4$ method. b) 100x magnification image, obtained via an optical microscope, highlights the inhomogeneity of the coating. 143
Figure 56: Transmittance spectra of TiO_2 thin films synthesised via the $TiCl_4$ method and spin coated at increasing RPM from 1000 to 8000. 144
Figure 57: Schematic of the operation principle of a ball milling machine. Collisions between the balls and the grinding medium cause a reduction in average particle size. 145
Figure 58: Transmittance spectra of the $Sr_4Al_{14}O_{25}$: Eu^{2+}, Dy^{3+} film which had been produced by ball milling and spin coated at 6000 RPM. 145
Figure 59: Schematic diagram to show the structure of the c-Si solar cells with laser grooved buried contact technology produced by NAREC and used in this work. Taken from [302]. 146
Figure 60: a) Real image of a soldered c-Si solar cell and b) a zoomed image of the cell to show the buried contacts. 147

Figure 61: Diagram of the experimental set up when characterising PV or LCPV cell performance under the solar simulator. 149
Figure 62: Diagram of the experimental set up when characterising PV or LCPV EQE with the Bentham PVE300. 151
Figure 63: I-V curve of cell 1, before and after coating with Sylgard. 152
Figure 64: I-V curve of cell 2, before and after coating with Sylgard. 153
Figure 65: I-V curve of cell 3, before and after coating with Sylgard doped with $Sr_4Al_{14}O_{25}$: Eu^{2+}, Dy^{3+}. 153
Figure 66: I-V curve of cell 4, before and after coating with Sylgard doped with $Sr_4Al_{14}O_{25}$: Eu^{2+}, Dy^{3+}. 153
Figure 67: a) Image of a solar cell before applying the Sylgard coating and b) after applying the coatings. 154
Figure 68: Reflectance spectrum of cell 3 before and after coating with Sylgard doped with $Sr_4Al_{14}O_{25}$: Eu^{2+}, Dy^{3+}. 155
Figure 69: I-V curve of cell 1, before and after coating with TiO_2. 156
Figure 70: I-V curve of cell 2, before and after coating with TiO_2. 156
Figure 71: I-V curve of cell 3, before and after coating with TiO_2 doped with $Sr_4Al_{14}O_{25}$: Eu^{2+}, Dy^{3+}. 157
Figure 72: EQE spectrum of cell 3, before and after coating with TiO_2 doped with $Sr_4Al_{14}O_{25}$: Eu^{2+}, Dy^{3+}. 157
Figure 73: Image of a c-Si solar cell coated with Sylgard-rare earth doped compound mixture via drop costing and fixed on an acrylic base. 158
Figure 74: PCE of the $Sr_4Al_{14}O_{25}$: Eu^{2+}, Dy^{3+} doped Sylgard devices of varying doping ratios at different solar irradiances. 163
Figure 75: J_{SC} of the $Sr_4Al_{14}O_{25}$: Eu^{2+}, Dy^{3+} doped Sylgard devices of varying doping ratios at different solar irradiances. 163
Figure 76: PCE of the $NaYF_4$: Er^{3+}, Yb^{3+} doped Sylgard devices of varying doping ratios at different solar irradiances. 164
Figure 77: J_{SC} of the $NaYF_4$: Er^{3+}, Yb^{3+} doped Sylgard devices of varying doping ratios at different solar irradiances. 164
Figure 78: Relative PCE gains for the $Sr_4Al_{14}O_{25}$: Eu^{2+}, Dy^{3+} doped Sylgard devices at different solar irradiances. 165
Figure 79: Relative J_{SC} gains for the $Sr_4Al_{14}O_{25}$: Eu^{2+}, Dy^{3+} doped Sylgard devices at different solar irradiances. 165
Figure 80: Relative PCE gains for the $NaYF_4$: Er^{3+}, Yb^{3+} doped Sylgard devices at different solar irradiances. 166
Figure 81: Relative J_{SC} gains for the $NaYF_4$: Er^{3+}, Yb^{3+} doped Sylgard devices at different solar irradiances. 166
Figure 82: I-V curves of for the $Sr_4Al_{14}O_{25}$: Eu^{2+}, Dy^{3+} doped Sylgard devices at different solar irradiances. 167
Figure 83: I-V curves of for the $NaYF_4$: Er^{3+}, Yb^{3+} doped Sylgard devices at different solar irradiances. 168
Figure 84: EQE spectra of the $Sr_4Al_{14}O_{25}$: Eu^{2+}, Dy^{3+} doped Sylgard devices. 169
Figure 85: EQE spectra of the $NaYF_4$: Er^{3+}, Yb^{3+} doped Sylgard devices. 169
Figure 86: 3D profile from various angles of the SEH concentrator and its dimensional parameters A, H, a and b. Taken from [39]. 173
Figure 87: Visual representation of how SEH concentrators can act as components of a BIPV system: a) a south-facing building front in the northern hemisphere with a window façade, b) a single window consisting of many LCPV arrays, c) a single

LCPV array of 18 silicon PV cells and SEH concentrators connected together to generate a power output and d) cross-section of a single cell LCPV module. 174
Figure 88: The simulated optical efficiency of various H/A ratio SEH concentrators when the incident radiation is at different angles of incidence. Taken from [39]. ... 174
Figure 89: Image of the metal casting mould used to produce a batch of SEH concentrators. 175
Figure 90: The four doping configurations of rare earth compounds incorporated into LCPV devices: a) doped optical coupling, b) homogenously doped concentrator, c) bottom doped concentrator and d) top doped concentrator. 176
Figure 91: Transmittance spectrum of the un-doped concentrator. 178
Figure 92: Transmittance spectra of the $Sr_4Al_{14}O_{25}$: Eu^{2+}, Dy^{3+} doped concentrators. 178
Figure 93: Transmittance spectra of the $NaYF_4$: Er^{3+}, Yb^{3+} doped concentrators. 178
Figure 94: Image of a single cell LCPV module to be characterised in this work. 179
Figure 95: Flow diagram to summarise the steps involved in fabricating a single cell PV or LCPV module. 179
Figure 96: PCE of the $Sr_4Al_{14}O_{25}$: Eu^{2+}, Dy^{3+} doped LCPV devices of varying doping ratios at different solar irradiances. 187
Figure 97: J_{SC} of the $Sr_4Al_{14}O_{25}$: Eu^{2+}, Dy^{3+} doped LCPV devices of varying doping ratios at different solar irradiances. 187
Figure 98: PCE of the $NaYF_4$: Er^{3+}, Yb^{3+} doped LCPV devices of varying doping ratios at different solar irradiances. 188
Figure 99: J_{SC} of the $NaYF_4$: Er^{3+}, Yb^{3+} doped LCPV devices of varying doping ratios at different solar irradiances. 188
Figure 100: Relative PCE gains for the $Sr_4Al_{14}O_{25}$: Eu^{2+}, Dy^{3+} doped LCPV devices at different solar irradiances. 189
Figure 101: Relative J_{SC} gains for the $Sr_4Al_{14}O_{25}$: Eu^{2+}, Dy^{3+} doped LCPV devices at different solar irradiances. 189
Figure 102: Relative PCE gains for the $NaYF_4$: Er^{3+}, Yb^{3+} doped LCPV devices at different solar irradiances. 190
Figure 103: Relative J_{SC} gains for the $NaYF_4$: Er^{3+}, Yb^{3+} doped LCPV devices at different solar irradiances. 190
Figure 104: I-V curves of for the $Sr_4Al_{14}O_{25}$: Eu^{2+}, Dy^{3+} doped optical coupling LCPV devices at different solar irradiances. 191
Figure 105: I-V curves of for the $Sr_4Al_{14}O_{25}$: Eu^{2+}, Dy^{3+} doped concentrator LCPV devices at different solar irradiances. 192
Figure 106: I-V curves of for the $NaYF_4$: Er^{3+}, Yb^{3+} doped optical coupling LCPV devices at different solar irradiances. 193
Figure 107: I-V curves of for the $NaYF_4$: Er^{3+}, Yb^{3+} doped concentrator LCPV devices at different solar irradiances. 194
Figure 108: EQE spectra of the $Sr_4Al_{14}O_{25}$: Eu^{2+}, Dy^{3+} doped optical coupling LCPV devices. 195
Figure 109: EQE spectra of the $Sr_4Al_{14}O_{25}$: Eu^{2+}, Dy^{3+} doped concentrator LCPV devices. 195
Figure 110: EQE spectra of the $NaYF_4$: Er^{3+}, Yb^{3+} doped optical coupling LCPV devices 196
Figure 111: EQE spectra of the $NaYF_4$: Er^{3+}, Yb^{3+} doped concentrator LCPV devices 196

Figure 112: The difference in relative PCE improvements as compared to un-doped Sylgard for LCPV modules with and coated PV cells without a concentrator for $Sr_4Al_{14}O_{25}$: Eu^{2+}, Dy^{3+} doping at different levels. 201
Figure 113: The difference in relative J_{SC} improvements as compared to un-doped Sylgard for LCPV modules with and coated PV cells without a concentrator for $Sr_4Al_{14}O_{25}$: Eu^{2+}, Dy^{3+} doping at different levels. 201
Figure 114: The difference in relative PCE improvements as compared to un-doped Sylgard for LCPV modules with and coated PV cells without a concentrator for $NaYF_4$: Er^{3+}, Yb^{3+} doping at different levels. 202
Figure 115: The difference in relative J_{SC} improvements as compared to un-doped Sylgard for LCPV modules with and coated PV cells without a concentrator for $NaYF_4$: Er^{3+}, Yb^{3+} doping at different levels. 202
Figure 116: Diagram to show how the adjustable inclined plane can be used to create an effective angle of incidence (θ) on an LCPV module when placed under the solar simulator. 204
Figure 117: The PCE of the $Sr_4Al_{14}O_{25}$: Eu^{2+}, Dy^{3+} doped LCPV devices under 1 sun illumination at angles of incidence from 0° to 80°. 210
Figure 118: The J_{SC} of the $Sr_4Al_{14}O_{25}$: Eu^{2+}, Dy^{3+} doped LCPV devices under 1 sun illumination at angles of incidence from 0° to 80°. 210
Figure 119: The PCE of the $NaYF_4$: Er^{3+}, Yb^{3+} doped LCPV devices under 1 sun illumination at angles of incidence from 0° to 80°. 211
Figure 120: The J_{SC} of the $NaYF_4$: Er^{3+}, Yb^{3+} doped LCPV devices under 1 sun illumination at angles of incidence from 0° to 80°. 211
Figure 121: Relative PCE gains for the $Sr_4Al_{14}O_{25}$: Eu^{2+}, Dy^{3+} doped LCPV devices under 1 sun illumination at angles of incidence from 0° to 80°..... 212
Figure 122: Relative J_{SC} gains for the $Sr_4Al_{14}O_{25}$: Eu^{2+}, Dy^{3+} doped LCPV devices under 1 sun illumination at angles of incidence from 0° to 80°..... 212
Figure 123: Relative PCE gains for the $NaYF_4$: Er^{3+}, Yb^{3+} doped LCPV devices under 1 sun illumination at angles of incidence from 0° to 80°..... 213
Figure 124: Relative J_{SC} gains for the $NaYF_4$: Er^{3+}, Yb^{3+} doped LCPV devices under 1 sun illumination at angles of incidence from 0° to 80°..... 213
Figure 125: Basic sandwich structure of a DSSC where the photoactive materials are contained within two conductive glass electrodes..... 217
Figure 126: The flow of electrons in a DSSC with reactions 1-5 occurring at the numbered locations..... 217
Figure 127: Energy level diagram of the steps within DSSC current flow: Photon absorption (1), electron injection into TiO_2 (2) and replenishment of dye (3). Recombination occurs via (4) and (5). Modified from [308]..... 219
Figure 128: EQE profile of a typical N719 dye based DSSC and the absorbance spectrum of N719 adsorbed on TiO_2 (top-right of the figure). Data from [317] and [318]..... 220
Figure 129: a) Device architecture with the spacer and connection points labelled and b) how the device was put together..... 225
Figure 130: Different ways of incorporating the spectral conversion materials onto the DSSC exterior glass substrate: a) and b) above or below the working electrode, c) and d) below or above the counter electrode. Taken from [329]..... 227
Figure 131: Different ways of incorporating the spectral conversion materials into the interior of a DSSC: a) Evenly throughout the TiO_2, b) at the top of the TiO_2, c)

above the TiO_2, d) throughout the electrolyte or e) on the counter electrode. Taken from [329]. *227*
Figure 132: Summary of the steps required to fabricate device types (a), (b), (c) and (e) as well as control DSSCs. *230*
Figure 133: Real life image of a complete fabricated DSSC of type (e). *230*
Figure 134: I-V curves for the $NaYF_4$: Er^{3+}, Yb^{3+} doped spin coated DSSCs at 1 sun. *232*
Figure 135: Transmittance spectra for the $NaYF_4$: Er^{3+}, Yb^{3+} doped spin coated DSSCs. *232*
Figure 136: I-V curves for the $Sr_4Al_{14}O_{25}$: Eu^{2+}, Dy^{3+} doped screen printed DSSCs at 1 sun. *234*
Figure 137: PCE against layer thickness (drop cast volume) for both rare earth doped compounds. *234*
Figure 138: I-V curves for the $Sr_4Al_{14}O_{25}$: Eu^{2+}, Dy^{3+} doped screen printed DSSCs at 1 sun. *235*
Figure 139: PCE against layer thickness (drop cast volume) for both rare earth doped compounds. *235*
Figure 140: EQE spectra for the control and best performing rare earth doped DSSCs for each material. *236*
Figure 141: I-V curves for the control screen printed DSSCs with SEH concentrators at varying irradiance levels. *243*
Figure 142: ΔP_{max} for the plain, top and bottom doped concentrators compared to without concentrators for the control DSSC at varying irradiance levels. *243*
Figure 143: I-V curves for the rare earth doped screen printed DSSCs with SEH concentrators at varying irradiance levels. *244*
Figure 144: ΔP_{max} for the plain, top and bottom doped concentrators compared to without concentrators for the rare earth doped DSSC at varying irradiance levels. *244*
Figure 145: Structure of the porphyrin dye LG5 used in the DSSCs in this section. Taken from [334]. *245*
Figure 146: J-V curves for the rare earth doped porphyrin-carbon counter electrode DSSCs under 1 sun. *249*
Figure 147: Normalized efficiency (as a fraction of the initial PCE) for the control and rare earth doped porphyrin-carbon counter electrode DSSCs under 1 sun. *249*
Figure 148: Real life image of porphyrin-carbon counter electrode DSSC. *250*
Figure 149: Real image of an LCPV module with 18 silicon solar cells attached to 18 SEH concentrators. This prototype has potential for BIPV. *257*
Figure 150: Graph of the sample mean PCEs of the $Sr_4Al_{14}O_{25}$: Eu^{2+}, Dy^{3+} doped screen printed DSSCs with their SE bars displayed. *275*
Figure 151: Graph of the sample mean PCEs of the $NaYF_4$: Er^{3+}, Yb^{3+} doped screen printed DSSCs with their SE bars displayed. *275*
Figure 152: The EQE profile for 0.25% w/w doped $Sr_4Al_{14}O_{25}$: Eu^{2+}, Dy^{3+} Sylgard PV cells predicted by the model compared to the bare and experimentally measured EQE. *281*
Figure 153: The EQE profile for 0.5% w/w doped $Sr_4Al_{14}O_{25}$: Eu^{2+}, Dy^{3+} Sylgard PV cells predicted by the model compared to the bare and experimentally measured EQE. *281*
Figure 154: The EQE profile for 1% w/w doped $Sr_4Al_{14}O_{25}$: Eu^{2+}, Dy^{3+} Sylgard PV cells predicted by the model compared to the bare and experimentally measured EQE. *282*

Figure 155: The EQE profile for 2% w/w doped $Sr_4Al_{14}O_{25}$: Eu^{2+}, Dy^{3+} Sylgard PV cells predicted by the model compared to the bare and experimentally measured EQE. 282
Figure 156: The EQE profile for 0.25% w/w doped $NaYF_4$: Er^{3+}, Yb^{3+} Sylgard PV cells predicted by the model compared to the bare and experimentally measured EQE. 283
Figure 157: The EQE profile for 0.5% w/w doped $NaYF_4$: Er^{3+}, Yb^{3+} Sylgard PV cells predicted by the model compared to the bare and experimentally measured EQE. 283
Figure 158: The EQE profile for 1% w/w doped $NaYF_4$: Er^{3+}, Yb^{3+} Sylgard PV cells predicted by the model compared to the bare and experimentally measured EQE. 284
Figure 159: The EQE profile for 2% w/w doped $NaYF_4$: Er^{3+}, Yb^{3+} Sylgard PV cells predicted by the model compared to the bare and experimentally measured EQE. 284
Figure 160: Relative J_{SC} gains for the $Sr_4Al_{14}O_{25}$: Eu^{2+}, Dy^{3+} doped Sylgard layers on PV cells (from the optical model and IPCE measurements) compared to that observed under the solar simulator. 288
Figure 161: Relative J_{SC} gains for the $NaYF_4$: Er^{3+}, Yb^{3+} doped Sylgard layers on PV cells (from the optical model and IPCE measurements) compared to that observed under the solar simulator. 289
Figure 162: Cross-section plot of the SEH concentrator studied in this thesis from the face-on perspective to its largest side. 291
Figure 163: Ray trace for 0° angle of incidence 293
Figure 164: Ray trace for 10° angle of incidence 293
Figure 165: Ray trace for 20° angle of incidence 294
Figure 166: Ray trace for 30° angle of incidence 294
Figure 167: Ray trace for 40° angle of incidence 295
Figure 168: Ray trace for 50° angle of incidence 295
Figure 169: Ray trace for 60° angle of incidence 296
Figure 170: Ray trace for 70° angle of incidence 296
Figure 171: Ray trace for 80° angle of incidence 297
Figure 172: Graphical representation of the J_{SC} predicted by the ray trace model and as measured experimentally for the un-doped LCPV modules under 1 sun of light at varying angles of incidence. 299
Figure 173: The positions of the absorption-emission centres within 5 horizontal slices that form the basis of the doped SEH concentrator model. 300
Figure 174: Probabilities of a ray of arbitrary λ_{em} entering at the x co-ordinate reaching the exit aperture for the control (un-doped), homogenously doped, top doped and bottom doped $Sr_4Al_{14}O_{25}$: Eu^{2+}, Dy^{3+} SEH concentrators. 303
Figure 175: Probabilities of a 400 nm ray entering at the x co-ordinate reaching the exit aperture for the control (un-doped), homogenously doped, top doped and bottom doped $Sr_4Al_{14}O_{25}$: Eu^{2+}, Dy^{3+} SEH concentrators. 310
Figure 176: Probabilities of a 410 nm ray entering at the x co-ordinate reaching the exit aperture for the control (un-doped), homogenously doped, top doped and bottom doped $Sr_4Al_{14}O_{25}$: Eu^{2+}, Dy^{3+} SEH concentrators. 310
Figure 177: Probabilities of a 400 nm ray entering at the x co-ordinate reaching the exit aperture for the control (un-doped), homogenously doped, top doped and bottom doped $NaYF_4$: Er^{3+}, Yb^{3+} SEH concentrators. 311

Figure 178: Probabilities of a 410 nm ray entering at the x co-ordinate reaching the exit aperture for the control (un-doped), homogenously doped, top doped and bottom doped $NaYF_4$: Er^{3+}, Yb^{3+} SEH concentrators..... 311

Figure 179: Predicted and observed relative J_{SC} gains for the bottom, top and homogenously doped $Sr_4Al_{14}O_{25}$: Eu^{2+}, Dy^{3+} concentrators against the un-doped concentrators. 313

Figure 180: Predicted and observed relative J_{SC} gains for the bottom, top and homogenously doped $NaYF_4$: Er^{3+}, Yb^{3+} concentrators against the un-doped concentrators. 314

List of Abbreviations

A – Absorptance

Abs – Absorbance

AM (1.5 G/D) – Air mass (1.5 Global/Direct)

A_{nr} – Non radiative decay rate (s^{-1})

A_r – Radiative decay rate (s^{-1})

a-Si – Amorphous silicon

b – Wien's displacement constant (2.90×10^{-3} m·K)

$B_{\lambda, T}$ – Spectral radiance ($Wm^{-2}nm^{-1}sr^{-1}$)

BA/BIPV – Building applied/ integrated photovoltaic(s)

BICPV – Building integrated concentrator photovoltaic(s)

c – Speed of light in a vacuum (299792458 ms^{-1})

C – Light concentration ratio

C - Y_2O_3: Yb^{3+}, Ho^{3+} (Chapter 5 only)

CET – Cooperative energy transfer

CIGS – Copper indium gallium selenide

CPC – Compound parabolic concentrator

CPS – Counts per second

CPV – Concentrating photovoltaic(s)

c-Si – Crystalline silicon

CSP – Concentrating solar power

CZTS – Copper zinc tin sulphide

d – Lattice spacing between ions (m)

DC – Downconversion

DF – Degrees of freedom

DSSC – Dye sensitized solar cell

e – Elementary charge (1.60×10^{-19} C)

E – Energy of a photon (eV)

E_G – Band gap energy (eV)

E_F – Fermi level (V)

ΔE – Energy gap between states (eV)

EDXS – Electron-dispersive x-ray spectroscopy

EMU – Energy migration upconversion

ePLQY – External photoluminescent quantum yield

EQE – External quantum efficiency

EQE J_{SC} – J_{SC} predicted by the experimental EQE data (mA/cm^2)

ESA – Excited state absorption

ESM – Emission spectral matching

ETU – Energy transfer upconversion

Expt. J_{SC} – J_{SC} measured experimentally (mA/cm^2)

eV – Electron volt (1.60×10^{-19} J)

EVA – Ethylene vinyl acetate

f_{abs} – Fraction of light absorbed

f_{trans} – Fraction of light transmitted

FEP – Fluorinated ethyl propylene

FF – Fill factor

FTO – Fluorine-doped tin oxide

G – Geometric concentration ratio

GDP – Gross domestic product

GSA – Ground state absorption

h – Planck's constant (6.63×10^{-19} Js)

H_A – Alternate hypothesis

H_0 – Null hypothesis

HCPV – High concentrating photovoltaic(s)

HJT – Heterojunction technology

HOMO – Highest occupied molecular orbital (eV)

I – Current (A)

I_0 – Saturation current (A)

I_{MP} – Current at max power output (A)

I_{SC} – Short-circuit current (A)

IICT – Indian Institute of Chemical Technology

iPLQY – Internal photoluminescent quantum yield

J – Total angular momentum quantum number

J_{SC} – Short-circuit current density (mA/cm^2)

k – Boltzmann constant (1.38×10^{-23} JK^{-1})

L – Total orbital angular momentum quantum number (Chapter 2)

L – Path length of ray (Chapter 6) (cm)

L_{esc} - Fraction of light lost via escape cone losses

L_{other} - Fraction light lost via other mechanisms

L_{reabs} - Fraction of light lost via reabsorption

LCOE – Levelised cost of electricity ($/kWh)

LCPV – Low concentrating photovoltaic(s)

LDS – Luminescent downshifting

LSC – Luminescent solar concentrator

LUMO - Lowest unoccupied molecular orbital

m_l – Azimuthal orbital angular momentum quantum number

m_s – Spin quantum number

MEG – Multiple exciton generation

Mod. J_{SC} – J_{SC} predicted by the optical model (mA/cm^2)

n – Refractive index

n – Sample size (6.3 only)

N – Population of excited states

n_0 – Refractive index of incident media

n_m – Refractive index of receiving media

NAREC – National Renewable Energy Centre

NEQE – Normalised external quantum efficiency (cm^2W^{-1})

NIR – Near infrared

OSC – Organic solar cell

P_{abs} – Probability of absorption

P_{reach} – Probability of reaching exit aperture

P_{in} – Power of incident radiation (W)

P3HT – Poly [3-hexylthiophene]

PA – Photon avalanche

PC – Polycarbonate

PCBM - Phenyl-C61-butyric acid methyl ester

PCE – Power conversion efficiency

PDMS – Polydimethylsilicone

PERC – Passivated emitter rear cell

PFCB – Polyfluorocyclobutane

PLQY - Photoluminescent quantum yield

PMMA – Polymethylmethacrylate

PPV – Polyphenylenevinylene

PSC – Perovskite solar cell

PV – Photovoltaic(s)

PVB - Polyvinyl butyral

QC – Quantum cutting

QD(s) – Quantum dot(s)

QDSC – Quantum dot solar cell

R – Reflectance

ΔR - Change in reflectance from addition of rare earth compound

R^2 – coefficient of determination

RET – Resonant energy transfer

RP – Redox potential

RPM – Revolutions per minute (min^{-1})

s – Sample standard deviation

S – Total spin quantum number

SE – Standard error of the sample mean

SEH – Square elliptical hyperboloid

SEM – Scanning electron microscopy

SHE – Standard hydrogen electrode

SR – Spectral response (A/W)

SSE – Sum of squared errors

SST – Total sum of squares

t - t-value

T – Temperature (K or °C)

T – Transmittance (from Chapter 3 onwards)

TBP - 4-tert-butylpyridine

TCO – Thin-film conducting oxide

TIR – Total internal reflection

TTA – Triplet-triplet annihilation

UC – Upconversion

UCNP – Upconversion nanoparticle

UV – Ultraviolet

V – Voltage (V)

V_C – Thermal voltage (V)

V_{MP} – Voltage at max power output (V)

V_{OC} – Open-circuit voltage (V)

W_p – Watt peak (W)

$\bar{x}$ - Sample mean

XRD – X-ray diffraction

Y - Y_2O_3: Yb^{3+}, Tm^{3+}, Ho^{3+}

z - z-value

α – Absorption coefficient (cm^{-1})

ε – Uncertainty error

η – Power conversion efficiency

η_{LDS} - LDS efficiency

η_{opt} – Optical efficiency

η_{PL} - iPLQY (Internal photoluminescent quantum yield)

θ – Angle of incidence, from the horizontal or vertical depending on context (°)

θ_C – Critical angle (°)

θ_i – Angle of incident ray (°)

θ_r – Angle of refracted ray (°)

θ_{TIR} – Angle of totally internally reflected ray (°)

λ – Wavelength (nm)

Δλ - Wavelength interval (nm)

λ_{max} – Peak wavelength intensity for a black body emission spectrum (nm)

Λ_{abs} – Absorbance scaling factor

μ – Population mean

$\varphi(\lambda)$ – Photon flux ($s^{-1}m^{-2}$)

φ – Angle of tangent from horizontal (6.4.2)

σ – Population standard deviation

σ_x – Uncertainty on variable x

τ – Time constant for decaying to a less excited state (s)

τ_r – Time constant for decaying radiatively to a less excited state (s)

List of Publications

Published by peer-reviewed journals:

1. J. Day, S. Senthilarasu, and T. K. Mallick, "Improving spectral modification for applications in solar cells: A review," *Renewable Energy,* vol. 132, pp. 186-205, 2019/03/01/ 2019.
2. J. Day, S. Senthilarasu, and T. K. Mallick, "Enhanced efficiency for building integrated concentrator photovoltaic modules based on rare earth doped optics," *Solar Energy Materials and Solar Cells*, vol. 199, pp. 83-90, 2019/09/01/ 2019.
3. J. Day, N. Islavath, L. Giribabu, S. Senthilarasu and T. K. Mallick, "Enhanced efficiency and stability of porphyrin-based DSSCs via incorporation of rare earth doped compounds at the photoelectrode." *Manuscript under preparation for submission in 2020.*
4. J. Day, S. Senthilarasu, and T. K. Mallick, "A 2D optical model for enhanced short-circuit current of concentrator photovoltaic modules through rare earth doped optics." *Manuscript under preparation for submission in 2020.*

Conference papers:

1. J. Day, S. Senthilarasu, and T. K. Mallick. “$Sr_4Al_{14}O_{25}$: Eu, Dy as a potential downconverter for crystalline-silicon solar cells.” 13th Photovoltaic Science Application and Technology · PVSAT 2017. Bangor, UK, 5-7 Apr 2017.
2. J. Day, S. Senthilarasu, and T. K. Mallick. “Rare Earth Doped Compounds for Enhancing the Efficiency of Silicon Building Integrated Concentrator PV via Spectral Conversion.” 35th European PV Solar Energy Conference and Exhibition · EUPVSEC 2018. Brussels, Belgium, 24-27 Sept 2017.

Chapter 1. Introduction

1.1 Background

Anthropogenic climate change is widely regarded as one of the greatest challenges facing humanity in the 21st century. This scenario has arisen, in part, due to our reliance on the combustion of fossil fuels such as coal, oil and natural gas to meet our energy needs. Therefore, the transition away from these power sources and towards more sustainable forms of energy will play a crucial role in mitigating the impact of climate change. The 2016 Paris Agreement within the United Nations Framework Convention on Climate Change [1] commits signatories to limit temperature increases to "well below 2°C above pre-industrial levels by 2100" and various national governments have their own ambitious greenhouse gas emission reduction targets; in June 2019 the UK committed to become a net zero greenhouse gas emitter by 2050 [2] and Norway aims to achieve the same status but by 2030 [3]. Even India with its rapidly growing economy and population hopes to reduce its greenhouse gas emissions per unit GDP 33-35% by 2030 against 2005 levels [4].

Carbon dioxide from fossil fuel burning leads to 65% of the global greenhouse gas emissions; the remainder coming from the carbon dioxide, methane, nitrous oxide and fluorinated gasses that accompany agriculture, industrial processes and land-use change [5]. In addition, energy production accounts for 72% of the global greenhouse gas emissions of which the three main areas responsible for 46% of these emissions are electricity, heating and transportation [6]. Each of these three sectors will need to be decarbonised but there will be a lot of overlap due to the potential electrification of heating and transport (i.e. as gas fired boilers to provide space heating and hot water and vehicles with internal combustion engines are likely to be replaced by electric alternatives). Hence it is arguable that finding cheap and reliable sources of electricity with heavily reduced carbon emissions is one of the key objectives in the fight against climate change. There are many different renewable and low-carbon technologies to harness cleaner electricity including nuclear, tidal, wave, geothermal, wind and solar power. Of these, solar power has by far the greatest potential; as seen in Figure 1, 23000 TW of the sun's energy falls on earth every second, several orders of magnitude greater than the 16 TW demand of human civilisation and the total energy

received each year by the sun is greater than the potential that could be obtained from the reserves of oil, coal, natural gas and uranium combined [7].

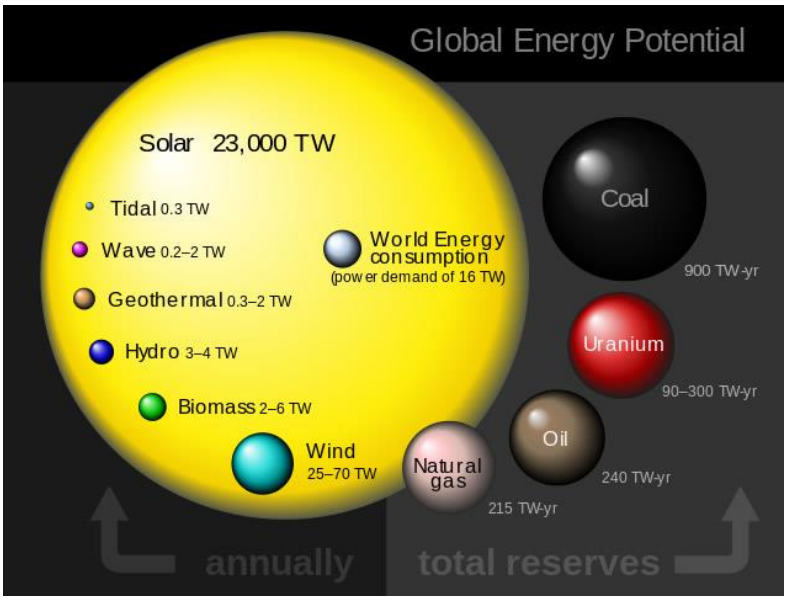

Figure 1: The global energy potential of various renewable and non-renewable sources. It can clearly be seen that solar is by far the energy source with the largest potential instantaneous power output at 23000 TW. Figure taken from [8].

Traditionally, some renewable energy sources (especially wind and solar) have been considered 'unreliable', in so far as their power output is highly dependent on the weather but as battery storage technology matures this issue will decline in significance, making 100% renewable electricity networks technically feasible. It then becomes a matter of finance, together with political will, to increase the deployment and generation capacities of these technologies in a timely manner. While unfortunately scientists are often excluded from the formation of energy policy, thankfully due to inevitable technological and market advances, solar has now become one of the cheapest forms of electricity with bids for tenders in the Middle East for large scale arrays being submitted at $0.02/kWh in 2018 [9]. Closer to the UK in Germany, utility scale solar PV is also the cheapest form of electricity alongside onshore wind at a cost as low as €0.04/kWh, whereas power from coal and gas fired power stations costs €0.05 and €0.08/kWh respectively [10]. However, ongoing research and innovation among the scientific community aims to bring these costs down further still.

There are two ways of generating electricity from sunlight, solar photovoltaics (PV) and concentrating solar power (CSP). Despite both requiring the same solar radiation as an input, the processes are completely dissimilar. CSP operates by

focussing sunlight onto a fluid which it heats, and the resulting steam is used to drive a turbine much like in a conventional fossil fuel power station. On the other hand, solar PV is based on the photovoltaic effect which was first observed by Becquerel in 1839 [11]. This phenomenon occurs in semiconductor materials that can covert the energy of an incident photon directly into electricity after it is absorbed to create an electron-hole pair which (provided they are kept apart) causes a solar cell to produce a steady current. Although CSP certainly has a role to play in providing cleaner energy, PV has several advantages over the technology including its ability to utilise non-direct (diffuse) radiation and minimal maintenance requirements. This means sizable energy yields can be produced from PV, practically all over the globe, at a lower cost than CSP which is only suitable for regions with high direct normal irradiance. Therefore, the scope of this thesis will be limited to solar PV and the search for methods and materials to enhance its performance, thereby lowering its deployment costs and easing in the transition to a zero-carbon economy.

1.2 Solar PV

The generation capacity of solar PV has undergone a rapid expansion in recent years (an estimated 512 GW of PV has been cumulatively installed worldwide as of 2018 [12] compared to 5.11 GW 2005 [13] and just 566 MW in 1998 [14], cf. Figure 2) and these values are predicted to continue to grow exponentially throughout the first half of the 21st century, reaching a capacity of 63.4 TW by 2050 [15]. This surge in activity has been due to and accompanied by plummeting costs of PV. Often quoted are the cost per watt peak ($/$W_p$, the power in watts at maximum output) and the levelized cost of electricity (LCOE) given in $/kWh. The former is simply the cost of the module divided by its maximum power output whereas the latter is the average cost of each unit of electricity generated over the system's lifetime. Naturally, both of these quantities have fallen dramatically in recent years; the most common types of solar PV cells that make up commercial modules have seen a drop in price from $77/$W_p$ in 1977 to less than $1/$W_p$ today, representing a compound cost reduction of approximately 75% per decade in a trend known as Swanson's law [16]. However, there are a range of solar PV technologies available each with varying performances and potential advances to be made, such that even lower cost clean sources of electricity can be realised.

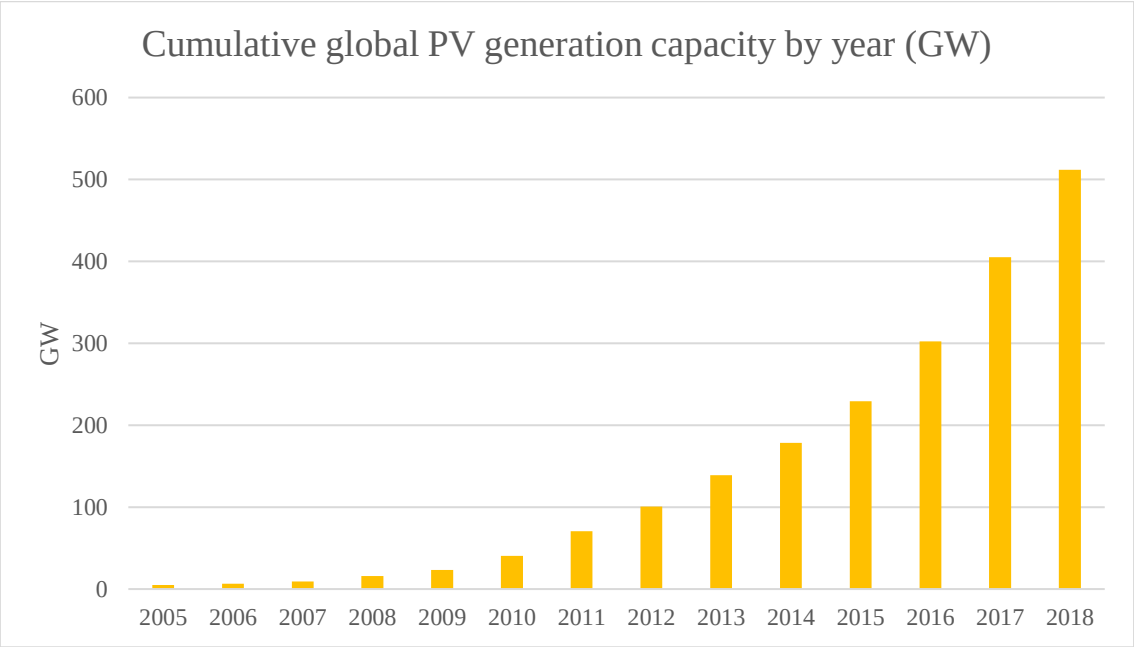

Figure 2: The cumulative solar PV generation capacity from 2005-2018. An exponential growth is observed with the total amount installed approximately doubling every 3 years in the last decade. Data from [12], [13] and [14].

1.2.1 Solar PV Technologies

The PV market of today is dominated by crystalline silicon (c-Si) solar cells, a well-established technology that has a 90% market share [17]. These so called 'first generation' cells can be further divided into mono-crystalline and multi-crystalline depending on their crystal structure. The designs of c-Si solar cells have evolved, and state-of-the-art devices are approaching their practical efficiency limits [18]. The cells can also be either mono-facial or bifacial, the latter having the potential to generate power when illuminated on both surfaces. However, the reliance on silicon wafers and other metals used in device architectures such as indium, tin and silver, along with resource intensive fabrication processes has driven the search for alternative materials.

Thin-film or 'second generation' technologies comprise of amorphous silicon (a-Si), copper indium gallium selenide (CIGS) and cadmium telluride (CdTe) solar cells. As the name suggests, these solar cells are much thinner than their c-Si predecessors, so use less material for environmental benefits and also have the advantageous properties of a low weight, semi-transparency and flexibility [19]. a-Si solar cells typically undergo hydrogenation to improve photoconductivity and

addition of carbon can raise the band gap leading to more efficient heterojunction structures [20]. Despite this environmental advantage, their efficiencies are typically lower than silicon, so their entry into the market has been gradual, only achieving a 10% market share.

Emerging or 'third generation' solar cells consist of organic solar cells (OSC), copper zinc tin sulphide (CZTS) solar cells, dye sensitized solar cells (DSSC), quantum dot solar cells (QDSC) and perovskite solar cells (PSC). Most of these technologies utilise nanostructures, and hence even fewer raw materials, to produce electricity and like second generation cells, they may be semi-transparent and flexible, giving rise to many useful potential applications. Perovskite in particular has attracted much interest with its remarkable rise in efficiency (from 3.8% in 2009, to 25.2% in 2019 [21, 22]), but issues with the long-term stability of all these technologies due to the sensitivity of their photoactive materials to heat, humidity and prolonged light exposure persist and it is this challenge that limits their wide scale commercial deployment.

Finally, tandem or multi-junction solar cells are a concept to harness a greater portion of the sunlight's energy (a central theme of this thesis) by combining materials which absorb different regions of the solar spectrum. This can be achieved by mechanically stacking two or more solar cells on top of each other or through lattice matching, a monolithic structure. Combinations of up to four group III-group V semiconductors in a monolithic structure have attained the highest efficiencies but there is immense potential for simpler tandem devices in which OSCs or a PSC would be fixed on top of a c-Si solar cell (leading to a potential device efficiency above 30% at a much lower cost than III-V technology). Oxford PV have already achieved 28.0% efficiency [23] for a perovskite-silicon tandem device and as part of a £5 million research project are targeting 37% within 5 years [24]. However, this method while yielding impressive results is prohibitively expensive to be a catch all solution to the issue of limited solar cell efficiency. The solar cells used for the experiments conducted within thesis, with the aim to enhance device efficiency and lower cost per watt without using multiple junctions, were c-Si and DSSCs whose structure and operation principles will be discussed in detail in 1.3 and 5.2 respectively. The record efficiency of various PV cell technologies and their potential cost per W_p are presented in Figure 4 and Table 1, respectively.

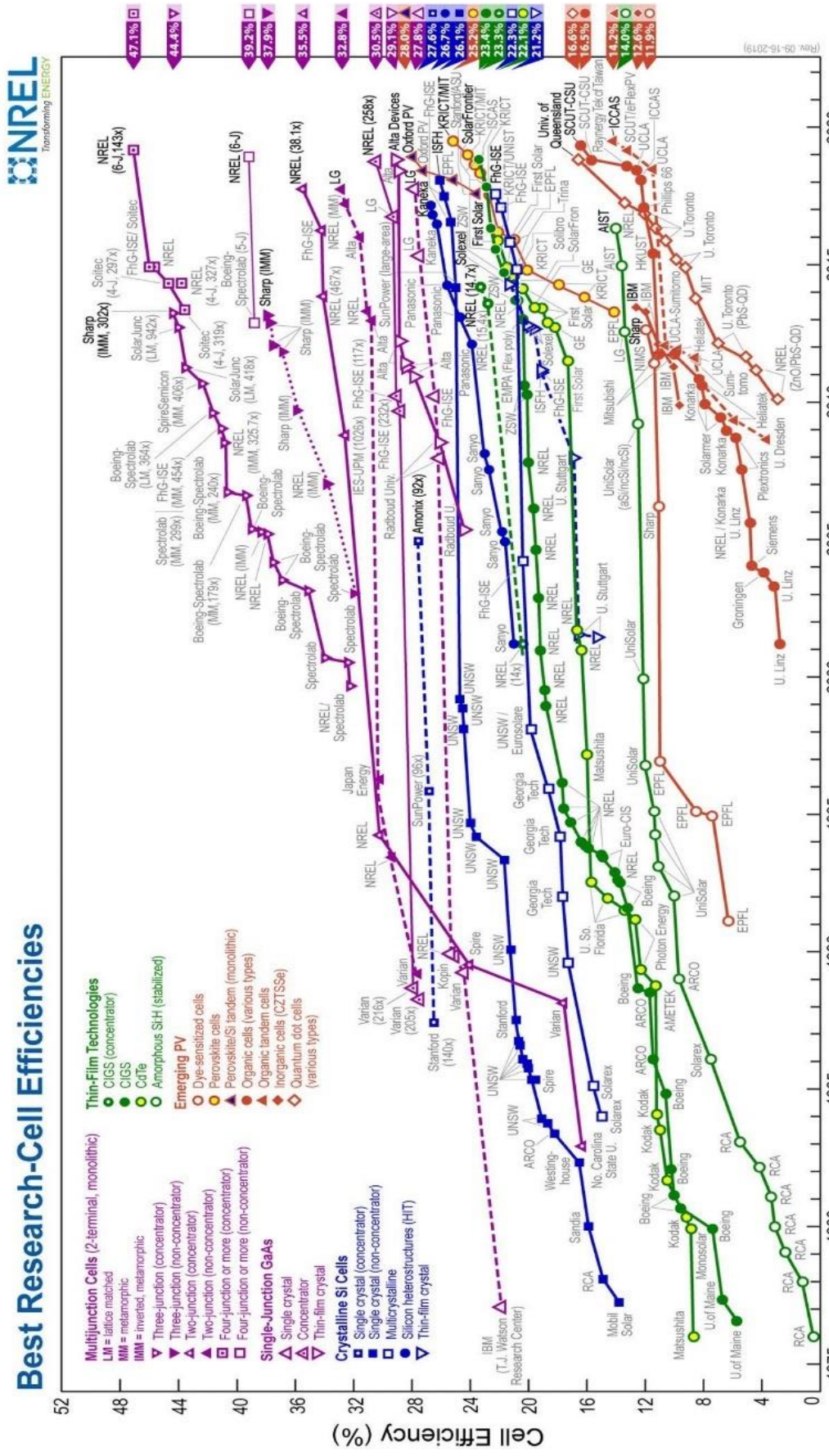

Figure 3: The contemporary maximum efficiency achieved by PV devices of different solar technologies since the 1970s as verified by the National Renewable Energy Laboratory [22].

Technology	Maximum efficiency (%)	Cost per W_p ($)	Ref.
Silicon (monocrystalline)	26.1	0.28	[25]
Silicon (multi-crystalline)	22.3	0.20	[25]
Silicon (amorphous)	14.0	0.30-0.40	[26]
Copper Indium Gallium Selenide	23.4	0.50	[27]
Cadmium Telluride	22.1	0.29	[28]
Dye Sensitized	11.9	0.25-0.40	[29]
Perovskite	25.2	0.10-0.20	[30]
Perovskite-Silicon Tandem	28.0	0.25-0.30	[31]
Concentrator Multi-junction	47.1	1.00	[32]

Table 1: Maximum cell efficiency and cost per W_p for various solar technologies. Maximum efficiencies from [22].

1.2.2 CPV

Optical concentrators have found a use in the PV sector as researchers seek to achieve the focussing of light onto smaller areas of solar cells. Concentrating PV (CPV), not to be confused with CSP, has a number of potential advantages including the increased light flux leading to higher cell efficiencies and reduced PV material usage to attain the same power output at a lower cost, by replacing large area cells with optical components [33].

The increased intensity light can be realised through the use of various optical systems; the most common approaches are Fresnel lenses, parabolic mirrors or 3D concentrators [34]. As shown in Figure 4, a Fresnel lens operates via refractive optics and parabolic mirrors by reflection, both focussing incoming rays onto a smaller receiver area. 3D static concentrators on the other hand work on the principle of total internal reflection which occurs when light travelling through a dielectric material of refractive index (n) encounters a boundary of another media (typically air where n ≈ 1) above a certain critical angle (θ_C) given by:

$$\theta_C = \sin^{-1}\left(\frac{1}{n}\right) \quad (1)$$

This process, in addition to the light that passes straight down through the exit aperture, causes higher concentrations of light to be attained on the solar cell. There are several possible geometrical designs of this type of concentrator as shown in Figure 5. Another class of static concentrator which has attracted much interest are luminescent solar concentrators (LSC). These have a different appearance as compared to conventional concentrators and operate on a distinct

yet novel concept; luminescent particles within the LSC can absorb and re-emit light which then undergoes total internal reflection (TIR) to be directed to the edges where PV cells are located [35].

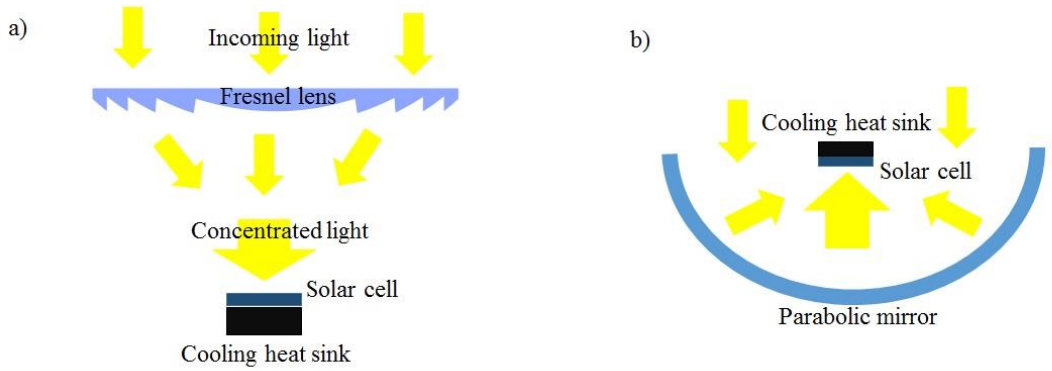

Figure 4: The working principles and designs of two types of optical concentrator used in HCPV systems: a) Fresnel lens and b) Parabolic reflecting mirror.

CPV systems can be categorised by their light concentration levels attained which are given in *n* suns or simply *n X*, where *n* is the number of times greater these values are than the ambient solar radiation intensity. There are no fixed definitions, but low concentrating PV (LCPV) devices typically operate at 1-10 *X* whereas high concentration PV (HCPV) systems operate at >1000 *X*. Medium concentration PV (MCPV) is occasionally classified as an intermediate level between the two extremes. Typically, Fresnel lenses and parabolic mirrors find applications in HCPV alongside small area, high efficiency multijunction III-V solar cells, whereas 3D static concentrators and LSCs are used for LCPV systems that typically utilise silicon PV [36].

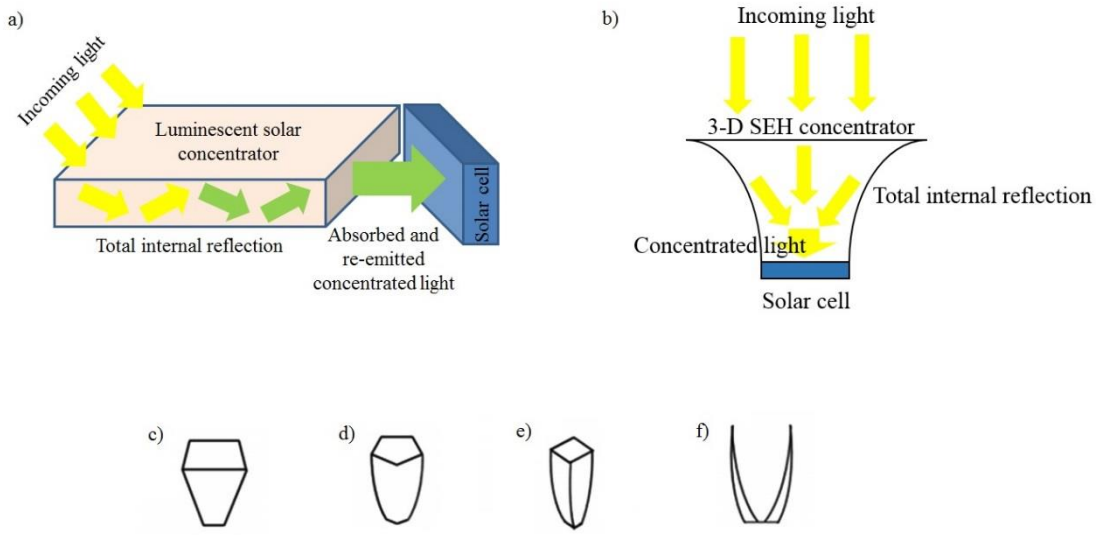

Figure 5: The designs of six types of optical concentrator used in LCPV systems that all operate via TIR: a) Luminescent solar concentrator, b) 3D static square elliptical hyperboloid (SEH) concentrator, c) 3D crossed V-trough, d) 3D polygonal compound parabolic concentrator (CPC), e) 3D crossed CPC and f) lens walled CPC.

As with solar cells, optical components will have a non-ideal efficiency since light is lost through various mechanisms including: unwanted reflection and chromatic aberration effects (in refractive optics), non-uniform surface smoothness and shading by the cell (in reflective optics), incoming light being at a greater incident angle than can be accepted by the concentrator, parasitic absorption by the transparent 3D concentrator medium or luminescent particles, scattering at interfaces and light escaping the concentrator (where in TIR based optics, the internally travelling light hits the sides at an angle less than θ_C) [37, 38]. To account for this, the terms geometric concentration ratio and optical efficiency are used to describe concentrators for solar photovoltaic applications. The geometric concentration ratio (G) is defined as the ratio of the area of the light collecting surface to the area of the illuminated cell. On the other hand, the optical efficiency (η_{opt}) is a measure that depends on the ratio of the light flux at the exit aperture of the concentrator to the light flux at its entry. The product of the optical efficiency and the geometric concentration ratio gives the intensity of the light (C, in terms of *n* suns) on the solar cell. It can also be calculated by comparing the power or current of the PV cell at 1 sun (i.e. with no concentrator) and with the concentrator (due to the linear relationship between light intensity and current/power for non-large *n*) [39].

As of 2017, cumulatively 370 MW of CPV generation capacity has been deployed worldwide (< 0.1% of the total global PV capacity which was 400 GW at the time). In addition, yearly installed CPV capacity has declined from a peak of 120 MW in 2012 to just 14 MW in 2016 as the technology struggled to compete with the falling costs of non-concentrating silicon modules. HCPV systems make up the overwhelming majority of this capacity and despite a short period of growth in 2012-14, the deployment of LCPV systems has flatlined [40]. The challenges faced by CPV which have prevented wider expansion of the sector include the expensive tracking mechanisms required (higher concentration level optics cannot utilise indirect or diffuse radiation, so require single or multi-axis tracking to follow the sun across the sky) and thermal management techniques to prevent overheating [41] (which lowers solar cell performance and in extreme cases destroys them entirely through cracking). Hence, it could be worth revaluating the potential of LCPV as a facilely produced and maintained alternative.

1.2.3 BIPV

Buildings use a significant portion of the world's total energy consumption (estimated at 36% in 2018 [42]), so making them more sustainable is a key task within the efforts of global decarbonisation. Furthermore, buildings being in control of their own electricity supply, decentralises the electricity network with technical and socioeconomic benefits. These challenges have led to a growing demand for building integrated PV (BIPV) systems in which the PV cells are incorporated into the architectural design for aesthetic, financial and performance benefits. Key elements of the building such as a façade, glasses and roofing may be replaced, in part or fully, with PV generating components. Designs have been proposed for BIPV to take many forms as shown in Figure 6. These not only include common parts of standard dwellings such as windows, glazing and tiles, but also novel urban architectures such as noise barriers or canopy shading. As of 2018, 2.3 GW of BIPV capacity has been installed worldwide [43] (< 1% of the total global PV capacity), and the BIPV sector is a rapidly growing market worth $(US) 1 billion in global annual commercial revenue and predicted to grow to $7 billion by 2026 [44]. These figures do not include building applied photovoltaics (BAPV) which is defined as PV not specifically designed for buildings but retrofitted to existing structures.

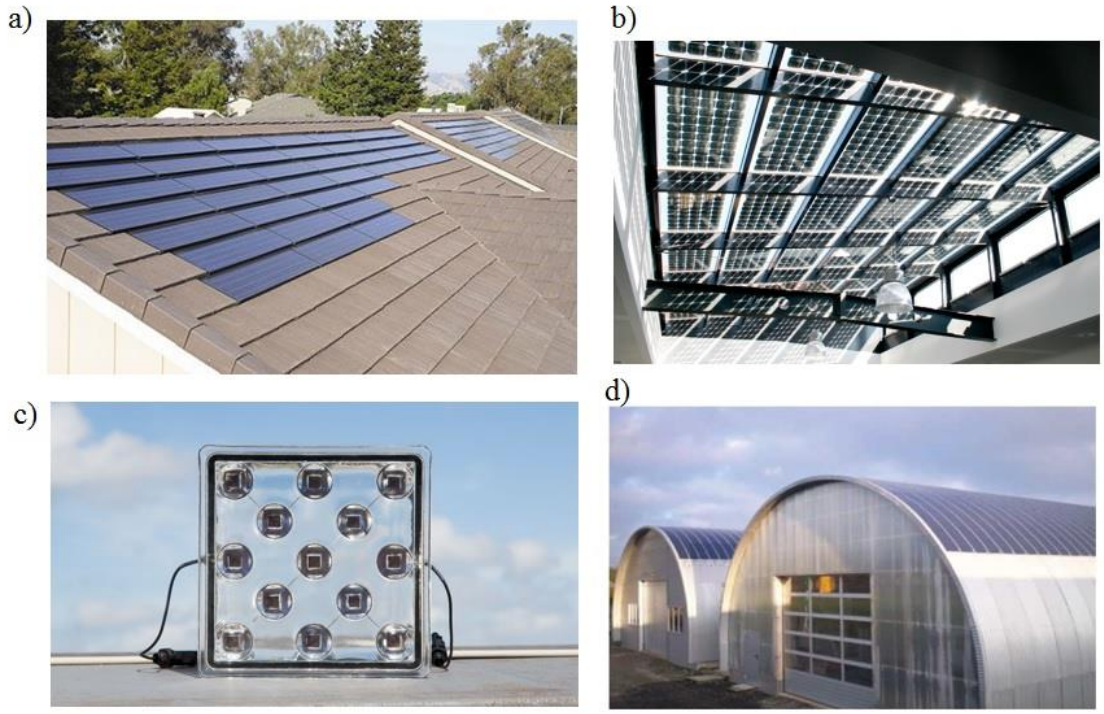

Figure 6: Images of BIPV systems: a) PV modules integrated as roof tiles for a slate effect [45], b) roof and ceiling made from PV modules for sky lighting effect [46], c) LCPV module based on SEH concentrators that could form part of a window due to high transparency [47] and d) flexible PV modules attached to the surface of a curved building [48].

The concepts of CPV and BIPV may be combined to give the field of building integrated concentrator PV (BICPV). This joining together of ideas can be beneficial for each field as the use of concentrators can add performance and architectural benefits. For example, LSCs with their range of potential colours depending on the luminescent materials are ideally placed to make stunning contributions to the architecture of a building. Furthermore, low concentration 3D static concentrators have been envisaged as semi-transparent building blocks when combined with an array of silicon cells.

This thesis will attempt to tie together the challenges of CPV and BIPV by primarily aiming to enhance the performance of a specific LCPV system with building integration potential. Firstly, in any attempt to improve device efficiency, the fundamentals of loss mechanisms within a solar cell must be clearly understood.

1.3 Fundamental Limits of Solar Cell Efficiency

To understand the fundamental limits of the efficiency of a solar cell, its source of input energy, the photons which make up the solar spectrum, must be considered. Photons are the quanta (pockets of defined energy) which carry the electromagnetic force and may interact with matter. The energy, *E*, of a photon is inversely proportional to its wavelength, *λ*, as given through the Planck relation:

$$E = \frac{hc}{\lambda} \qquad (2)$$

In this expression, *h* is the Planck constant (6.63×10^{-34} J s) and *c* the speed of light in a vacuum (299792458 m/s). The sun, the ultimate source of all light the Earth receives, is a G type star with a surface temperature of approximately 6000 K, which if assumed to be a black body (a good approximation) leads to an emitted spectrum with the following profile according to Planck's law, in which $B_{\lambda,T}$ is the spectral radiance (measured in power per unit solid angle, area and wavelength), T is temperature of the black body and k the Boltzmann constant (1.38×10^{-23} J/K) .

$$B_{\lambda,T} = \frac{2hc^2}{\lambda^5} \frac{1}{\exp\left(\frac{hc}{\lambda kT}\right) - 1} \qquad (3)$$

The primary concern for collecting solar energy then becomes not the spectrum emitted by the sun, called the radiance, but the radiation power received per unit area and wavelength here on the Earth, known as the irradiance. This can be estimated at the edge of the Earth's atmosphere, by multiplying the sun's black body spectral radiance by its surface area then dividing by the area of a sphere with radius 1 astronomical unit (1.50×10^{11} m, the distance from the Earth to the sun) [49]. Clearly as a result of absorption from the Earth's atmosphere, especially at certain wavelengths due to the presence of ozone, oxygen, water vapour and carbon dioxide, the solar irradiance spectrum at ground level will differ significantly from that at the edge of space. This leads to concept of an air mass (AM) solar spectrum which accounts for the presence of these gasses. The most commonly used are AM 0 (i.e. no atmosphere), AM 1 (when the light has travelled through one atmosphere to a horizontal panel directly under the sun, useful for regions close to the equator) and AM 1.5 (when the sun is at a zenith angle of

48° on a south facing panel at a pitch of 37°, a good approximation for northern hemisphere latitudes close to the world's major population centres in Asia, Europe and North America). AM 1.5 can be further divided into 1.5 D and 1.5 G; D only accounts for the direct radiation received whereas G includes the global radiation received from other sources (reflection and scattering) with an irradiance value of 963.8 W/m^2 based on data averaged from the 48 contiguous US states. AM 1.5 G has become the standard test condition for evaluating solar cell performance and its irradiance is often normalised to 1000 W/m^2 for convenience [49]. The key spectral irradiance profiles are presented in Figure 7.

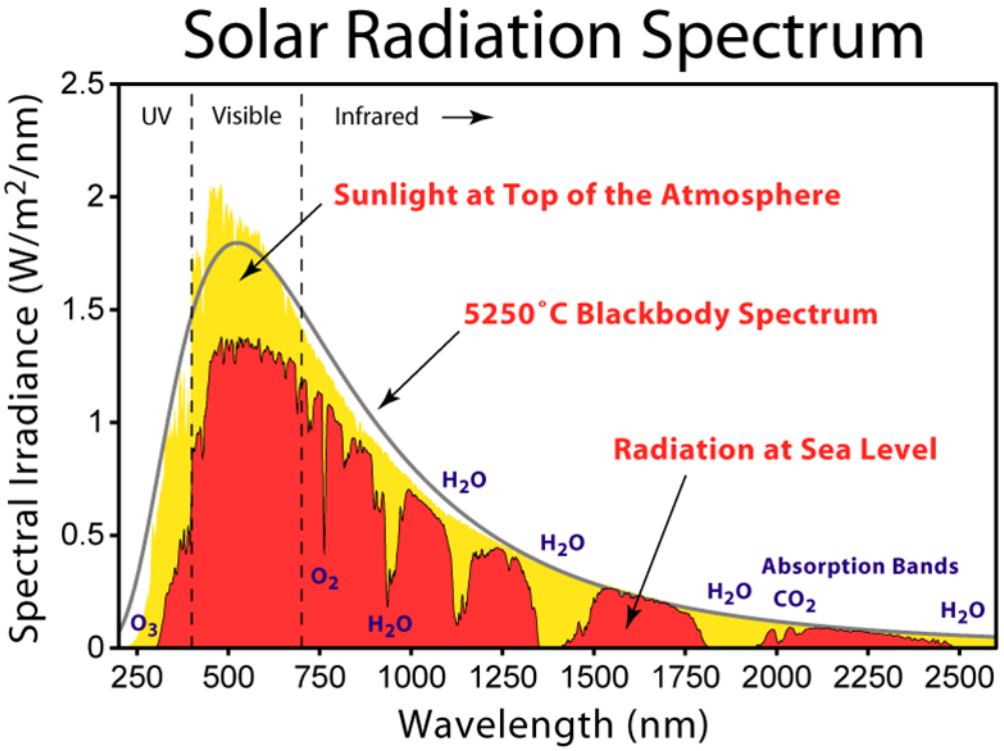

Figure 7: The solar irradiance spectrum here at Earth in terms of: that derived from the black body spectrum of the sun (black line), the actual radiation received at the top of the Earth's atmosphere, AM0 (shaded yellow) and the actual radiation received at the Earth's surface after absorption by the atmosphere, AM 1.5 (shaded red) [50].

Once the input energy and spectrum has been determined, the efficiency and loss mechanisms of an arbitrary solar cell may be explored. A property of any semiconductor is the band gap energy (E_G) which is the difference in energy between the valence band and conduction band. These are the two states where electrons can exist, either fixed to an atom as in an insulator or free to flow around the material like in a conductor (cf. Figure 8).

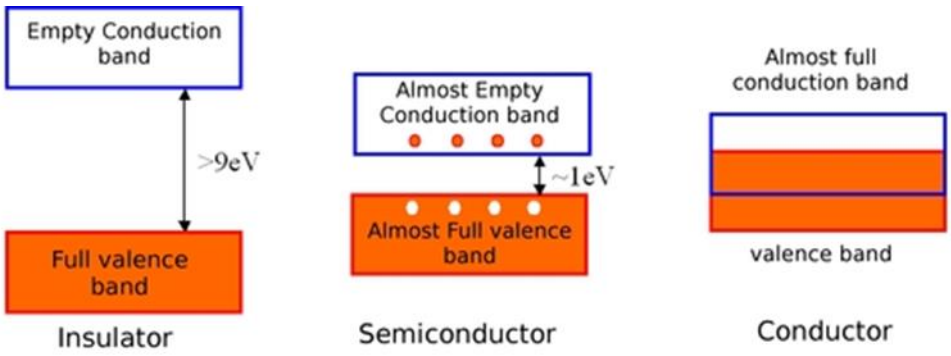

Figure 8: A simple diagram of the band structure in three types of material. In insulators the valence bands are full and there is a large energy gap between this band and the conduction band. Conversely for conductors, the electrons can move freely between the two bands. Finally, in semiconductors the energy gap between the valence and conduction band is smaller such that a photon can promote an electron to the conduction band and create a hole. This process is known as the photovoltaic effect [51].

The photovoltaic effect allows for electrons in semiconductors to be promoted to the conduction band via the absorption of a photon. In reality, the incident photons on a solar cell have a range of energies as per the AM 1.5 G spectrum. This means if a photon with $E < E_G$ falls on a solar cell its energy is insufficient to release electrons into the conduction band and it is not absorbed, so no current is generated; for c-Si solar cells, 20% of the total spectrum has energy less than E_G and is not harnessed for electrical power [52]. On the other hand, for photons with energy $E > E_G$, current is generated but the conduction band electrons now possess excess kinetic energy which is dissipated as heat via emission of phonons into the lattice as electrons relax to the edge of the conduction band (sometimes referred to as thermalisation losses, which account for 35% of incident spectral power for c-Si [53]). Collectively, these issues are known as the 'spectral mismatch' and are arguably the fundamental reason for limiting the efficiency of a single junction cell under ambient sunlight. The different PV technologies described in 1.2.1 will have different band gaps, so these losses will vary depending on the semiconductor properties; in c-Si E_G = 1.1 eV whereas for a-Si, E_G = 1.7 eV, so a higher portion of the spectrum (almost 50%) will be non-absorbed and lower portion (14%) lost through thermalisation [54].

Moving beyond the solar spectrum, the dynamics and collection of charge carriers (electrons and holes) within a solar cell must also be considered. A typical silicon solar cell has a p-n junction which forms when a p-type semiconductor (with an excess of holes attained by doping impurities that accept electrons such as boron) comes into contact with an n-type semiconductor (with an excess of

electrons achieved by doping electron donator impurities like phosphorus). In this case, the boundary becomes a depleted region with no excess charge carriers as electrons from the n-type semiconductor fill vacant holes at the edge of the p-type (and vice versa, as holes travel from the p-type to the n-type to accept electrons), creating an electric field between the two areas since the n-type semiconductor is now positively charged at its edge and the p-type negatively at its. Upon illumination, electron-hole pairs can be formed in the p or n-type layer of the cell but to generate a current they must make it out of their layer and around the cell through surface or rear conducting contacts, where electrons may do work if connected to an external load via metallic contacts as shown in Figure 9.

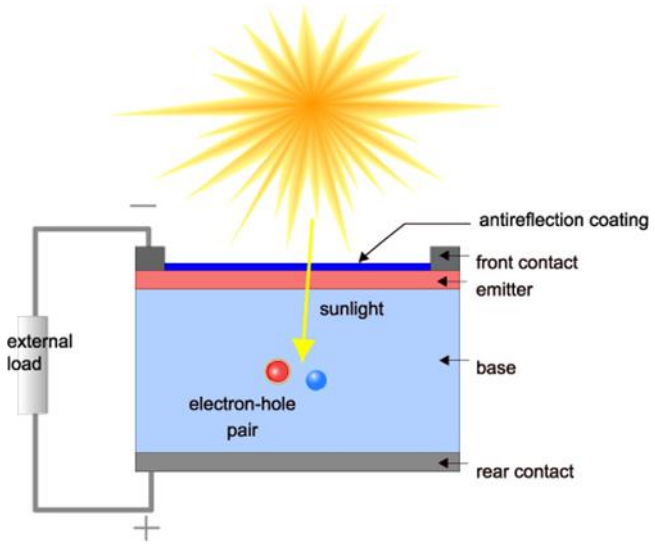

Figure 9: The structure and working principle of a typical single junction silicon solar cell. Electron-hole pairs are generated by photons in the p-type base and the charges travel in opposite directions; electrons across the p-n junction to the emitter and front contact, and holes to the rear contact. When the front and rear contacts are connected via an external load a light generated current flows [55].

The n-doped silicon 'emitter' typically is situated on top of the p-doped 'base' and as in a diode, the p-n junction acts to restrict the flow of charge to unidirectional; due to the electric field, electrons can only move from the p-type to the n-type whereas holes can only move from the n-type to the p-type. Nevertheless, electrons in the p-type region and holes in the n-type are minority charge carriers, so have a limited lifetime and diffusion length before they may recombine with a majority charge carrier, emitting a photon (radiative recombination) or phonon (non-radiative recombination) in the process [55].

However, electron-hole pair generation from photon absorption/radiative recombination is a reversible process, and the principle of detailed balance states

that: *"Corresponding to every individual process there is a reverse process, and in a state of equilibrium the average rate of every process is equal to the average rate of its reverse process"* [56]. This means, at equilibrium, the rate of electron-hole pair generation must equal the rate of recombination. Therefore, the radiative recombination of charge carriers within the cell are another fundamental and unavoidable source of efficiency loss. In 1960 using this principle, Shockley and Queisser produced a model for the maximum theoretical limit of the efficiency of a single junction cell of arbitrary band gap and under the radiation of a blackbody sun. It was found for c-Si cells (E_G = 1.1 eV) that the highest possible efficiency would be approximately 30% [57].

The current-voltage (*I-V*) relationship (and hence output power) for an ideal cell was also determined to be:

$$I = I_{SC} + I_0 \left(1 - \exp\left(\frac{V}{V_C}\right)\right) \qquad (4)$$

Where I_{SC} is the short-circuit current (sometimes denoted J_{SC} when referring to a current per unit area or current density) and is equal to the current when $V = 0$ (i.e. when the cell is short circuited). It is an intrinsic property of a cell depending on the rate of electron-hole pair generation which itself is related to E_G (the higher value of E_G, the lower the I_{SC} and vice versa) and light intensity (I_{SC} rises linearly with increasing irradiance). I_0 is the saturation current which ultimately depends on the rate of recombination within the cell and V_C is the thermal voltage given by:

$$V_C = \frac{kT}{e} \qquad (5)$$

In this is expression e = 1.60 × 10^{-19} C, the elementary charge. The open-circuit voltage (V_{OC}) can also be defined for the condition when $I = 0$ (i.e. when the circuit is open).

$$V_{OC} = V_C \ln\left(\frac{I_{SC}}{I_0} + 1\right) \qquad (6)$$

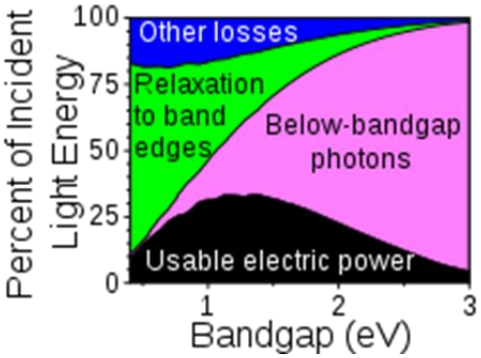

Figure 10: Graph to show the useable electrical power and sources of efficiency loss for single junction solar cells of varying band gap under the Shockley-Queisser model. The maximum theoretical efficiency is approximately 30% for a 1.1 eV band gap device [58].

Through analysis of the dependence of I_0 on temperature, V_{OC} can be shown to decrease sharply with increased temperature and from the linear relationship of light intensity and I_{SC}, it can be shown V_{OC} rises logarithmically with light concentration. Furthermore, and in contrast to I_{SC}, a higher E_G of the semiconductor leads to a greater V_{OC}. Hence, when selecting the optimal band gap for a single junction solar cell there is a trade-off in the voltage and current produced, in turn affecting the maximum performance but as seen in the above Figure 10, an E_G of 1.1 eV as per c-Si is a sensible value for harnessing the most usable electrical power. The output power is given by the voltage multiplied by the current and will be a maximum at the point V_{MP}, I_{MP} on the graph (cf. Figure 11).

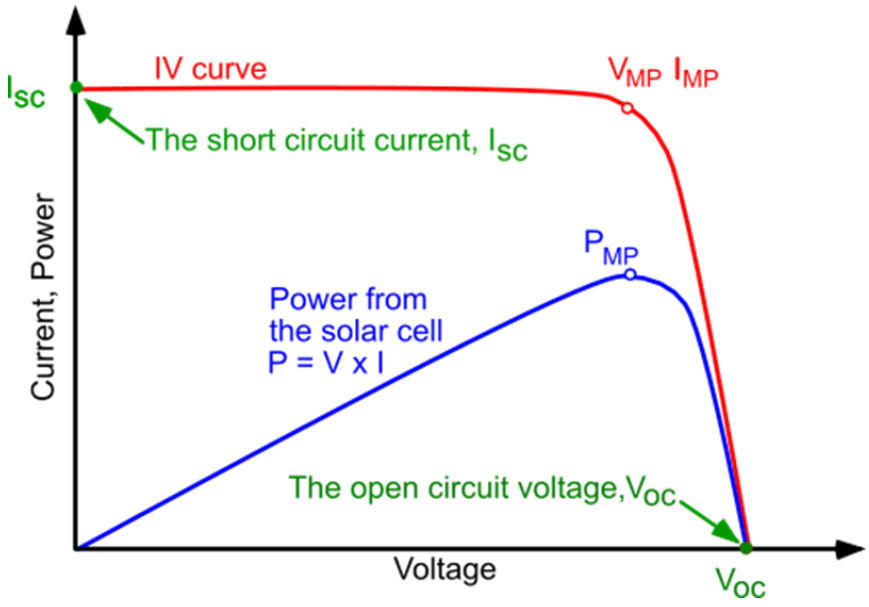

Figure 11: A typical I-V profile of a solar cell (the red curve) in which the y-intercept is the I_{SC} and x-intercept V_{OC}. The blue curve is the power generated by the cell which reaches a maximum at point V_{MP} and I_{MP} [59].

The fill factor (FF) may also be defined as [59]:

$$FF = \frac{I_{MP}V_{MP}}{I_{SC}V_{OC}} \quad (7)$$

In this relation, V_{MP} and I_{MP} are the respective voltage and current at the maximum power output. This relationship can be quantitatively measured for real devices, by connecting them to an I-V tracer which can apply a bias to give an I-V curve. The peak power output of the cell divided by the incident light intensity (usually 1000 W/m^2) will give the efficiency of the device, often called the power conversion efficiency (PCE).

Another type of efficiency can also be of interest, the external quantum efficiency (EQE) at a given incident photon wavelength (λ) which may be defined as follows:

$$EQE = \frac{number\ of\ charge\ carrier\ pairs\ generated}{number\ of\ incindent\ photons} \quad (8)$$

The EQE varies as a function of wavelength as photons of different energies will generate photons with various degrees of effectiveness; photons with $E < E_G$ will not lead to charge carrier generation, so will have an EQE of 0%. The internal quantum efficiency (IQE) can also be defined as the number of charge carriers generated divided by the number of photons actually absorbed by the solar cell, in order to account for optical losses. The short circuit current density can be obtained from an input irradiance spectrum and photon flux φ(λ) from the EQE using the formula:

$$J_{SC} = e \int_{\lambda_{min}}^{\lambda_{max}} \varphi(\lambda) EQE(\lambda)\, d\lambda \quad (9)$$

In a real cell, the EQE is reduced at short wavelengths due to front surface recombination and at longer wavelengths ($E \approx E_G$) due to recombination at the rear surface [60]. The EQE is related to another quantity, the spectral response (SR) which is simply given by the output current divided by the incident radiation power at a certain wavelength and measured in A/W. For an ideal cell, its SR profile should be a right-angled triangle rising from the origin with a maximum value at $\lambda = hc/E_G$ before falling to zero for $\lambda > E_G$. For the same reasons as with EQE, the SR profile is different due to due to front and rear surface recombination

effects. It is easier to experimentally measure spectral response directly than EQE, so it is the quantity recorded initially in characterisation. Spectral response can then be converted to EQE using the following relation [61]:

$$EQE = \frac{1239.8 \times SR}{\lambda\,(nm)} \qquad (10)$$

As previously discussed, radiative recombination is unavoidable in solar cells and the spontaneous emission from this process is dependent on temperature and limits the voltage, fill factor and efficiency of the cell. For c-Si cells every 1°C increase in temperature leads to a 2-2.3 mV decrease in voltage and 0.4-0.5% relative decrease in PCE [62]. Therefore, cooling solar cells, particularly in LCPV systems, through passive and active techniques, such as circulating water or placing wax materials in a rear container to capture the heat and use it to change their phase, lowering the cell temperature since the energy is absorbed as latent heat, have been researched as a way to lower their operating temperature and improve electrical performance.

Avoidable recombination in c-Si cells may also be reduced by techniques such as a passivated emitter rear cell (PERC) design and heterojunction technology (HJT). In the former, a dielectric passivation layer is added to the base of the solar cell to greatly reduce the rate of recombination at the rear interface [63], and in the latter, the p-type c-Si (emitter in Figure 9) is replaced by thin layers of a-Si, lowering the front surface recombination, reducing production costs and leading to smaller performance curtailment at higher temperatures (only -0.2% per °C, meaning they have high potential for use in LCPV systems [64]). These methods have led to significant advances in c-Si device performance, as demonstrated by Figure 3 in which their maximum efficiency growth has stagnated in recent years, leading many to predict practical limits are within reach. Other non-fundamental losses include optical losses due to non-complete absorption of the semiconductor material, shading from metal contacts and reflection of useful photons occurring at its front surface. Again, these issues have been widely studied and may soon be practically eliminated through the ongoing use of anti-reflective coatings [65], textured front surfaces, transparent conducting oxides and metal nanoparticles to scatter light which increases its path length (and hence absorption probability) within the cell [66]. Finally, parasitic shunt and series resistance losses may hamper cell efficiency and their

causes must be considered in cell design. Shunt resistances occur due to alternative paths forming for the charge carriers to travel, often as a result of material impurities. On the other hand, series resistance takes place due to lateral conduction in the semiconductor, the contact resistance (between the semiconductor and metal contact) and the resistance of the metal contacts themselves.

Since the above-mentioned issues have been largely solved by as described techniques, limiting their occurrence will be beyond the scope of this thesis. Neglecting non-radiative recombination, it is the wavelength profile of the incident photons responsible for the majority of fundamental losses in a solar cell, so it is this that will emerge as a focus of the work presented.

The Shockley-Queisser model has proven highly useful for describing the behaviour of single junction solar cells, however, and fortunately for photovoltaics researchers, a number of assumptions in the model don't necessarily have to be adhered to. Firstly, it was assumed the incoming light was of the ambient solar intensity which as seen through the development of CPV systems, doesn't have to be the case. The short-circuit current increases linearly with light intensity and the open-circuit voltage rises logarithmically, so the efficiency of single junction devices will be enhanced under greater concentrations of light, up to a maximum of 40% at 46200 suns [67] (the highest achievable geometric concentration of solar radiation).

Secondly, their model only considered single junction solar cells and from Figure 3 it can be observed multi-junction solar cells have already achieved higher efficiencies than the Shockley-Queisser limit (47.1% in 2019). This method attempts to overcome the spectral mismatch by utilising semiconductors of varying bandgaps to absorb different regions of the solar spectrum in a more optimal manner. De Vos produced a detailed balance calculation for a solar cell made from an infinite stack of differing band gap semiconductors and derived a maximum theoretical device efficiency of 68% under 1 sun [68]. This value could potentially reach 86% under the highest solar concentration which is the same for the separately derived thermodynamic limit; if we consider the solar cell to be a Müser engine operating between 290 K (Earth temperature) and 6000 K (sun temperature) [69]. Wurfel and others have used thermodynamic approaches to

derive efficiency limits and models for various solar cell scenarios and these are presented in a recent review by Rawat et al [67].

Given these promising hypothetical efficiencies, it may seem that multi-junction solar cells combined with HCPV should be the priority of solar researchers. However, as seen in 1.2.2, there are practical problems around their wide scale deployment and prohibitive costs. As a result, it is more than worthwhile to explore alternative ways of achieving higher efficiencies at a lower cost per watt, potentially leading to a paradigm shift in how solar cell performance is optimised. Proposed concepts include: multiple exciton generation (MEG) in which multiple electrons may be promoted to the conduction band by a single photon (EQEs of greater than 100% have been demonstrated in QDSCs by Semonin et al in 2011 [70]), intermediate band photovoltaics in which impurities allow for sub E_G photons to reach the conduction band via an intermediate energy level (the potential of this approach is immense but increased recombination has limited its effectiveness [71]), and finally spectral conversion, where the incident photons rather than the PV cells themselves are modified. It is the latter which of interest to this thesis, as there is a mature and evolving field of literature to drive these investigations on and materials may be applied (with relative ease) to existing solar cells without having to modify their internal structure.

1.4 Spectral Conversion

Spectral conversion is a phenomenon which changes the energy of a photon after it is absorbed by a molecule. Therefore, it can be regarded as a form of photoluminescence; for most cases fluorescence but occasionally phosphorescence depending on the spin states and decay lifetime. Spectral conversion can be a Stokes or anti-Stokes shift, depending on whether the emitted light is of a lower or higher energy. This area of interest has applications in diverse areas of physics including lighting displays and medical imaging. Naturally, this thesis will attempt to assess the potential impact of materials exhibiting this behaviour on photovoltaics, as first proposed by Wolf in 1960 [72].

The three process of note are upconversion (UC), downconversion (DC) and luminescent downshifting (LDS). The basic concept of each is outlined in Figures 12 and 13, while subsequent sections elucidate how these processes may aid solar cell performance.

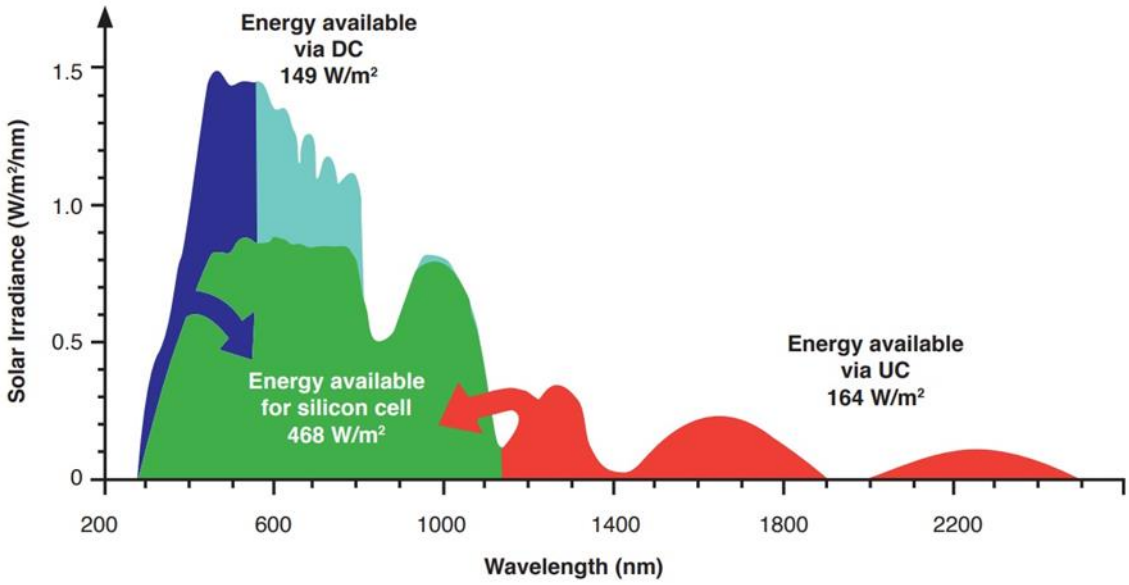

Figure 12: The basic concept of spectral conversion is to harness more energy from the parts of the spectrum that are not fully utilised. The green shaded area represents the energy that can be used by a silicon solar cell, the red that which may be captured via UC of low energy photons and the blue that which can be utilised by DC of high energy photons.

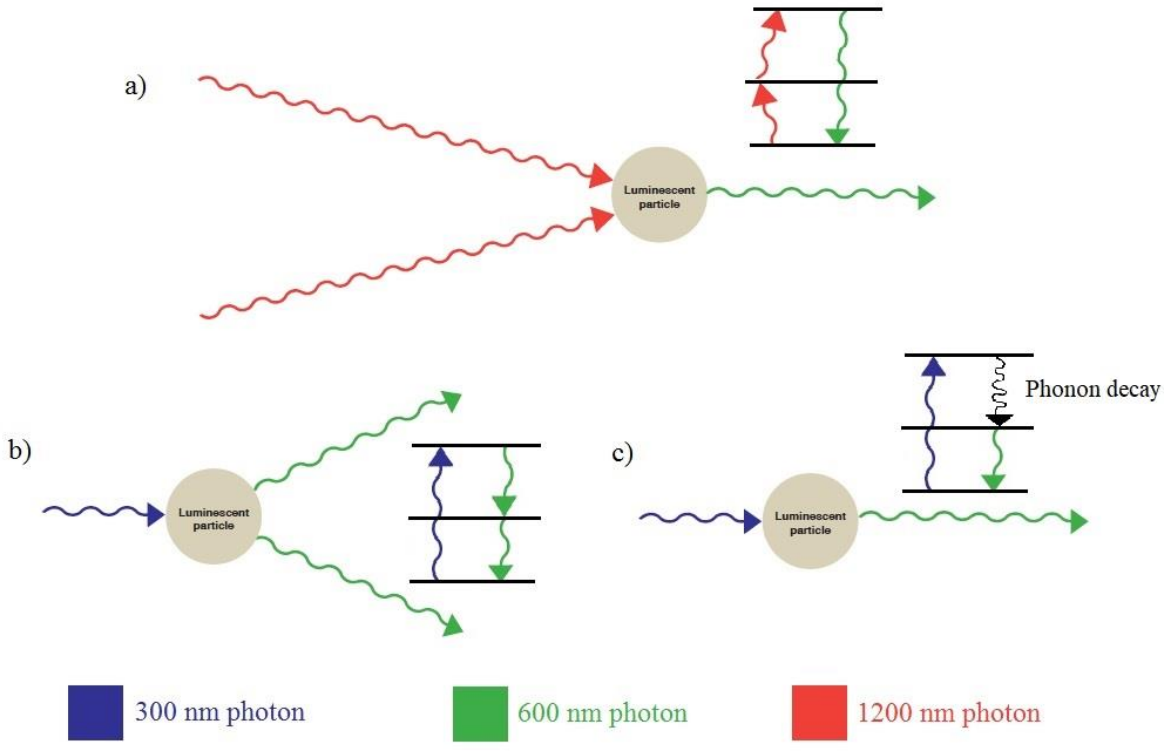

Figure 13: Examples of three spectral conversion processes: a) UC where two low energy photons are combined to make a single higher energy photon, b) DC where the energy of one high energy photon is split between two lower energy photons and c) LDS where the energy of a single high energy photon is reduced. The generalised energy level picture is also shown for each process.

1.4.1 Upconversion

Upconversion (UC) is an anti-Stokes shift process whereby the energy of two low energy photons are combined into a single higher energy photon, following absorption and reemission by a luminescent particle. First observed by Bloembergen, this phenomenon has the potential to improve solar cell performance since incident photons with $E < E_G$ may undergo UC to become a photon with $E \geq E_G$, increasing the amount of current able to be generated [73]. Trupke et al showed the theoretical efficiency limit of a solar cell, if all sub band gap photons could be harnessed via UC, increases to 47.6% at 1 sun illumination and 63.2% at the highest possible light concentrations [74].

UC layers have typically been placed below a solar cell (cf. Figure 14), so that light transmitted by the solar cell is then captured and redirected towards a bifacial cell with the aid of a reflector, once its photons' energies have been converted [53]. However, this conceptual design is not always the case and, as shall become apparent, for emerging solar technologies the UC materials may be incorporated within the photoactive layers.

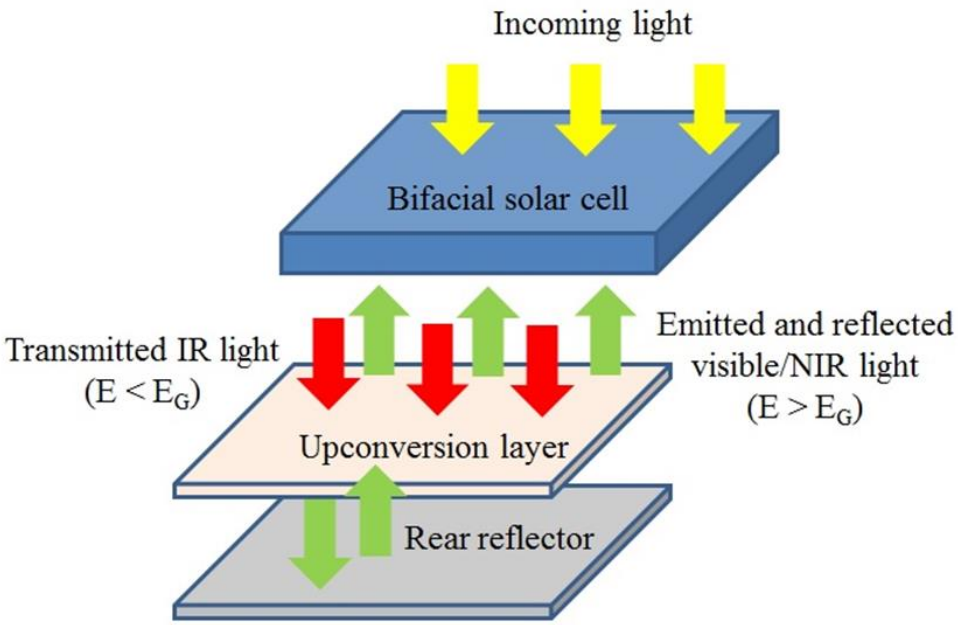

Figure 14: Design of a UC-PV system in which transmitted sub-band gap radiation is absorbed by the UC layer and converted to wavelengths that can be used to generate current upon being re-directed to the bifacial solar cell above.

UC processes have been observed in several luminescent particles such as rare earth ion containing compounds, organometallic dyes or quantum dots (QDs); a detailed collection of studies on the application of specific compounds will be presented in chapter 2. However, proposed mechanisms for each of these materials are presented in Figure 15. Firstly, UC in rare earth ions has been shown to occur via 5 proposed mechanisms [75, 76]:

1. Ground state absorption / excited state absorption (GSA/ESA), a process involving one ion in which an electron is elevated to an excited state after absorbing a photon. It then absorbs a secondary photon while in the excited state, taking the electron to a higher energy level still, before decaying radiatively to the ground state during which a photon with the combined energies of the two absorbed photons is emitted.

2. Energy transfer upconversion (ETU), a process involving two ions where both absorb a photon to an excited state before one ion (the sensitizer) transfers its energy to the other (the activator). The activator then emits a higher energy photon when it returns to its ground state.

3. Photon avalanche (PA) upconversion occurs when there is an energy mismatch between absorbed photons and the intermediate/final states, causing an exponential population of intermediate excited states via cross relaxation resonance.

4. Cooperative energy transfer (CET), a three-step process involving three ions in which two sensitizer ions are excited and transfer their energy to a third ion in the ground state.

5. Energy migration upconversion (EMU), a four-step process that takes place in a core-shell nanostructure and uses four ions: a sensitizer, accumulator, migrator and activator.

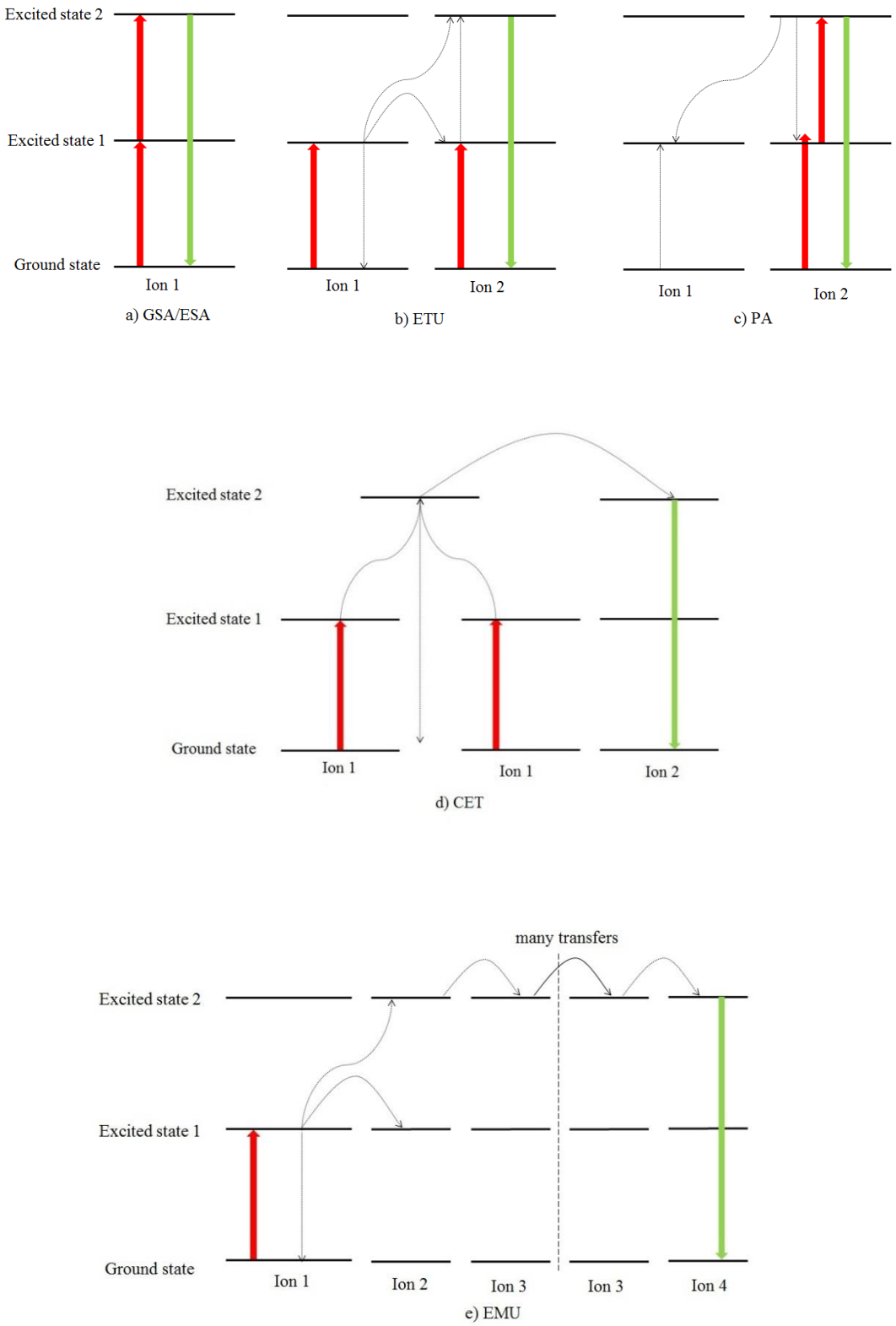

Figure 15: Energy level diagram representation for the proposed UC mechanisms within rare earth ions: a) excited state absorption (ESA), b) energy transfer upconversion (ETU), c) photon avalanche (PA), d) co-operative energy transfer (CET) and e) energy migration upconversion (EMU). Modified from [75].

UC in organometallic dyes can happen via a different process called triplet-triplet annihilation (TTA) involving the spin states of a molecule. The steps are summarised by Cheng [77] and presented in Figure 16:

1. A low energy photon is absorbed by a sensitizer in the ground state.
2. Intersystem crossing introduces the first triplet state.
3. The energy from this triplet state is transferred via a (Dexter) triplet energy transfer process to a ground state emitter molecule which is excited to a triplet state.
4. TTA then occurs when two emitters in the excited triplet state undergo a collisional complex, yielding one in a (higher) excited singlet state and one in the ground state.
5. The excited singlet state decays, emitting a higher energy photon

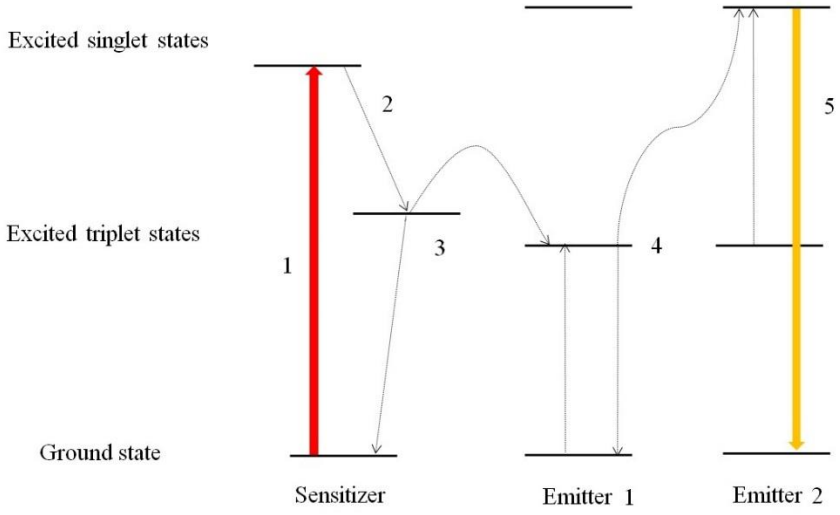

Figure 16: Energy level diagram for the states and steps involved in UC via TTA. The numbered processes are referred to in the text. Modified from [77].

UC may also occur within QDs, semiconductor nanocrystals whose electron-hole pairs are confined in 3D space, via two mechanisms outlined in the diagram below. The absorption properties of QDs depend on their size, which makes them ideal for photoluminescence and PV applications as they can be fine-tuned to respond to a particular wavelength [78]. In a typical system, two QDs of varying band gap are connected by a semiconductor rod. For UC to occur, a photon undergoes absorption in the lower energy QD, creating an electron-hole pair. Then, a second photon is absorbed by the same QD which permits the hole to tunnel the potential barrier into the higher band gap QD. Finally, the hole recombines and emits a photon of higher energy than the ones absorbed. There

are two ways this process can take place as shown in Figure 17 through direct intraband hole absorption or Auger mediation [79].

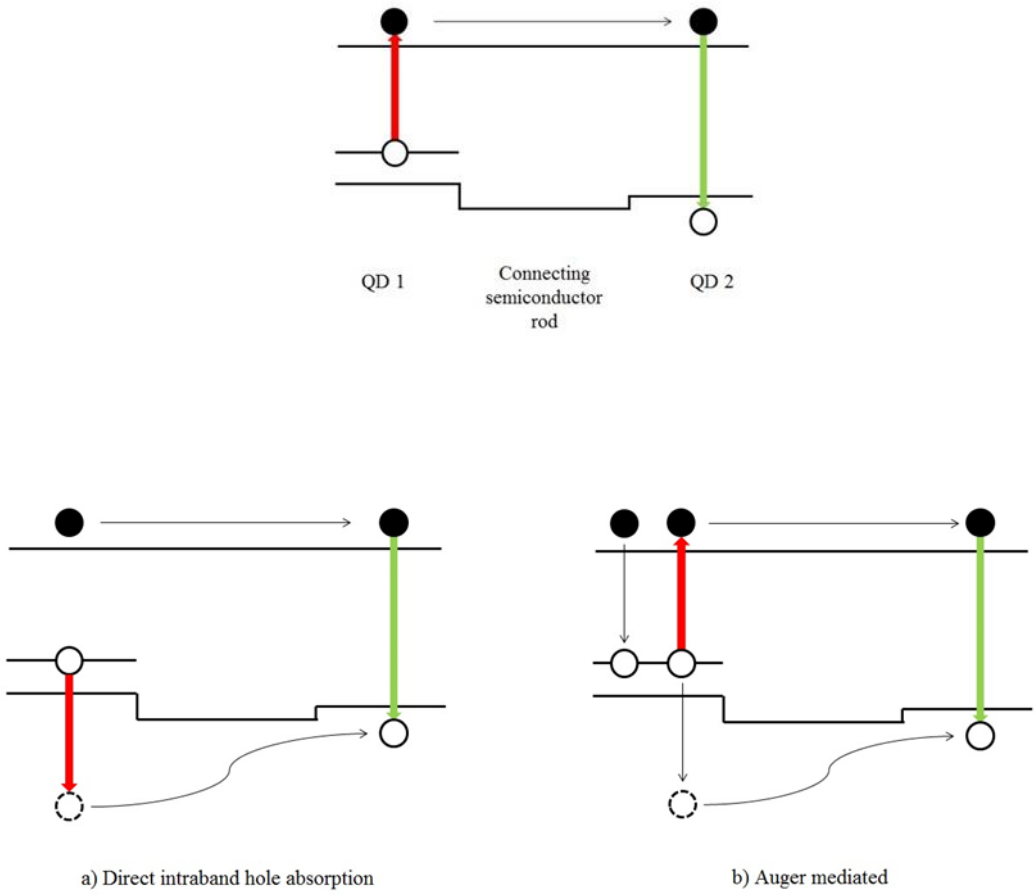

Figure 17: Diagram of the potential UC processes within QD nanostructures. The overall process for QDs 1 and 2 which are connected by a semiconductor rod is shown at the top of the figure. This can occur in two ways: a) direct intraband hole absorption and b) an Auger mediated process. Modified from [79].

Finally, UC can happen via a different concept altogether; rather than relying on absorption and emission from the energy levels within molecules, the same outcome can follow the heating of a material, resulting in so-called 'thermal upconversion'. This is achieved by shifting the peak wavelength of an object's blackbody spectrum to a shorter wavelength which accompanies a rise in temperature due to Wien's displacement law:

$$\lambda_{max} = \frac{b}{T} \quad (11)$$

In this formula λ_{max} is the peak wavelength, T the temperature of the body and b Wien's displacement constant equal to 2.90×10^{-3} m K. As demonstrated in Figure 18, ions in the lattice may absorb low energy photons which then undergo

relaxation via multi-phonon emission, leading to a temperature increase of the material through energy transfer. Hence, the blackbody is shifted, meaning a greater number of high energy photons are emitted. If this emitted thermal radiation can be directed towards a solar cell, then it will result in a greater portion of the originally incident radiation being above the bandgap and able to generate electricity, thus enhancing the performance of the PV device [80].

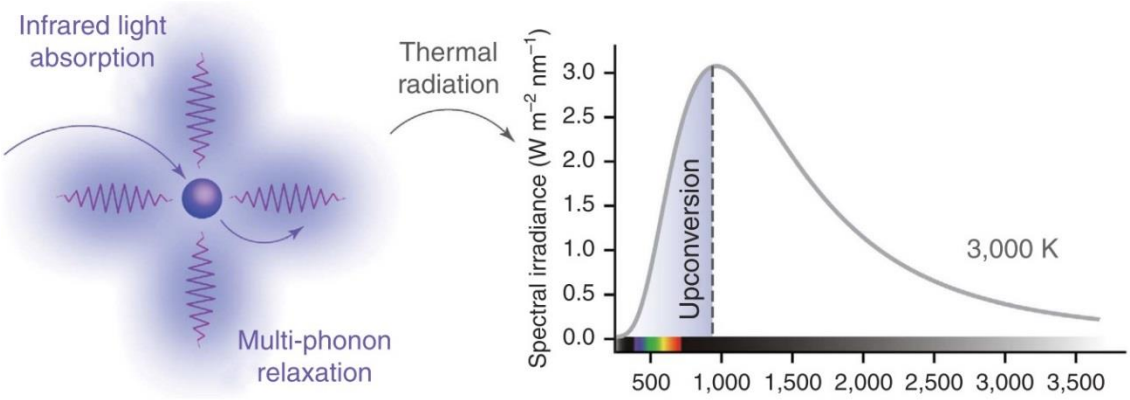

Figure 18: The concept of UC via thermal radiation. Infrared photons are absorbed by a material and, by multi-phonon relaxation, raise the material's temperature. This in turn shifts the peak of the emitted black body radiation towards the visible and UV part of the spectrum, meaning UC of photons has taken place. Taken from [80].

1.4.2 Downconversion

Downconversion (DC) can be considered the inverse of UC; a Stokes process in which a high energy photon splits its energy between two lower energy photons after being absorbed by a luminescent particle that re-emits two photons. This can also enhance solar cell output because incident photons with $E > E_G$ contribute to thermalisation losses, so provided the DC emission still has greater energy than the band gap, these losses will be reduced as two electrons can be promoted to the edge of the conduction band (instead of one electron with a higher energy level). Trupke et al calculated the maximum theoretical efficiency of a 1.1 eV band gap silicon solar cell under 1 sun illumination could increase to 38.6% through the incorporation of an optimal DC layer [81] (higher than permitted by the Shockley-Queisser model).

In contrast to UC materials, a DC layer would be ideally situated on top of the solar cell (cf. Figure 19) where it can absorb short wavelength radiation (which

yields a low EQE) and emit higher wavelength photons with a corresponding improved EQE value for the cell. For the overall power conversion efficiency to improve, it is vital the layer is transparent to regions of the spectrum which provide a good ratio of charge carriers generated per incident photon [82].

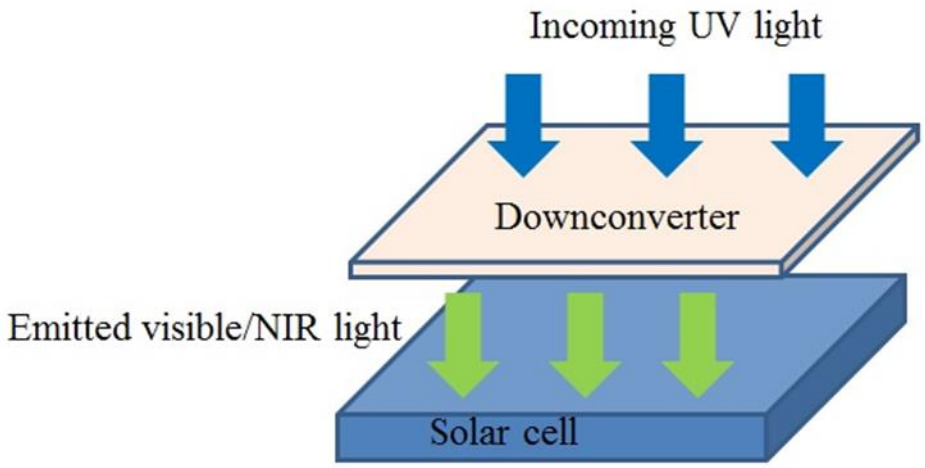

Figure 19: Design of a DC-PV system in which incoming short wavelength light is absorbed by the DC layer placed above the solar cell. The photons are then re-emitted at wavelengths which cause less thermalisation losses, increasing the overall efficiency of the PV.

As with UC, the materials in which DC processes may be instigated include rare earth ions, organic dyes and quantum dots. Furthermore, the dominant mechanisms (presented in Figure 20) appear similar to UC in reverse. These are [75]:

1. Reverse GSA/ESA, a process involving one ion in which the electron is this time instead promoted to a higher energy level after absorbing a high energy photon. It then decays in two stages to the ground state, via an excited state, emitting two lower energy photons in the duration.

2. Resonant energy transfer (RET) can take place in two or three ions. A high energy photon is absorbed by the first ion and its energy is either a) fully transferred to two further ions which excites them to states from which they will decay to the ground state and emit a low energy photon each or b) partially transferred to a single other ion via one of two mechanisms, which will cause that ion to enter an excited state followed by low energy photon

emission. The original absorbing ion is also left in an excited which will emit another low energy photon upon returning to the ground state.

3. Reverse CET where a single ion absorbs a high energy photon and transfers its energy simultaneously to two other ions, promoting them to an excited state and leading to the emission of two low energy photons when they decay to the ground state.

Unfortunately, detailed mechanisms for DC in non-rare earth ions are sparsely reported in the literature.

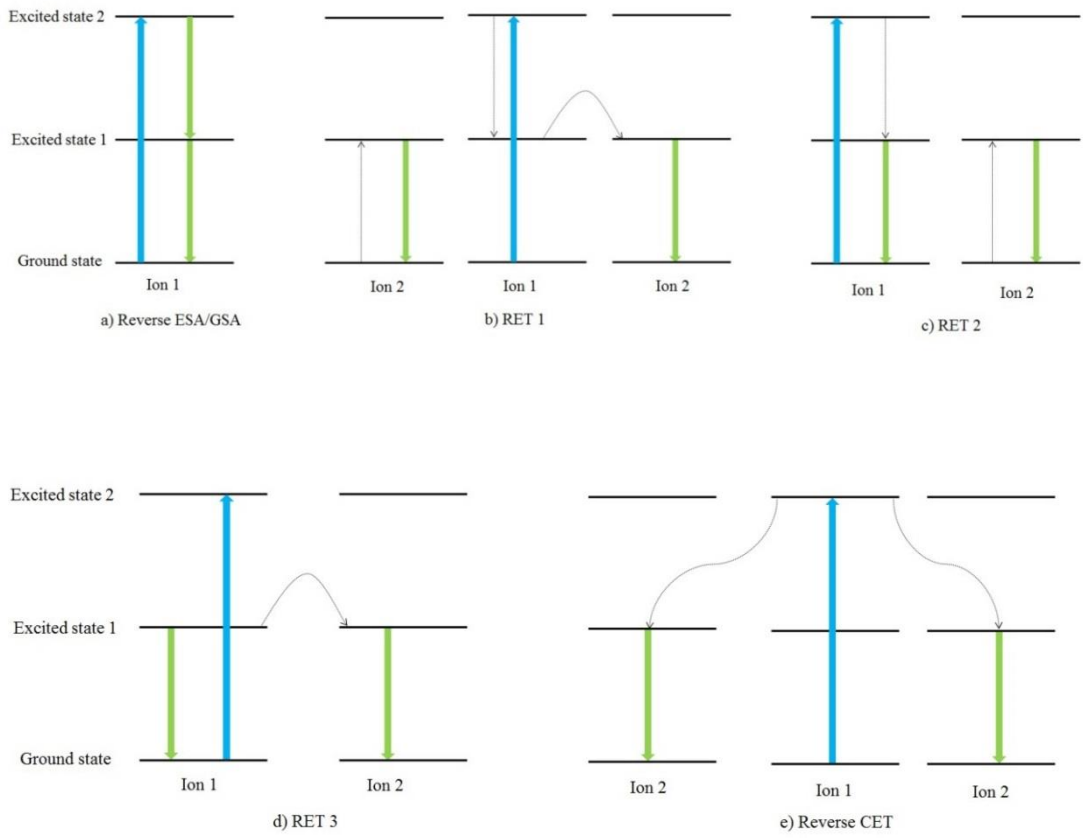

Figure 20: Energy level diagram of the proposed DC mechanisms within rare earth ions: a) ESA in reverse, b), c), and d) resonant energy transfer between two ions and e) CET. Modified from [75].

1.4.3 Luminescent Downshifting

Luminescent downshifting (LDS) is another Stokes process but differs from DC in that only one lower energy photon is emitted per absorbed photon. This means it is not possible to exceed the Shockley-Queisser limit through a LDS layer alone since no extra photons are created, so still only one charge carrier pair is being

generated per incoming photon [75]. As with DC, LDS layers may be applied on top of a solar cell to achieve a higher performance by changing the profile of the incident light from shorter to longer wavelengths, with a practical net gain in efficiency as long as the layer has a high transmittance to the lower energy photons. Although, van Sark et al believe improved front surface passivation techniques could render LDS layers atop PV cells obsolete [83].

Like the other spectral conversion processes, LDS also occurs in rare earth doped compounds, dyes and quantum dots. However, as shall be seen in chapter 2, the dyes and quantum dots used for LDS investigations have shown more replicable success than those in UC and are more widely commercially available. Furthermore, LDS has been particularly of interest for LCPV applications within LSCs. Luminescent solar concentrators coupled to single junction solar PV cells were shown by Rau et al to have the same theoretical maximum efficiency as the Shockley-Queisser limit [84]. Although, unlike UC and DC, mechanisms are not widely reported in the literature, so less is known about the specific energy transfer process. Despite the lack of a clear description in the literature, from first principles a mechanism is hereby proposed involving the non-radiative transfer of energy from a high level, post-high energy photon absorption, to a lower intermediate state from which a lower energy photon can be emitted. One pictorial representation of these steps is given by Figure 21 which shows the states being excited by an incoming photon and losing some of this energy to the lattice, then decaying to the ground state emitting a lower energy photon.

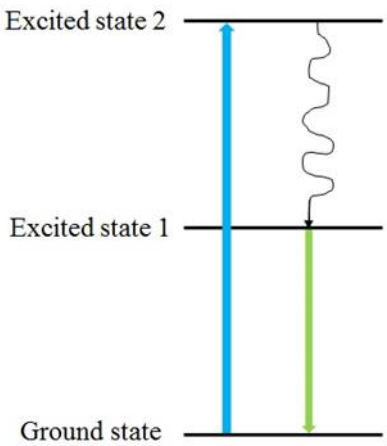

Figure 21: Energy level diagram of one proposed simple mechanism for LDS in which an absorbed high energy photon decays non-radiatively to an intermediate state, before emitting a single lower energy photon.

1.5 Chapter Overviews and Aims

The aims of the project must follow the widely used SMART criteria.

Specific: A clear problem must be identified from the gaps in the current knowledge field and investigations planned around them.
Measurable: How to quantitatively evaluate the impact of the proposed methods on solar cell performance?
Attainable: The aims must be sensible given the facilities and expertise available. For example, breaking the Shockley-Queisser limit via UC or DC which has yet to be achieved, would be very ambitious.
Relevant: The outcomes must be relevant to the field of solar PV and add meaningful value to the tree of knowledge.
Time-bound: The tasks to be conducted must be able to be carried out in the allotted timescale for a typical doctorate degree (3-4 years).
Therefore, the primary aim of this thesis is:

- To develop a cost-effective method for incorporating spectral conversion materials into established and emerging types of solar PV cells and technologies with the aim to increase efficiency and electrical power output.

To achieve this the following procedure will be followed:

- Select a suitable spectral conversion material to be used for this purpose and study its material properties.
- Carry out experiments on PV cells containing these materials
- Justify that the enhanced performance is due to this material and critically assess its potential impact on the search for lower cost PV modules.

This general methodology used will be outlined further in the following descriptive overview of the chapters whose layout comprises this thesis.

1.5.1 Chapter 2

In chapter 2, an unrestricted literature search is conducted across a wide range of online sources and studies from the early attempts of spectral conversion to up-to-date results are catalogued. This will demonstrate the evolving nature of the research area and its application to a range of solar cell technologies.

Through critical analysis, gaps in the knowledge field have been identified and these gaps will be explored throughout the experimental and theoretical investigations of this thesis. These knowledge gaps were found to be consistent with the aims of this thesis, in that beyond LSCs, spectral conversion techniques have not been applied in LCPV systems.

1.5.2 Chapter 3

In chapter 3, a study on the effect of selected rare earth doped compounds known to exhibit spectral conversion on silicon PV cells is presented. These compounds which form the basis for investigations in subsequent chapters, were $NaYF_4$: Er^{3+}, Yb^{3+} and $Sr_4Al_{14}O_{25}$: Eu^{2+}, Dy^{3+} (the colon indicating the rare earth ions replace the heavy metal in the chemical formula at fixed percentages). First, a best approach method of applying the materials above the silicon cells is determined. Then the electrical characterisation methods are outlined and results from coated silicon PV cells presented.

1.5.3 Chapter 4

In chapter 4, the same materials are applied into an LCPV system based on square elliptical hyperboloid (SEH) 3D static concentrators coupled to silicon PV cells. By varying the doping ratio and configuration, different systems were characterised in an attempt to find the optimal design. Then, these results were compared to the same modules without concentrators to determine the effect of the LCPV and the variation in performance enhancement with angle of incidence was also explored.

1.5.4 Chapter 5

In chapter 5, the effect of rare earth doped compounds on emerging photovoltaic technologies is investigated. DSSC devices of different layer thickness and containing the spectral conversion materials in varying locations are fabricated in house. The same concentrators are then added atop the DSSCs to see the effect of spectral conversion within an emerging cell based LCPV system.

1.5.5 Chapter 6

In chapter 6, mathematical techniques are used to scrutinise the consistency and reproducibility of the experiments, a cost analysis is presented for scaled up systems and mathematical models are utilised to give justification for the results.

1.5.6 Chapter 7

In chapter 7, the key findings from each chapter are summarised and conclusions drawn from the research undertaken with recommendations then made on where future studies should focus attention to maximise the impact of this thesis.

1.5.7 Expectations

As shall become apparent in chapter 2, spectral conversion has not been the silver bullet that it may first appear. However, small efficiency increases for a low cost would still be desirable and a useful addition to the web of PV knowledge. With this is in mind, an expectation shall be set for the devices to show a relative enhanced efficiency of 5% through the addition of spectral conversion materials and cost per watt should be lowered rather than increased.

Chapter 2. Literature Review

2.1 Introduction

Upconversion as a phenomenon was first envisaged in 1959 by Bloembergen [73] who proposed the energy levels in rare earth ions could absorb IR radiation and re-emit at higher photon energies, naming them ‘quantum counters’. Just a year later, the potential for PV was realised by Wolf [72]. In recent years, more novel molecules have been used for spectral conversion, including dyes and quantum dots, but initially the traditionally used rare earth ions will be the focus of discussion. Throughout the rest of this chapter, a thorough literature review is conducted, outlining the evolution of the field of spectral conversion from a theoretical concept with little practical application, to state-of-the-art materials with a substantial impact on laboratory PV device performance.

By the end of the review, knowledge gaps are identified, particularly around the cost aspect of these enhancements and suggestions made where this thesis should focus in order to be a useful addition to the field of knowledge.

2.2 Rare Earth Ions and Early Spectral Conversion Experiments

Rare earth elements (NB this term will be used to mean the lanthanides, elements 57-71, neglecting Sc and Y) in their 3+ (trivalent) ion form have a diverse range of energy levels due to their electron configuration, $1s^2\ 2s^2\ 2p^6\ 3s^2\ 3p^6\ 3d^{10}\ 4s^2\ 4p^6\ 4d^{10}\ 5s^2\ 5p^6\ 4f^n$ with $0 \leq n \leq 14$. The abundance of states in this 4f subshell leads to a diverse range of possible absorption and emission events. Although f-f transitions are parity forbidden, the introduction of a crystal field by doping the rare earth ions into a lattice (usually an oxide or halide compound) permits these transitions to occur [85]. Dieke studied the states in the ions of different elements and presented them in diagrams, as shown in Figure 22, giving a visual representation of just how many possible energy levels there are [86]. Auzel further gave an extensive review of mechanisms responsible for their transitions at a level beyond the scope of this investigation [87]. These states of the outermost unfilled subshell are often given in term symbols of the general form:

$$^{2S+1}L_J \qquad (12)$$

Wherein *S* is the total spin quantum number (sum of the individual spin quantum numbers, m_s, which can either be ± ½), *L* is the total orbital angular momentum quantum number (sum of the individual azimuthal orbital angular momentum numbers, m_l, which take possible values in integer steps from *-l* to + *l* where *l* = *0, 1, 2* and *3* for s, p, d and f orbitals respectively, and are denoted by spectroscopic notation, letters for *L = 0-9* are shown in Table 2) and *J* is the total angular momentum quantum number which has a range of possible values from |*L - S*| *to L + S* in steps of 1.

L	0	1	2	3	4	5	6	7	8	9
Letter	S	P	D	F	G	H	I	K	L	M

Table 2: The letters used to represent the respective total orbital angular momentum quantum numbers in the term symbol notation.

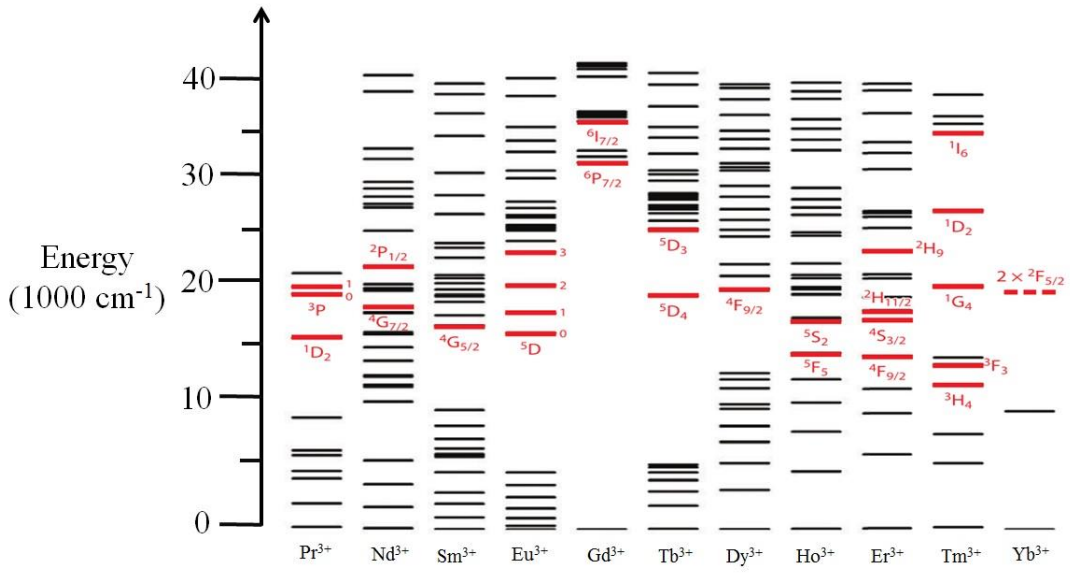

Figure 22: A Dieke style diagram which shows the energy levels of trivalent rare earth ions. The red highlighted states are able to undergo UC when excited.

Hund's rules can be used to determine the term symbol for the ground state of a given electron configuration. These rules are such that:

1. S is maximised for a given configuration of electrons
2. L is maximised for a given configuration of electrons
3. If half or less of the subshell is filled then *J* for the ground state is equal to its minimum value, |*L - S*|, else if more than half of the subshell is occupied then *J* for the ground state takes its maximum value, *L + S* [88].

So, for example, the Er^{3+} ground state's term symbol can be derived by first considering the number of electrons (for Er atomic number = 68, so its trivalent ion will have 65 electrons, hence the outer subshell will be $4f^{11}$), then applying Hund's rules to the subshell, while also obeying the Pauli exclusion principle which means no two electrons can occupy the same state within a quantum system (i.e. they can't have the same quantum numbers, m_s and m_l, within the same subshell). Therefore, if S is maximised, then all seven of the energy levels will be filled with a +½ electron. This leaves four electrons, which by applying the second rule, will fill the m_l = 0, 1, 2 and 3 energy levels. *L* and *S* can be found to be 6 and 3/2, by summing the values for m_s and m_l respectively as represented pictorially in Figure 23. Finally, since the subshell is at more than half its full capacity, then $J = L + S = 15/2$. Thus, the Er^{3+} ground state's term symbol can be written $^4I_{15/2}$.

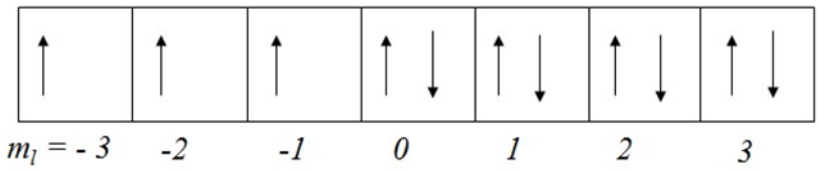

Figure 23: Electron configuration for the 4f subshell of Er^{3+} derived via Hund's rules with m_s = +½ denoted by upward arrows and m_s = -½ denoted by downward arrows.

Based on these transitions, which can occur when the ground state is elevated by the energy of an incident photon, several ions (either alone or combined with another) have been of particular interest for spectral conversion applications and will be discussed subsequently. Most notably for UC are Er^{3+} with its absorption peak at 1523 nm and emission at 980 nm, following decay from the excited state, $^4I_{11/2}$, to the ground state, $^4I_{15/2}$ [89]. This is promising for c-Si solar cells, since there is strong IR radiation in the AM 1.5 G solar spectrum around 1500-1750 nm and the bang gap of a c-Si device is approximately 1100 nm, so the UC emission could potentially allow the cell to harness more of the ambient sunlight. Furthermore, the Yb^{3+}-Er^{3+} pair as shown in Figure 24 has been of interest due to its absorption at 980 nm and emission across the visible spectrum, occurring efficiently due to Yb^{3+} acting as a sensitizer for ETU with its large cross section [90] (9.11×10^{-21} cm^{-2} at 976 nm for the $^2F_{7/2}$ to $^2F_{5/2}$ transition). This behaviour highlights its potential for applications to higher band gap cells such as a-Si or

DSSCs for which $E_G \approx 1.7$ eV (or 730 nm). In addition tri-doped Er^{3+} -Yb^{3+}- Nd^{3+} particles could capture further radiation still for these cell technologies through 808 nm excitation [91].

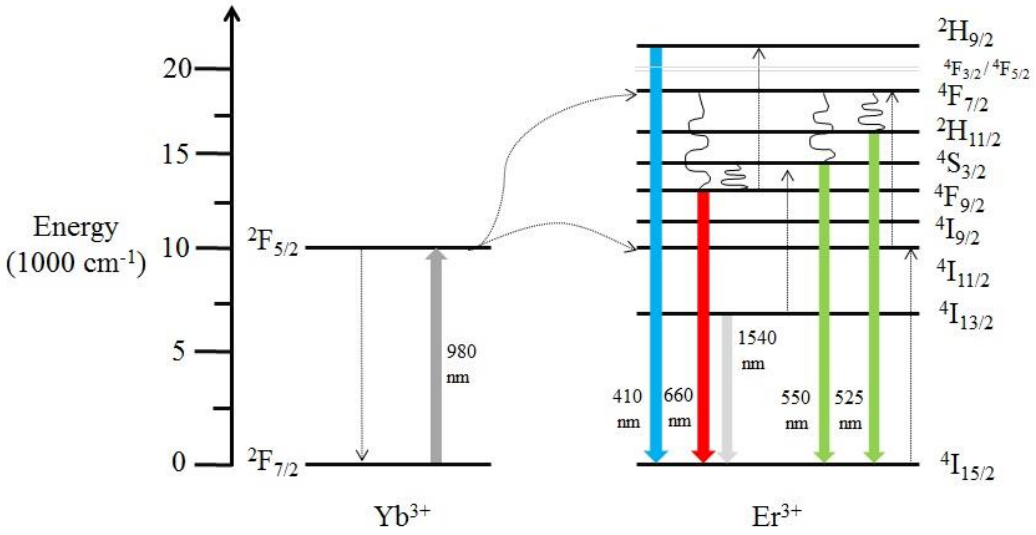

Figure 24: Energy level diagram which shows the potential emissions from the Yb^{3+}-Er^{3+} ion pair. In this representation the dashed arrows correspond to energy transfer between ions, the curly arrows non-radiative decay and the solid arrows radiative decay of that colour. Modified from [92].

Two additional candidate ions which may demonstrate potential for UC have been Ho^{3+} [93] (absorbing in the 1150-1225 nm region due to the $^5I_5$ to $^5I_8$ transition and emitting at 910 nm) and Tm^{3+} [94] (with two absorption peaks at 1210 and 1640 nm because of excitation from the $^3H_6$ ground state to either the $^3H_5$ or $^3F_4$ energy level, leading to emission of wavelength 808 nm). Since there are such a wide variety of energy levels in the 4f orbital, other rare earth ions have shown energy level transitions relevant for UC to be technically possible. In 2013, Huang et al catalogued an extensive list of processes for Pr^{3+}, Nd^{3+}, Tb^{3+} and Dy^{3+} [75]. However weak intensity of emission limits their potential and Yang et al concluded in 2014 [93] that efficient processes were restricted to Er^{3+}, Tm^{3+} and Ho^{3+} ions (notwithstanding the use of Yb^{3+} sensitizers). There is even scope for these rare earth ions to be used in tandem to capture an even wider portion of the spectrum, as proposed by Lahoz et al who in 2011 conceptualised a bifacial c-Si PV device with a reflector and two UC layers beneath it, one containing Ho^{3+} to capture 1150-1225 nm photons and the other Er^{3+} to utilise the 1480-1580 nm radiation [95]; though as of 2019, no such system has been fabricated.

On the other hand, the idea of dividing a UV photon into two visible photons through DC was originally developed by Dexter in 1957 [96]. This process is sometimes called quantum cutting (QC) to differentiate it from LDS (in which a UV photon reduces its energy to emit a single visible photon). In addition, LDS is confusingly in some instances classed together with QC as a subcategory of DC, but in this thesis, DC will be used only to refer to QC as introduced in 1.4.2. Although in terms of choice of rare earth ion, LDS and DC lanthanide materials can be viewed from a similar perspective as the initial ground state to be excited will often be the same, but emission processes differ due to rates of radiative or non-radiative decay and efficiency of emission. Furthermore, there appears to be slightly more variation in the potential ions with PV applications for DC studies; in the state-of-the-art studies, Eu^{3+} commonly features throughout the literature (sometimes paired with Gd^{3+}, as Wegh et al first observed highly efficient DC processes in an Eu^{3+}- Gd^{3+} system [97]) and other combinations of ion paired with Yb^{3+} such as: Tb^{3+}, Tm^{3+}, Er^{3+}, Pr^{3+}, Ho^{3+}, Dy^{3+} or Nd^{3+} [75, 98]. Likewise, Eu^{3+} and other lanthanides co-doped alongside Yb^{3+} are frequently used for LDS applications, although as will be seen, there are much greater uses of dyes and QDs in pure LDS studies. Finally, Eu^{2+} is a fantastic sensitizer of trivalent ions for LDS and DC applications [99] with its emission relevant energy levels shown alongside those of Dy^{3+} in Figure 25.

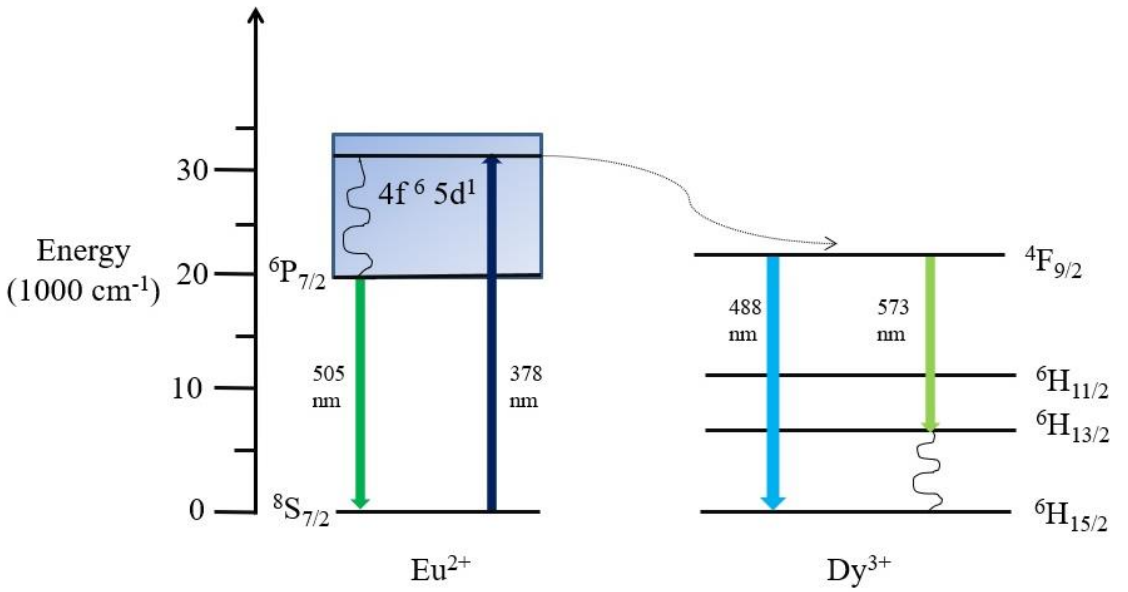

Figure 25: Energy level diagram which shows the potential emissions from the Eu^{2+}-Dy^{3+} ion pair. Modified from [100] and [101].

Initially, it was envisaged the materials that demonstrated UC would be doped into the PV cells themselves, in so called impurity photovoltaics [102]. These

attempts were of limited success and it wasn't until 1996 when Gibart's group applied an external vitroceramic doped with Yb^{3+} and Er^{3+} of 100 μm thickness to the rear of a GaAs doped solar cell [103]. After being illuminated by an 892 nm laser (below the GaAs band gap) at an intensity of 25.6 W/cm^2, an EQE of 2.5% for the device was recorded. This approach was deemed more appropriate than impurity PV since the performance enhancements were more pronounced and, importantly, the UC layer could be optimised independently of the solar cell. Then in the mid-2000s, Shalav and Richards's groups' work could be acknowledged for reigniting an interest in the sector with their studies on UC, DC and LDS. 20% Er^{3+} doped $NaYF_4$ was fixed in a transparent oil medium to the rear of a bifacial c-Si solar cell and an EQE of 3.4% achieved under illumination by a 6 mW laser, at an excitation wavelength of 1523 nm [85]. This was a significant result, although potential for practical applications were concluded to be limited due to the narrow excitation spectrum and poor efficiency of the UC process at lower concentrations of light; in an ideal case the cell's power conversion efficiency could only be raised 2.4% (absolute) through this method, while Tm^{3+} and Ho^{3+} ions were also investigated but were unable to be characterised because of their weak performance at the excitation power densities. It was suggested this meant UC may be limited to silicon photodiodes rather than PV for practical applications.

Simultaneously, the group catalogued DC and LDS materials [104]. DC, despite having theoretical benefits due to better performance at lower light intensities, was not reported to be applicable to PV systems at the time (since then successful studies have been reported and are discussed in 2.5) due to the losses from the DC emitting layer and low irradiance of UV light at the necessary excitation wavelengths. They predicted LDS to have the most potential of the three spectral conversion processes and this had an established presence in the literature of successful trials; in 1979, Hovel et al used ruby sheets (Cr^{3+}: Al_2O_3, transition metal ions also exhibit luminescence) and organic dye containing fluorescent sheets (Plexiglass 2184) in an attempt to increase the efficiency of GaAlAs-GaAs, GaAs, a-Si, c-Si and CdS/Cu_2S PV by fixing the layer above the solar cells with a refractive index matched adhesive [105]. All the devices showed enhanced EQE under high energy photons and their power conversion efficiencies under AM0 were measured to increase from 14% to 15% for GaAlAs-GaAs with Plexiglass 2184, 3% to 3.5% for CdS/Cu_2S with Plexiglass 2814, no

increase for a-Si with Plexiglass (due to the decreased EQE at longer wavelengths) and 9 to 9.3% for GaAs with ruby. Additionally a ruby sheet atop a commercial c-Si had its EQE measured only and it was expected an absolute power conversion efficiency increase of 1-2% could be achieved under AM 0, although all these results would have been less successful in AM 1 or AM 1.5 G conditions due to the reduced short wavelength intensity (and hence less LDS taking place). LDS within LSCs as proposed by Weber and Lamb in 1976 [106], was identified in 2006 by Richards as an area of upmost interest going forward and advances in this sector are analysed in 2.7.

Since this time period, research has focused on the range of materials available for spectral conversion processes and their optimisation with respect to the following parameters: choice of host lattices and/or matrices, layer thickness, doping ratio (e.g. weight or molar percentage of rare earth ion in a compound) and maximising the quantum efficiency of the spectral conversion process. Spectral conversion materials have also been applied to a wider type of solar cells (DSSCs, PSCs, QDSCs etc) reflecting the progress made in this parallel field of evolving PV technologies as shall be discussed in subsequent subsections.

2.3 Spectral Conversion Efficiency Limitations and Optimisation Parameters

Like solar cells, a quantum efficiency may be defined for spectral conversion processes. In the literature, this is often known as the photoluminescent quantum yield and as with the quantum efficiency for a solar cell, it may be stated as an internal or external result. The internal photoluminescent quantum yield (iPLQY) is given by:

$$iPLQY = \frac{number\ of\ photons\ emitted}{number\ of\ photons\ absorbed} \quad (13)$$

And external photoluminescent quantum yield (e-PLQY) by:

$$ePLQY = \frac{number\ of\ photons\ emitted}{number\ of\ incident\ photons} \quad (14)$$

For example, perfectly efficient UC, LDS and DC processes would have ePLQYs of 50%, 100% and 200% respectively. ePLQY can be measured with an

integrating sphere using a method described by Johnson et al [102]. In some cases, investigations have focussed on spectral conversion materials purely to determine their PLQYs for hypothetical PV applications. However, increasingly spectral conversion materials have been applied with solar cells to observe performance improvements. In such investigations the power conversion efficiency, J_{SC} and EQE can all be measured through the use of either a solar simulator (a lamp with an irradiance profile replicating AM 1.5 G) or a monochromatic illumination source. Due to the dependence of EQE on light intensity, when quoting an EQE with a monochromatic source it is useful to state a normalised EQE defined as:

$$NEQE = \frac{EQE}{incident\ light\ power\ density} \qquad (15)$$

However, some spectral conversion processes (UC in particular) have a non-linear dependence on light concentration, therefore caution should be exercised when comparing NEQEs [107]. In these instances, the iPLQY obeys a power law such that:

$$iPLQY \propto P_{in}^{n} \qquad (16)$$

Where P_{in} is the power of the incident radiation and n the number of steps in the mechanism, so a two-step ETU process would exhibit a quadratic dependence on the power of the incoming light. Conversely, the EQE of single junction solar cells has a linear relationship with increasing intensity. If these processes are combined for an overall UC-PV system, the emitted photoluminescence can be assumed to be the proportional to the number of sub-band gap electron-hole pairs generated, so the following equation applies:

$$EQE \propto \frac{P_{in}^{n}}{P_{in}} \propto P_{in}^{(n-1)} \qquad (17)$$

Therefore, for an ETU dominated process with $n = 2$, the EQE is predicted to scale linearly with increased light concentration. This expectation holds at low irradiances but at high light intensity deviates from the linear relationship due to competing mechanisms [108]. In general, the photoluminescent yield of the UC process rises with light concentration, so spectral conversion processes may have potential in CPV systems.

There are three processes identified by Shalav which cause suboptimal quantum yields within a UC ion [85]. These include non-radiative relaxation, radiative relaxation to a state other than that which results in photon emission of the desired wavelength and cross-relaxation between ions. When selecting a compound to be a part of a spectral conversion material, these are the fundamental losses which must be minimised.

Since the spectral conversion processes are transfers between energy states, they can accurately be modelled by simulations. The essential dynamics of a luminescent system are underlined by the following rate equation [75]:

$$\frac{dN}{dt} = -(A_r + A_{nr})N \qquad (18)$$

In which *N* is the population of excited states and A_r and A_{nr} are the radiative and non-radiative decay rates. It can be seen from this equation that in the case for zero illumination, *N(t)* decays exponentially from *N(t = 0) = N(0)* such that:

$$N(t) = N(0)e^{-\frac{t}{\tau}} \qquad (19)$$

Where the time constant, τ, is given as:

$$\tau = \frac{1}{(A_r + A_{nr})} \qquad (20)$$

The quantum efficiency of the process can then be calculated as the ratio of radiative decay rate to total depopulation rate such that:

$$iPLQY = \frac{A_r}{(A_r + A_{nr})} = \frac{\tau_r}{\tau} \qquad (21)$$

The time constant, τ, can be measured directly from experiment (by observing photoluminescent decay times) whereas τ_r can be calculated from Judd-Ofelt theory [109]. Empirical observations have led to an energy gap law:

$$A_{nr} = A_{nr}(0)e^{-\alpha(\Delta E)} \qquad (22)$$

In this equation, $A_{nr}(0)$ and α are constants that depend on the host lattice and ΔE is the gap in energy between the states in the rare earth ion. Thus, it can be seen that the non-radiative decay rate decays exponentially with increasing difference in energy levels. Layne et al experimentally measured A_{nr} for a range of ΔE values and oxide host lattices [110]. The results showed that A_{nr} and hence

the quantum yield of the spectral conversion process, depends heavily on the choice of host lattice as well. The physical behaviour responsible for this is the phonon energy of the lattice; in general, compounds with lower phonon energies have a lower non-radiative decay rate due to more phonons being required to cause a decay through multi-phonon emission. It has been proposed that if more than six phonons are necessary for a non-radiative decay event then radiative relaxation will dominate, leading to higher photoluminescent quantum yields [111]. This means that the selection of host lattice is a key factor in determining the effectiveness of spectral conversion to improve the performance of a solar cell. Of the common anionic combinations of atoms which could be used in the rare earth containing lattices, the lowest phonon energies are halides and oxides. Oxides have a typical phonon energy of 600 cm^{-1} and halide phonon energies decrease with increasing atomic number: 355 cm^{-1} for F^-, 260 cm^{-1} for Cl^-, 172 cm^{-1} for Br^- and 144 cm^{-1} for I^-. Despite the lowest energies occurring in bromide and iodide, their hygroscopic properties limit their use for practical applications [112].

The ideal compounds were identified in 2015 by Sun et al as REF_3, REOF or $MREF_n$ (with RE = rare earth ion, M = Li, Na, K, Ba; n = 4, 5) [90]. Chemical stability is another important factor and oxysulfide compounds (of the form RE_2O_2S) also possess low phonon energies (< 500 cm^{-1}) and impressive quantum yields [113]. Subsequently, it is unsurprising that one of the most studied compounds has been $NaYF_4$ either when doped with Er^{3+} or co-doped with Yb^{3+}-Er^{3+}. $NaYF_4$ can exist in two crystal structures, a cubic α-phase and a hexagonal β-phase. The β-phase has been shown to yield higher photoluminescent emission than the α-phase, so it is desirable to fabricate β-$NaYF_4$ whilst keeping the cubic impurity levels to a minimum [114]. In 2004 Kramer reported a widely replicated synthesis technique to produce pure β-$NaYF_4$ via a hydrothermal method with an optimised preparation temperature of 600°C [115]. Many other methods have been proposed to synthesise rare earth ion doped compounds including: solid-state reaction, combustion synthesis, template technology, solvothermal synthesis, glass melting, thermal decomposition, co-precipitation, sol-gel method, aqueous precipitation, thermal growth, pulsed laser deposition, vertical Bridgman and an ion-exchange process [75]. Considerations will have to be made as to which are more cost effective and environmentally friendly

(especially with regards to the maximum temperature required), if commercial production was to go ahead.

Furthermore, when measuring the ePLQY or iPLQY, the spectral broadness of the excitation source can have a noticeable effect. Arnaoutakis et al prepared Er^{3+} doped $NaYF_4$ and by using relevant filters and a quartz tungsten halogen lamp were able to observe an increase in iPLQY from 1.61% to 4.27% upon widening the incoming spectral range from 1500-1550 nm to 1400-1600 nm [89]. MacDougall et al also investigated this area and found the iPLQY of Er^{3+} doped β-$NaYF_4$ rose to 16.2% from 8.7% when broadening the excitation bandwidth from 12 nm to 61 nm [116]. Despite the success of $NaYF_4$, alternative host lattices have been studied and proposed for UC-PV applications. ZBLAN, a glass containing fluorides of Zr, Ba, Ln, Al and Na, has attained an ePLQY of 12.7% when doped with Er^{3+} [117]. Other compounds that have attracted interest are BaY_2F_8 and Gd_2O_2S which have given ePLQYs of 9.5% and 12.7% when doped with 30% Er^{3+} and 10% Er^{3+} respectively [118, 119]. Even with their lower ePLQYs, oxides and oxyfluorides may still be viable options due to their stability. In a recent study by Markose et al, Er^{3+} and Yb^{3+} ions were co-doped into Y_2O_3, YOF and YF_3. YF_3 demonstrated the most efficient UC process but YOF (the second highest performing lattice) was deemed the most suitable for commercial applications due to its excellent chemical and thermal stability [120].

Host lattices for DC and LDS applications tend to be similar in composition as those used for UC; $NaYF_4$, $LiYF_4$, metal oxides, phosphates, oxyfluorides and various glasses have been studied extensively. De la Mora et al state that host materials must exhibit high transmittance, photo-stability, excitation energy, absorption strength, chemical and thermal stability as well as low scattering [98]. It is further argued that host materials should be highly crystalline with few defects and impurities as this prevents energy migration that leads to parasitic non-radiative recombination. In addition, Huang et al suggest for LDS it is particularly important to have large Stokes shifts, i.e. a minimal overlap between the excitation and emission spectra, in order to minimise the self-absorption losses within the material [75]. DC and LDS also have an advantage over UC in that because they only involve the absorption of a single incoming photon, they are linear processes in respect to the iPLQY formula with n = 1, resulting in more viability to increase PV efficiency at lower light concentrations [83]. The iPLQYs

of DC materials have been theoretically calculated (by analysing the energy transfer between states) to be in excess of 150%, in cases approaching almost 200% for Eu^{3+} doped $LiGdF_4$ [97]. However, measuring the ePLQY, of greater relevance for practical PV applications, experimentally is more challenging. Although in 2012, Fan et al were able to record for the first time an ePLQY of over 100% for Er^{3+} and Yb^{3+} co-doped La_2O_2S using an integrating sphere. LDS ePLQYs are typically over 80% for the best rare earth ion containing compounds and 50-65% for QDs [121]. Dyes have the most promising PLQYs at around 90% but issues with their stability are a concern for their long term exposure [122].

The doping ratio of an ion in the host lattice is another crucial factor in determining the efficiency of photoluminescent processes. If the concentration is too low, then the distance between ions will be high and insufficient photons absorbed along with a low energy transfer rate (and hence less undergo spectral conversion), whereas if the concentration is too high, cross-relaxation processes between ions will dominate to hamper the efficiency [123]. Hence it is necessary to find the appropriate balance, typically around 25% (by mole) for Er^{3+} doped $NaYF_4$ as derived by Ivaturi et al [124] and varying for differently composed materials. For co-doped rare earth ion $NaYF_4$, the sensitizer Yb^{3+} ion is typically doped at a level of 18% by mole and the emitter Er^{3+} ion at 2%. In an optimisation study for a different host material, Tikhomirov et al prepared Yb^{3+} and Er^{3+} co-doped oxyfluoride glasses in many distinct doping ratios which exhibited UC and DC behaviours under 980 and 380 nm excitation respectively; it was found the 1.5 % Er^{3+} and 4.5% Yb^{3+} displayed the strongest UC emission and 1 % Er^{3+} and 4% Yb^{3+} the most intense DC [125]. In addition, Eu^{3+} doped $LiGdF_4$ phosphors were recently found to have an optimal molar concentration of 35% to maximise DC emission [126].

The optimal doping level also changes with increased light concentration; Fischer et al have studied the relationship between incident excitation power density and Er^{3+} doping concentration in the widely cited lattices, $NaYF_4$ and Gd_2O_2S [127]. Through calculations and experiment, it was observed the optimum ion doping level decreases as light concentration increases. The particle size and shape can further determine photoluminescent properties in rare earth ion doped compounds. Kramer et al's particles were typically 1-3 μm crystals, sometimes forming aggregates which could be broken up via mortar and pestle,

whereas in recent years spectral conversion particles have been made at much smaller scales (particularly for application to emerging PV cells). In 2009, Lim et al investigated the dependence of particle size and shape on luminescent behaviour for Yb^{3+} and Er^{3+} co-doped $NaYF_4$ nanocrystals between 10 and 130 nm in size and of different shapes (either spherical or rod). It was found that the smaller particles exhibited greatly decreased luminescent intensity and the surface area to volume ratios affected the level of green as compared to red emission; contrary to previous studies, a small particle size or high surface area to volume ratio resulted in higher rates of green emission [128]. Li et al have reported a technique for the same material which controls the size and shape of the particles during synthesis by adjusting the precursor and solvent ratios respectively [129]. Despite higher particle size benefiting the PLQY, at sizes over 100 nm unwanted optical effects like scattering can occur, reducing the amount of spectral conversion emission that will reach the solar cell [130]. On the contrary, for very small DC particles, an increase in emission intensity was observed for particles between 15-40 nm compared to those of size 150 nm, so it is important to determine the exact morphology-luminescence relationship for each potential spectral conversion material [131]. Furthermore, when applying these materials into the devices themselves (as happens with emerging PV) particle size and agglomerations must be kept to a minimal level to avoid interfering with the charge transport properties, and as shall be presented in 2.8, nanoscale phenomena can be utilised to benefit the overall spectral conversion process.

Finally, the compounds usually exist in powder form so need to be embedded within a complex, in order to form a layer which can be applied to a solar cell. In choosing this host complex, it is vital that the material is transparent to the areas of the spectrum that the spectral conversion material emits in. Polyfluorocyclobutane (PFCB) has been a popular choice for UC studies involving $NaYF_4$ due to its similar refractive index to the phosphor, minimising scattering losses, and high transparency to NIR photons. As the doping level of the rare earth ion within the compound must be optimised, so should the ratio of the spectral conversion material to the host matrix. Ivaturi et al showed the optimal ratio of Er^{3+} doped $NaYF_4$ to PCFB as 84.9% by weight [124]. Likewise for DC and LDS, transparent polymers have been utilised such as

polymethylmethacrylate (PMMA) and ethylene vinyl acetate (EVA), as well as silicates and silica nitrides with dual functional anti-reflective properties [132, 133]. Innovative optical materials for LSC fabrication will be presented in 2.7.2. The thickness of the layer plays a role too and Boccolini et al attributed re-absorption as a source of loss should this value be un-optimised and carried out simulations to determine the ideal depth for maximum emission of UC photons [134]. The same group developed an optical model to determine the most suitable thickness for a DC layer which was validated by tests on Ce^{3+} and Yb^{3+} co-doped borate glass [134]. Moreover, Lipovšek et al produced a similar work for LDS layers using 3D ray tracing and Mie scattering theory to predict the maximum J_{SC} gains on an OSC before experimental confirmation, accounting for the following LDS layer parameters: layer thickness, phosphor particle size, distribution and concentration by volume [135]. Thickness may also be varied by changing the spin speed if applying with a spin coater or by modifying the mesh size if screen printing (two common methods of applying films, which will be discussed later in this thesis).

All of the aforementioned criteria affect the performance of the spectral conversion process. However, absorption coefficients and excitation spectra must be improved and broadened to maximise the ePLQY and impact on solar cells. There are several emerging methods at the nanoscale to rectify these material limitations which will be presented in 2.8 and the optimisation of the spectral conversion materials continues to feature alongside their application to solar cells in the most recent studies.

2.4 State-of-the-art Upconversion Materials

Here results from up-to-date and innovative studies of UC materials applied to various PV technologies are reported.

2.4.1 Upconversion for Silicon PV

Since Shalav's group's work in 2006-7 there has been a rapid growth in the effectiveness of UC layers applied to silicon PV cells. In 2011, Goldschmidt et al applied 20% Er^{3+} doped $NaYF_4$ to a silicon solar cell and when characterised under broadband 1460-1600 nm radiation, the UC process efficiency was 1.03% [52]. The corresponding relative increase in power conversion efficiency under ambient sunlight would only be a paltry 0.014% which was deemed far too low to

have a significant impact. However, by 2013 relative efficiency improvements of up to 0.16% were found to be viable through the application of 25% Er^{3+} doped $NaYF_4$ to a silicon device, following a J_{SC} of 4.03 mA/cm^2 that had been observed under 1450-1600 nm illumination [136]. In addition, the group developed a method to calculate the spectral mismatch which allows the quantum yield at different solar concentrations to be determined. Results from 2015 demonstrate further progress still; 30% Er^{3+} doped BaY_2F_8 has attained a J_{SC} improvement of (17.2 ± 3.0) mA/cm^2 at 95 suns [118]. This is equal to a relative enhancement of (0.55 ± 0.14) %, a 35-fold increase on the values reported in 2011. In 2018, the same group tested bifacial c-Si cells combined with UC layers of either 10% Er^{3+} doped Gd_2O_2S or 25% Er^{3+} doped $NaYF_4$ to achieve J_{SC} enhancements of 8.2 and 9.4 mA/cm^2 respectively under 94 sun illumination. Although not as large as the increase recorded for BaY_2F_8 this still shows promising progress for a lower light concentration level. Excitingly, the devices were also characterised when exposed to real sunlight conditions (the first time ever for a UC-PV system) where they showed results consistent with those predicted from the solar simulator and spectral mismatch calculations [137]. In all these experiments the UC layer was placed beneath a bifacial PV cell as outlined in Figure 14 in 1.4.1. However, occasionally the UC particles have been placed on top of the device for added beneficial anti-reflective properties. This was the case for Chen et al, who added Er^{3+}-Yb^{3+} and Ho^{3+}-Yb^{3+} doped $La_2Mo_2O_9$ layers on top of the solar cell [138]. Despite a low UC contribution, increases in efficiency between 1.5% and 2.7% were observed due to the layer's anti-reflective properties.

Due to their higher band gap, it is predicted that a-Si solar cells have greater potential efficiency gains to be realised than their c-Si counterparts from UC. In 2010, an enhancement in J_{SC} of 0.01 mA/cm^2 was observed under 980 nm illumination by de Wild et al for an a-Si:H solar cell that contained $NaYF_4$ doped with 18% Yb^{3+} and 2% Er^{3+} on its rear face [139]. This value was only twice the background dark current, so again not deemed to be of significance. However, suggestions were made on how to improve the efficiency by reducing channels of energy loss in the system; the biggest factor was the poor response of the cell to rear-side illumination from radiation that had undergone UC. In a subsequent investigation, Qu et al synthesised rare earth co-doped β-$NaYF_4$ phosphors with the following compositions: 20% Yb^{3+}, 1 % Er^{3+}; 25% Yb^{3+}, 1 % Ho^{3+}; and 60%

Yb^{3+}, 0.5 % Tm^{3+} and applied them to a-Si:H solar cells, either as a solid or colloid slice [140]. The solid slice Er^{3+} ion containing device performed the best, recording a J_{SC} enhancement of 0.1 mA/cm^2 under monochromatic 980 nm illumination and an efficiency improvement of 7.3% under AM 1.5 G relative to the reference cell without any additional layers. The group attributed these results to an improved scattering function and enhanced absorption in the NIR region; to assess the impact of UC processes alone, a $NaYF_4$ layer without any rare earth ions was applied and a relative increase in efficiency of 6.3% was observed.

Moreover in 2015, Chen's group reported an improvement over $NaYF_4$ as a host lattice for high band gap PV applications by using 28% Er^{3+} doped $BaCl_2$ instead. Unlike Yb^{3+}, Er^{3+} co-doped $NaYF_4$ which is often only excited at 980 nm illumination, this material was able to utilise radiation at two distinct peaks, 808 and 980 nm [141]. Upon broadband excitation (>800 nm), its emission was intense across 410-667 nm, demonstrating substantial potential for a-Si solar cells. Using the same material, the J_{SC} of an a-Si:H solar cell under simulated NIR sunlight increased to 0.6 mA/cm^2 [142]. Meanwhile, Jia et al have also used Ho^{3+} or Pr^{3+} doped $BaCl_2$ to attain respective J_{SC} measurements of 0.25 mA/cm^2 and 0.16 mA/cm^2 for an a-Si:H device under broadband >800 nm illumination [143]. Conversely, Er^{3+} doped LaF_3 embedded in an oxyfluoride ceramic has shown a remarkable 1.72 mA/cm^2 J_{SC} under tri-wavelength simultaneous excitation at 1530, 980 and 808 nm [144]. This value was 1.77 times greater than the sum of the J_{SC} measurements obtained for monochromatic illumination at each of these wavelengths, highlighting the synergistic nature of multi-wavelength excitation.

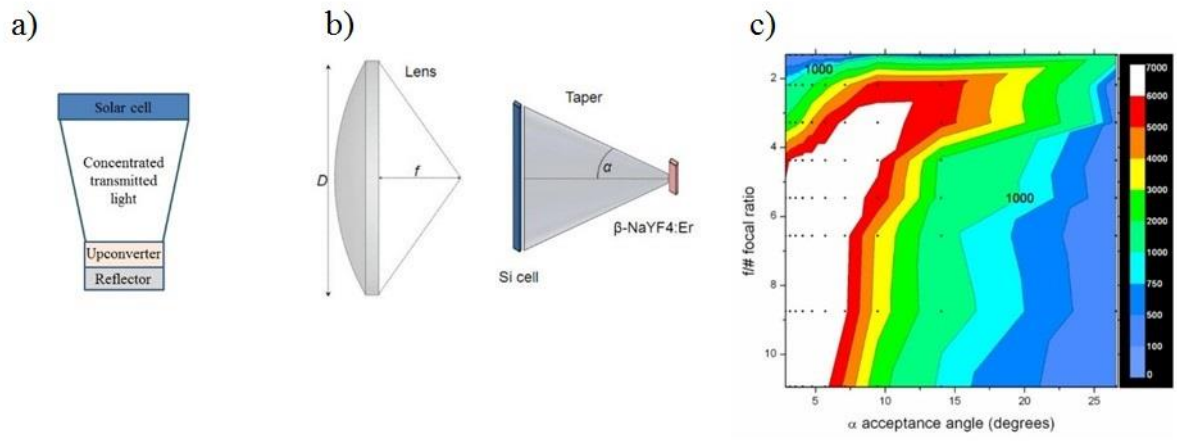

Figure 26: Two ways concentrating optics can be integrated with UC: a) cross-section of a single cell UC-CPV module in which a CPC is placed between the PV cell and UC layer in order to increase the intensity of the light that reaches it, b) the schematic of a modelled CPV system in which the parameters α (acceptance angle) and f/D (focal ratio) are varied [89] and c) simulations show high concentrations of 1000 suns can be achieved at the UC layer in this set up.

Optical concentrators, as outlined in 1.2.2, have been proposed for deployment in UC-PV systems. This has the advantage of increasing the effectiveness of UC due to its non-linear relationship with light intensity. A hypothetical design was proposed by Goldschmidt et al in 2008, which was predicted to raise the efficiency of a bifacial silicon solar cell from 23% to 25% [145]. Fischer et al were able to use a Fresnel lens to concentrate light to high levels onto an Er^{3+} doped $NaYF_4$ layer. At an intensity of 210 suns, J_{SC} increased by 13.1 mA/cm^2 and relative efficiency by 0.19% [146]. One issue that needs addressing is the variation in optimal solar concentration between the PV cell and the UC layer to maximise system performance; integrated optics could be one way to tackle this imbalance. Optical fibres in combination with dielectric tapers are components which could reach light concentrations of 2000 suns at specified wavelengths relevant to a given PV system [147]. This method has been used to achieve increased response in a UC-PV system under sub band gap illumination and it was shown the light intensities at the cell's surface and UC layer could be independently optimised [148]. Arnaoutakis et al built on this concept by fabricating a system with compound parabolic concentrators placed between a bifacial silicon solar cell and UC layers, as outlined in Figure 26 [149]. An EQE of 1.80% upon excitation by a 1523 nm source at 0.024 W/cm^2 power density was attained for the system with the integrated optics compared to 1.33% for the PV cell-UC layer without concentrators (these values correspond to NEQEs of 0.75 cm^2/W and

0.54 cm^2/W). Geometrical optical simulations based on ray tracing and Monte Carlo techniques have been carried out for UC-CPV set ups to determine how to achieve maximum concentration of light. Arnaoutakis' group modelled the design shown in the Figure 26 and showed a concentration of 6000 suns was realisable for acceptance angles < 10° and focal ratio greater than 3 [89]; intensities of this magnitude would result in highly effective UC layers and higher PV performance (provided the solar cell was thermally isolated). The optimal doping levels of rare earth ions with regards to variation in light intensity as per Fischer et al's study, should also be considered for UC-CPV systems [127].

In 2014, Wang's group showed UC with a process efficiency of 16% could be realised through the thermal radiation method discussed in 1.4.1. Yb^{3+} doped ZrO_2 was selected for its excellent thermal conductivity, high melting point and strong infrared absorption properties [80]. In contrast to UC via other mechanisms, multi-phonon relaxation becomes a desirable process since it leads to heat being transferred to the lattice, raising its temperature. The sample powder was heated to 2850 K under illumination at 976 nm by a 570 W/cm^2 laser beam and Wien's displacement law along with considered conduction losses were used to derive the efficiency. Concentrated white light was also used in order to determine the effect on solar cell performance and compare with the commonly used Er^{3+} doped $NaYF_4$; the fluoride yielded greater improvements at low irradiances whereas the oxide achieved better results at the highest light concentrations. When designing physical thermal UC-PV systems, it is of vital importance to thermally isolate the solar cell from the radiation source due to the decreased efficiency that accompanies an increase in PV temperature. One solution could be to place the optical concentrator beneath a bifacial device, so that transmitted photons could be focussed onto a thermal UC layer, then redirected back towards the cell. Boriskina and Chen envisaged a thermal UC-PV platform with angular selectivity through utilising nanomaterials or a small aperture cavity [150] and other designs (cf. Figure 27). This system could have a maximum theoretical UC efficiency of 73%, corresponding to a silicon PV efficiency of 45%. In 2015, an a-Si cell showed a 1 mA/cm^2 photocurrent under 808-1064 nm illumination by using thermal UC material $CeVO_4$, showing the immense potential of this approach to wide band gap solar technologies [151].

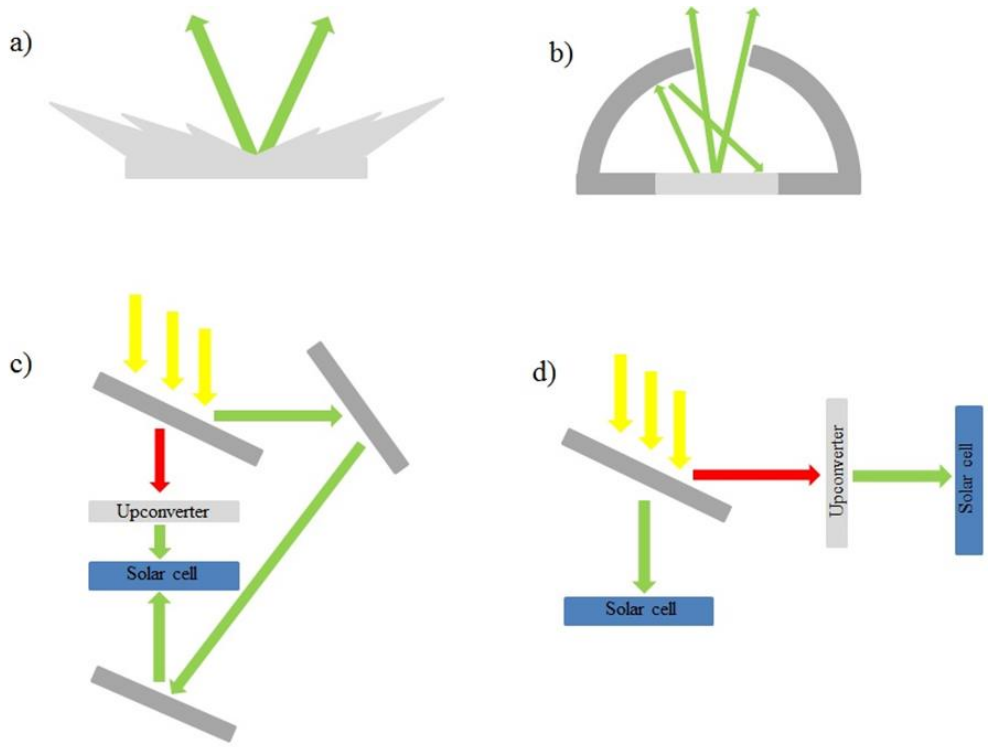

Figure 27: Designs of potential UC via thermal radiation systems: a) angular selectivity by surface nano-patterning, b) enclosing the upconverter into a reflective cavity with small aperture, c) geometrical and spectral splitting of sunlight onto a cell and d) same concept as c) but with two cells. Modified from [150].

2.4.2 Upconversion for Emerging PV

UC has increasingly been applied to third generation or emerging PV technologies. This includes DSSCs, OSCs, QDSCs and PSCs. These cells are in a strong position to benefit from UC due to their generally high band gap energies (like a-Si) and nanoscale thin film structure which allows for facile incorporation of luminescent particles.

DSSCs typically use Ru-carboxyl group based dyes (such as N-719) that fail to absorb photons effectively when their wavelength is greater than 700 nm [152]. This means UC can enhance DSSC performance by allowing more of the spectrum to be captured by the dye. In a first attempt at this approach, Shan and Demopoulos added Yb^{3+}-Er^{3+} co-doped LaF_3 into the TiO_2 electron transport layer of a DSSC [153]. Despite an increased response at NIR wavelengths, the overall efficiency of the cell declined because of increased charge carrier recombination at the electrode interfaces. In 2010, Xie's group achieved better outcomes by fabricating DSSCs in which the Yb^{3+}-Er^{3+} ions were directly doped into the TiO_2 particles that make up one layer of the device [154]. This led to incident 980 nm light undergoing UC and being converted into 510-700 nm

wavelengths which could be used by the DSSC to generate electricity. Under AM 1.5 G solar simulated radiation, an efficiency of 7.28% was recorded for the rare earth doped TiO_2 cell and 6.41% for a reference DSSC without any added ions, thus, a relative efficiency increase of 13.6% was observed. The ratio of rare earth ion to TiO_2 was optimised at 1:3 and the incorporation of these impurities resulted in another advantage by acting as a p-type dopant which raised the TiO_2 Fermi level and the redox potential of the electrolyte, hence producing a higher DSSC voltage. Advances in nanotechnology have allowed for new methods to enhance UC. In 2013, Ramasamy and Kim prepared a novel rear reflecting structure utilising Ag reflectors and Fe^{3+} doped β-$NaGdF_4$: Yb^{3+} - Er^{3+} UC nanoparticles (UCNPs) [155]. The addition of Fe^{3+} was found to increase the UC emission 30-fold and the dual functional Ag further enhanced the UC process by increased scattering and surface-coupled plasmon emission (this phenomenon will be further explored in section 2.8.4). In 2017, Han et al achieved a 27% relative increase in DSSC efficiency through the use of Er^{3+} - Yb^{3+} CeO_2 spheres as UCNPs, highlighting the progress that has been made in this field since 2010 [156].

OSCs contain conjugated polymers like polyphenylenevinylene (PPV) derivatives or poly [3-hexylthiophene] (P3HT) to act as electron donors along with a fullerene derivative, Phenyl-C_{61}-butyric acid methyl ester (PCBM), electron acceptor [157]. The EQE of OSCs is negligible beyond 800 nm, so UC could utilise higher wavelengths to generate more current and improve the device efficiency. In 2012, Wang et al added a layer consisting of Yb^{3+} - Er^{3+} co-doped MoO_3 under the photoactive P3HT-PCBM region of the cell and a mild increase of <1% in J_{SC} was detected at an irradiance level of 1 sun [158]. To result in better J_{SC} gains the following recommendations were made: higher ePLQY of rare earth doped compound, deployment of light trapping or photon management and thicker UC films. At the same time, Adikaari et al alternatively applied Ho^{3+}-Yb^{3+} co-doped Y_2BaZnO_5 layers onto the front and rear of OSCs [159]. As expected, the device with the UC layer at its rear performed best, achieving a J_{SC} of 0.016 mA/cm^2 and EQE of 0.0052% under a 986 nm excitation source of intensity 0.39 W/m^2. Although this result was very small, calculations showed a wider excitation spectrum and more transparent electrodes could lead to performance enhancements on par with those achieved for a-Si and an overall absolute power

conversion efficiency increase of 0.45%. Two years later, Chen et al utilised $Yb3^{+}$-Er^{3+} doped β-$NaYF_4$ UC particles in a PMMA matrix and a silver reflector to improve the J_{SC} of an OSC by 22.2% [160]. However, the overwhelming majority of this additional current was generated by a greater amount of transmitted visible light being reflected back towards the cell; it was estimated only 1.6% of the J_{SC} enhancement was due to UC and poor performance under low solar concentrations meant it was unlikely to have a major impact on OSC design until further progress is made. Most recently in 2018, Wang et al have added $NaYF_4$: Yb^{3+}, Er^{3+} particles into a P3HT: PCMB type OSC and reported enhanced charge transport and J_{SC} measurements of 8.3% [161].

UC via TTA could be an alternative to rare earth ion doped compounds in OSCs with Zhao et al cataloguing several organometallic complexes with potential for use as sensitizers and acceptors in a TTA process [162]. Schulze et al explored this concept with tests on three solar cells (two OSCs of different acceptor-donor polymer pairs and one a-Si device) after developing theoretical models. Proof-of-principle 0.2% J_{SC} improvements were achieved but needed to be 2 to 3 orders of magnitude higher to be meaningful for those devices [163]. Despite these limitations, TTA molecules might still prove to be superior to rare earth ion compounds due to their higher PLQYs at lower irradiances. To realise this, the concentration of sensitizers must be optimised which was practically difficult in their organic solvent; the incorporation of the molecules into a solid-state material such as nanoparticles or a polymer film might be one avenue to this outcome.

QDSCs are yet another emerging PV technology that stand to benefit from UC. A fascinating property of QDs that makes them exciting for use in solar PV is that their absorption properties are dependent on size. This means it is possible to synthesise QDs so that they are fine tuned to absorb at specific wavelengths. Nevertheless, QDSCs will still have a limited absorption range and commonly are limited to utilising photons of wavelength less than 700 nm [164]. There had been few instances in the literature of UC studies involving QDSCs until 2014, when Wang et al synthesised and applied a Tm^{3+} - Yb^{3+} - Er^{3+} tri-doped $NaYF_4$ phosphor into the photo-anode of a CdS/CdSe QDSC through annealing [165]. This device achieved a power conversion efficiency of 4.37%, corresponding to relative efficiency and J_{SC} increases of 20% and 17.6% respectively. It was also noted the annealing treatment contributed to this positive result by removing

defects that cause charge carrier recombination in the device. Further efficiency improvements were noted in 2017 by Ramachari et al who incorporated Yb^{3+} - Er^{3+} co-doped ZrO_2 into a QDSC, resulting in a relative power conversion efficiency of 55%, and Sun et al who added Mn^{2+}-Yb^{3+} - Er^{3+} tri-doped $NaYF_4$ into the photoanode of a QDSC for a 42.6% relative PCE enhancement [166, 167].

PSCs based on the crystal structure known as perovskite have shown a rapid increase in efficiency as outlined in 1.2.1. Even more excitingly, their higher stability and performance compared to DSSCs makes them prime candidates for commercial deployment in the near future with $41 million invested in Oxford PV in early 2019 to bring the technology ready for market [168, 169]. The PSC cell absorption profile is limited to photons of wavelength below 800 nm, so like other emerging technologies can benefit from UC applications to harness a wider range of the incoming solar spectrum. This was proposed by Wang in 2014 [165] and in recent years UC materials have successfully been incorporated into PSCs to improve device performance but there have been different methods used when adding these materials into the system. For example, Chen et al placed a highly transmitting to visible wavelengths $LiYF_4$: Yb^{3+}, Er^{3+} single crystal on top of a PSC to increase the relative power conversion efficiency by 7.9% under 7-8 suns [170]. On the other hand, He et al, Roh et al and Wang et al all added UCNPs directly into the TiO_2 mesoporous layer of the electrode, achieving relative power conversion efficiency increases of 6.0%, 13.7% and 20.8% respectively. Similarly, as with DSSC investigations, there could be additional benefits from the incorporation of nanoparticles inside the photoactive device layers, such as helping ensure quality perovskite crystal growth and structure [171-173]. A summary of the best UC materials and their impact on solar cells is provided in Table 3.

UC material	$\lambda_{excitation}$ (nm)	$\lambda_{emission}$ (nm)	Solar cell	Device response	Ref
20% Er^{3+} doped $NaYF_4$	1460-1600	980	c-Si	+0.69 mA/cm^2 J_{SC} under 732 suns	[52]
25% Er^{3+} doped $NaYF_4$	1450-1600	980	c-Si	+4.03 mA/cm^2 J_{SC} under 77 suns	[136]
25% Er^{3+} doped $NaYF_4$	1450-1600	980, 805, 655, 540	c-Si	+13.1 mA/cm^2 J_{SC} under 210 suns	[146]
30% Er^{3+} doped BaY_2F_8	1493	1000	c-Si	+17.2 mA/cm^2 J_{SC} under 95 suns	[118]
25% Er^{3+} doped $NaYF_4$	1450-1600	980, 830, 665, 550	c-Si	+9.4 mA/cm^2 J_{SC} under 94 suns (real sunlight)	[137]
10% Er^{3+} doped Gd_2O_2S	1450-1600	980, 830, 665, 550	c-Si	+8.2 mA/cm^2 J_{SC} under 94 suns (real sunlight)	[137]
25% Er^{3+} doped $NaYF_4$	1523	980	c-Si	1.33% EQE (without optic) and 1.80% EQE (with optic) under 0.024 W/cm^2 laser	[149]
28% Er^{3+} doped $BaCl_2$	808, 980	667, 546, 530, 496, 455, 410	a-Si:H	+0.6 mA/cm^2 J_{SC} under bi-wavelength 70 and 100 mW lasers	[142]
5% Pr^{3+} doped $BaCl_2$	2190, 2000, 1596, 1460, 980, 850	636, 610, 537, 470	a-Si:H	+0.16 mA/cm^2 J_{SC} under concentrated broadband >800 nm illumination	[143]

15% Ho^{3+} doped $BaCl_2$	1610, 1157, 900	658, 546, 489	a-Si:H	+0.25 mA/cm^2 J_{SC} under concentrated broadband >800 nm illumination	[143]
3% Er^{3+} doped LaF_3 in oxyfluoride ceramic	808, 980, 1530	657, 542	a-Si:H	+1.72 mA/cm^2 J_{SC} under tri-wavelength 1400, 1200 and 800 W/cm^2 lasers	[144]
$CeVO_4$ via thermal UC	1064, 980, 808	750-700	a-Si:H	+0.91 mA/cm^2 J_{SC} under 831 W/cm^2	[151]
20% Yb^{3+} - 1% Er^{3+} co-doped $NaYF_4$	980	650, 536, 518	a-Si:H	+1.74 mA/cm^2 J_{SC} and +0.41% PCE under AM 1.5 G	[140]
Yb^{3+} - Er^{3+} co-doped TiO_2 (25% w/w)	980	700-510	DSSC	+0.87% PCE under AM 1.5	[154]
0.7% Yb^{3+} - 2.9% Er^{3+} co-doped CeO_2	980	525-680	DSSC	+1.54% PCE under AM 1.5	[156]
20% Yb^{3+} - 2% Er^{3+} co-doped $NaYF_4$	975	655, 540	OSC	+0.46% PCE under AM 1.5 G	[160]
Yb^{3+} - Er^{3+} co-doped $NaYF_4$ (0.5% w/w in P3HT:PCBM)	980	550-750	OSC	+0.44% PCE under AM 1.5 G and 980 nm laser	[161]
0.2% Tm^{3+} - 20% Yb^{3+} - 1.5% Er^{3+} tri-doped $NaYF_4$	980	650, 540, 520, 475, 400	QDSC	+2.15 mA/cm^2 J_{SC} and +0.73% PCE (+17.6% and 20% relative increases) under AM 1.5 G	[165]
1% Yb^{3+} - 1% Er^{3+} co-doped ZrO_2	970	725-500	QDSC	+1.06% PCE (+55% relative increase) under 0.1 W/cm^2	[166]

Mn^{2+}-Yb^{3+} - Er^{3+} tri-doped $NaYF_4$ (8% w/w in TiO_2)	980	660, 540, 520	QDSC	+6.61 mA/cm^2 J_{SC} and +1.42% PCE (+45.1% and +42.7% relative increases) under AM 1.5 G	[167]
2% Yb^{3+} - 1% Er^{3+} co-doped $LiYF_4$	1540, 980	700-500	PSC	+0.87% PCE (+7.9% relative increase) under 7-8 suns	[170]
20% Yb^{3+} - 2% Er^{3+} co-doped $NaYF_4$	980	655, 543, 523, 408	PSC	+1.9% PCE (+13.7% relative increase) under AM 1.5 G	[172]
6% Yb^{3+} - 13% Er^{3+} co-doped TiO_2 nanorod arrays	980	512-680	PSC	+2.6% PCE (+20.8% relative increase) under AM 1.5 G	[173]

Table 3: Summary of the UC materials used, and PV device performance enhancements noted in recent studies on various solar cell technologies.

2.5 State-of-the-art Downconversion Materials

Whereas UC allows for the harnessing of sub band gap photons, DC can lead to better PV performance following illumination by short wavelength photons. In c-Si solar cells, the losses due to thermalisation from high energy photons are greater than those for non-absorption of sub band gap photons. Many emerging solar cell technologies also suffer from UV sensitivity which can degrade their performance over time, so DC could provide dual benefits for their efficacy.

As well as the ions listed in 2.1, DC may be aided by the use of other species to increase the absorption cross section and broaden the excitation spectrum. These often come in the form of divalent (2+) rare earth ions such as Eu^{2+} or Yb^{2+} and occasionally transition metal ions like Mn^{2+} [174]. Tai et al have shown Eu^{2+} to behave as an effective energy sensitizer for Yb^{3+} in a $SrAl_2O_4$ host lattice, attaining a 147.3% ePLQY under a 450 W Xe lamp with a broad range of 250-450 nm radiation being absorbed and emitted in the NIR region, where it could be better utilised by a c-Si solar cell [99].

2.5.1 Downconversion for Silicon PV

Before 2015, there were few instances where DC-PV systems had been fabricated and their electrical performance characterised. This was to change when in that year, Gonzalez-Perez et al applied a Eu^{3+} doped complex in PMMA to a c-Si solar cell via spin coating or tape casting [175]. The EQE of the device increased by 5.8% at 280 nm as a result of the strong excitation band from 250-360 nm with emission at 615 nm. The film also possessed a high thermal stability, meaning it could be facilely introduced to the silicon PV module assembly and potentially in CPV as well. Meanwhile, Dumont et al fabricated a DC layer made from Tb^{3+} - Yb^{3+} co-doped Silicon-Nitride by magnetron co-sputtering [133]. After characterising the material, they noted their novel optimisation approach yielded improved results compared to previous works; at 325 nm illumination there was efficient 980 nm emission and the coating demonstrated anti-reflective properties, making it an ideal DC layer candidate. Moreover, Florêncio et al have reported a 7% relative increase in the efficiency of a commercial silicon cell through the use of their Tb^{3+} - Yb^{3+} co-doped tellurite glass, compared to that measured for glass without doping [176]. Then in 2018, Li et al reported c-Si solar cells topped with PMMA mixed with Ce^{3+}- Yb^{3+} co-doped $Y_3Al_5O_{12}$ applied via spin coating demonstrating enhanced relative PCEs of 4.86% and 6.04% at illumination levels of 1 sun and 4 suns respectively. The increased performance at higher light intensity was attributed to higher temperatures leading to more phonons in the lattice and ultimately more efficient energy transfer and DC emission [177].

2.5.2 Downconversion for Emerging PV

DC materials have also been utilised within emerging PV technologies. In a similar vein to 2.4.2, these particles have often been incorporated into the active layers of the device. Yao et al have added Eu^{3+}-Dy^{3+} co-doped ZnO into the TiO_2 photoanode of a DSSC along with graphene loading which reduced recombination and interfacial resistance [178]. They observed a 4.8% power conversion efficiency for the best performing device with a Eu^{3+}-Dy^{3+}: ZnO doping level of 1.75% w/w, corresponding to a relative improvement of 245% compared to the pure TiO_2 device and 105% to the TiO_2 and graphene containing cell. At the same time, Sun et al added Eu, Dy co-doped $Sr_4Al_{14}O_{25}$ into the TiO_2 photoanode of a CdS QDSC, enhancing the power conversion efficiency by 37% relative to a control cell (of 1.02% power conversion efficiency) through DC and

beneficial scattering processes [179]. Then in 2016, Hou et al introduced a Eu^{3+} doped $ZnGa_2O_4$ nanophosphor into the TiO_2 layer of a PSC [180]. This resulted in an increased J_{SC} of 4.08 mA/cm^2 and 34.4% higher relative power conversion efficiency because of better light harvesting. Alternatively, in 2019, Jia et al synthesised Eu^{3+}: $NaYF_4$ nanocrystals and applied them to the non-conducting front side of the conductive glass of a PSC [181]. This led to a relative efficiency gain of 17.7% and J_{SC} improvement of 2.50 mA/cm^2 and additionally, the samples with the nanocrystals exhibited a smaller I-V hysteresis than was observed in the control devices. The best DC materials are summarised in Table 4.

DC material	λ excitation (nm)	λ emission (nm)	Solar cell	Device response	Ref
Tb^{3+} - Yb^{3+} in silicon nitride matrix	325	980	c-Si	N/A	[133]
Eu^{3+} containing aromatic complex in PMMA	250-360	665	c-Si	+5.8% EQE under 100W Xe lamp	[175]
Tb^{3+} - Yb^{3+} co-doped tellurite glass	355, 482	548, 980	c-Si	+7% relative PCE under 0.1 W/cm^2	[176]
Ce^{3+}- Yb^{3+} co-doped $Y_3Al_5O_{12}$	460	550, 1030	c-Si	+4.86% and +6.04% relative PCE under 0.1 and 0.4 W/cm^2	[177]
Eu^{3+} - Dy^{3+} co-doped ZnO (alongside graphene loading)	338, 394	394, 458, 483, 575, 593, 611	DSSC	+6.06 mA/cm^2 and +3.18% PCE (212% and 245% relative increases) under 0.1 W/cm^2	[178]

Eu^{2+} - Dy^{3+} co-doped $Sr_4Al_{14}O_{25}$	300-450	450-500	QDSC	+2.62 mA/cm^2 and +0.38% PCE (+35.5% and +37.3% relative increases)	[179]
Eu^{3+} doped $ZnGa_2O_4$	380-500	450-720	PSC	+3.48 mA/cm^2 and +3.67% PCE (17.2% and 34.4% relative increases) under AM 1.5 G	[180]
Eu^{3+} doped $NaYF_4$	325, 375	615, 700	PSC	+2.50 mA/cm^2 and +3% PCE (+12.1% and +17.7% relative increases) under AM 1.5	[181]

Table 4: Summary of the DC materials used, and PV device performance enhancements noted in recent studies on various solar cell technologies.

2.6 State-of-the-art Luminescent Downshifting Materials

LDS materials have been deployed to improve the efficiency of solar cells, especially in second generation thin film technologies such as CdTe and CIGS that have poor EQEs when under illumination by UV or blue light. Simple analytical optical models have been produced by Rothemund et al to assess the potential effectiveness of LDS layers and theoretical EQE enhancements attainable [182]. The materials used for LDS investigations tend to be more varied than UC and DC, where rare earth ion doped compounds dominate the literature, with more QDs and dyes having been cited. LDS materials also feature prominently in LCPV literature due to their use for LSC-PV systems and this area of knowledge shall be reviewed in depth in the following section (2.7).

2.6.1 Luminescent Downshifting for Silicon PV

An LDS layer consisting of Eu^{3+} doped gadolinium oxysulfide embedded in polyvinylpyrrolidone (PVP) was prepared by Hung and Chen for applying to a multi-crystalline-Si solar cell [183]. When exposed to ambient solar illumination conditions (AM 1.5 G) an enhanced J_{SC} of 6 mA/cm^2 and power conversion efficiency of 2.53% (24.2% relative increase) were measured compared to a bare cell; the respective improvements were 2.6 mA/cm^2 and 1.12% (9.45% relative)

compared to cell coated in pure PVP (which has anti-reflective properties), highlighting the significant impact of LDS via the rare earth ion doped compound. In addition, the material was low-cost and prepared by a simple method, two important factors for potential commercialisation. Likewise, Ho et al prepared two Eu^{2+} doped phosphor species mixed with SiO_2 and the solution was placed on top of a silicon cell via spin coating; the cell's J_{SC} increased by 19.85% and the power conversion efficiency went up by 15.97% relative to a control device due to forward scattering and broadband (512-610 nm) LDS emission [184]. As well as LDS within dual functional anti-reflective coatings or the encapsulant, it may take place within the glass covering of a solar cell. Tm^{3+} doped fluoride glasses have been investigated by Maalej et al who recorded a smaller 1.4% relative power conversion efficiency gain when the glass was placed above a silicon cell compared to an un-doped glass [185]. For scaled up commercial applications the glass would have to have a greater absorption for more LDS photons be collected by the solar cell.

2.6.2 Luminescent Downshifting for Thin-film PV

CdTe and CIGS are the prime PV beneficiaries of LDS due to their very poor spectral response to short wavelength light. In 2016, Uekert et al synthesised nanostructured organo-silicon luminophores impregnated in EVA or polyvinyl butyral (PVB) to behave as an LDS layer for a CIGS cell [186]. Under UV light, the device demonstrated a remarkably improved EQE at 360 nm from 1% to 55% and when exposed to AM 1.5 G illumination, a relative power conversion efficiency gain of 4.3%. Conversely, Ross et al doped EVA and fluorinated ethylene propylene (FEP) with an organic dye to produce two different cover sheets which could be placed on two CdTe modules [132]. The dyes used were perylene and naphtalimide fluorphores from the BASF Lumogen F series (V570, Y083, Y170 and O240). These materials demonstrated strong absorption peaks in the 375 – 520 nm range and emission peaks from 425 – 575 nm with high iPLQYs from 88-100%. The EVA-dye covered module recorded an improved J_{SC} of 9.7% and an enhancement of 5.3% was observed for the dye in FEP. QDs have also found applications in LDS-PV studies; Hodgson et al encapsulated commercially available CdS_xSe_{1-x}/ZnS QDs (supplied by Cytodiagnostics Inc) with an iPLQY of 51% and emission peak of 540 nm into a PMMA film at various doping concentrations [187]. They found the 192 µg/mm^3 layer improved the EQE

the most at short wavelengths but the 48 µg/mm^3 had the best overall J_{SC} gain of 1.7%. Furthermore, rare earth ions continue to be used in LDS studies for thin film PV. In 2016, Song et al prepared Mn^{2+}-Eu^{3+} co-doped phosphate glasses (with an excitation peak of 392 nm and emission peak of 615 nm) which were applied to CdS/CdTe cells and resulted in an improved relative power conversion efficiency of 7.14% and J_{SC} gain of 5.6% [188]. Theoretical simulations were used to support the results and it was noted that the thickness of the LDS layer is a vital parameter to be optimised since a thicker layer will lead to improved EQE at short wavelengths but higher absorption losses at longer wavelengths, so a balance must be struck to maximise the overall J_{SC}. LDS materials with high potential for applications are listed in Table 5.

LDS material	$\lambda_{excitation}$ (nm)	$\lambda_{emission}$ (nm)	Solar cell	Device response	Ref
Eu^{3+} doped Gd_2O_2S	200-350	624	c-Si	+6.47 mA/cm^2 and +2.67% PCE under 1 sun	[183]
Eu^{2+} doped phosphors in SiO_2	250-360	512, 610	c-Si	+19.85% J_{SC} and +16% relative PCE under AM 1.5 G	[184]
Tm^{3+} doped fluoride glass	355, 482	548, 980	c-Si	+1.4% relative PCE under AM 1.5 G	[185]
Organo-silicon lumiphores in EVA or PMMA	375	575	CIGS	+54% EQE at 360nm and +4.3% relative PCE under AM 1.5 G	[186]
Organic dyes in EVA and FEP	375, 475, 500, 520	425, 525, 560, 575	CdTe	+5.3% and +9.7% J_{SC} under 1.5 AM G	[132]

QDs in PMMA	300-500	540	CdTe	+1.7% PCE under AM 1.5 G	[187]
Mn^{2+} - Eu^{3+} doped phosphate glass	392	615	CdTe	+7.14% relative PCE under 0.1 W/cm^2	[188]
Dyes in PMMA	425-475	500-650	CdTe	+5% relative J_{SC} (non-concentrating) and up to +20% relative J_{SC} (concentrating) under 300 W Xenon lamp	[217]

Table 5: Summary of the LDS materials used, and PV device performance enhancements noted in recent studies on various solar cell technologies.

2.7 Luminescent Solar Concentrators

LSCs were first proposed by Weber and Lambe in 1976 [106]. Unlike the other types of solar concentrator in 1.2.2, these optical devices can modify the wavelength of the incident spectrum via LDS as well as increasing light concentration. Despite their lower concentration ratios than HCPV, LSCs have attracted much research interest and show immense potential for commercialisation due to their pleasing aesthetic and low fabrication cost [189]. This is because a concentrator which emits at the sides but is transparent through one axis can be attractively integrated with building design either as a roof light or window façade. Furthermore, the small area of active PV cell required reduces module prices and because the concentrator can utilise diffuse as well as direct solar radiation, expensive tracking mechanisms are not required [190]. Recalling the working principle of an LSC as presented in Figure 5, the fundamental efficiency limitations, loss mechanisms, state-of-the-art materials and designs, in addition to applications for BIPV will now be presented.

2.7.1 Luminescent Solar Concentrator Efficiency

The maximum theoretical efficiency of an ideal LSC-PV module was shown by Rau et al [84] to be identical to a single junction solar cell under the classical Shockley-Queisser limit as introduced in 1.3. However, real world devices have struggled to attain this performance, with 7.7% power conversion efficiency (i.e. the power output of the solar cell divided by the power of light going into the LSC), the highest reported value in the literature as of 2019 [191]. This discrepancy is due to five sources of energy loss from a physical LSC (cf. Figure 28) which include: (i) the so-called escape cone of photons which have undergone luminescence but are emitted at a solid angle that allows them to leave the LSC via an undesired surface, (ii) the non-100% luminescent quantum efficiency (LQE) of the luminescent process which is defined the same way as i-PLQY, (iii) the limited absorption cross section and excitation spectrum of the luminescent species compared to the range of photons in sunlight, (iv) re-absorption of emitted photons if the emission spectrum of the luminescent species overlaps with is absorption spectrum (called self-absorption) and (v) optical losses from surface reflectance or scattering and host matrix absorption. In a recent study Tummeltshammer et al were able to analyse each source of loss and compare them relative to each other for various LSCs; escape cone losses and non-100% quantum yields were found to be the dominant loss channels [192]. It is hoped that recent advances in dealing with these challenges will soon allow LSC-PV modules to surpass 10% power conversion efficiency [193]. As in 1.2.2, the optical efficiency (η_{opt}) of an LSC can also be defined as the power of the light emitted at the edges divided by the power of the incident light.

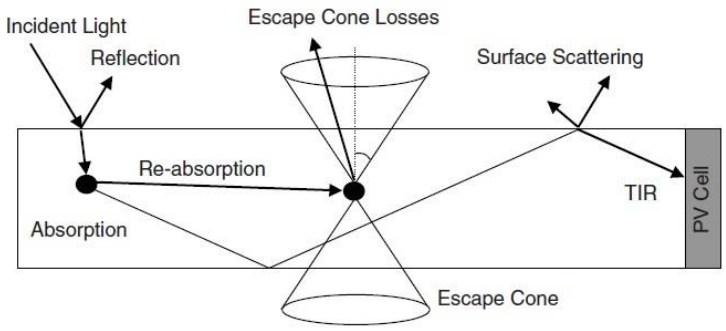

Figure 28: The paths through which the major sources of optical loss occur in an LSC: reflection, reabsorption, escape cone losses and surface scattering. Taken from [194].

2.7.2 Luminescent Solar Concentrator Materials

There are two considerations when selecting materials for an LSC: the host matrix and the luminescent specie. The former appears initially to be a relatively solved problem in that the widely available PMMA is frequently used throughout the literature in LSC fabrication. This is because it has the following advantageous properties for an LSC host matrix: (i) high transparency to visible/near-infrared light, (ii) a suitable refractive index ($n \approx 1.5$), (iii) ease of mixing with luminescent species, (iv) sensible cost, (v) non-harmfulness and (vi) low weight. Glasses with their greater stability to UV radiation than polymers have also been considered for LSC fabrication [195]. Zettl et al investigated 7 other potential host materials including 5 polycarbonates (PCs) which share an advantage with glass over PMMA; both possess higher mechanical and chemical stability but PCs maintain the low weight of a polymer [196]. In their investigation an LSC made from compact disc PC achieved the same optical efficiency as a PMMA device (8.9%). There have been novel host matrices developed by Chowdhury et al [197] (an eco-friendly biopolymer made from cellulose nanocrystals) and Chou et al [198] (a flexible LSC made from polydimethylsiloxane), both achieving respectable efficiencies.

The criteria for selecting a luminescent specie for use in LSC are often the same for an LDS layer. Ideal molecules should have the following properties [199]: (i) a wide excitation range within a suitable area of the solar spectrum (i.e. where the PV cell's photo-response is low) and high absorption cross section, (ii) a narrow emission band where the PV cell's EQE is highest, (iii) minimum overlap between absorption and emission spectra, (iv) a high LQE close to 100% and (v) long term stability over a module's intended lifetime. Commonly used materials include Lumogen dyes (which come in a variety of colours), rare earth ions (such as Eu^{3+}) and quantum dots such as PbS, CdSe/CdS or CdSe/ZnS. Silicon [200] or colloidal carbon [201] QDs have also been investigated as more benign alternatives to the potentially harmful lead or cadmium containing compounds with the latter demonstrating high stability under UV illumination. For commercialisation, there will need to be considerations of the environmental impact and safety of both the host matrix and luminescent specie.

2.7.3 Luminescent Solar Concentrator Designs

In addition to material selection, there are parameters which can vary when designing an LSC such as the size of the concentrator and ratios of the lengths of certain edges or areas of surfaces. Using the standard cuboid LSC as an example, with regards to its 2D cross-section shown in Figure 28 and defining its base length, L, and height, H, two more quantities can be introduced: the *geometric gain* (*G*) = *L/nH* where *n* is the number of edges with PV (or in general *G* = *area of illuminated concentrator surface/area of PV*) and the *aspect ratio* (AR) = *L/H* [191]. Another important quantity is the *concentration ratio*, *C*, (i.e. the ratio of the light intensity at the PV divided by the incident light intensity) given mathematically by $C = \eta_{opt} \times G$ as introduced in 1.2.2. This ratio is sometimes calculated by *C* = *power of cells when attached to the LSC / power of bare cells* at the same irradiance, assuming the power output is linearly related to light concentration (a good approximation for these levels of intensity). It is important to get these dimensions optimised for both performance and economic reasons. Evidently larger sides will require a greater area of PV cell which increases cost, so *H* needs to be kept relatively small. Furthermore, it is beneficial for the optical path length to be shorter to reduce host matrix absorption losses, meaning $L >> H$ is undesirable. In general, a higher geometric gain will lead to more concentrated light but a lower optical efficiency (η_{opt}), resulting a trade-off [202]. Models have been employed either by ray tracing or detailed balance calculations to aid in optimal design [203]. However, when we introduce practical considerations on solar cell sizes, a very small *H* is ruled out. Therefore most laboratory LSC devices typically have $H \approx$ 1-10 mm with *AR*s and *G*s of 2-10 [191]. Given that reported optical efficiencies range from 11-35%, even obtaining a $C > 1$ can be challenging feat to achieve [204].

In recent years, there have been variations on the standard design from Figure 5. Wu's group have proposed a tandem LSC device in which two LSCs containing different luminescent species will be stacked on top of each other. The top LSC will absorb shorter wavelength light (utilising it for edge placed PV) and transmit the longer wavelengths which can then be absorbed by the bottom LSC and generate additional power [205]. It was concluded this could be advantageous to doping multiple species in the same LSC. There have also been devices fabricated where the luminescent specie is contained within a thin film at the top

or bottom of the LSC, as opposed to being doped homogenously throughout the host matrix [206]. This can have the advantage of a greater optical efficiency by reduced self-absorption losses. The state-of-the-art efficiencies achieved by [191] resulted from luminescent films being deployed at the base of the LSC. Doping concentration of the luminescent specie can also be an important factor in optimising LSC design; at too low levels there will be insufficient absorption and emission whereas at too high levels scattering and reabsorption losses increase along with the LSC's opacity which is undesirable for BICPV applications, so a compromise must be found [207].

In more extreme variations on LSC design, the assumption that the concentrator must be a cuboid has been challenged. Various 3D shaped LSCs have been reported including: cylindrical array [208] (sometimes in the form of thin optical fibres [209]), planar circular [210] and wedge designs [211]. Cylindrical arrays can have an optical efficiency of up to 1.9 times greater than conventional LSCs provided luminescence takes place near the surface, and if the cylinders are placed alongside each other, escape cone losses can be reduced through reabsorption into the adjacent concentrator [212]. A simple geometric observation shows planar circular LSCs to have a theoretical *G* 1.13 times greater than cuboids, although their inability to tessellate would be a barrier when scaling up [213]. On the other hand, the wedge design does not have this problem whilst having the advantage of reduced escape cone and host matrix absorption losses due to the light hitting the top surface at increasingly oblique angles. In a comparative study, simulations from Hughes et al resulted in a lower peak efficiency for the wedge compared to a planar cuboid, but over the course of a year the wedge would have generated substantially more electricity due to a better performance when the sun is lower in the sky [211].

Finally, the incorporation of PV with an LSC must be considered, chiefly the type of solar cell and its position of placement. Established PV technologies like silicon cells appear most frequently in the literature because of their low cost per watt and suitability for the emission profile of common luminescent species; Assadi et al give a recent review outlining key results [204]. GaAs [214] and GaInP [215] cells also feature, whereas there have been few instances of LSCs coupled to emerging PV technologies. However, in separate investigations in 2015, LSCs were combined with fibre dye-sensitized [216] and CdTe/CdS solar

cells [217]. It is expected that integration of LSCs with emerging PV will be an area of interest going forward as their cost per watt decreases and because they could benefit relatively more from LDS due to their poor short wavelength response, if luminescent species with appropriate absorption and emission spectra are developed. In an up-to-date study Brennan et al coupled an LSC with a planar dye-sensitized solar cell achieving proof of principle integration and an estimated power conversion efficiency of 2.71% [218].

In the standard LSC design a PV cell is attached with a transparent adhesive to one or more of its edges. In some cases, the cell is only attached to one edge with mirrors placed at the other three, in order to achieve a higher concentration of light on the PV. However, coating all four edges in PV can sometimes be beneficial; Sloof et al recorded a 4.6% power conversion efficiency for single edge LSC-PV whereas a 7.1% efficiency was attained for cells on all four edges [219]. The group also observed a modest increase in performance when the cells were connected in parallel rather than series. Zhang et al went beyond the standard design by mounting one, two or three small PV cells on a portion of the base of the LSC with mirrors fixed on all the side edges [220]. The results were remarkable in that the two cell LSC device achieved a 20% lower cost per watt than a commercial silicon PV module. Moreover, Markman et al showed light concentration on cells could be further increased by up to 35% (whilst maintaining >90% of the original optical efficiency) through the addition of non-imaging optics such as CPCs at all the edges of an LSC, resulting in greater device power output at a negligible extra cost [221].

2.7.4 Luminescent Solar Concentrators for BIPV

LSCs have immense potential for BIPV, a rapidly growing sector, because of their transparency, low cost, light weight and pleasing aesthetic. Commercial BIPV modules available in the UK today are based on established thin film technologies such as CdTe or amorphous silicon [222, 223], or non-luminescence concentrating PV [224], although LSCs are expected to play a large part in future BIPV market growth; major electronics company Philips already has 14 patents for LSC devices [225].

As part of a building an LSC-PV module could broadly be a component of either a window façade or roofing structure. There is also scope for LSCs to be utilised

in non-building urban architecture such as noise barriers alongside highways [226] or canopy shading [227] for carparks. Having discussed recent advances in LSC design and materials at the laboratory device scale, studies are now presented involving larger scale modules with potential commercialisation opportunities and the challenges they face. For maximum transparency and atheistic value, each LSC-PV unit would want to be relatively large ($\gtrsim 0.1\ m^2$) in area (so that a mesh appearance is avoided). This means scaled up LSCs would suffer from additional losses such as greater unwanted self and host matrix absorption because of their larger size. Merkx et al through their models showed the optimal luminescent specie doping concentration level changes depending on LSC size, adding further design complications [228]. For a 1 m^2 module they estimated a theoretical maximum efficiency of 9% and a practical efficiency limit of 6%. It is this low power to area ratio which has hampered further deployment of LSCs. Tsoi estimated only 5 kWh per day could be generated by a 60 m^2 LSC-PV module in favourable sunlight conditions (less than a third of the daily electricity demand of a typical household in a developed nation) [229]. An additional material barrier to LSC commercialisation is the long-term stability of either their luminescent dye or host matrix, since a module marketed as part of a building that generates electricity would ideally need to keep producing power for at least 10 years before replacement. Despite their lower efficiencies and issues around dye stability, the commercial opportunities for LSCs as part of a window integrated PV system should not be underestimated. The fact that LSCs can come in a range of colours (due to different dyes being used) allows for some truly stunning visual architectures to be realised, as seen in Figure 29.

a)

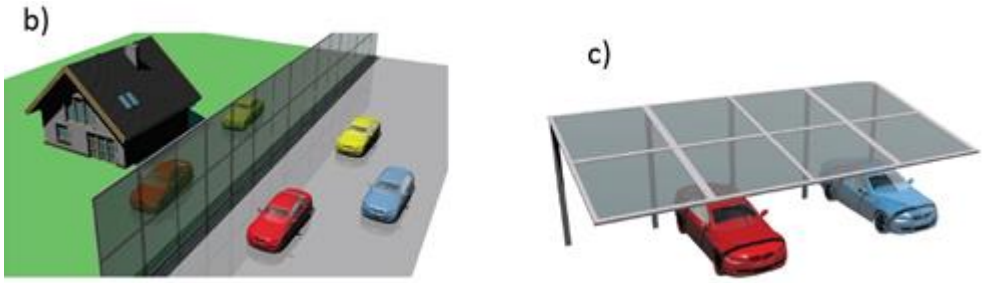

Figure 29: Potential BIPV applications of LSCs: (a) Façade of the Palais du Congrès in Montréal; these windows are only decorative but LSC-PV systems of a similar appearance could one day be widespread, (b) LSC could function as a roadside noise barrier or (c) a canopy for parked vehicles. Taken from [227].

Kerrouche et al provided some insight into how small LSCs could be attractively pieced together by 3D ray tracing simulations and fabricating 70 LSCs of 5 different colours in order to replicate a stained-glass window [230]. The experimental and theoretical values were in agreement to within 7%, highlighting the value of this approach to the design of arbitrary window patterns based on LSCs. Similarly, in 2017, van Sark et al designed and characterised a 1 m^2 module made from different coloured LSCs inspired by the rectangular geometries of Dutch artist Piet Mondrian [231]. A peak 2 W of electricity could be generated, enough to charge two mobile devices, meaning a small utility could accompany its decorative effect. Despite their novel futuristic look, there will need to be studies into the social acceptability of coloured windows to end users including building occupants and urban planners. In one such investigation, Vossen et al used a red LSC module to cover different sized portions of the sole window illuminating a model room [232]. Then volunteers were subjected to the varying light levels and asked to complete a questionnaire on the visual comfort. It was found an LSC which covered 25% of the total window area was viewed most favourably by the participants.

In contrast to their range of colours, an additional property of LSCs which has attracted interest with regards to BIPV is their ability to be transparent and colourless. This can be achieved if the luminescent specie emits outside of the visible range of the spectrum. Meinardi et al have constructed a large-area colourless LSC based on $CuInSe_xS_{2-x}$ QDs which absorb visible light and have an emission peak of 960 nm [233]. At a size of 0.0144 m^2, the device achieved an optical efficiency of 3.2% and had the added benefit of containing no toxic heavy metals. Yang et al provide an up-to-date review of the challenges facing

transparent colourless LSCs and the materials available [234]. From their considerations, the authors concluded the theoretical and practical efficiency limits of visibly transparent LSCs were closing in on those of transparent PV technologies and that research should focus on optimising the luminescent materials. Conversely, LSCs have been fabricated to have a frosted glass effect in which visible light is sent to the edges by scattering alone [210]. These LSCs could have uses in BIPV for when a low transparency is required (e.g. for privacy).

Another benefit of LSC based windows is to allow for enhanced thermal regulation of buildings in both hot and cold climates. An LSC-PV module could be contained within double or triple glazing window units, providing additional thermal insulation and complimentary electricity generation [227]. In depth studies on the heat related performance and insulation benefits of LSC-PV windows are lacking but for semi-transparent thin-film PV, it has been found a triple glazed system achieves a 6% reduction on annual space heating energy consumption compared to a double glazed one, whilst achieving a similar electrical efficiency [235]. Alternatively, for when there is too much sunlight, Aste et al have developed the concept of a smart window utilising LSC technology [236]. In their design a fanlight consisting of 4 yellow LSC-PV modules was fixed above a regular glass double glazed window. Through sensors and motors powered by the LSC-PV, reflective venetian blinds located inside the lower window could be altered to regulate the intensity of light coming into the room. Batteries were incorporated to allow for 5 days of stored PV electricity and a light-shelf beneath the LSC-PV modules (protruding in and out of the window) acted to reduce glare, heat gain and yellow light entering the room. Real images of these aforementioned devices are shown in Figure 30.

Figure 30: Examples of real LSC-PV modules for applications in BIPV: (a) Roof Leaf module design [237], (b) smart window powered by yellow LSC-PV [236] and (c) greenhouse made from red LSC-PV [238].

From the literature, it appears LSCs for BIPV are more suitable and studied in their application as windows. This could be because of their better electrical response at indirect angles, so LSCs are better placed to compete with established PV technology when fixed to the side of a building as opposed to its top. However, opportunities for roof lighting and falling costs per watt could lead to a growing interest in this area. In an intriguing study, Corrado et al fabricated a 22.3 m^2 greenhouse from red LSC-PV modules of varying designs and observed its electrical behaviour over one year [238]. It was found 57.4 kWh/m^2 annually could be generated from the best performing panels, a 37% improvement on the reference greenhouse with non-LSC PV incorporated. Remarkably, the LSCs showed no decline in their performance over the course of the trial and the effect on plant growth was neutral to positive. Thus, greenhouses made from LSC-PV modules could have a major impact in meeting the electricity demands of the horticultural sector (typically 20 kWh/m^2 per year). For more conventional buildings, Reinders et al have developed a 0.11 m^2 LSC-PV module called Leaf Roof [237]. With a design appearance resembling a leaf, these modules are visually appealing when interconnected and come in various

colours each with high efficiencies reported (5.8% for red and 5.5% for green). Leaf Roof has an extra advantage over silicon PV modules in that its lower thermal conductivity (due to the use of PMMA instead of glass) results in peak temperatures 15°C lower than standard silicon PV systems when exposed to intense sunlight. This cooling effect benefits the electrical performance of PV which can lose 0.4% of its power per °C increase. Finally, Vishwanathan et al have modelled and fabricated bent LSC-PV modules which can compete efficiency wise with flat LSC-PV; the bent modules had a slight lower efficiency at 2.4% vs 2.9% for the flat ones [239]. Notwithstanding the slight decrease, this could have positive implications for the realisation of LSC BIPV roofing in a range of curved surfaces.

2.8 Nanoscale Phenomena to Enhance Spectral Conversion

Recent progress in nanotechnology has made it possible to engineer nanostructures to aid spectral conversion processes (especially UC). A major problem resulting in the limited efficiency improvements from UC is the limited absorption spectrum of the rare earth ions; comparing the absorption regions of Yb^{3+}- Er^{3+} and Er^{3+} to the AM 1.5 G spectrum, it can be observed that 1050-1350 nm and >1580 nm photons are not captured. Furthermore, the UC emission is often of low intensity. Both of these issues can potentially be rectified through the use of nanoscale phenomena.

2.8.1 Quantum Dots as Rare Earth Ion Sensitizers

QDs have been proposed to be used alongside rare earth ions, to widen the latter's excitation range. In 2010, Pan et al introduced PbS quantum dots into a Yb^{3+}- Er^{3+} doped oxide UC layer [240]. These added QDs effectively widened the absorption spectrum of the rare earth ions by allowing photons in the 1200-1500 nm range to be absorbed which would otherwise be transmitted, then emitting them at 1530 nm wavelengths which could be used by the Yb^{3+}- Er^{3+} pair. Upon application to a bifacial silicon solar cell a 60% J_{SC} enhancement was observed for the PbS-UC layer compared to the UC layer without QDs. By 2014, the same group carried out tests on rear coated industrial cells and despite the low contribution to EQE at 1500 nm (smaller than the background noise from the measuring instrument), the reflection losses were reduced by 20% across the

spectrum [241]. This method has been used less often of late, as alternative ways of broadening the absorption spectra have been explored.

2.8.2 Photonic Crystals

Photonic crystals are another nanostructure which can be used for enhanced spectral conversion. These are optical nanostructures that influence photon behaviour in solids which means they have potential to improve UC-PV system performance by managing the wavelengths and direction of emitted light [242]. In 2015, Marcos-Hueso et al coupled PbSe QDs with InP graphite lattice photonic crystals and UC properties were significantly improved [243]. The photonic crystal behaved as a wavelength modifier by blue shifting the QD emission leading to a reduction in re-absorption and focussing the spectrum to the point where strongest rare earth ion absorption occurs. As a result, the amount of QD emission matching the UC absorption increased 158%. In addition, vertical emission grew by a factor of 7.8, ideal for a spectral concentrator since it would reduce scattering and lead to a greater portion of photons reaching the cell.

2.8.3 Core-Shell Nanostructures

Spectral conversion particles typically have a small physical size which can limit their absorption and hence the ePLQY of the process. One possible solution is to add antenna ligands to rare earth ions to increase their absorption cross section. Zou et al have reported a 3300-fold enhancement in UC luminescent intensity in β-$NaYF_4$ nanoparticles through the addition of a cyanine dye (IR-806) [245]. This meant 700-850 nm radiation was able to be captured by the dye and its energy passed to the rare earth ions via a fluorescence resonance energy transfer process, after which UC can occur. Further developments on the application of dyes as ligands to improve UC are presented in a letter by Huang [246].

Designing UCNPs with a core-shell nanostructure has also been suggested to absorb a broader part of the spectrum [90]. These structures would be composed from a core of rare earth ions encompassed by a layered shell of phosphor and insulator (such as SiO_2) to electrically isolate the UC particles and reduce recombination. Multi-shelled structures are also achievable and have excellent potential for increasing the amount of radiation absorbed by assigning a rare earth ion and region of the spectrum to a corresponding layer (demonstrated in Figure 32). This concept has been demonstrated by Shao et al who in 2015

fabricated a multi-shell consisting of (from centre to surface): 10 % Er^{3+} doped $NaYF_4$ @ $NaYF_4$ @ 10 % Ho^{3+} doped $NaYF_4$ @ $NaYF_4$ @ 1% Tm^{3+} doped $NaYF_4$ @ $NaYF_4$ (the @ notation is used to denote increasing distance from the core). These ions were able to absorb up to 270 nm of the spectrum; 1120-1190 nm, 1190-1260 nm and 1450-1580 nm for Ho^{3+}, Tm^{3+} and Er^{3+} respectively [247]. The use of inert pure $NaYF_4$ layers helped minimise cross relaxation losses and the lack of absorption at 1350-1450 nm is not too problematic since this portion of the spectrum is heavily absorbed by the Earth's atmosphere. DC core-shell nanostructures are less frequently cited for PV applications, although tri-doped Ce^{3+}- Er^{3+} - Yb^{3+} $BaLuF_5$ with distinct active layers have been prepared for potential use in fibre optic communications [248].

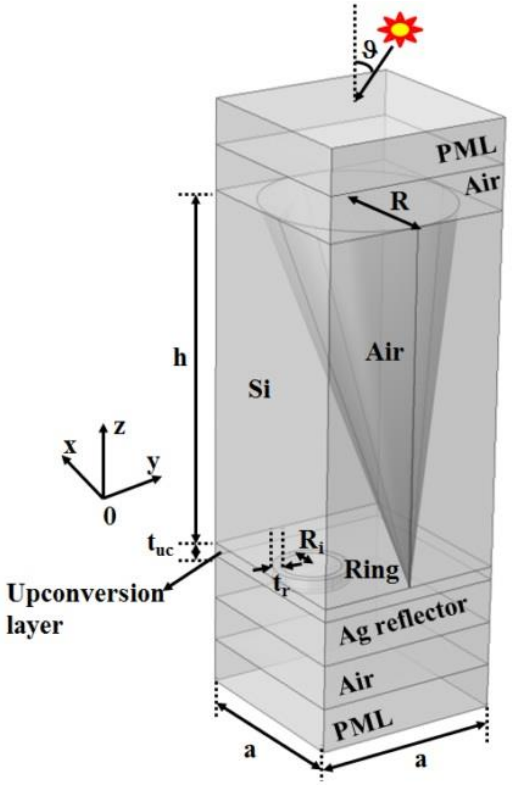

Figure 31: Unit cell of the synergistic plasmonic and photon crystal structure, containing perfectly matched layers which are labelled PML. Taken from [244].

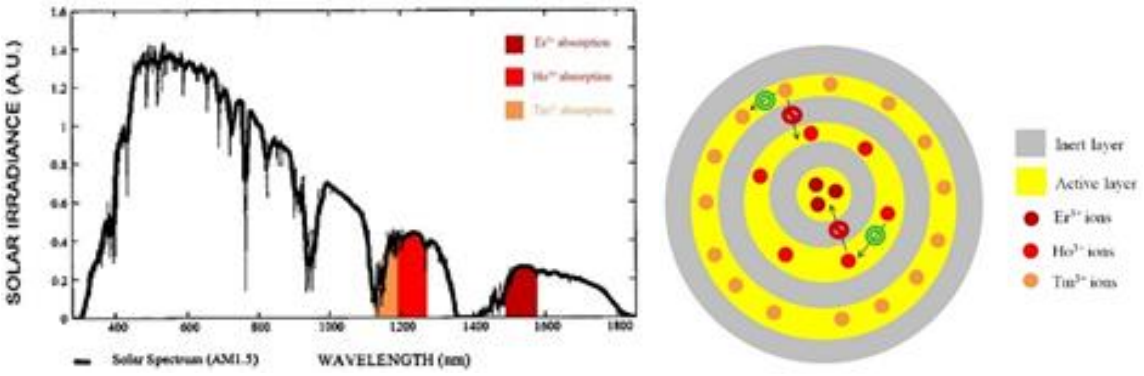

Figure 32: 2D cross-section of the core-shell nanostructure with separate rare earth ions in each active layer. The ions absorb at different wavelengths and are kept apart by an inert layer that prevents them from interacting with each other which would lead to energy losses. By using three ions, a wider region of the spectrum can be harnessed as shown on the diagram. Modified from [247].

2.8.4 Plasmon Resonance

Plasmons are quasiparticles which accompany the quanta of vibrations in the electron density of a metal. Surface plasmon resonance is a phenomenon that can occur at the interface between two materials when the incoming radiation frequency matches that of the electron oscillations, resulting in increased photon intensity being emitted from the surface. This could be used to benefit UC applications to PV by ensuring the higher energy radiation which reaches the cell is of a greater power density [249]. Plasmon resonance is often realised through core-shell structured UCNPs; Atre et al designed a structure consisting of a UC dielectric core surrounded by a crescent shaped Ag shell [250]. They observed a 100-fold increase in the power of the emitted above band gap radiation towards the solar cell and postulated these nanostructure techniques would eventually lead to low cost single junction cells overcoming the Shockley-Queisser limit. Liu et al went further by preparing Au decorated core-shell β-$NaYF_4$:Er^{3+}/Yb^{3+}@SiO_2 UCNPs and applying them to a DSSC [251]. The UCNPs with the Au surface were able to attain J_{SC} measurements 13.3% greater than for a DSSC containing the same UCNPs but without the Au shell. In 2016, Luoshan et al carried out a similar investigation on DSSCs but added an extra TiO_2 layer on the outer layer of their UCNPs to act as a transport channel for generated electrons, increase dye loading and prevent contact between Au and the electrolyte [252]. Their methods led to a 38.2 % improvement in J_{SC} over a DSSC without UCNPs and a 5.4% J_{SC} enhancement over the device with β-$NaYF_4$:Er^{3+}-Yb^{3+}@SiO_2@Au UCNPs. This approach has also been utilised in LDS investigations. Ahmed et al added Au nanoparticles to their CdSe/ZnS QDs and fabricated plasmonic-LDS

layers which demonstrated improved short wavelength EQE and J_{SC} in both c-Si and DSSCs; the plasmonic-LDS layers improved J_{SC} by 7.67% relative to the reference cell and 5.71% relative to LDS layers without the Au nanoparticles for c-Si, and by 8.11% and 5.93% for DSSCs in the same scenarios [253]. Then in 2019, Garcia et al reported Eu^{3+} and Ag LDS nanoparticle containing tellurite glass covers that improved silicon solar cell PCE 12.71% relative due to plasmonic enhancement [254].

Furthermore, in latest studies, advanced nanostructures have been utilised for enhancing LSC performance. Liu et al added SiO_2 particles to a QD LSC which improved the efficiency by 60% relative to the original device due to beneficial scattering of incident light, increasing the probability of absorption by the QDs [255]. Likewise, El-Bashir et al used gold and silver nanoparticles to enhance the luminescence of a thin film LSC via localised surface plasmon resonance, achieving a relative efficiency increase of up to 53.2% [256]. In another landmark study, Bronstein et al created photonic mirrors with spectrally selective reflectance to trap light once it has undergone luminescence, greatly reducing escape cone losses and increasing the light concentration on the PV cell by a factor of 30 (the highest figure to date for an LSC) [257].

As well as core-shell UCNPs, there are potential synergies from combining plasmon resonance with photonic crystals in order to trap light and aid the UC process in thin film PV technologies. Le and John proposed a slanted conical photonic crystal structure above core-shell rings and a UC layer [244] (cf. Figure 31). Through modelling, it was found this system could realise an IR spectral intensity 1400 times greater than that of AM 1.5 G, meaning the UC process would be much more efficient. This design also had the benefit of improved light trapping and absorption for light at incident angles up to 60°, highlighting its potential for capturing diffuse radiation.

2.9 Challenges and Opportunities

There has been significant progress made in the field of spectral conversion, especially in recent years, with enhanced efficiencies report for a range of PV technologies but key problems prevent its widespread commercial deployment. These factors can be broken down into material and cost related problems. The material issues include the non-ideal efficiency of the spectral conversion

processes (especially at low light concentrations for UC), their limited absorption spectra (particularly for UC) and making sure the light that has undergone spectral conversion reaches the solar cell. As seen in 2.8.1-4, nanotechnologies may address some of these concerns, but these complicated structures will surely add to the fabrication costs.

2.9.1 Solar Cells Designed for Upconversion

In the hitherto presented studies, the solar cells used were not designed specifically for UC. The established silicon devices were sourced externally, and emerging technology cells fabricated according to previously published methods. It could be argued that an area to be taken forward by researchers would be the design of solar cells specifically for use alongside UC materials. Rüdiger et al suggest practical ways to achieve this by implementing three criteria for bifacial solar cells used together with UC: a very high transmittance to photons with wavelength greater than 1200 nm for maximum illumination of the UC layer, a high EQE on the rear of the cell to wavelengths at which UC photons are emitted and a generally high power conversion efficiency to maximise the output power [258]. Using data from 2014, they concluded a 3% relative enhancement in power conversion efficiency was attainable through optimised cell designs and the group then fabricated a bifacial n-type silicon solar cell that attained an EQE of 1.69% under 1508 nm illumination at an irradiance of 1091 W/m^2. When normalised to give an NEQE, this corresponded to a 5-fold increase over previously published results without optimised solar cells. They also noted a textured (as opposed to planar) surface on both sides improved performance and anti-reflective coating design considerations led to a trade-off between maximising cell efficiency (due to improved EQE at short to mid wavelengths) and UC performance; since the former is always the primary objective and UC impact is small, it should never be compromised at the expense of greater sub band gap transmission. Nevertheless, the design with a double layer (40 nm a-SiN_x:H, 80 nm SiO_2) on the front surface and single layer (120 nm a-SiN_x:H) on the rear surface showed the highest potential across all wavelengths. Further considerations include the upscaling to a module scale and stability of the UC materials over the typical lifetime of a solar PV system. Furthermore, in 2019 Ho et al deposited a SiO_2 layer containing Yb^{3+} - Er^{3+} co-doped YF_3.within matrix

grooves at the base of a c-Si solar cell; through combined UC and surface passivation, a relative PCE improvement of 13.26% was recorded [259].

2.9.2 Simultaneous Up and Downconversion or Luminescent Downshifting

One approach, which appears to be the logical conclusion, to get the most potential from sunlight is the idea of simultaneous up and downconversion (or LDS). If successfully implemented, it would allow solar cells to utilise sub band gap photons and reduce losses from thermalisation that occur due to short wavelength light. This could potentially increase solar cell efficiency to a greater level than the Shockley-Queisser limit, even accounting for the additional losses that would occur from the DC/LDS potentially absorbing photons that could be utilised by the UC material.

Yao et al have shown this concept by using rare earth co-doped ZnO UC and DC layers which were incorporated into a DSSC [260]. The rare earth ion pair used for the DC layer was Eu^{3+}- Tm^{3+} and Yb^{3+}- Er^{3+} functioned as the UC layer. A remarkable relative power conversion efficiency enhancement of 70.4% was recorded for the UC and DC layer containing device compared to a pure TiO_2 electrode device. This result also corresponds to a 53.6%, 25.4% and 14.5% relative increase on the ZnO/TiO_2, Yb^{3+}-Er^{3+}: ZnO/TiO_2 and Eu^{3+}- Tm^{3+}: ZnO/TiO_2 photoanode devices respectively, highlighting the recombination reducing effect of the DC layer. Likewise for a-Si cells, Song et al prepared tri-doped Yb^{3+} - Ce^{3+} - Er^{3+} ZBLA fluoride glasses which could convert both UV (280-350 nm) and NIR (900 -1100 nm) photons to visible (500 – 700 nm) emission through UC and LDS, raising the power conversion efficiency of the device by up to 7.6% [261]. In 2018 the simultaneous use of LDS and UC has also been reported by Ha et al within an LSC-PV system. The application of a Pd meso-tetraphenyl-tetrabenzoporphine complex alongside 9,10-bis(phenylethynyl)anthracene that demonstrated TTA-UC into the LSC was able to improve the PCE of a coupled DSSC by 27% relative to the same system based on LDS alone [262].

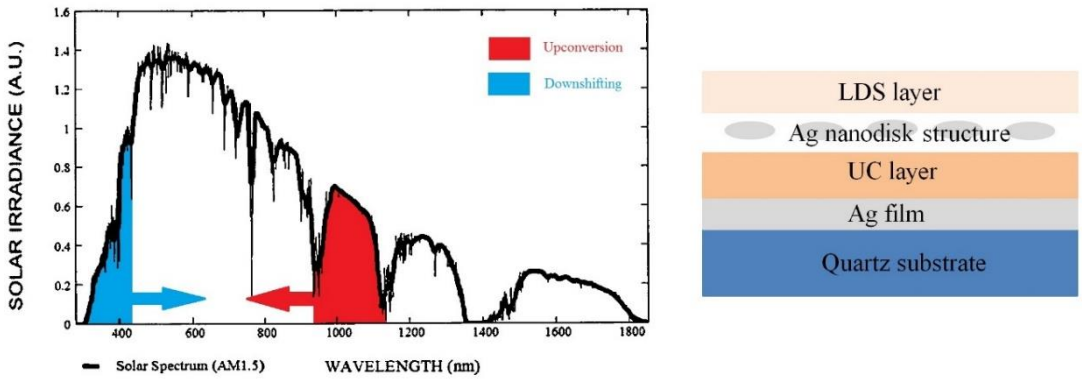

Figure 33: Representation of the promising prospect of simultaneous UC and LDS which shifts light from both short and long wavelength parts of the spectrum, along with the design of the prepared layers which can achieve this for a PV cell. Modified from [263].

Nanostructures have also been used to demonstrate simultaneous UC and LDS. In 2015, Lee et al designed and constructed a metal nanodisk-insulator-metal structure (cf. Figure 33) that dually enhanced UC and LDS via plasmon resonance [263]. It was fabricated by a nanotransfer method printing technique which can be replicated over a large surface area and achieved increased luminescence factors of 174 and 29 for UC and LDS respectively, demonstrating immense potential for raising the efficiency of high band gap cells. Excitingly, some rare earth ion doped compounds have been shown to possess both UC and DC or LDS properties under illumination by different wavelengths. These multi-modal phosphors include: Er^{3+} doped K_2YbF_5 (yellow-orange emission under 355, 532 and 980 nm excitation), Tb^{3+} - Yb^{3+} co-doped lithium borate glass (visible and 976 nm emission under 266, 355 and 976 nm excitation) and Tb^{3+} - Yb^{3+} co-doped $GdPO_4$ (green and 980 nm emission under UV and 980 nm excitation) [264-266]. These all have the potential to aid solar cell efficiency by allowing them to use both UV and IR radiation more effectively. Interestingly, the widely used Er^{3+} - Yb^{3+} co-doped $NaYF_4$ can also be added to this category of materials, since Aarts et al showed it to exhibit DC emission of 650 nm and 980 nm upon excitation by 380 nm illumination [267]. Furthermore, Gavrilović et al have prepared Eu^{3+} and Yb^{3+}-Er^{3+} doped $GdVO_4$ nanoparticles via a reverse micelle method, exhibiting green emission due to both UV and NIR excitation, so this compound too has potential as a multifunctional UC and DC material [268].

2.9.3 Costs of Spectral Conversion Materials

Quantitative financial considerations and comparisons must be made between spectral conversion and alternative approaches to realise low cost, high efficiency PV devices that harness a wider range of the solar spectrum. Due to the high production costs of multijunction cells and their unsuitability for many irradiance regions, it could be more attractive to develop relatively smaller efficiency gains at a much lower additional cost, thereby reducing the cost per W_p.

The EPHOCELL project conducted research in this area, under the European Union's 7th Funding Programme between 2007 and 2013, by being one of the first groups to carry out a cost-benefit analysis based on the materials they had developed, and future idealised systems, for application to c-Si, a-Si and DSSCs [269]. They made the reasonable assumption that the additional cost is proportional to the enhancement in efficiency. The materials synthesised were Eu^{3+} and Tb^{3+} based complexes for LDS and perylene/Pd-octaethylporphyrin for UC which achieved relative J_{SC} enhancements of 2.7% and 3% respectively and were determined to have high stability over a 10-year period. The minimum costs per additional W_p for the LDS and UC to be viable were calculated to be €0.011 and €0.096. It was also envisaged by 2020, the revenue from this type of technology would be worth €3.05 million.

In 2018, Day et al presented a formula derived from first principles to determine the condition such that an efficiency increasing modification to a PV system would lower the overall cost per W_p. For any cell of cost, C_{cell}, maximum power output, P_{max}, and cost per W_p equal to C_{cell} / P_{max} , the new cost per W_p resulting from an enhanced performance (ΔPCE) at a cost $C_{modification}$, will be given by [29]:

$$New\ cost\ per\ watt\ peak = \frac{C_{cell}+C_{modification}}{(1+\Delta PCE)P_{max}} \qquad (23)$$

This general formula can be used to directly contrast cost with any approach used to raise power conversion efficiency. Moreover, if the above expression is compared with the original cost per W_p of the unmodified cell and each side divided by C_{cell} / P_{max}, the resulting equation provides the condition for the modification to lower the cost per W_p.

$$\frac{1+\frac{C_{modification}}{C_{cell}}}{1+\Delta PCE} < 1 \qquad (24)$$

Through the use of the above equation, approximate costs of the rare earth ion doped compound (making the assumption that their cost is similar to the rare earth element and the host lattice reagents are negligible), the costs of solar cell technologies from Table 1 and the *ΔPCE* enhancements from the most recent studies, an interesting approximation can be made, the maximum mass of rare earth metal than can be added per W_p of solar cell while still leading to a reduced cost per W_p. These values are calculated in Table 6.

Rare earth ion	Process	ΔPCE relative (%)	Solar cell	Maximum mass of ion to reduce cost per W_p (mg/W)	Ref
Er^{3+} - Yb^{3+}	UC	20.8	PSC	0.16	[173]
Eu^{3+}	DC	34.4	PSC	0.06	[180]
Eu^{2+}	LDS	16.0	c-Si	0.15	[184]
Eu^{3+} - Dy^{3+}	UC/DC	70.4	DSSC	0.44	[260]

Table 6: Estimates for the maximum mass of rare earth ion that can be added per Wp of solar cell power output to still reduce the cost per Wp, using ΔPCE data from state-of-the-art studies presented in this chapter.

In one of the few studies cited thus far to consider cost, Le Donne et al carried out a basic cost analysis on the Eu^{3+} doped complex used as an LDS material for c-Si cells in their work [270]. They estimated the cost per W_p could potentially decrease by €0.06. Alternatively, Schulze et al have proposed Zn porphyrin dyes as sensitizers for TTA based UC; these materials yield comparable photoluminescent performances but at a much lower cost than the heavier rare earth ion containing compounds since Zn only costs approximately $2/kg [271]. In 2018, Sutherland et al analysed the economics of a tandem LSC architecture based on colloidal QDs which could be scaled to large areas [272]. The cost per watt was found to be 13% lower as compared to typical c-Si modules, with the potential for a 34% reduction through further material and design optimisation. Although improving the stability of the LSCs should be a priority since their lifetimes were only 9 and 38 months for the top and bottom concentrator respectively, significantly less than a commercial c-Si module.

2.9.4 Future Outlook for Spectral Conversion Materials

The following factors are suggested areas of significance where future research should be focussed in order to advance the viability of this approach. Firstly, the

optimisation of materials used in spectral conversion is clearly a priority for this field. The low PLQY and narrow absorption of UC materials has prohibited their wide scale use. Various methods have been proposed to overcome these issues, but there must also be more comparative analyses between the different available host lattices. $NaYF_4$ has emerged as the most promising candidate but there needs to be thorough research into its synthesis to improve quantum yields or see if another compound could be a more suitable host lattice. In 2017, Kumar et al summarised most recent advances for $NaYF_4$ [273] and the following year Nair et al reported a facile precipitation synthesis method for rare earth doped BaY_2F_8 [274]. Meanwhile, Favilla et al carried out a comparative analysis of two different Er^{3+} doped fluoride compounds, $LiYF_4$ and BaY_2F_8. The latter achieved a 6.8% EQE at 1494 nm illumination (at spectral intensity equivalent to 8600 suns) and the better performance was explained from static and dynamic crystal properties derived from spectroscopic studies [275]. On the other hand, moving away from rare earth ion doped fluorides or oxides and towards TTA in organometallic dyes may be an attractive alternative due to their better performance at ambient solar light concentrations and potentially lower material costs.

LDS and DC investigations have produced more pronounced impacts on PV device performance by improving response to short wavelength photons at lower solar irradiances. However, there is further work to be done on dye stability and optimising the process efficiencies. LSCs are a particular area where there is immense potential for spectral conversion, perhaps its greatest single application. LSC research has as well come a long way in the last 40 years from a theoretical concept, to test laboratory devices of improving efficiency and now a budding commercial technology with module scale systems being fabricated. In order to reach the mass market, the following research challenges should be overcome: (i) material optimisation for scaled up LSC modules in terms of minimising self-absorption losses and maximising power to area ratio, whilst maximising long term stability and minimising cost per watt, harmfulness and environmental impact, (ii) applying the nanostructures to achieve light trapping and enhanced luminescence on a larger scale, through the aid of modelling to determine practicality, (iii) applying LSCs to emerging types of solar cell technology as their respective costs come down and (iv) a plan for BIPV market share growth by

catering to specific building and end user needs from the various LSC applications and module appearances available. To summarise, LSCs provide unique opportunities for BIPV, predominantly as attractive, electricity generating window façades with potential benefits for thermal regulation, but also in other niche architectural areas such as greenhouses, public art spaces and noise barriers. If studies continue at their current rate of innovation, it is highly likely we will see these colourful technologies realised as part of our human landscape in the coming decades. However, one area that could be explored more is the deployment of spectral conversion materials in LCPV systems beyond the standard LSC design.

Another material issue in the long term which will need addressing is their safety and environmental impact. Lesyuk et al have recently developed Cd free QD LDS layers, containing instead Zn-Cu-In-S/ZnS as the light converting materials. The simulations and experiments carried out showed that if ePLQYs of >80% could be achieved, this would be a viable approach for significant improvements in device performance [276]. In addition, costs must be kept minimal so that the enhanced performance can ultimately significantly lower the cost per watt, which is necessary if this approach is to emerge as a serious competitor to other methods of capturing a greater portion of incident sunlight.

However, as well as competing against other approaches that can harness more of the solar spectrum, there is potential for spectral conversion to be used alongside these methods rather than instead of them. Rudiger et al imagined the application of UC to III-V silicon tandem solar PV devices, in which the effect of UC would be more beneficial for a given performance due to the silicon cells lower current than when used in non-tandem systems [258]. Additionally, this author would envisage some potential for the application of DC or LDS layers to the PSC part of a PSC/c-Si tandem PV system which is widely touted as a low-cost, clean energy generation solution. Finally, Shpaisman et al predicted practical efficiencies of 38% could be attained for a single junction cell (beyond the Shockley-Queisser limit) through the combined use of MEG and UC [277]. However, the process efficiencies in their model were optimistic; 25% for UC and 70% for MEG, both higher than the best performing materials have achieved.

2.10 Relation of Knowledge Gaps to Thesis

In this chapter spectral conversion has been reviewed as a means to attain higher performance for a range of solar cell technologies After overviewing the fundamental concepts and materials available, many studies have been presented that have attempted to apply these processes in order to utilise the spectrum of light incident on solar devices more effectively. It might not be the silver bullet it first appears, but there has certainly been considerable development in the field from a purely academic exercise to one achieving growing demonstrable improvements in the performance of laboratory PV devices. One observation from surveying the literature is that in the studies quoting the highest increases in performance, it is often secondary effects that are responsible for a large proportion of these J_{SC} or power conversion efficiency enhancements, especially in emerging PV technologies. This can be interpreted in two ways; that spectral conversion in itself may be of limited practical applications, or more optimistically that these dual functionalities increase the scope for its potential, since the end result of higher device performance and lower cost per W_p are the important outcomes regardless of the exact mechanism behind the cause.

Lowering cost will be a major theme of this project and a key element of this then becomes the choice of spectral conversion material to work with; the three options are rare earth doped compounds, dyes or QDs. The latest methods using nanostructures to develop the highest performing spectral conversion materials are likely to be cost prohibitive, until innovative ways are found to scale up production. For example, in comparing the price of those commercially available from Sigma Aldrich, Er^{3+}, Yb^{3+} doped $NaYF_4$ powder of particle size 1-5 μm costs £135 for a 25 g sample [278], whereas the same rare earth ions doped into $NaYF_4$ 20 nm nanoparticles cost £223 for 0.01 g dissolved in 1 ml of toluene [279]. Therefore, state-of-the-art nano-engineering techniques, newly synthesised materials and material optimisation will therefore be beyond the scope of this thesis. Alternatively, the Lumogen series of dyes have been used widely for LSCs and LDS layers to great effect but there are issues with their long term stability to sunlight (their PLQY drops to 80% of its peak value after one year [280]) and the cost of these materials, although not extortionate, still comes in high at €7000-9000/kg at an industrial scale [38]. CdSe/ZnS core-shell structured QDs have

also performed well but are currently very expensive, costing £561 per 25 mg [281]. Considering these factors, it is the rare earth doped compounds that are deemed the most sensible choice of material.

CPV is one area where spectral conversion has excellent potential; LSCs have already demonstrated this but one area lacking is the application of spectral conversion to other LCPV systems. The 3D static concentrators, that demonstrate similar potential for attractive BIPV systems, have yet to be tested for enhancements via spectral conversion. Designing a new concentrator would again, like working with new materials, be above the level of depth required for this work. So, of the available 3D concentrators, SEH are selected because of their use in proposed BIPV systems, simple fabrication procedure and suitable geometric concentration ratio. Additionally, it has been observed that the most successful UC results have occurred under high intensity light concentration, >90 suns, which for practical applications fall under HCPV that are not considered due to high costs and unsuitability for global deployment. Therefore, the primary focus will be on DC/LDS processes in the 300-500 nm region of the spectrum because these have showed more signs of progress than UC at irradiances <10 suns.

Next the PV cells themselves must be chosen, using a similar vein of thought to decide. Since c-Si cells have issues with lower short wavelength spectral response, have had rare earth doped compounds successfully applied to them and are a mature technology that makes up the overwhelming majority of installations today with suitability for use in LCPV, they were chosen as the PV cell to consist of the bulk of investigations. Furthermore, PV cells with spectral conversion materials tend to be characterised under 1 sun but illuminating them at different fractional levels of solar irradiance could yield better understanding of the impact of spectral conversion at different light intensities. In addition, by changing the angle of incidence of light on the concentrator-cells, it can be proven that spectral conversion is a viable approach for off-normal incident radiation in these systems.

By acknowledging the rapidly evolving market it was also deemed necessary to try these same methods on an emerging PV technology as well. Ideally this should be PSCs due to their rapidly growing efficiency and path to commercialisation, but through their fabrication process, it is still difficult to

produce quality and stable devices in air. As a result, DSSCs which lack the higher efficiencies of PSCs but are simpler to fabricate and are still likely to have a growing share of the PV market in years to come, are chosen to be investigated. DSSCs have benefitted immensely from spectral conversion via rare earth containing compounds and the materials used in cutting edge work take advantage of nanoscale phenomena to achieve the best results. However, for cost reasons it would be interesting to see what may be achieved by simpler materials (the same ones to be used for c-Si). The jury is still out on whether an external layer or adding spectral conversion particles internally is best for PSCs, but the latter appears to have worked best for DSSCs, so this seems the logical option for subsequent experimental work. Also, the variation of spectral conversion enhancements with respect to the layer thickness within an emerging PV device and how it varies with incident light concentration are other areas lacking in the literature which will be explored in this thesis. As with c-Si devices, there is a lack of DSSCs tested under varying light concentrations, both sub-1 sun and coupled to a 3D concentrator. The exact specifications for which spectral conversion materials were used, how they were integrated with the relevant PV and LCPV systems and how the electrical performance is characterised in a way consistent with the established literature are given in chapters 3, 4 and 5.

Finally, simple mathematical models will be used to justify experimental results which is important to deepen the understanding of underlying principles. Ray tracing has been utilised with great effect for modelling all sorts of concentrators including LSCs and systems combined with spectral conversion materials. Nevertheless, for the specific 3D static concentrators (CPC and SEH), there has been little theoretical enquiries into the nature of how adding impurities will affect their optical properties and performance of the coupled PV. This thesis will also aim to give an overview of the material costs involved and apply a simple cost-analysis to determine the potential economic benefits of spectral conversion, something again lacking a clear presence in the literature. The holistic scope of the work is summarised in Figure 34.

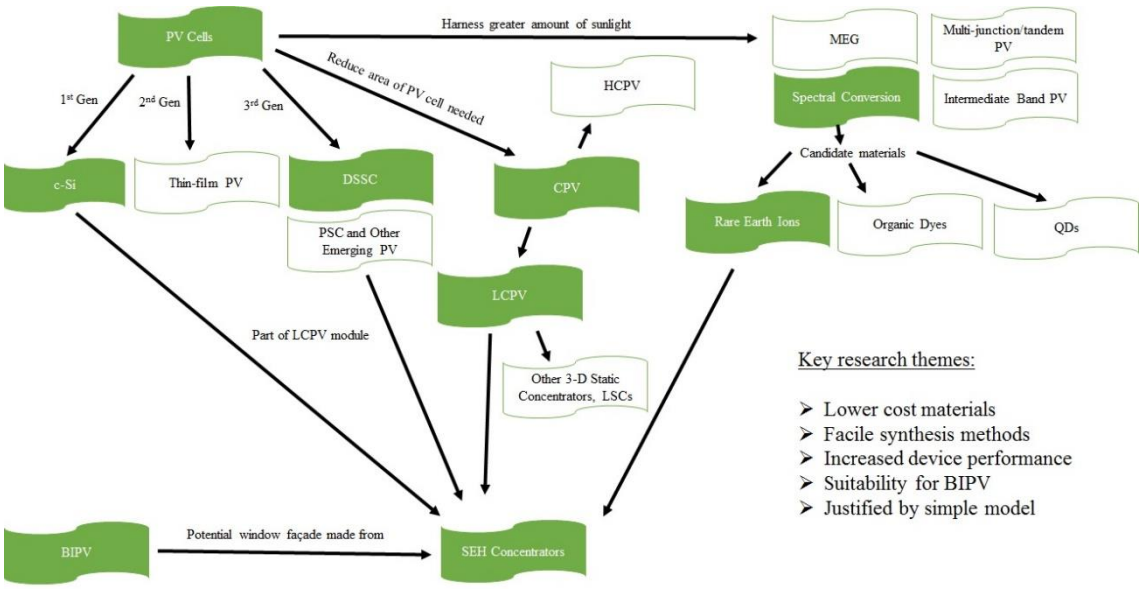

Figure 34: Nexus of issues and research themes addressed in this thesis based on the web of current PV technology and knowledge. Topics within green boxes fall within the scope of this work and white boxes are beyond that which is considered.

Chapter 3. Material Properties, Characterisation Methods and Application to Silicon PV

3.1 Introduction

In this chapter the two rare earth compounds which form the basis of subsequent investigations are presented and characterised through UV-Vis spectroscopy, SEM, XRD and photoluminescent spectroscopy. The silicon solar cells used in chapters 3 and 4 are also described and characterisation procedures (through the solar simulator and IPCE) outlined. Thin films containing the two rare earth compounds in different media (TiO_2 and Sylgard) are first prepared separately on glass substrates and then applied as a coating to individual solar cells to study their impact on device performance.

3.2 Choice of Materials

The spectral conversion materials of primary concern for this thesis ($Sr_4Al_{14}O_{25}$: Eu^{2+}, Dy^{3+} and $NaYF_4$: Er^{3+}, Yb^{3+}) were judged on the criteria outlined towards the end of chapter 2. These included: low-cost, commercial availability, non-toxicity, demonstrating luminescence in regions of relevance for given solar PV technologies and ease of application to form a film above the cell. Also, of importance were the materials possessing high quantum efficiencies for the relevant spectral conversion processes. These were expected to be high because the chosen materials were metal oxides and halides (which have low phonon energies, thus a greater iPLQY). Moreover, previous works had measured the iPLQY to be 80.4% for $Sr_4Al_{14}O_{25}$: Eu2+, Dy3+ and 64% for $NaYF_4$: Yb^{3+} Er^{3+} [179, 267].

3.2.1 $Sr_4Al_{14}O_{25}$: Eu^{2+}, Dy^{3+}

The first rare earth doped compound to be selected was $Sr_4Al_{14}O_{25}$: Eu^{2+}, Dy^{3+}. This non-toxic material is a beige powder demonstrating highly persistent blue-green luminescence due to the presence of rare earth ions and has primarily found commercial use in ‘glow in the dark’ lighting displays [282] (cf. Figure 35).

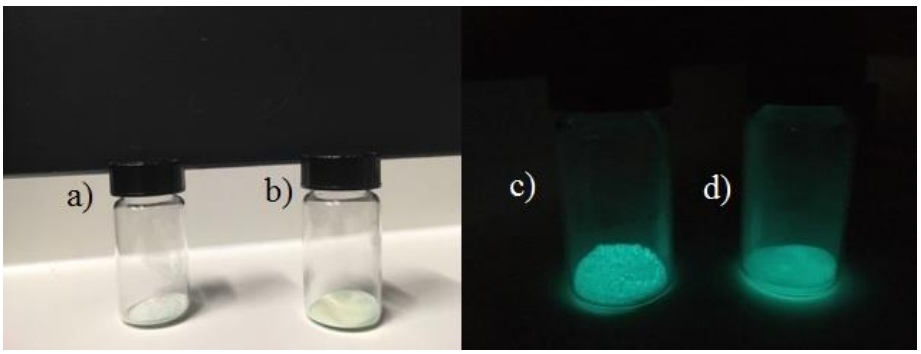

Figure 35: $Sr_4Al_{14}O_{25}$: Eu^{2+}, Dy^{3+} powder in vessels: a) ground and b) unground. Persistent phosphorescence was observed after exposure to simulated sunlight in both samples: c) ground and d) unground.

Strontium aluminate comes in different chemical formula and structures. These are $SrAl_2O_4$ or $SrAl_4O_7$ (monoclinic), $Sr_3Al_2O_6$ (cubic), $SrAl_{12}O_{19}$ (hexagonal) and $Sr_4Al_{14}O_{25}$ (orthorhombic) [283]. $Sr_4Al_{14}O_{25}$ was chosen due to its lower price than $SrAl_2O_4$ and suitable photoluminescent properties for solar cells as demonstrated by Sun et al in 2014 [179]. In their work, cited in 2.5.2, $Sr_4Al_{14}O_{25}$: Eu^{2+}, Dy^{3+} was used to enhance QDSC efficiency by 37% relative. Interestingly, the phosphorescence was able to drive a current for 1 minute after illumination, meaning there is at least conceptual potential for glow in the dark solar cells, although this innovative aspect will not be further investigated in this work. Sun et al's photoluminescence spectra showed that $Sr_4Al_{14}O_{25}$: Eu^{2+}, Dy^{3+} was excited by photons from 300-450 nm (with a peak at 365 nm) and re-emitted them at 450-550 nm (with a peak at 490 nm).

Despite the strong performance of ZnO in an earlier work [178], where a J_{SC} enhancement of +6.06 mA/cm^2 was achieved, and its low cost per kg due to the wide availability of Zn, $Sr_4Al_{14}O_{25}$ was selected as a host material for two reasons. Firstly, because the ZnO was deployed alongside graphene loading which was the main effect in raising device performance (compared to a graphene loaded DSSC without rare earth doped ZnO, the J_{SC} was only raised by 4.26 mA/cm^2), so it felt more appropriate to test a material which had demonstrated enhanced PV characteristics on its own. And secondly, because rare earth doped ZnO was not commercially available and synthesising rare earth doped compounds from their essential reagents was deemed to be beyond the scope of this work.

Given these properties, $Sr_4Al_{14}O_{25}$: Eu^{2+}, Dy^{3+} of 99% purity was sourced from Sigma Aldrich. In this product the doping level of Eu and Dy were 6% and 10% respectively and emission was described as blue-green, consistent with Sun et

al. It also had a quoted particle size of 180 mesh (74-88 μm) and initial studies showed the material too coarse to be effectively incorporated with solvents. To resolve this issue, an agate mortar and pestle was used to grind the powder for 30 minutes, in order to reduce the particle size and produce a finer powder that would be easier to mix into an embedding agent.

3.2.2 $NaYF_4$: Er^{3+}, Yb^{3+}

It goes without saying that from the previous chapter, $NaYF_4$: Er^{3+}, Yb^{3+} has featured heavily in spectral conversion studies. As well as application for UC from 980 nm excitation, Aarts et al demonstrated potential for DC through 380 nm and 451 nm excitation [267]. The transitions from $^2H_{11/2}$ to $^4I_{15/2,}$ $^4F_{9/2}$ to $^4I_{15/2,}$ $^4S_{3/2}$ to $^4I_{13/2}$ and $^4I_{11/2}$ to $^4I_{15/2}$ are responsible for emission at wavelengths 550 nm, 650 nm, 840 nm and 980 nm respectively. The relative strength of the emission at these different wavelengths depends on the concentration of the Yb^{3+} ion. Following this potential, a commercially available sample of $NaYF_4$: Er^{3+}, Yb^{3+} was supplied from Sigma Aldrich, containing 3% Er^{3+} and 20% Yb^{3+}. The particle size was quoted as 1-5 μm and the emission described as green to NIR. In addition, the substance was a white powder as shown in Figure 36 and much finer than the $Sr_4Al_{14}O_{25}$: Eu^{2+}, Dy^{3+} sample, so grinding it in order to reduce average particle size was not deemed necessary.

Figure 36: $NaYF_4$: Er^{3+}, Yb^{3+} powder in a vessel. Unlike the $Sr_4Al_{14}O_{25}$: Eu^{2+}, Dy^{3+} sample, it did not exhibit phosphorescence once the lights had been turned off after exposure to sunlight, so the lifetimes of its photoexcited states are much shorter.

3.3 Initial Characterisation

It is important to characterise materials via established procedures which are used throughout the field because it will help verify the manufacture claims about their properties. The following techniques were used: x-ray diffraction, scanning

electron microscopy and photoluminescent spectroscopy. The basic principles of each of these methods are briefly discussed and the relevant data for the chosen rare earth doped compounds presented.

3.3.1 X-ray Diffraction

X-ray diffraction (XRD) is a powerful technique used to study crystalline materials that can determine their structures, phases, preferred crystal orientations, crystallinity, strain and defects [284]. The fundamental principle behind XRD is the diffraction patterns that occur from the elastic scattering of monochromatic x-rays passing through a crystalline structure, due to their wavelengths being of similar size to the lattice spacing much like how gratings can produce optical effects for visible light. This interaction was discovered by Von Laue in 1912, and soon after in Manchester, UK, Bragg derived the conditions for constructive interference [285]:

$$n\lambda = 2d \sin\theta \qquad (25)$$

In this equation, *d* is the lattice spacing between the ions, *θ* the angle between the incident beam and the horizontal, *λ* the wavelength of the x-ray and *n* a positive integer. From Figure 37, it can be seen the expression shows the path difference between the two rays undergoing diffraction to be consistent with the described equation, with constructive interference occurring when this is equivalent to an integer number of wavelengths.

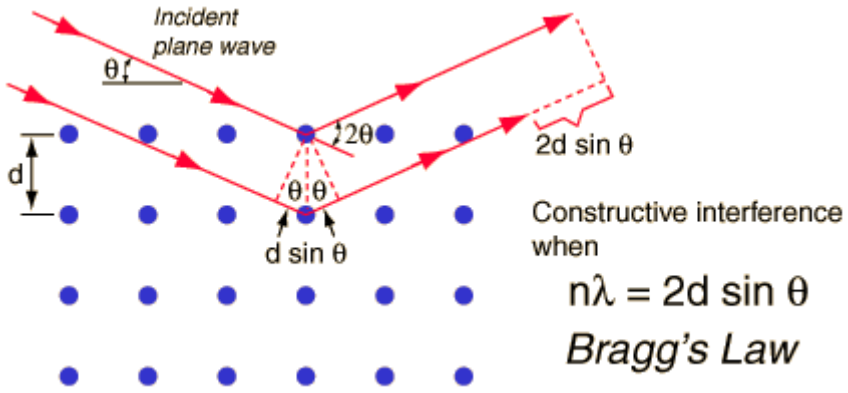

Figure 37: Representation of the derivation of Bragg's law of x-ray diffraction. Lattice ions separated by a distance, d, and subject to an x-ray beam of angle θ to the horizontal, will result in constructive interference when integer multiples of the wavelength are equal to 2dsin θ. Taken from [286].

These points which represent atoms, ions or molecules in a given crystal structure will be arranged into a repeating unit cell. When a sample powder is

characterised its composite unit cells will be randomly orientated. Thus, through varying the angle of the incident beam (as per Figure 38) and measuring the resulting intensity of the collected x-rays, all possible diffraction patterns can be observed [287]. Materials have a characteristic 'fingerprint' distribution of the peaks obtained, so by comparing the results from the measured sample to that from a standard database, the phase and structure may be determined. Since the angle between the incident ray and diffracted beam is 2θ, XRD data outputs are mostly given as intensity (in counts) on the y-axis and 2θ on the x-axis.

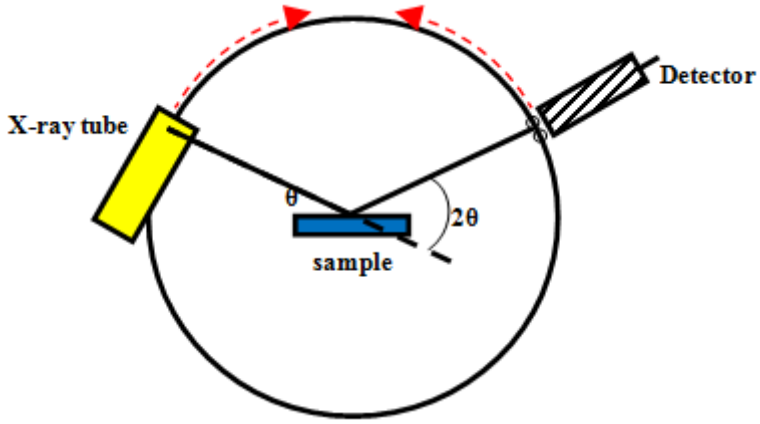

Figure 38: The simple layout of an x-ray diffractometer. The x-ray tube and detector can move along the circumference of the circle so that θ and 2θ can be varied to produce a profile. Taken from [287].

In these investigations, a *Siemens* D5000 Powder Diffractometer was used for analysing the rare earth doped compounds. The x-ray tube used a radiation source containing a Cu anode powered by a 40 kV voltage and 30 mA current to produce *K-α* x-rays of wavelength 1.54 Å. To prepare the materials for XRD, powders were placed in a sample holder (cleaned thoroughly with ethanol) and glass pressed across them to make the substance flat and uniform. Then, they were placed in the machine where they would sequentially be elevated to the platform and exposed to the x-ray beam for the duration of the scanning program. The program took measurements for 2θ = 2-70° in steps of 0.02° at a rate of 1 step/s.

The results for the XRD of the two materials are given in Figure 39. The output data could be smoothed using an operation in the software (this factor was set to 0.05, for the displayed graphs). Despite the still noisy spectra, comparing that obtained for $Sr_4Al_{14}O_{25}$: Eu^{2+}, Dy^{3+} with another work, it can be seen the peaks at 2θ = 25°, 28°, 31° and 34° align [288]. Likewise, for the much cleaner $NaYF_4$:

Er^{3+}, Yb^{3+} spectrum, the peaks at 2θ = 18°, 30°, 31°, 43° and 53°, match with those identified in Wu et al's work [289]. This indicates the materials possess a crystal structure consistent with the literature and they are of the high purity levels claimed. The International Centre for Diffraction Data (ICDD) profiles for the closest in chemical composition to each material within the power diffraction database are also shown in Figures 40 and 41.

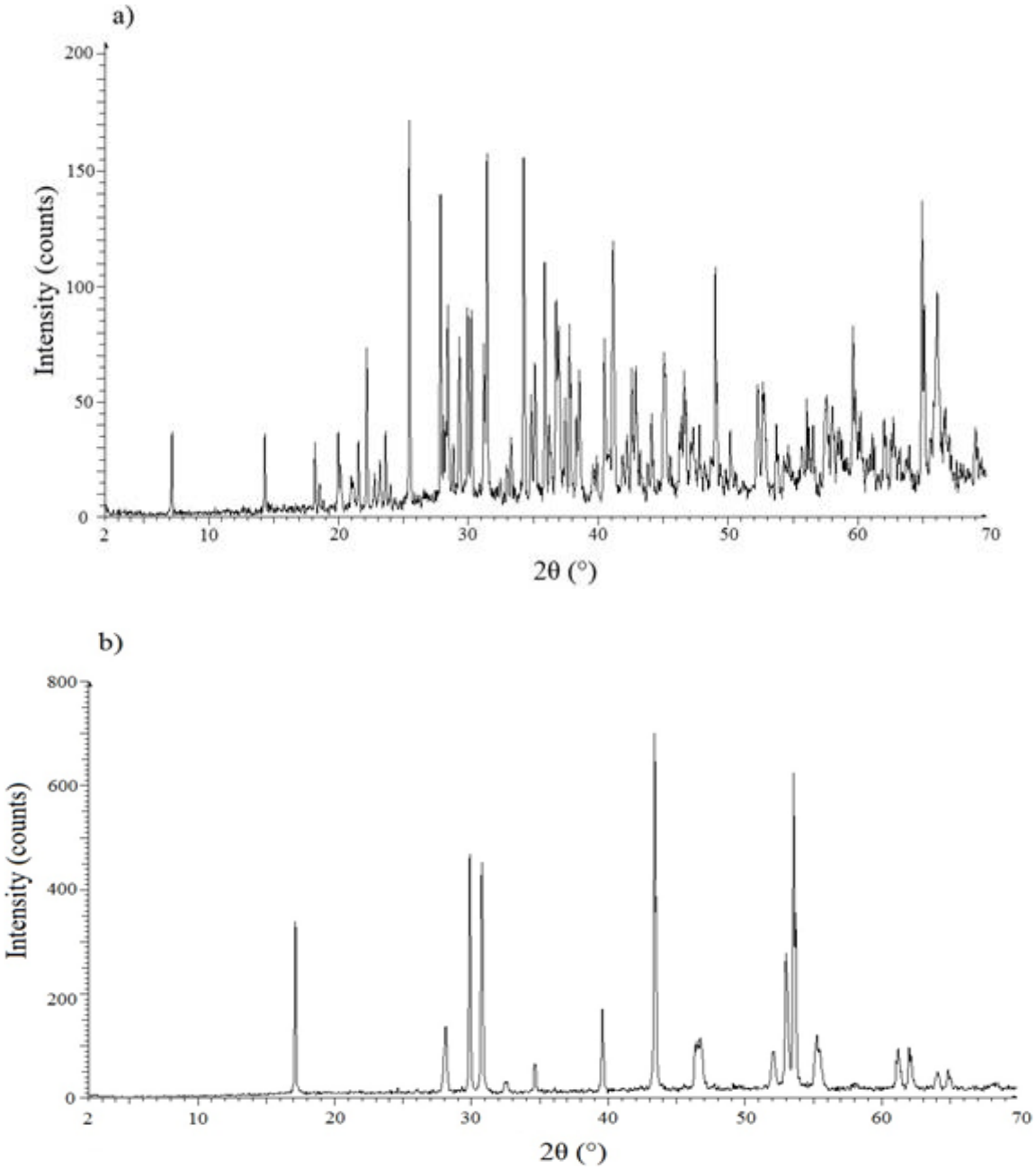

Figure 39: XRD profiles obtained for: a) the ground $Sr_4Al_{14}O_{25}$: Eu^{2+}, Dy^{3+} and b) $NaYF_4$: Er^{3+}, Yb^{3+} powder.

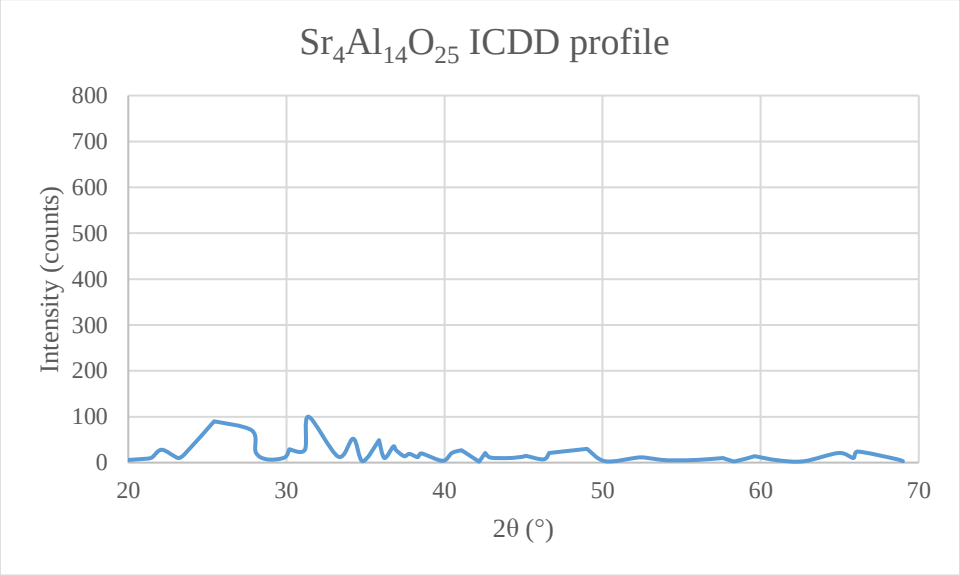

Figure 40: ICDD profile for $Sr_4Al_{14}O_{25}$ from the powder diffraction profile database.

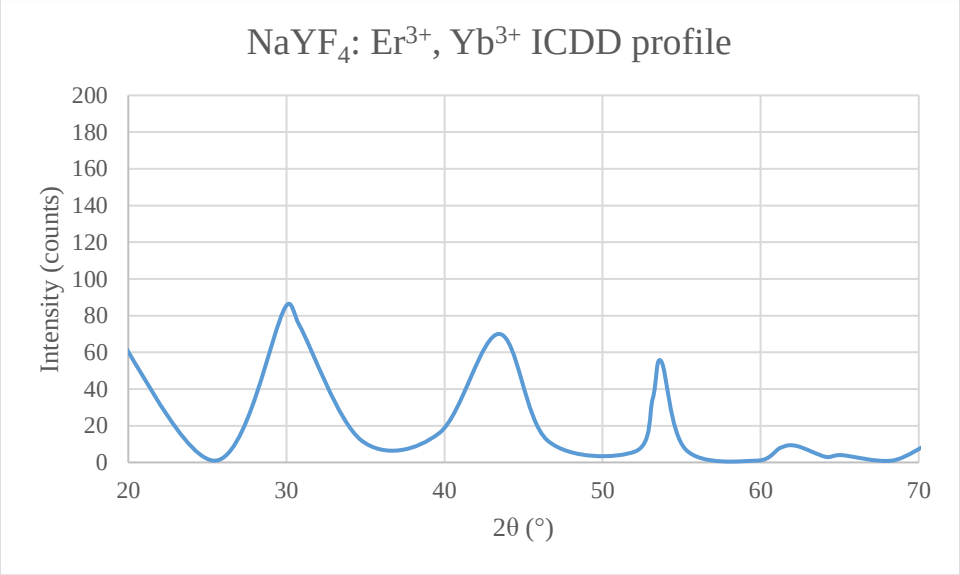

Figure 41: ICDD profile for $NaYF_4$: Er^{3+}, Yb^{3+} from the powder diffraction profile database.

3.3.2 Scanning Electron Microscopy

Scanning electron microscopy (SEM) is another widely used and highly useful experimental method that allows materials to be seen at the nanoscale, beyond the limitations of traditional optical microscopes. SEM works by accelerating electrons to high energies and bombarding a target sample with them, generating signals from the resulting interactions which can then be used to produce digital images. The two processes which can be detected to aid in microscopy are secondary electrons and back scattered electrons. Secondary electrons are a beam of lower energy electrons emitted from the sample, following exposure to the primary high energy beam whereas back scattered electrons are of the same

initial high energy. These can both be detected by an Everhart-Thornley detector [290], surrounded by a Faraday cage, which coverts them into digital signals for image processing. Furthermore, electron-dispersive x-ray spectroscopy (EDXS) often accompanies SEM, since the high energy electrons can lead to x-ray emission from the atoms within the sample and by observing the characteristic peaks in the spectra of these energies, the elements present may be identified.

For this thesis, the *FEI* Quanta FEG 650 SEM was used to obtain images of the rare earth doped compounds and other thin films and conduct basic EDXS. This equipment can attain magnification levels of 100,000 times higher resolution than the naked eye through accelerating electrons to a potential of up to 30 kV and it also has EDXS capabilities. The samples were placed onto a carbon stub in order to reduce background contributions to the signal and then carefully onto a stage within a vacuum chamber. Some materials require further measures, in the form of a gold sputtered coating [291] to eliminate charge build-up which lowers the quality of SEM images, but this was not deemed necessary for gathering these images. Finally, the parameters of the electron beam were set, and images sent to the computer display. These images for the $Sr_4Al_{14}O_{25}$: Eu^{2+}, Dy^{3+} samples, before and after grinding, are displayed in Figure 42.

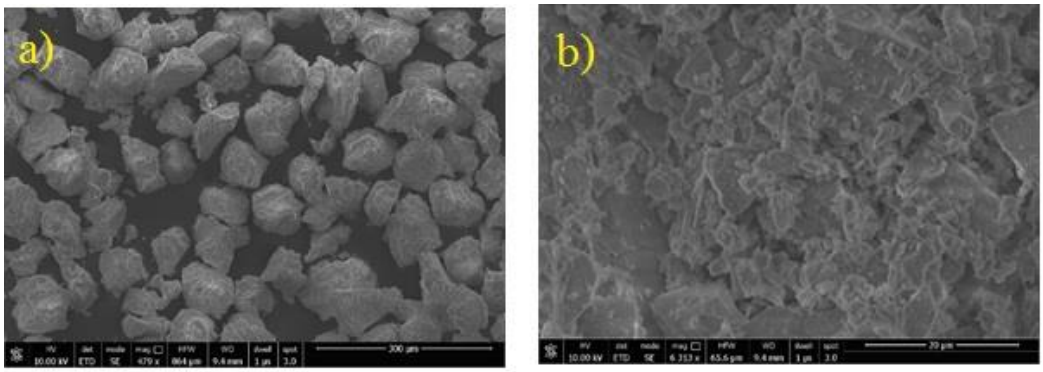

Figure 42: SEM images obtained for the $Sr_4Al_{14}O_{25}$: Eu^{2+}, Dy^{3+} powder samples: a) unground and b) ground.

3.3.3 Photoluminescent Spectroscopy

Photoluminescent spectroscopy is an experimental technique that yields information about the range of wavelengths that excite and are emitted by a material that exhibits photoluminescence. In order to characterise the photoluminescent materials featured in this a work, an FS5 Spectrofluorometer (Edinburgh Instruments) was used. This equipment contains a 150 W xenon arc lamp as a light source and monochromators based on reflective optics in a

Czerny-Turner design that provides an accurate focus at all wavelengths and minimal stray light [292]. The beam incident on a sample has high brightness and a variable bandwidth from 0-30 nm, before passing into one of three detectors: a reference detector (to correct for fluctuations in the light source), a transmission detector (for absorbance) and a single-photon counting detector to give highly sensitive measurements of the amount of emitted radiation in counts per second (CPS). The detectors can also have their bandwidth altered from 0-30 nm.

Before conducting an excitation or emission scan, the 'plug and play' aspect of the machine's accompanying Fluoracle® software is utilised to vary the excitation and emission detection wavelengths and bandwidth parameters to obtain a maximal instantaneous CPS measurement; a wider emission and excitation bandwidth sharply increases the CPS (typically signal bandwidths of 1-3 nm ensured quality spectra). The values quoted in the literature as the excitation and emission peaks for $Sr_4Al_{14}O_{25}$: Eu^{2+}, Dy^{3+} and $NaYF_4$: Er^{3+}, Yb^{3+} were used a starting point and were indeed close to the values that produced the highest CPS values. The CPS value should ideally be ≈ 1 million for emission and excitation peaks to yield a decent spectrum, although this number shouldn't go over 1.5 million as this has the potential to damage the detectors (a red text warning would display, if this situation arose).

The measurements were taken for the $Sr_4Al_{14}O_{25}$: Eu^{2+}, Dy^{3+} and $NaYF_4$: Er^{3+}, Yb^{3+} powders themselves in cuvettes and for the rare earth compounds mixed in a transparent polymer coating on glass (preparation steps for this thin film are given in 3.4). The thin film sample excitation and emission spectra were more relevant for practical considerations than those observed for the powders and the coatings with a doping level of 1% yielded strong spectra and are closest to the average concentration, so are the measurements presented subsequently. Furthermore, both ground and coarse $Sr_4Al_{14}O_{25}$: Eu^{2+}, Dy^{3+} powders were illuminated, and similar profiles observed, so the grinding had not significantly affected its photoluminescent properties. Excel was then used to perform baseline corrections and normalisation, producing the excitation and emission spectra for $Sr_4Al_{14}O_{25}$: Eu^{2+}, Dy^{3+} and $NaYF_4$: Er^{3+}, Yb^{3+} that are shown in Figures 43-46. It can be seen that $Sr_4Al_{14}O_{25}$: Eu^{2+}, Dy^{3+} is broader in its excitation and emission peaks at 360 and 495 nm respectively, each with a Gaussian profile. On the other hand, $NaYF_4$: Er^{3+}, Yb^{3+} shows narrower excitation peaks spread

across the visible spectrum with two modes of photoluminescence observed; one under 380 nm excitation with the most intense emission occurring from 650-680 nm, and another following excitation at 450 nm, with the most prominent emission peak at 553 nm. Furthermore, it was of interest to see if UC could be observed in $NaYF_4$: Er^{3+}, Yb^{3+} by exciting at 979 nm. This sample had primarily been described as a phosphor which exhibits green emission under UV-blue excitation, so may have been prepared primarily for this purpose. However, since it possesses the same chemical structure, it was shown to exhibit small visible UC under NIR illumination (Figure 46). It is also proposed that 979 nm emission may be present under UV-blue illumination but unable to be observed due to the 870 nm limit on the detectors.

The emission spectra of the different doping levels, 0.25% to 2%, (with constant bandwidth to compare relative peak intensity) are also shown in Figures 47 and 48 for each material, which as expected, display an increased CPS with doping concentration. However, as will be seen in 3.4.2, the transmittance also decreases sharply with increased rare earth compound concentration level, so the optimal concentration for improving solar cell performance may lie between the extremes. Finally, and of interest to this study for PV cells where the incident solar radiation comprises of a range of wavelengths, and ultimately their use with LCPV concentrators that absorb UV radiation, it was deemed necessary to excite the materials at 400-440 nm in 10 nm intervals and constant bandwidth, to verify emission can take place at these wavelengths and classify their emission peaks. It can be seen from the resulting spectra for both materials shown in Figures 49 and 50, that significant photoluminescence does indeed still occur, and a redshift is observed in the emission peak with increasing excitation wavelength.

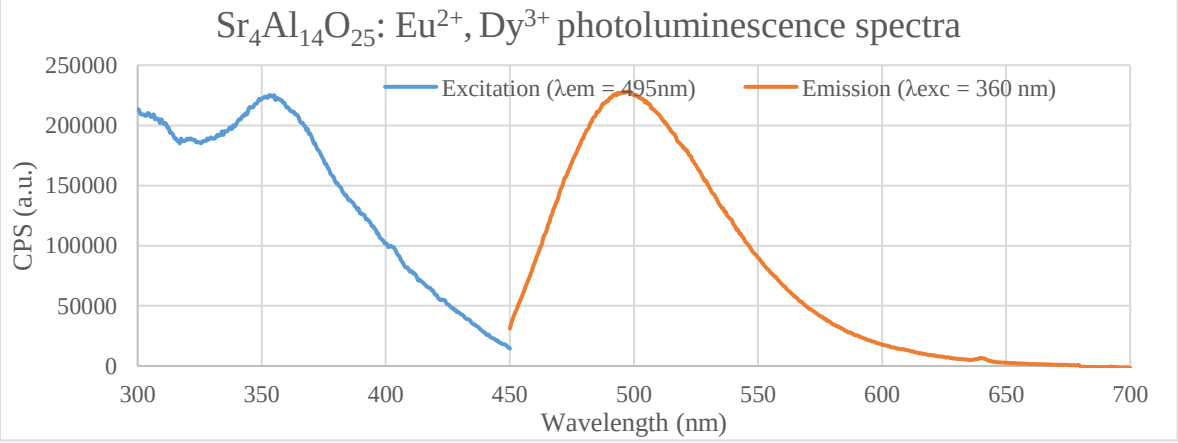

Figure 43: Photoluminescence spectra for 1% $Sr_4Al_{14}O_{25}$: Eu^{2+}, Dy^{3+} doped thin film.

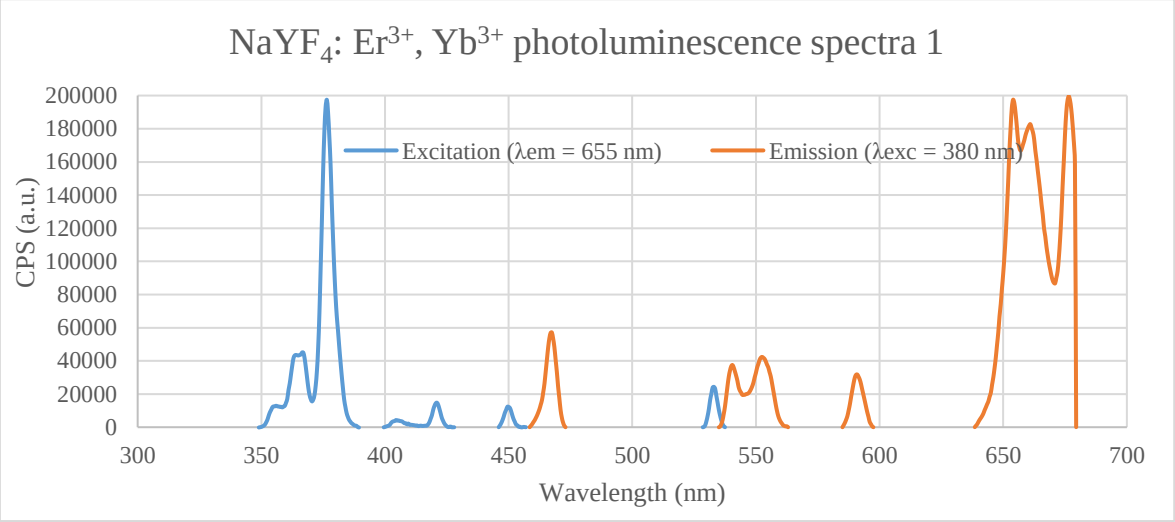

Figure 44: First photoluminescence spectra for 1% $NaYF_4$: Er^{3+}, Yb^{3+} doped thin film.

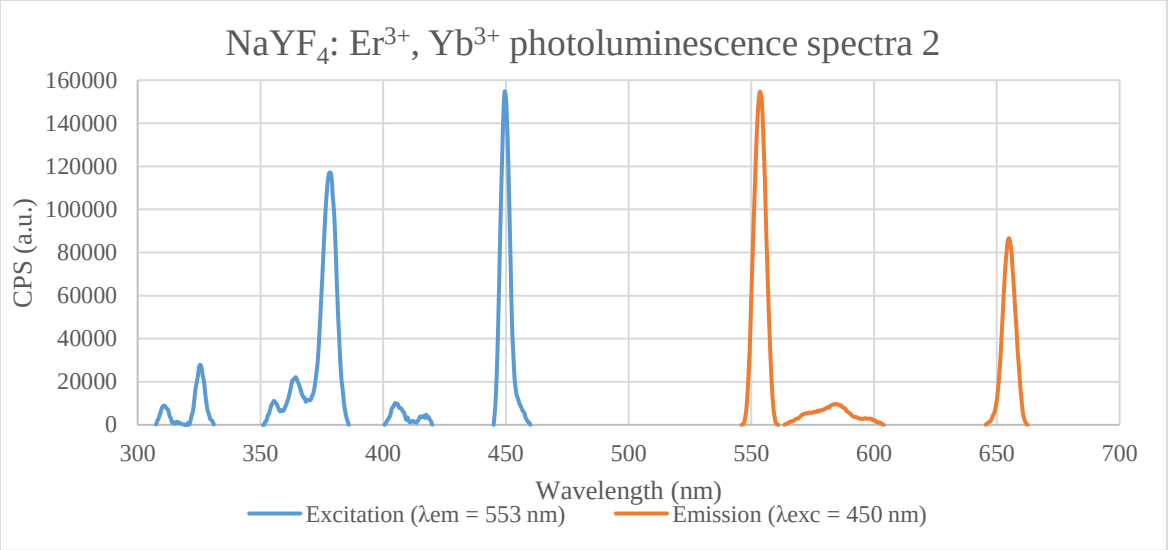

Figure 45: Second photoluminescence spectra for 1% $NaYF_4$: Er^{3+}, Yb^{3+} doped thin film.

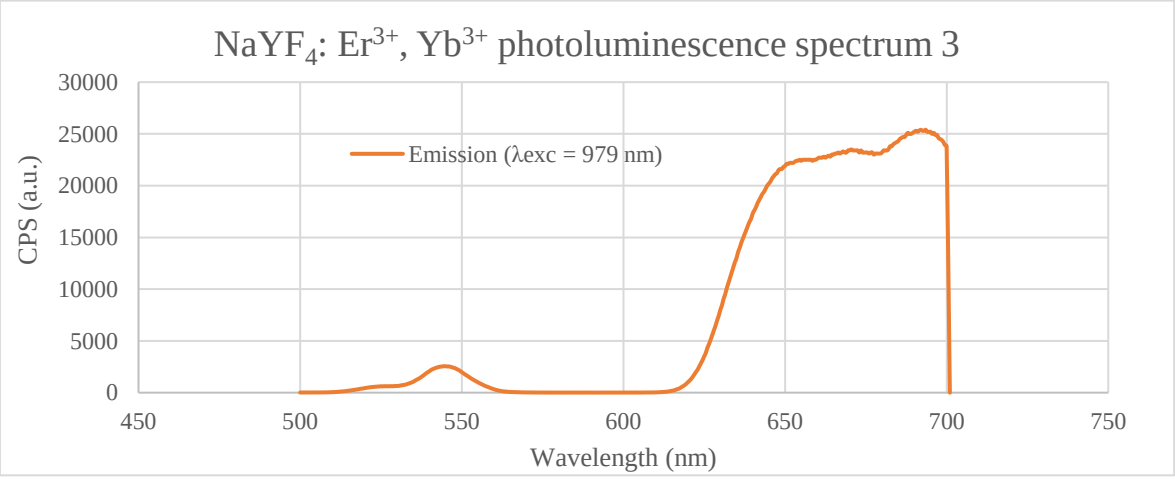

Figure 46: Emission spectrum for 1% $NaYF_4$: Er^{3+}, Yb^{3+} doped thin film under 979 nm excitation.

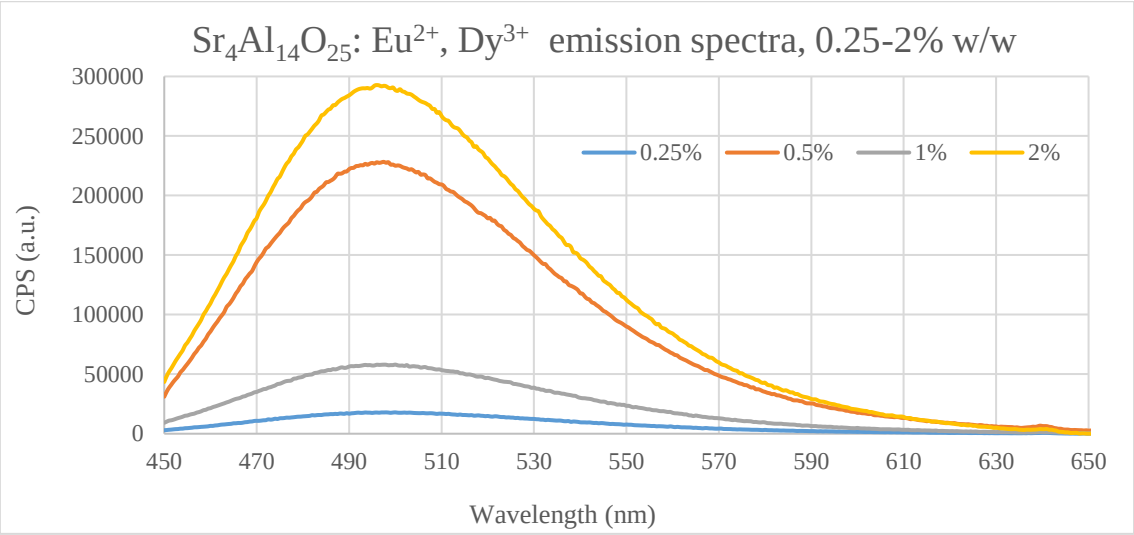

Figure 47: Relative emission spectra for 0.25, 0.5, 1 and 2% doped $Sr_4Al_{14}O_{25}$: Eu^{2+}, Dy^{3+} doped thin films under 360 nm excitation.

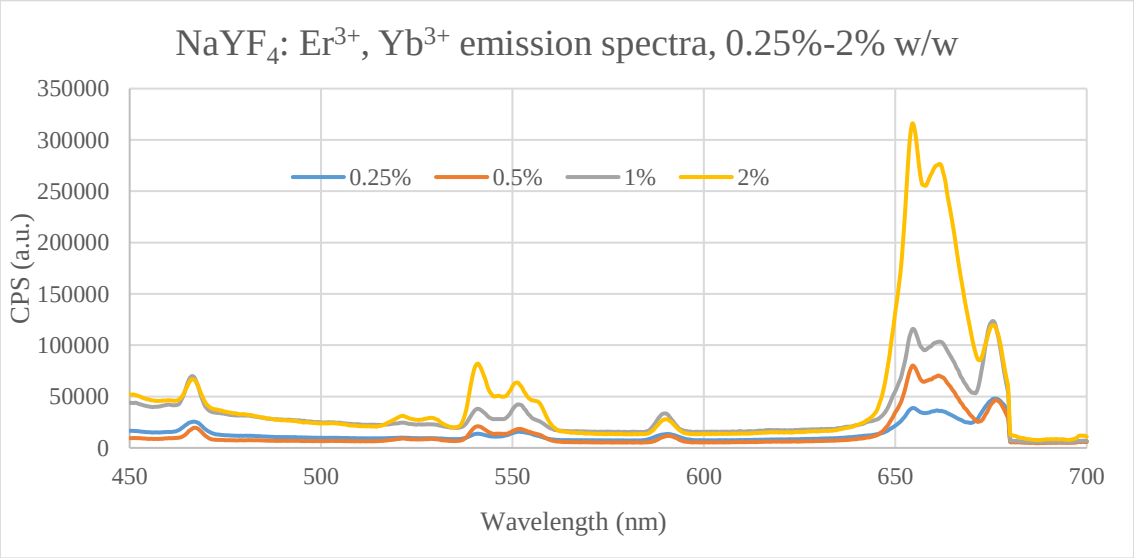

Figure 48: Relative emission spectra for 0.25, 0.5, 1 and 2% doped $NaYF_4$: Er^{3+}, Yb^{3+} doped thin films under 380 nm excitation.

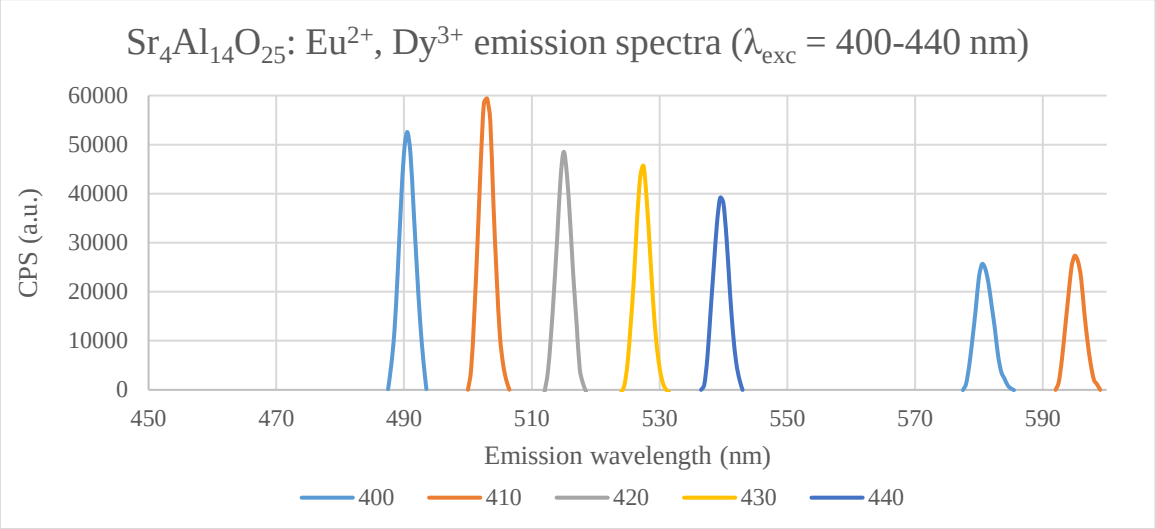

Figure 49: Relative emission spectra for the 1% $Sr_4Al_{14}O_{25}$: Eu^{2+}, Dy^{3+} doped thin films under 400, 410, 420, 430 and 440 nm excitation.

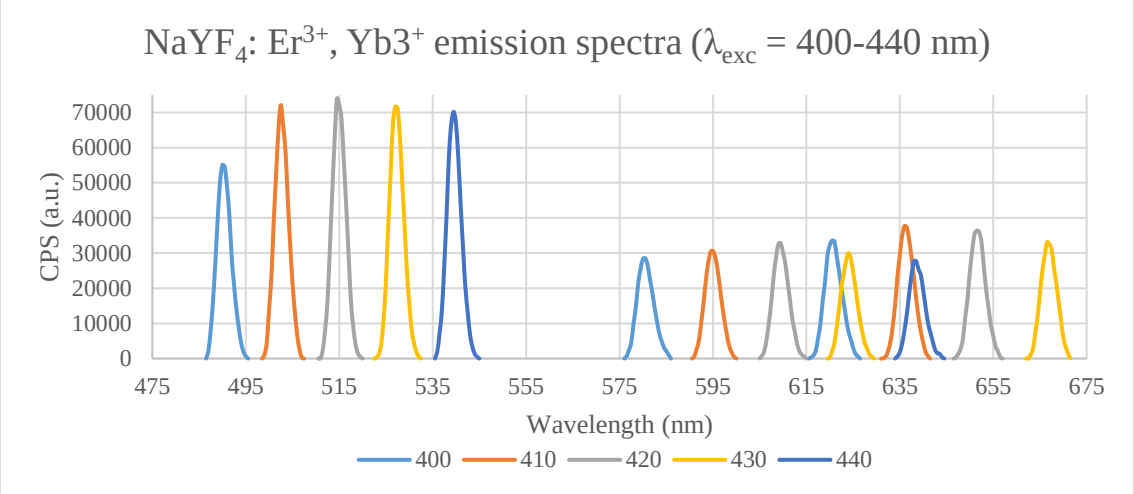

Figure 50: Relative emission spectra for the 1% $NaYF_4$: Er^{3+}, Yb^{3+} doped thin films under 400, 410, 420, 430 and 440 nm excitation.

3.4 Thin Film Preparation and Characterisation

The materials existed in a powder form and as discussed in 2.3, need to be embedded within a near-transparent medium in order to be applied as a thin film and ultimately on top of a solar cell. In this subsection different experimental techniques and materials for achieving this are elucidated.

3.4.1 Spin Coating

Spin coating is a common procedure used to apply a thin film to a substrate. Its main advantage over other coating techniques is its simplicity for achieving a uniform film. However, one drawback is that a large amount (up to 90%) of the coating fluid is wasted as it flies off the edge, meaning it can sometimes be not very cost effective. In a spin coating process, a small quantity (of order 100 μl) of

fluid, consisting of the particles desired to form a layer from dissolved in a solvent, is released drop by drop from a micropipette onto a substrate attached via suction from a vacuum pump to a platform which rapidly rotates (typically 1000-10000 RPM) for a short period of time, usually around a minute. There are two dispense techniques, static and dynamic, depending on whether the substrate is stationary or already revolving when the liquid is applied. During rotation, the centripetal force and surface tension act on the fluid pulling it outwards to produce an even coating [293]. The solvent is then evaporated, mostly from airflow throughout the spinning, while remnants can be removed through either drying in air or heating on a hot plate.

The main parameter for determining the thickness of the film is the spin speed. The two quantities are connected by the following relationship:

$$t \propto \frac{1}{\sqrt{\omega}} \qquad (26)$$

In this expression, t is the film thickness and ω the angular velocity of the substrate. The spin coater used to apply films was a *MIDAS* SPIN-1200D which had a rotation speed range from 300 to 7000 RPM with a quoted accuracy of 1%. Up to 20 ‘recipes’ may be created and stored using the arrow buttons and display screen to set the spin speeds, acceleration times and spin times, with multiple steps available for a single procedure. It was important to optimise the spin coating method in order to avoid the common pitfalls which lead to a non-uniform coating. Figure 51 shows six of these frequent mistakes and their characteristic appearance on the substrate. These patterns include: air bubbles on the surface (from air bubbles in the fluid or a faulty micropipette tip), outward streaks (from too high a fluid dispensing rate), swirl (from the fluid hitting the substrate too far from the centre and too short a spin time), circle in the centre (from off centre fluid deposition or a fault with the vacuum chuck), uncoated areas (from an insufficient volume of fluid dispensed) and pinholes (from impurities in the dispensing fluid or substrate surface). When initially trialling the spin coating technique, many of these resemblances were observed, so were sought to be avoided by following the as described troubleshooting steps [294].

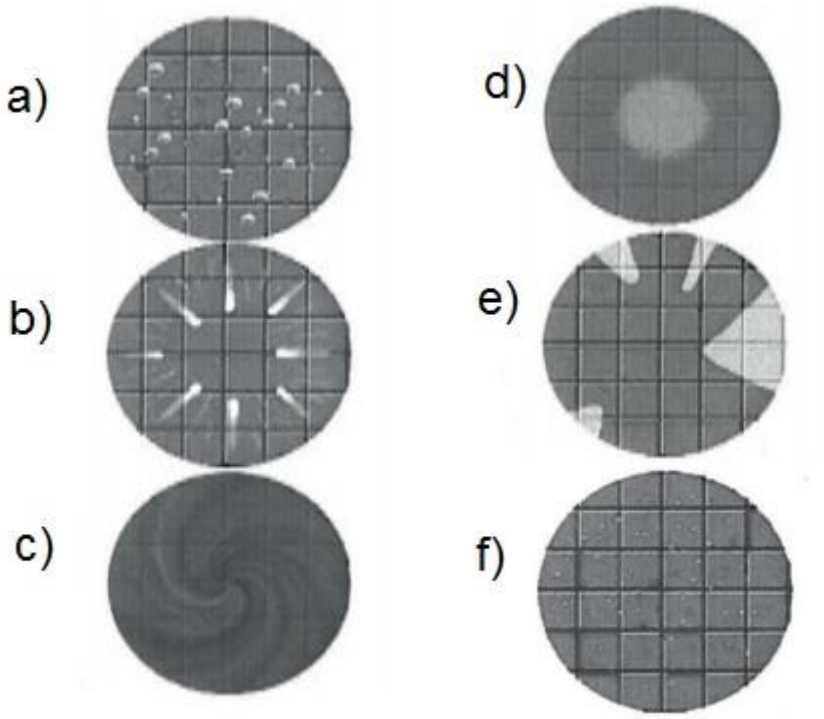

Figure 51: Common spin coating error patterns: a) air bubbles on wafer surface, b) comets, streaks or flares, c) swirl pattern, d) centre circle chuck mark, e) uncoated areas and f) pinholes. Taken from [294].

3.4.2 UV-Vis Spectroscopy

UV-Vis spectroscopy is a vital tool in solar energy materials research that allows the optical properties of matter to be determined. In classical optics, when light interacts with a body, there are three possibilities; it can be absorbed by the material, transmitted through the material or reflected by the surface. These can be quantified by defining the transmittance, *T*, and reflectance, *R*, which are given as the ratio of the power of the transmitted light (P_T) and reflected light (P_R) respectively, to the incident light (P_0).

$$T = \frac{P_T}{P_0} \qquad (27)$$

$$R = \frac{P_R}{P_0} \qquad (28)$$

The light absorbed by the material or absorptance, *A*, can then be calculated as such:

$$A = 1 - T - R \qquad (29)$$

Another quantity that can be derived from UV-Vis spectroscopy is called the absorbance (*Abs*) and is often stated in studies. It is a measure of the amount of radiation that is not transmitted (including reflection and absorption) and is defined as follows:

$$Abs = -\log T \qquad (30)$$

Each of these properties will be highly wavelength dependent, hence in this method, the light source used is able to vary its wavelength across the UV, visible and NIR regions of the electromagnetic spectrum. The machine used for measuring the transmittance was a *Perkin Elmer* UV/VIS/NIR Spectrophotometer Lambda 1050 model. This equipment uses halogen tungsten and deuterium light sources along with double holographic grating monochromators to produce an operating range of illumination from 175-3300 nm. To obtain data, samples are placed in a compartment where they are exposed to the radiation and in the path of high sensitivity photomultipliers and Peltier-controlled detectors, to send signals to a computer display [295].

The UV *WinLab*™ software was used to initialise the system, by selecting the range of wavelengths to be measured, scanning speed (fixed at 3.7 nm/s) and number of samples to be measured. For most studies, the range chosen was 300 – 1100 nm because beyond these wavelengths were of less concern for the relevant solar cells to which the materials would be applied. In the case of a sample consisting of a thin film on a glass substrate, two possible transmittance measurements could be obtained. At the start of the run, a 100% *T* correction is requested which will be used to give the desired transmittance data for the remaining scans. If the transmittance of the entire material, including the substrate, is needed then for the 100% *T* correction, the sample compartment is left empty. However, if the transmittance of only the thin film coating is required, then placing a clean, bare identical glass substrate in the illumination area during this period will allow it to be 'subtracted' from the rest of the samples, meaning the transmittance data will only be for what is on top of the substrates. The latter procedure is useful since for solar cell coatings, only the transmittance of the thin film is of interest. Absorbance could also be measured directly, but since all the software does is apply the above equation, these values could be more aptly calculated from the transmittance data. Any potential solar cell coating will need

to have a high transmittance in the areas of high EQE, so as not to significantly affect the amount of light reaching the solar cell and hamper the device performance.

3.4.3 Sylgard

Sylgard184® is the commercial name of polydimethylsilicone (PDMS), a polymer elastomer and solar cell encapsulant with excellent optical and adhesive properties. These include high transparency (for wavelengths relevant to silicon solar cells), a refractive index of approximately 1.4 across visible and NIR wavelengths (so it is suitable for use as an optical coupling in 3D static LCPV modules made from glass or other transparent polymers), a relatively long pot life (2 hours), a facile and room temperature curing process, chemical inertness and thermal stability up to 200°C [296].

The Sylgard184® set comes in two parts, A and B. In order to make the encapsulant these parts must be mixed together at a ratio of 10 parts A to 1 part B. To achieve a homogenous resulting layer, it is important to minimise the bubble formation during preparation. Therefore, the mixing was carried out in a larger radius beaker and stirred at an appropriately slow speed to fully merge the components without generating lots of air pockets. More importantly, a vacuum oven (MTI technologies EQ-DZF-6210 Vacuum Oven) was used to degas the solution (by exposing the solution to a very low pressure, trapped air would be able to escape) at several stages in the mixing process: when part A was measured out, when part A and B were fully mixed and after any particles were dispersed into the Sylgard.

Given the aforementioned beneficial properties of Sylgard, it could be used as a near-transparent embedding media for the spectral conversion materials $Sr_4Al_{14}O_{25}$: Eu^{2+}, Dy^{3+} and $NaYF_4$: Er^{3+}, Yb^{3+}. This was realised by adding the rare earth compound powders in specified amounts to Sylgard once parts A and B had been mixed and using a magnetic stirrer for several minutes to disperse the particles in a similar method to Qu et al [140]. However, the high viscosity of the Sylgard partially limited the effectiveness of the stirring, so to further ensure a homogenous distribution, the mixture was subjected to ultra-sonication by placing the beaker in the bath of a Hilsonic® ultra-sonicator for 10 minutes.

Deposition of the Sylgard on substrates was achieved either by the spin coating method or drop casting in which the coating is simply applied in a small amount and left to spread across the surface while it sets. Again, the high viscosity of the solution limited the effectiveness of dynamic spin coating as the micropipette was unable to intake or dispense the fluid properly. Therefore, static spin coating was used in some early tests, but the films were not very uniform, so ultimately drop casting proved the more effective technique. In Figures 52 and 53 are shown the UV-Vis spectra for Sylgard with added rare earth doped compounds prepared to these methods in weight percentages of 0% (i.e. no rare earth compound), 0.25%, 0.5%, 1% and 2% and drop cast on acrylic substrates.

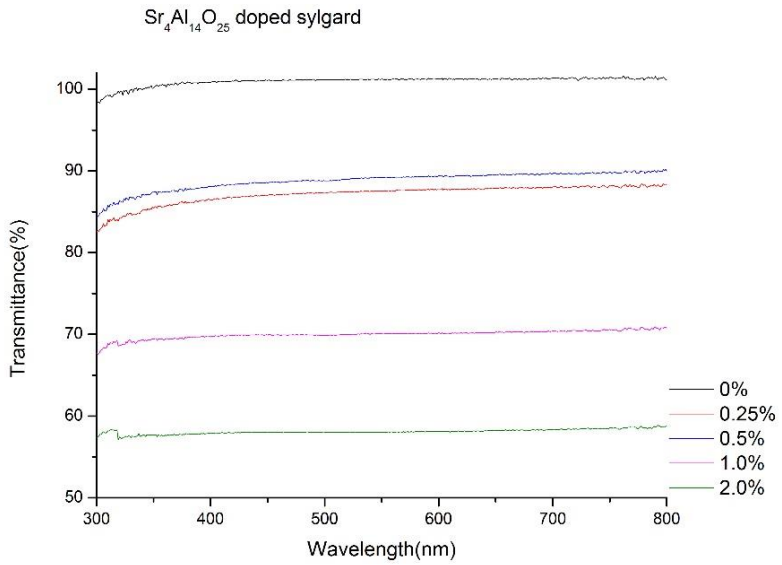

Figure 52: Transmittance of the $Sr_4Al_{14}O_{25}$: Eu^{2+}, Dy^{3+} doped Sylgard layers, in concentrations by weight from 0-2%, drop casted on acrylic.

As expected, there is a clear decrease in transmittance with an increase in rare earth compound concentration. Furthermore, NaYF4: Er3+, Yb3+ appears to have a higher transmittance across most visible wavelengths for a given weight percentage and most spectra show a lower transmittance from 300-400 nm, indicating possible absorption from the rare earth ions. Thus, potential was demonstrated for application to silicon solar cells.

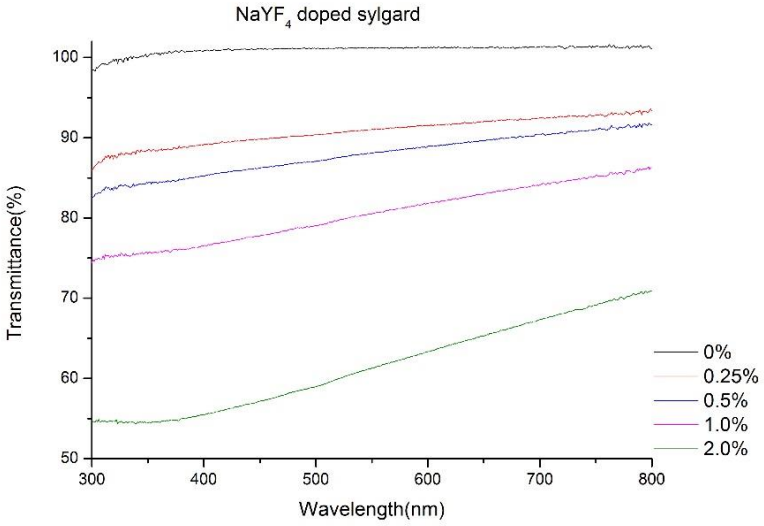

Figure 53: Transmittance of the $NaYF_4$: Er^{3+}, Yb^{3+} doped Sylgard layers, in concentrations by weight from 0-2%, drop casted on acrylic.

3.4.4 TiO_2

Titanium dioxide (TiO_2) is a metal oxide compound which has found several applications including in paints, plastics, paper textiles and inks, corrosion-resistant coatings, anti-bacterial agents, cosmetics, water and air purification and food additives [297]. It occurs naturally in different crystal forms, the most common being rutile and anatase; the former is more compact and opaquer, the latter possesses greater transparency and stability at nanoscales. More recently and with regards to solar energy, anatase TiO_2 has been used as the electron transport layer in emerging PV technologies such as PSCs and DSSCs. This is due to its excellent optical, structural and electronic properties that allow it to form a mesoporous scaffold to undergo dye adsorption or aid perovskite growth, which when on top of a transparent conducting oxide coated glass forms the working electrode of a PV device. For current to flow upon exposure to light, other components must be added which will be presented alongside operating principles in detail in section 5.2. In addition to uses in emerging PV, TiO_2 has also been suggested as a coating for silicon solar cells due to its anti-reflective behaviour as well as high transparency, low cost per area and chemical stability [298].

The TiO_2 primarily used in these investigations was a Greatcell 18NR-T transparent titania paste. This initially takes the form of a yellow paste that contains 20 nm TiO_2 particles, at a concentration of 19% by weight, within organic binders. This paste may be applied to a substrate by spin coating (following

dilution and mixing in ethanol to reduce viscosity), screen printing or doctor blading (these latter two processes will be discussed for DSSC fabrication in chapter 5). Once the film has been coated, it must be heated to 500°C to evaporate the binders and leave a sintered deposition.

The rare earth compounds could be added to the TiO_2 solution before it was spin coated by mixing in a vortex mixer (Stuart SA8) and further treated by ultra-sonication. This is not an ideal method, since the particles did not readily dissolve and disperse (recalling from 3.4.1 impurities would affect coating quality) but initial tests showed the films to be of acceptable standards and UV-Vis spectroscopy showed a high transparency (cf. Figure 54). Therefore, these films were to be further investigated and applied to solar cells.

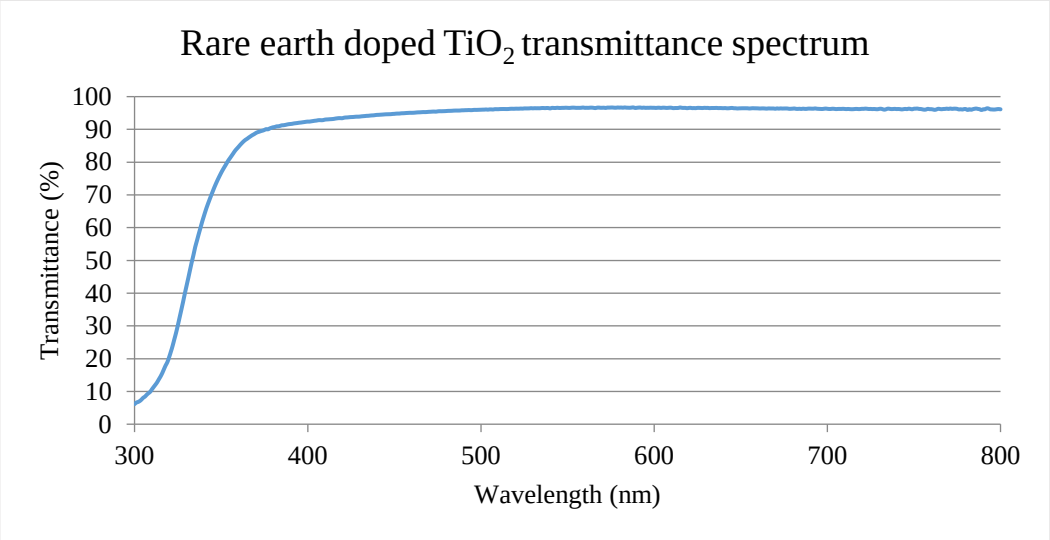

Figure 54: Transmittance spectrum of TiO_2 (Greatcell 18NR-T) containing 10% $Sr_4Al_{14}O_{25}$: Eu^{2+}, Dy^{3+} by weight and spin coated at 6000 RPM on a glass substrate.

It was also proposed to produce TiO_2 in house, rather than rely on the costlier pre-prepared paste. In order to do this $TiCl_4$ was sourced from Sigma Aldrich (≥ 99% purity) and reacted with high quality ethanol (≥ 99.5% purity) to form titanium ethoxide ($Ti_4(CH_2CH_2O)_{16}$), in a sol-gel method previously proposed by Zhu et al [299]. The overall reaction is expected to be:

$$4\ TiCl_4 + 16\ CH_3CH_2OH \rightarrow Ti_4(CH_2CH_2O)_{16} + 16\ HCl \qquad (31)$$

The resulting $Ti_4(CH_2CH_2O)_{16}$ can then, after deposition, be heated to undergo hydrolysis when exposed to air at its surface, leading to the formation of a pure TiO_2 film [300].

$$Ti_4(CH_2CH_2O)_{16} + 8\ H_2O \rightarrow 4\ TiO_2 + 16\ CH_3CH_2OH \qquad (32)$$

This synthesis was attempted by adding 1.5 ml of $TiCl_4$ to 6 ml of ethanol and mixing vigorously by a magnetic stirrer for 30 minutes. During the reaction, heat and clouds of HCl gas were emitted from the beaker and the resulting product was a yellow-green gel. Like Sylgard, this was mixture was highly viscous, so a further few drops of ethanol were added to reduce the viscosity, easing its transfer to a glass substrate via dynamic spin coating. 75 µl of this liquid was dispensed at 5 varying spin speeds (1000, 2000, 4000, 6000 and 8000 RPM) for one minute, before annealing the samples at 450°C for 30 minutes with a ramp time of 3°C/minute to complete the TiO_2 layer formation. The resulting films were characterised by UV-Vis spectroscopy (Figure 56) to determine their transmittance and an optical microscope (100 times zoom) to analyse their uniformity (Figure 55). However, these transmittances were deemed too low and films of too low quality, from their unideal synthesis, to be of use for solar cell applications.

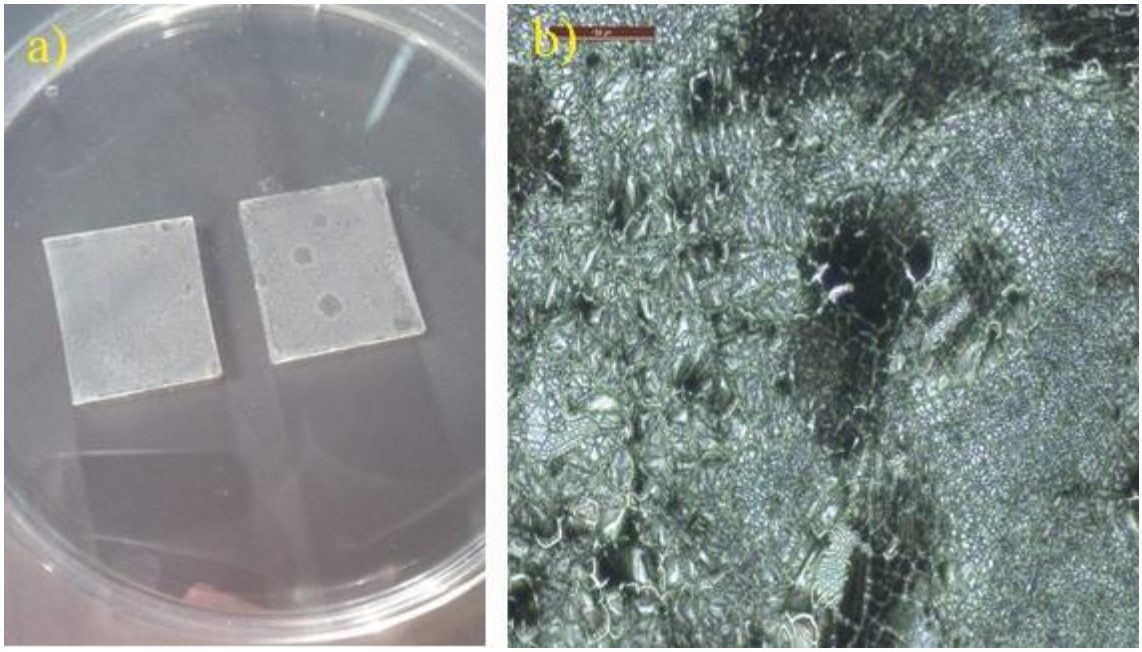

Figure 55: a) Picture of two films of TiO_2 synthesised via the $TiCl_4$ method. b) 100x magnification image, obtained via an optical microscope, highlights the inhomogeneity of the coating.

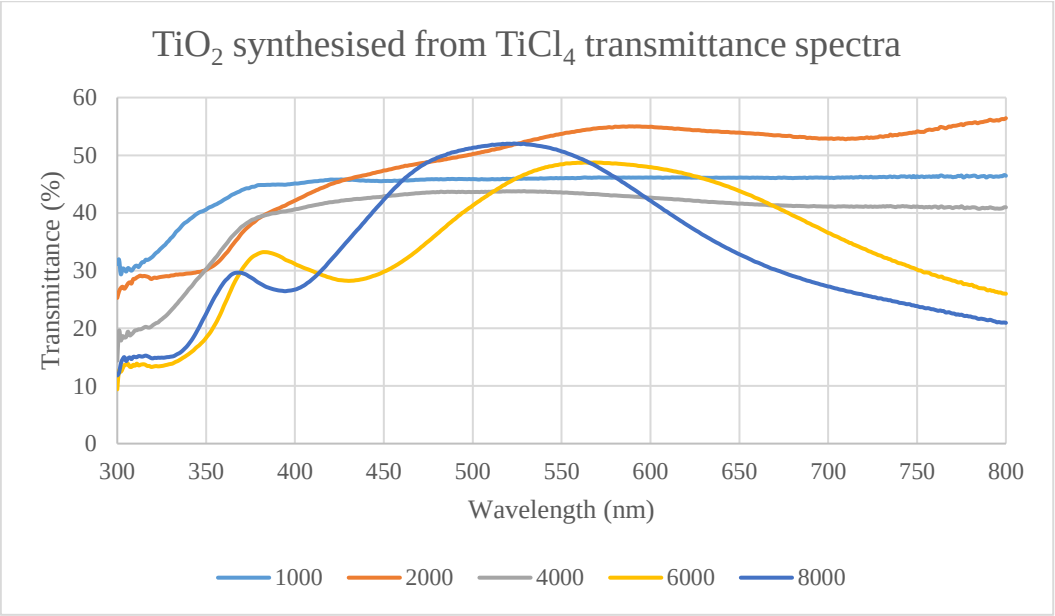

Figure 56: Transmittance spectra of TiO_2 thin films synthesised via the $TiCl_4$ method and spin coated at increasing RPM from 1000 to 8000.

3.4.5 Ball Milling in Ethanol Solvent

$Sr_4Al_{14}O_{25}$: Eu^{2+}, Dy^{3+} in its powdered form was insoluble in ethanol but if the particle size could be greatly reduced, it may be suspended in solution and spin coated to form a layer. This led to another way of getting the powders to form a thin film without the use of an embedding media being explored. Ball milling is a method which involves placing a material in a cylindrical vessel with inert, rigid spheres and subjecting it to a rotational force. This causes the balls to act as a grinding medium and reduces the particle size of the powder through repeated collisions (cf. Figure 57). It is also important for the balls and jar coating to be of similar material and wear resistant. The milling can be carried out in the presence or absence of a liquid, known as dry milling and wet milling respectively. Wet milling is recommended for achieving particle sizes smaller than 1 µm, so would be used in this situation [301] and a *Retsch* Planetary Ball Mill 100 capable of rotation speeds up to 650 RPM was to be used in these studies. In this machine, a 50 ml jar filled with 100g of 1 mm diameter Al_2O_3 balls, 2g of $Sr_4Al_{14}O_{25}$: Eu^{2+}, Dy^{3+} and ethanol (mixed into the other contents of the jar with a spatula until there was a slurry consistency) was placed on the rotation platform and set to 350 RPM for 1 hour. Afterwards, the jar was emptied, and the grinding balls separated by a sieve mesh. The filtered homogenous solution was then spin coated on glass substrates at 1000, 3000 and 6000 RPM for 1 minute. The samples were then dried for 18 hours either in air at room temperature or on a hot plate at 100°C.

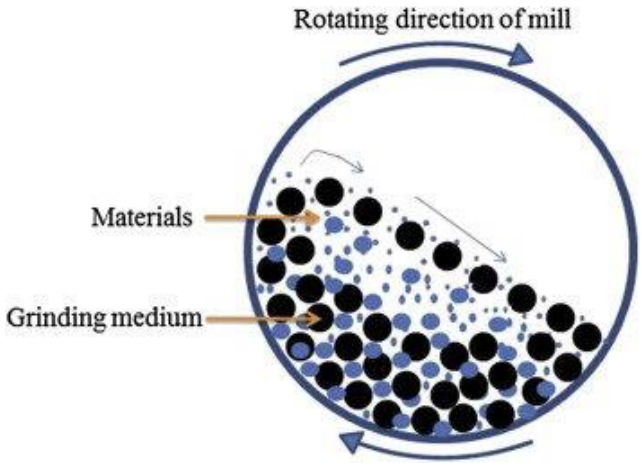

Figure 57: Schematic of the operation principle of a ball milling machine. Collisions between the balls and the grinding medium cause a reduction in average particle size.

As shown in Figure 58, the reduction in transmittance from 300-420 nm suggests absorption is taking place, which is consistent with the excitation profile of $Sr_4Al_{14}O_{25}$: Eu^{2+}, Dy^{3+}. Despite promising optical properties, this method, though potentially useful for application of a layer in an emerging PV cell was deemed unsuitable to be deployed to silicon solar cells, since their surface structure is not as flat as glass which will affect film quality, the temperature required could damage the PV and because the encapsulant is usually located between the cell and the cover glass anyway, doped Sylgard was considered to be of the most practical interest for experiments.

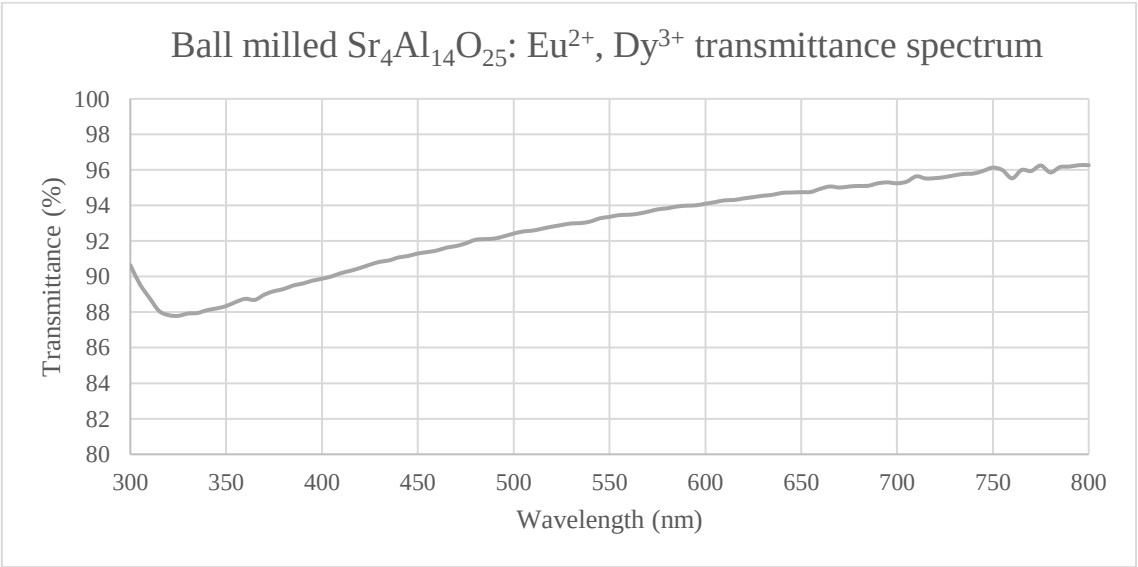

Figure 58: Transmittance spectra of the $Sr_4Al_{14}O_{25}$: Eu^{2+}, Dy^{3+} film which had been produced by ball milling and spin coated at 6000 RPM.

3.5 Silicon PV Device Preparation

In this section the properties of the silicon solar cells that formed the basis of subsequent investigations are described, along with the methods used to modify their surface and prepare them for electrical characterisation.

3.5.1 Silicon Solar Cells

The solar cells used in the majority of this thesis were pre-manufactured c-Si devices with an active area of 1 cm^2 provided by the National Renewable Energy Centre (NAREC). These cells were chosen because of their high performance, low cost and suitability for use in LCPV conditions. The stated electrical parameters under 1 sun concentration were a PCE of 17%, J_{SC} of 32 mA/cm^2 and V_{OC} of 0.56 V. These respectable properties are a result of the laser grooved buried contact technology, outlined in Figure 59, leading to reduced shading losses and improved charge carrier collection. In addition, the textured Si_3N_4 surface causes more light to be captured and current generated [302].

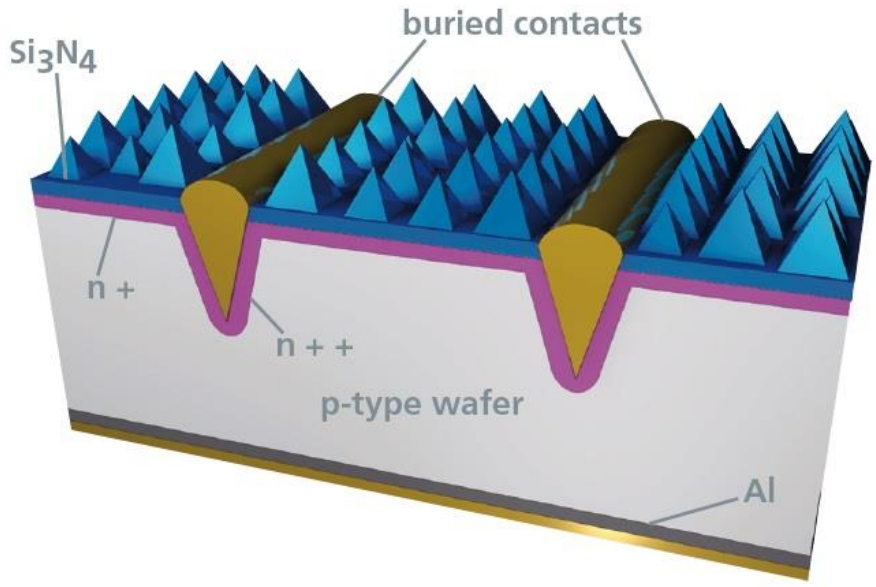

Figure 59: Schematic diagram to show the structure of the c-Si solar cells with laser grooved buried contact technology produced by NAREC and used in this work. Taken from [302].

The cells arrive without external wiring contacts (see Figure 60) which makes them very difficult to extract a load from and characterise their electrical properties. Therefore, all solar cells were soldered (using a *Weller* WD1 soldering kit at 350^{o}C) with aluminium wire at the top and bottom surfaces and a light brush

from a flux pen (RS 251-3637) was applied prior to soldering, in order to help the solder flow cleanly on to the metal surface. Once soldering was completed a multi-meter (Fluke 117) was used to check the voltage of the devices (under ambient room lighting conditions) to verify the device was functioning properly; the contribution of these voltage fluctuations to measurement uncertainty is discussed in 6.3.2.

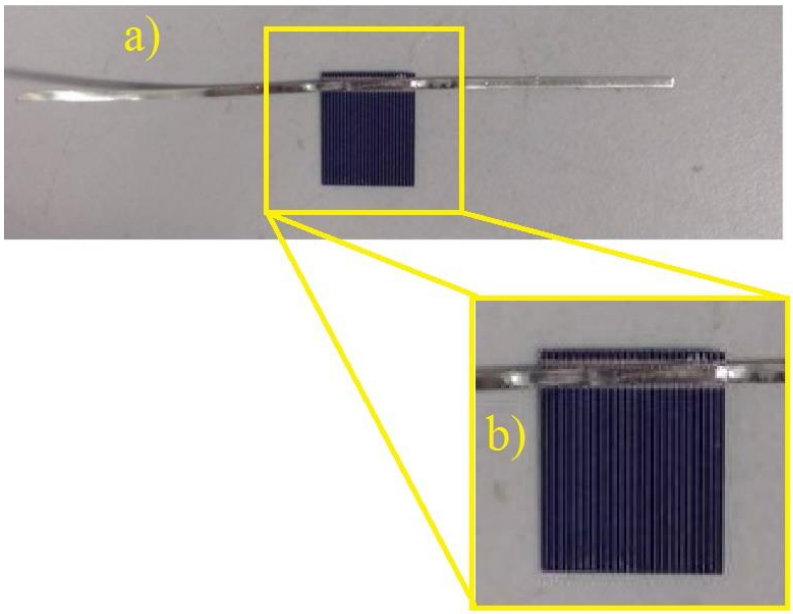

Figure 60: a) Real image of a soldered c-Si solar cell and b) a zoomed image of the cell to show the buried contacts.

3.5.2 Application of Thin Film

The films were applied to these c-Si solar cells using the methods as previously described in this chapter (spin coating and drop casting) and components of solutions will be discussed as results are presented in 3.7.

The Sylgard-rare earth doped compound mixture was static spin coated by applying a small drop (approximately 0.5 ml) on to the middle of the soldered solar cell and rotating at a speed of 8000 RPM for 5 minutes. The coatings were then left to cure by placing on a hot plate at 75°C for 5 minutes.

On the other hand, the TiO_2-rare earth doped compound composite was spin coated dynamically at 6000 RPM for 1 minute. However, a potential problem arose due to the high annealing temperature required by the TiO_2 (500°C which would crack the PV cells, rendering them unusable) but a solution was found by decreasing the hot plate temperature to 100°C while increasing the exposure time from 3 to 24 hours, allowing the binders to fully evaporate and layer to form.

When drop casting the Sylgard-rare earth doped compound mixture, a small amount of approximately 0.5 ml was poured gently, directly from the mixing beaker. To make sure the Sylgard could spread over an area without sticking the solar cell to the table, another surface was needed to act as a permanent backing fixture for the device. For this purpose, 3 mm thick Plexiglas® acrylic sheets were cut into 4 cm × 4 cm squares and a boundary created using glue from a glue gun (Loctite® Hot Melt) to prevent Sylgard leakage. Prior to drop casting the cells were then placed close to the centre of this square and the soldered metal contacts over its edges.

3.6 Electrical Performance Characterisation Methods

After applying the coatings, the c-Si devices needed to have their electrical properties (PCE, EQE, J_{SC} and V_{OC}) measured. This was accomplished through illuminating them with a solar simulator or tuneable laser and connecting them to electronic equipment that could send data to a computer.

3.6.1 Solar Simulator

Solar simulators are essential laboratory equipment used by researchers and industry to test PV device efficiency and other electrical performance parameters (PCE, FF, J_{SC} and V_{OC}) under standard conditions [303]. The solar simulator used in these studies was an A+A+A+ *Wacom*® Super Solar Simulator containing a powerful 2000 W xenon arc lamp that can produce highly collimated (to within ± 3°) illumination to replicate sunlight with an approximate spectral irradiance (with temporal intensity stability to within ± 1%) as per the AM 1.5 G spectrum. The intensity of the light was then able to be controlled by a piece of equipment and software called HelioCon (*Voss electronic* GmbH) with a high accuracy adjustment rate of 0.1 W/m^2 per step.

Devices to be measured are placed on a stage under the lamp as per Figure 61 (which can illuminate an area of 441 cm^2) and to obtain electrical performance data, an I-V tracer (EKO MP-160i) must be electrically connected to both terminals of a solar cell. This equipment is able to produce an I-V curve made of 256 data points with an accuracy of ± 0.5%, by varying the emulated impedance from zero to infinity whilst sweeping across the operating voltage range (from V_{OC} to V = 0) of the cell. Prior to measurement, the device parameters must be inputted on the MP-160i software including: active and total PV area, rated

voltage and current (i.e. maximum values expected) and sweep time; a sweep time of 5 secs was used to prevent the high efficiency cells storing charge [304].

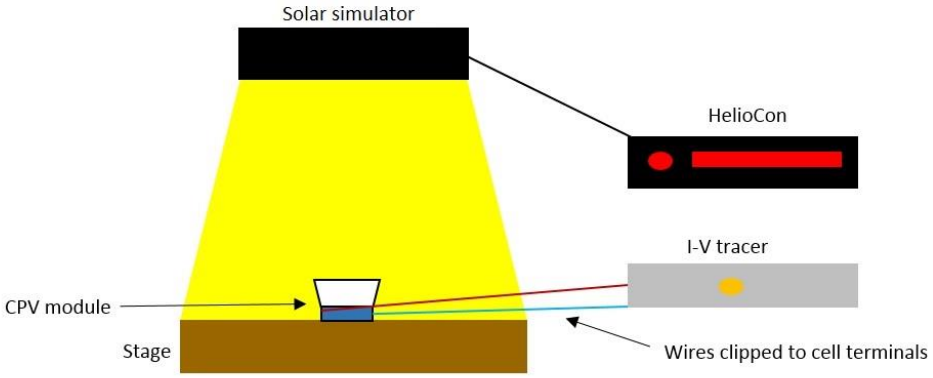

Figure 61: Diagram of the experimental set up when characterising PV or LCPV cell performance under the solar simulator.

It is important to confirm that the lamp is of a known irradiance for a given HelioCon value, so this simulator has been calibrated through Fraunhoffer Institute, ISE in Frieburg, Germany by a special reference cell (WPVS, S/N 10510-0401) that is carefully stored in the vicinity. Before each measurement session, the reference cell is tested to obtain an I_{SC} value that must be its quoted value of 127 mA (to a level of ±0.05 mA) for a solar simulator irradiance of 1000 W/m^2 (i.e. 1 sun). Due to the linear relationship between I_{SC} and light intensity, different irradiance levels (n suns, where n < 1) of interest for this study could be realised by altering the HelioCon value until a reference cell I_{SC} measurement of n × 127 mA had been obtained for n = 0.4, 0.6 and 0.8; for their typical values, refer to Table 7. The HelioCon values to achieve a desired reference current varied slightly over the lifetime of the investigations and this source of error will be discussed in 6.3.2.

Light intensity (suns or W/m^2)	Reference cell I_{SC} (mA)	HelioCon value (arb. units)
1 or 1000	127	730
0.8 or 800	101.6	550
0.6 or 600	76.2	260
0.4 or 400	50.8	80

Table 7: The reference cell I_{SC} required for the light intensity to be calibrated to the appropriate level and corresponding HelioCon value.

The simulator takes power from a three-phase AC supply (400 V voltage, 16A current and 50 Hz frequency) which is converted to DC by a full-wave rectifier,

and through the use of an internal light monitor and feedback circuit is able to stabilise the lamp's irradiance to a constant level of ± 1% (for a given HelioCon value). Recalling from 1.3 the performance of solar cells is affected by temperature, so it is vital to keep this invariable throughout experiments in order to achieve reproducible results. Despite the lamp having inbuilt cooling and propeller exhaust fans, these are insufficient to prevent a notable warming of surroundings by several °C. Therefore, to mitigate this problem, the room was intended to be kept at a constant temperature of 25°C with the help of an additional wall mounted air conditioning unit.

To test an as fabricated in 3.5.1 silicon PV device, the solar cell was placed on a stage under the lamp and both its front and rear conducting contacts connected via crocodile clips to the I-V tracer. The relevant area and electrical parameters were selected, and the lamp was switched on. Two I-V curves were produced per cell after 30 and 60 s. This timing procedure was chosen to allow the system to reach a steady state, 'charge up' the phosphor and allow for a second measurement (to improve reliability and reproducibility).

3.6.2 Incident Photon-to-electron Conversion Efficiency

As well as the aforementioned electrical properties which can be derived through the use of a solar simulator, it is important in this work to quantify how the solar cells respond to different spectral regions of the incident sunlight through an EQE measurement. This can be carried out through the use of a *Bentham PVE300* incident photon-to-electron conversion efficiency (IPCE, another name for EQE) system which contains a tuneable monochromatic laser (*Bentham* TMc300) that can be used to provide illumination to a PV cell across discrete integer wavelengths from 300-2500 nm. The light source originates from a 75 W xenon or 100 W quartz tungsten lamp (depending on the target wavelength) and undergoes dispersion at one of three grated surfaces to reach an exit slit in a Czerny-Turner arrangement of optics with focal length 300 mm, producing a 0.36 cm^2 monochromatic beam (after travelling through a reflective relay optic) to an accuracy of ±0.2 nm below 1100 nm and ±0.4 nm above 1100 nm. This light is incident upon a 400 cm^2 gold coated mount (cf. Figure 62) where solar cells can be placed and which sits on a motorised stage that can be remotely moved in the X and Y direction to ensure the sample device is appropriately illuminated (for consistency this was always the centre of the cell).

BenWin+ software was used to control the equipment and show collected data. When measuring silicon cells, the 'transformer mode with stages' was selected and scans were set to run between 300 and 1100 nm in intervals of 10 nm. Prior to commencing measurements, the PVE300 had been calibrated using a reference silicon cell (15968 Si) which gave a known characteristic output current for each wavelength. A data correction is then applied, so that when PV cells of unknown current are measured, the signal can be automatically displayed as a spectral response (and converted to an EQE spectra through an option in the software). In order to retrieve an electrical signal (and hence EQE spectra) a robust, gold tipped spring probe was held on the front metal contact of the solar cell. The probe was connected to a transformer using a coaxial cable and to complete the circuit it was grounded via a connecting wire to the gold plate which in turn had the back metal contact pressed onto it by another spring probe. The transformer then has another coaxial cable at its output feeding into a pre-amplifier (*Bentham* S400 474) and signal detection unit (*Bentham* S400 417) that is able to display the data on the computer. Three scans were taken for each of the PV cells and an average spectrum calculated to improve reproducibility.

In addition to EQE, this system was also used for another function, to measure the optical property of reflectance. This could be done by placing a mirror beneath the tuneable light source to redirect the beam towards an integrating sphere. This integrating sphere could be connected by a coaxial cable to another input on the amplifier and processing unit, bypassing the transformer so that the signal becomes direct current. After being calibrated by a white reflectance standard, samples placed at the exit aperture of the sphere will have their percentage reflectance measured by the system and displayed through the *BenWin+* software.

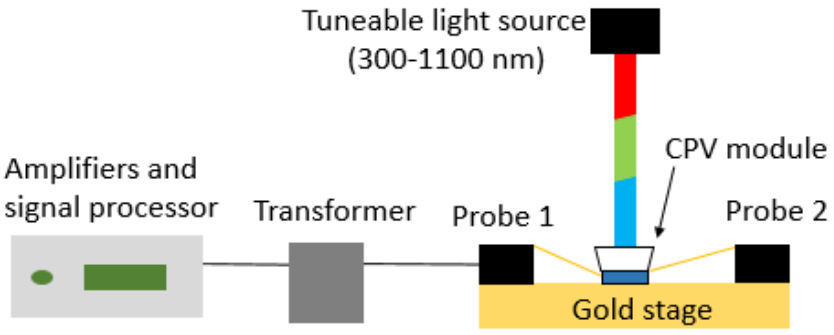

Figure 62: Diagram of the experimental set up when characterising PV or LCPV EQE with the Bentham PVE300.

3.7 Results

The results from three investigations of different coatings on silicon solar cells are presented in the following subsections.

3.7.1 Sylgard Static Spin Coated

In the first trial investigation, a sample of four silicon solar cells (described in 3.5.1) had a coating applied to their front surface by a static spin coating method (3.5.2); two with pure Sylgard and two with Sylgard containing 8.3% $Sr_4Al_{14}O_{25}$: Eu^{2+}, Dy^{3+} by weight. The cells had their efficiencies and J_{SC} tested both before and after the coating was applied. These values are stated in the subsequent Tables 8-9 and I-V curves from the solar simulator are given in Figures 63-66.

Cell and Coating	Bare η (%)	Coated η (%)	Δη from Coating (%)
Cell 1 – Sylgard only	15.10	14.75	-2.32
Cell 2 – Sylgard only	15.01	15.27	+1.73
Cell 3 – Sylgard and $Sr_4Al_{14}O_{25}$: Eu^{2+}, Dy^{3+}	14.09	14.20	+0.78
Cell 4 – Sylgard and $Sr_4Al_{14}O_{25}$: Eu^{2+}, Dy^{3+}	14.14	13.74	-2.83

Table 8: PCE measurements and relative PCE changes for the solar cells when bare and then when spin coated with Sylgard or $Sr_4Al_{14}O_{25}$: Eu^{2+}, Dy^{3+} doped Sylgard.

Cell and Coating	Bare J_{SC} (mA)	Coated J_{SC} (mA)	ΔJ_{SC} from Coating (%)
Cell 1 – Sylgard only	35.400	34.336	-3.01
Cell 2 – Sylgard only	35.015	34.869	-0.42
Cell 3 – Sylgard and $Sr_4Al_{14}O_{25}$: Eu^{2+}, Dy^{3+}	35.285	34.796	-1.38
Cell 4 – Sylgard and $Sr_4Al_{14}O_{25}$: Eu^{2+}, Dy^{3+}	34.456	33.344	-3.33

Table 9: J_{SC} measurements and relative J_{SC} changes for the solar cells when bare and then when spin coated with Sylgard or $Sr_4Al_{14}O_{25}$: Eu^{2+}, Dy^{3+} doped Sylgard.

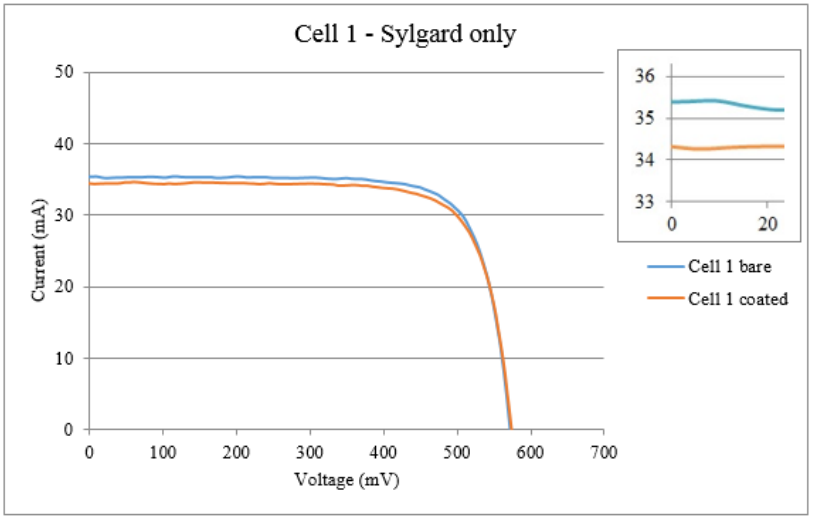

Figure 63: I-V curve of cell 1, before and after coating with Sylgard.

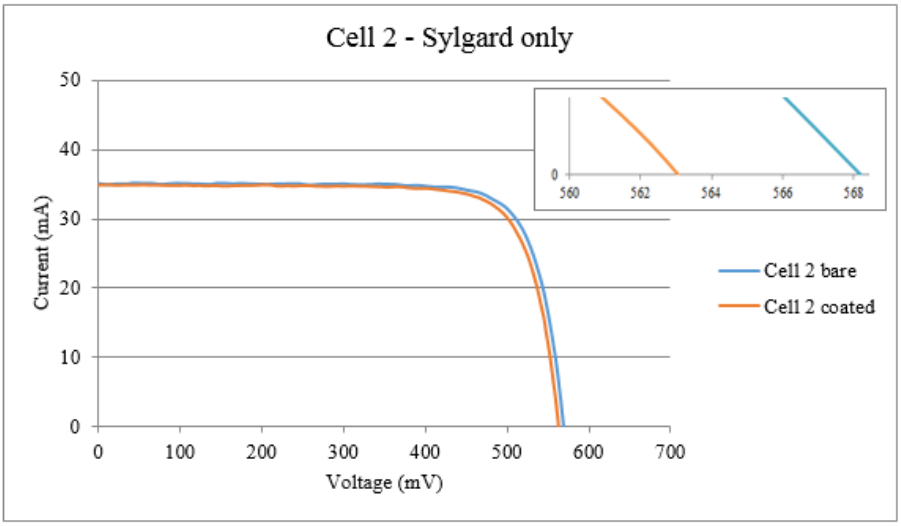

Figure 64: I-V curve of cell 2, before and after coating with Sylgard.

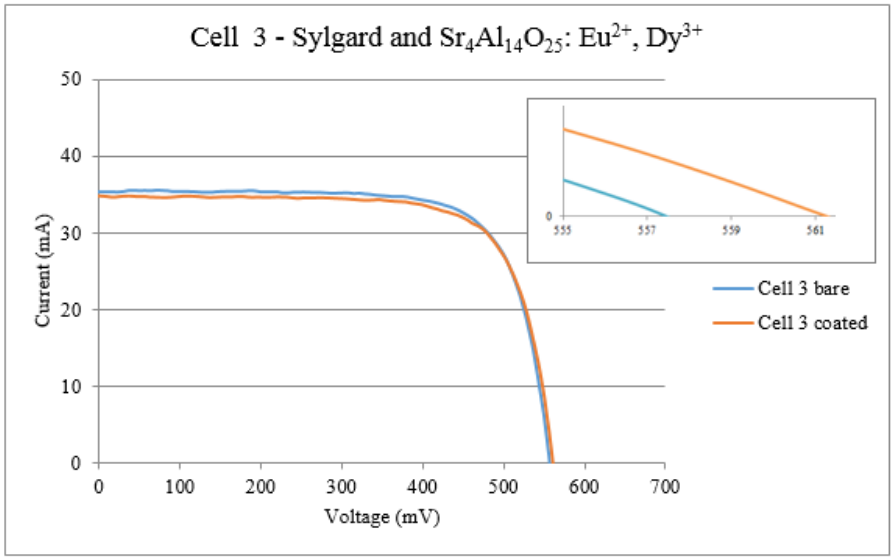

Figure 65: I-V curve of cell 3, before and after coating with Sylgard doped with $Sr_4Al_{14}O_{25}$: Eu^{2+}, Dy^{3+}.

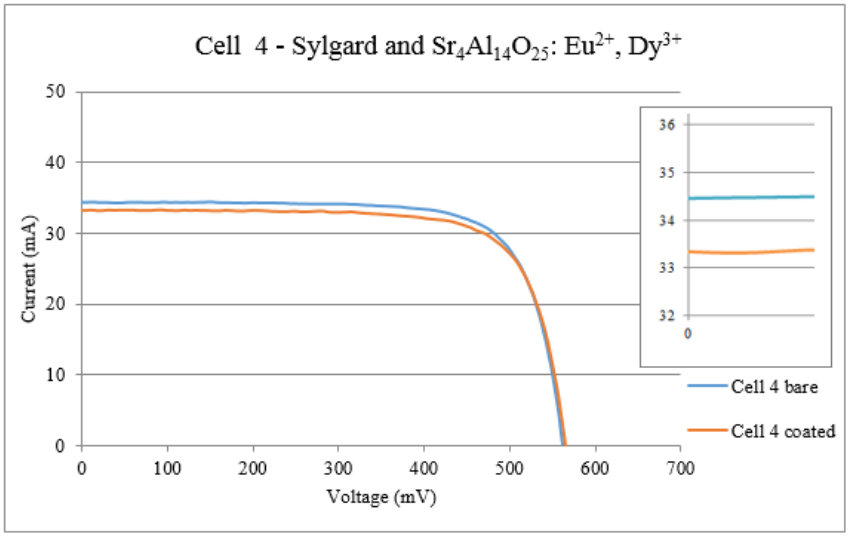

Figure 66: I-V curve of cell 4, before and after coating with Sylgard doped with $Sr_4Al_{14}O_{25}$: Eu^{2+}, Dy^{3+}.

The results give an unclear picture; while two devices show an increase in PCE, two do not and all four cells show a reduction in J_{SC}. This could be due to a non-uniform coating, too a high doping ratio of $Sr_4Al_{14}O_{25}$: Eu^{2+}, Dy^{3+} and that the powder was unground, meaning its transmittance was too low in regions where PV spectral response is high. Furthermore, because this was a preliminary study there were some flaws in the methods. Firstly, the sample size of cells needed to be larger than just two and secondly, comparing bare cells with coated cells for changes in performance is not the most logical approach. This is because in real commercial PV systems, the cell is always coated by an encapsulant layer. Therefore, a more meaningful comparison would be between cells of similar intrinsic bare efficiencies coated with just Sylgard and those with rare earth doped compound containing Sylgard, as per the middle columns in the earlier Tables 8-9.

Despite these shortcomings, one benefit of this technique was the verification that $Sr_4Al_{14}O_{25}$: Eu^{2+}, Dy^{3+} doped Sylgard layers on PV cells possess anti-reflective attributes, as shown by Figures 67 and 68; in this instance the coating shows reduction in reflectance at UV and blue wavelengths. In addition, this effect can be seen in the image of the un-coated and coated devices, which appear visibly less blue.

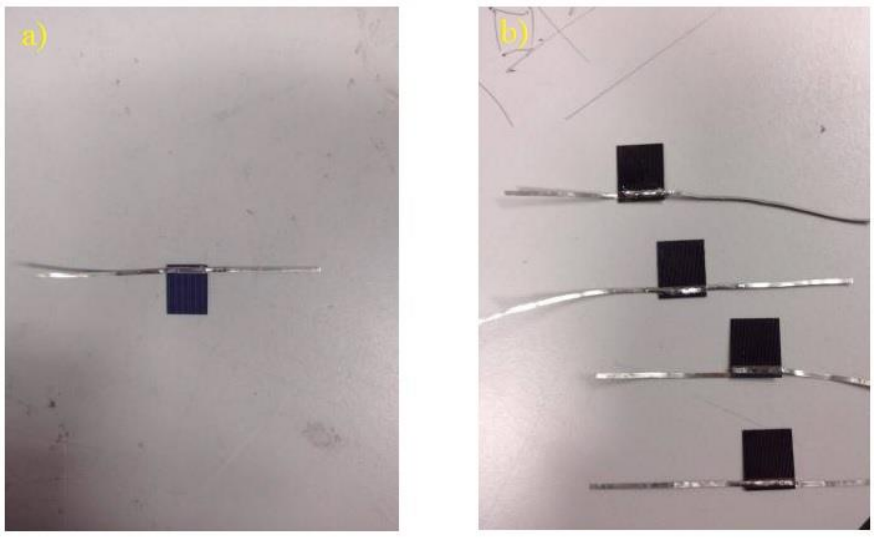

Figure 67: a) Image of a solar cell before applying the Sylgard coating and b) after applying the coatings.

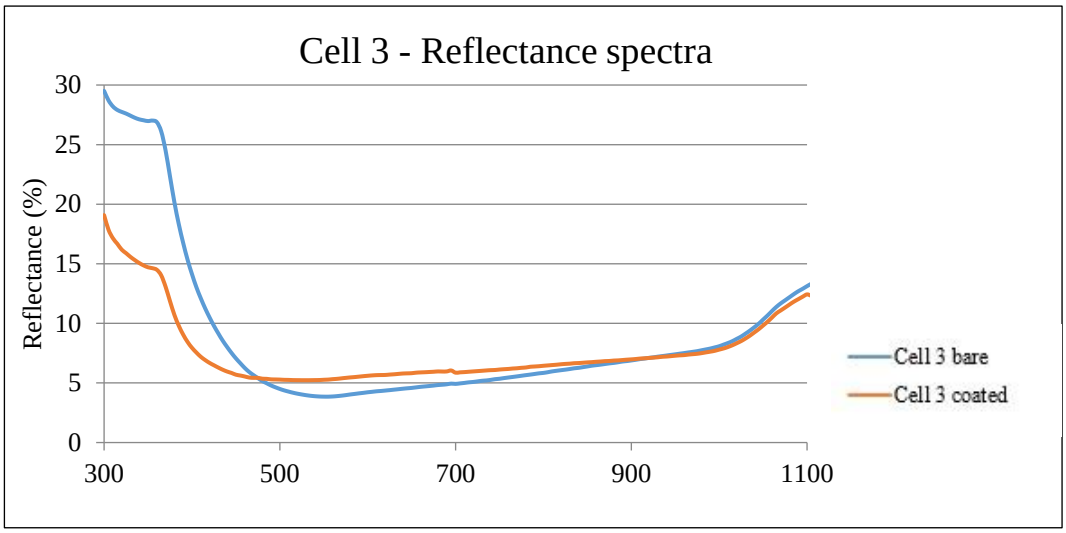

Figure 68: Reflectance spectrum of cell 3 before and after coating with Sylgard doped with $Sr_4Al_{14}O_{25}$: Eu^{2+}, Dy^{3+}.

3.7.2 TiO_2 Dynamic Spin Coated

In the second preliminary run of experiments, TiO_2 (Greatcell 18NR-T) diluted with ethanol was used as the embedding agent and particles of $Sr_4Al_{14}O_{25}$: Eu^{2+}, Dy^{3+} mixed in according to 3.4.4, before applying the resulting solution by dynamic spin coating to two silicon solar cells and pure TiO_2 to two more devices. Again, the results (Tables 10 and 11, Figures 69-72) are inconclusive but show a sharp decrease for the cell containing the TiO_2 and rare earth doped compound. This could be due to its lower transmittance, especially across the 300-400 nm region, as shown by an EQE measurement of this sample. This area of the spectrum has a similar energy to the band gap of TiO_2, so despite the thinness of the film, lots of optical power is lost this way. Again the doping level of the rare earth material may have been too high at 10% w/w of the spin coating solution and the electrical properties of cell 1 may have been compromised when performing the bare measurement, since the I-V curve is distorted in a way that implies shunt resistance effects.

Cell and Coating	Bare η (%)	Coated η (%)	Δη from Coating (%)
Cell 1 – TiO_2 only	10.96	13.42	+22.4
Cell 2 – TiO_2 only	13.48	13.26	-1.63
Cell 3 – TiO_2 and $Sr_4Al_{14}O_{25}$: Eu^{2+}, Dy^{3+}	15.02	13.28	-12.6
Cell 4 – TiO_2 and $Sr_4Al_{14}O_{25}$: Eu^{2+}, Dy^{3+}	13.84	-	-

Table 10: PCE measurements and relative PCE changes for the solar cells when bare and then when spin coated with TiO_2 or $Sr_4Al_{14}O_{25}$: Eu^{2+}, Dy^{3+} doped TiO_2.

Cell and Coating	Bare J_{SC} (mA)	Coated J_{SC} (mA)	ΔJ_{SC} from Coating (%)
Cell 1 – TiO_2 only	36.570	33.729	-7.77
Cell 2 – TiO_2 only	37.462	36.547	-2.44
Cell 3 – TiO_2 and $Sr_4Al_{14}O_{25}$: Eu^{2+}, Dy^{3+}	36.174	33.673	-6.91
Cell 4 – TiO_2 and $Sr_4Al_{14}O_{25}$: Eu^{2+}, Dy^{3+}	35.412	-	-

Table 11: J_{SC} measurements and relative J_{SC} changes for the solar cells when bare and then when spin coated with TiO_2 or $Sr_4Al_{14}O_{25}$: Eu^{2+}, Dy^{3+} doped TiO_2.

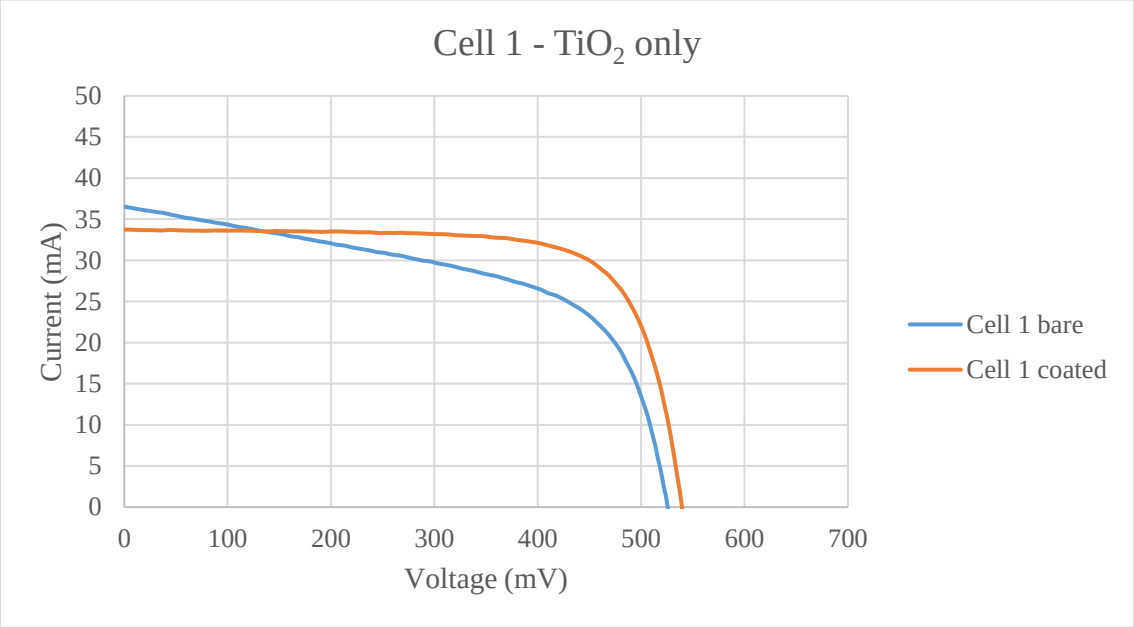

Figure 69: I-V curve of cell 1, before and after coating with TiO_2.

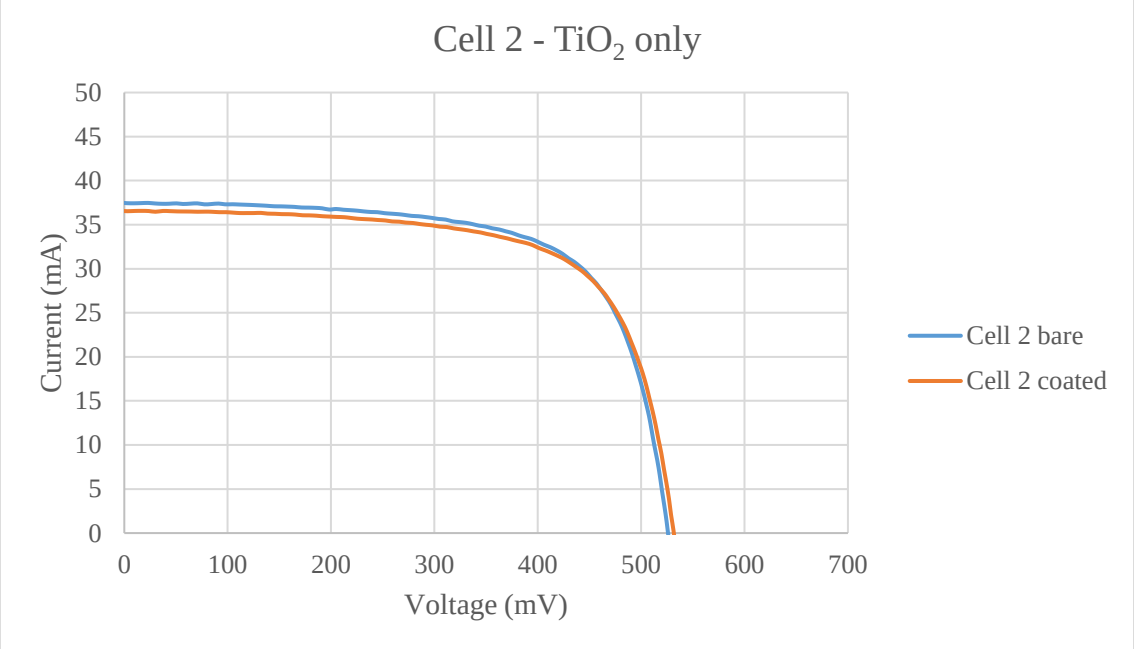

Figure 70: I-V curve of cell 2, before and after coating with TiO_2.

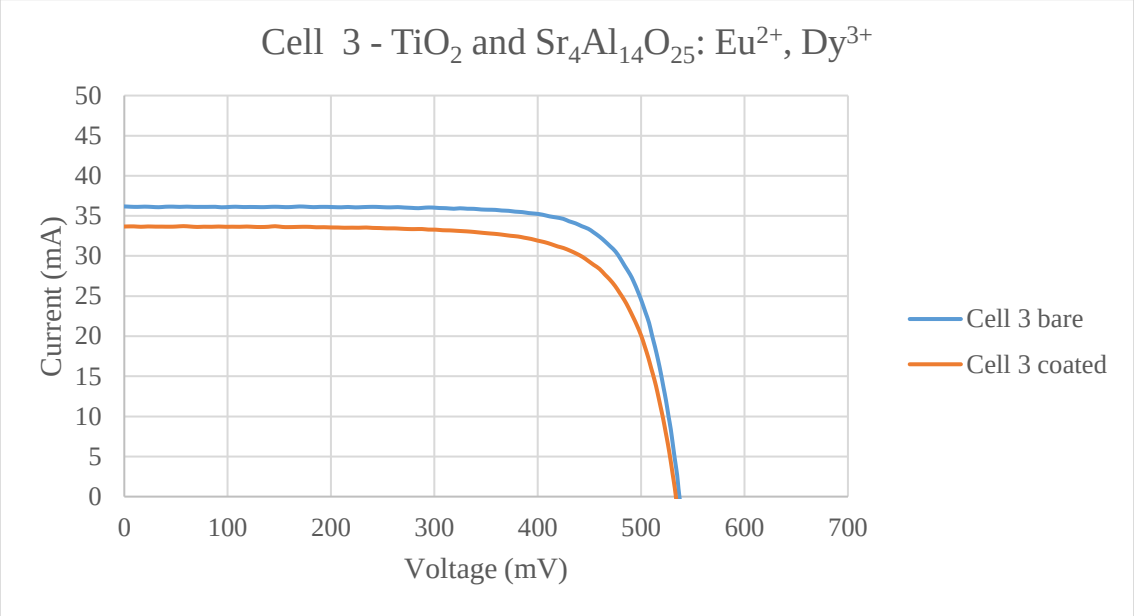

Figure 71: I-V curve of cell 3, before and after coating with TiO_2 doped with $Sr_4Al_{14}O_{25}$: Eu^{2+}, Dy^{3+}.

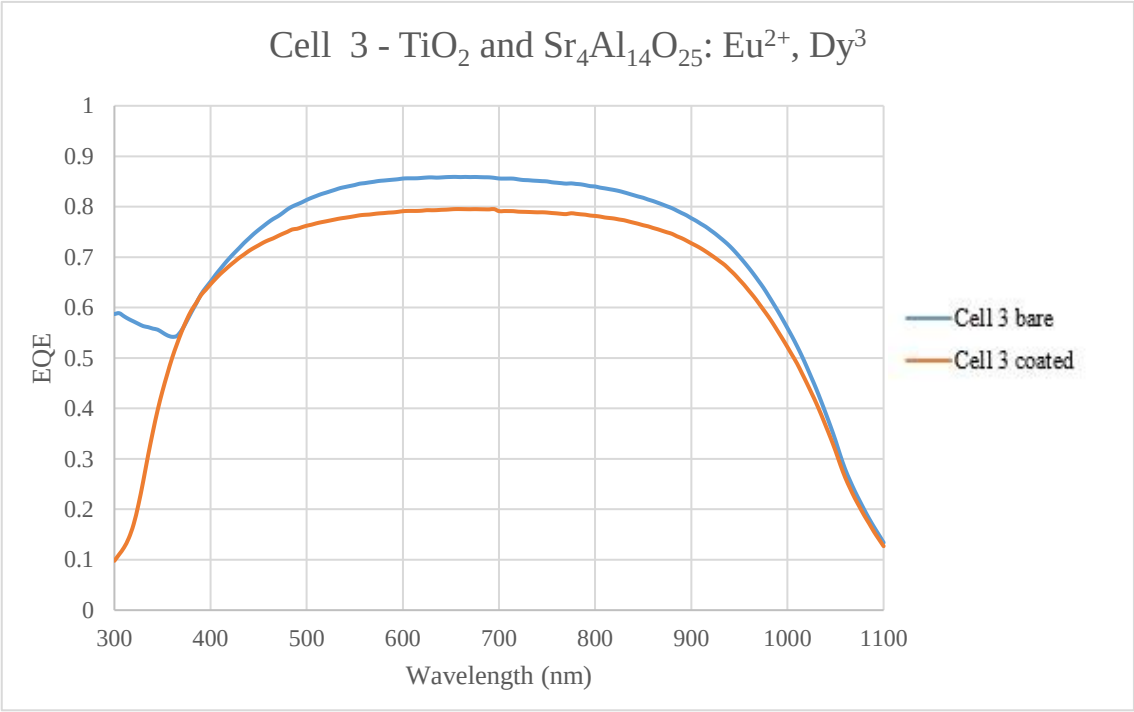

Figure 72: EQE spectrum of cell 3, before and after coating with TiO_2 doped with $Sr_4Al_{14}O_{25}$: Eu^{2+}, Dy^{3+}.

One positive observation, however, is that the EQE is less reduced, almost being equivalent to that of the bare cell at 370-420 nm. This could be because of LDS or DC taking place as photons of these wavelengths correspond to the excitation energies required for these processes to occur. Due to this subsection's work being carried in parallel with 3.7.1, there remain the methodological issues

outlined previously. So, moving forward, it is a priority to compare like with like, by making solar cells of as close to the same bare cell efficiencies as possible.

3.7.3. Sylgard drop casted

In the third and major study of this chapter, based on the drawbacks of the preliminary work, silicon cells would be coated with Sylgard in 5 different weight ratios (0%, 0.25%, 0.5%, 1%, 2%) applied via drop casting to make a device looking like Figure 73. A larger sample size of three cells per design specification would be used and the devices checked prior to coating with a multi-meter, to ensure that their electrical performance properties were as invariant as possible. Also, in this study $NaYF_4$: Er^{3+}, Yb^{3+} was deployed for the first time, because it was deemed important to try another material that may have better optical and spectral conversion properties.

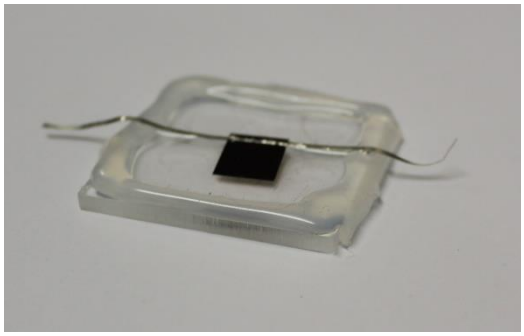

Figure 73: Image of a c-Si solar cell coated with Sylgard-rare earth doped compound mixture via drop costing and fixed on an acrylic base.

The results obtained from the solar simulator and Bentham PVE300 are displayed graphically in the following Figures 74-85 and numerically in the Tables 12-28. The value taken as the PCE and J_{SC} measurement for each specification was the maximum, or champion, value for that set. The mean values and standard deviations are discussed as part of a sensitivity analysis with statistical methods in 6.3.2.

It can be seen from the data, that these results were much more consistent and promising than those derived in 3.7.1 and 3.7.2. At 1 sun illumination, the highest PCEs attained were 16.31% for 0.5% $Sr_4Al_{14}O_{25}$: Eu^{2+}, Dy^{3+} doping and 16.75% for 1% doped $NaYF_4$: Er^{3+}, Yb^{3+}. These correspond to relative efficiency increases of 2.1% and 4.3% compared to the control device, with a pure Sylgard coating and PCE of 15.98%. Similarly, as expected to accompany improved PCE, the J_{SC} went up from 36.33 mA/cm^2 for the control device to 37.55 mA/cm^2 and

37.02 mA/cm^2 for the best performing $Sr_4Al_{14}O_{25}$: Eu^{2+}, Dy^{3+} and $NaYF_4$: Er^{3+}, Yb^{3+} device. Interestingly for the $NaYF_4$: Er^{3+}, Yb^{3+} devices, it was not the same cell which produced the highest PCE and J_{SC}; the 2% doped Sylgard generating an additional 0.05 mA.

Furthermore, in this study, the light irradiance was varied using the HelioCon to obtain data for the electrical performance at 0.4, 0.6 and 0.8 suns. As intuition would predict, the cells demonstrated a lower J_{SC} with decreasing light intensity; in line with the linear relationship outlined in chapter 1. On the other hand, the PCE was largely unaffected by the HelioCon variation because the cell efficiency is much less sensitive to relatively small changes in incident power (from 0.4 to 1 sun). All cells containing rare earth doped layers demonstrated an increased PCE, except in a handful of instances: 1% $Sr_4Al_{14}O_{25}$: Eu^{2+}, Dy^{3+} and 0.25%, 0.5% and 2% $NaYF_4$: Er^{3+}, Yb^{3+} at 0.4 suns irradiance, and 0.5% and 2% $NaYF_4$: Er^{3+}, Yb^{3+} at 0.6 suns irradiance.

Another figure of merit is how the relative PCE and J_{SC} enhancements vary with solar irradiance which are succinctly displayed in Figures 78-81. For $Sr_4Al_{14}O_{25}$: Eu^{2+}, Dy^{3+} doped layers, the J_{SC} and PCE tend to rise with increasing light concentration at low irradiances before reaching a peak at 0.8 suns. The rise is more drastic for the 0.5% and 1% doping levels; the 0.5% also achieves the peak relative PCE gain for this material of +5.36% at 0.8 suns. Alternatively, $NaYF_4$: Er^{3+}, Yb^{3+} follows a stranger pattern in relative PCE and J_{SC} enhancements, in which the percentage gains fall between 0.4 and 0.6 suns (except for two PCE measurements), but then ascending to another localised peak at 0.8 suns before decreasing again at 1 sun (except for the 0.5% and 2% samples which increase in PCE at 1 sun). Again, the maximum relative PCE enhancement of +4.86% can be found for a 1% doping level at 0.8 suns.

Finally, particular attention is drawn to the 1% doped $Sr_4Al_{14}O_{25}$: Eu^{2+}, Dy^{3+} and $NaYF_4$: Er^{3+}, Yb^{3+} samples, which show an abnormal trend at 0.4 suns. The former material exhibits a sharp decrease in PCE, while the latter a modest increase, going against the pattern observed in their respective other doping level samples. This could be justified if the relationship between doping level and performance enhancement is considered to be a polynomial that varies at each light intensity. Thus, a 1% doping level at 0.4 suns illumination could be interpreted as a local minimum for $Sr_4Al_{14}O_{25}$: Eu^{2+}, Dy^{3+} or local maximum for

$NaYF_4$: Er^{3+}, Yb^{3+}. Conversely, the large drop in $Sr_4Al_{14}O_{25}$: Eu^{2+}, Dy^{3+} performance may go beyond what is expected by the local minimum explanation, so could be the result of a systematic error in the fabrication or characterisation procedure (although this risk was minimised by testing 3 copies of each sample).

The V_{OC} and FF data for the PV devices tested are presented in Tables 20-27 for completeness. As can be observed, there is little clear relationship apparent and these quantities are not of direct interest for spectral conversion studies, so will be omitted in the following chapters. The small and seemingly random changes in FF and V_{OC} could be from the I_{SC} dependence in the FF formula (although its impact is small as three other unrelated variables are in the expression) and amount of light reaching the cell (since V_{OC} is logarithmically dependent on light concentration).

Finally, EQE measurements between 300 and 1100 nm are presented in Figures 84 and 85. It can be observed that for 0.5% and 1% doping level $Sr_4Al_{14}O_{25}$: Eu^{2+}, Dy^{3+} coated devices showed an improved EQE between 320 and 450 nm; at 400 nm these increases are 2.9% and 1.7%. Likewise, for the PV with $NaYF_4$: Er^{3+}, Yb^{3+} layers, similar increases in EQE in these regions of the spectrum were observed but interestingly were more pronounced for the 0.25% and 2% doping levels with increases of 2.24% and 2.13% compared to the control device at 400 nm. This indicates the c-Si PV cell below is utilising short wavelength solar radiation more effectively when both materials are deployed, which could be due to the photons undergoing spectral conversion processes such as LDS or DC. These do not represent short wavelength enhancements as significant in some of the studies cited in chapter 2 but nonetheless are respectable for the simplicity and low cost of the materials used, and still can explain the improved J_{SC} as measured by the solar simulator. Although, perhaps the 1% $NaYF_4$: Er^{3+}, Yb^{3+} could have expected greater EQE gains around 400 nm; its greater overall PCE could be due to higher transmittance at longer wavelengths that are used by the PV cell.

The physical reasons behind these results will be explored in future chapters which will attempt to build on understanding the results from underlying principles. However, at this stage one factor that becomes apparent is the doping level of the rare earth ions within the layer. For example, the localised maxima for peak performance at 0.5% for $Sr_4Al_{14}O_{25}$: Eu^{2+}, Dy^{3+} could indicate that at lower ratios

less effective LDS/DC takes place due to insufficient particle concentration and that at higher levels, the spectral conversion occurs less due to competing optical processes. Also, worth mentioning is the dependence of the spectral conversion process on light intensity, a theme which will be investigated further in the following chapter where LCPV systems are considered. A relationship between light intensity and the efficiency of the process could yield information about the energy transfer mechanism, as per the discussions in chapter 2. For practical applications, the better relative performance at 0.8 suns is exciting because it is often necessary to improve device performance in lower light conditions, which make up a large amount of the illumination conditions for many regions including the UK.

Doping (w/w %)	η (%)	J_{SC} (mA/cm^2)	Δη (%)	Δ J_{SC} (%)
0.0	15.976	36.330	-	-
0.25	16.239	36.721	+1.65	+1.08
0.5	16.312	37.552	+2.10	+3.36
1.0	16.232	36.768	+1.60	+1.21
2.0	16.070	36.982	+0.59	+1.79

Table 12: PCE and J_{SC} data for drop casted $Sr_4Al_{14}O_{25}$: Eu^{2+}, Dy^{3+} doped Sylgard devices at 1 sun irradiance.

Doping (w/w %)	η (%)	J_{SC} (mA/cm^2)	Δη (%)	Δ J_{SC} (%)
0.0	16.066	29.683	-	-
0.25	16.589	30.046	+3.25	+1.22
0.5	16.928	30.667	+5.36	+3.32
1.0	16.635	30.109	+3.54	+1.44
2.0	16.528	30.186	+2.87	+1.69

Table 13: PCE and J_{SC} data for drop casted $Sr_4Al_{14}O_{25}$: Eu^{2+}, Dy^{3+} doped Sylgard devices at 0.8 suns irradiance.

Doping (w/w %)	η (%)	J_{SC} (mA/cm^2)	Δη (%)	Δ J_{SC} (%)
0.0	16.225	22.443	-	-
0.25	16.542	22.501	+1.95	+0.26
0.5	16.728	23.029	+3.10	+2.61
1.0	16.295	22.391	+0.43	-0.23
2.0	16.225	22.443	-	-

Table 14: PCE and J_{SC} data for drop casted $Sr_4Al_{14}O_{25}$: Eu^{2+}, Dy^{3+} doped Sylgard devices at 0.6 suns irradiance.

Doping (w/w %)	η (%)	J_{SC} (mA/cm^2)	Δη (%)	Δ J_{SC} (%)
0.0	15.833	14.751	-	-
0.25	16.040	14.776	+1.31	+0.17
0.5	15.920	14.956	+0.55	+1.39
1.0	15.088	14.677	-4.71	-0.50
2.0	15.875	14.873	+0.27	+0.83

Table 15: PCE and J_{SC} data for drop casted $Sr_4Al_{14}O_{25}$: Eu^{2+}, Dy^{3+} doped Sylgard devices at 0.4 suns irradiance.

Doping (w/w %)	η (%)	J_{SC} (mA/cm^2)	Δη (%)	Δ J_{SC} (%)
0.0	15.976	36.330	-	-
0.25	16.100	36.794	+0.78	+1.28
0.5	16.180	36.544	+1.28	+0.59
1.0	16.747	36.968	+4.83	+1.76
2.0	16.474	37.017	+3.12	+1.89

Table 16: PCE and J_{SC} data for drop casted $NaYF_4$: Er^{3+}, Yb^{3+} doped Sylgard devices at 1 sun irradiance.

Doping (w/w %)	η (%)	J_{SC} (mA/cm^2)	Δη (%)	Δ J_{SC} (%)
0.0	16.066	29.683	-	-
0.25	16.645	30.555	+3.60	+2.94
0.5	16.141	29.988	+0.47	+1.03
1.0	16.848	30.329	+4.86	+2.18
2.0	16.479	29.904	+2.57	+0.74

Table 17: PCE and J_{SC} data for drop casted $NaYF_4$: Er^{3+}, Yb^{3+} doped Sylgard devices at 0.8 suns irradiance.

Doping (w/w %)	η (%)	J_{SC} (mA/cm^2)	Δη (%)	Δ J_{SC} (%)
0.0	16.225	22.443	-	-
0.25	16.233	22.520	+0.05	+0.34
0.5	15.863	21.923	-2.23	-2.32
1.0	16.560	22.047	+2.06	-1.76
2.0	15.882	22.200	-2.12	-1.08

Table 18: PCE and J_{SC} data for drop casted $NaYF_4$: Er^{3+}, Yb^{3+} doped Sylgard devices at 0.6 suns irradiance.

Doping (w/w %)	η (%)	J_{SC} (mA/cm^2)	Δη (%)	Δ J_{SC} (%)
0.0	15.563	14.946	-1.71	+1.32
0.25	15.285	14.647	-3.46	-0.71
0.5	16.380	14.745	+3.46	-0.04
1.0	15.565	14.695	-1.69	-0.38
2.0	15.563	14.946	-1.71	+1.32

Table 19: PCE and J_{SC} data for drop casted $NaYF_4$: Er^{3+}, Yb^{3+} doped Sylgard devices at 0.4 suns irradiance.

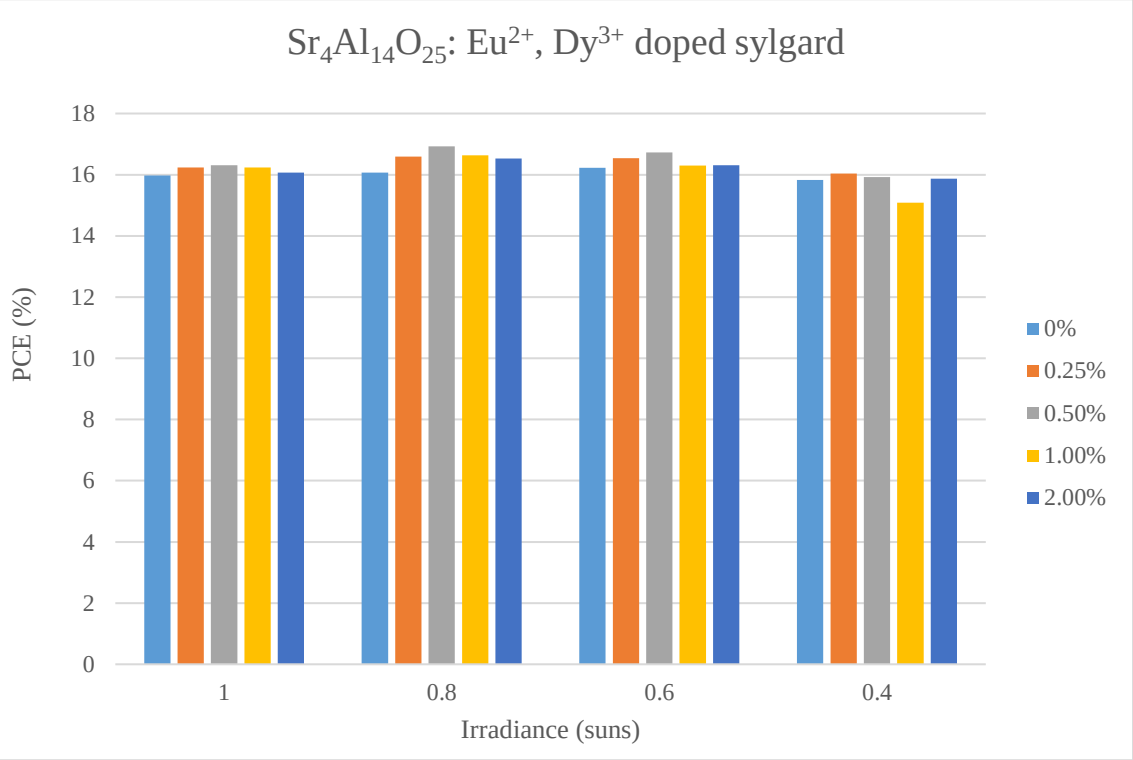

Figure 74: PCE of the $Sr_4Al_{14}O_{25}$: Eu^{2+}, Dy^{3+} doped Sylgard devices of varying doping ratios at different solar irradiances.

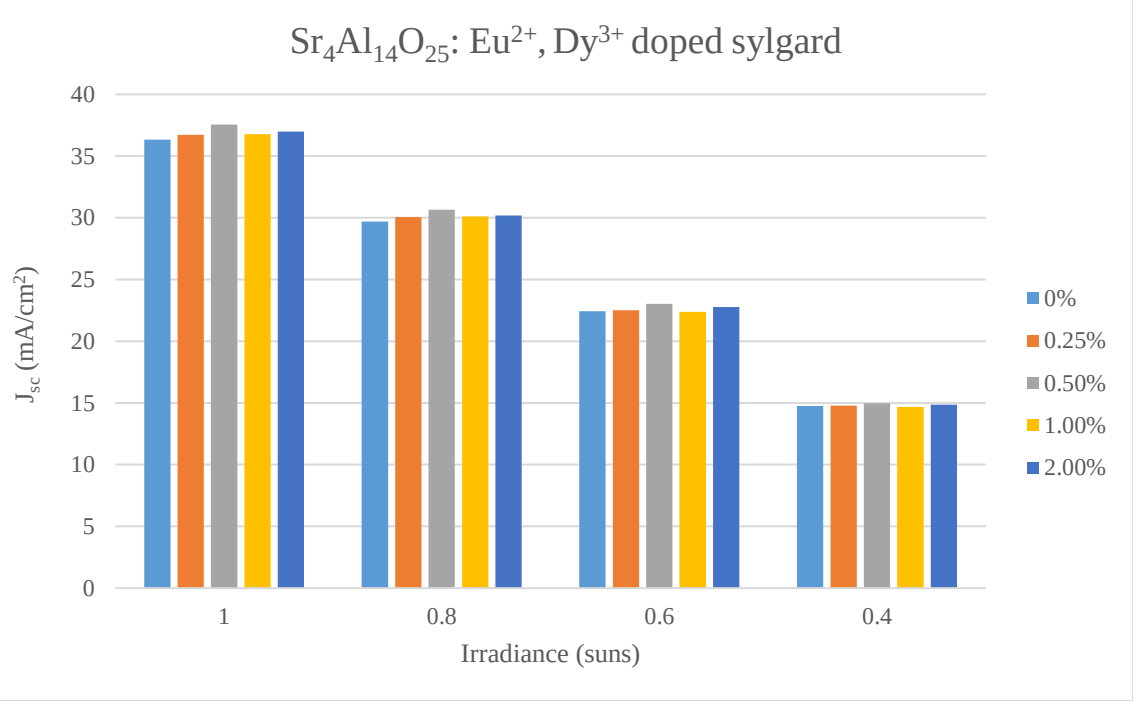

Figure 75: J_{SC} of the $Sr_4Al_{14}O_{25}$: Eu^{2+}, Dy^{3+} doped Sylgard devices of varying doping ratios at different solar irradiances.

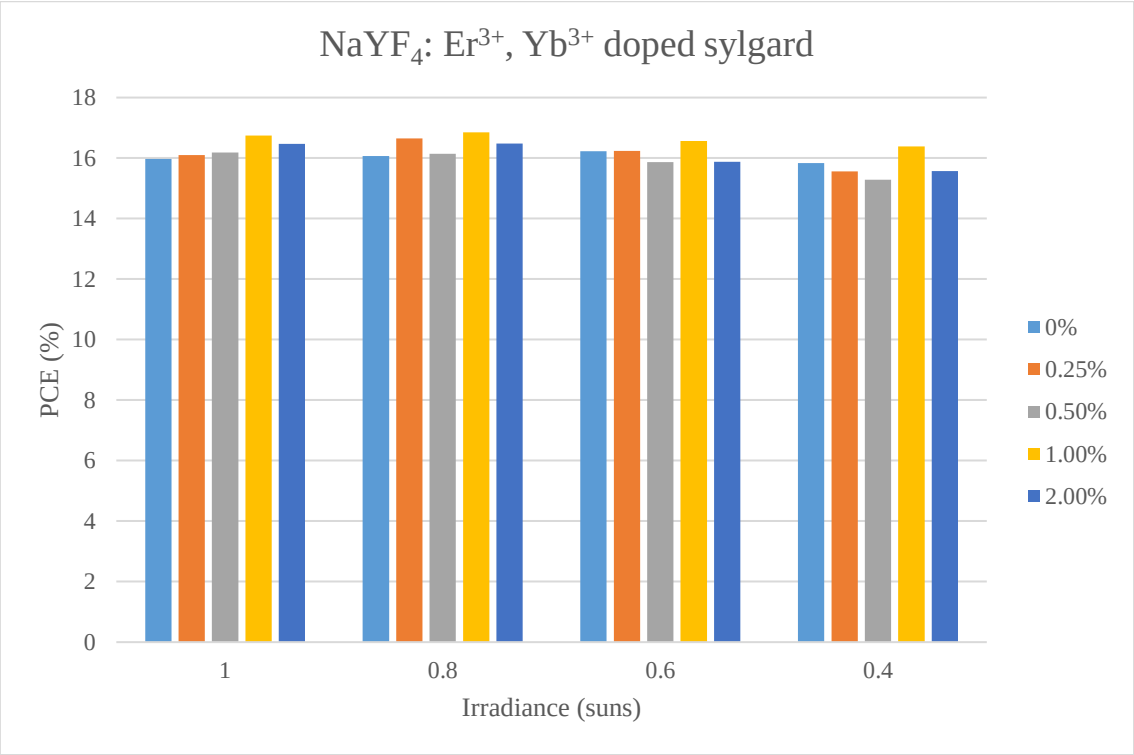

Figure 76: PCE of the $NaYF_4$: Er^{3+}, Yb^{3+} doped Sylgard devices of varying doping ratios at different solar irradiances.

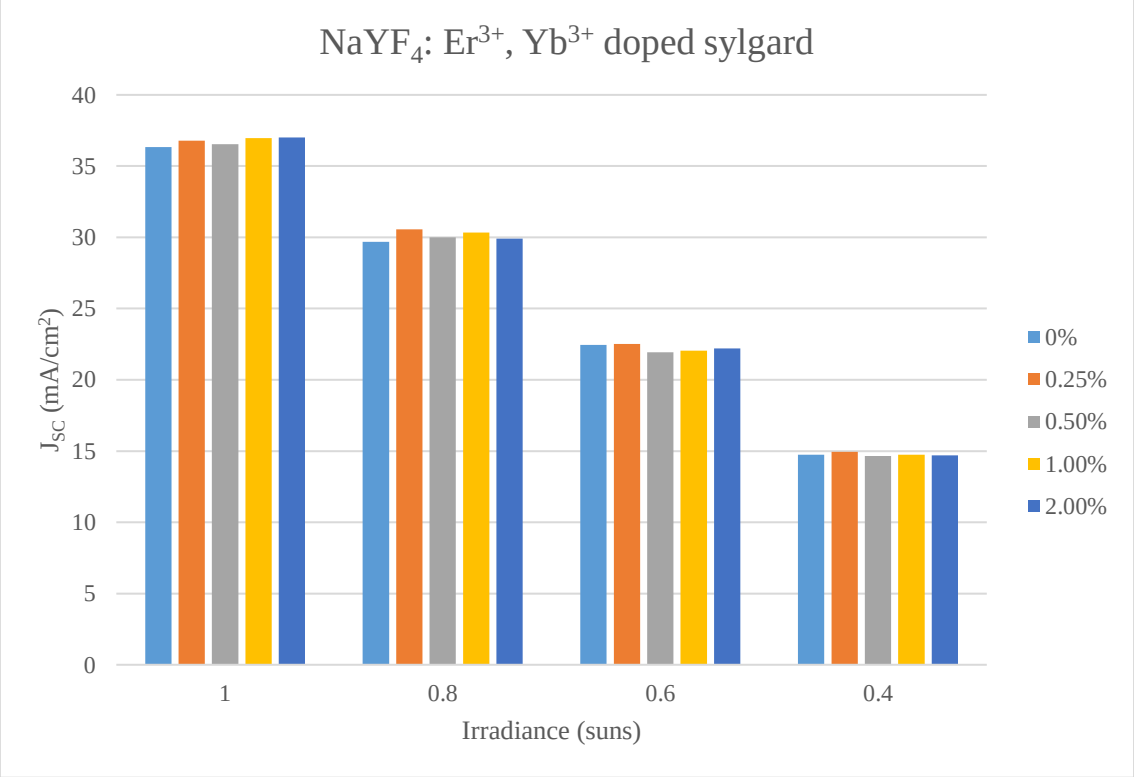

Figure 77: J_{SC} of the $NaYF_4$: Er^{3+}, Yb^{3+} doped Sylgard devices of varying doping ratios at different solar irradiances.

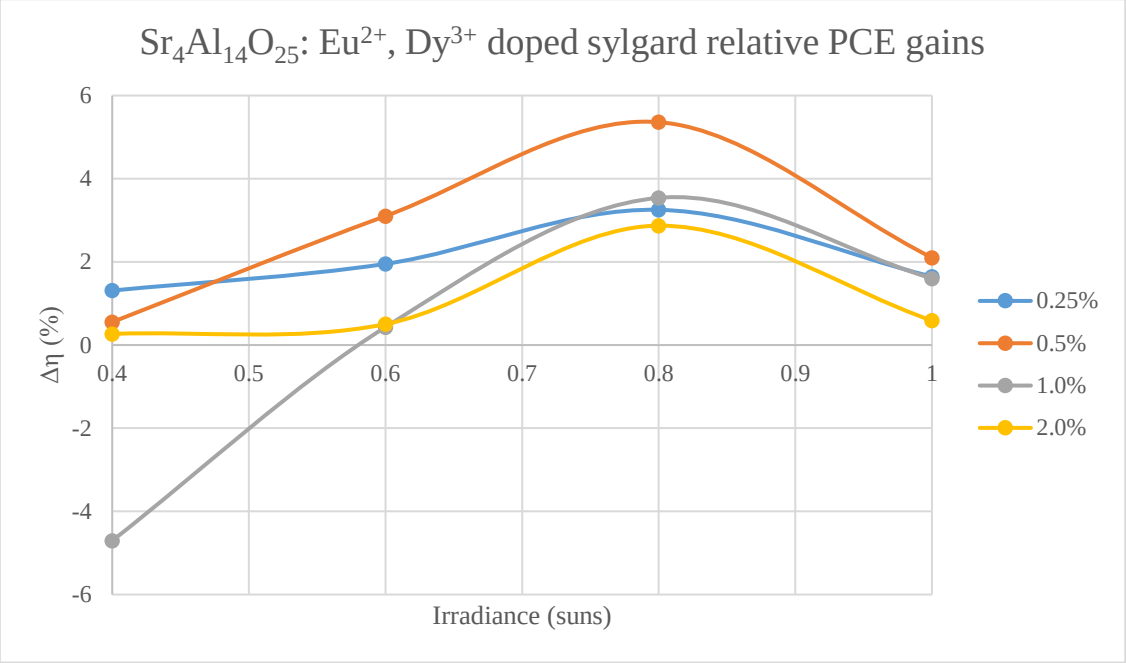

Figure 78: Relative PCE gains for the $Sr_4Al_{14}O_{25}$: Eu^{2+}, Dy^{3+} doped Sylgard devices at different solar irradiances.

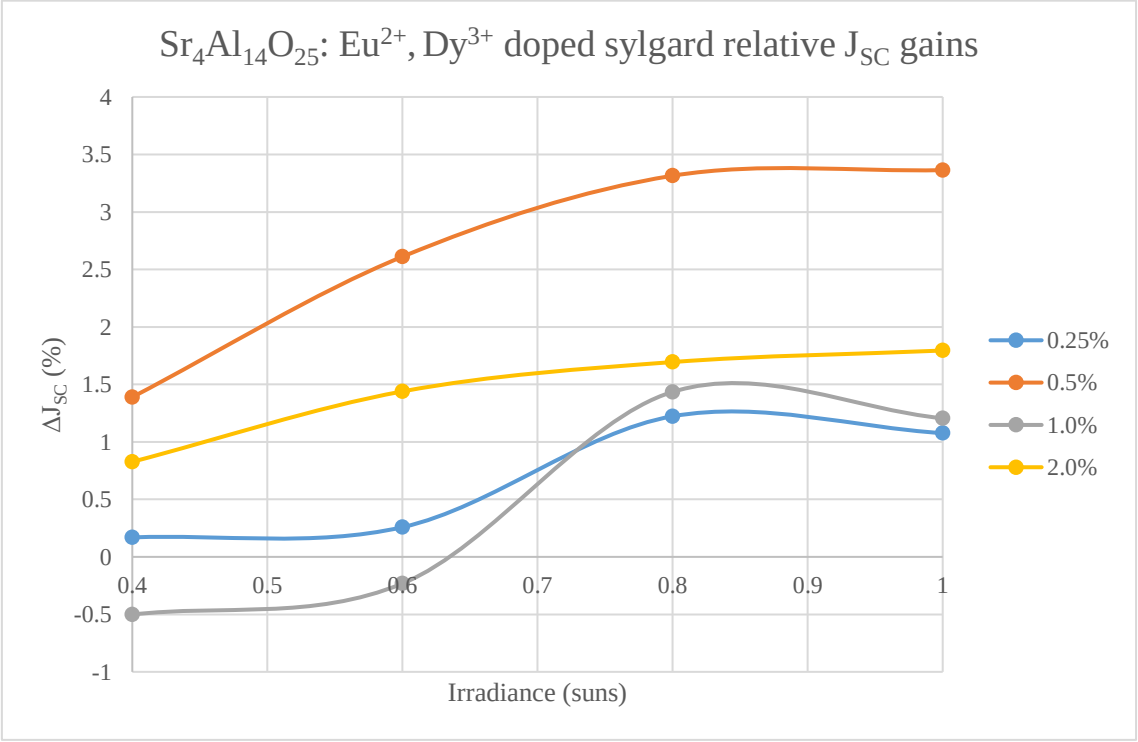

Figure 79: Relative J_{SC} gains for the $Sr_4Al_{14}O_{25}$: Eu^{2+}, Dy^{3+} doped Sylgard devices at different solar irradiances.

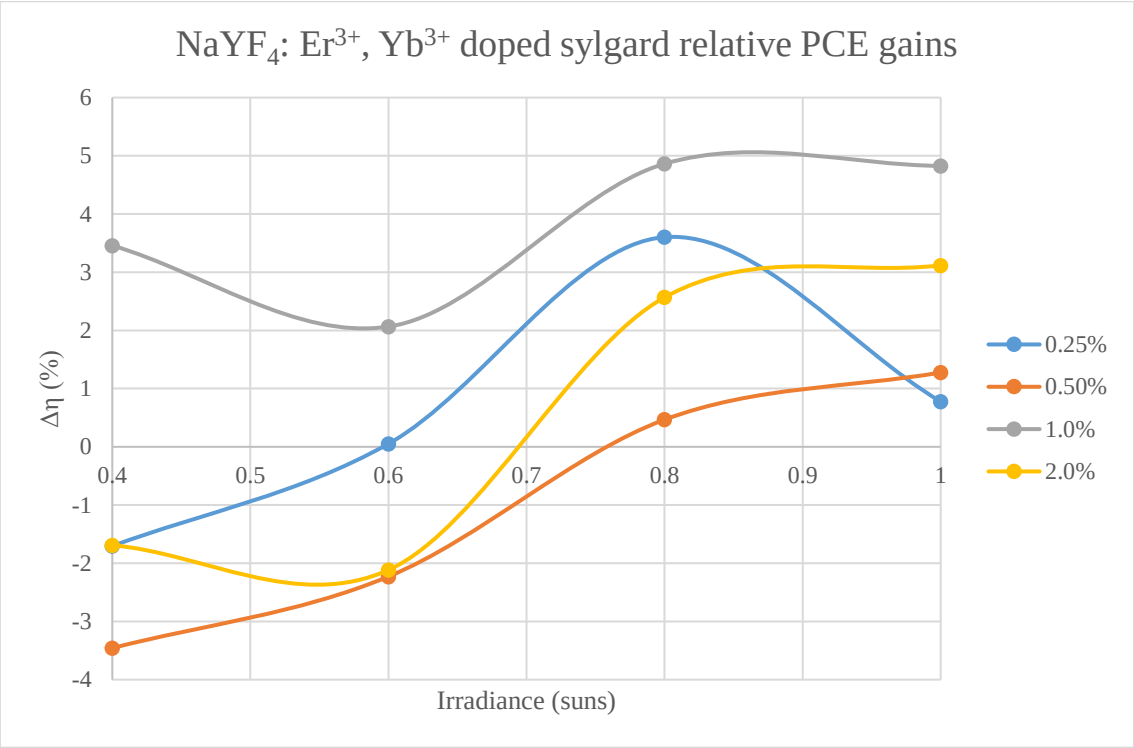

Figure 80: Relative PCE gains for the $NaYF_4$: Er^{3+}, Yb^{3+} doped Sylgard devices at different solar irradiances.

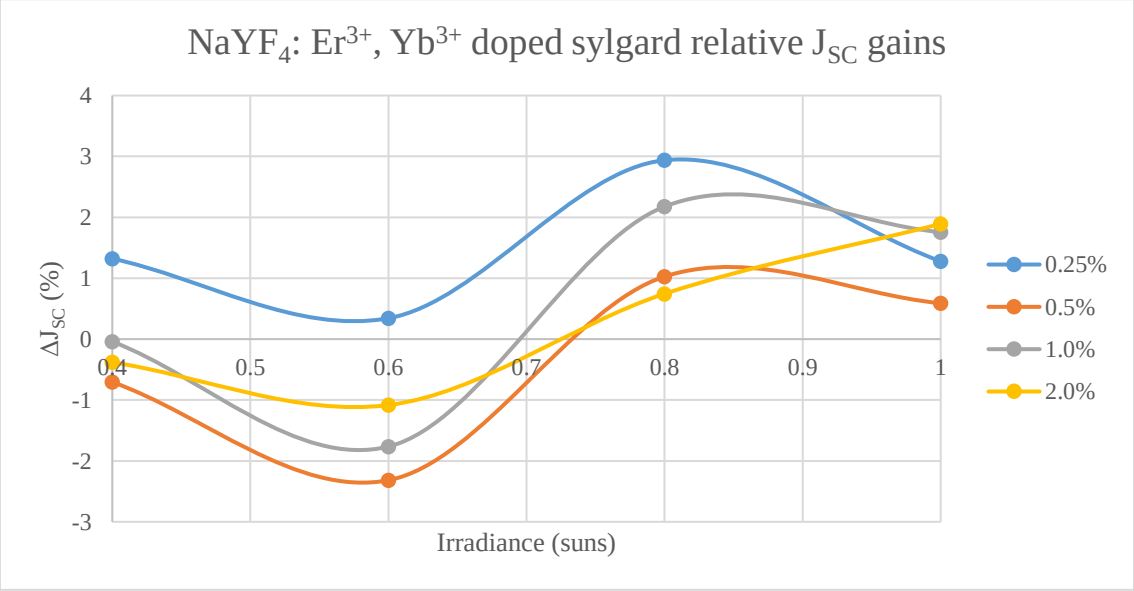

Figure 81: Relative J_{SC} gains for the $NaYF_4$: Er^{3+}, Yb^{3+} doped Sylgard devices at different solar irradiances.

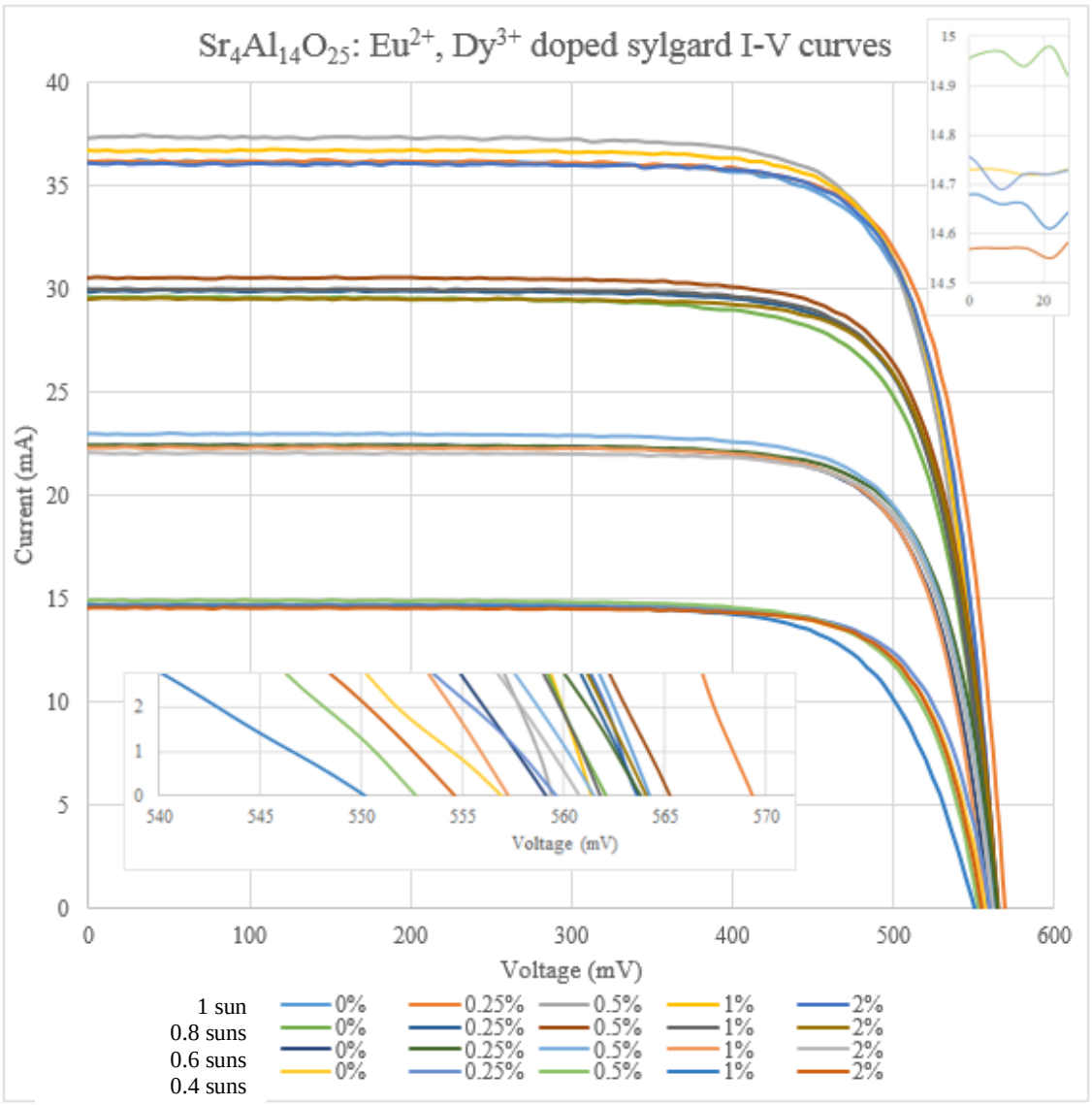

Figure 82: I-V curves of for the $Sr_4Al_{14}O_{25}$: Eu^{2+}, Dy^{3+} doped Sylgard devices at different solar irradiances.

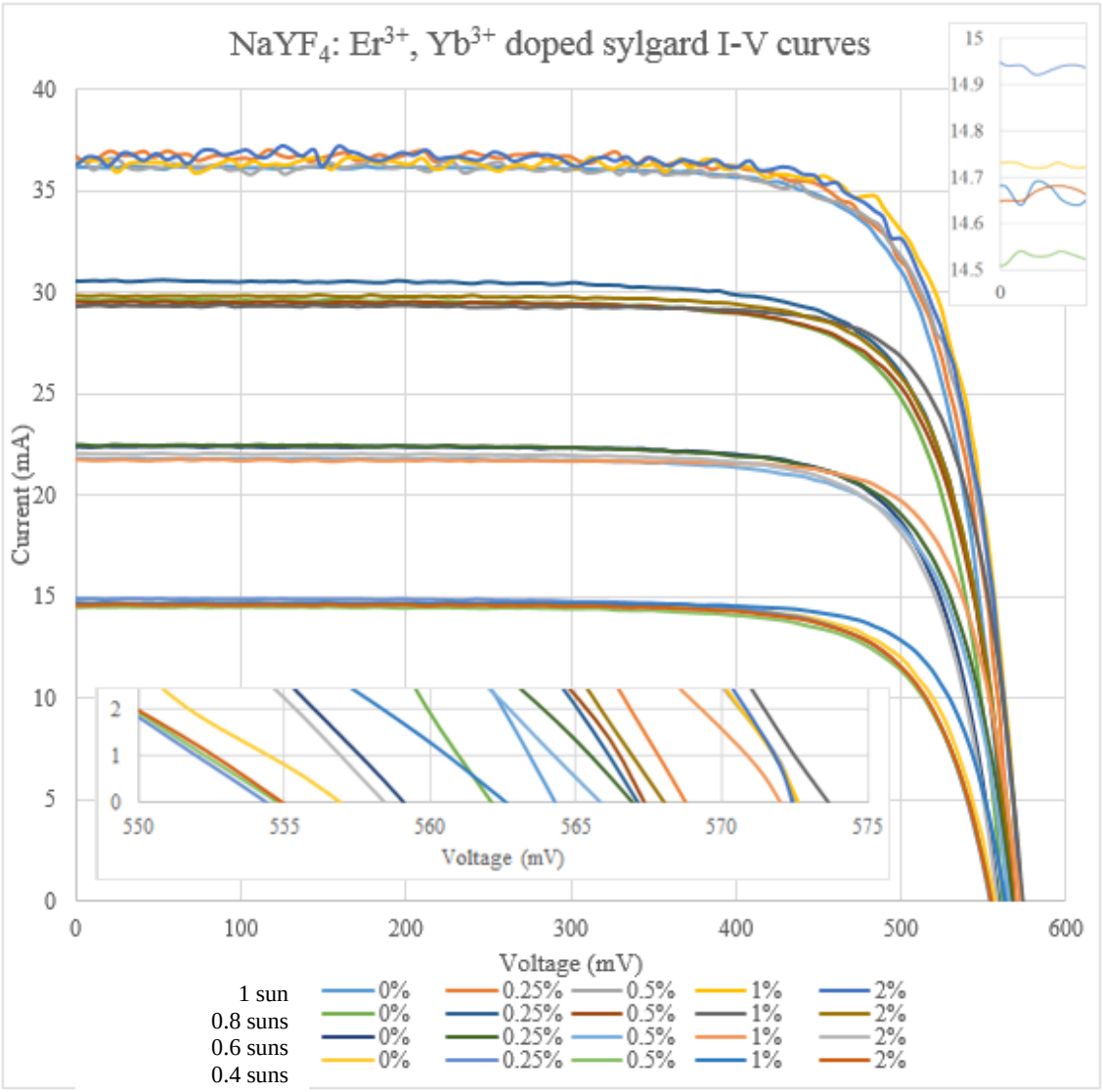

Figure 83: I-V curves of for the $NaYF_4$: Er^{3+}, Yb^{3+} doped Sylgard devices at different solar irradiances.

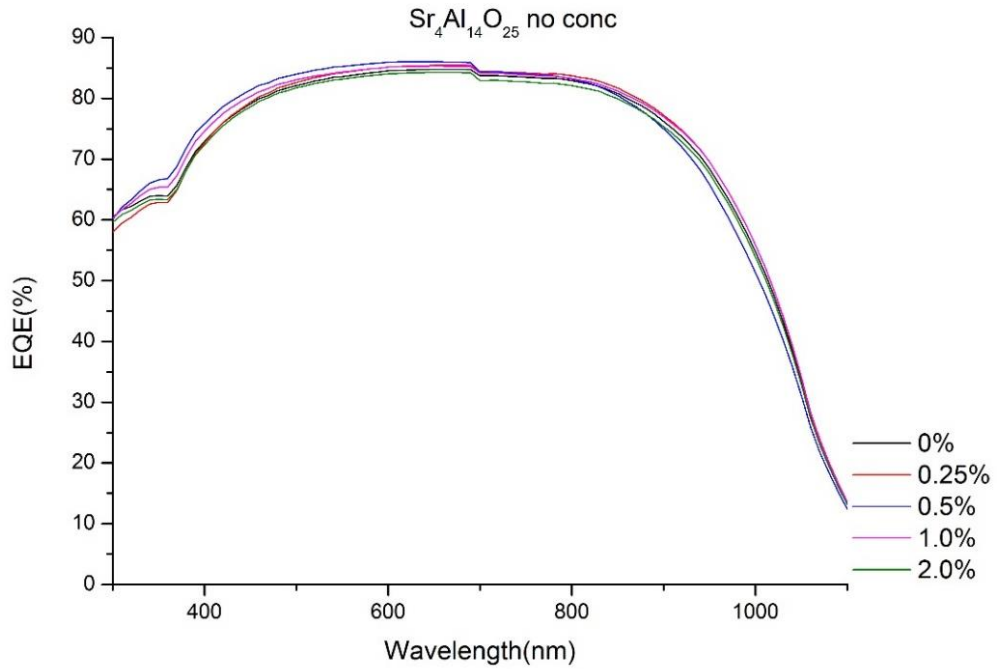

Figure 84: EQE spectra of the $Sr_4Al_{14}O_{25}$: Eu^{2+}, Dy^{3+} doped Sylgard devices.

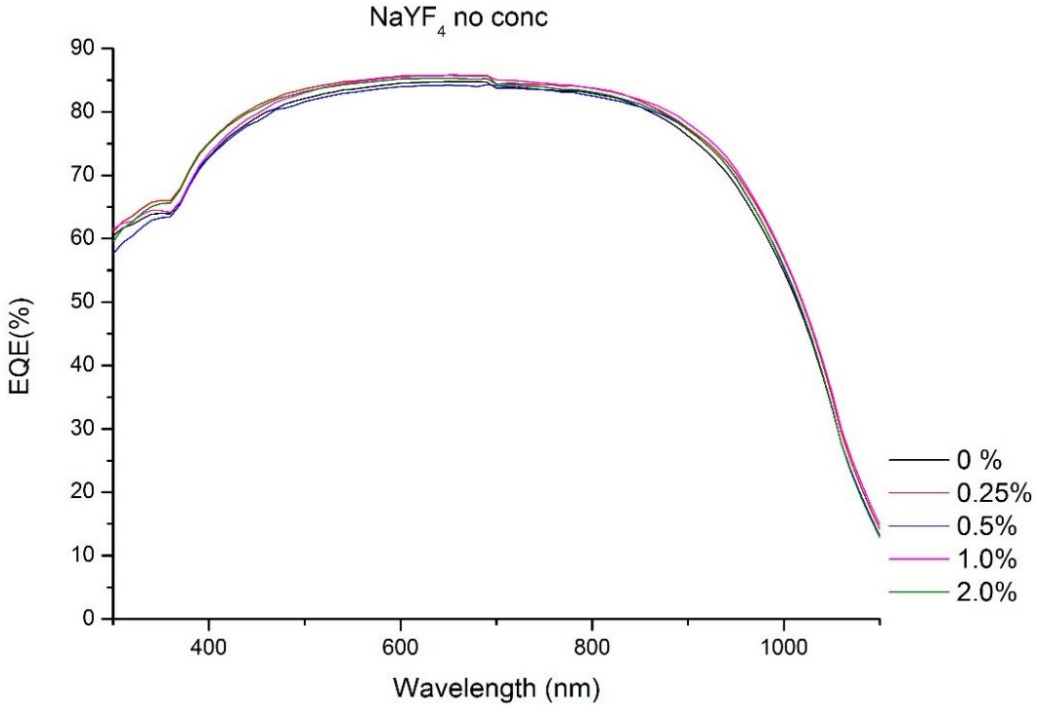

Figure 85: EQE spectra of the $NaYF_4$: Er^{3+}, Yb^{3+} doped Sylgard devices.

Doping (w/w %)	V_{OC} (mV)	FF	V_{OC} (%)	Δ FF (%)
0.0	564.272	0.779	-	-
0.25	569.269	0.777	+0.89	-0.32
0.5	559.508	0.776	-0.84	-0.38
1.0	562.292	0.785	-0.35	+0.75
2.0	563.641	0.771	-0.11	-1.07

Table 20: V_{OC} and FF data for drop casted $Sr_4Al_{14}O_{25}$: Eu^{2+}, Dy^{3+} doped Sylgard devices at 1 sun irradiance.

Doping (w/w %)	V_{OC} (mV)	FF	V_{OC} (%)	Δ FF (%)
0.0	562.419	0.770	-	-
0.25	567.538	0.778	+0.91	+1.09
0.5	565.209	0.781	+0.50	+1.48
1.0	561.771	0.787	-0.12	+2.19
2.0	564.106	0.777	+0.30	+0.86

Table 21: V_{OC} and FF data for drop casted $Sr_4Al_{14}O_{25}$: Eu^{2+}, Dy^{3+} doped Sylgard devices at 0.8 suns irradiance.

Doping (w/w %)	V_{OC} (mV)	FF	V_{OC} (%)	Δ FF (%)
0.0	559.061	0.776	-	
0.25	563.832	0.782	+0.85	+0.83
0.5	561.490	0.776	+0.43	+0.04
1.0	557.308	0.783	-0.31	+0.98
2.0	560.760	0.766	+0.30	-1.22

Table 22: V_{OC} and FF data for drop casted $Sr_4Al_{14}O_{25}$: Eu^{2+}, Dy^{3+} doped Sylgard devices at 0.6 suns irradiance.

Doping (w/w %)	V_{OC} (mV)	FF	V_{OC} (%)	Δ FF (%)
0.0	556.812	0.771	-	-
0.25	559.630	0.776	+0.51	+0.63
0.5	552.695	0.770	-0.74	-0.09
1.0	550.109	0.747	-1.20	-3.06
2.0	554.595	0.770	-0.40	-0.16

Table 23: V_{OC} and FF data for drop casted $Sr_4Al_{14}O_{25}$: Eu^{2+}, Dy^{3+} doped Sylgard devices at 0.4 suns irradiance.

Doping (w/w %)	V_{OC} (mV)	FF	V_{OC} (%)	Δ FF (%)
0.0	564.272	0.779	-	-
0.25	568.730	0.769	+0.79	-1.27
0.5	572.443	0.773	+1.45	-0.75
1.0	572.525	0.791	+1.46	+1.53
2.0	572.405	0.777	+1.44	-0.23

Table 24: V_{OC} and FF data for drop casted $NaYF_4$: Er^{3+}, Yb^{3+} doped Sylgard devices at 1 sun irradiance.

Doping (w/w %)	V_{OC} (mV)	FF	V_{OC} (%)	Δ FF (%)
0.0	562.419	0.770	-	-
0.25	567.113	0.768	+0.83	-0.19
0.5	567.380	0.759	+0.88	-1.42
1.0	573.659	0.775	+2.00	+0.62
2.0	568.028	0.776	+1.00	+0.81

Table 25: V_{OC} and FF data for drop casted $NaYF_4$: Er^{3+}, Yb^{3+} doped Sylgard devices at 0.8 suns irradiance.

Doping (w/w %)	V_{OC} (mV)	FF	V_{OC} (%)	Δ FF (%)
0.0	559.061	0.776	-	-
0.25	566.954	0.763	+1.41	-1.68
0.5	565.84	0.767	+1.21	-1.11
1.0	571.985	0.788	+2.31	+1.55
2.0	562.054	0.764	+0.54	-1.57

Table 26: V_{OC} and FF data for drop casted $NaYF_4$: Er^{3+}, Yb^{3+} doped Sylgard devices at 0.6 suns irradiance.

Doping (w/w %)	V_{OC} (mV)	FF	V_{OC} (%)	Δ FF (%)
0.0	556.812	0.771	-	-
0.25	554.388	0.751	-0.44	-2.56
0.5	554.759	0.752	-0.37	-2.42
1.0	562.640	0.790	+1.05	+2.42
2.0	554.939	0.763	-0.34	-0.98

Table 27: V_{OC} and FF data for drop casted $NaYF_4$: Er^{3+}, Yb^{3+} doped Sylgard devices at 0.4 suns irradiance.

3.8 Conclusion

To conclude, in this chapter the rare earth compounds, $Sr_4Al_{14}O_{25}$: Eu^{2+}, Dy^{3+} and $NaYF_4$: Er^{3+}, Yb^{3+}, had their properties successfully verified in terms of their XRD and photoluminescence profiles. Thin films containing 10% w/w $Sr_4Al_{14}O_{25}$: Eu^{2+}, Dy^{3+} in TiO_2 and 8.3% w/w in Sylgard were constructed but were not initially effective at improving solar cell efficiency. However, grinding the $Sr_4Al_{14}O_{25}$: Eu^{2+}, Dy^{3+} and applying at a lower weight percentage (0.25-2%) in Sylgard did appear to raise performance; at 1 sun the PCE was enhanced by up to 2.1% (for the 0.5% w/w doping level) relative to the control device. Likewise, $NaYF_4$: Er^{3+}, Yb^{3+} when applied in the same way, achieved an even better relative PCE increase of 4.8% under the same conditions. The irradiance level was varied and the PCE gains were shown to be lower at 0.4 and 0.6 suns in both materials but greater at 0.8 suns for $Sr_4Al_{14}O_{25}$: Eu^{2+}, Dy^{3+}. Finally, IPCE measurements showed up to a 2.9% absolute rise in EQE at 400 nm, indicating spectral conversion could have been responsible for this behaviour.

Chapter 4. Application to Low Concentrator Photovoltaic Modules

4.1 Introduction

To build on the findings from the previous chapter, the same silicon solar cells are now coupled with SEH concentrators to form single cell LCPV modules with potential BIPV applications. The SEH concentrator is introduced while the geometry and fabrication processes for the different ways of adding rare earth compounds into the system are elucidated. The modules are characterised, again at varying light intensity, and relative performance improvements compared with the non-LCPV cell analogues from chapter 3. Finally, because of the importance of off-normal irradiance in real systems, the LCPV modules are tested at varying angles of incident radiation.

4.2 Square Elliptical Hyperboloid Concentrators

Square elliptical hyperboloid (SEH) concentrators are 3D static, non-imaging optical devices suitable for applications in low concentration PV. Developed by Sellami et al from 2012, the SEH concentrator operates via total internal reflection. Incoming light passes into the elliptical entrance aperture and is focussed to a square exit aperture at the base of the concentrator, where it then reaches a solar cell via an optical coupling and generates electricity. This design has a relatively high optical efficiency at a wide range of acceptance angles compared to other 3D static concentrators, which is important to allow LCPV systems to utilise diffuse as well as direct radiation. The concentrator is typically made from glass or a transparent polymer which could be polyurethane, PDMS or PMMA. Polyurethane is generally regarded as the best choice due to its lower cost and shrinkage coefficient [305].

SEH concentrators have further attracted interest due to their potential for BIPV; prototype semi-transparent modules have been proposed and fabricated for ultimate use as part of an aesthetically pleasing window façade with added insulation benefits, reducing the heating demand for a building. The conceptual design for such an electricity generating window front is shown in Figure 87. An advantage of using SEH concentrators in these BIPV systems is that for the same

level of transparency and power output, 60% less cells are required than in a non-concentrating BIPV module [305].

There are four key geometrical parameters that determine the performance of an SEH concentrator as shown in Figure 86. These are: the height of the concentrator from base to top (*H*), the side length of the square base (*A*) and the semi-major (*b*) and semi-minor (a) axes of the top ellipse. For a generalised SEH concentrator the geometrical concentration ratio, *G,* and concentration ratio, *C*, (as described in 1.2.2) ratio are given by:

$$G = \frac{\pi ab}{A^2} \qquad (33)$$

$$C = \eta_{opt} \times \frac{\pi ab}{A^2} \qquad (34)$$

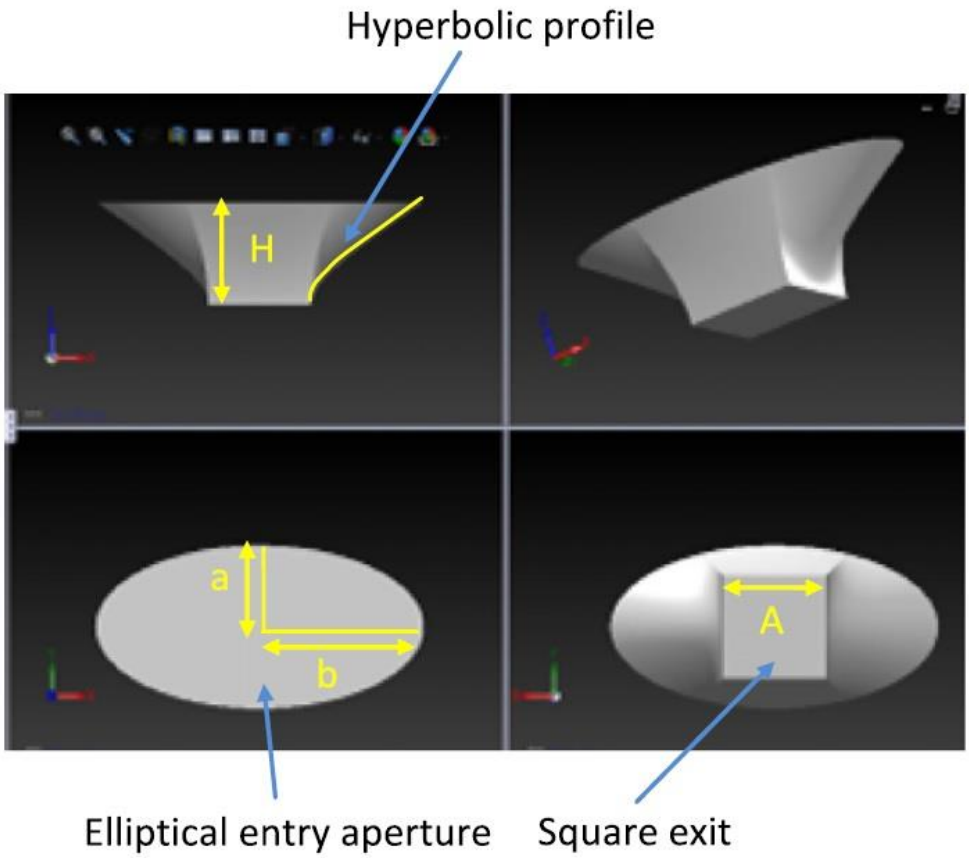

Figure 86: 3D profile from various angles of the SEH concentrator and its dimensional parameters A, H, a and b. Taken from [39].

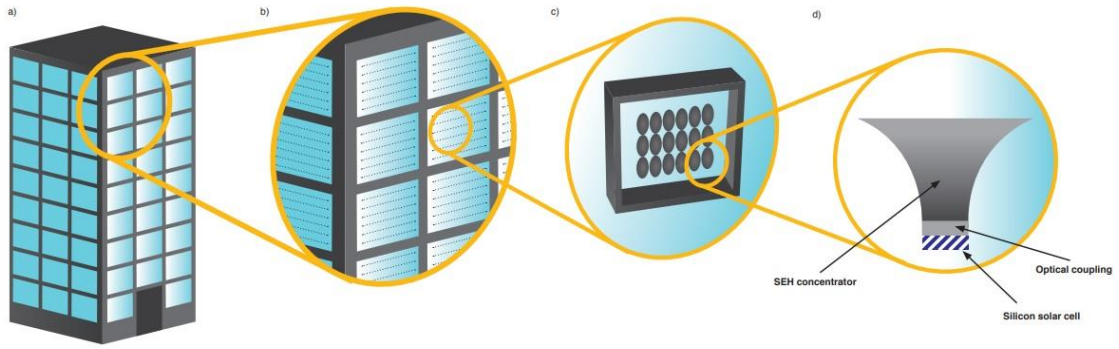

Figure 87: Visual representation of how SEH concentrators can act as components of a BIPV system: a) a south-facing building front in the northern hemisphere with a window façade, b) a single window consisting of many LCPV arrays, c) a single LCPV array of 18 silicon PV cells and SEH concentrators connected together to generate a power output and d) cross-section of a single cell LCPV module.

In this work the SEH concentrators used had constant dimensions of: *a = 0.75 cm*, *b = 1.5* cm, *A = 1* cm and *H = 1.5* cm. So, with these values *G = 3.534*. These parameters were varied and optimised in a previous in-depth work [39], so their variation does not fall within the scope of this thesis. For interest, the optical efficiencies of SEH concentrators with different H/A ratios are shown in Figure 88, where it can be seen the chosen dimensions for this work exhibit a higher optical efficiency at wider acceptance angles. This, in addition to the reduced material usage of a lower H/A, means that H/A = 1.5 is an appropriate selection despite a lower peak optical efficiency at normal irradiance.

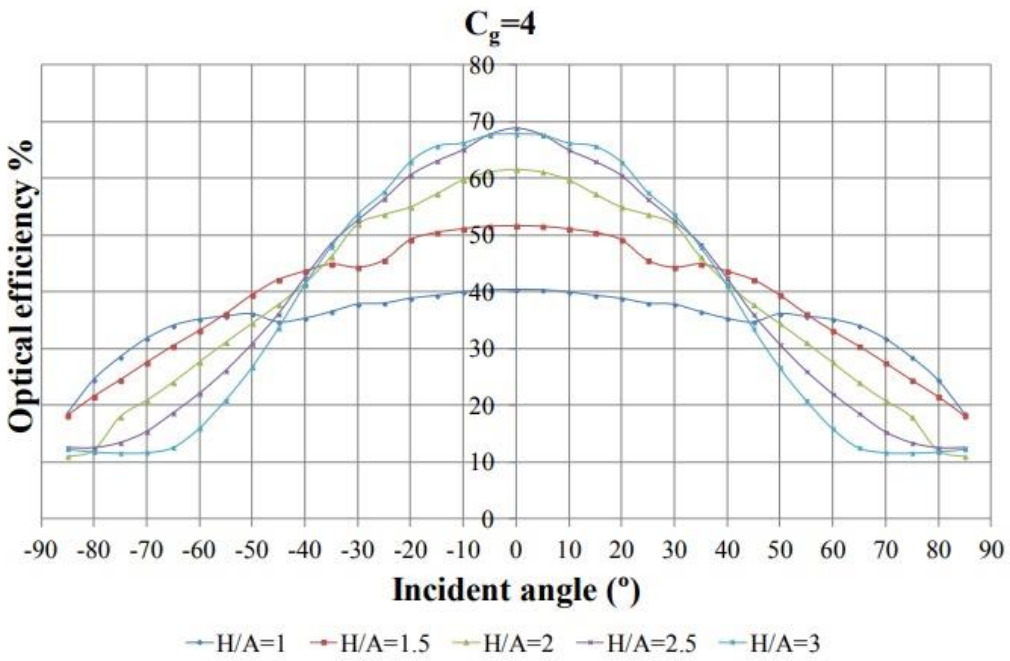

Figure 88: The simulated optical efficiency of various H/A ratio SEH concentrators when the incident radiation is at different angles of incidence. Taken from [39].

4.3 Concentrator Photovoltaic Module Fabrication

In order to fabricate these concentrators, a metal casting mould, as shown in Figure 89, with the shape to produce an SEH concentrator of the as described parameters was used. The concentrators were to be made from Crystal Clear® 200, a polyurethane based casting resin. When set, this material is highly transparent, non-brittle, UV resistant and has a refractive index of 1.50, all ideal properties for use in LCPV systems. Like Sylgard, the Crystal Clear® 200 comes in two parts, A and B, which must be mixed carefully at a ratio of 10:9.

Figure 89: Image of the metal casting mould used to produce a batch of SEH concentrators.

For this part of this study, four geometric configurations of adding rare earth doped compounds into single cell modules LCPV were proposed which are displayed in Figure 90: (i) by adding the particles into the whole concentrator homogenously, labelled in graphs as H, (ii) by adding the particles exclusively to the bottom portion (approximately 20% by volume) of the concentrator, labelled as B, (iii) by adding them solely to the top section (approximately 20% by volume) of the concentrator, labelled T, and (iv) by adding them into the optical coupling between the concentrator and PV cell (in the same weight ratios of 0%, 0.25%, 0.5%, 1.0% and 2.0%, labelled as x syl for an x% doping level when compared to doped concentrators). The latter method is of particular interest since this system will be a replica of the Sylgard coated PV cells studied in 3.7.3 but with a concentrator on top, meaning the relative effects of spectral conversion can be compared in concentrating and non-concentrating PV. The control devices were the ones without any rare earth compound augmentations (i.e. 0% doped optical

coupling and un-doped concentrator, labelled C) and would be the baseline to which the doped LCPV devices could be compared. In these regards, this study can be considered a novel work because the question of optimally adding spectral conversion materials to SEH concentrators has yet to be explored.

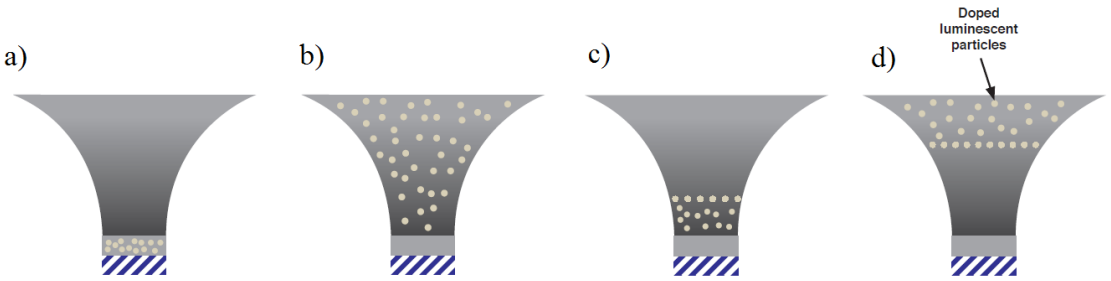

Figure 90: The four doping configurations of rare earth compounds incorporated into LCPV devices: a) doped optical coupling, b) homogenously doped concentrator, c) bottom doped concentrator and d) top doped concentrator.

To fabricate the concentrator the relevant weights of part A and B were measured, so that they could be mixed at a 10:9 ratio. As with the Sylgard procedure, the vacuum oven was utilised in order to reduce bubble formation but this time both precursors A and B were exposed to low pressure before mixing. If a rare earth compound was desired to be placed in the concentrator, then the appropriate amount was measured and added to part B before dispersing with a magnetic stirrer and further degassed. Part B was chosen over part A due to its lower viscosity which allowed for easier dispersion. Initial tests used rare earth compound by weight contents of 1% and 0.5% but these devices clearly had a low visible transparency, so would not be suitable for further use with PV cells. 0.1% was found to be a suitable weight level so was chosen for all homogenously and partially doped concentrators.

Since the optical depth is much thicker than the thin films in non-concentrating PV, it is essential to produce high quality concentrators to ensure consistent results. To further avoid air pockets the components were stirred very gently, although still to a speed and duration that allowed for the reaction to complete (or else the resin would not fully set). Also, when mixing it was important to use a large based beaker, high surface area stirrer and large quantity of resin (typically 300 g) as this was empirically observed to yield better outputs. Each individual mould compartment to form one SEH concentrator used approximately 3.5g of resin (63 g for the whole mould), which unfortunately led to material wastage.

Furthermore, Crystal Clear has a much shorter pot life than Sylgard of only 20 minutes, thus time was of the essence and an optimised procedure necessary.

Once satisfactorily mixed, the resin was poured into the casting mould in one smooth filling motion down the side of one of the mould's compartments (again to avoid air gap growth) and subjected to a final degassing. Another variation in the fabrication occurred if a concentrator was required to limit the rare earth compound content to its top or base. In these cases, two separate mixtures were prepared (one with and one without the rare earth compound added) and the mould was filled to the appropriate level with each beaker.

Finally, the mould was left to cure for 16 hours in air at room temperature. Before pouring the resin, the mould had been treated with Smooth-on Universal™ mould release (to aid with removal of the concentrators) and tightened with bolts to a sheet of glass and metal base to prevent leakage. At times, the glass had become stuck to the concentrators and was difficult to remove but application of heat and repeated twisting through a vice clamp allowed the glass to be removed, after which concentrators could be pushed out through the top of the mould by applying a force to the gaps at the base.

The UV-Vis transmittance spectra of concentrators were recorded using the Perkin Elmer UV/VIS/NIR Spectrophotometer Lambda 1050. As shown in Figure 91, an un-doped concentrator has a transmittance of approximately 65% across visible wavelengths, although it sharply drops to 0% below 400 nm. This leads to less photons in the UV region reaching the solar cell and partially limits the effectiveness of the rare earth doped compounds which can absorb UV radiation. However, because they can also absorb blue wavelengths, increases in EQE may still be observed around 400-450 nm. The transmittance spectra of the concentrators containing the rare earth doped compounds at the top, bottom and homogenously throughout the concentrator are also presented in Figures 92 and 93. It can be observed from these spectra that the doped concentrators still exhibit similar transmittance levels with regards to the beam incident at the centre of the top elliptical entrance aperture, with the exception of the bottom doped $NaYF_4$: Er^{3+}, Yb^{3+} and homogenously doped $Sr_4Al_{14}O_{25}$: Eu^{2+}, Dy^{3+} samples. Therefore, performance enhancements can be realistically expected for most of the proposed LCPV device architectures.

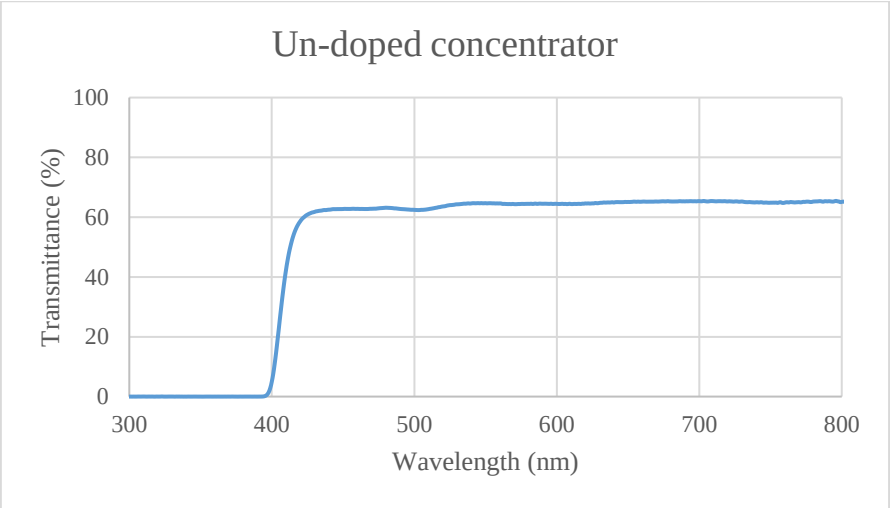

Figure 91: Transmittance spectrum of the un-doped concentrator.

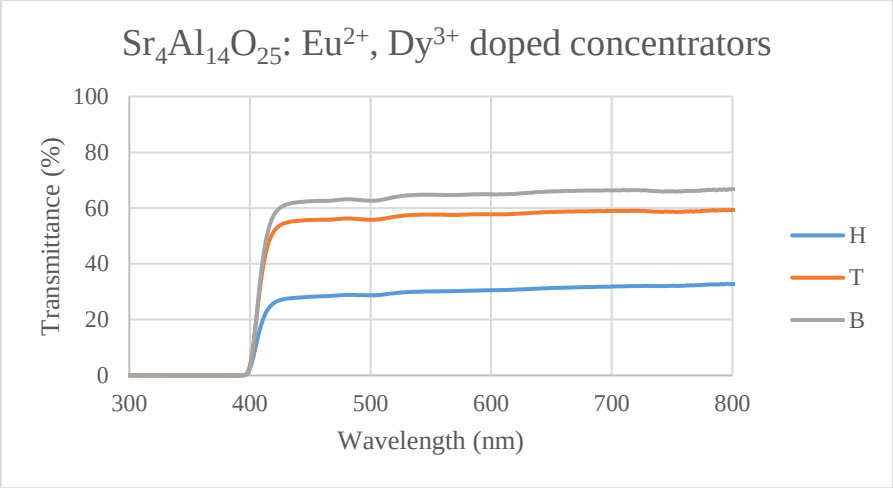

Figure 92: Transmittance spectra of the $Sr_4Al_{14}O_{25}$: Eu^{2+}, Dy^{3+} doped concentrators.

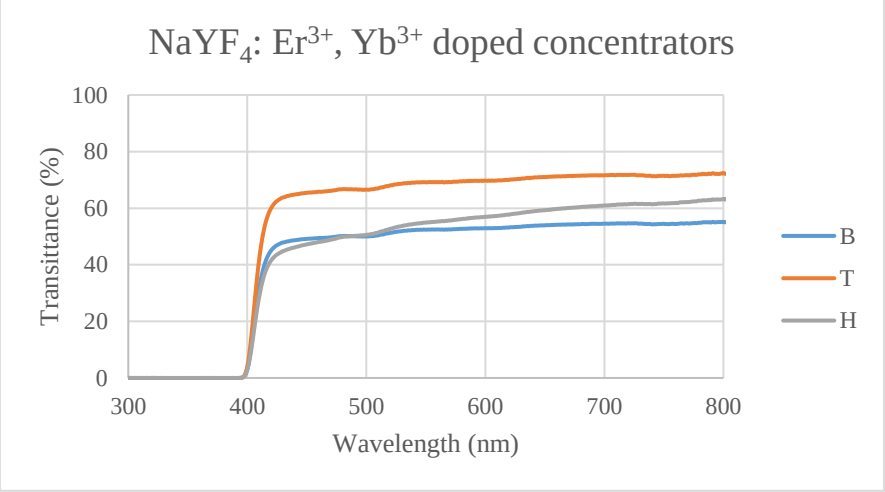

Figure 93: Transmittance spectra of the $NaYF_4$: Er^{3+}, Yb^{3+} doped concentrators.

Once the rigid concentrators had been demoulded, they could be combined with silicon cells as prepared in 3.5.1 to form a single cell PV module. This was achieved by preparing a layer of Sylgard (without any rare earth doped compound for doped concentrators or the control, and with rare earth doped compounds for un-doped concentrators) and placing a small amount on the silicon cell situated on an edge protected acrylic base, in the exact way as the drop casting procedure from the previous chapter. However, the concentrators could then be stuck on top of the PV cells by gently pressing them down on them for several seconds. Care was taken to ensure the concentrators were not at an angle and then the sample devices were left to set for a further 48 hours at room temperature. At the end of this period, the concentrators had become permanently affixed to the PV cell via the Sylgard optical coupling and the devices were ready for electrical characterisation (cf. Figure 94). A full graphical summary of these steps in the procedure for producing an LCPV or coated PV cell can be found in Figure 95.

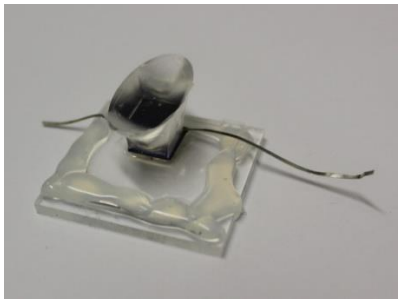

Figure 94: Image of a single cell LCPV module to be characterised in this work.

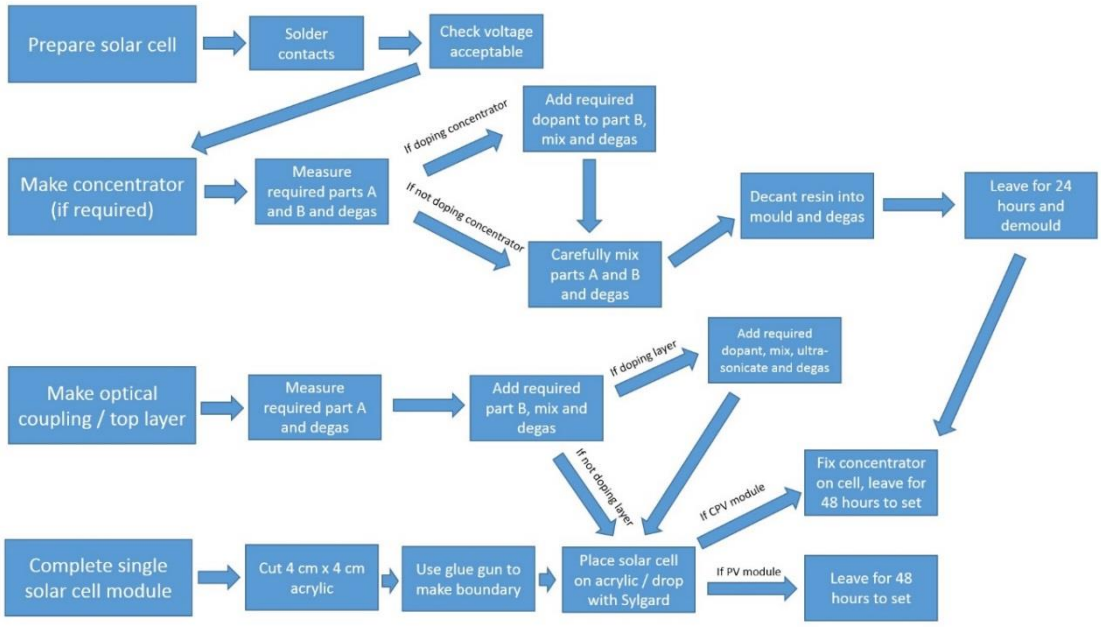

Figure 95: Flow diagram to summarise the steps involved in fabricating a single cell PV or LCPV module.

4.4 Results

Once fabricated, the devices were characterised through the solar simulator and IPCE with the same methods as chapter 3. The PCE and J_{SC} for the LCPV devices obtained under the solar simulator are displayed graphically in Figures 96-103 and numerically in Tables 28-35. In this investigation, the control device, with no rare earth doped compound, showed a PCE of 9.38% under 1 sun illumination. It can clearly be seen from the data that in general the devices containing either of the rare earth doped compounds exhibited increased electrical performance. Only the 1% and 2% w/w doped $Sr_4Al_{14}O_{25}$: Eu^{2+}, Dy^{3+} optical coupling, homogenously $Sr_4Al_{14}O_{25}$: Eu^{2+}, Dy^{3+} doped concentrator and bottom doped $NaYF_4$: Er^{3+}, Yb^{3+} failed to demonstrate increased PCE at all irradiances with PCE reductions ranging from 0.0% to -2.3%. At 1 sun, the highest PCE attained was 10.42% for an $NaYF_4$: Er^{3+}, Yb^{3+} containing device and 9.92% by the addition of $Sr_4Al_{14}O_{25}$: Eu^{2+}, Dy^{3+}; these correspond to relative enhancements of 11.1% and 5.7% respectively. These impressive results were obtained for the 1% w/w doped $NaYF_4$: Er^{3+}, Yb^{3+} optical coupling and top doped $Sr_4Al_{14}O_{25}$: Eu^{2+}, Dy^{3+} concentrator.

As expected J_{SC} enhancements accompanied improvements in PCE. The control device had a J_{SC} of 71.97 mA/cm^2 at 1 sun, whereas at the same light intensity the highest J_{SC} recorded was 77.78 mA/cm^2 (an 8.1% relative increase) for the 1% doped $NaYF_4$: Er^{3+}, Yb^{3+} LCPV device (unsurprisingly the same specification that attained the highest PCE). However, for $Sr_4Al_{14}O_{25}$: Eu^{2+}, Dy^{3+} containing devices at 1 sun, there was a discrepancy between the device with the greatest J_{SC} and highest PCE; the bottom doped concentrator achieved a J_{SC} of 75.24 mA/cm^2 (a 4.6% relative increase to the control), while the highest PCE device, the top doped concentrator achieved a slightly lower J_{SC} of 75.17 mA/cm^2 (a 4.4% relative enhancement). Although, this is not totally unanticipated since the bottom doped concentrator $Sr_4Al_{14}O_{25}$: Eu^{2+}, Dy^{3+} device still showed a respectable relative PCE increase of 5.3%, not to dissimilar from the 5.7% realised for the champion $Sr_4Al_{14}O_{25}$: Eu^{2+}, Dy^{3+} top doped concentrator. The y-axis intercepts on the I-V curves, Figures 104-107, also demonstrate these J_{SC} enhancements whilst the closely together x-axis intercepts indicate small variation in V_{OC}, which recalling from solar cell theory is to be expected since the J_{SC} is determined by

rate of electron-hole pair generation that is more likely to be influenced by spectral conversion.

Then as with the results presented in 3.7.3, the effect of subjecting the devices to varying levels of solar irradiance (1 sun and 0.8, 0.6 and 0.4 suns) was studied. This time, a relationship was often observed such that the PCE and J_{SC} gains were more pronounced at lower irradiances. For example, the 1% optical coupling doped $NaYF_4$: Er^{3+}, Yb^{3+} device exhibited an 11.1% relative PCE gain at 1 sun, but 15.5% and 17.7% at 0.6 and 0.4 suns respectively. The same phenomenon is recorded for $Sr_4Al_{14}O_{25}$: Eu^{2+}, Dy^{3+} containing LCPV devices, in that the top doped concentrator displayed a 5.7% PCE enhancement at 1 sun compared to a 14.0% increase at 0.4 suns. In addition, the J_{SC} measurements followed a similar pattern, with maximum relative J_{SC} gains of +16.3% and +13.8% occurring at 0.4 suns irradiance for the champion $NaYF_4$: Er^{3+}, Yb^{3+} and $Sr_4Al_{14}O_{25}$: Eu^{2+}, Dy^{3+} containing devices respectively. On the other hand, there are some cases where this trend was not observed; for the homogenously doped $Sr_4Al_{14}O_{25}$: Eu^{2+}, Dy^{3+} concentrator, $Sr_4Al_{14}O_{25}$: Eu^{2+}, Dy^{3+} doped optical couplings (all concentrations) and the $NaYF_4$: Er^{3+}, Yb^{3+} doped concentrators (all spatial configurations), the maximum PCE gain was observed at either 0.6 or 0.8 suns.

Furthermore, it is noteworthy to contrast the performance between the different types of doped concentrators and doped optical couplings for both spectral conversion materials. In $Sr_4Al_{14}O_{25}$: Eu^{2+}, Dy^{3+}, it was the concentrators that achieved the best performance parameters but in $NaYF_4$: Er^{3+}, Yb^{3+}, the doped optical couplings. However, despite $NaYF_4$: Er^{3+}, Yb^{3+} doped concentrators generally performing weaker, the homogenously doped concentrator LCPV device outperformed that of its $Sr_4Al_{14}O_{25}$: Eu^{2+}, Dy^{3+} analogue; at 1 sun the $NaYF_4$: Er^{3+}, Yb^{3+} homogenously doped concentrator achieved a relative PCE gain of 1.7% whereas its $Sr_4Al_{14}O_{25}$: Eu^{2+}, Dy^{3+} counterpart showed a decrease in PCE of 2.3%. Likewise, for the doped optical couplings, there was a variance in the optimal doping concentration between the two compounds. For $NaYF_4$: Er^{3+}, Yb^{3+} doped optical coupling devices, the 1% w/w dominated across all irradiance levels but for their $Sr_4Al_{14}O_{25}$: Eu^{2+}, Dy^{3+} equivalents, it was the 0.25% w/w and 0.5% w/w that achieved the best PCE at 1 and 0.6 suns, and 0.8 and 0.4 suns respectively.

The EQE spectra of the LCPV devices, an important aspect of spectral conversion investigations, are presented in Figures 108-111. From these it can be seen that the EQEs obtained for cells containing both materials increased and were consistent with the findings from the solar simulator studies, such that the better performing devices exhibited higher EQEs. Of relevance to this work, the EQE increase was particularly observed in the 400-500 nm region, indicating DC or LDS taking place to aid spectral response to those wavelengths. The champion $Sr_4Al_{14}O_{25}$: Eu^{2+}, Dy^{3+} device showed an absolute rise in EQE of 3.53% at 450 nm and an even larger enhancement of 3.96% was recorded for the best performing $NaYF_4$: Er^{3+}, Yb^{3+} at the same wavelength. In the middle of the illumination range (600-800 nm), the difference between the doped LCPV modules and control device becomes less significant. This is to be expected since these wavelengths are not within the excitation range of the rare earth compounds, so no spectral conversion would occur. Higher doping level devices also exhibit lower EQEs in this part of the spectrum because of their lower transparency. Then at longer illumination wavelengths, although not the primary focus of this investigation nor as impactful, there could be minor evidence of UC aiding the performance of the $NaYF_4$: Er^{3+}, Yb^{3+} containing devices. Considering its excitation potential at 980 nm, the EQE of the $NaYF_4$: Er^{3+}, Yb^{3+} doped optical coupling devices all increase up to a maximum of 1.55% at this wavelength, whereas their $Sr_4Al_{14}O_{25}$: Eu^{2+}, Dy^{3+} counterparts all decrease in EQE substantially at this wavelength by up to -3.29% (bar the 1% w/w measurement). Finally, and unfortunately, no increase in EQE can take place below 400 nm, despite being within a strong excitation range of both materials, due to the poor transmittance of the polyurethane concentrator in those regions of the spectrum.

After quantitatively analysing the results, it is then important to attempt to understand them further in terms of the underlying physical process and how they depend on the parameters of choice of compound, doping concentration level and system geometry. The better performance of $NaYF_4$ Er^{3+}, Yb^{3+} could potentially be attributed to its smaller particle size leading to fewer scattering losses, a higher quantum yield and wider spectral excitation range. Another strong case for the results observed is the fact that for $NaYF_4$ Er^{3+}, Yb^{3+}, the most intense photoluminescent emission occurs at 650-675 nm whereas for $Sr_4Al_{14}O_{25}$: Eu^{2+}, Dy^{3+} the emission peaks at 500 nm. This dissimilarity could have

an impact on the effectiveness of the material at improving LCPV performance since the EQE of the bare solar cells used in these experiments is 83.8% at 500 nm and 85.9% at 650 nm. So, the $NaYF_4$ Er^{3+}, Yb^{3+} could be better as its emitted photons lead to the generation of more photocurrent.

However, this does not explain why the $Sr_4Al_{14}O_{25}$: Eu^{2+}, Dy^{3+} doped concentrators outperform those containing $NaYF_4$ Er^{3+}, Yb^{3+}. One possible theory is that the $Sr_4Al_{14}O_{25}$: Eu^{2+}, Dy^{3+} suffer from less self-absorption losses since there is little overlap in the emission and excitation spectrum, whereas $NaYF_4$: Er^{3+}, Yb^{3+} can be excited at wavelengths of 450 nm and 980 nm, where it demonstrates a little emission. These greater self-absorption losses will become more apparent over longer optical path lengths which results in more photons lost as the emitted light passes through the concentrator, hence the $NaYF_4$: Er^{3+}, Yb^{3+} doped concentrator's lower performance. As a corollary, the reason that better PCE and J_{SC} measurements were recorded for the $NaYF_4$: Er^{3+}, Yb^{3+} doped optical couplings could be due the shorter optical path lengths involved following a photon absorption and re-emission event.

In addition, the better results from the $Sr_4Al_{14}O_{25}$: Eu^{2+}, Dy^{3+} containing concentrators when doped at the top or bottom of the SEH can be explained by conclusions from a prior work; LSCs containing thin films of rare earth ion compounds have been demonstrated to greater PV performance than homogenously doped concentrators by making sure that spectral conversion processes occur near the boundaries of the concentrator, which reduces optical losses [191]. Conversely, the homogenously doped $NaYF_4$: Er^{3+}, Yb^{3+} concentrator may have performed better than its $Sr_4Al_{14}O_{25}$: Eu^{2+}, Dy^{3+} analogue, simply because of its greater transmittance across visible wavelengths, meaning a greater number of photons reach the PV cell.

As was seen in 2.3 and 2.7, the doping concentration of the rare earth compound is a major factor in the effectiveness of a spectral conversion layer or optical efficiency of an LSC, so is a vital parameter to be optimised. Recall that if the doping level is too low, insufficient absorption and thus spectral conversion will occur, while if it is too high, then the transparency of the layer will be parasitically reduced across the spectrum and energy transfer between ions will further reduce the spectral conversion quantum efficiency. For the doped optical coupling $NaYF_4$: Er^{3+}, Yb^{3+} containing devices, the 1% w/w concentration achieved the

best results which suggests at lower doping ratios insufficient spectral conversion was taking place and at 2% w/w, the PCE gain is smaller due to lower transmittance of the layer or even less efficient spectral conversion due to energy transfer between ions. Likewise, the same logic can partially explain the superior performance of the 0.25% and 0.5% w/w $Sr_4Al_{14}O_{25}$: Eu^{2+}, Dy^{3+} devices whose lower value could indicate greater scattering losses. However, since the maximum enhancements were sometimes obtained for the lowest concentration levels considered in this study, the true optimal value could be lower than 0.25% w/w or alternatively, lie somewhere between 0.25% and 0.5% w/w. The variance in optimal doping ratio for $Sr_4Al_{14}O_{25}$: Eu^{2+}, Dy^{3+} doped optical couplings also raises the question if the spectral conversion processes are dependent on incident light intensity. LDS and DC have been proposed to be independent of light intensity while the J_{SC} of the PV cell falls linearly with decreasing irradiance. Therefore, the greater J_{SC} enhancements observed at lower irradiances could be because LDS and DC process are able to occur at the same rate as higher irradiances, providing relatively greater numbers of photons to fall on the PV cell and generate current. On the other hand, UC is a non-linear process whose quantum yield falls with incident light intensity. Despite UC only occurring mildly in $NaYF_4$: Er^{3+}, Yb^{3+}, this could explain the better performance of the doped optical coupling devices, since the light there will be at a higher concentration than in the concentrator, and the localised peaks in J_{SC} and PCE gains at 0.8 suns for various $NaYF_4$: Er^{3+}, Yb^{3+} containing LCPV device configurations (since below 0.8 suns the impact of the UC process on device performance could be negligible).

Doped optical coupling (w/w %)	η (%)	J_{SC} (mA/cm^2)	Δη (%)	Δ J_{SC} (%)
0.0	9.382	71.970	-	-
0.25	9.798	73.619	+4.43	+2.29
0.5	9.778	74.949	+4.22	+4.14
1.0	9.338	72.207	-0.70	+3.19
2.0	9.382	73.302	+0.00	+1.85
Doped concentrator (w/w %)	**η (%)**	**J_{SC} (mA/cm^2)**	**Δη (%)**	**Δ J_{SC} (%)**
0.1 (Homogenous)	9.167	69.976	-2.29	-2.77
0.1 (Top)	9.916	75.168	+5.69	+4.44
0.1 (Bottom)	9.883	75.243	+5.34	+4.55

Table 28: J_{SC} and PCE data for $Sr_4Al_{14}O_{25}$: Eu^{2+}, Dy^{3+} doped LCPV devices at 1 sun irradiance.

Doped optical coupling (w/w %)	η (%)	J_{SC} (mA/cm^2)	Δη (%)	Δ J_{SC} (%)
0.0	8.871	53.856	-	-
0.25	9.521	57.647	+7.33	+7.04
0.5	9.574	58.568	+7.92	+8.75
1.0	8.938	55.480	+0.75	+3.28
2.0	9.225	57.431	+3.99	+6.64
Doped concentrator (w/w %)	**η (%)**	**J_{SC} (mA/cm^2)**	**Δη (%)**	**Δ J_{SC} (%)**
0.1 (Homogenous)	8.873	53.719	+0.03	-0.25%
0.1 (Top)	10.079	59.807	+13.61	+11.05
0.1 (Bottom)	9.660	60.313	+8.89	+11.99

Table 29: J_{SC} and PCE data for $Sr_4Al_{14}O_{25}$: Eu^{2+}, Dy^{3+} doped LCPV devices at 0.8 suns irradiance.

Doped optical coupling (w/w %)	η (%)	J_{SC} (mA/cm^2)	Δη (%)	Δ J_{SC} (%)
0.0	8.860	40.490	-	-
0.25	9.458	43.188	+6.75	+6.66
0.5	9.398	43.746	+6.08	+8.02
1.0	8.873	41.890	+0.15	+3.37
2.0	9.085	42.894	+2.54	+5.94
Doped concentrator (w/w %)	**η (%)**	**J_{SC} (mA/cm^2)**	**Δη (%)**	**Δ J_{SC} (%)**
0.1 (Homogenous)	8.843	40.525	-0.19	+0.09
0.1 (Top)	9.960	45.198	+12.42	+11.63
0.1 (Bottom)	9.367	45.039	+5.72	+11.23

Table 30: J_{SC} and PCE data for $Sr_4Al_{14}O_{25}$: Eu^{2+}, Dy^{3+} doped LCPV devices at 0.6 suns irradiance.

Doped optical coupling (w/w %)	η (%)	J_{SC} (mA/cm^2)	Δη (%)	Δ J_{SC} (%)
0.0	8.448	26.670	-	-
0.25	8.920	28.141	+5.59	+5.52
0.5	8.945	28.627	+5.89	+7.34
1.0	8.448	27.320	+0.00	+2.95
2.0	8.525	28.140	+0.92	+5.38
Doped concentrator (w/w %)	**η (%)**	**J_{SC} (mA/cm^2)**	**Δη (%)**	**Δ J_{SC} (%)**
0.1 (Homogenous)	8.403	26.537	-0.53	-0.50
0.1 (Top)	9.633	29.890	+14.03	+12.07
0.1 (Bottom)	9.523	30.346	+12.73	+13.78

Table 31: J_{SC} and PCE data for $Sr_4Al_{14}O_{25}$: Eu^{2+}, Dy^{3+} doped LCPV devices at 0.4 suns irradiance.

Doped optical coupling (w/w %)	η (%)	J_{SC} (mA/cm^2)	Δη (%)	Δ J_{SC} (%)
0.0	9.382	71.970	-	-
0.25	10.011	75.237	+6.70	+4.54
0.5	10.032	76.536	+6.93	+6.34
1.0	10.423	77.783	+11.10	+8.08
2.0	9.875	74.632	+5.25	+3.70
Doped concentrator (w/w %)	**η (%)**	**J_{SC} (mA/cm^2)**	**Δη (%)**	**Δ J_{SC} (%)**
0.1 (Homogenous)	9.542	73.454	+1.71	+2.06
0.1 (Top)	9.446	72.296	+0.68	+0.45
0.1 (Bottom)	9.164	70.049	-2.32	-2.67

Table 32: J_{SC} and PCE data for $NaYF_4$: Er^{3+}, Yb^{3+} doped LCPV devices at 1 sun irradiance.

Doped optical coupling (w/w %)	η (%)	J_{SC} (mA/cm^2)	Δη (%)	Δ J_{SC} (%)
0.0	8.871	53.856	-	-
0.25	9.691	59.850	+9.24	+11.13
0.5	9.356	60.689	+5.47	+12.69
1.0	10.249	61.925	+15.53	+14.98
2.0	9.620	59.071	+8.44	+9.68
Doped concentrator (w/w %)	**η (%)**	**J_{SC} (mA/cm^2)**	**Δη (%)**	**Δ J_{SC} (%)**
0.1 (Homogenous)	9.754	59.800	+9.95	+11.03
0.1 (Top)	9.484	58.373	+6.90	+8.39
0.1 (Bottom)	9.311	57.338	+4.96	+6.47

Table 33: J_{SC} and PCE data for $NaYF_4$: Er^{3+}, Yb^{3+} doped LCPV devices at 0.8 suns irradiance.

Doped optical coupling (w/w %)	η (%)	J_{SC} (mA/cm^2)	Δη (%)	Δ J_{SC} (%)
0.0	8.860	40.490	-	-
0.25	9.750	45.350	+10.05	+12.00
0.5	9.787	45.785	+10.46	+13.08
1.0	10.230	46.865	+15.46	+15.74
2.0	9.652	44.945	+8.94	+11.00
Doped concentrator (w/w %)	**η (%)**	**J_{SC} (mA/cm^2)**	**Δη (%)**	**Δ J_{SC} (%)**
0.1 (Homogenous)	9.537	44.431	+7.64	+9.51
0.1 (Top)	9.413	43.787	+6.25	+8.14
0.1 (Bottom)	9.127	42.426	+3.01	+4.78

Table 34: J_{SC} and PCE data for $NaYF_4$: Er^{3+}, Yb^{3+} doped LCPV devices at 0.6 suns irradiance.

Doped optical coupling (w/w %)	η (%)	J_{SC} (mA/cm^2)	Δη (%)	Δ J_{SC} (%)
0.0	8.448	26.670	-	-
0.25	9.460	29.950	+11.99	+12.30
0.5	9.518	30.341	+12.67	+13.76
1.0	9.940	31.013	+17.67	+16.28
2.0	9.350	29.728	+10.68	+11.47
Doped concentrator (w/w %)	**η (%)**	**J_{SC} (mA/cm^2)**	**Δη (%)**	**Δ J_{SC} (%)**
0.1 (Homogenous)	9.160	29.118	+8.43	+9.18
0.1 (Top)	8.965	28.492	+6.12	+6.83
0.1 (Bottom)	8.705	27.793	+3.05	+4.21

Table 35: J_{SC} and PCE data for $NaYF_4$: Er^{3+}, Yb^{3+} doped LCPV devices at 0.4 suns irradiance.

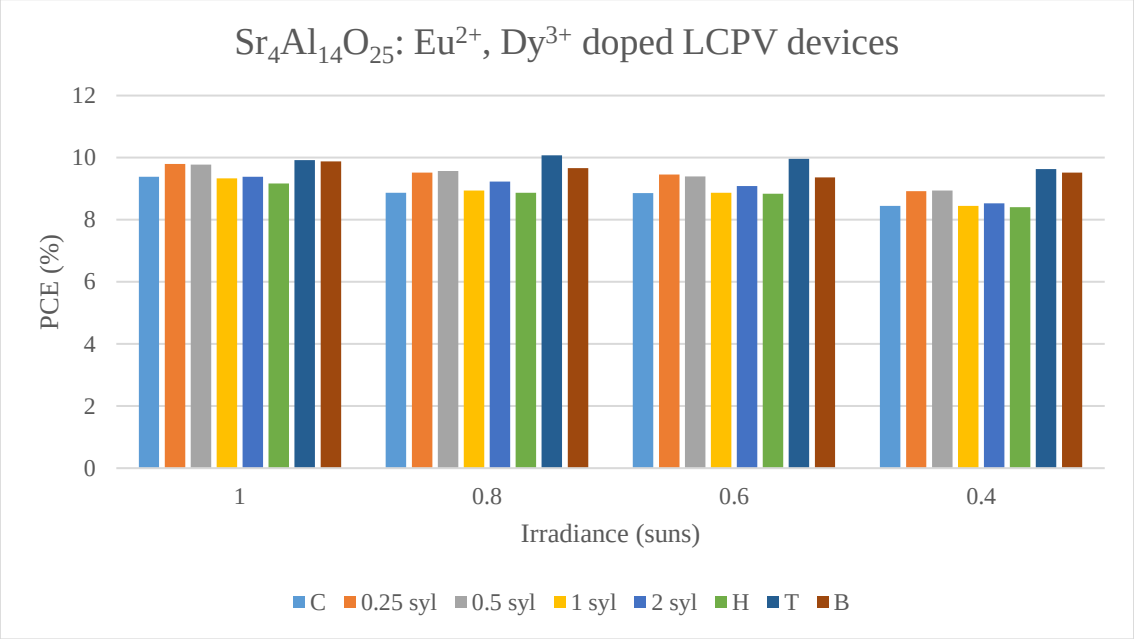

Figure 96: PCE of the $Sr_4Al_{14}O_{25}$: Eu^{2+}, Dy^{3+} doped LCPV devices of varying doping ratios at different solar irradiances.

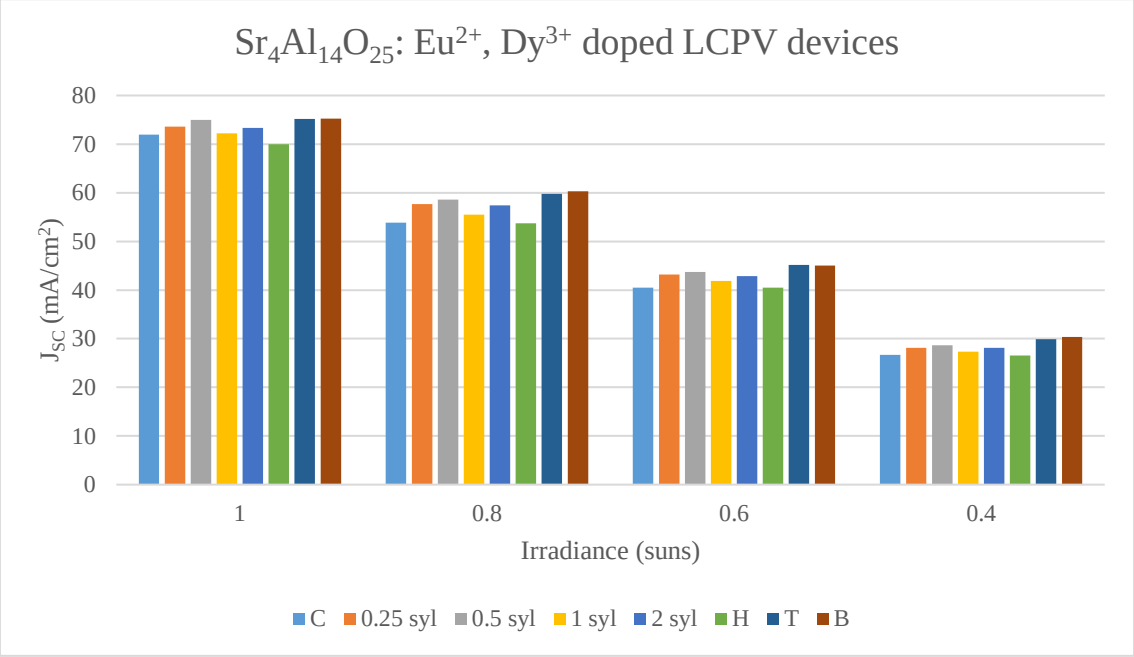

Figure 97: J_{SC} of the $Sr_4Al_{14}O_{25}$: Eu^{2+}, Dy^{3+} doped LCPV devices of varying doping ratios at different solar irradiances.

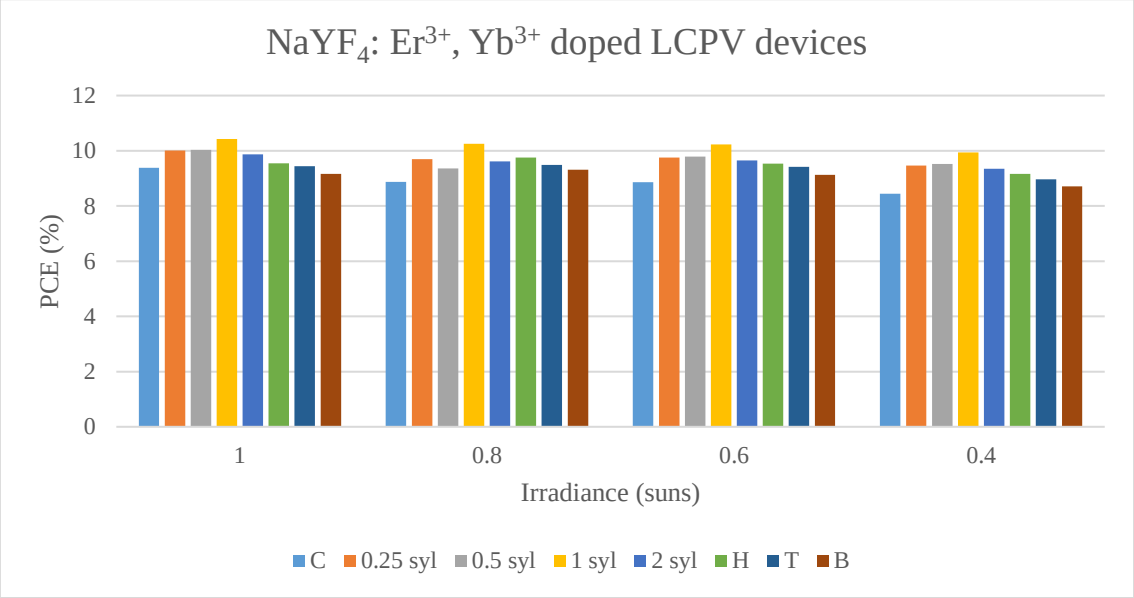

Figure 98: PCE of the $NaYF_4$: Er^{3+}, Yb^{3+} doped LCPV devices of varying doping ratios at different solar irradiances.

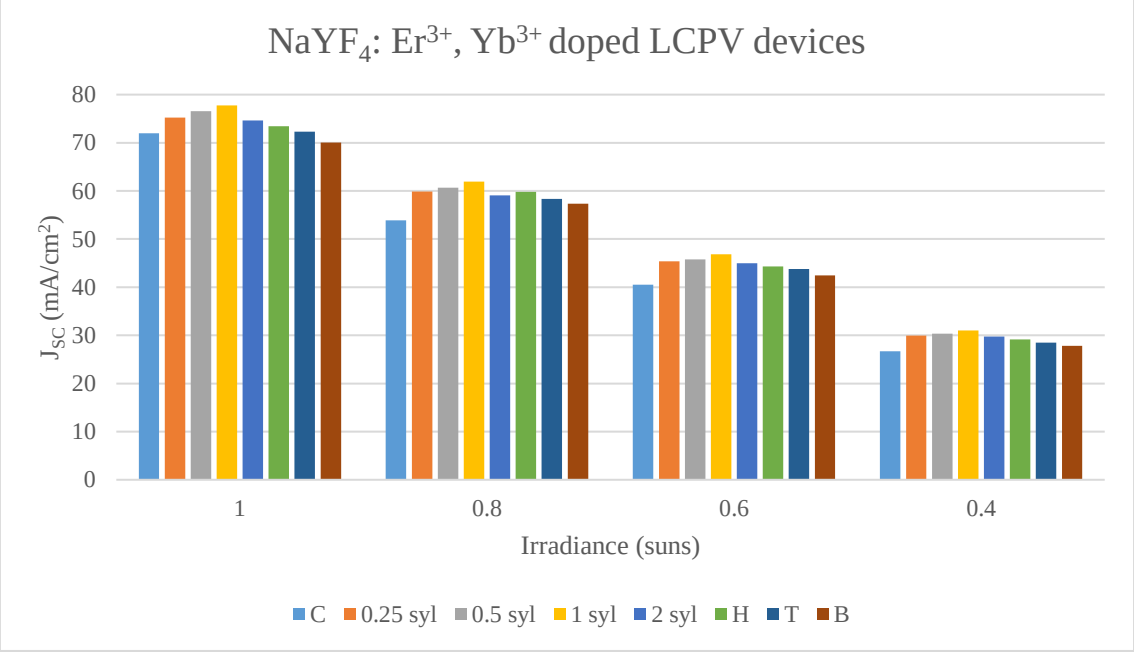

Figure 99: J_{SC} of the $NaYF_4$: Er^{3+}, Yb^{3+} doped LCPV devices of varying doping ratios at different solar irradiances.

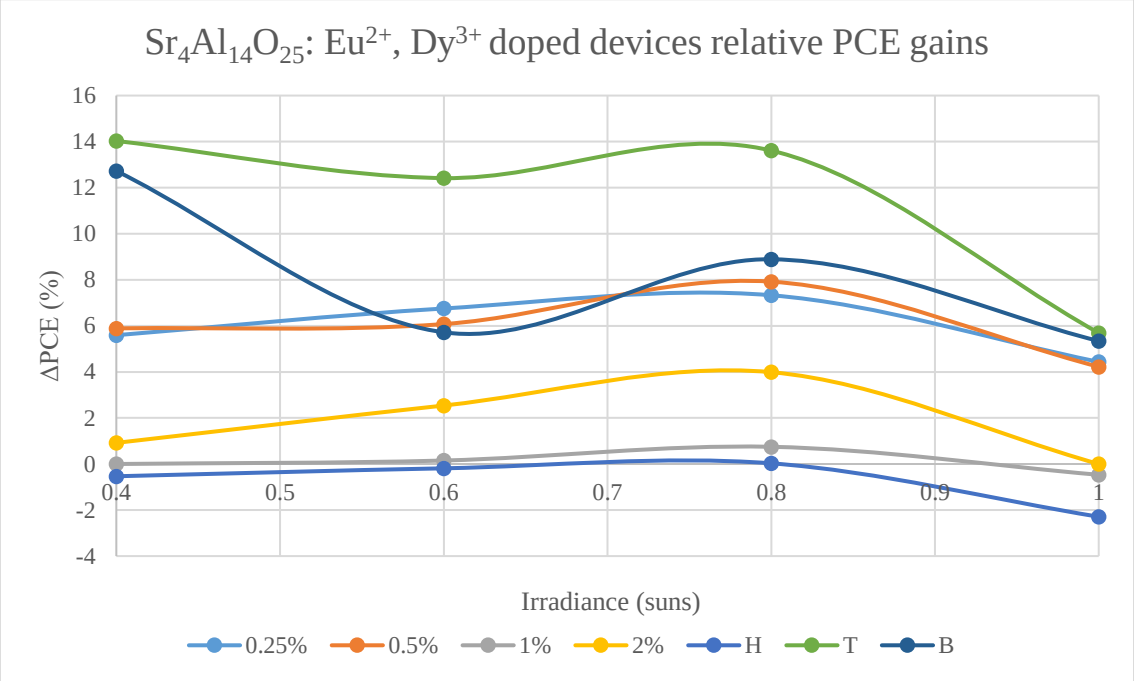

Figure 100: Relative PCE gains for the $Sr_4Al_{14}O_{25}$: Eu^{2+}, Dy^{3+} doped LCPV devices at different solar irradiances.

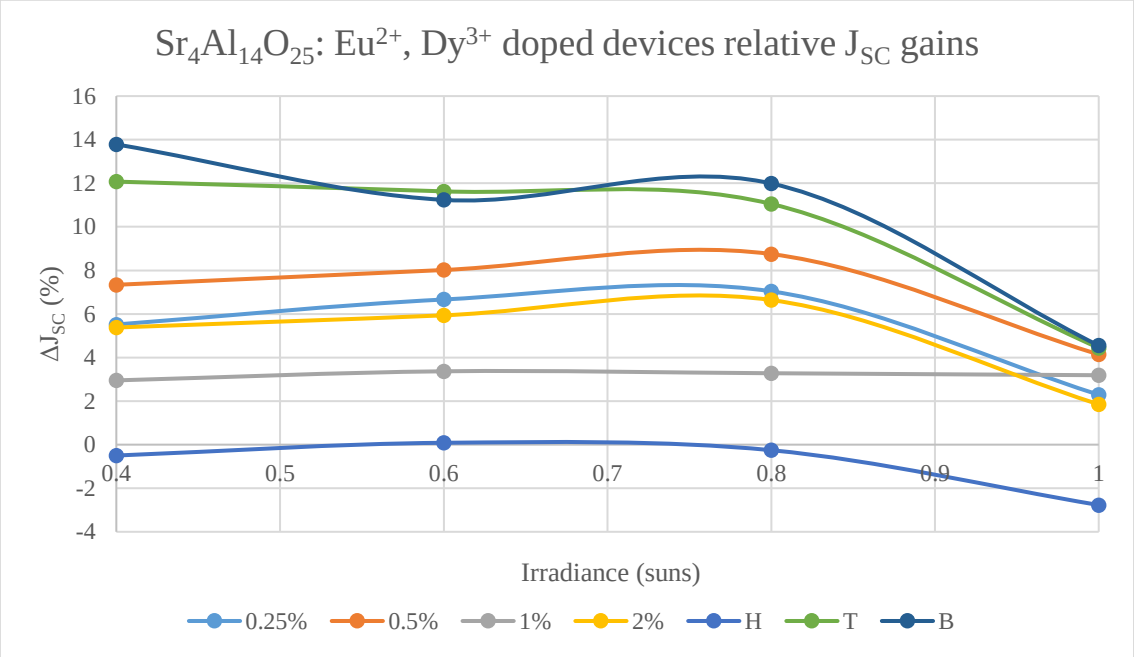

Figure 101: Relative J_{SC} gains for the $Sr_4Al_{14}O_{25}$: Eu^{2+}, Dy^{3+} doped LCPV devices at different solar irradiances.

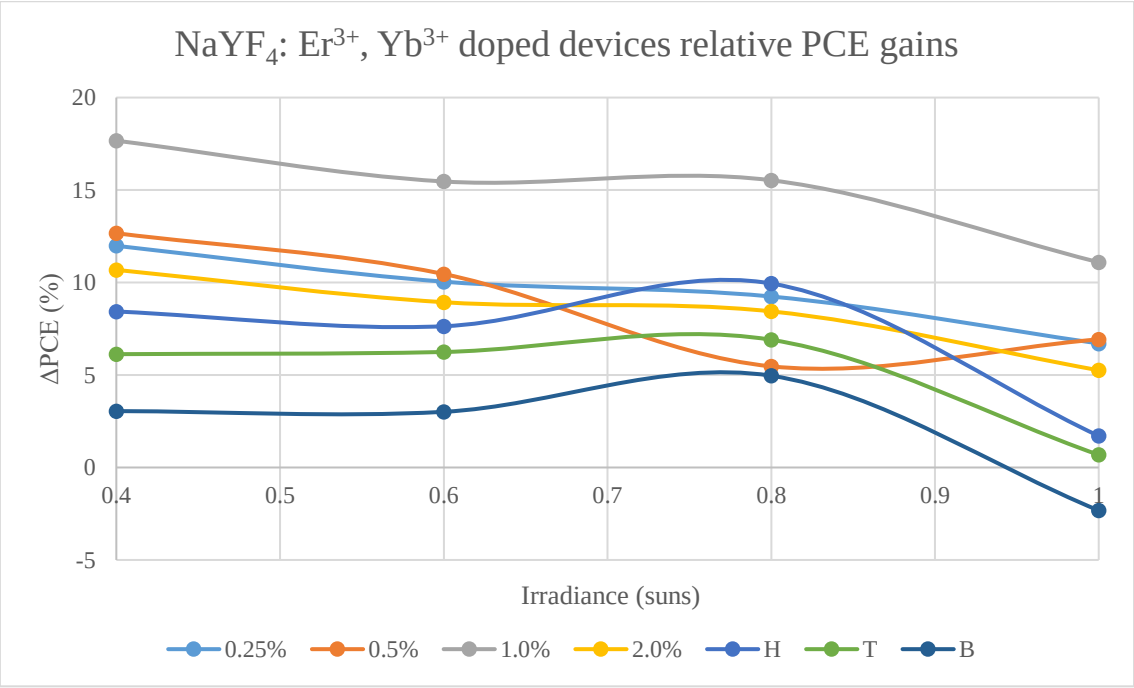

Figure 102: Relative PCE gains for the $NaYF_4$: Er^{3+}, Yb^{3+} doped LCPV devices at different solar irradiances.

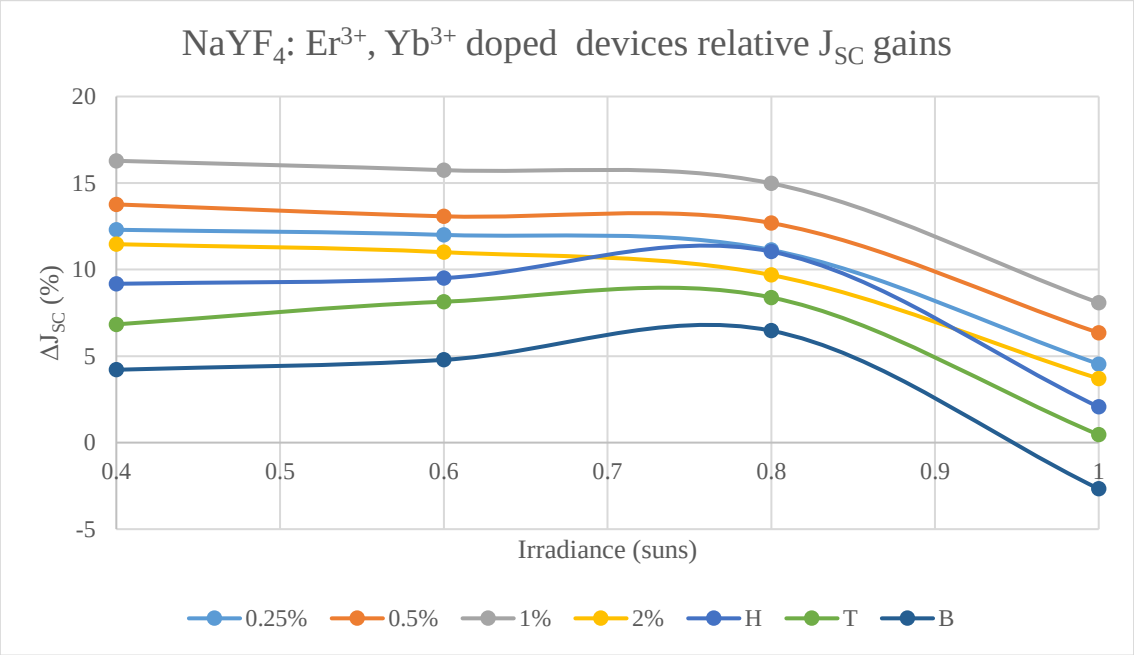

Figure 103: Relative J_{SC} gains for the $NaYF_4$: Er^{3+}, Yb^{3+} doped LCPV devices at different solar irradiances.

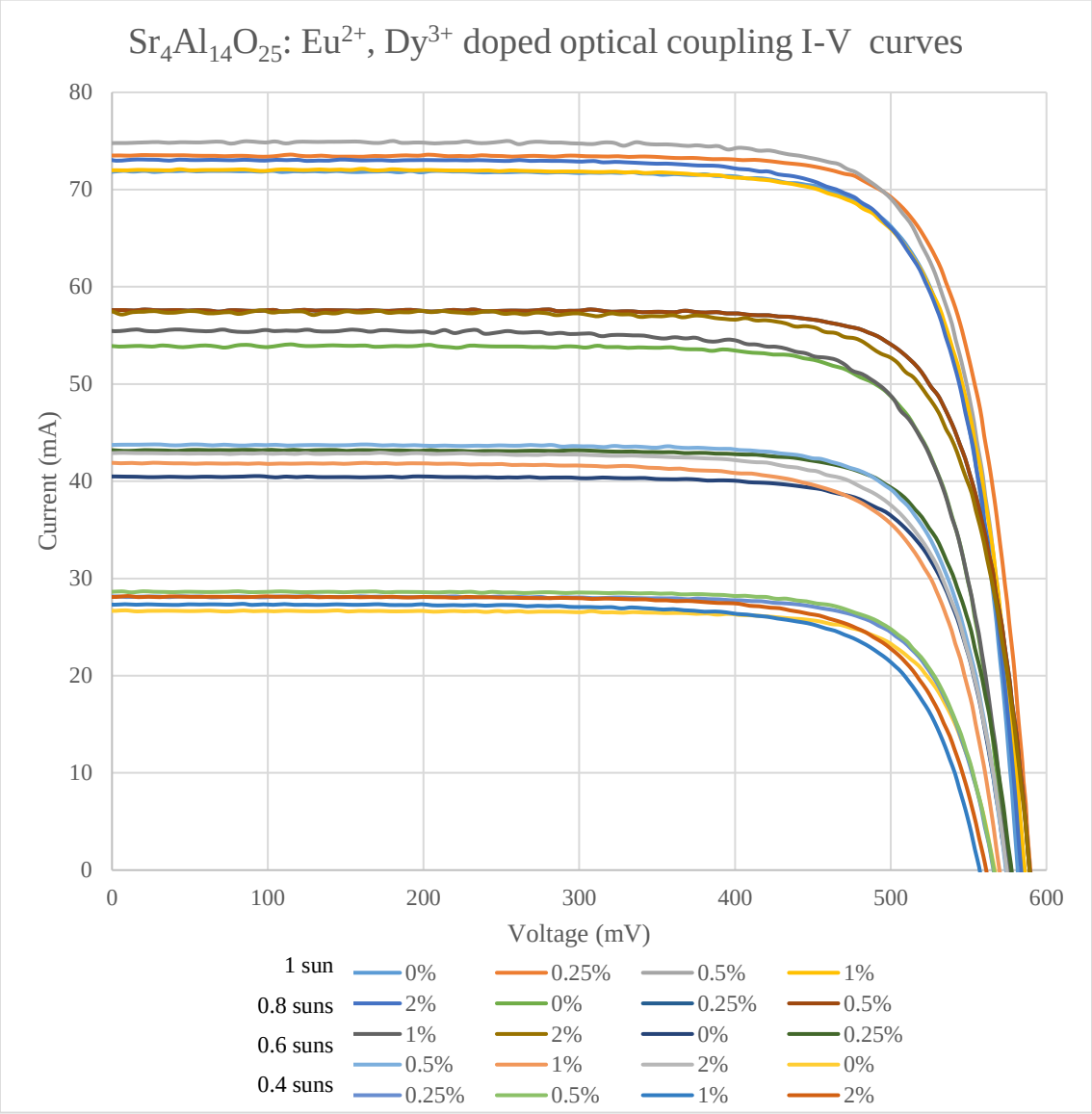

Figure 104: I-V curves of for the $Sr_4Al_{14}O_{25}$: Eu^{2+}, Dy^{3+} doped optical coupling LCPV devices at different solar irradiances.

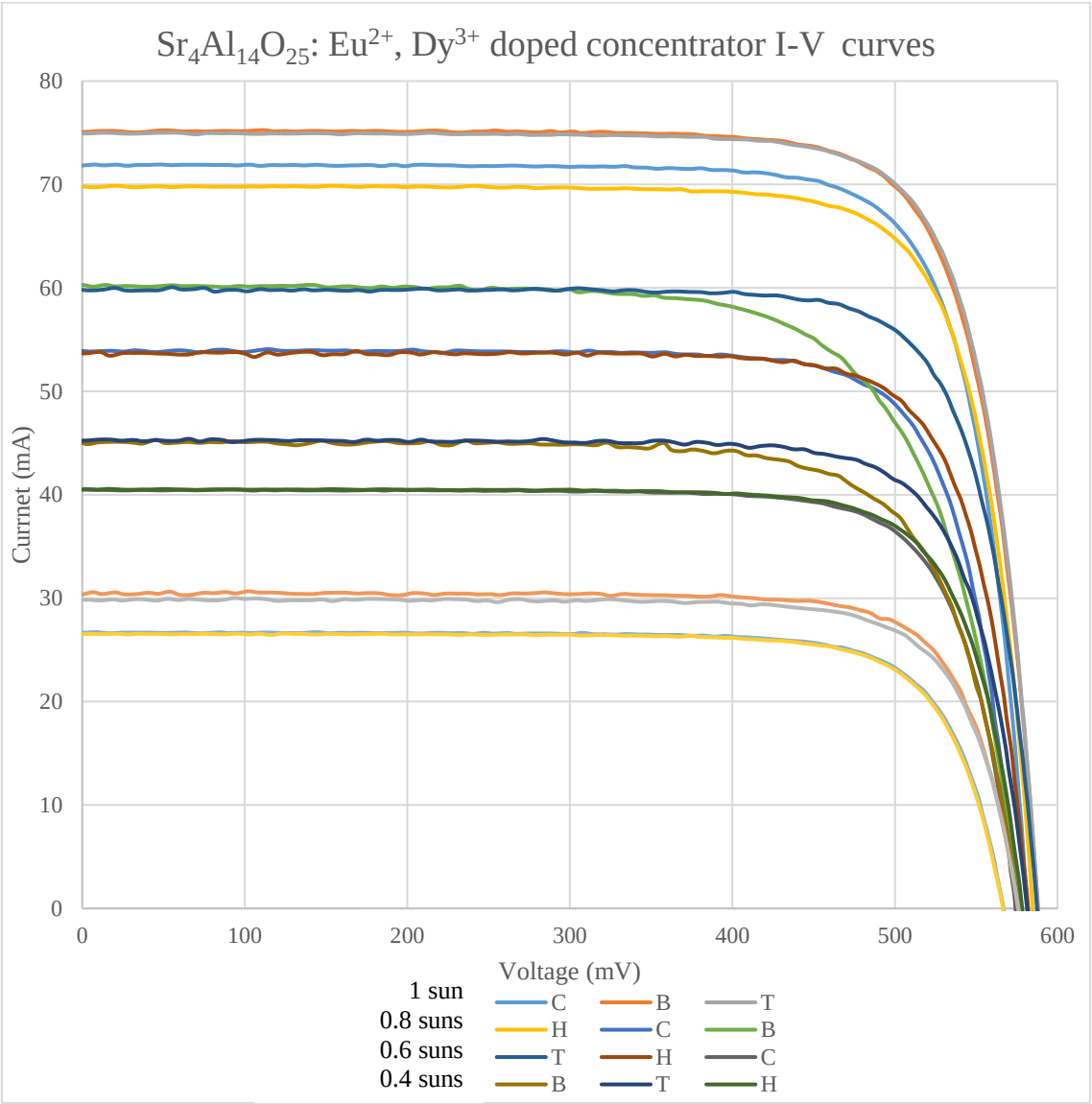

Figure 105: I-V curves of for the $Sr_4Al_{14}O_{25}$: Eu^{2+}, Dy^{3+} doped concentrator LCPV devices at different solar irradiances.

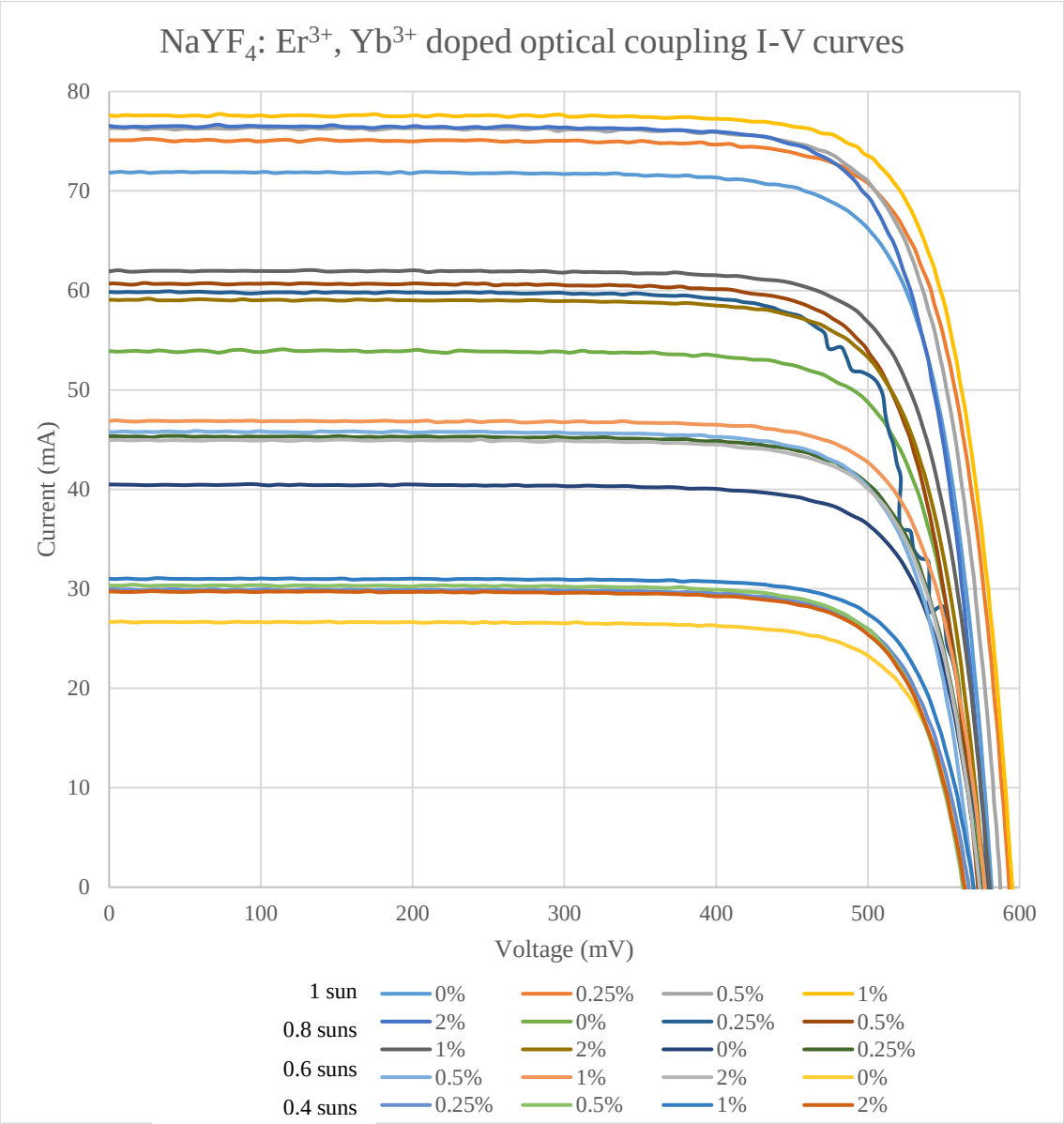

Figure 106: I-V curves of for the $NaYF_4$: Er^{3+}, Yb^{3+} doped optical coupling LCPV devices at different solar irradiances.

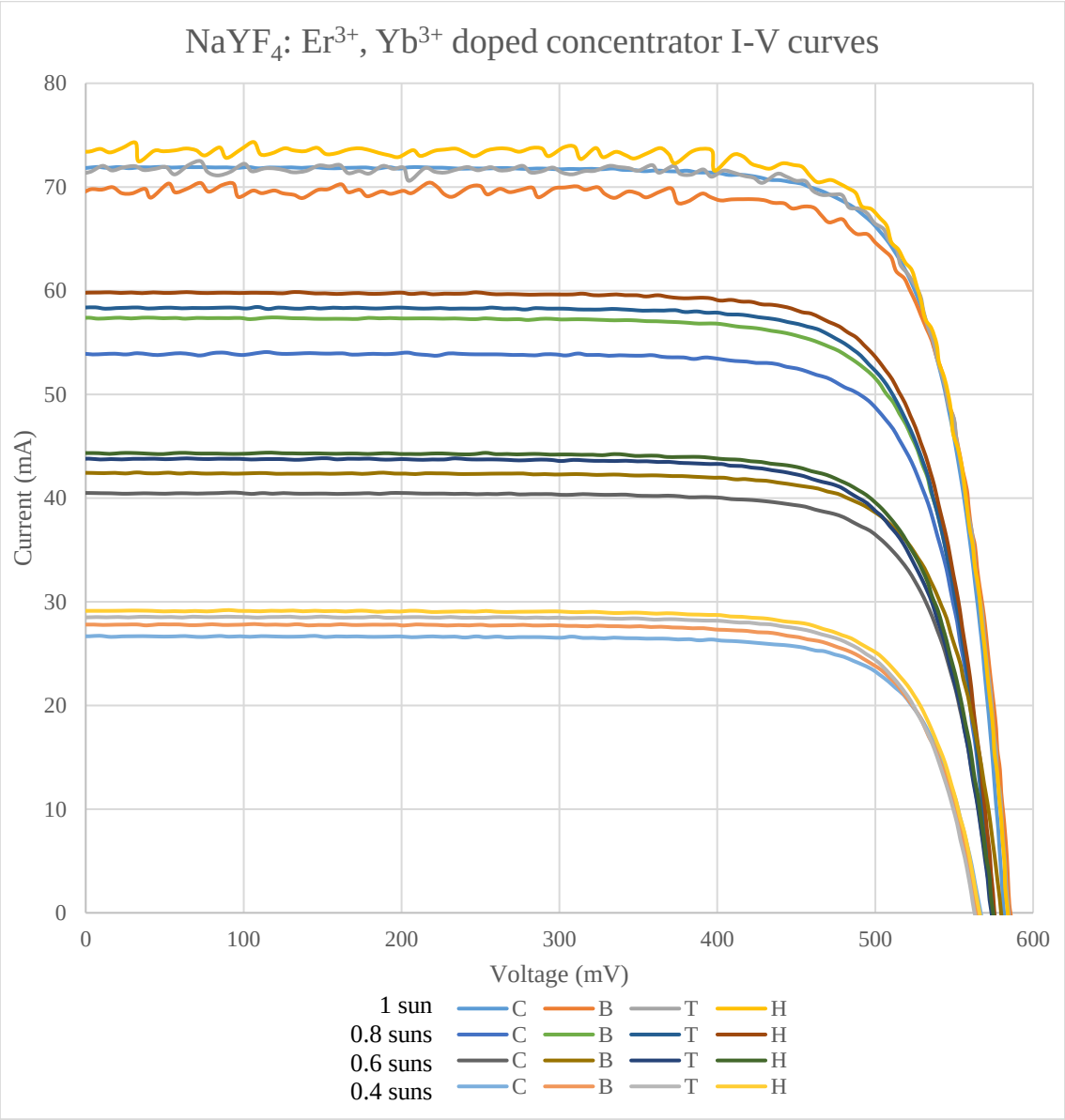

Figure 107: I-V curves of for the $NaYF_4$: Er^{3+}, Yb^{3+} doped concentrator LCPV devices at different solar irradiances.

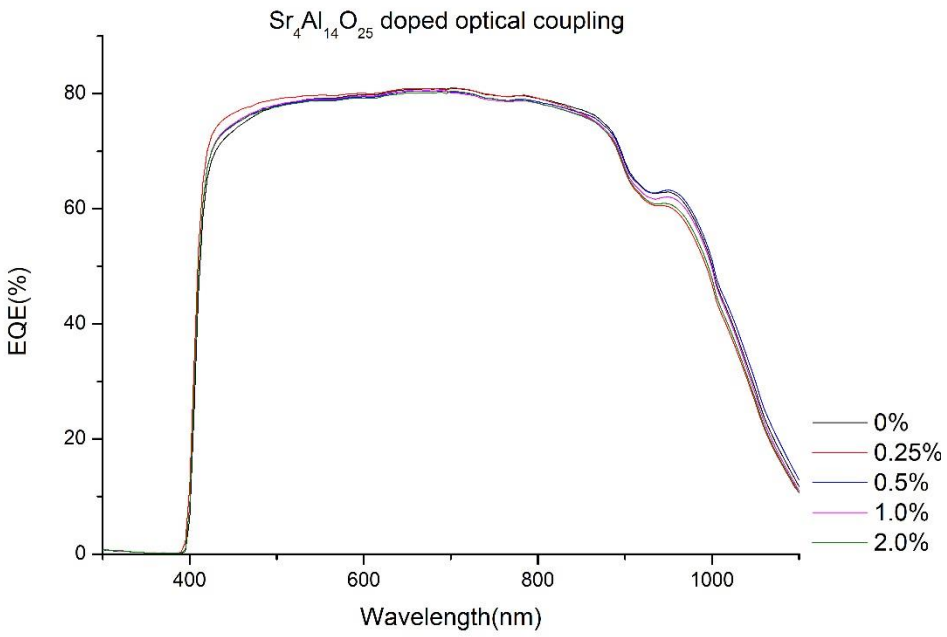

Figure 108: EQE spectra of the $Sr_4Al_{14}O_{25}$: Eu^{2+}, Dy^{3+} doped optical coupling LCPV devices.

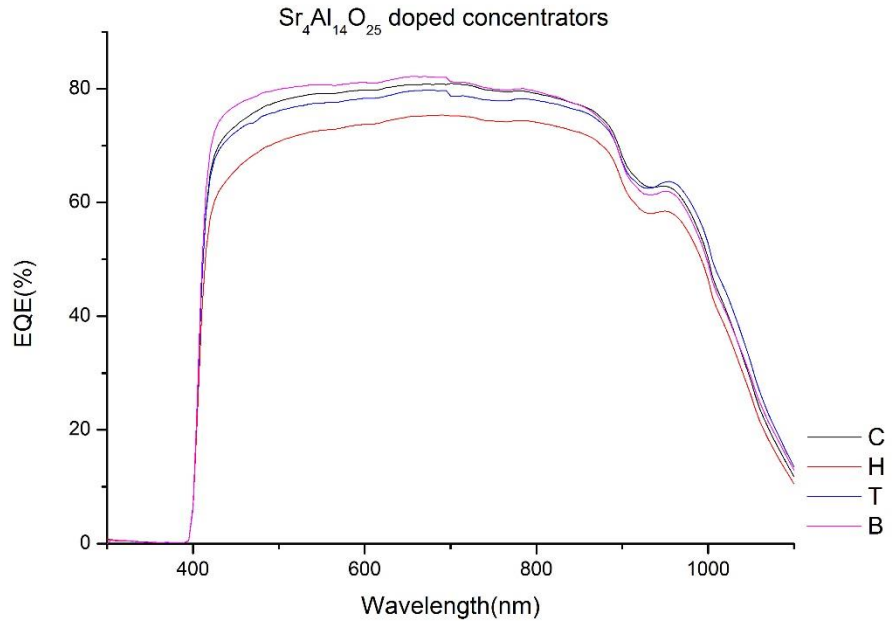

Figure 109: EQE spectra of the $Sr_4Al_{14}O_{25}$: Eu^{2+}, Dy^{3+} doped concentrator LCPV devices.

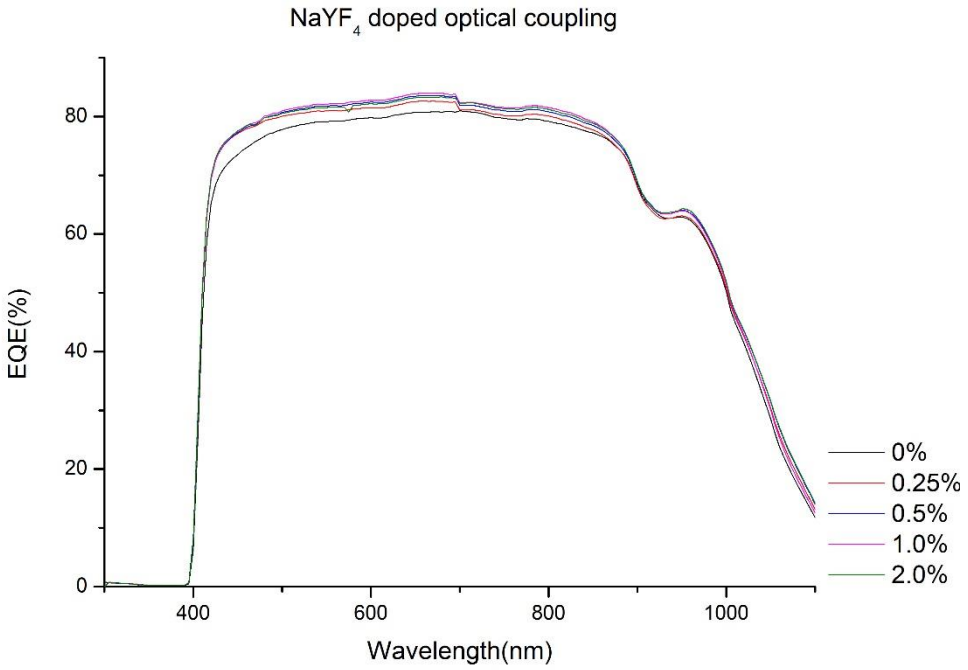

Figure 110: EQE spectra of the $NaYF_4$: Er^{3+}, Yb^{3+} doped optical coupling LCPV devices

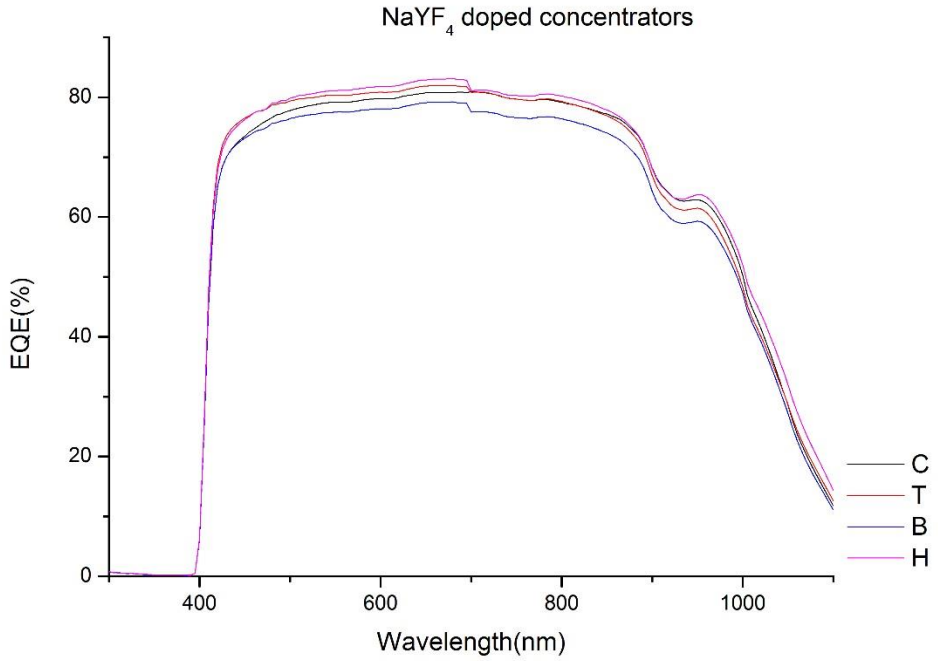

Figure 111: EQE spectra of the $NaYF_4$: Er^{3+}, Yb^{3+} doped concentrator LCPV devices

4.5 Comparing the Effect of Concentrator vs. No Concentrator

It was of interest to consider the difference in performance enhancements between the doped optical coupling LCPV modules and the Sylgard coated non-concentrating PV cells. In order to quantitatively contrast their behaviour, the relative enhancements in PCE and J_{SC} for the non-LCPV cells ($\Delta\eta_2$ and ΔJ_{SC2}) were subtracted from their respective doped optical coupling LCPV values ($\Delta\eta_1$ and ΔJ_{SC1}) for the same rare earth compound weight level, such that:

$$\Delta\,(\Delta\eta) = \Delta\eta_1 - \Delta\eta_2 \qquad (35)$$

$$\Delta\,(\Delta J_{SC}) = \Delta J_{SC1} - \Delta J_{SC2} \qquad (36)$$

The values for Δ (Δη) and Δ (ΔJ_{SC}) are presented numerically in the following Tables 36-43 and demonstrated graphically in Figures 112-115. From the data, it can be seen that in nearly all cases and for both materials the relative PCE and J_{SC} gains are greater, often significantly, for the cells in LCPV modules than in their analogues without a concentrator. At 1 sun of light intensity, the 0.25% and 0.5% w/w doped $Sr_4Al_{14}O_{25}$: Eu^{2+}, Dy^{3+} LCPV devices displayed differences in relative PCE enhancements of 2.8% and 2.1% respectively as compared to the same layers atop PV cells but without concentrators. At the same illumination level for $NaYF_4$: Er^{3+}, Yb^{3+} containing devices, even greater discrepancies were seen; the 0.25%, 0.5% and 1.0% w/w doping levels showed stark 5.9%, 5.7% and 6.3% differences in PCE enhancement with regards to the addition of an SEH concentrator. Furthermore, again these findings were more pronounced at lower irradiances, such that Δ (Δη) rose to a maximum of 5.3% and a remarkable 16.1% for 0.5% w/w $Sr_4Al_{14}O_{25}$: Eu^{2+}, Dy^{3+} and 0.5% w/w $NaYF_4$: Er^{3+}, Yb^{3+} respectively (the latter corresponding to a relative PCE gain of -3.5% without the concentrator and +12.7% with the concentrator). Moreover, the Δ (ΔJ_{SC}) largely followed a similar pattern as described for the Δ (Δη), although while Δ (ΔJ_{SC}) were positive for all irradiance values, Δ (Δη) was negative for 1% w/w $Sr_4Al_{14}O_{25}$: Eu^{2+}, Dy^{3+} at 0.6, 0.8 and 1 suns and 2% w/w $Sr_4Al_{14}O_{25}$: Eu^{2+}, Dy^{3+} at 1 sun only.

There are three proposed physical reasons for this behaviour. Firstly, that the UC process is non-linear, so is more effective at the higher light concentrations in the optical couplings of the LCPV modules which can justify why the $NaYF_4$: Er^{3+}, Yb^{3+} containing layers strongly benefit from the addition of a concentrator. However, this does not explain the phenomena for $Sr_4Al_{14}O_{25}$: Eu^{2+}, Dy^{3+} since no UC is expected to take place and LDS and DC are unaffected by light intensity. This leads to an alternative theory that the increased performance for both compounds in the LCPV devices is because the light which enters the region containing spectral conversion materials comes from a media through which a portion of it will have undergone TIR, instead of straight from the air in the case of the PV cells with coatings. After TIR, the incoming light rays will be at non-normal angles to the optical coupling, with their paths unaffected due to the effectively identical refractive index between the SEH concentrator and Sylgard, resulting in a longer optical path length through the rare earth doped region, and ultimately more spectral conversion events taking place leading to greater PV cell performance enhancement. In addition, this change in the boundary conditions may also have an effect on escape cone and surface scattering losses, with further impact on the measured parameters. And finally, another reason could be that the optical couplings are thinner in the LCPV devices. Although care was taken to ensure otherwise, the pressure of the fixing of a concentrator on top might have made the layers thinner in the LCPV systems, leading to less optical losses occurring and higher device performances.

It also worth comparing the different optimal doping levels for each material in the optical coupling of the LCPV devices and solely coated PV cells. Across irradiance levels, these ratios are essentially unchanged between the concentrator and non-concentrator modules, remaining at 0.25% or 0.5% w/w for the $Sr_4Al_{14}O_{25}$: Eu^{2+}, Dy^{3+} and 1% for the $NaYF_4$: Er^{3+}, Yb^{3+} devices. This is not unreasonable because in predominantly LDS and DC exhibiting materials, the best performing rare earth compound concentration levels should not change with light intensity. However, the differences between the relative PCE and J_{SC} gains with the addition of concentrators did increase significantly for other doping ratios, particularly at the lower irradiance levels for the 1% w/w doped $Sr_4Al_{14}O_{25}$: Eu^{2+}, Dy^{3+} and the 0.25%, 0.5% and 2% w/w doped $NaYF_4$: Er^{3+}, Yb^{3+} containing devices.

Again, abnormal trends are observed for the 1% doped coatings of both materials, but this time in the relationship between the difference in performance enhancement (for devices with and without a concentrator) and illumination level. In addition, the discrepancy is now most apparent at 0.8 suns instead of 0.4 suns for both $Sr_4Al_{14}O_{25}$: Eu^{2+}, Dy^{3+} and $NaYF_4$: Er^{3+}, Yb^{3+}. This shift is likely due to the change in the intensity of light falling on the solar cell arising from the fixing of a concentrating optic, which affects the enhancement from spectral conversion and because LCPV devices showed greater performance increases than those studied in chapter 3, the earlier effects at 0.4 suns are less accounted for. Furthermore, because this anomalous behaviour is repeated for separately prepared 1% doped LCPV samples, it decreases the likelihood that abnormalities in the 1% doped layer coated PV results were due to a systematic error.

To summarise, these results suggest that spectral conversion could be relatively more effective for improving performance in LCPV, especially for BIPV applications where a high power per unit area is desirable. Contrasting the measured EQEs of the devices with and without concentrators further supports this hypothesis, since in the absence of concentrators at 450 nm, the EQE for $Sr_4Al_{14}O_{25}$: Eu^{2+}, Dy^{3+} and $NaYF_4$: Er^{3+}, Yb^{3+} only increased 2.25% and 1.79% respectively. These values are relatively 36% and 55% lower than the highest EQE enhancements for the best $Sr_4Al_{14}O_{25}$: Eu^{2+}, Dy^{3+} and $NaYF_4$: Er^{3+}, Yb^{3+} containing LCPV devices. However, one disadvantage of spectral conversion in LCPV is that no photons of wavelength less than 400 nm are utilised due to the opacity of the SEH concentrators in this region of the spectrum.

Doping (w/w %)	$\Delta\eta_1$ (%)	ΔJ_{SC1} (%)	$\Delta\eta_2$ (%)	ΔJ_{SC2} (%)	Δ ($\Delta\eta$) (%)	Δ (ΔJ_{SC}) (%)
0.25	+4.43	+2.29	+1.65	+1.08	+2.79	+1.21
0.5	+4.22	+4.14	+2.10	+3.36	+2.12	+0.78
1.0	-0.70	+3.19	+1.60	+1.21	-2.07	+1.98
2.0	+0.00	+1.85	+0.59	+1.79	-0.59	+0.06

Table 36: Difference in the relative PCE and J_{SC} gains between the LCPV and non-LCPV devices containing $Sr_4Al_{14}O_{25}$: Eu^{2+}, Dy^{3+}at 1 sun irradiance.

Doping (w/w %)	$\Delta\eta_1$ (%)	ΔJ_{SC1} (%)	$\Delta\eta_2$ (%)	ΔJ_{SC2} (%)	Δ ($\Delta\eta$) (%)	Δ (ΔJ_{SC}) (%)
0.25	+7.33	+7.04	+3.25	+1.22	+4.07	+5.82
0.5	+7.92	+8.75	+5.36	+3.32	+2.56	+5.43
1.0	+0.75	+3.28	+3.54	+1.44	-2.79	+1.84
2.0	+3.99	+6.64	+2.87	+1.69	+1.12	+4.94

Table 37: Difference in the relative PCE and J_{SC} gains between the LCPV and non-LCPV devices containing $Sr_4Al_{14}O_{25}$: Eu^{2+}, Dy^{3+}at 0.8 suns irradiance.

Doping (w/w %)	$\Delta\eta_1$ (%)	ΔJ_{SC1} (%)	$\Delta\eta_2$ (%)	ΔJ_{SC2} (%)	Δ ($\Delta\eta$) (%)	Δ (ΔJ_{SC}) (%)
0.25	+6.75	+6.66	+1.95	+0.26	+4.80	+6.40
0.5	+6.08	+8.02	+3.10	+2.61	+2.97	+5.41
1.0	+0.15	+3.37	+0.43	-0.23	-0.28	+3.60
2.0	+2.54	+5.94	+0.50	+1.44	+2.04	+4.50

Table 38: Difference in the relative PCE and J_{SC} gains between the LCPV and non-LCPV devices containing $Sr_4Al_{14}O_{25}$: Eu^{2+}, Dy^{3+}at 0.6 suns irradiance.

Doping (w/w %)	$\Delta\eta_1$ (%)	ΔJ_{SC1} (%)	$\Delta\eta_2$ (%)	ΔJ_{SC2} (%)	Δ ($\Delta\eta$) (%)	Δ (ΔJ_{SC}) (%)
0.25	+5.59	+5.52	+1.31	+0.17	+4.28	+5.35
0.5	+5.89	+7.34	+0.55	+1.39	+5.34	+5.95
1.0	+0.00	+2.95	-4.71	-0.50	+4.71	+3.45
2.0	+0.92	+5.38	+0.27	+0.83	+0.65	+4.55

Table 39: Difference in the relative PCE and J_{SC} gains between the LCPV and non-LCPV devices containing $Sr_4Al_{14}O_{25}$: Eu^{2+}, Dy^{3+}at 0.4 suns irradiance.

Doping (w/w %)	$\Delta\eta_1$ (%)	ΔJ_{SC1} (%)	$\Delta\eta_2$ (%)	ΔJ_{SC2} (%)	Δ ($\Delta\eta$) (%)	Δ (ΔJ_{SC}) (%)
0.25	+6.70	+4.54	+0.78	+1.28	+5.93	+3.26
0.5	+6.93	+6.34	+1.28	+0.59	+5.65	+5.76
1.0	+11.10	+8.08	+4.83	+1.76	+6.27	+6.32
2.0	+5.25	+3.70	+3.12	+1.89	+2.14	+1.81

Table 40: Difference in the relative PCE and J_{SC} gains between the LCPV and non-LCPV devices containing $NaYF_4$: Er^{3+}, Yb^{3+} at 1 sun irradiance.

Doping (w/w %)	$\Delta\eta_1$ (%)	ΔJ_{SC1} (%)	$\Delta\eta_2$ (%)	ΔJ_{SC2} (%)	Δ ($\Delta\eta$) (%)	Δ (ΔJ_{SC}) (%)
0.25	+9.24	+11.13	+3.60	+2.94	+5.64	+8.19
0.5	+5.47	+12.69	+0.47	+1.03	+5.00	+11.66
1.0	+15.53	+14.98	+4.86	+2.18	+10.67	+12.81
2.0	+8.44	+9.68	+2.57	+0.74	+5.87	+8.94

Table 41: Difference in the relative PCE and J_{SC} gains between the LCPV and non-LCPV devices containing $NaYF_4$: Er^{3+}, Yb^{3+} at 0.8 suns irradiance.

Doping (w/w %)	$\Delta\eta_1$ (%)	ΔJ_{SC1} (%)	$\Delta\eta_2$ (%)	ΔJ_{SC2} (%)	Δ ($\Delta\eta$) (%)	Δ (ΔJ_{SC}) (%)
0.25	+10.05	+12.00	+0.05	+0.34	+9.99	+11.66
0.5	+10.46	+13.08	-2.23	-2.32	+12.69	+15.39
1.0	+15.46	+15.74	+2.06	-1.76	+13.40	+17.51
2.0	+8.94	+11.00	-2.12	-1.08	+11.05	+12.09

Table 42: Difference in the relative PCE and J_{SC} gains between the LCPV and non-LCPV devices containing $NaYF_4$: Er^{3+}, Yb^{3+} at 0.6 suns irradiance.

Doping (w/w %)	$\Delta\eta_1$ (%)	ΔJ_{SC1} (%)	$\Delta\eta_2$ (%)	ΔJ_{SC2} (%)	Δ ($\Delta\eta$) (%)	Δ (ΔJ_{SC}) (%)
0.25	+11.99	+12.30	-1.71	+1.32	+13.69	+10.98
0.5	+12.67	+13.76	-3.46	-0.71	+16.12	+14.47
1.0	+17.67	+16.28	+3.46	-0.04	+14.21	+16.32
2.0	+10.68	+11.47	-1.69	-0.38	+12.37	+11.85

Table 43: Difference in the relative PCE and J_{SC} gains between the LCPV and non-LCPV devices containing $NaYF_4$: Er^{3+}, Yb^{3+} at 0.4 suns irradiance.

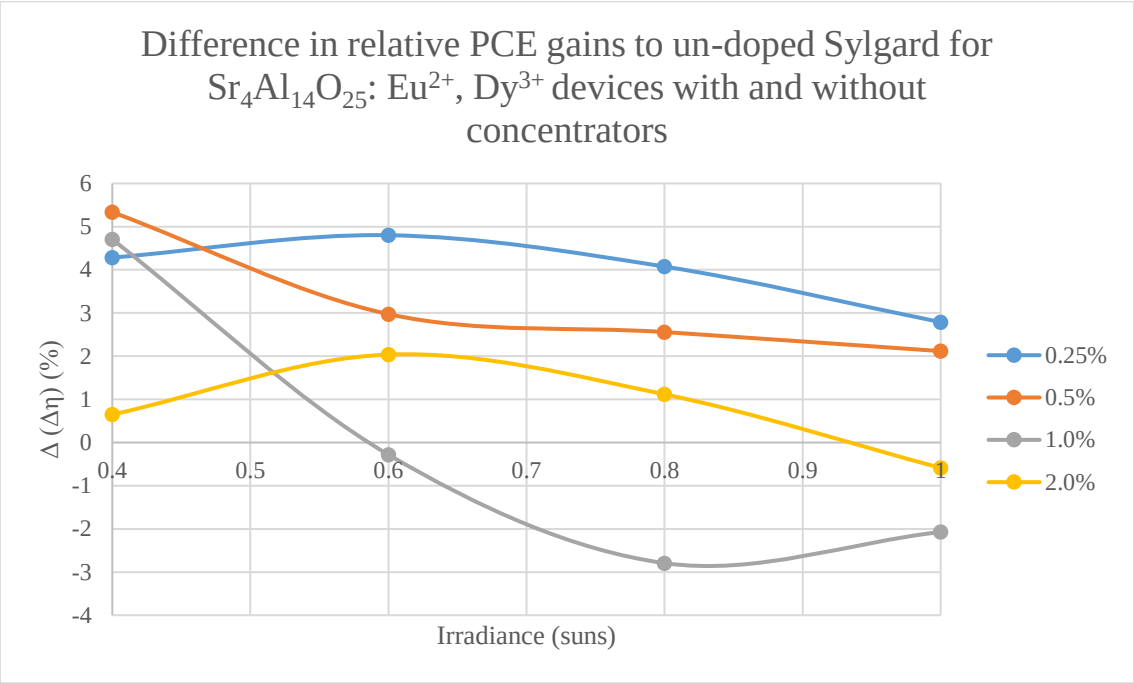

Figure 112: The difference in relative PCE improvements as compared to un-doped Sylgard for LCPV modules with and coated PV cells without a concentrator for $Sr_4Al_{14}O_{25}$: Eu^{2+}, Dy^{3+} doping at different levels.

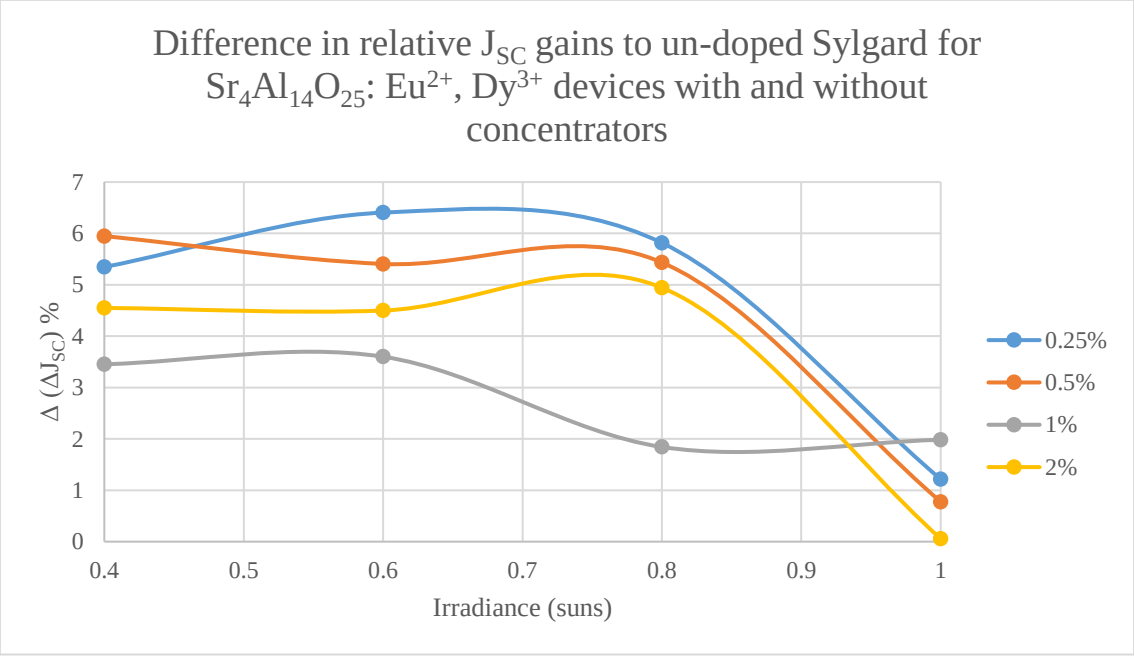

Figure 113: The difference in relative J_{SC} improvements as compared to un-doped Sylgard for LCPV modules with and coated PV cells without a concentrator for $Sr_4Al_{14}O_{25}$: Eu^{2+}, Dy^{3+} doping at different levels.

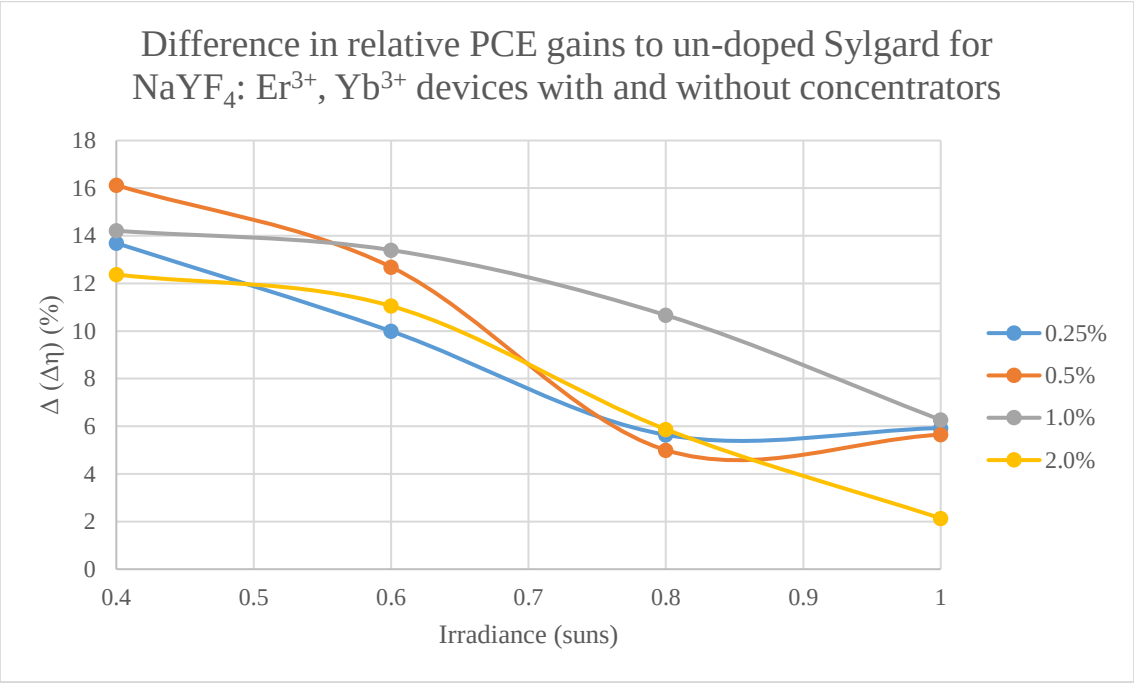

Figure 114: The difference in relative PCE improvements as compared to un-doped Sylgard for LCPV modules with and coated PV cells without a concentrator for $NaYF_4$: Er^{3+}, Yb^{3+} doping at different levels.

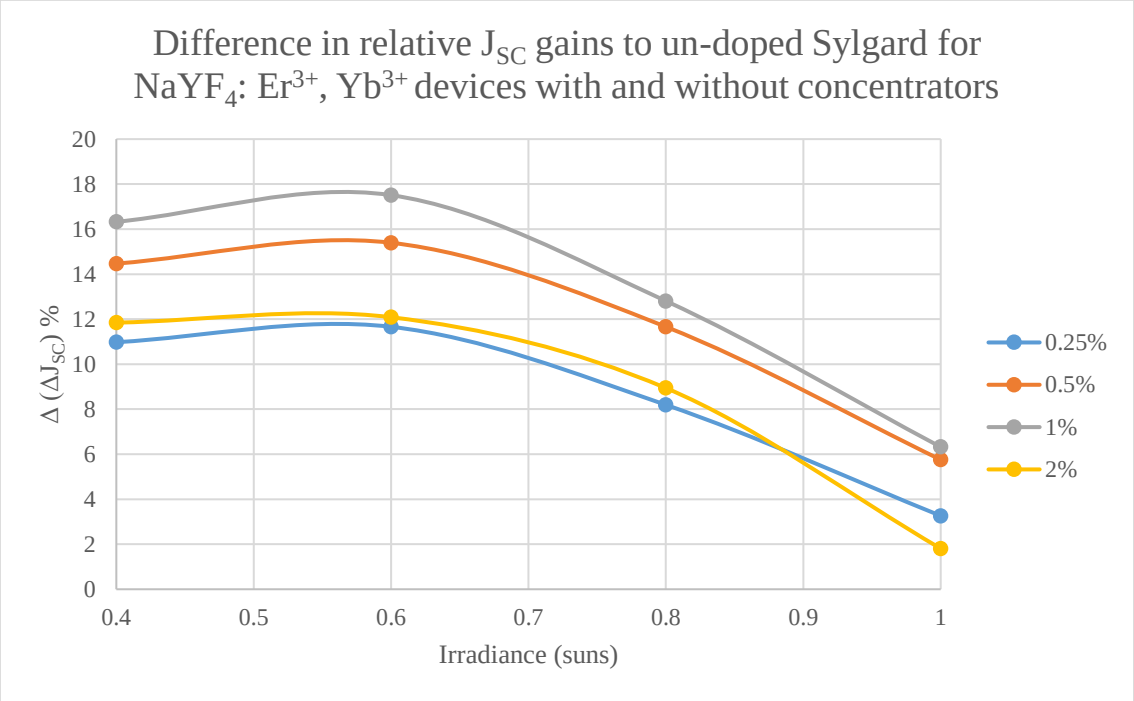

Figure 115: The difference in relative J_{SC} improvements as compared to un-doped Sylgard for LCPV modules with and coated PV cells without a concentrator for $NaYF_4$: Er^{3+}, Yb^{3+} doping at different levels.

4.6 Effect of the Angle of Incidence

The investigations so far have been testing devices under illumination which is incident perpendicular to the surface of the concentrator (or at an angle of incidence of 0°). However, for realistic situations of LCPV deployment, and especially in BIPV, it is important to consider the case when the incoming radiation is at a non-normal angle of incidence. This is because over the course of the day in the absence of a solar tracker, sunlight will typically be striking the concentrator at various angles of incidence from 0 to 90°. Also, depending on the local climate conditions, diffuse radiation could make up a large amount of the total light received, so how effectively the LCPV module responds to high angle of incidence light can have a strong effect on the energy generation yield.

As shown in the earlier Figure 88, when optimising the SEH design parameters Sellami et al studied the optical efficiency of the concentrator over a range of acceptance angles from both theoretical calculations and experimental observations. They found an advantage of the SEH design was its wide acceptance angles, so it was of interest to verify this behaviour was replicated following the addition of rare earth containing compounds. The necessity to consider off-normal angles of incidence is further amplified in this work, since the behaviour of the spectral conversion materials will be affected by the change in optical path length that occurs at varied angle of incidence. To quantitatively investigate this, an angle adjustable inclined plane was placed on the stage under the simulator to which the previously fabricated LCPV devices were attached. By locating the solar cells and concentrators on an inclined surface (attaching with Blu Tack), the collimated illumination would now be at an angle of incidence equal to the angle of inclination of the plane from the horizontal (see Figure 116). The devices could then be connected to the I-V tracer to provide electrical characterisation at a range of solar angles of incidence.

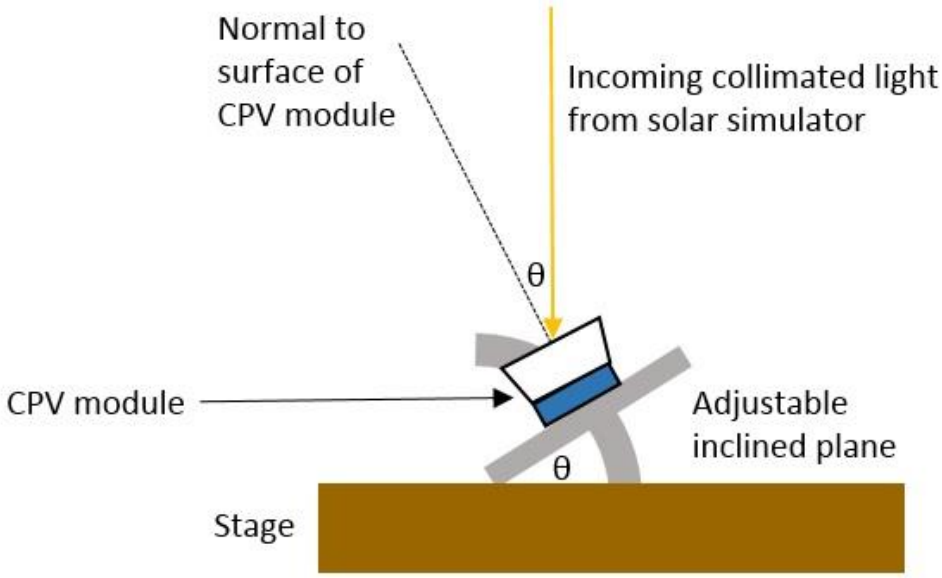

Figure 116: Diagram to show how the adjustable inclined plane can be used to create an effective angle of incidence (θ) on an LCPV module when placed under the solar simulator.

The pitch of the plane was adjusted from 10° to 80 in 10° intervals, with PCE and J_{SC} measurements taken at each inclination for an irradiance of 1 sun only (the same constant light intensity that was used for the earlier '1 sun' characterisations for 0° angle of incidence). These values are presented numerically in the Tables 44-59 and graphically in Figures 117-120. It can be seen from the data that the enhanced electrical performance also occurs at higher angles of incidence. In general, larger angles of incidence correspond to greater relative PCE and J_{SC} improvements. It can be seen from Figures 121 and 123 that from 0° to 20° for both compounds and most configurations, the relative PCE gains rise to a peak of +24.0% for the 1% w/w optical coupling doped $NaYF_4$: Er^{3+}, Yb^{3+} and +23.0% for the top doped concentrator $Sr_4Al_{14}O_{25}$: Eu^{2+}, Dy^{3+} device. As the angle of incidence is further increased from 30° to 60°, the relative PCE improvements, though positive, display a quasi-sinusoidal behaviour over this range. For example, the top doped concentrator $Sr_4Al_{14}O_{25}$: Eu^{2+}, Dy^{3+} exhibited a local minimum at 30° where a 16.8% relative PCE increase is observed (down from 23.0% at 20°), which subsequently rose and fell in turn to local maxima and minima at 40° and 50° with PCE enhancements of 18.9% and 15.3% respectively. Similar patterns were observed across a range of doping configurations for both

rare earth compounds. Then finally at high angles of incidence (70° and 80°), there is another sudden jump in the relative PCE enhancement for most devices; 8.1% to 41.7% and 19.3% to 69.5% between 70° and 80° for the top and bottom doped $NaYF_4$: Er^{3+}, Yb^{3+} concentrators respectively. Figures 122 and 124 show that the same behaviour was recorded for the J_{SC} measurements.

In terms of the underlying reasons for these observations, it is proposed that the change in optical path length could be responsible for these J_{SC} and PCE enhancements. As the light travels further through the concentrator or doped optical coupling layer, it increases the chance of absorption and re-emission by the rare earth compound particles, hence a greater amount of additional current is produced. However, the sinusoidal profiles of the J_{SC} and PCE enhancements indicate that the situation is not simply this straightforward. The presence of minima and maxima suggests that there is a trade-off between increasing the amount of spectral conversion taking place and other factors that may depend on angle of incidence such as parasitic absorption by the polyurethane concentrator medium, surface reflectance and optical losses in the SEH through non-occurrence of TIR. The sharp increase in performance enhancement between 70° and 80° could demonstrate this and further understanding of the paths of rays within the doped concentrators will be developed in chapter 6. Nevertheless, these preliminary results imply that this technique of rare earth compound addition can successfully be used for enhancing the performance of LCPV modules when exposed to sunlight of off-normal angles of incidence, which is vital for real world BIPV applications.

Doped optical coupling (w/w %)	η (%)	J_{SC} (mA/cm^2)	Δη (%)	Δ J_{SC} (%)
0.0	7.940	59.612	-	-
0.25	8.874	65.744	+11.76	+10.29
0.5	8.959	66.812	+12.83	+12.08
1.0	8.453	64.030	+6.46	+7.41
2.0	8.674	66.314	+9.24	+11.24
Doped concentrator (w/w %)	**η (%)**	**J_{SC} (mA/cm^2)**	**Δη (%)**	**Δ J_{SC} (%)**
0.1 (Homogenous)	8.084	60.176	+1.81	+0.95
0.1 (Top)	9.389	69.158	+18.25	+16.01
0.1 (Bottom)	9.226	70.822	+16.20	+18.80

Table 44: PCE and J_{SC} data for $Sr_4Al_{14}O_{25}$: Eu^{2+}, Dy^{3+} doped LCPV devices at 10° angle of incidence.

Doped optical coupling (w/w %)	η (%)	J_{SC} (mA/cm^2)	Δη (%)	Δ J_{SC} (%)
0.0	7.298	54.509	-	-
0.25	8.234	61.462	+12.83	+12.76
0.5	8.067	60.910	+10.54	+11.74
1.0	7.938	61.930	+8.77	+13.61
2.0	8.001	61.762	+9.63	+13.31
Doped concentrator (w/w %)	**η (%)**	**J_{SC} (mA/cm^2)**	**Δη (%)**	**Δ J_{SC} (%)**
0.1 (Homogenous)	7.768	57.891	+6.44	+6.20
0.1 (Top)	8.978	66.270	+23.02	+21.58
0.1 (Bottom)	8.874	66.432	+21.59	+21.87

Table 45: PCE and J_{SC} data for $Sr_4Al_{14}O_{25}$: Eu^{2+}, Dy^{3+} doped LCPV devices at 20° angle of incidence.

Doped optical coupling (w/w %)	η (%)	J_{SC} (mA/cm^2)	Δη (%)	Δ J_{SC} (%)
0.0	6.761	49.991	-	-
0.25	7.684	57.527	+13.65	+15.07
0.5	6.929	52.655	+2.48	+5.33
1.0	6.911	54.482	+2.22	+8.98
2.0	6.991	53.836	+3.40	+7.69
Doped concentrator (w/w %)	**η (%)**	**J_{SC} (mA/cm^2)**	**Δη (%)**	**Δ J_{SC} (%)**
0.1 (Homogenous)	6.664	49.833	-1.43	-0.32
0.1 (Top)	7.895	58.372	+16.77	+16.77
0.1 (Bottom)	7.873	59.028	+16.45	+18.08

Table 46: PCE and J_{SC} data for $Sr_4Al_{14}O_{25}$: Eu^{2+}, Dy^{3+} doped LCPV devices at 30° angle of incidence.

Doped optical coupling (w/w %)	η (%)	J_{SC} (mA/cm^2)	Δη (%)	Δ J_{SC} (%)
0.0	5.280	40.759	-	-
0.25	5.890	44.490	+11.55	+9.15
0.5	5.924	45.139	+12.20	+10.75
1.0	6.162	48.297	+16.70	+18.49
2.0	6.432	50.245	+21.82	+23.27
Doped concentrator (w/w %)	**η (%)**	**J_{SC} (mA/cm^2)**	**Δη (%)**	**Δ J_{SC} (%)**
0.1 (Homogenous)	5.645	42.347	+6.91	+3.90
0.1 (Top)	6.280	47.205	+18.94	+15.81
0.1 (Bottom)	6.682	50.095	+26.55	+22.91

Table 47: PCE and J_{SC} data for $Sr_4Al_{14}O_{25}$: Eu^{2+}, Dy^{3+} doped LCPV devices at 40° angle of incidence.

Doped optical coupling (w/w %)	η (%)	J_{SC} (mA/cm^2)	Δη (%)	Δ J_{SC} (%)
0.0	4.137	32.389	-	-
0.25	5.101	41.050	+23.30	+26.74
0.5	4.552	34.625	+10.03	+6.90
1.0	4.705	36.854	+13.73	+13.79
2.0	4.905	38.781	+18.56	+19.74
Doped concentrator (w/w %)	**η (%)**	**J_{SC} (mA/cm^2)**	**Δη (%)**	**Δ J_{SC} (%)**
0.1 (Homogenous)	4.500	34.401	+8.77	+6.21
0.1 (Top)	4.772	35.988	+15.35	+11.11
0.1 (Bottom)	5.375	41.088	+29.93	+26.86

Table 48: PCE and J_{SC} data for $Sr_4Al_{14}O_{25}$: Eu^{2+}, Dy^{3+} doped LCPV devices at 50° angle of incidence.

Doped optical coupling (w/w %)	η (%)	J_{SC} (mA/cm^2)	Δη (%)	Δ J_{SC} (%)
0.0	2.571	20.205	-	-
0.25	3.679	28.489	+43.10	+41.00
0.5	2.745	21.891	+6.77	+8.34
1.0	3.171	26.636	+23.34	+31.83
2.0	3.265	26.661	+26.99	+31.95
Doped concentrator (w/w %)	**η (%)**	**J_{SC} (mA/cm^2)**	**Δη (%)**	**Δ J_{SC} (%)**
0.1 (Homogenous)	2.556	20.281	-0.58	+0.38
0.1 (Top)	3.128	24.322	+21.66	+20.38
0.1 (Bottom)	3.472	27.151	+35.04	+34.38

Table 49: PCE and J_{SC} data for $Sr_4Al_{14}O_{25}$: Eu^{2+}, Dy^{3+} doped LCPV devices at 60° angle of incidence.

Doped optical coupling (w/w %)	η (%)	J_{SC} (mA/cm^2)	Δη (%)	Δ J_{SC} (%)
0.0	1.536	12.434	-	-
0.25	1.540	13.500	+0.26	+8.57
0.5	1.788	14.440	+16.41	+16.13
1.0	2.051	17.944	+33.53	+44.31
2.0	1.958	16.249	+22.47	+30.62
Doped concentrator (w/w %)	**η (%)**	**J_{SC} (mA/cm^2)**	**Δη (%)**	**Δ J_{SC} (%)**
0.1 (Homogenous)	1.252	10.422	-18.49	-16.18
0.1 (Top)	1.886	15.183	+22.79	+22.11
0.1 (Bottom)	2.202	17.650	+43.36	+41.95

Table 50: PCE and J_{SC} data for $Sr_4Al_{14}O_{25}$: Eu^{2+}, Dy^{3+} doped LCPV devices at 70° angle of incidence.

Doped optical coupling (w/w %)	η (%)	J_{SC} (mA/cm^2)	Δη (%)	Δ J_{SC} (%)
0.0	0.561	4.880	-	-
0.25	0.715	7.330	+27.45	+50.24
0.5	0.649	6.151	+15.69	+26.05
1.0	1.013	8.524	+80.57	+74.67
2.0	0.935	8.099	+66.67	+65.96
Doped concentrator (w/w %)	**η (%)**	**J_{SC} (mA/cm^2)**	**Δη (%)**	**Δ J_{SC} (%)**
0.1 (Homogenous)	0.672	5.844	+19.79	+19.75
0.1 (Top)	0.698	6.150	+24.42	+26.02
0.1 (Bottom)	1.022	8.649	+82.17	+77.23

Table 51: PCE and J_{SC} data for $Sr_4Al_{14}O_{25}$: Eu^{2+}, Dy^{3+} doped LCPV devices at 80° angle of incidence.

Doped optical coupling (w/w %)	η (%)	J_{SC} (mA/cm^2)	Δη (%)	Δ J_{SC} (%)
0.0	7.940	59.612	-	-
0.25	9.398	70.068	+18.36	+17.54
0.5	9.558	71.858	+20.38	+20.54
1.0	9.751	71.920	+22.81	+20.65
2.0	9.314	70.258	+17.30	+17.86
Doped concentrator (w/w %)	**η (%)**	**J_{SC} (mA/cm^2)**	**Δη (%)**	**Δ J_{SC} (%)**
0.1 (Homogenous)	9.108	68.413	+14.71	+14.76
0.1 (Top)	8.647	64.967	+8.90	+8.98
0.1 (Bottom)	8.861	66.311	+11.60	+11.24

Table 52: PCE and J_{SC} data for $NaYF_4$: Er^{3+}, Yb^{3+} doped LCPV devices at 10° angle of incidence.

Doped optical coupling (w/w %)	η (%)	J_{SC} (mA/cm^2)	Δη (%)	Δ J_{SC} (%)
0.0	7.298	54.509	-	-
0.25	8.561	64.540	+17.31	+18.40
0.5	8.436	63.939	+15.59	+17.30
1.0	9.046	67.426	+23.95	+23.70
2.0	8.338	62.878	+14.25	+15.35
Doped concentrator (w/w %)	**η (%)**	**J_{SC} (mA/cm^2)**	**Δη (%)**	**Δ J_{SC} (%)**
0.1 (Homogenous)	8.450	63.876	+15.79	+17.18
0.1 (Top)	8.079	61.696	+10.70	+13.18
0.1 (Bottom)	8.008	60.740	+9.73	+11.43

Table 53: PCE and J_{SC} data for $NaYF_4$: Er^{3+}, Yb^{3+} doped LCPV devices at 20° angle of incidence.

Doped optical coupling (w/w %)	η (%)	J_{SC} (mA/cm^2)	Δη (%)	Δ J_{SC} (%)
0.0	6.761	49.991	-	-
0.25	7.368	56.023	+8.98	+12.07
0.5	8.063	61.700	+19.26	+23.42
1.0	7.952	59.322	+17.62	+18.67
2.0	7.483	56.535	+10.68	+13.09
Doped concentrator (w/w %)	**η (%)**	**J_{SC} (mA/cm^2)**	**Δη (%)**	**Δ J_{SC} (%)**
0.1 (Homogenous)	7.145	54.511	+5.68	+9.04
0.1 (Top)	7.223	55.607	+6.83	+11.23
0.1 (Bottom)	7.383	56.248	+9.20	+12.52

Table 54: PCE and J_{SC} data for $NaYF_4$: Er^{3+}, Yb^{3+} doped LCPV devices at 30° angle of incidence.

Doped optical coupling (w/w %)	η (%)	J_{SC} (mA/cm^2)	Δη (%)	Δ J_{SC} (%)
0.0	5.280	40.759	-	-
0.25	6.185	47.319	+17.14	+16.09
0.5	6.730	51.150	+27.46	+25.49
1.0	6.866	51.536	+30.04	+26.44
2.0	6.118	46.602	+15.87	+14.34
Doped concentrator (w/w %)	**η (%)**	**J_{SC} (mA/cm^2)**	**Δη (%)**	**Δ J_{SC} (%)**
0.1 (Homogenous)	6.245	47.712	+18.28	+17.06
0.1 (Top)	5.885	45.787	+11.46	+12.34
0.1 (Bottom)	5.838	44.800	+10.57	+9.91

Table 55: PCE and J_{SC} data for $NaYF_4$: Er^{3+}, Yb^{3+} doped LCPV devices at 40° angle of incidence.

Doped optical coupling (w/w %)	η (%)	J_{SC} (mA/cm^2)	Δη (%)	Δ J_{SC} (%)
0.0	4.137	32.389	-	-
0.25	5.044	38.941	+21.92	+20.23
0.5	5.481	42.646	+32.49	+31.67
1.0	5.543	42.236	+33.99	+30.40
2.0	4.874	37.503	+17.81	+15.79
Doped concentrator (w/w %)	**η (%)**	**J_{SC} (mA/cm^2)**	**Δη (%)**	**Δ J_{SC} (%)**
0.1 (Homogenous)	4.971	38.610	+20.16	+19.21
0.1 (Top)	4.848	38.003	+17.19	+17.33
0.1 (Bottom)	4.940	37.917	+19.41	+17.07

Table 56: PCE and J_{SC} data for $NaYF_4$: Er^{3+}, Yb^{3+} doped LCPV devices at 50° angle of incidence.

Doped optical coupling (w/w %)	η (%)	J_{SC} (mA/cm^2)	Δη (%)	Δ J_{SC} (%)
0.0	2.571	20.205	-	-
0.25	3.026	24.111	+17.70	+19.33
0.5	3.577	28.502	+39.13	+41.06
1.0	3.891	30.564	+51.34	+51.27
2.0	2.900	22.970	+12.80	+13.68
Doped concentrator (w/w %)	**η (%)**	**J_{SC} (mA/cm^2)**	**Δη (%)**	**Δ J_{SC} (%)**
0.1 (Homogenous)	3.188	25.365	+24.00	+25.54
0.1 (Top)	3.160	25.308	+22.91	+25.26
0.1 (Bottom)	3.527	27.446	+37.18	+35.84

Table 57: PCE and J_{SC} data for $NaYF_4$: Er^{3+}, Yb^{3+} doped LCPV devices at 60° angle of incidence.

Doped optical coupling (w/w %)	η (%)	J_{SC} (mA/cm^2)	Δη (%)	Δ J_{SC} (%)
0.0	1.536	12.434	-	-
0.25	1.739	14.290	+13.22	+14.93
0.5	2.042	16.652	+32.94	+33.92
1.0	1.948	15.863	+26.83	+27.58
2.0	1.669	13.850	+8.66	+11.39
Doped concentrator (w/w %)	**η (%)**	**J_{SC} (mA/cm^2)**	**Δη (%)**	**Δ J_{SC} (%)**
0.1 (Homogenous)	1.791	14.833	+16.60	+19.29
0.1 (Top)	1.661	13.879	+8.14	+11.62
0.1 (Bottom)	1.832	14.781	+19.27	+18.88

Table 58: PCE and J_{SC} data for $NaYF_4$: Er^{3+}, Yb^{3+} doped LCPV devices at 70° angle of incidence.

Doped optical coupling (w/w %)	η (%)	J_{SC} (mA/cm^2)	Δη (%)	Δ J_{SC} (%)
0.0	0.561	4.880	-	-
0.25	0.697	6.170	+24.24	+26.43
0.5	0.712	6.252	+26.92	+28.11
1.0	0.779	6.750	+38.86	+38.32
2.0	0.609	5.352	+8.56	+9.67
Doped concentrator (w/w %)	**η (%)**	**J_{SC} (mA/cm^2)**	**Δη (%)**	**Δ J_{SC} (%)**
0.1 (Homogenous)	0.803	6.490	+43.14	+32.99
0.1 (Top)	0.795	7.047	+41.71	+44.41
0.1 (Bottom)	0.951	8.075	+69.52	+65.47

Table 59: PCE and J_{SC} data for $NaYF_4$: Er^{3+}, Yb^{3+} doped LCPV devices at 80° angle of incidence.

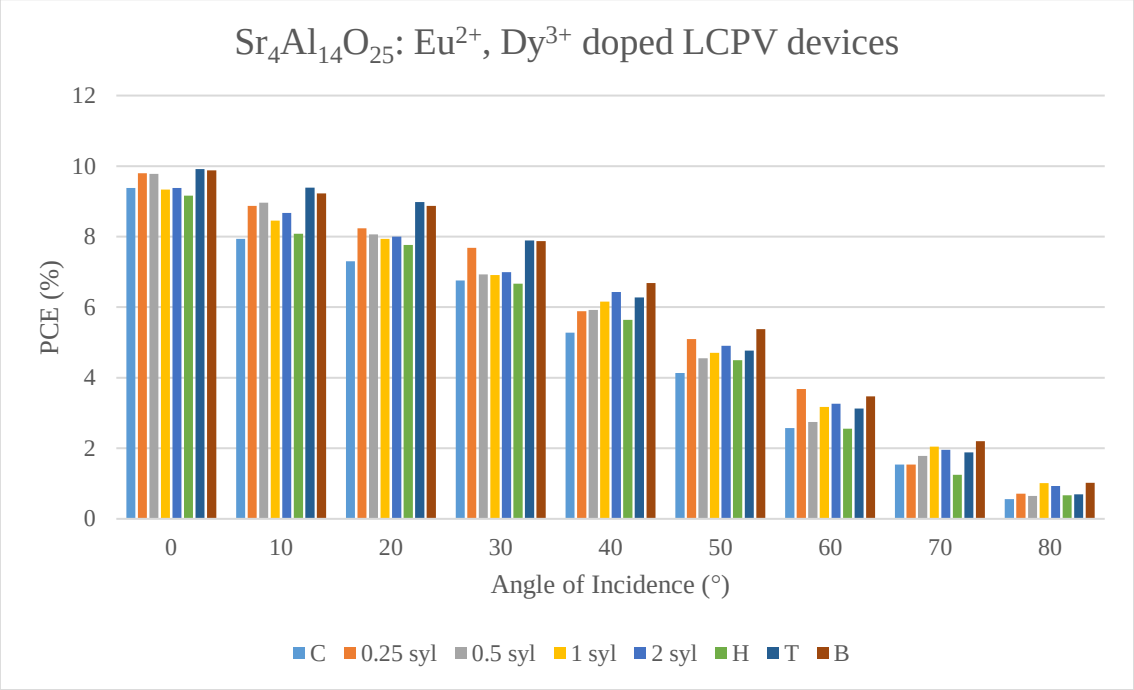

Figure 117: The PCE of the $Sr_4Al_{14}O_{25}$: Eu^{2+}, Dy^{3+} doped LCPV devices under 1 sun illumination at angles of incidence from 0° to 80°.

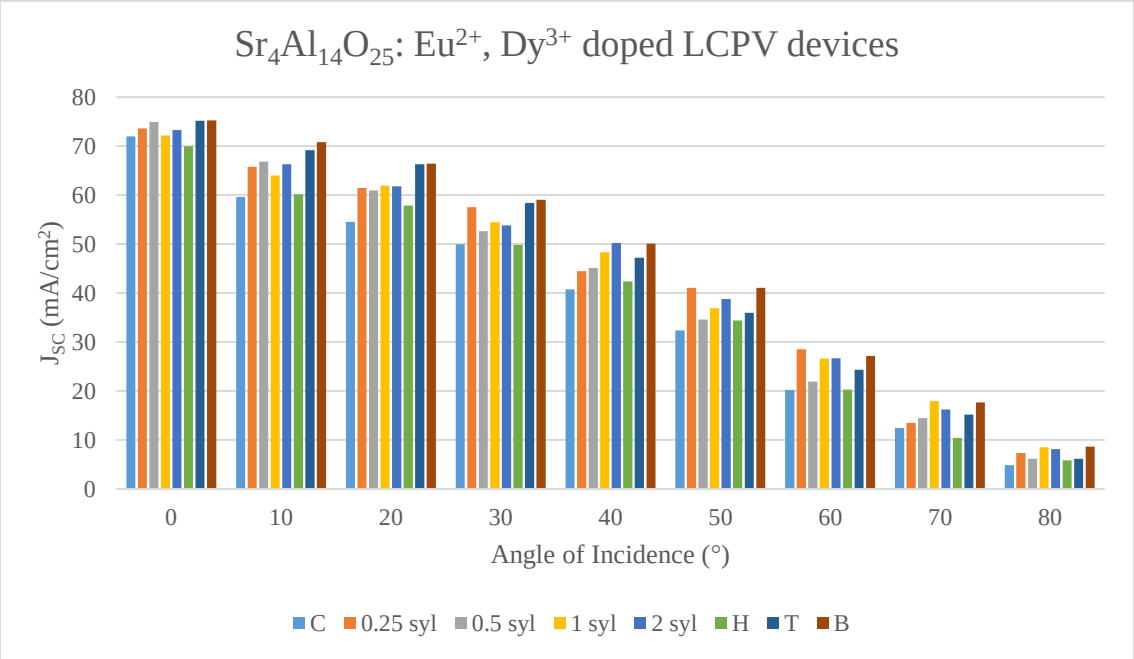

Figure 118: The J_{SC} of the $Sr_4Al_{14}O_{25}$: Eu^{2+}, Dy^{3+} doped LCPV devices under 1 sun illumination at angles of incidence from 0° to 80°.

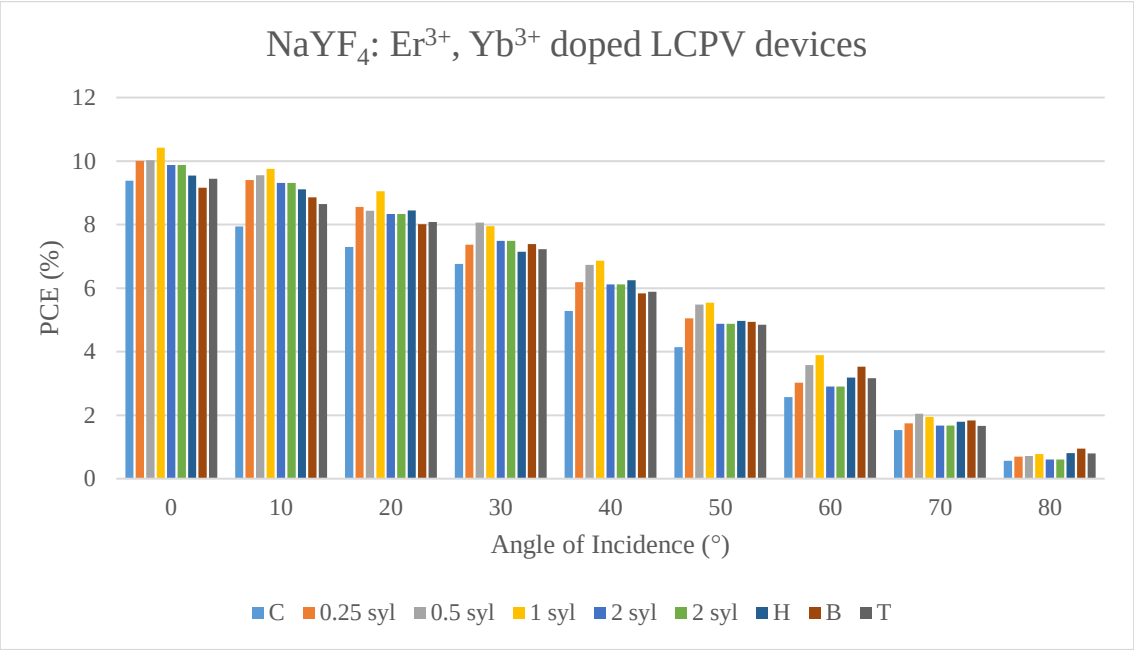

Figure 119: The PCE of the $NaYF_4$: Er^{3+}, Yb^{3+} doped LCPV devices under 1 sun illumination at angles of incidence from 0° to 80°.

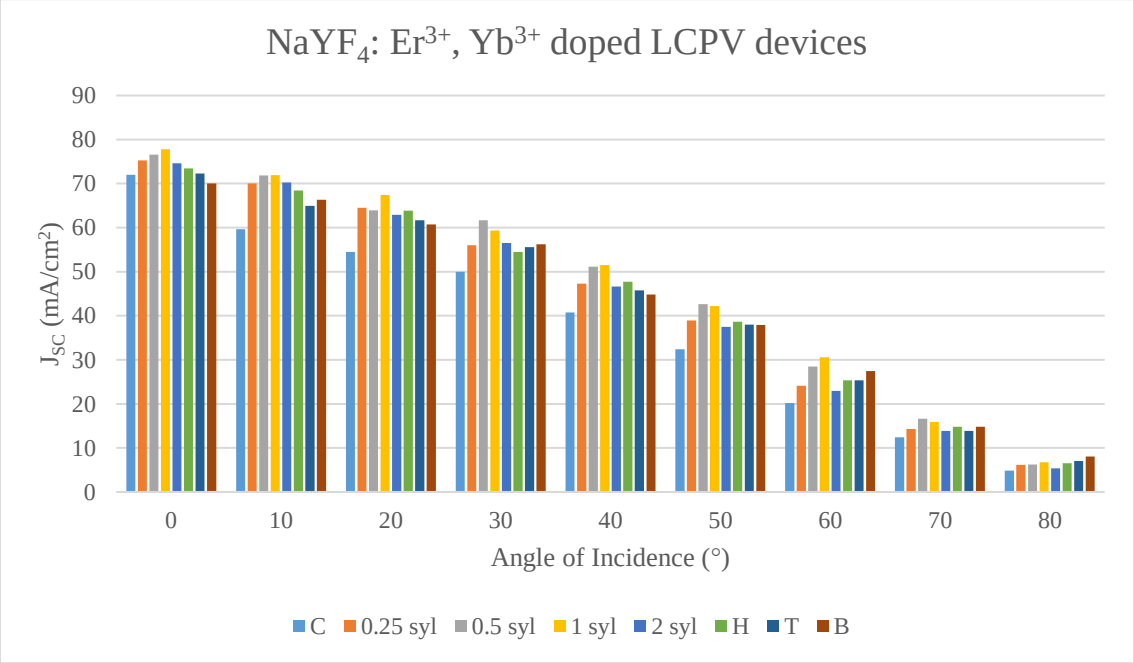

Figure 120: The J_{SC} of the $NaYF_4$: Er^{3+}, Yb^{3+} doped LCPV devices under 1 sun illumination at angles of incidence from 0° to 80°.

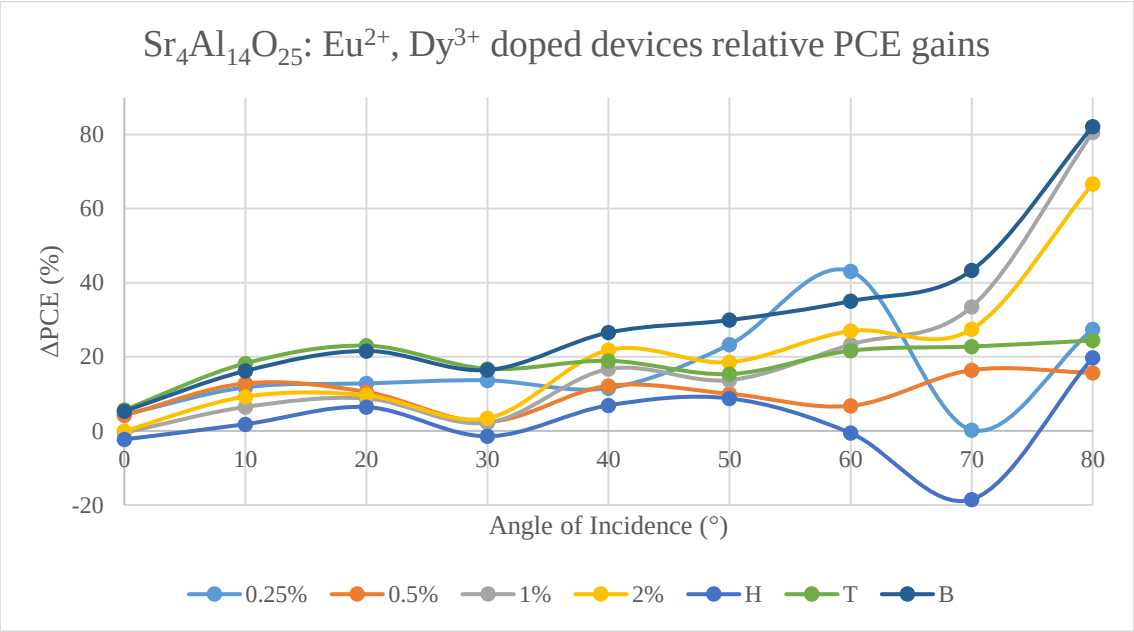

Figure 121: Relative PCE gains for the $Sr_4Al_{14}O_{25}$: Eu^{2+}, Dy^{3+} doped LCPV devices under 1 sun illumination at angles of incidence from 0° to 80°.

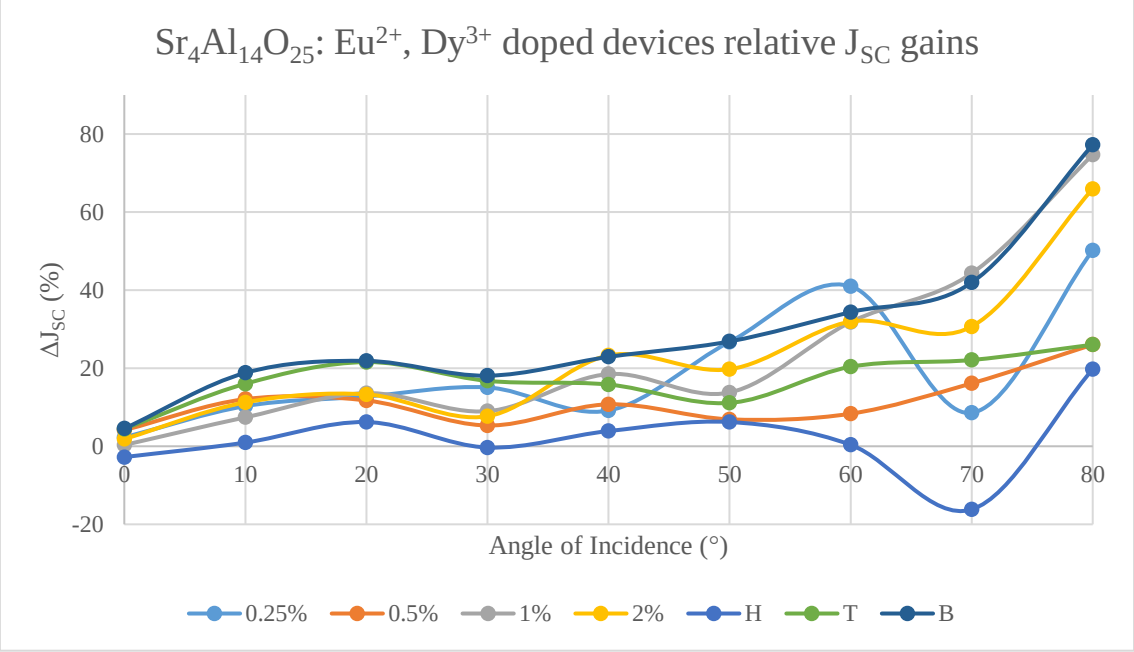

Figure 122: Relative J_{SC} gains for the $Sr_4Al_{14}O_{25}$: Eu^{2+}, Dy^{3+} doped LCPV devices under 1 sun illumination at angles of incidence from 0° to 80°.

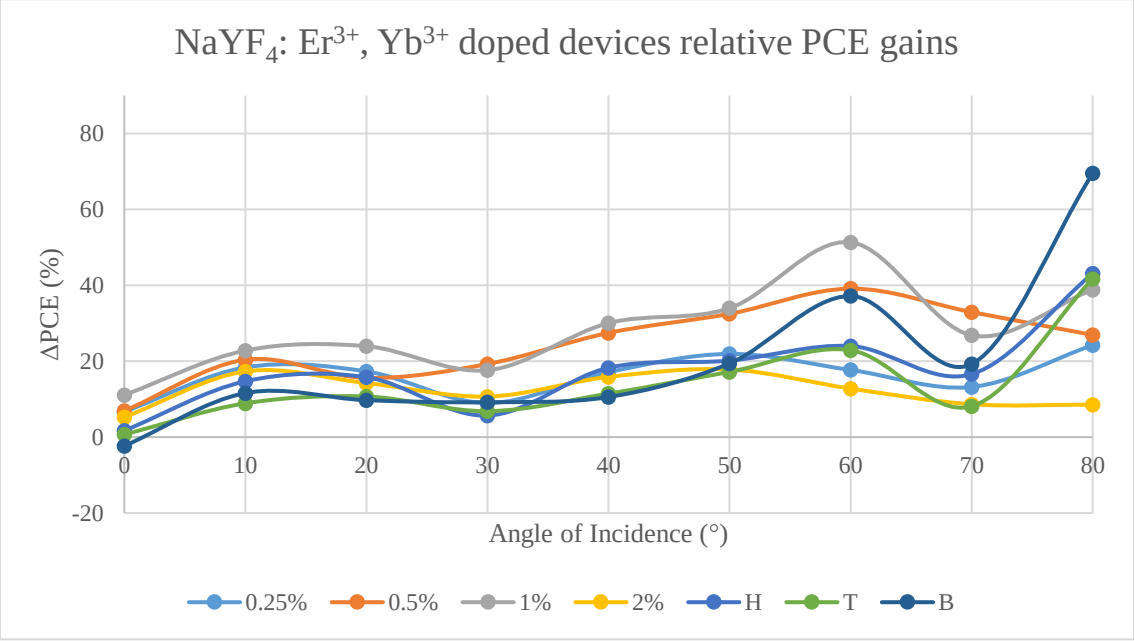

Figure 123: Relative PCE gains for the $NaYF_4$: Er^{3+}, Yb^{3+} doped LCPV devices under 1 sun illumination at angles of incidence from 0° to 80°.

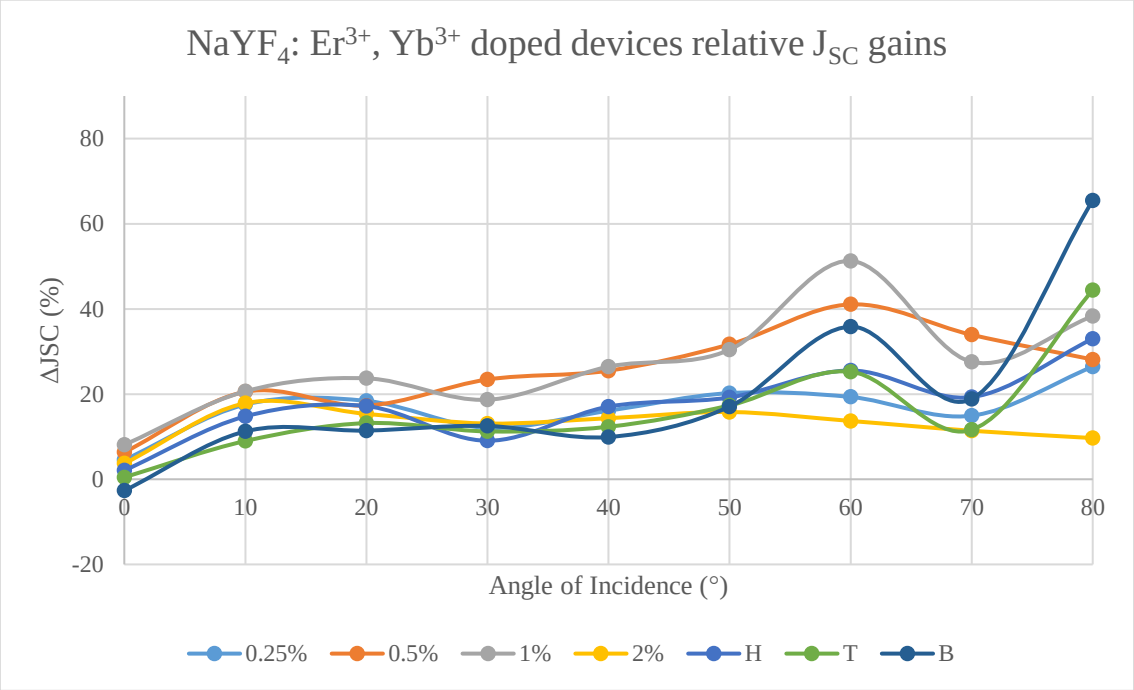

Figure 124: Relative J_{SC} gains for the $NaYF_4$: Er^{3+}, Yb^{3+} doped LCPV devices under 1 sun illumination at angles of incidence from 0° to 80°.

4.7 Conclusion

In this chapter, the LCPV modules displayed increased performance upon addition of both rare earth compounds. $Sr_4Al_{14}O_{25}$: Eu^{2+}, Dy^{3+} was found to produce greater PCE enhancements whilst being doped at 0.1% w/w into the top or bottom layer of an SEH concentrator whereas $NaYF_4$: Er^{3+}, Yb^{3+} was more

effective at improving PCE when doped in the optical coupling (between the concentrator and the PV cell). At 1 sun the $Sr_4Al_{14}O_{25}$: Eu^{2+}, Dy^{3+} top doped concentrator achieved the best PCE gain for that material of 5.7%, while $NaYF_4$: Er^{3+}, Yb^{3+} doped at 1% w/w in the optical coupling attained a PCE enhancement of 11.1%. This time the lower irradiances produced stronger relative PCE increases, the champion $NaYF_4$: Er^{3+}, Yb^{3+} category displaying a 17.7% rise at 0.4 suns. Furthermore, when the doped optical coupling LCPV devices were compared to their analogues from chapter 3 without the concentrators, it was seen that the enhancements were far greater through the addition of an SEH optic, especially at lower irradiances; a maximum difference in relative PCE gains with and without a concentrator of 16.1% was recorded for 0.5% w/w doped $NaYF_4$: Er^{3+}, Yb^{3+} at 0.4 suns. Again, EQE went up by almost 4% at 450 nm for $NaYF_4$: Er^{3+}, Yb^{3+} and 3.5% for $Sr_4Al_{14}O_{25}$: Eu^{2+}, Dy^{3+} containing devices, providing further evidence for spectral conversion playing a role in these observations and physical reasons for the patterns noted were proposed. Finally, the rare earth doped LCPV devices were able to raise device PCE at wide angles of incidence (important when considering suitability for practical irradiance conditions). The increased performance was particularly noted at the wide angles of 60° and 80°.

Chapter 5. Application to Dye Sensitized Solar Cells

5.1 Introduction

Following the successful application of $Sr_4Al_{14}O_{25}$: Eu^{2+}, Dy^{3+} and $NaYF_4$: Er^{3+}, Yb^{3+} to silicon-based PV and LCPV devices, it was now time to explore the effects of the same two rare earth compounds when applied to DSSCs. First, the structure and operating principles of a DSSC are discussed, as well as the different possible techniques for incorporating rare earth compounds into the device. Then batches of DSSCs containing the rare earth compounds in different thicknesses and configurations are fabricated; first by spin coating and then by screen printing, and their performance characterised by the solar simulator and IPCE. The best SEH concentrators from chapter 4 are also attached to some of the DSSCs, to see the effect on power output and J_{SC}. Finally, results from a collaborative study involving alternative DSSC materials and spectral conversion compounds are presented.

5.2 Dye Sensitized Solar Cells

Dye sensitized solar cells (DSSCs) were first conceived by O'Regan and Grätzel in 1991 [306] and have exciting properties that could realise lower cost PV modules. Despite their drawbacks in terms of lower efficiency (a record of 11.9% as of 2019 [22]) and reduced stability limiting their commercial application, their simple fabrication process has made them an appealing member of the third generation of solar PV technologies. Their range of available colours and ability to be attached to flexible substrates, means attractive and innovative module architectures can be realised, leading to potential BIPV applications. They are also an environmentally promising cell as their photoactive components are able to be recycled after exposure to alkaline solution [307] and unlike most PSCs, they do not contain any toxic lead.

It has been seen in 2.4.2 and 2.5.2 that DSSCs have benefitted from the addition of spectral conversion materials with impressive performance enhancements observed. In order to incorporate the materials used thus far into DSSCs, their structure and operating principles must be appreciated.

5.2.1 Dye Sensitized Solar Cell Operating Principles

The basic structure of a DSSC and the type of device to be studied in this chapter is presented in Figure 125. Each of these components play a role in a light driven electrochemical reaction which generates current between the two electrodes when they are connected via an external load. The transparent glass coated with a thin-film conducting oxide (TCO), usually fluorine-doped tin oxide (FTO), allows light to enter the cell through the working electrode. Then, the photosensitive dye molecules which have been adsorbed to a mesoporous layer TiO_2 are able to absorb photons and excite the dye from its ground state to an excited state. Following absorption, the excited dye electron is injected into the conduction band of the TiO_2, leaving behind a hole in the dye. This hole is then filled by an electron donated from an I^- ion in the electrolyte which is oxidised to I. When many of these events occur simultaneously, two I molecules react with an I^- to produce the triiodide ion I_3^-. This ion subsequently is broken down to three I^- ions, through the acceptance of two electrons taken from the counter electrode; the same electrons that were released in the working electrode and reached the counter electrode via an external load. Thus, the flow of current is completed and is steadily sustained by the redox reaction taking place within the electrolyte. These steps are summarised in Figure 126 and the following reactions [308].

$$1.\ S + hu \rightarrow S^*$$

$$2.\ S^* \rightarrow S^+ + e^- (TiO_2)$$

$$3.\ 2S^+ + 3I^- \rightarrow 2S + I_3^-$$

$$4.\ I_3^- + 2e^- \rightarrow 3I^-$$

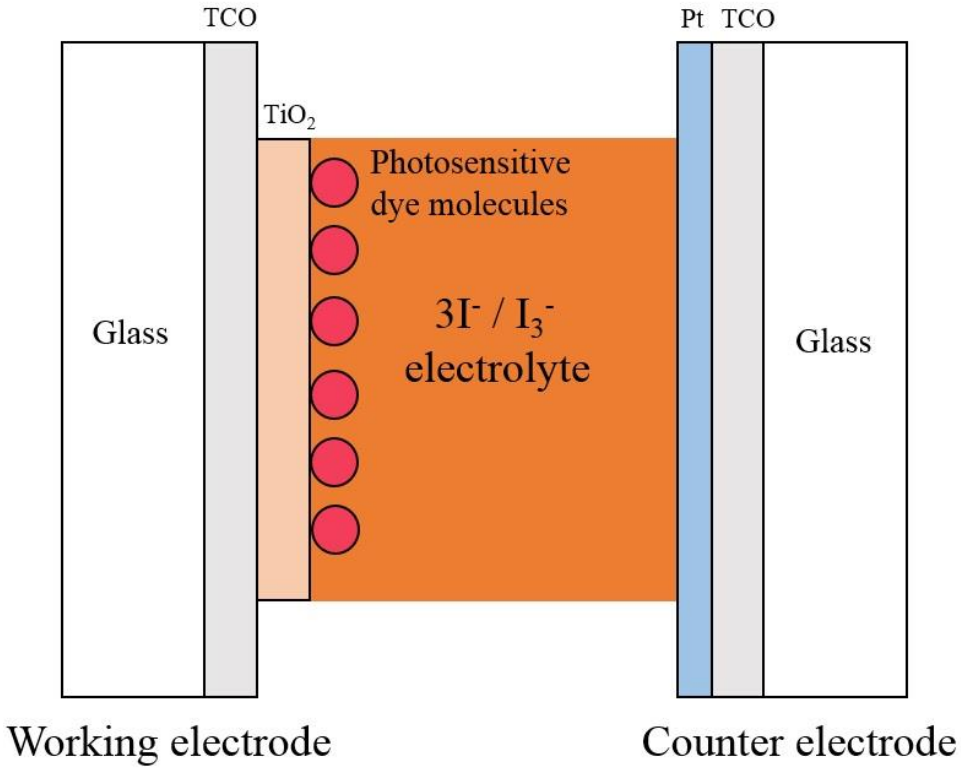

Figure 125: Basic sandwich structure of a DSSC where the photoactive materials are contained within two conductive glass electrodes.

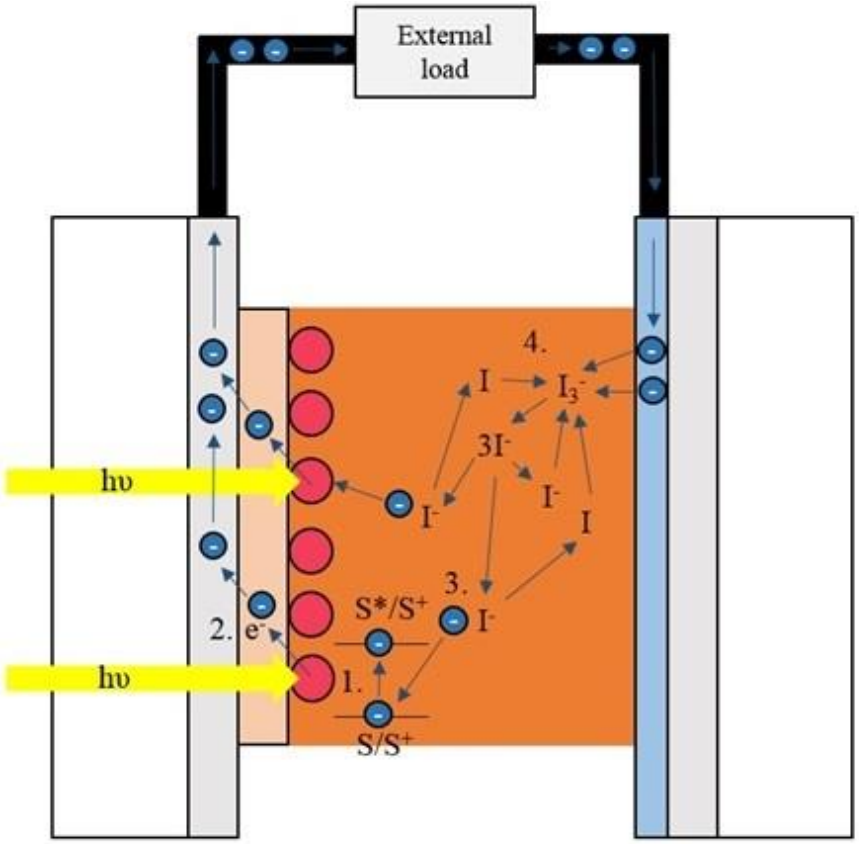

Figure 126: The flow of electrons in a DSSC with reactions 1-5 occurring at the numbered locations.

5.2.2 Dye Sensitized Solar Cell Limitations

The limitations on DSSC performance and issues that prevent their more widespread use can be divided into theoretical and practical concerns. Fundamentally, the power conversion efficiency is limited by four energy levels to be found in the cell's material components: the ground state of the photosensitizer dye, S, equivalent to the highest occupied molecular orbital (HOMO); the excited state, S*, approximately equal to the lowest unoccupied molecular orbital (LUMO); the Fermi level of the TiO_2 layer (E_F) and redox potential of the electrolyte ion pair (RP) [308]. Just as with E_G in single junction solar cells, the difference in energies between LUMO and HOMO, places a limit on the range of photons that can be absorbed and generate current. For the most often used dyes this value is approximately 1.7 eV, meaning only sunlight of wavelength 730 nm or less will be able to produce an electrical response. This is a greater portion of the spectrum than for c-Si with an E_G of 1.1 eV, resulting in significantly more power losses due to the spectral mismatch in DSSCs. Tandem DSSC-silicon structures have been proposed to overcome this, reaching a PCE over 18% [309]. Moreover, E_F is the energy required to add an electron into the system (in this case from the dye molecule into the working electrode) and is close to the conduction band level of the TiO_2, while RP is a measure of the tendency of the ion pair ($3I^-/I_3^-$) to gain or lose electrons. Both of these energy levels in addition to HOMO and LUMO can be defined relative to a standard hydrogen electrode (SHE) and are shown in Figure 127.

For electrons to keep moving and hence photocurrent to flow effectively, two further difference in energy level conditions must be satisfied. Firstly, LUMO must be more negative than the conduction band of the TiO_2 in order to ensure electrons are injected at a sufficient rate. Secondly, HOMO must be more positive than RP, so that dye electrons are likewise replenished with optimal effectiveness. The discrepancies in these values compared to HOMO and LUMO (or over-potentials) limit the potential difference of electrons travelling between the two electrodes and hence curtail the maximum theoretical voltage of the device to the approximate difference between E_F and RP, whereas for silicon cells, V_{OC} is essentially limited by the rate of radiative recombination alone. The higher V_{OC} of DSSCs, is also consistent with the concept of a higher E_G resulting in a greater V_{OC}. Although interestingly, in contrast to silicon solar cells, DSSCs

actually increase in performance with higher temperature which could have implications for their use in LCPV [310].

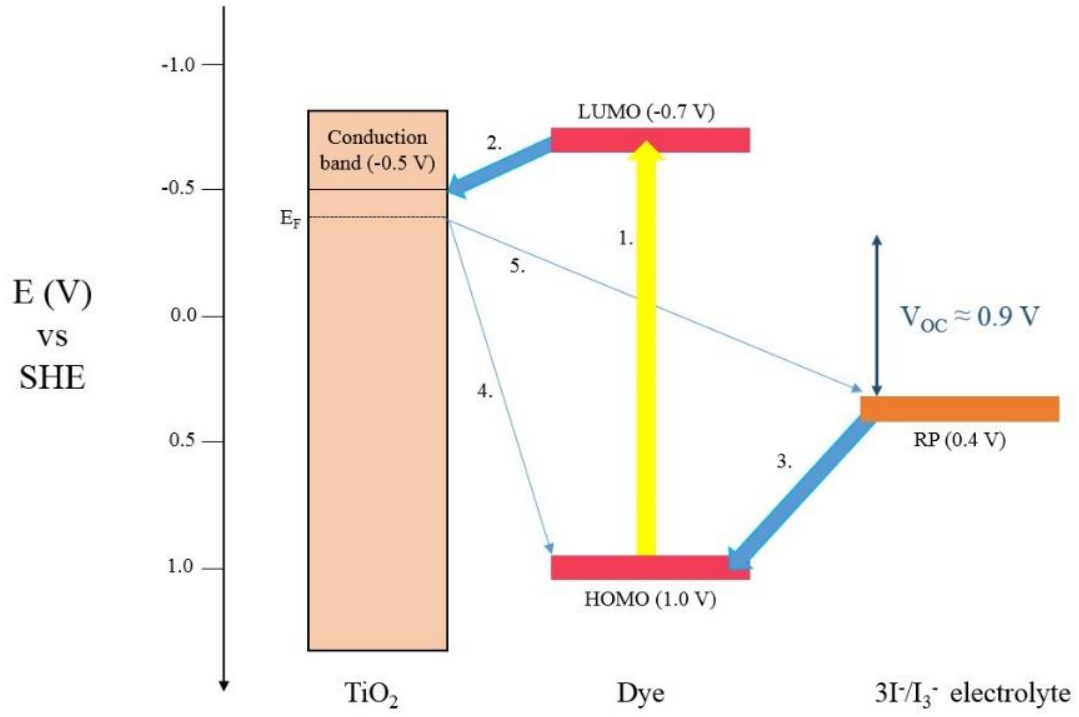

Figure 127: Energy level diagram of the steps within DSSC current flow: Photon absorption (1), electron injection into TiO_2 (2) and replenishment of dye (3). Recombination occurs via (4) and (5). Modified from [308].

A further contrast between silicon PV and DSSCs is that the holes and electrons become physically separated upon injection into the TiO_2 such that recombination does not occur through the same charge carrier interactions as within a p-n junction-based cell. However, recombination in DSSCs still does occur through two predominant routes, between the electrons injected into the TiO_2 and either the dye cations or I_3^- ions. Typically and fortunately for the cell's performance, these processes happen over much longer timescales (microseconds to milliseconds) compared to the injection from the dye which is ultrafast, in the order of 10^{-12} s [311]. Although in reality, structural imperfections such as contact between the working electrode's TCO or TiO_2 uncoated with dye and the electrolyte can hamper device performance by amplifying these effects. Nevertheless, the charge transport properties and power conversion efficiency can be further improved by the addition of a compact $TiCl_4$-treated TiO_2 layer at the TCO-TiO_2 boundary [312] or co-adsorbing the TiO_2 with 4-tert-butylpyridine

(TBP) [313] which reduce TCO-electrolyte and TiO_2-electrolyte recombination respectively.

Another practical factor which then limits DSSC efficiency is the absorption of the dye. The widely used N719 when adsorbed to TiO_2 has the absorbance spectrum profile shown in the top right of Figure 128, where it can be seen that the absorption coefficient is reduced between 380 and 450 nm and is effectively zero at wavelengths over 730 nm. The device EQE corresponds well with the absorption spectrum of the dye, while the use of multiple dyes in a tandem electrode structure which can absorb different wavelengths has been studied by Baranwal et al to yield a higher EQE profile across more wavelengths and PCE of 7.1% [314].

Notwithstanding the different band gap energies, the EQEs of DSSCs typically are lower than silicon, with high quality devices peaking at around 70% at 540 nm, while silicon cells exhibit EQE > 80% for 450-850 nm. This could be because it is harder to ensure all photons are absorbed in a nanoscale structure than in a traditional wafer-based cell due to the different absorption coefficients. However, if the dye adsorbed TiO_2 layer is made too thick the sheet resistance will rise, reducing performance [315], so the right balance must be struck; a thickness of ~10 μm is usually optimal [316].

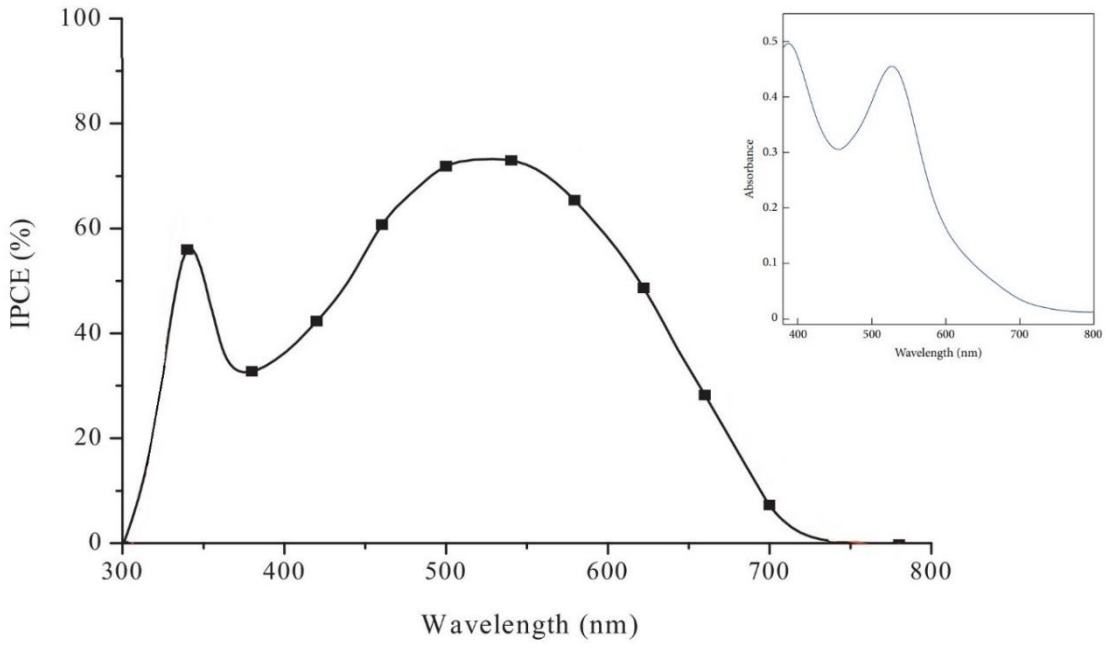

Figure 128: EQE profile of a typical N719 dye based DSSC and the absorbance spectrum of N719 adsorbed on TiO_2 (top-right of the figure). Data from [317] and [318].

Due to their multiple material components, unlike silicon or other single junction PV cell technologies, the performance is not primarily dependant on one quantity (E_G or LUMO minus HOMO) alone and the voltage of a DSSC is affected by lots of factors, so one cannot simply plug 1.7 eV into the Shockley-Queisser equation to determine maximum PCE. In 2009, Snaith estimated if a dye could absorb up to 940 nm with an over-potential of just 0.4 V, then a DSSC with efficiency of 20% would be theoretically achievable, while 13.4% was the maximum attainable PCE based on the properties of, at the time, state-of-art materials for liquid electrolyte DSSCs [319]. Mohamed et al have identified practical considerations for the ideal properties of each component to maximise the PCE: high transparency and high conductivity for the TCO coated glass; high surface area, high catalytic activity and high stability for the counter electrode coating; optimum redox, high stability and good solvent for the electrolyte; wide-range absorption, high absorption coefficient, high-anchoring propensity and high stability for the dye; high surface area, high stability and high conductivity for the mesoporous working electrode layer and that the photoactive region should be highly sealed [320].

In addition to maximising performance, in order to be a successful alternative to silicon PV, the power output must be stable over long term exposure to light and the ambient environment, since module lifetime is just as important as efficiency and cost for the commercial viability of a PV technology. In their detailed review of stability issues pertaining to emerging PV, the following are identified as problems by Castro-Hermosa et al: electrolyte leakage, evaporation of the electrolyte solvent, degradation and depletion of the I_3^- ion, desorption of the dye from the TiO_2, degradation of the dye molecules, corrosion of the counter electrode coating and surface contamination of either electrode. These can be caused by a combination of improper sealing, thermal stress and the subjection of the cell to UV radiation, moisture and oxygen, all of which accelerate dye degradation [321]. In the long term, replacement of the liquid electrolyte by solid state hole transport materials such as 2,2′,7,7′-tetrakis-(N,N-di-p-methoxyphenylamine)9,9′-spirobifluorene (spiro-MeOTAD) [322], widely used in PSCs, or phosphonium organic ionic plastic crystals with hydrophilic silica [323] could tackle these issues. Sharma et al reviewed areas to focus on for improving their performance which included co-sensitisation with dyes to broaden the absorption spectrum, increasing the TiO_2 porosity and counter electrode surface

area through nanostructures such as with nanorods or nanowires, and of relevance to this work, the addition of luminescent materials such as rare earth ion doped oxides to change the composition of incoming light. There is also an added advantage of LDS or DC spectral conversion in DSSCs as it can limit the exposure of the dye to high energy UV photons, to the benefit of device stability [310].

Having discussed DSSC operating principles and contemporary issues around their effectiveness, this work will forthwith focus on the common $I_3^-/3I^-$ system because of its facile synthesis and low cost. Even if ultimately it may be replaced by solid state DSSCs, the operating principles and structure are largely similar, so the successful demonstration of the $NaYF_4$: Er^{3+}, Yb^{3+} and $Sr_4Al_{14}O_{25}$: Eu^{2+}, Dy^{3+} materials added into various parts of the cell will be a useful addition of knowledge for future cell designs.

5.3 Dye Sensitized Solar Cell Fabrication

The DSSCs were made using a method similar to that reported by Narra et al and widely used in the publications of the University of Exeter group [324].

The working electrodes consisted of FTO coated (to act as the TCO) 2 cm x 2 cm square pieces of glass of 2.2 mm thickness (Pilkington). FTO conductance was quoted by the supplier as 13 Ω/sq and this was verified by a multi-meter check. After cutting to the desired size, the substrates for the working electrode were thoroughly cleaned through a number of steps. First the glass pieces were placed in a beaker containing deionised water and swilled by hand several times to remove shards. Then they were subjected to ultra-sonication for 15 minutes in a beaker of deionised water and again in ethanol. Finally after drying with hot air, further cleaning was conducted by placing the substrates in an Ozone UV cleaner (Ossila) for 15 minutes which blasts the surface with high energy activated oxygen atoms, breaking contaminants down into volatile compounds and resulting in a highly clean substrate [325].

Once the substrates had been prepared, the TiO_2 layer could be added in one of two ways, spin coating or screen printing. In each case, the material used to form the TiO_2 was 18NR-T transparent Titania paste (Greatcell). This mixture consists of 20 nm TiO_2 nanoparticles and organic binder molecules that when heated dissipate, leaving behind a uniform, mesoporous layer. Spin coating as

described in 3.4.1 is a method to deposit thin films on substrates. The 18NR-T paste is too thick and viscous to be spin coated, so is mixed with ethanol in a 1:3 weight ratio and 100 µl dropped by micropipette dynamically onto the FTO substrate at 3000 RPM for 60s. The edges were coated with tape to give a coating area of 1cm^2 and prevent TiO_2 going all the way to edge. This is necessary as to extract a current to an external load and thus characterise device performance, some FTO must be uncovered.

Screen printing, on the other hand, is a method of depositing layers in which a sample of material is forced downwards manually with a squeegee through a mesh onto the substrate below. Unlike spin coating, it does not require a non-viscous solution, so the 18NR-T paste can be used directly, and it typically provides thicker layers (approx. 6 µm per print as opposed to 100 nm for spin coating). The thickness of the resultant layer is determined by the level of spacing in the mesh; the more compact the mesh pattern, the smaller volume of material deposited, leading to a thinner layer and vice versa [326]. The screen printer used for the fabrication of these devices was a 43T mesh, meaning it had 43 threads per cm of length. A small spatula was used to smear approximately 0.1g of paste on the higher boundary of the mesh (from where the squeegee would be pulled down from) and then carefully but firmly, a stroke of the squeegee would press the material down onto the centre of the glass below, producing a square coating of area 0.28 cm^2. Two layers were added to give a thickness of ~12 µm and when screen printing, between the additions of layers, the substrates were kept on a hot plate (Stuart) at a temperature of 120°C for 10 minutes. Both sides of the mesh and squeegee were rubbed cleaned between depositions with ethanol in order to ensure a consistent procedure and no remnants from previous prints would be deposited. Also, when adding another layer, it is essential the second layer overlaps as closely as possible with the first layer for maintaining a uniform layer thickness and device active area. To achieve this a marker pen was used, on the reverse side of the FTO glass, to trace an outline of the first layer which could be seen through the screen printer and used as a visual reference in order to align subsequent layers. Lastly, in the case of screen printing only, a further TiO_2 scattering layer was added using Greatcell 18NR-AO. In contrast to 18NR-T, this material consists of larger TiO_2 nanoparticles (approximately 450 nm in size) again mixed with smaller 20 nm TiO_2 nanoparticles and organic binders that

upon heating forms an opaque layer. This functions as a light scattering layer, and improves the DSSC performance by increasing the path length of the incoming photons and hence their chance of absorption by the dye and generating current [327].

After applying the layers, to finalise the desired structure and film quality of the TiO_2 layers, the coated substrates must be annealed to a high temperature over several hours. For this step, the partially complete working electrodes were placed on another hot plate (PR5, Harry Gestigkeit GmbH) which had a programmable temperature control and timer that can manage the time taken to reach a desired temperature (called ramp time) and time held at that temperature (known as hold time). The hot plate was set to expose the substrates to the following conditions: 20°C to 150°C with a 5 minute ramp time and held for 5 minutes, 150°C to 250°C with a 5 minute ramp time and held for 10 minutes, 250°C to 375°C with a 5 minute ramp time and held for 10 minutes, 375°C to 500°C with a 15 minute ramp time and held for 30 minutes, and finally, 500°C to 40°C with a 90 minute ramp time after which the substrates could be removed from the hot plate. The peak temperature of 500°C is required to fully evaporate the organic binders present in the pastes and give them the desired uniform structure (mesoporous with a large surface area to aid dye adsorption and one that promotes beneficial scattering). It is also important to set the cooling time for such a length, so that the glasses do not crack upon rapid decrease in temperature.

Next the annealed TiO_2 coated FTO glasses must be soaked in a dye solution for 24 hours with their TiO_2 side face up, so gravity aids adsorption. The dye solution consists of N719 powder (Ossila) which has been prepared into a 0.2 mM solution by dissolving and mixing thoroughly in a conical flask with ethanol at a concentration of 12 mg of powder per 100 ml of solvent. The dye is a Ru containing complex with the central transition metal ion surrounded by a range of organic functional groups; the precise chemical composition of the powder is $C_{58}H_{86}N_8O_8RuS_2$, full name Ditetrabutylammoniumcisbis(isothiocyanato)bis(2,2′-bipyridyl-4,4′-dicarboxylato)ruthenium(II). Once made up, this dye solution could be stored for future use by covering the flask's exterior in foil and its top in Parafilm® to prevent exposure to light and air, which would cause the dye solution to degrade and evaporate respectively.

After allowing sufficient time for the dye to be adsorbed to the TiO_2 layer, the substrates were carefully removed and dried with hot air. The fabrication of the working electrode was now complete, and the device almost ready to be put together. However, before placing the two electrodes in contact, there is one further consideration. As seen in earlier Figure 125, for DSSC operation the electrolyte must be spatially contained between the dye-adsorbed TiO_2 layer and Pt counter electrode. In this study, the working electrodes have only a dye-adsorbed TiO_2 coated area of 0.28 cm^2 for screen printing or 1 cm^2 for spin coating on a 2 cm x 2 cm substrate. This means if the two electrodes are simply stuck together, the uncoated FTO of the working electrode will be in contact with the electrolyte solution or Pt opposite, which respectively create a path for the charges to recombine or a short-circuit. Hence it is necessary to use a spacer, stuck around the edges of the TiO_2 layer in a square annulus shape, to contain the electrolyte. The material used for this purpose was Surlyn®, a 30 µm thick co-polymer of ethylene and methyl acrylic acid with good chemical and mechanical stability, along with adhesiveness on heating.

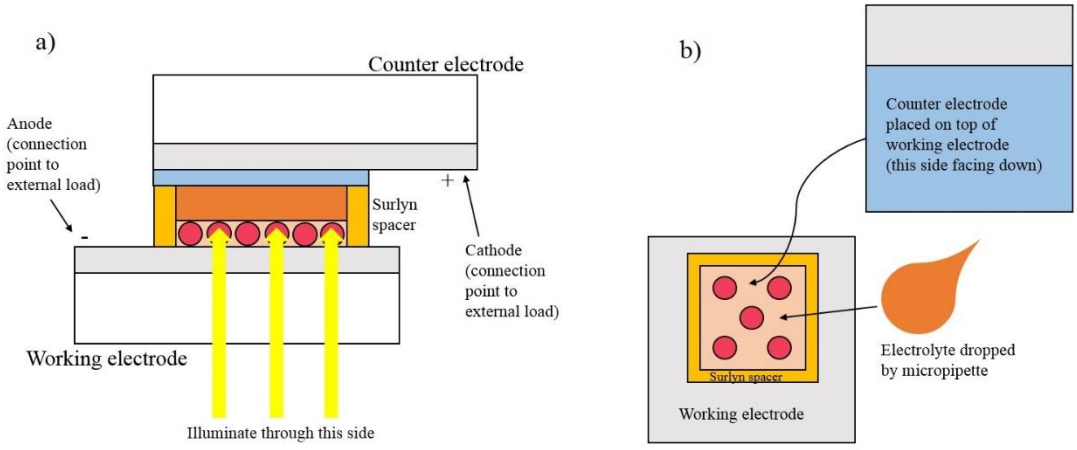

Figure 129: a) Device architecture with the spacer and connection points labelled and b) how the device was put together.

Once the appropriately shaped spacers had been cut and placed on the working electrode, the counter electrodes were prepared for completing the device architecture. This process was much simpler, since no additional layers are required to be added to the already Pt coated FTO glasses. These counter electrodes were provided by Greatcell and came in strips of 7 which had to be cut to their 3 cm x 2 cm sizes; the glass thickness was 3 mm and just 2 cm x 2

cm had been coated in the Pt catalyst (since only the area that would be in contact with the electrolyte requires it). The counter electrodes were cleaned in a similar method to the FTO substrates (ultra-sonication in deionised water, then ethanol, followed by UV cleaning). Finally, the I^-/I_3^- electrolyte solution (containing 0.4 M LiI, 0.4 M tetrabutylammonium iodide, and 0.04 M I_2 dissolved in 0.3 M N-methylbenzimidazole in acetonitrile and 3-methoxypropionitrile solvent mixture at 1:1 volume ratio) that had been previously prepared according to Senthilarasu et al [328] was dropped by a micropipette in a 30 µl quantity onto the dye-adsorbed TiO_2 and the counter electrode placed on top (Pt facing down) to give the sandwich device structure shown in Figure 129. This was also done on a 100°C hotplate to melt the Surlyn and tweezers were used to press the sides together and keep the electrolyte evenly distributed. For practical reasons (e.g. cells couldn't be kept on the hot plate too long or electrolyte would evaporate), ring binders were also used to fix the electrodes and provide a more mechanically stable DSSC. It is possible (and more ideal) to fill the electrolyte via a hole in the counter electrode which can be sealed with more Surlyn, although this was not deemed a necessary step for these investigations.

5.4 Incorporation of Spectral Conversion Materials

The procedure described so far is for the fabrication of plain DSSCs to act as control devices containing N719 adsorbed TiO_2 at the photoanode only, but when DSSCs containing spectral conversion materials were required, the rare earth compounds must be incorporated at some stage of the process. It was seen in 2.4.2 and 2.5.2 that various rare earth doped compounds have been added into DSSCs and other emerging PV cells in a range of configurations, predominantly internally within the layers of the working electrode or externally on the glass that faces the incoming illumination. The spectral conversion properties of $NaYF_4$: Er^{3+}, Yb^{3+} and $Sr_4Al_{14}O_{25}$: Eu^{2+}, Dy^{3+} were suitable as they could potentially absorb in the 380-450 nm region of the spectrum where EQE is low and re-emit at > 500 nm where spectral response is greater.

To probe these differences further, in 2017 Hosseini et al [329] critically compared an extensive catalogue of DSSC studies which had applied the luminescent particles in nine regions of the device structure as shown in Figures 130 and 131.

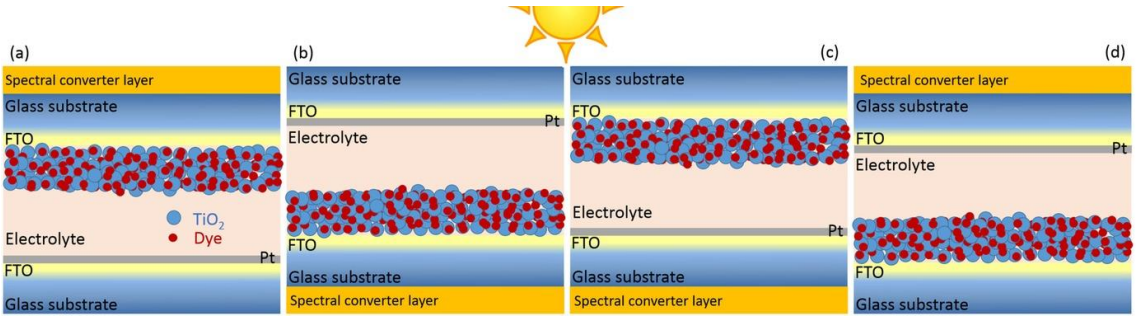

Figure 130: Different ways of incorporating the spectral conversion materials onto the DSSC exterior glass substrate: a) and b) above or below the working electrode, c) and d) below or above the counter electrode. Taken from [329].

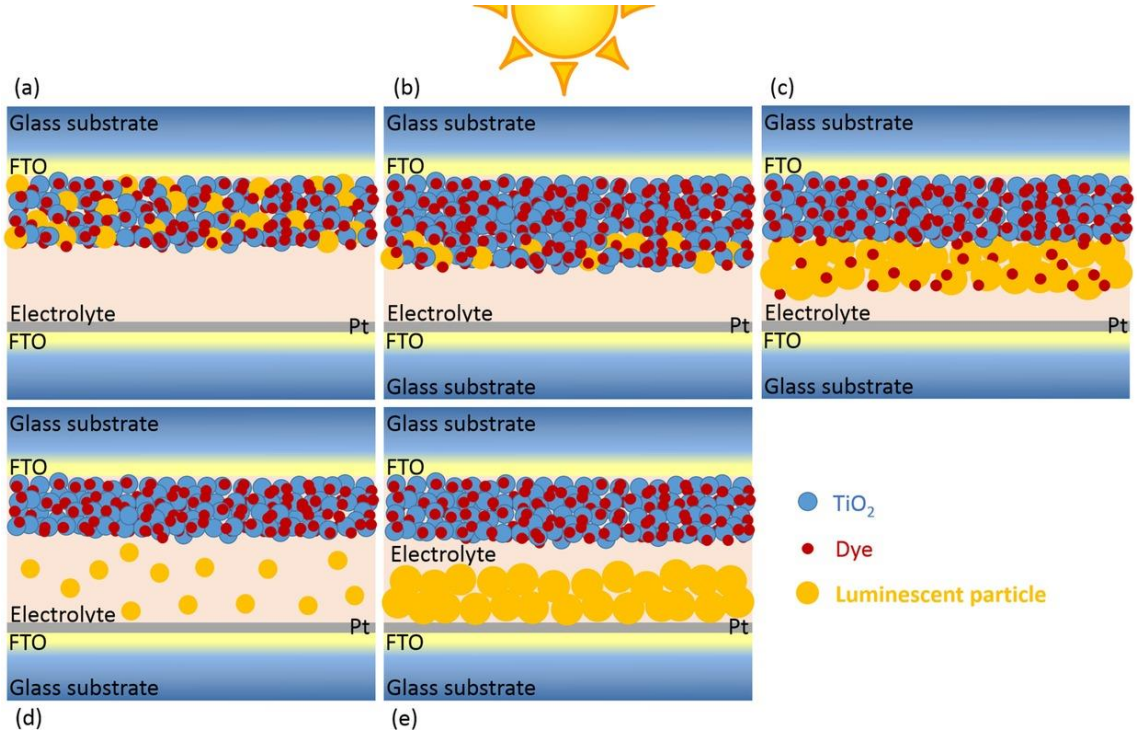

Figure 131: Different ways of incorporating the spectral conversion materials into the interior of a DSSC: a) Evenly throughout the TiO_2, b) at the top of the TiO_2, c) above the TiO_2, d) throughout the electrolyte or e) on the counter electrode. Taken from [329].

In subsequent investigations, the doping was opted to be added internally to the device, as opposed to above or below the glass substrate of either electrode. This was due to higher efficiency enhancements having been observed for these configurations and additional functional benefits such as raising E_F of the TiO_2 (and hence the cell voltage) and the ability to act as a light scattering material. The configurations of (a), (b) and (c) in Figure 131 were chosen as the predominant structures to be investigated due to the higher enhancements reported, as well as (e) because of the novelty of it not having been attempted in any of the studies presented by Hosseini et al.

In the first trial study, using the spin coated DSSC fabrication technique, $NaYF_4$: Er^{3+}, Yb^{3+} (chosen over $Sr_4Al_{14}O_{25}$: Eu^{2+}, Dy^{3+} due to its better performance in chapters 3 and 4) was dispersed in the TiO_2 to give an (a) type device. A simple mixing technique was used such that varying weight ratios of $NaYF_4$: Er^{3+}, Yb^{3+} (0%, 0.25%, 0.5%, 1% and 2%) were mixed with 18NR-T paste and ethanol, first manually in a vortex mixer (Stuart), then through ultra-sonication for 15 minutes. As will be seen in the results, this crude approach together with the thinness of TiO_2 layer from spin coating led to a lower efficiency and less meaningful results.

Therefore, for the following studies, care was taken to prepare a mixture of rare earth compound that could be well applied to the electrode with a uniform and mesoporous structure, as seen in Figure 131. Furthermore, a more rigorous preparation process was needed to reduce particle size (since the devices are at nanoscale, any internally added particles should ideally be too). To achieve this, the two rare earth materials were in turn mixed in a mortar and pestle with the same organic binders present in 18NR-T/18NR-AO in order to give a good film quality upon annealing. The binder molecules used were ethyl cellulose (Sigma) and α-terpineol (Sigma). In order to make the mixture, first 1 g of either $Sr_4Al_{14}O_{25}$: Eu^{2+}, Dy^{3+} or $NaYF_4$: Er^{3+}, Yb^{3+} was added to 1.2 ml of ethanol and ground firmly with an agate mortar and pestle. Meanwhile, 1g of ethyl cellulose was separately added to 2 ml of ethanol in a small beaker placed on a 70°C hotplate, creating a viscous gel. Next 200 µl of this mixture was added to the rare earth compound-ethanol powder along with a further 200 µl of α-terpineol, and thorough grinding in the mortar and pestle continued for 10 minutes. Additional rare earth compound or ethanol was added if the mixture became too thin or thick respectively. Then the addition of 200 µl of both binders and mixing for 10 minutes was repeated four times, such that the paste had been ground for a total of 50 minutes. This procedure resulted in two smooth but gel like pastes with a similar texture to the 18NR-T/AO materials but greyish-white in colour for the $NaYF_4$: Er^{3+}, Yb^{3+} containing sample and beige for that made from $Sr_4Al_{14}O_{25}$: Eu^{2+}, Dy^{3+}. Then finally, to allow the particles for use in different proposed methods of incorporation into the DSSC, each mixture was divided into two portions; one was set aside as prepared and the other was to be further mixed with an equal mass of TiO_2 paste (18NR-AO) in ethanol; this was done for 1 hour by magnetic stirring. The mixture of TiO_2 and rare earth compound paste would be used for making cells to the

design of Figure 131 (b) whereas the purely $Sr_4Al_{14}O_{25}$: Eu^{2+}, Dy^{3+} or $NaYF_4$: Er^{3+}, Yb^{3+} pastes would be utilised for methods (c) and (e).

All that remained to be considered after this synthesis was how to apply the pastes and solutions to the electrodes during device fabrication. Screen printing was found not to be effective for applying either the rare earth compound pastes or rare earth compound-TiO_2 solutions due to their thickness and low viscosity respectively. Therefore, three alternative methods were used: spin coating, drop casting and doctor blading. Only the latter technique has not been introduced thus far; doctor blading is fairly similar to screen printing, but there is no mesh and instead a rigid object (such as a glass rod or rectangular piece of glass) is used as the squeegee by pulling in one direction to distribute a thin film of material on a substrate that has been masked (e.g. covered with tape on the area that no deposition is required). For the construction of a device like (c), after the deposition of two 18NR-T layers via screen printing, a layer of the desired rare earth compound paste was added by doctor blading. Likewise, for (e), the cleaned and dried Pt counter electrodes were coated in a 0.28 cm^2 area of rare earth compound paste via doctor blading. On the other hand, for (b) type devices, the rare earth compound-TiO_2 mixture was added either by drop casting a blob (of varying volumes, 25 µl, 50 µl, 100 µl and 200 µl to control the layer thickness) in the central area of the first two 18NR-T layers over a hot plate at 120°C and spreading with the micropipette tip, or for a very thin layer, by spin coating (after masking outside the 18NR-T layers as per doctor blading) 100 µl at 3000 RPM for 1 minute.

In all cases where rare earth compounds were added, the same annealing and cooling procedure (up to and down from 500°C) was followed and two identical copies of each device configuration were made to improve reproducibility of the work (except for the control devices, for which a total of six devices were made since they were going to be compared against all other samples, so needed a more accurate set of measurements). These steps are summarised by Figure 132 and a real image of a completed DSSC device is shown in Figure 133.

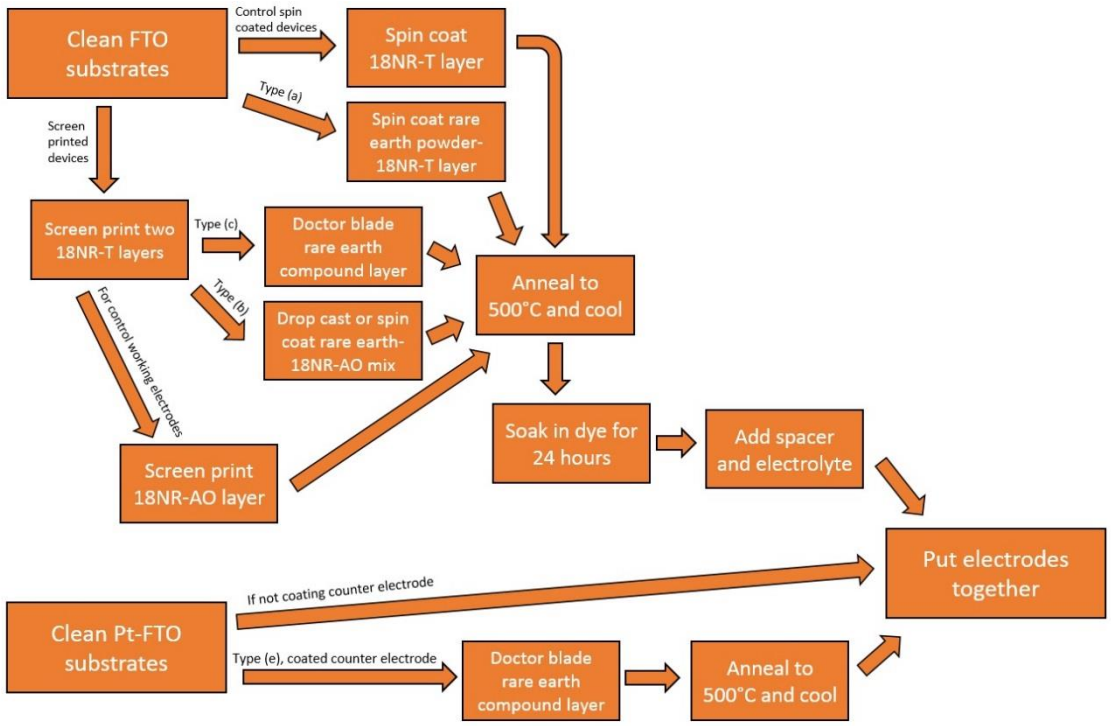

Figure 132: Summary of the steps required to fabricate device types (a), (b), (c) and (e) as well as control DSSCs.

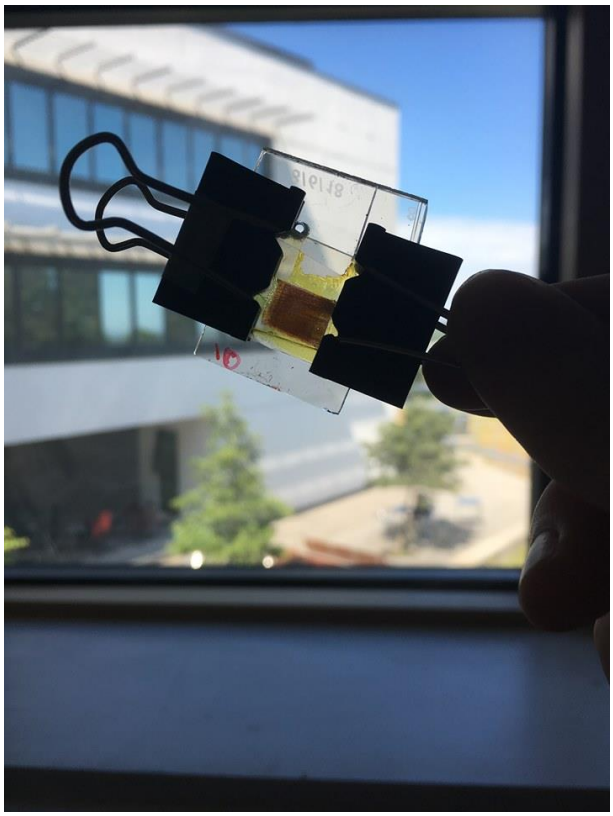

Figure 133: Real life image of a complete fabricated DSSC of type (e).

5.5 Results

5.5.1 Indoor Characterisation under the Solar Simulator

The DSSCs were first tested under the solar simulator by connecting the I-V tracer clips to the DSSC anode and cathode as shown in Figure 128. The same general procedure was followed as in chapters 3 and 4 whereby devices had two measurements recorded following illumination for 30 seconds and 60 seconds. It was also important to characterise within a reasonably quick timeframe following device fabrication, since DSSCs may lose quality after prolonged exposure to the ambient environment.

The electrical performance parameters for the spin coated devices are given in Tables 60 and 61, and their I-V curves and transmittance spectra (from UV-Vis spectrometry) given in Figures 134 and 135 respectively. Furthermore, the numerical data for the much more extensive study on screen printed DSSCs are presented in Tables 62-65 with I-V curves in Figures 136 and 138. For clarity in the tables and I-V curves, the devices are denoted by DB for the doctor bladed on TiO_2 (Figure 131 (a)), SC for the spin coated TiO_2-rare earth mixture (b), DC x µl for the drop casting by x µl of the TiO_2-rare earth mixture (b) and DB CE for the doctor bladed counter electrode (e). Additionally, the variations in PCE and J_{SC} enhancements with layer thickness for the drop casted TiO_2-rare earth compound mixtures are presented in Figures 137 and 139. It should be finally added that as in chapter 3 and 4, the presented data are for the device displaying the champion PCE (although for the control, it is the champion from the median of the three produced batches each of two devices).

Doping (w/w %)	η (%)	J_{SC} (mA/cm^2)	Δη (%)	Δ J_{SC} (%)
0	0.164	0.511	-	-
0.25	0.206	0.461	+25.61	-9.78
0.5	0.052	0.177	-68.29	-65.36
1.0	0.120	0.256	-26.83	-49.90
2.0	0.136	0.324	-17.07	-29.72

Table 60: PCE and J_{SC} data for $NaYF_4$: Er^{3+}, Yb^{3+} doped spin coated DSSCs at 1 sun.

Doping (w/w %)	V_{OC} (mV)	FF	ΔV_{OC} (%)	Δ FF (%)
0	764.222	0.420	-	-
0.25	832.753	0.547	+8.97	+30.24
0.5	741.967	0.399	-2.91	-5.00
1.0	830.053	0.583	+8.61	+38.81
2.0	804.300	0.525	+5.24	+25.00

Table 61: V_{OC} and FF data for $NaYF_4$: Er^{3+}, Yb^{3+} doped spin coated DSSCs at 1 sun.

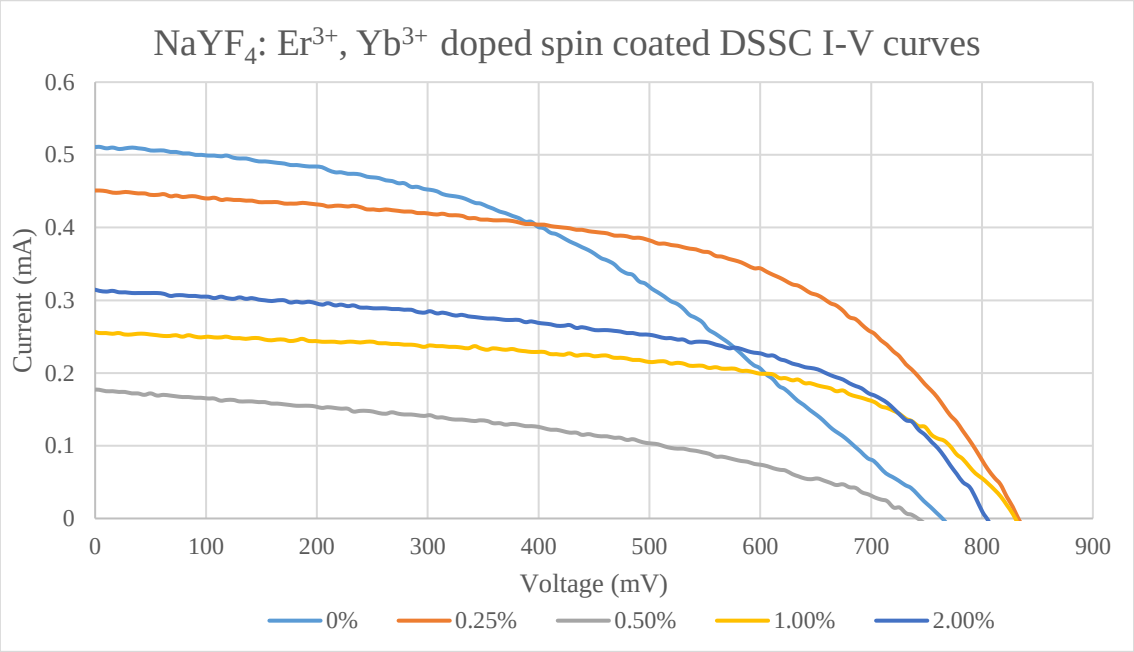

Figure 134: I-V curves for the $NaYF_4$: Er^{3+}, Yb^{3+} doped spin coated DSSCs at 1 sun.

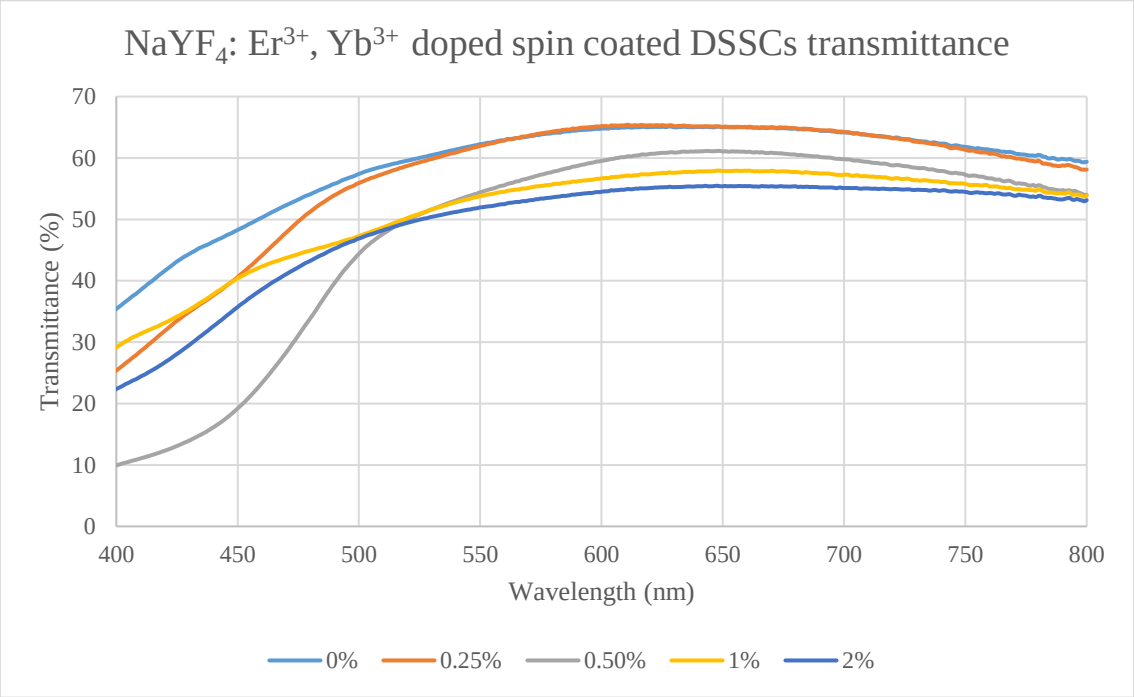

Figure 135: Transmittance spectra for the $NaYF_4$: Er^{3+}, Yb^{3+} doped spin coated DSSCs.

Device Category	η (%)	J_{SC} (mA/cm^2)	Δη (%)	Δ J_{SC} (%)
Control	3.456	6.639	-	-
Doctor bladed on TiO_2	3.218	6.482	-6.89	-2.37
Spin coated TiO_2 mixture	3.588	6.970	+3.82	+4.99
Drop cast TiO_2 mixture (25 µl)	4.088	8.650	+18.27	+30.29
Drop cast TiO_2 mixture (50 µl)	3.804	8.088	+10.07	+21.83
Drop cast TiO_2 mixture (100 µl)	3.502	8.868	+1.33	+33.57
Drop cast TiO_2 mixture (200 µl)	2.792	6.698	-19.21	+0.89
Doctor bladed counter electrode	4.321	11.481	+25.04	+72.94

Table 62: PCE and J_{SC} data for $Sr_4Al_{14}O_{25}$: Eu^{2+}, Dy^{3+} doped screen printed DSSCs at 1 sun.

Device Category	V_{OC} (mV)	FF	ΔV_{OC} (%)	Δ FF (%)
Control	849.892	0.613	-	-
Doctor bladed on TiO_2	864.978	0.574	+1.78	-6.36
Spin coated TiO_2 mixture	855.000	0.604	+0.60	-1.47
Drop cast TiO_2 mixture (25 µl)	804.000	0.588	-5.40	-4.08
Drop cast TiO_2 mixture (50 µl)	832.934	0.572	-2.20	-6.69
Drop cast TiO_2 mixture (100 µl)	767.925	0.514	-9.64	-16.15
Drop cast TiO_2 mixture (200 µl)	779.612	0.546	-8.27	-10.93
Doctor bladed counter electrode	797.600	0.475	-6.15	-22.51

Table 63: V_{OC} and FF data for $Sr_4Al_{14}O_{25}$: Eu^{2+}, Dy^{3+} doped screen printed DSSCs at 1 sun.

Device Category	η (%)	J_{SC} (mA/cm^2)	Δη (%)	Δ J_{SC} (%)
Control	3.456	6.639	-	-
Doctor bladed on TiO_2	2.142	3.846	-38.02	-42.07
Spin coated TiO_2 mixture	3.701	7.485	+7.09	+12.74
Drop cast TiO_2 mixture (25 µl)	4.303	9.004	+24.50	+35.63
Drop cast TiO_2 mixture (50 µl)	5.303	12.412	+53.44	+86.96
Drop cast TiO_2 mixture (100 µl)	2.798	5.439	-19.04	-18.07
Drop cast TiO_2 mixture (200 µl)	2.871	6.479	-16.94	-2.42
Doctor bladed counter electrode	5.029	11.921	+45.53	+79.55

Table 64: PCE and J_{SC} data for $NaYF_4$: Er^{3+}, Yb^{3+} doped screen printed DSSCs at 1 sun.

Device Category	V_{OC} (mV)	FF	ΔV_{OC} (%)	Δ FF (%)
Control	849.892	0.613	-	-
Doctor bladed on TiO_2	836.700	0.666	-1.55	+8.65
Spin coated TiO_2 mixture	851.700	0.585	+0.21	-4.57
Drop cast TiO_2 mixture (25 µl)	775.800	0.606	-8.72	-1.14
Drop cast TiO_2 mixture (50 µl)	779.007	0.544	-5.99	-11.26
Drop cast TiO_2 mixture (100 µl)	788.800	0.652	-7.19	+6.36
Drop cast TiO_2 mixture (200 µl)	756.500	0.591	-10.99	-3.59
Doctor bladed counter electrode	798.000	0.526	-6.11	-14.19

Table 65: V_{OC} and FF data for $NaYF_4$: Er^{3+}, Yb^{3+} doped screen printed DSSCs at 1 sun.

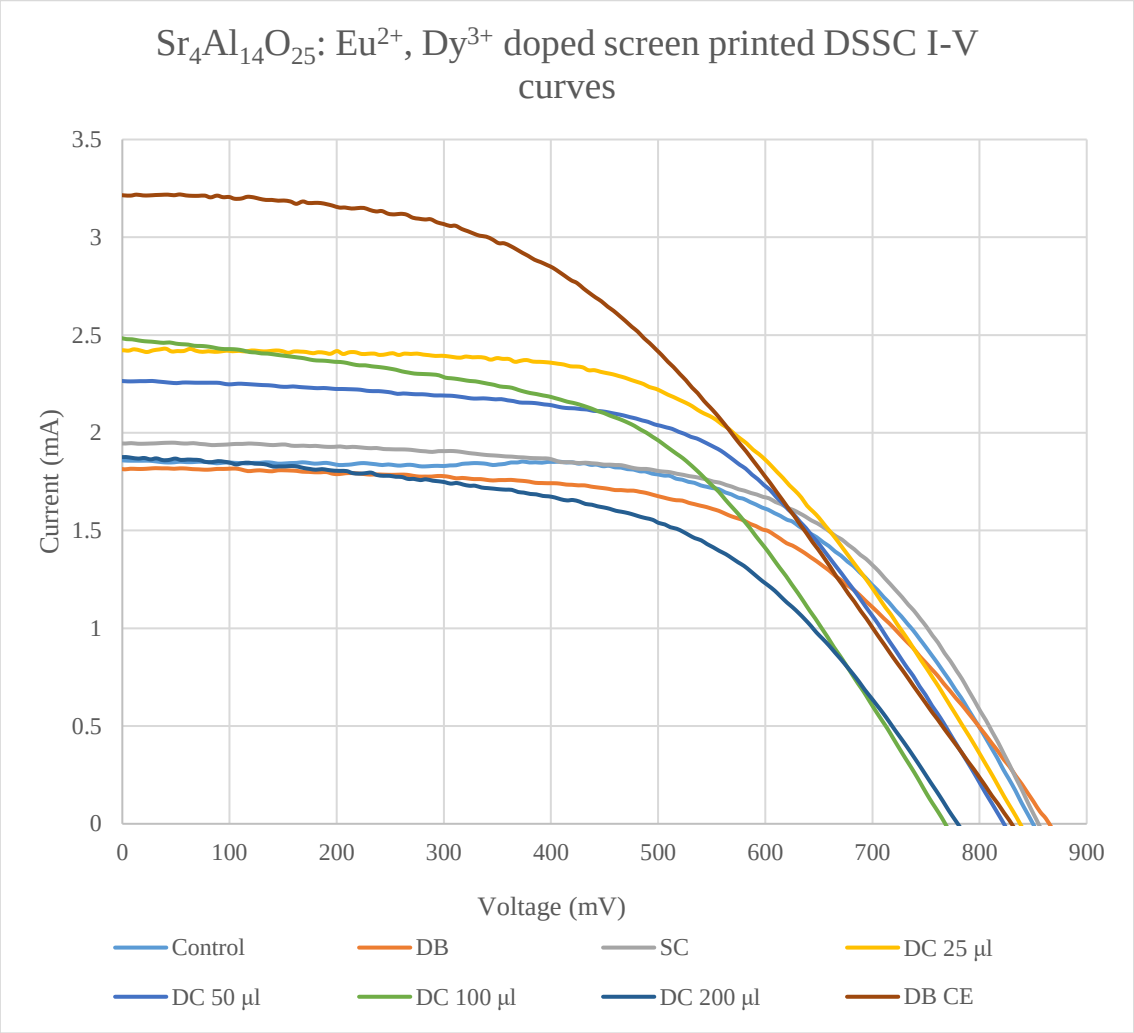

Figure 136: I-V curves for the $Sr_4Al_{14}O_{25}$: Eu^{2+}, Dy^{3+} doped screen printed DSSCs at 1 sun.

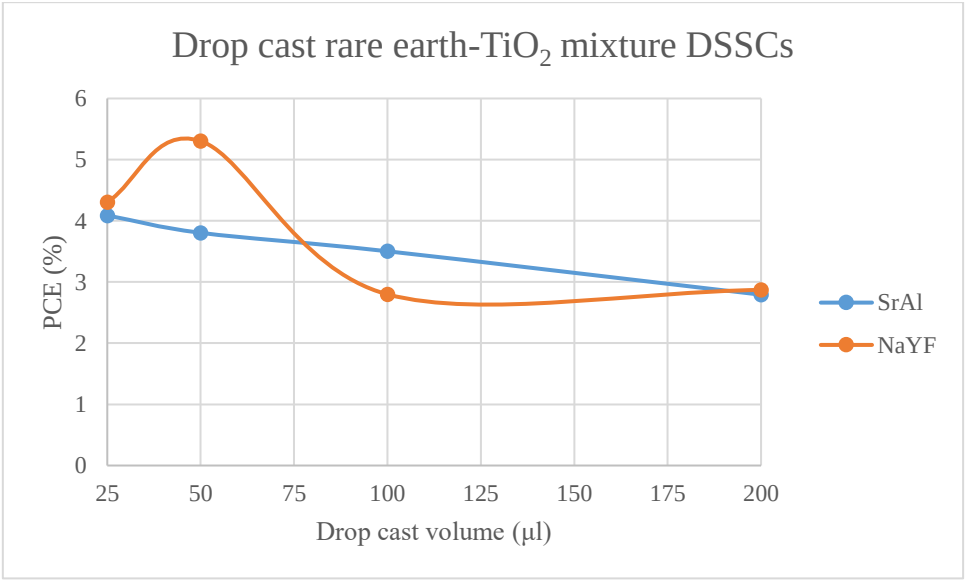

Figure 137: PCE against layer thickness (drop cast volume) for both rare earth doped compounds.

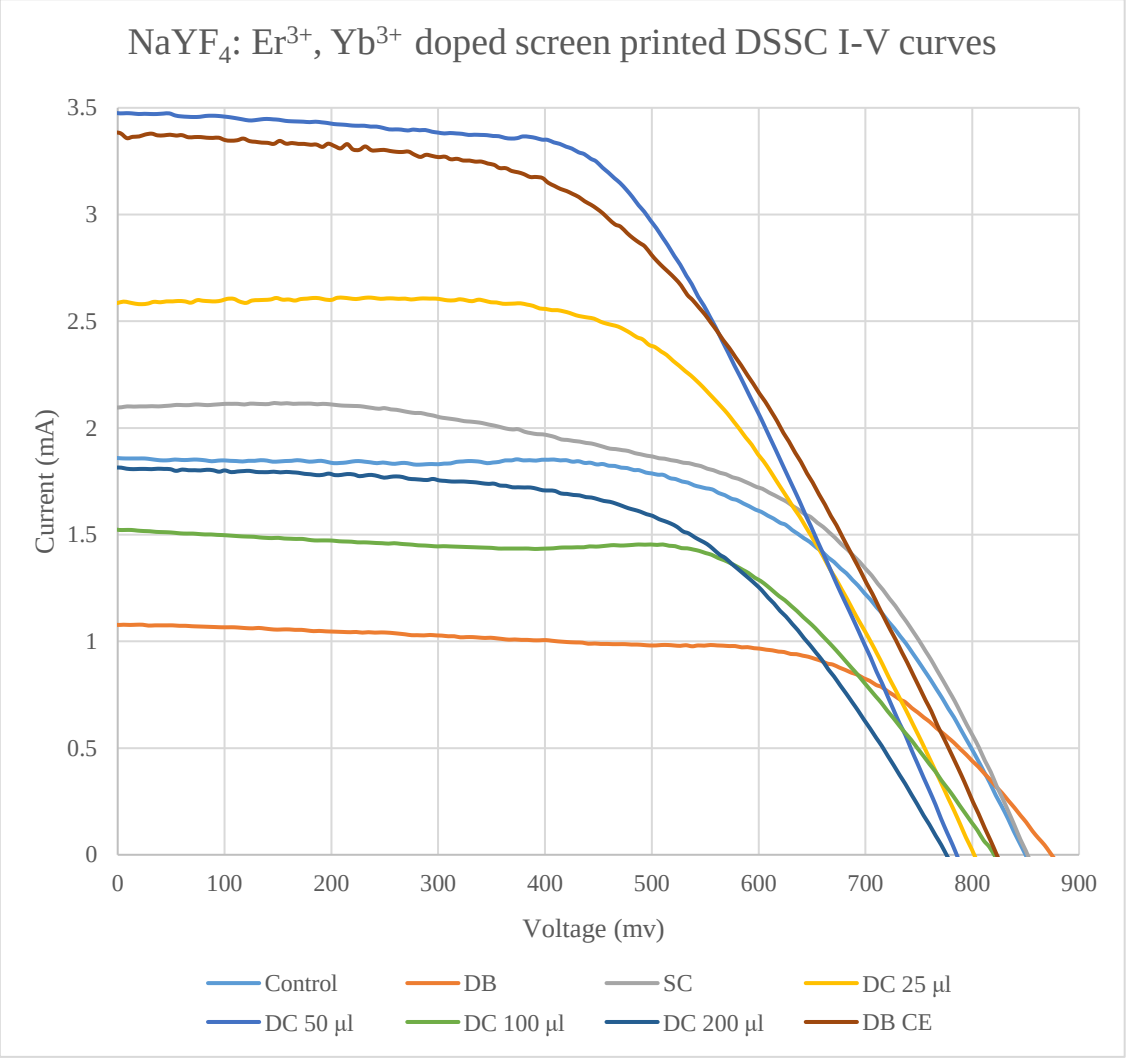

Figure 138: I-V curves for the $Sr_4Al_{14}O_{25}$: Eu^{2+}, Dy^{3+} doped screen printed DSSCs at 1 sun.

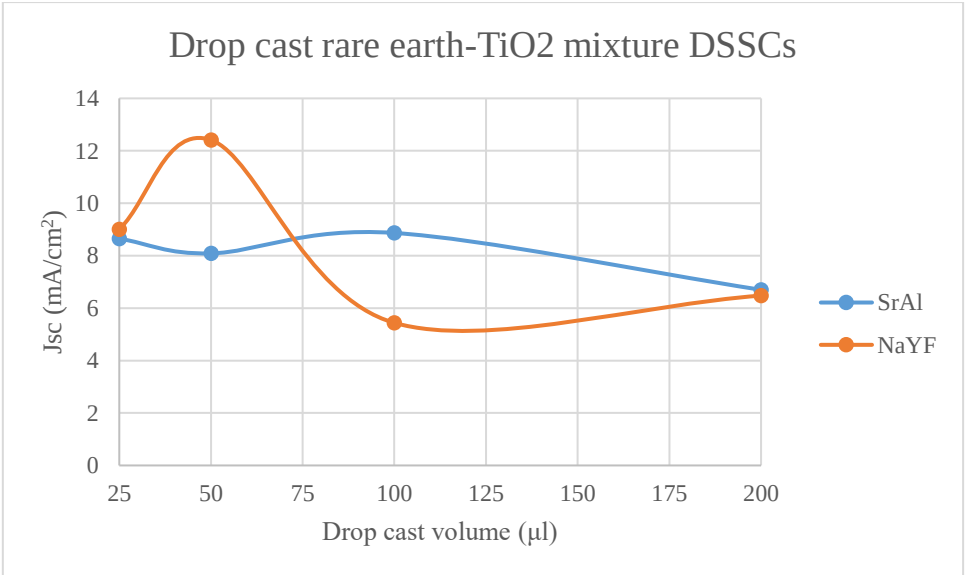

Figure 139: PCE against layer thickness (drop cast volume) for both rare earth doped compounds.

5.5.2 Incident Photon-to-electron Conversion Efficiency

It was also intended, as with the silicon PV devices, to measure the EQE of the DSSCs with the Bentham PVE300. This was possible by following a different characterisation procedure, necessary due to the lower current signals of a DSSC. In this case, the transformer was not used and instead the direct current mode of the signal processor was chosen. The connections were set up in a similar way to when reflectance measurements were made in chapter 3, such that the test cell was connected directly to the 497 current pre-amplifier which had an output to the 496 lock in amplifier. In addition, the chopper was turned off (because of the weaker signal from DSSCs) and the wire connecting the cell and the 497 was a coaxial cable with one end split into two cables, so that two further crocodile clip wires could be attached to their ends and to the DSSC anode and cathode respectively. Finally, the calibration was applied in the same method as before, but the silicon reference cell was connected without transformer and into the 497. The resulting spectra for the control DSSC and best performing rare earth doped device are shown in Figure 140.

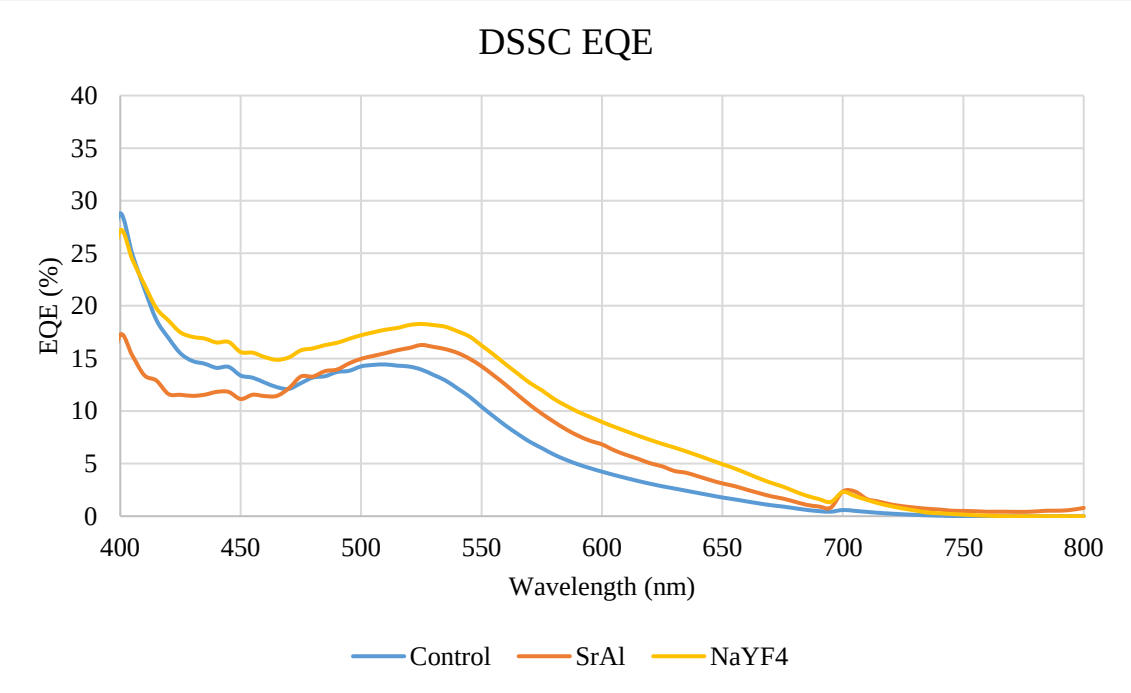

Figure 140: EQE spectra for the control and best performing rare earth doped DSSCs for each material.

5.5.3 Discussion

It can be noted from the data and I-V curves that, in general, the presence of rare earth doped compounds increased the performance characteristics of the DSSCs, particularly the PCE and J_{SC} which are of primary concern in this work. It was observed that the spin coated devices clearly performed worse than the DSSCs with screen printed working electrodes. This was likely because of their TiO_2 layer being so thin, meaning much less of the incident light can be absorbed and converted to current. However, the high transparency of these cells could lead to more potential for spin coated devices, following a more optimal fabrication procedure and the addition of rare earth compound (albeit primitively), still resulted in increased performance for the 0.5% w/w doped $NaYF_4$: Er^{3+}, Yb^{3+} in TiO_2. In addition, the rise in V_{OC} for 3 out of 4 of these doped devices could be due to the change in Fermi level raising the electron potential or reduced recombination at the working electrode interface [260]. Although, this benefit in the majority of cases was outweighed by the decrease in J_{SC} (perhaps due to weaker dye adsorption and hence absorption in the presence of $NaYF_4$: Er^{3+}, Yb^{3+}) that hampered the overall PCE.

The screen printed DSSCs on the other hand achieved PCEs, over an order of magnitude greater than their spin coated counter parts and more recognisable performance enhancements owing to their greater layer thickness and more meticulous method of adding the rare earth compounds. For example, the control spin coated TiO_2 electrode DSSC with no added rare earth compound achieved a PCE of 0.16% compared to 3.46% for its control screen printed counterpart (a 22-fold increase). Likewise, the J_{SC} between the two fabrication methods rose from 0.51 mA/cm^2 for spin coating to 6.64 mA/cm^2 for screen printing (a 13-fold increase). The FFs and V_{OC} did not change so drastically but were still slightly higher for the screen printed control device at 0.61 and 850 mV vs 0.42 and 764 mV for the un-doped spin coated DSSC.

In most instances, the devices containing the spectral conversion materials showed higher PCE and J_{SC} with the exceptions of the rare earth compound only doctor bladed layer on top of the TiO_2 (for both materials), the 200 µl drop casted TiO_2-$Sr_4Al_{14}O_{25}$: Eu^{2+}, Dy^{3+} mixture and the 100 and 200 µl drop casted TiO_2-$Sr_4Al_{14}O_{25}$: Eu^{2+}, Dy^{3+} mixture. As with chapter 3 and 4, the PCE and J_{SC} increases were correlated across all devices, meaning more current being

generated is primarily responsible for the enhanced performance. Although unlike the spin coated devices, the addition of rare earth compounds did not consistently raise the V_{OC} or FF, as this time these quantities were mostly decreased.

In terms of PCE, the stronger performing devices for both materials were the (25 and 50 µl) drop casted TiO_2-rare earth mixture and doctor bladed counter electrode as compared to the other methods of applying the TiO_2 rare earth mixture. The reasons for this could be because of the thicker layer, leading to more potential for interaction with the spectral conversion particles and because of optical scattering, increasing the light path travelled and current generated. Also the fact the impurities are located at the top of the mesoporous TiO_2 and not throughout it means dye adsorption is not curtailed, which is why a high J_{SC} is still recorded [330]. On the contrary, the large enhancement from the unconventional approach of coating the counter electrode, could be down to the lack of interference with the charge carrier dynamics of the DSSC's working electrode, with the rare earth layer acting separately to capture more light via spectral conversion or even simple optical reflection. However, there is an effect on the charge-carrier behaviour at the counter electrode, as demonstrated by a decrease in FF and V_{OC} but compensated by a sharp increase in J_{SC}. These changes could be because the sheet resistance goes up (lowering FF) and a mismatch to the electrolyte redox potential is introduced, increasing the over-potential (lowering V_{OC}) but quickening the replenishment of ions (raising J_{SC}) [331].

Comparing the two rare earth compounds, for $Sr_4Al_{14}O_{25}$: Eu^{2+}, Dy^{3+}, the best device was the coated counter electrode which displayed a 4.32% PCE and J_{SC} of 11.48 mA/cm^2, corresponding to relative increases of 25% and 73% compared to the control device. However, for $NaYF_4$: Er^{3+}, Yb^{3+}, the coated counter electrode was the second most improved device and the single highest PCE (across both rare earth compounds) was recorded for the 50 µl drop casted TiO_2-rare earth compound mixture. This DSSC exhibited a remarkable increase in its PCE and J_{SC} to 5.30% and 12.41 mA/cm^2 respectively (53% and 87% relative enhancements).

The relationship between the layer thicknesses of each drop casted material mixture was also explored as shown in Figures 137 and 139. It can be seen in general that for both materials the thinner drop casted layers performed better,

although the optimum for $NaYF_4$: Er^{3+}, Yb^{3+} was deemed to be 50 µl and 25 µl for $Sr_4Al_{14}O_{25}$: Eu^{2+}, Dy^{3+}. These discrepancies could be due to the different absorption coefficients of the two materials and there could be evidence of consistency with the earlier silicon PV investigations. In chapter 4, it was claimed the homogenously doped $NaYF_4$: Er^{3+}, Yb^{3+} concentrator performed better over longer optical path lengths due to its lower absorption coefficient. The same theory would explain why a thicker layer of $NaYF_4$: Er^{3+}, Yb^{3+} is required to deliver the best performance enhancement. However, as seen by the 100 µl and 200 µl measurements, if the layer becomes too thick, then parasitic absorption will dominate the desirable optical and luminescent processes. Alternatively, too thin a layer is not good as demonstrated by the poorer performances of both the spin coated TiO_2-rare earth mixtures. This also means, there must be an optimal thickness for the $Sr_4Al_{14}O_{25}$: Eu^{2+}, Dy^{3+} doped TiO_2 between that of the spin coated and 25 µl drop casted layer.

Lastly, and in contrast to earlier chapters, the DSSC EQE measurements were inconclusive and not immediately indicative of spectral conversion being very responsible for increased performance. This is because they did not show much improvement in EQE at the expected wavelengths of rare earth compound excitation (400-450nm) whereas they surprisingly did show a higher spectral response in the 500-650 nm region. Positively, the EQE profile of the control cell did follow approximately the predicated shape according to Figure 128, in which EQE broadly follows the absorption of the N719 dye, with peaks at < 400 nm and 520 nm, and no response beyond 730 nm where the dye cannot absorb photons. Although, in these fabricated cells the minimum has shifted towards 450 nm which is unusual. This could be for one of two reasons; either a systematic error from the measuring equipment or the suggestion that the increased performance is not down to spectral conversion alone. This would mean the better performance across all wavelengths is due to some other process such as scattering or anti-reflective properties. In fact, if spectral conversion was dominant, one would expect the $Sr_4Al_{14}O_{25}$: Eu^{2+}, Dy^{3+} to outperform $NaYF_4$: Er^{3+}, Yb^{3+} in terms of PCE and J_{SC} as the emission wavelength of the former (500 nm) corresponds better to a high EQE for N719 based DSSCs than the latter's 660 nm. Nevertheless, this does not necessarily mean spectral conversion is not taking place, rather it just may be dominated by the other processes which are

amplified because unlike the silicon cells, these materials are located inside the PV cell itself.

5.6 SEH Concentrators on DSSCs

Concentrators can be coupled with DSSCs to increase the light flux and hence power output from a device [332]. This reduces the area of cells required and can potentially lower electricity costs. Moreover, since the rare earth doped compound SEH concentrators (particularly the top and bottom doped $Sr_4Al_{14}O_{25}$: Eu^{2+}, Dy^{3+} varieties) were effective in improving the efficiency of silicon PV cells, it would be interesting to see if this enhancement could be repeated for DSSCs. To test this concept, 3 concentrators were placed on top two types of DSSC and their performance was characterised under the solar simulator. The DSSCs to be tested were the un-doped control device (the natural choice to see if the doped concentrators themselves could raise device performance) along with a rare earth doped DSSC, $Sr_4Al_{14}O_{25}$: Eu^{2+}, Dy^{3+} - TiO_2 mixture 100 µl drop casted. The concentrators used were the 0.1% w/w $Sr_4Al_{14}O_{25}$: Eu^{2+}, Dy^{3+} top and bottom doped concentrators (as they gave the best results in chapter 4), as well as the plain SEH concentrator to act as a control. Although they are not ideally shaped, having a 1 cm^2 exit aperture on to 0.28 cm^2 active area of DSSC, they should still attain a higher light concentration incident on the device. Furthermore, illumination levels were varied to 1, 0.8, 0.6 and 0.4 sun(s) in order to see if any effects similar to those in chapter in 4 would be observed (e.g. if performance enhancement changes with reduced light irradiance).

The key results are displayed in Tables 66-69 with I-V curves in Figures 141 and 143. The scope of this presented data was limited to maximum power output, P_{max}, and J_{SC} instead of PCE (because the increased receiving area of the module as in chapter 4 will lower the PCE for LCPV devices and the main motivation of using concentrators is to get more power per area not a higher PCE). ΔP_{max} and ΔJ_{SC} are defined relative to the DSSC type with no concentrator (i.e. no comparison between doped and control DSSC) and the former is shown for each type of concentrator in Figures 142 and 144. It is noted that at 1 sun, P_{max} was increased by all concentrators to a maximum of 1.32 mW for the control DSSC and 1.24 mW for the doped DSSC, relative enhancements of 36.3% and 26.4% respectively. As expected, increased J_{SC} accompanied these enhancements, rising up to 48.3% and 32.7% for the control and doped DSSC.

It was the bottom doped concentrator that achieved these best results, followed by the plain (un-doped) concentrator and top doped concentrator. The optical efficiencies of the concentrators in this set up can be calculated by dividing the J_{SC} with the concentrator by the J_{SC} without the concentrator and multiplying by G (=3.534), and are 41.9%, 39.3% and 38.0% for the bottom doped, plain and top doped concentrators respectively, using data for the control cell. The reason for the better performance of the bottom doped concentrator could be that more emission was originating from closer to the cell, so that the radiation cone reaching it is a larger portion of the total emitted in all directions. Likewise, the top doped concentrator fails to raise efficiency because a smaller portion of its emission reaches the cell. This idea will be further explored in a model that features in the next chapter.

Furthermore, the un-doped DSSC may have been enhanced more relatively because less light of the spectral conversion excitation wavelength is reaching the cell when a concentrator is placed above. However, by observing the data for lower irradiances, it can be seen a similar phenomenon to chapter 4 is observed in that the rare earth containing device's performance is relatively more enhanced at lower irradiances. For example, considering the bottom doped concentrators, at 0.8 suns the doped DSSC sees a ΔP_{max} of 37.8% vs 34.2% for the control DSSC. Similarly, at 0.6 and 0.4 suns the doped DSSC records a greater ΔP_{max} (4.7% higher at 0.6 suns and 8.9% higher at 0.4 suns). This finding could be attributed to the same behaviour proposed in the earlier chapter in that the spectral conversion quantum yield and cell collection efficiency fall at different rates with reduced light intensity.

Device Category	P_{max} (mW)	J_{SC} (mA/cm^2)	ΔP_{max} (%)	ΔJ_{SC} (%)
Control DSSC (no concentrator)	0.968	6.639	-	-
Control DSSC (plain conc.)	1.267	9.225	+30.93	+38.95
Control DSSC (top concentrator)	1.223	8.914	+26.39	+34.27
Control DSSC (bottom conc.)	1.319	9.843	+36.29	+48.25
Doped DSSC (no concentrator)	0.981	8.868	-	-
Doped DSSC (plain conc.)	1.172	11.214	+19.53	+26.46
Doped DSSC (top concentrator)	1.126	10.575	+14.85	+19.25
Doped DSSC (bottom conc.)	1.240	11.768	+26.41	+32.70

Table 66: P_{max} and J_{SC} data for control and rare earth doped screen printed DSSCs with SEH concentrators under 1 sun.

Device Category	P_{max} (mW)	J_{SC} (mA/cm^2)	ΔP_{max} (%)	ΔJ_{SC} (%)
Control DSSC (no concentrator)	0.802	5.425	-	-
Control DSSC (plain conc.)	1.046	7.421	+30.32	+36.80
Control DSSC (top concentrator)	0.996	7.054	+24.08	+30.02
Control DSSC (bottom conc.)	1.077	7.764	+34.19	+43.12
Doped DSSC (no concentrator)	0.773	6.757	-	-
Doped DSSC (plain conc.)	0.993	8.946	+28.56	+32.40
Doped DSSC (top concentrator)	0.990	8.868	+28.09	+31.24
Doped DSSC (bottom conc.)	1.065	9.736	+37.80	+44.08

Table 67: P_{max} and J_{SC} data for control and rare earth doped screen printed DSSCs with SEH concentrators under 0.8 suns.

Device Category	P_{max} (mW)	J_{SC} (mA/cm^2)	ΔP_{max} (%)	ΔJ_{SC} (%)
Control DSSC (no concentrator)	0.605	3.893	-	-
Control DSSC (plain conc.)	0.780	5.354	+28.98	+37.52
Control DSSC (top concentrator)	0.759	5.218	+25.46	+34.04
Control DSSC (bottom conc.)	0.813	5.686	+34.44	+46.06
Doped DSSC (no concentrator)	0.617	5.068	-	-
Doped DSSC (plain conc.)	0.792	6.614	+28.38	+30.51
Doped DSSC (top concentrator)	0.792	6.668	+28.38	+31.57
Doped DSSC (bottom conc.)	0.858	7.321	+39.10	+44.47

Table 68: P_{max} and J_{SC} data for control and rare earth doped screen printed DSSCs with SEH concentrators under 0.6 suns.

Device Category	P_{max} (mW)	J_{SC} (mA/cm^2)	ΔP_{max} (%)	ΔJ_{SC} (%)
Control DSSC (no concentrator)	0.410	2.414	-	-
Control DSSC (plain conc.)	0.535	3.282	+30.29	+35.95
Control DSSC (top concentrator)	0.515	3.136	+25.38	+29.88
Control DSSC (bottom conc.)	0.542	3.332	+31.92	+38.02
Doped DSSC (no concentrator)	0.406	3.129	-	-
Doped DSSC (plain conc.)	0.534	4.164	+31.43	+33.11
Doped DSSC (top concentrator)	0.497	3.893	+22.33	+24.43
Doped DSSC (bottom conc.)	0.568	4.518	+39.83	+44.41

Table 69: P_{max} and J_{SC} data for control and rare earth doped screen printed DSSCs with SEH concentrators under 0.4 suns.

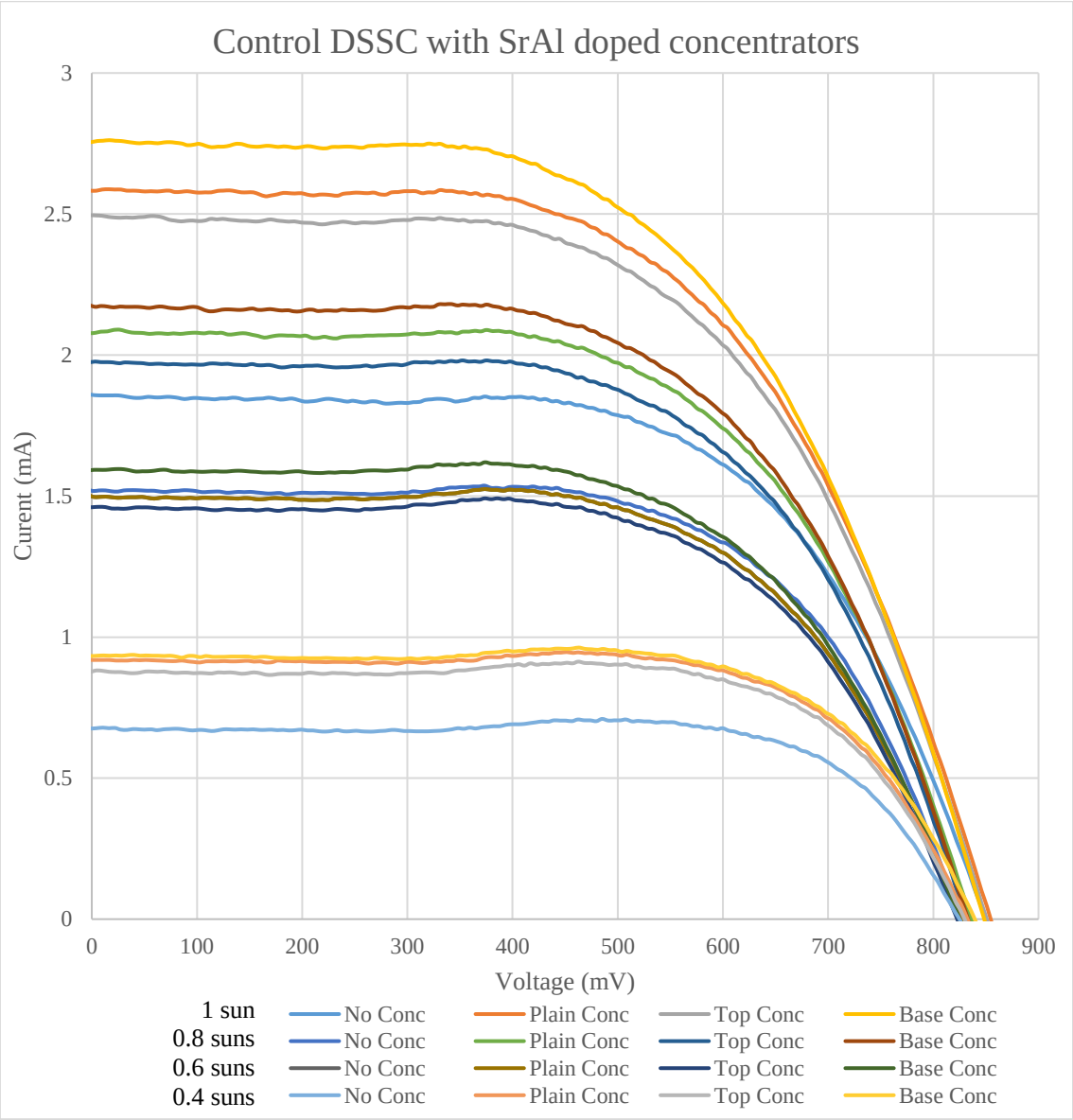

Figure 141: I-V curves for the control screen printed DSSCs with SEH concentrators at varying irradiance levels.

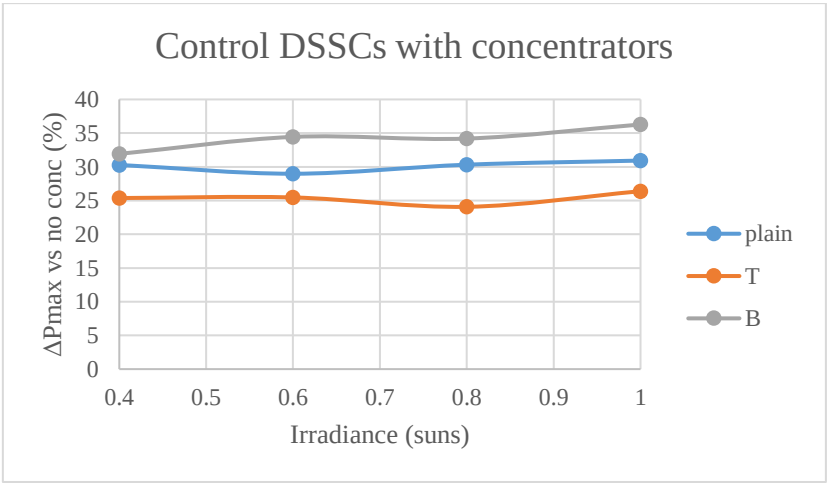

Figure 142: ΔP_{max} for the plain, top and bottom doped concentrators compared to without concentrators for the control DSSC at varying irradiance levels.

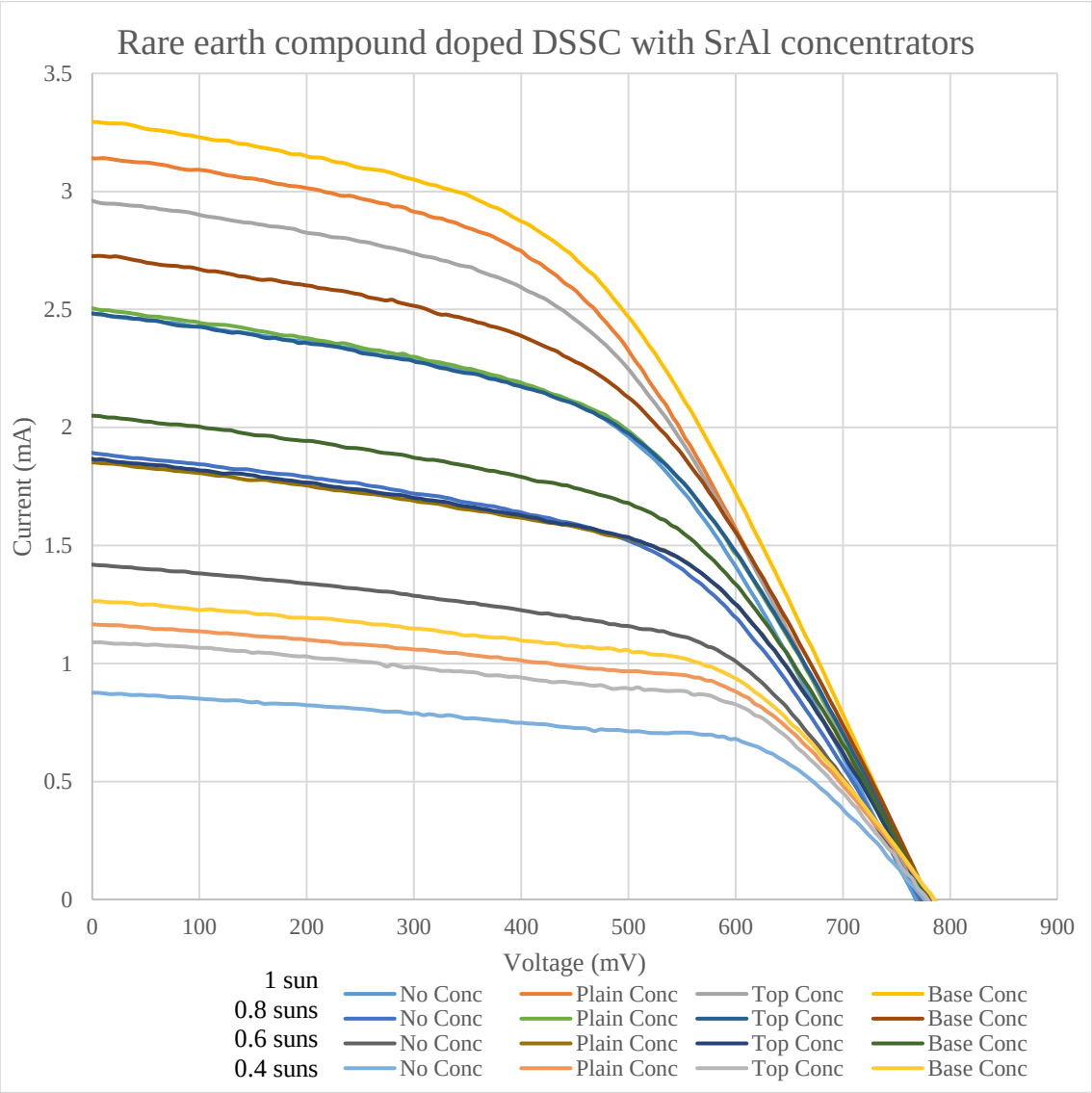

Figure 143: I-V curves for the rare earth doped screen printed DSSCs with SEH concentrators at varying irradiance levels.

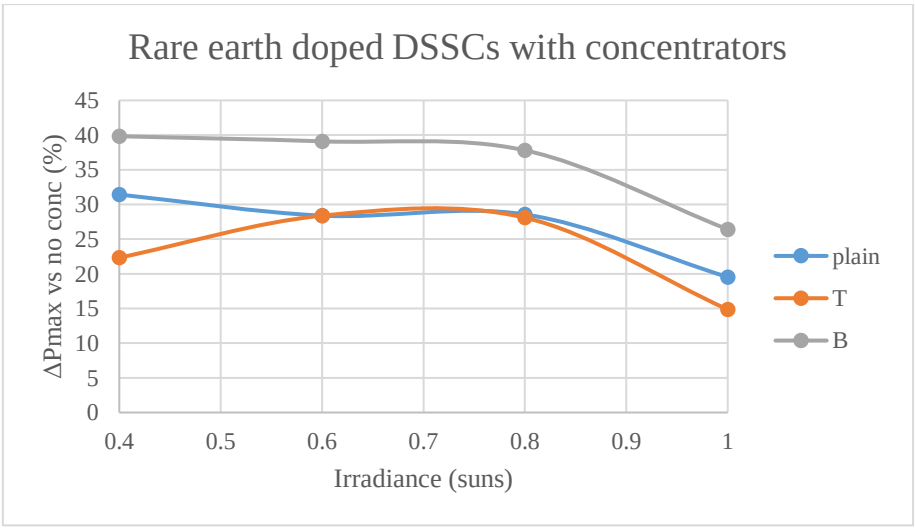

Figure 144: ΔP_{max} for the plain, top and bottom doped concentrators compared to without concentrators for the rare earth doped DSSC at varying irradiance levels.

5.7 Y_2O_3: Yb^{3+}, Tm^{3+}, Ho^{3+} and Y_2O_3: Yb^{3+}, Ho^{3+} in Porphyrin-Carbon Counter Electrode Based DSSCs

Another type of DSSC that utilised a different dye and counter electrode as opposed to the widely used N719 and Pt coated FTO was fabricated in collaboration with Dr. Nanaji Islavath at the Indian Institute of Chemical Technology (IICT), Hyderabad, India. The basic device sandwich structure and operating principle were the same as earlier Figure 125, with a dye adsorbed TiO_2 working electrode and $I_3^-/3I^-$ electrolyte solution providing the necessary steps for the generation of current. However, the devices in this subsection used a type of porphyrin dye as a photosensitizer instead of N719. This class of dyes have long been investigated as an alternative DSSC material due to their intense visible light absorption, easily tuneable electronic structure and modifiable core. Further motivation comes from their potential lower cost than ruthenium based N719 because porphyrin molecules can contain inexpensive metals such as zinc at their coordination centre or even no metal at all [333]. Although one factor that has held back porphyrin dyes' widespread use in devices is their poor response to light at wavelengths around 600 nm. Nevertheless, recent advances in the designing of donor-π-acceptor (D-π-A) dyes, in which an organic molecule and carboxyl group are attached to opposing sides of the porphyrin macrocycle, have led to significantly higher device efficiencies due to the enhanced light absorption. Specifically, work by Krishna et al has identified LG5 (structure outlined in Figure 145) as a strongly performing and highly stable dye, demonstrating DSSC PCE above 10% and 8% after 1000 hours of exposure [334]. Thus, there is exciting potential from LG5, so it is an ideal type of dye to explore in DSSC spectral conversion studies.

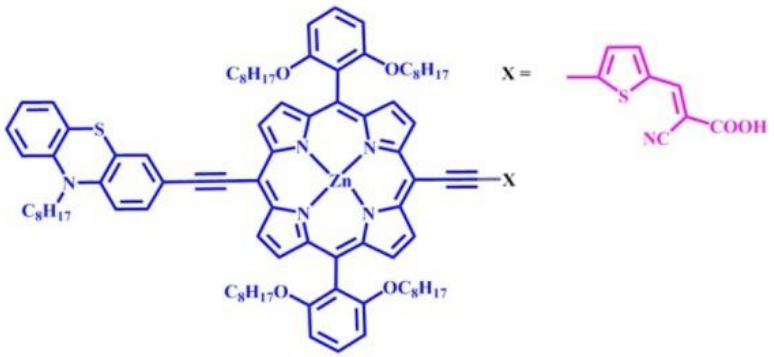

Figure 145: Structure of the porphyrin dye LG5 used in the DSSCs in this section. Taken from [334].

Likewise, the counter electrode, until now made from Pt (which contributes significantly to the device cost) was replaced with a cheaper option. Carbon is deemed a suitable alternative due to its low cost, high surface area to volume ratio, catalytic activity, electrical conductivity, thermal stability, corrosion resistance and reactivity with respect to the reduction of the I_3^- ion. A review of advances in carbon electrodes and a critical comparison with metallic options are presented by Wu et al [331]; from their analysis carbon is shown to be the most popular choice for counter electrode coatings featuring in 23% of DSSC articles and 47% of patents as of 2017. The new allotrope, graphene, may present further opportunities due to its excellent electrical properties but is currently limited by its high production cost.

In order to make this alternative counter electrode, an FTO glass substrate (with a prior drilled small aperture to allow the injection of liquid electrolyte) was coated with graphite/carbon paste (Elcocarb B/SP from Solaronix) by a doctor blading method. This paste contains 1-20 µm graphite particles and carbon black nanoparticles, like the 18NR-T, in a viscous gel of organic binders that on heating forms an opaque black, conductive and mesoporous layer. Through covering the rest of the 2 cm x 2 cm FTO substrate with tape, a 1 cm^2 square of carbon paste was deposited via doctor blading, then removing the tape and annealing at 200°C in a furnace oven for 30 minutes.

Furthermore, the rare earth compounds used to dope these types of devices were also different, having been prior synthesised by the IICT group. The two materials of focus were Y_2O_3: Yb^{3+}, Tm^{3+}, Ho^{3+} and Y_2O_3: Yb^{3+}, Ho^{3+}, known respectively as Y and C. Chemically identical compounds have demonstrated photoluminescence in the form of UC emission at visible wavelengths 550 nm for the co-doped Y_2O_3 and 550 nm along with 475 nm for the tri-doped Y_2O_3 at NIR 980 nm excitation [335, 336]. Furthermore Huang et al have listed transitions in the Ho^{3+} and Tm^{3+} ions with strong intensity that would produce 450-675 nm emission through DC of high energy photons; $^1G_4 \rightarrow {}^3H_6$ or $^3F_4$ in Tm^{3+} would result in the emission of a 475 or 650 nm photon and $^5S_2$ or $^5F_4 \rightarrow {}^5I_8$ in Ho^{3+} causes a 540 nm photon to be emitted [75].

Physically, they were both whitish powders and like the previously used compounds, the two new luminescent materials had to be prepared into a gel or solution, so that a thin film that could be applied to the working electrodes of a

DSSC; as with prior work, the materials were to be incorporated within the mesoporous TiO_2 layer. This was achieved by taking 10 mg of Y and C in separate vials and adding 100 µl of deionised water to each and subjecting to ultra-sonication for 5 minutes. Next, 2.5 ml of ethanol was added to the resulting mixtures and they were sonicated for a further 5 minutes. Then, 100 µl of concentrated hydrochloric acid was pipetted dropwise and ultra-sonication undertook for another 5 minutes, before finally adding a further 2.5 ml of ethanol and sonicating for 20 minutes, until the solution was homogenous and clearer in colour. It had been initially suggested to add this solution to the base of the working electrode, so it would sit entirely below the TiO_2 layer an act as a transparent blocking layer, although early tests from spin coating the solution on a glass substrate and drying in a furnace at 150°C, did not produce a quality film, despite displaying a high transparency. Therefore, it was decided to disperse them evenly within the mesoporous layer as per earlier Figure 131 (a).

Next, to combine this mixture with the TiO_2 paste, 100 mg of 18NR-T (the same material from the same supplier that had been used for the rest of this chapter's devices) was placed in an agate mortar and 1200 µl of the Y or C solution was added in batches and mixed thoroughly with the pestle for 20 minutes. During this process a change in colour from orange to blue was observed and it was calculated that the rare earth compound content of the TiO_2 anode would be 2.3% w/w. The resulting rare earth compound-TiO_2 composite was to be doctor bladed, as opposed to screen printed as per previous samples. It was doctor bladed in an identical technique to how the carbon counter electrodes were made to produce a coating but with a slightly smaller square area of 0.81 cm^2. This was then annealed up to 500°C for 30 minutes in the furnace oven and cooled over a period of 90 minutes.

In an analogous procedure as before, the working electrodes were then soaked in the pre-prepared LG5 porphyrin dye for 24 hours. After removing from the dye and drying, Surlyn spacer was cut to size and placed around the boundaries of the active area. Finally, the triiodide liquid electrolyte (of same composition as used previously in 5.3) was injected into the device and the hole was sealed. Once fabricated, devices were tested under the group's solar simulator (Newport, 94043A), a different model but one that had still been calibrated to AM 1.5 G conditions by an NREL reference cell. Naturally, a control device with no Y or C

in the TiO_2 layer was fabricated for the purpose of comparison. Unfortunately, the first batch of devices performed poorly which was attributed to the presence of hydrochloric acid increasing recombination pathways, so fresh ones were made that added TBP in 0.5 M concentration to the electrolyte, in order to mitigate this effect. The results for these devices are shown in Figures 146 and 147 and Tables 70 and 71, along with a real image of this type of DSSC in Figure 148.

It can be seen that the Y containing devices performed better than the control, exhibiting relative increases in PCE and J_{SC} of 10.3% and 8.5% respectively, whereas the C containing DSSCs recorded slightly weaker PCE and J_{SC} values (relative decreases of 5.3% and 6.8% respectively, compared to the control). The parameter enhancements through the addition of Y could be attributed to the additional current generated by the UC of NIR photons and DC of UV photons. The presence of three rare earth ions in Y as opposed to just two in C could explain the superior performance of the former, since it leads to more possible transitions for spectral conversion processes and hence Y could absorb a wider part of the spectrum. Moreover, the Yb^{3+} ion could potentially sensitise both the Ho^{3+} and Tm^{3+} ions to make their emission more effective. Also, of note, the V_{OC} for both rare earth compound doped DSSCs was higher (implying a higher Fermi level), while FF was lowered with respect to the un-doped DSSC.

Finally, and a unique focus of this subsection, the PCE was recorded for the classes of device at several intervals over a 90-day exposure to ambient air and sunlight. Here the effect of the rare earth doping became more apparent as after 90 days, the Y doped device remarkably retained 40% of its original PCE compared to just 5% for the control device over the same period. C also kept 18% of its initial PCE over the course of the observations. It can therefore be concluded that the presence of the rare earth compound significantly increases the stability of the device PCE over time by spectral conversion of the incident UV radiation, which slows the degradation of the dye.

Device type	η (%)	J_{SC} (mA/cm^2)	Δη (%)	Δ J_{SC} (%)
Control (TiO_2 only)	8.90	17.49	-	-
C-TiO_2	8.43	16.31	-5.28	-6.75
Y-TiO_2	9.82	18.97	+10.34	+8.46

Table 70: PCE and J_{SC} data for control and rare earth doped porphyrin-carbon counter electrode DSSCs under 1 sun.

Device type	V_{OC} (mV)	FF	ΔV_{OC} (%)	Δ FF (%)
Control (TiO_2 only)	752	0.677	-	-
C-TiO_2	773	0.669	+2.79	-1.18
Y-TiO_2	791	0.655	+5.19	-3.25

Table 71: V_{OC} and FF data for control and rare earth doped porphyrin-carbon counter electrode DSSCs under 1 sun.

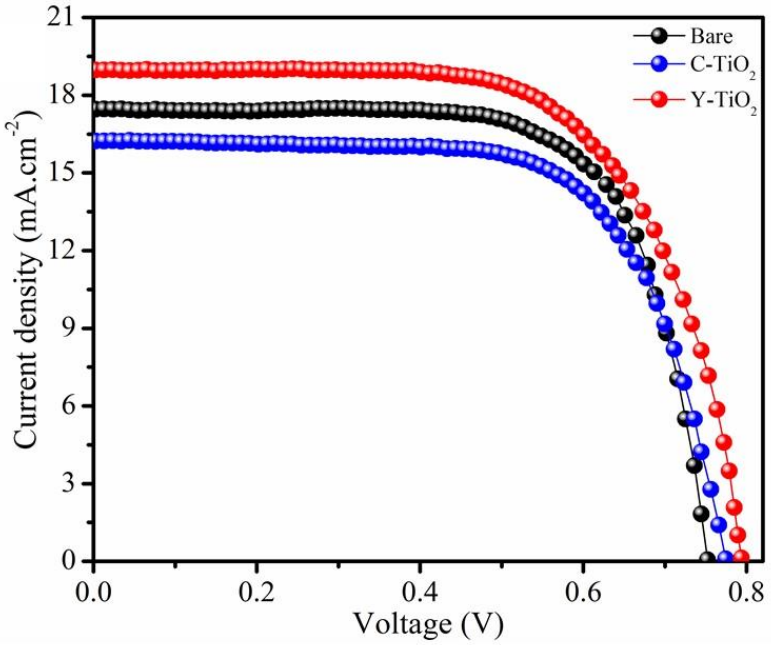

Figure 146: J-V curves for the rare earth doped porphyrin-carbon counter electrode DSSCs under 1 sun.

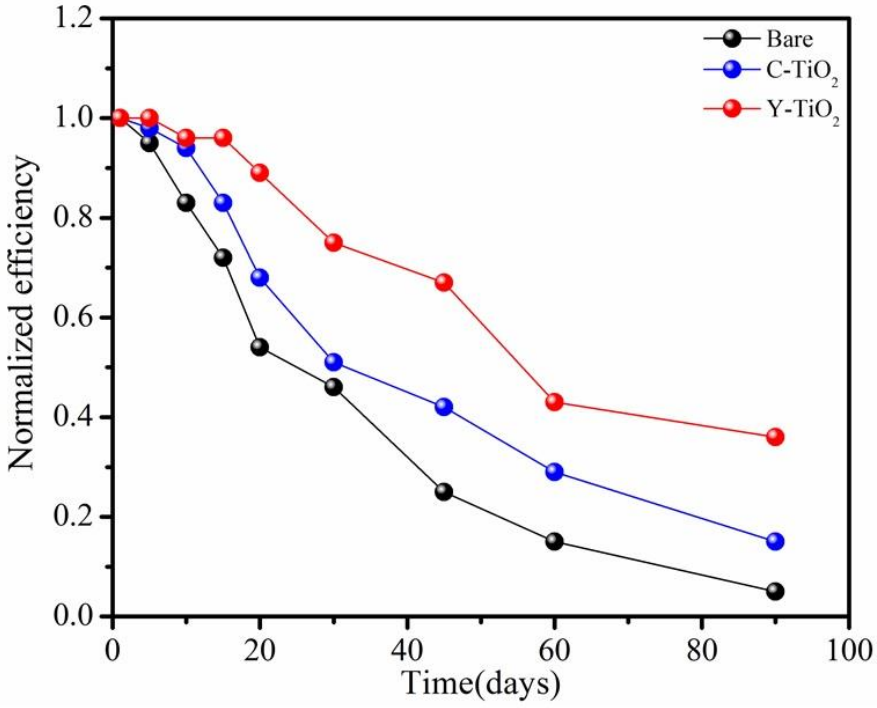

Figure 147: Normalized efficiency (as a fraction of the initial PCE) for the control and rare earth doped porphyrin-carbon counter electrode DSSCs under 1 sun.

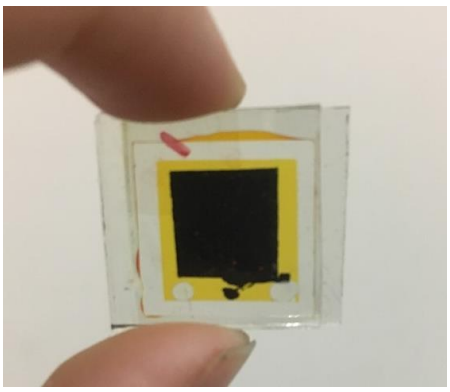

Figure 148: Real life image of porphyrin-carbon counter electrode DSSC.

5.8 Conclusion

In this chapter, DSSCs were successfully fabricated and shown to demonstrate enhanced PCE from the addition of $Sr_4Al_{14}O_{25}$: Eu^{2+}, Dy^{3+} and $NaYF_4$: Er^{3+}, Yb^{3+}. The spin coated devices performed much poorer than the screen printed devices which was expected in hindsight due to their thinner TiO_2 layer and non-uniform dispersal of rare earth compound (although PCE did increase modestly from 0.16% to 0.21% for the 0.5% w/w $NaYF_4$: Er^{3+}, Yb^{3+} doped spin coated electrode). For the screen printed devices, the best performances were recorded for the smaller drop cast quantities of the TiO_2-rare earth mixtures and rare earth paste doctor bladed counter electrodes (a novel way of incorporating the layer). 50 µl drop cast $NaYF_4$: Er^{3+}, Yb^{3+} achieved the best DSSC PCE of 5.30% whereas for the $Sr_4Al_{14}O_{25}$: Eu^{2+}, Dy^{3+} devices, the doped counter electrode displayed the highest PCE of 4.32% (although further study on the charge dynamics of this approach is recommended). Moreover, EQE measurements were inconclusive as to the cause of the enhanced PCE, as unlike for silicon devices, there were no increases in the EQE in the expected regions of the spectrum. On the contrary, EQE was improved across visible wavelengths for both rare earth compounds, indicating scattering might be the dominant effect. The bottom doped $Sr_4Al_{14}O_{25}$: Eu^{2+}, Dy^{3+} SEH concentrators were also able to increase P_{max} (by up to 36.3% at 1 sun) but not by as much as for silicon LCPV, owing to their exit aperture being too large. Finally, through a collaborative study, porphyrin dye-carbon electrode based DSSCs with added Y_2O_3: Yb^{3+}, Tm^{3+}, Ho^{3+} achieved a PCE of 9.82% (compared to 8.90% for the control) and exhibited greatly enhanced stability (8 times more PCE than the control after 90 days exposure) from less UV entering the system due to the spectral conversion of high energy photons.

Chapter 6. Financial, Statistical and Optical Models

6.1 Introduction

Having gathered a large amount of empirical data, it was necessary to theorise the potential impact, statistical confidence and physical processes related to the experiments. Therefore, this chapter concerns calculations and models arising for these three aspects of this work. Firstly, using the information from how much was paid for the materials, a basic cost analysis was conducted, which yielded the cost per watt of the devices tested in chapters 3, 4 and 5. Secondly, t and z statistics were used to test the hypothesis that the true mean of the PCE of rare earth compound containing silicon PV and LCPV devices was higher than that of the control group. This was done using two standard deviations (one based on the observed PCE fluctuations within an identically produced sample and one based on a semi-empirical propagated standard error). Then finally, two optical models were used to predict the J_{SC} enhancements for the different configurations of silicon-based devices in chapter 3 and 4. The first of these (for the non-concentrating silicon PV cells) had been developed by another group, and the second of which, for the LCPV cells, was built from first principles with the help of 2D ray tracing in MATLAB.

6.2 Cost Analysis

Cost per W_p is an important parameter in solar cell research for increasing PV deployment and its minimisation is a higher priority in practice than the attractive headline PCE values. Therefore, it was deemed necessary and of interest to compare the cost per W_p of the devices at different rare earth doping levels, in order to see if the increased electrical power output came at an additional cost or not. By using the information available from prices paid to the suppliers for each of the materials, the fabrication cost of each PV and LCPV device studied in chapters 3, 4 and 5 could be calculated component-wise. Prices are given in US$ and converted from GBP at the May 2018 exchange rate of £1 = $1.38. Similarly, Greatcell which supplies many materials used for DSSCs are based in Australia, so costs are converted at the rate of AU$1 = US$0.70.

6.2.1 Silicon PV and LCPV devices

Firstly, the silicon PV and LCPV devices in chapter 3 and 4 are considered which consist of the following materials whose costs are given in Table 72. In addition, the high-performance silicon solar cells provided by NAREC cost $1.38 each.

Material	Unit Cost ($)	Unit Mass (g)	Cost per gram ($)	Supplier
$Sr_4Al_{14}O_{25}$: Eu^{2+}, Dy^{3+}	76.50	25	3.06	Sigma-Aldrich
$NaYF_4$: Er^{3+}, Yb^{3+}	164.00	25	6.56	Sigma-Aldrich
Crystal Clear 200	366.76	6900	0.053	Benam
Sylgard 184	276.00	1100	0.25	Univar

Table 72: Costs of the materials required for fabrication of the silicon PV and LCPV devices.

If only the material costs are considered (no labour, machinery etc.), no wastage occurs and the cost of other minor components (acrylic base, glue, solder, flux remover, metal contacts and mould remover) are assumed to be negligible, then the fabrication costs of the coated PV cells or LCPV devices can be calculated. Since the amount of Sylgard used per device was approximately 0.5g and each SEH concentrator weighed 4g, the fabrication costs of the un-doped control PV and LCPV devices are $1.51 and $1.72 respectively. Similarly, by adding the cost of the relevant amount of rare earth compound used, the fabrication costs of all doping level devices can be derived individually. Then finally, dividing these values by the maximum power outputs observed under characterisation at 1 sun illumination gives the cost per W_p; these are all presented for each device type in Tables 73-76.

$Sr_4Al_{14}O_{25}$: Eu^{2+}, Dy^{3+} doping level (w/w %)	Max Power Output (W)	Device Cost ($)	Cost per W_p ($/W)
0 (no doping)	0.0160	1.505	94.20
0.25	0.0162	1.509	92.92
0.5	0.0163	1.513	92.75
1.0	0.0162	1.52	93.64
2.0	0.0161	1.536	95.58

Table 73: Cost analysis for the $Sr_4Al_{14}O_{25}$: Eu^{2+}, Dy^{3+} doped coated PV devices.

$NaYF_4$: Er^{3+}, Yb^{3+} doping level (w/w %)	Max Power Output (W)	Device Cost ($)	Cost per W_p ($/W)
0 (no doping)	0.0160	1.505	94.20
0.25	0.0161	1.513	93.98
0.5	0.0162	1.521	94.00
1.0	0.0167	1.538	91.84
2.0	0.0165	1.571	95.36

Table 74: Cost analysis for the $NaYF_4$: Er^{3+}, Yb^{3+} doped coated PV devices.

$Sr_4Al_{14}O_{25}$: Eu^{2+}, Dy^{3+} doping level (w/w %)	Max Power Output (W)	Device Cost ($)	Cost per W_p ($/W)
0 (no doping)	0.0332	1.720	51.81
0.25 (optical coupling)	0.0346	1.724	49.78
0.5 (optical coupling)	0.0346	1.728	50.00
1.0 (optical coupling)	0.0331	1.735	52.36
2.0 (optical coupling)	0.0332	1.751	52.80
0.1 (throughout conc.)	0.0324	1.732	53.47
0.1 (top of concentrator)	0.0350	1.722	49.15
0.1 (base of concentrator)	0.0349	1.722	49.31

Table 75: Cost analysis for the $Sr_4Al_{14}O_{25}$: Eu^{2+}, Dy^{3+} doped LCPV devices.

$NaYF_4$: Er^{3+}, Yb^{3+} doping level (w/w %)	Max Power Output (W)	Device Cost ($)	Cost per W_p ($/W)
0 (no doping)	0.0332	1.720	51.81
0.25 (optical coupling)	0.0354	1.728	48.85
0.5 (optical coupling)	0.0354	1.736	48.98
1.0 (optical coupling)	0.0368	1.753	47.59
2.0 (optical coupling)	0.0349	1.786	51.17
0.1 (throughout conc.)	0.0337	1.746	51.78
0.1 (top of concentrator)	0.0334	1.725	51.68
0.1 (base of concentrator)	0.0324	1.725	53.27

Table 76: Cost analysis for the $NaYF_4$: Er^{3+}, Yb^{3+} doped LCPV devices.

It can be clearly seen from the data that the cost per W_p falls for both the PV and LCPV silicon-based devices in nearly all cases compared to the un-doped controls, sans the 2% doped PV coatings for both materials. The greatest reductions in cost per W_p are achieved for $NaYF_4$: Er^{3+}, Yb^{3+} despite it being the more expensive of the two rare earth doped compounds; $NaYF_4$: Er^{3+}, Yb^{3+} reaches a minimum of $91.84 for PV cells and $47.59 LCPV devices, corresponding to a 2.5% and 8.1% fall through the addition of this material. $Sr_4Al_{14}O_{25}$: Eu^{2+}, Dy^{3+} on the other hand, only attains maximum cost per W_p reductions of 1.5% for coated PV cells and 4.8% in LCPV devices, though this is still respectable. It is also of note that the LCPV registered lower cost per W_p in general, regardless of the effect of rare earth compounds. By comparing the un-doped Sylgard coated PV cell and un-doped LCPV device, it is seen the mere addition of an SEH concentrator cuts the cost per W_p approximately in half. This supports the idea that an advantage of LCPV is lower costs due to less area of cell being required to generate the same power output because of the higher incident light intensity.

In their 2016 review, Yang et al [337] present the costs of the typical latest BIPV modules which range from $4.1-$24.5/W_p. These values are higher than conventional PV costs and the devices fabricated in this work are higher still.

However, from being fabricated only at the laboratory scale, the costs of rare earth doped LCPV modules are not too far off the upper limit of $24.5 and significant further reductions would be expected to be possible, following larger production quantities due to economies of scale.

6.2.2 DSSC devices

A second cost analysis is then carried out for the screen printed DSSCs using the same approach as 6.2.1 and based on the material costs per unit given in Table 77.

Material	Unit Cost ($)	Unit size	Cost per unit ($)	Supplier
FTO glass sheet	67.60	225 electrodes	0.21	Pilkington
Pt counter electrode	70.00	28 electrodes	2.50	Greatcell
18NR-T paste	52.01	10g	5.20	Greatcell
18NR-AO paste	77.99	10g	7.80	Greatcell
I_3/I^- electrolyte	338.10	50ml	6.76	Sigma-Aldrich
N719 dye powder	412.62	1g	412.62	Ossila
High purity ethanol	57.96	1000ml	0.06	Sigma-Aldrich
Ethyl cellulose	62.61	250g	0.25	Sigma-Aldrich
α-terpineol	54.01	50ml	1.08	Sigma-Aldrich
Elcocarb B/SP paste	360.74	20g	18.04	Solaronix
TBP	112.62	25g	4.50	Sigma-Aldrich

Table 77: Costs of the materials required for fabrication of the silicon PV and LCPV devices.

The dye solution, synthesised at 12 mg of powder per 100 ml of ethanol, has a high initial outlay of $10.77 per 100 ml. However, this can be re-used, theoretically infinite times (or in practice to produce tens of batches of devices, at ten or more to a batch), provided it is kept airtight and in foil, to prevent solvent evaporation and degradation by light. Therefore, this aspect of the cost per device shall be approximated to zero. Considering the rest of its constituent components and neglecting the spacer, a control DSSC contains 1 piece of FTO glass (the substrate for its working electrode), 1 Pt counter electrode, 30 μl of electrolyte, 2 layers of 18NR-T and 1 layer of 18NR-AO. If each screen printed layer is assumed to require 0.05 g of the paste to produce then a device cost of $3.82 is derived for the control cell.

The costs of the rare earth compounds from the previous section can then be used to calculate the costs of the doped cells. However, it is not as straightforward a calculation this time as they are not simply added alone, but as part of a synthesised gel or solution. Nevertheless, the components of these substances'

cost and mass are known from the fabrication procedure in 5.4, so calculations can be performed to yield the desired information. By assuming half the ethanol had evaporated during the grinding, it was found the rare earth compound pastes cost \$1.21/g and \$2.03/g for $Sr_4Al_{14}O_{25}$: Eu^{2+}, Dy^{3+} and $NaYF_4$: Er^{3+}, Yb^{3+} respectively. On the other hand, when mixed in a 1:1 weight ratio with 1 part 18NR-AO in 3 parts ethanol for the rare earth-TiO_2 mixture drop casted or spin coated layers, the cost per gram of solution was \$1.61 for $Sr_4Al_{14}O_{25}$: Eu^{2+}, Dy^{3+} and \$2.15 for $NaYF_4$: Er^{3+}, Yb^{3+}. Each doctor bladed layer was assumed to use 0.05 g of substance and the spin coated or drop coated solution's mass was calculated from its volume by assuming the same density as water (since the presence of pastes would raise it above the 0.79 g/cm^3 of ethanol).

The costs per watt peak for each doping configuration (as obtained from their PCE data for 1 sun illumination) could then be calculated and are shown in Tables 78 and 79. The procedures for the rare earth mixtures and lower masses applied meant all modified DSSCs, except the doctor bladed counter electrode, were actually cheaper to produce than the control device, meaning cost per watt was nearly always lower. Again, as with silicon the best performing device (50 µl drop casted $NaYF_4$: Er^{3+}, Yb^{3+}-TiO_2 mixture) had the lowest cost per watt at \$2390/W_p versus \$3950/W_p for the control (a 39.6% decrease). The most cost effective $Sr_4Al_{14}O_{25}$: Eu^{2+}, Dy^{3+} containing device also lowered its cost of power to \$3030/W_p (a 23.2% drop), although this was actually the sample with the 2nd highest power output (25 µl drop casted $Sr_4Al_{14}O_{25}$: Eu^{2+}, Dy^{3+}-TiO_2 mixture) as opposed to the one with a higher PCE and fabrication cost (doctor bladed counter electrode).

It was also of interest to consider the cost-benefit of the addition of concentrators to DSSCs, the costs of which are known from 6.2.1, so the device cost of an SEH-DSSC pair can easily be derived. These are shown in Table 80 for the data obtained under 1 sun irradiance. The analysis showed a reduction in cost of up to 22.4% through the addition of a 0.1% w/w base doped $Sr_4Al_{14}O_{25}$: Eu^{2+}, Dy^{3+} concentrator. The reduction for the rare earth doped DSSC was not as large (-16.2%) but a reduction none the less, so the addition of SEH concentrators is a viable option to further bring down cost per watt.

Device categories for $Sr_4Al_{14}O_{25}$: Eu^{2+}, Dy^{3+} doped DSSCs	Max Power Output (mW)	Device Cost ($)	Cost per W_p ($/W)
Control	0.968	3.823	3949
Doctor bladed (not in TiO_2)	0.901	3.494	3878
Spin coated TiO_2 mixture	1.005	3.594	3577
Drop cast TiO_2 mixture (25 µl)	1.145	3.473	3034
Drop cast TiO_2 mixture (50 µl)	1.065	3.513	3298
Drop cast TiO_2 mixture (100 µl)	0.981	3.594	3665
Drop cast TiO_2 mixture (200 µl)	0.782	3.755	4803
Doctor bladed counter electrode	1.210	3.884	3210

Table 78: Cost analysis for the $Sr_4Al_{14}O_{25}$: Eu^{2+}, Dy^{3+} doped screen printed DSSC devices.

Device categories for $NaYF_4$: Er^{3+}, Yb^{3+} doped DSSCs	Max Power Output (mW)	Device Cost ($)	Cost per W_p ($/W)
Control	0.968	3.823	3949
Doctor bladed (not in TiO_2)	0.600	3.535	5894
Spin coated TiO_2 mixture	1.036	3.648	3520
Drop cast TiO_2 mixture (25 µl)	1.205	3.487	2894
Drop cast TiO_2 mixture (50 µl)	1.485	3.541	2385
Drop cast TiO_2 mixture (100 µl)	0.783	3.648	4656
Drop cast TiO_2 mixture (200 µl)	0.804	3.863	4805
Doctor bladed counter electrode	1.408	3.925	2787

Table 79: Cost analysis for the $NaYF_4$: Er^{3+}, Yb^{3+} doped screen printed DSSC devices.

Device categories for DSSCs with concentrators	Max Power Output (mW)	Device Cost ($)	Cost per W_p ($/W)
Control DSSC (no concentrator)	0.968	3.823	3949
Control (plain concentrator)	1.267	4.038	3187
Control (top doped concentrator)	1.223	4.040	3303
Control (base doped concentrator)	1.319	4.040	3063
Doped DSSC (no concentrator)	0.981	3.594	3665
Doped (plain concentrator)	1.172	3.809	3250
Doped (top doped concentrator)	1.126	3.811	3385
Doped (base doped concentrator)	1.240	3.811	3073

Table 80: Cost analysis for the control and rare earth doped screen printed DSSC devices with SEH concentrators.

The costs in this subsection do seem nonsensically high, but results from the cells being produced at a very small scale with specialised externally produced components such as the Pt electrodes, and would drastically fall with larger production scales; Calogero et al have shown at a bigger scale N719-TiO_2 based DSSCs can be produced for as little as \$2.8/W_p [338]. If the same percentage decrements could be applied to this value through the addition of rare earth materials, then this approach is indeed a worthy endeavour.

Finally, the costs may also come down from replacing the Pt with carbon at the counter electrode and N719 dye with porphyrin. A full cost analysis for all the porphyrin dye-based electrodes is unavailable as the material costs for the rare earth doped Y_2O_3 and porphyrin solution are unknown. However, if the cost of

the dye is assumed to negligible like N719 because of multiple soaking cycles, then the control device without any added rare earth compound can have its cost per watt found since the Elcocarb BS/P paste and TBP are known costs. Like before, 0.05 g of 18NR-T is assumed for the working electrode, and 0.05 g of Elcocarb BS/P paste for the counter electrode. The remaining components are two FTO glass substrates and 30 µl of electrolyte as before but this time with 0.5 M TBP added (which only has a mass of 1.9 mg so just adds < $0.01 to the cost). Collating this information leads to a derived DSSC fabrication cost of $1.81, which with a higher power output of 7.21 mW causes the cost per watt peak to reduce drastically to $251/$W_p$ (~10 times lower than the best N719 dye-Pt counter electrode devices).

6.2.3 Commercialisation Opportunities

Having studied the cells at the 1-100 mW scale, it is finally necessary to predict how much power they could theoretically produce over a larger area. In prototype LCPV module blocks that use SEH concentrators of the same dimensions in this work, 18 silicon cells and optics are contained in a 17.6 cm x 17.6 cm semi-transparent block of area 0.031 m^2 (shown in Figure 149). Using this information, a hypothetical large system can have its peak power output estimated, firstly by finding the power output per m^2, which would be 19.3 W/m^2 for the un-doped control modules and 21.4 W/m^2 for the best performing rare earth containing devices (1% $NaYF_4$: Er^{3+}, Yb^{3+} doped optical coupling). This is another advantage of PCE enhancement because a higher power per unit area is a useful quantity to have for BIPV systems.

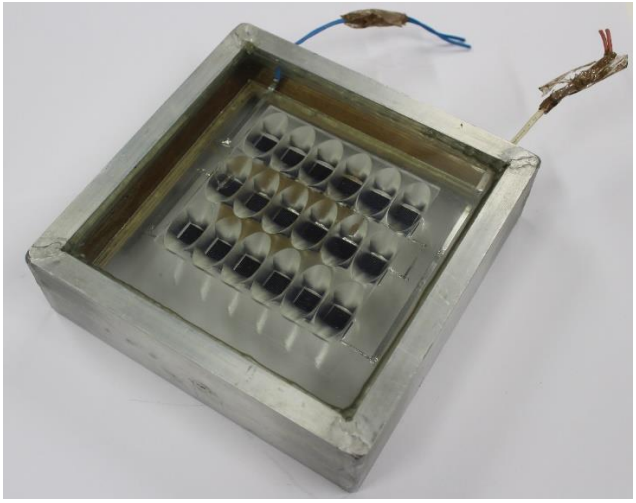

Figure 149: Real image of an LCPV module with 18 silicon solar cells attached to 18 SEH concentrators. This prototype has potential for BIPV.

Then to envisage the effects of these modules at a commercial scale, consider a typical cuboidal tower with a height of 100 m and width of 15 m that could potentially have 1500 m^2 of glass cladding on its south face. Replacing this entirely with BIPV modules of the types studied here would lead to a maximum generation potential of 29.0 kW_p at a tentative cost of $1.50 million if the un-doped LCPV were used and 32.1 kW_p at a cost of $1.53 million if the optimal rare earth doped devices were deployed, with both scenarios considering the basic materials alone. To compare these figures with conventional PV, as of 2019 in the UK, commercial non-concentrating mono-crystalline solar PV panels at single-building use scale typically cost around $\$0.85/W_p$ while generating 185 W/m^2 [339], so the same area system (again from a material only perspective) would provide 277 kW_p output at a cost of $236,000. Thus, on the surface, window based BIPV, like the modules studied here, seems a much more expensive and less desirable option. It is also likely a building of that size would require a larger peak electricity demand than ~30 kW, so this type of BIPV would only claim to be able to supplement a building's energy requirements at peak generation times as opposed to allowing it to run off-grid. Furthermore, due to both systems having a pitch of 90° relative to the celestial zenith, they would rarely generate at their peak power derived from AM 1.5 G conditions. Although, as a trade-off they would enjoy reasonably high power production in the morning and evening hours when the sun is lower in the sky.

Nevertheless, the added benefits of optical semi-transparency and insulation, to respectively reduce heating and lighting costs, could be extra advantageous factors for the LCPV modules. In addition, the conventional PV panels have a weight of 11.7 kg/m^2 whereas the semi-transparent modules would likely be less than this, so would cause less structural issues for the tower that become more important the taller a building becomes. Also, and clearly, for a project of this scale the production cost would come down significantly if the LCPV modules were being produced in such large quantities. Specific aspects to consider would be: identifying processes that can be automated (e.g. 3D printing the concentrators), the polymer to be used (in terms of cost and environmental impact), increasing the geometrical concentration ratio while maintaining high optical efficiency across wide angles of incidence (so that the more power can be

obtained from the cells), market research to find the most socially acceptable designs and adherence to building regulations in the given polity.

Scaling up (or upscaling) production of processes for PV material fabrication is an important area of research, particularly for emerging technologies like DSSCs and PSCs with BIPV applications [340]. It is likely they would ultimately take different geometries to the small screen printed squares in these test devices and DSSCs of the liquid electrolyte form are limited in commercial uses because of their stability issues. However, if it assumed that this latter problem can be solved in the coming years, while maintaining a similar device PCE, then it is a worthwhile exercise to speculate how much power they could generate at a larger scale.

Going by the data from chapter 5, the control DSSCs (N719 dye-Pt counter electrode) would have a peak power output of 2.42 W/m^2 in the design of 0.28 cm^2 active area on 2 cm^2 substrates, whereas the best performing rare earth containing DSSCs would yield 3.71 W/m^2. Alternatively, the control porphyrin-carbon electrode DSSCs could yield 18.8 W/m^2 (from its higher PCE and active area) and the Y doped version would yield 19.9 W/m^2 (more than the un-doped silicon LCPV module). The peak power output of the earlier described building's south facade coated instead with on-glass DSSCs would be 3.63 kW_p, 5.57 kW_p, 28.2 kW_p and 29.9 kW_p for the devices in ascending power output (summarised in Table 81). Notwithstanding their lower power, the two N719-Pt counter electrode devices would be more transparent as they do not contain a jet-black counter electrode and have less area of the substrate coated with photoactive materials. Although at the scale of this work's production, the costs of these areas of cells would be astronomical at $14.3 million and $13.3 million for the un-doped and optimally doped DSSCs respectively. The porphyrin control devices would still be very costly too at a grand total of $7.08 million.

Again, and obviously, moving beyond the laboratory scale would drastically bring down these costs. There would be lots of considerations for aspiring manufacturers including how large an area of the substrate to actually coat, the best electrode coating process, the temperatures needed to be attained and energy for machinery required, minimisation of waste (particularly TiO_2 pastes), which processes can be automated, recyclable parts to enable a circular economic process and sourcing as many components in the lab internally

(although this can require more skilled chemists' labour). To give one example, Pt could be thermally deposited within a production line, in situ by the cell manufacturer, at a much lower cost than buying from an external supplier (which was the majority of the cost for this thesis' devices). Furthermore, inkjet printing of a concentrated dye solution has been proposed as a method to speed up the manufacturing process and reduce material wastage by removing the need for a lengthy soaking of the electrode in the dye [341].

Finally, LCPV may offer exciting opportunities for DSSC in BIPV, as the cells can be made in a range of colours and spatial arrays, to produce more power from less active area of cell which in turn brings down costs. If a concentrator-DSSC system was specifically designed to achieve a light concentration of >5 suns on a cell, then cost per watt would fall substantially since the concentrator fabrication cost is <10% that of the cell. Perhaps even higher light intensities are possible and studying the behaviour of cells at higher temperatures will help set practical limitations of this approach [332]. Moreover, if the costs of a carbon-porphyrin device can fall by a factor of 100 upon scaling from mW to W production (like the N719-Pt devices studied by [338]) while maintaining stability, then combined with concentrators, DSSCs would become a very attractive option for BIPV.

Device category	Power per area (W/m^2)	Cost per area ($/m^2$)
Silicon LCPV module (plain)	19.3	1000
Silicon LCPV module (doped)	21.4	1020
Standard mono-c-Si PV module	185	157
N719-Pt DSSC module (plain)	2.42	9560
N719-Pt DSSC module (doped)	3.71	8850
Porphyrin-carbon module (plain)	18.8	4720
Porphyrin-carbon module (doped)	19.9	N/A

Table 81: Power and cost per area of different BIPV technologies presented in this work compared with that of a commercial standard mono-c-Si PV module.

6.3 Sensitivity Analysis

When undertaking experimental investigations, it is essential to include an analysis that considers the sources of error. Errors can be statistical or systematic, meaning they occur either due to random fluctuations (e.g. in the accuracy of measuring equipment) which will vary (usually about a normal distribution) with each repetition of an experiment or by a fault with the equipment or flawed methodology that will apply a consistent offset or multiplying factor to the observed data [342]. Systematic errors are difficult to detect and quantify, and because the equipment had been calibrated to a high level and experiments were

based on established procedures, they are hereby neglected in this analysis. Thus, a statistical approach is taken, from two different aspects, to quantitatively analyse the uncertainty for the silicon PV and LCPV device PCE measurements and yield levels of confidence in the overall results.

6.3.1 Pure Statistical Analysis of Results

First, a basic statistical analysis of the PCE results obtained in 3.7.3 and 4.4 was conducted to determine the level of significance of the findings and justify their validity (i.e. that the observed performance enhancements were genuine and not a statistical fluke). PCE is chosen to be analysed here over J_{SC}, since it is the measured parameter of most importance in this work. As a starting step in this approach, rather than taking the maximum PCE value of the three devices, the sample mean, $\bar{x}$, and sample standard deviation, s, were calculated using the formulae below for each batch of three identical PV or LCPV devices (where x_i corresponds to an individual PCE measurement and n the sample size, equal to 3).

$$\bar{x} = \frac{1}{n}\sum_{i=1}^{n} x_i \tag{37}$$

$$s = \sqrt{\frac{1}{n}\sum_{i=1}^{n}(x_i - \bar{x})} \tag{38}$$

Once these values had been calculated for each configuration of cells, it was required to use a statistical test that can compare two sample means of unknown population standard deviation (σ) and different sample standard deviation, to determine the difference in their population or true means (μ). The term population here refers to a hypothetical infinitely sized batch of PV or LCPV devices of the given design speciation that follow a normal distribution of PCE about μ and standard deviation σ. To say with confidence that the true mean PCE of one type of device with added rare earth ions (μ_1) is greater than that of the control cells without any such addition (μ_2), the Welch t-test was conducted [343]. This test is useful for comparing two means from small sample sizes of unknown population standard deviation and gives a probability (p-value) as its output from

two parameters, the t-value (t) and number of degrees of freedom (DF), which can in turn be calculated from the $\bar{x}$, *s and n* of two samples. The resulting p-value can then be ultimately used to test the null hypothesis (H_0) in a one-sided test that the true population mean of the PCE of a class of rare earth compound doped PV or LCPV devices (μ_1) was greater than the true population mean of the control (μ_2), to a given level of confidence, against the alternate hypothesis (H_a) that $\mu_1 \leq \mu_2$ (i.e. the control device is just as efficient). Typically, throughout science, this level can be 95% or 99%. Alternatively, significance levels are given by 100% minus the confidence level, so for 95% and 99% the corresponding significance levels would be 5% and 1%.

$$H_0: \mu_1 > \mu_2$$

$$H_A: \mu_1 \leq \mu_2 \quad (39)$$

In this test, the t-values are calculated using the formula below with n_1 and n_2 always equal to 3, $\bar{x}_2$ and s_2 always remaining that of the control device and $\bar{x}_1$ and s_1 changing to the values of the PV or LCPV cell it is being compared with.

$$t = \frac{\overline{x_1} - \overline{x_2}}{\sqrt{\frac{s_1^2}{n_1} + \frac{s_2^2}{n_2}}} \quad (40)$$

Translating a t-value into a probability then requires knowledge of the number of degrees of freedom, DF, which can be estimated by the Welch-Satterthwaite equation given below [344]. DF is always greater than the larger of $n_1 - 1$ and $n_2 - 1$ and less than $n_1 + n_2 - 2$ (so in this case $2 < DF < 4$). Traditionally DF is rounded down to the nearest integer but in computational calculations this is unnecessary [345].

$$DF = \frac{\left(\frac{s_1^2}{n_1} + \frac{s_2^2}{n_2}\right)^2}{\frac{s_1^4}{n_1^2(n_1-1)} + \frac{s_2^4}{n_2^2(n_2-1)}} \quad (41)$$

Then an online calculator [346] was used to perform a one-sided test and derive a p-value (the probability, P ($T \leq t$)) from the t-value and DF calculated for each comparison. If the p-value was less than the critical level of 0.05 and 0.01 (for 5% and 1% significance), then we accept the null hypothesis that the true mean PCE of the group of PV or LCPV devices containing rare earth ions is greater than that

of the control cell to that level of significance. Alternatively, if the p-value is greater than 0.05 or 0.01, the alternative hypothesis must be accepted, and it cannot be said with statistical confidence of 99% or 95% that the device has a higher PCE than the control. Another useful way of interpreting the p-value is that it is the probability of rejecting the null hypothesis. Given this fact, the calculated p-value subtracted from one will be equal to the probability that the null hypothesis is true (i.e. P ($\mu > \mu_{control}$)). The results from the Welch's t-test are shown for all configurations of doped silicon PV and LCPV cells in Tables 82-97. If a significance of 5% is attained, the final cell in that row is coloured light green and dark green for a significance of 1%. For some devices, the p-value was <0.001, in which case P ($\mu > \mu_{control}$) is >0.999.

Doped optical coupling (w/w %)	$\bar{x}$ (%)	s (%)	t	DF	P ($\mu > \mu_{control}$)
0.0	9.102	0.247	-	-	-
0.25	9.000	0.513	-0.312	2.884	0.388
0.5	9.434	0.397	1.226	3.349	0.850
1.0	9.141	0.089	0.257	2.508	0.592
2.0	9.137	0.180	0.196	3.656	0.571
Doped concentrator (w/w %)	**$\bar{x}$ (%)**	**s (%)**	**t**	**DF**	**P ($\mu > \mu_{control}$)**
0.1 (Homogenous)	8.774	0.304	-1.449	3.842	0.112
0.1 (Top)	9.808	0.104	4.555	2.681	0.988
0.1 (Bottom)	9.723	0.164	3.624	3.470	0.966

Table 82: Results of t-test for $Sr_4Al_{14}O_{25}$: Eu^{2+}, Dy^{3+} doped LCPV devices at 1 sun.

Doped optical coupling (w/w %)	$\bar{x}$ (%)	s (%)	t	DF	P ($\mu > \mu_{control}$)
0.0	8.370	0.154	-	-	-
0.25	8.819	0.509	0.289	2.362	0.602
0.5	9.235	0.381	2.128	2.634	0.932
1.0	8.881	0.078	1.521	2.961	0.887
2.0	8.895	0.238	1.010	3.418	0.811
Doped concentrator (w/w %)	**$\bar{x}$ (%)**	**s (%)**	**t**	**DF**	**P ($\mu > \mu_{control}$)**
0.1 (Homogenous)	8.515	0.254	-1.255	3.293	0.146
0.1 (Top)	9.892	0.134	9.863	3.928	>0.999
0.1 (Bottom)	9.624	0.215	5.863	3.623	0.997

Table 83: Results of t-test for $Sr_4Al_{14}O_{25}$: Eu^{2+}, Dy^{3+} doped LCPV devices at 0.8 suns.

Doped optical coupling (w/w %)	$\bar{x}$ (%)	s (%)	t	DF	P ($\mu > \mu_{control}$)
0.0	8.703	0.157	-	-	-
0.25	8.662	0.567	-0.119	2.305	0.457
0.5	9.123	0.403	1.683	2.594	0.897
1.0	8.751	0.087	0.461	3.120	0.662
2.0	8.711	0.270	0.043	3.218	0.516
Doped concentrator (w/w %)	**$\bar{x}$ (%)**	**s (%)**	**t**	**DF**	**P ($\mu > \mu_{control}$)**
0.1 (Homogenous)	8.462	0.270	-1.337	3.214	0.134
0.1 (Top)	9.787	0.123	9.422	3.778	>0.999
0.1 (Bottom)	9.143	0.254	3.778	3.336	0.962

Table 84: Results of t-test for $Sr_4Al_{14}O_{25}$: Eu^{2+}, Dy^{3+} doped LCPV devices at 0.6 suns.

Doped optical coupling (w/w %)	$\bar{x}$ (%)	s (%)	t	DF	P ($\mu > \mu_{control}$)
0.0	8.295	0.170	-	-	-
0.25	8.158	0.549	-0.412	2.381	0.357
0.5	8.597	0.466	1.053	2.523	0.809
1.0	8.312	0.117	0.140	3.541	0.552
2.0	8.278	0.180	-0.116	3.987	0.457
Doped concentrator (w/w %)	**$\bar{x}$ (%)**	**s (%)**	**t**	**DF**	**P ($\mu > \mu_{control}$)**
0.1 (Homogenous)	8.040	0.257	-1.433	3.472	0.118
0.1 (Top)	9.537	0.071	11.661	2.677	0.999
0.1 (Bottom)	9.133	0.335	3.865	2.968	0.984

Table 85: Results of t-test for $Sr_4Al_{14}O_{25}$: Eu^{2+}, Dy^{3+} doped LCPV devices at 0.4 suns.

Doped optical coupling (w/w %)	$\bar{x}$ (%)	s (%)	t	DF	P ($\mu > \mu_{control}$)
0.0	9.102	0.247	-	-	-
0.25	9.126	0.640	0.059	2.585	0.521
0.5	9.780	0.179	3.846	3.641	0.989
1.0	10.182	0.268	5.127	3.975	0.997
2.0	9.708	0.133	3.734	3.070	0.984
Doped concentrator (w/w %)	**$\bar{x}$ (%)**	**s (%)**	**t**	**DF**	**P ($\mu > \mu_{control}$)**
0.1 (Homogenous)	9.356	0.147	1.527	3.249	0.891
0.1 (Top)	9.330	0.157	1.346	3.387	0.869
0.1 (Bottom)	9.107	0.045	0.035	2.130	0.512

Table 86: Results of t-test for $NaYF_4$: Er^{3+}, Yb^{3+} doped LCPV devices at 1 sun.

Doped optical coupling (w/w %)	$\bar{x}$ (%)	s (%)	t	DF	P ($\mu > \mu_{control}$)
0.0	8.370	0.154	-	-	-
0.25	8.820	0.631	0.239	2.237	0.584
0.5	9.567	0.172	6.280	3.949	0.998
1.0	9.965	0.290	6.513	3.041	0.996
2.0	9.507	0.142	6.441	3.973	0.998
Doped concentrator (w/w %)	**$\bar{x}$ (%)**	**s (%)**	**t**	**DF**	**P ($\mu > \mu_{control}$)**
0.1 (Homogenous)	9.438	0.225	4.504	3.536	0.993
0.1 (Top)	9.340	0.137	5.135	3.945	0.996
0.1 (Bottom)	9.245	0.054	5.469	2.488	0.990

Table 87: Results of t-test for $NaYF_4$: Er^{3+}, Yb^{3+} doped LCPV devices at 0.8 suns.

Doped optical coupling (w/w %)	$\bar{x}$ (%)	s (%)	t	DF	P ($\mu > \mu_{control}$)
0.0	8.703	0.157	-	-	-
0.25	8.807	0.701	0.251	2.200	0.588
0.5	9.544	0.172	6.261	3.968	0.998
1.0	9.938	0.287	6.544	3.100	0.997
2.0	9.532	0.122	7.229	3.764	0.999
Doped concentrator (w/w %)	**$\bar{x}$ (%)**	**s (%)**	**t**	**DF**	**P ($\mu > \mu_{control}$)**
0.1 (Homogenous)	9.285	0.191	4.081	3.858	0.992
0.1 (Top)	9.278	0.160	4.444	3.998	0.994
0.1 (Bottom)	9.103	0.031	4.336	2.152	0.978

Table 88: Results of t-test for $NaYF_4$: Er^{3+}, Yb^{3+} doped LCPV devices at 0.6 suns.

Doped optical coupling (w/w %)	$\bar{x}$ (%)	s (%)	t	DF	P ($\mu > \mu_{control}$)
0.0	8.295	0.170	-	-	-
0.25	8.499	0.718	0.479	2.224	0.663
0.5	9.255	0.186	6.594	3.968	0.999
1.0	9.644	0.299	6.796	3.174	0.997
2.0	9.252	0.107	8.237	3.372	0.999
Doped concentrator (w/w %)	**$\bar{x}$ (%)**	**s (%)**	**T**	**DF**	**P ($\mu > \mu_{control}$)**
0.1 (Homogenous)	8.906	0.186	4.196	3.969	0.993
0.1 (Top)	8.798	0.151	3.831	3.941	0.990
0.1 (Bottom)	8.647	0.041	3.478	2.235	0.969

Table 89: Results of t-test for $NaYF_4$: Er^{3+}, Yb^{3+} doped LCPV devices at 0.4 suns.

Doping (w/w %)	$\bar{x}$ (%)	s (%)	t	DF	P ($\mu > \mu_{control}$)
0.0	15.515	0.400	-	-	-
0.25	15.951	0.207	1.674	2.999	0.904
0.5	15.573	0.543	0.150	3.679	0.556
1.0	15.699	0.378	0.580	3.987	0.703
2.0	15.587	0.675	0.158	3.252	0.558

Table 90: Results of t-test for $Sr_4Al_{14}O_{25}$: Eu^{2+}, Dy^{3+} doped Sylgard PV cells at 1 sun.

Doping (w/w %)	$\bar{x}$ (%)	s (%)	t	DF	P ($\mu > \mu_{control}$)
0.0	15.809	0.182	-	-	-
0.25	16.285	0.218	2.904	3.878	0.977
0.5	16.087	0.619	0.745	2.342	0.738
1.0	16.056	0.414	0.945	2.744	0.790
2.0	16.059	0.601	0.688	2.363	0.724

Table 91: Results of t-test for $Sr_4Al_{14}O_{25}$: Eu^{2+}, Dy^{3+} doped Sylgard PV cells at 0.8 suns.

Doping (w/w %)	$\bar{x}$ (%)	s (%)	t	DF	P ($\mu > \mu_{control}$)
0.0	15.715	0.419	-	-	-
0.25	16.100	0.319	1.266	3.736	0.861
0.5	15.947	0.586	0.558	3.622	0.695
1.0	15.759	0.380	0.136	3.963	0.551
2.0	15.829	0.640	0.259	3.450	0.595

Table 92: Results of t-test for $Sr_4Al_{14}O_{25}$: Eu^{2+}, Dy^{3+} doped Sylgard PV cells at 0.6 suns.

Doping (w/w %)	$\bar{x}$ (%)	s (%)	t	DF	P ($\mu > \mu_{control}$)
0.0	15.197	0.486	-	-	-
0.25	15.504	0.388	0.857	3.812	0.779
0.5	15.305	0.479	0.275	3.999	0.602
1.0	14.951	0.116	-0.852	2.225	0.238
2.0	15.235	0.726	0.076	3.494	0.528

Table 93: Results of t-test for $Sr_4Al_{14}O_{25}$: Eu^{2+}, Dy^{3+} doped Sylgard PV cells at 0.4 suns.

Doping (w/w %)	$\bar{x}$ (%)	s (%)	t	DF	P ($\mu > \mu_{control}$)
0.0	15.515	0.400	-	-	-
0.25	15.761	0.240	0.915	3.269	0.789
0.5	15.748	0.306	0.801	3.744	0.765
1.0	16.283	0.354	2.489	3.941	0.966
2.0	15.887	0.455	1.062	3.936	0.825

Table 94: Results of t-test for $NaYF_4$: Er^{3+}, Yb^{3+} doped Sylgard PV cells at 1 sun.

Doping (w/w %)	$\bar{x}$ (%)	s (%)	t	DF	P ($\mu > \mu_{control}$)
0.0	15.809	0.182	-	-	-
0.25	16.131	0.416	1.227	2.327	0.843
0.5	15.952	0.226	0.852	3.822	0.778
1.0	16.350	0.367	2.287	2.927	0.946
2.0	15.905	0.443	0.348	2.654	0.623

Table 95: Results of t-test for $NaYF_4$: Er^{3+}, Yb^{3+} doped Sylgard PV cells at 0.8 suns.

Doping (w/w %)	$\bar{x}$ (%)	s (%)	t	DF	P ($\mu > \mu_{control}$)
0.0	15.715	0.419	-	-	-
0.25	15.734	0.390	0.059	3.979	0.522
0.5	15.593	0.194	-0.458	2.823	0.340
1.0	15.863	0.545	0.372	3.753	0.635
2.0	15.549	0.372	-0.512	3.944	0.318

Table 96: Results of t-test for $NaYF_4$: Er^{3+}, Yb^{3+} doped Sylgard PV cells at 0.6 suns.

Doping (w/w %)	$\bar{x}$ (%)	s (%)	t	DF	P ($\mu > \mu_{control}$)
0.0	15.197	0.486	-	-	-
0.25	15.189	0.308	-0.023	3.385	0.491
0.5	14.892	0.308	-0.918	3.384	0.210
1.0	15.512	0.623	0.690	3.776	0.735
2.0	14.997	0.473	-0.511	3.997	0.318

Table 97: Results of t-test for $NaYF_4$: Er^{3+}, Yb^{3+} doped Sylgard PV cells at 0.4 suns.

The results from the t-test show a generally good agreement with the conclusions in chapter 4 drawn from the champion PCE values, particularly for the best performing LCPV devices (top and bottom doped $Sr_4Al_{14}O_{25}$: Eu^{2+}, Dy^{3+} concentrators and 0.5%, 1% and 2% w/w doped $NaYF_4$: Er^{3+}, Yb^{3+} optical couplings) which at 1 sun exhibited the highest levels of confidence (all over 95%) that their true means were higher than that of the control. The notion of better performance at lower irradiance is also supported since the 0.5% and 2% doped $NaYF_4$: Er^{3+}, Yb^{3+} optical couplings saw their confidence levels increase from 95% at 1 sun to over 99% at 0.4, 0.6 and 0.8 suns. It also noteworthy that at <1 sun irradiance, the doped $NaYF_4$: Er^{3+}, Yb^{3+} concentrators all showed high confidence (>95%) of enhanced performance, meaning they are essentially as effective as the doped optical couplings, while the $Sr_4Al_{14}O_{25}$: Eu^{2+}, Dy^{3+} doped optical couplings did not improve their PCE to 95% confidence at any illumination level. These discrepancies from the earlier narrative are the result of applying more statistical rigour, since the champion of each configuration could have been a mild outlier and the range of measurements within a sample were not considered.

The findings from chapter 3, on the other hand, are partially backed up by this analysis, since the best devices for each material by champion PCE value (0.25% w/w for $Sr_4Al_{14}O_{25}$: Eu^{2+}, Dy^{3+} and 1% w/w doped optical coupling $NaYF_4$: Er^{3+},

Yb^{3+}) were the only two samples to reach 95% confidence and at the irradiance levels where their PCE measurements were highest, highlighting a good level of consistency between 3.7.3 and this subsection. However, although their sample means are almost exclusively higher than the control, other doping levels do not demonstrate a higher true PCE mean to a 95% level of confidence at any intensity level. Nevertheless, this does provide further evidence for the finding that the addition of concentrators improves the PCE of rare earth compound layer coated PV cells more effectively than in their absence. Although one caution when performing these kinds of tests that should be noted is the possibility for type 1 and 2 errors, in which respectively, an actually true H_0 is rejected or an in reality false H_0 is accepted. The probability of these occurring are the p-value for type 1 and one minus the p-value for type 2. Since p-values are small by definition for accepted H_0 they are quite unlikely to occur, but type 2 errors are relatively likely to occur for several p-values, particularly ones just above the critical value of 0.05. Hence, the binary nature of hypothesis testing that treats a p-value of 0.06 and 0.99 identically by rejecting both could be regarded as a minor drawback of this approach.

6.3.2 Analysis via Propagated Sources of Error

Another way to estimate the error and statistical significance of the results could be to consider the physical sources of uncertainty in the experiment, and from first principles, derive an expression for the standard deviation of the entire population of solar cells (σ). Then it would be possible to calculate the standard error (SE) for a given sample mean using the equation:

$$SE = \frac{\sigma}{\sqrt{n}} \qquad (42)$$

Then one could simply perform a two sample z-statistic from the formula below (where z is the standard normal distribution, $\bar{x}_1$ and SE_1 are the sample mean and standard error of the rare earth compound containing device and $\bar{x}_2$ and SE_2 that for the control).

$$z = \frac{\overline{x_1} - \overline{x_2}}{\sqrt{{SE_1}^2 + {SE_2}^2}} \qquad (43)$$

This approach does not require DF to find the corresponding p-values (which are found from an online calculator [347]) and are equal to the level of significance.

Finally, from looking at the significance level, the same hypothesis test in 6.3.1 is conducted. For a one-sided test the critical z values are 1.64 and 2.33 for p-values of 0.05 and 0.01 (95% and 99% confidence) respectively. The same logic applies as 6.3.1 that one minus the p-value gives P ($\mu > \mu_{control}$).

The five fundamental sources of experimental error to be considered in deriving σ are: temperature of room fluctuations, intrinsic solar cell quality variation within the batch from NAREC, solar simulator lamp intensity fluctuations, I-V tracer accuracy and fluctuations in the transmittance of concentrators (for the LCPV devices only). This excludes any uncertainty that may arise due to imperfections in the fabrication procedure and all variations are assumed to follow a normal distribution. In order to quantitatively evaluate these factors' contributions towards uncertainty, it must first be considered to study the components of a PCE measurement, using the formula.

$$PCE = \frac{P_{out}}{P_{in}} = \frac{I_{MP}\, V_{MP}}{P_{in}} \qquad (44)$$

Therefore, the overall PCE error, σ_{PCE}, will depend on the uncertainties of each of the parameters, I_{MP}, V_{MP} and P_{in} which can be given by σ_I, σ_V and σ_P, respectively. Once these values are known, the individual parameter errors may be propagated using the equation below, (a special case from the exact formula for propagation of error, when the powers of all variables are 1 or -1), to derive the magnitude of σ_{PCE}.

$$\sigma_{PCE} = PCE\sqrt{\left(\frac{\sigma_I}{I_{MP}}\right)^2 + \left(\frac{\sigma_V}{V_{MP}}\right)^2 + \left(\frac{\sigma_P}{P_{in}}\right)^2} \qquad (45)$$

Further calculation is required to determine the initial values of σ_I, σ_V and σ_P which all have their own sources of uncertainty from the factors mentioned earlier (for simplicity it will be assumed σ_I and σ_V scale with the errors of J_{SC} and V_{OC}, $I_{MP} = J_{SC}$ and rises linearly with light intensity, and $V_{MP} = V_{OC}$ and is independent of light intensity). If there are multiple errors, ε, present in a measurement, x, then provided they are all independent of one another [348], their root sum square gives a combined overall uncertainty for that variable, σ_x.

$$\sigma_x = \sqrt{\sum_{i=0}^{n} \varepsilon_i{}^2}$$

(46)

This is the case for I_{MP} and V_{MP} measurements. For example, the current at maximum power, has quantifiable component errors from the accuracy on the I-V tracer (± 0.5% or ± 0.005I_{MP} mA), the fluctuations in lamp intensity over time (± 1% or ± 0.01I_{MP} mA) and, for LCPV devices, from the uncertainty on the quality of the concentrator (± 3.5% or ± 0.035I_{MP} mA). The latter stems from the presence of tiny bubbles and shape variation in some of the concentrators and was calculated from the standard deviation of their transmittance measurements for a sample of 17 doped and un-doped concentrators. Using the above formula, these errors were combined to yield σ_I = 0.0112I_{MP} and 0.0367I_{MP} for the PV and LCPV devices respectively.

Likewise, V_{MP} also depends on the accuracy on the I-V tracer, so any measurements come with an error of ± 0.5% or ± 0.005V_{MP} mV. Two additional uncertainties on this variable originate from the fluctuations in room temperature and intrinsic silicon PV cell quality. These are quantified by the standard deviation of the temperature of the room (which was recorded periodically throughout device characterisation and varied between 24.9°C and 29.1°C) multiplied by 2.2 mV (the effect on V_{OC} per °C temperature difference) and the standard deviation of the multi-meter recorded voltages (that varied between 300 and 390 mV), to give errors of ± 2.4 mV and ± 21 mV for the temperature and cell quality issue respectively. Combining again leads to a σ_V = 21.32 mV or 0.0381V_{MP} and is the same for LCPV and PV devices.

Finally, the uncertainty on P_{in} is only affected by one factor, the lamp intensity, so σ_P = 0.01P_{in} W. Now σ_I, σ_V and σ_P have been quantified, σ_{PCE} can be calculated using the earlier formula. This is equal to 0.0538PCE for LCPV devices and 0.0410PCE for the coated PV cells. Due to the cancellation of terms in the formula, σ_{PCE} is unaffected by the change in irradiance level, although as apparent from its linear dependence on PCE, higher performing devices will exhibit a greater absolute error.

Now the standard deviation of the population is now known, a standard error, *SE*, can be given for each sample mean and the calculated z and p-values for two sets of data used to test the hypothesis that the true mean of one type of device is greater than the control's. The resulting data is given in Tables 98-113 in the same style as 6.3.1 with P ($\mu > \mu_{control}$) and green shading used to indicate the samples with the highest confidence levels that their true mean is greater than that of the control.

Doped optical coupling (w/w %)	$\bar{x}$ (%)	SE (%)	z	P ($\mu > \mu_{control}$)
0.0	9.102	0.283	-	-
0.25	9.000	0.280	-0.258	0.398
0.5	9.434	0.293	0.814	0.792
1.0	9.141	0.284	0.097	0.539
2.0	9.137	0.284	0.086	0.534
Doped concentrator (w/w %)	**$\bar{x}$ (%)**	**SE (%)**	**z**	**P ($\mu > \mu_{control}$)**
0.1 (Homogenous)	8.774	0.273	-0.835	0.202
0.1 (Top)	9.808	0.305	1.697	0.955
0.1 (Bottom)	9.723	0.302	1.501	0.933

Table 98: Results of z-test for $Sr_4Al_{14}O_{25}$: Eu^{2+}, Dy^{3+} doped LCPV devices at 1 sun.

Doped optical coupling (w/w %)	$\bar{x}$ (%)	SE (%)	z	P ($\mu > \mu_{control}$)
0.0	8.730	0.271	-	-
0.25	8.819	0.274	0.230	0.591
0.5	9.235	0.287	1.279	0.900
1.0	8.881	0.276	0.391	0.652
2.0	8.895	0.276	0.427	0.665
Doped concentrator (w/w %)	**$\bar{x}$ (%)**	**SE (%)**	**z**	**P ($\mu > \mu_{control}$)**
0.1 (Homogenous)	8.515	0.264	-0.568	0.285
0.1 (Top)	9.892	0.307	2.835	0.998
0.1 (Bottom)	9.624	0.299	2.215	0.987

Table 99: Results of z-test for $Sr_4Al_{14}O_{25}$: Eu^{2+}, Dy^{3+} doped LCPV devices at 0.8 suns.

Doped optical coupling (w/w %)	$\bar{x}$ (%)	SE (%)	z	P ($\mu > \mu_{control}$)
0.0	8.703	0.270	-	-
0.25	8.662	0.269	-0.106	0.542
0.5	9.123	0.283	1.072	0.858
1.0	8.751	0.272	0.125	0.550
2.0	8.711	0.271	0.020	0.508
Doped concentrator (w/w %)	**$\bar{x}$ (%)**	**SE (%)**	**z**	**P ($\mu > \mu_{control}$)**
0.1 (Homogenous)	8.462	0.263	-0.639	0.508
0.1 (Top)	9.787	0.304	2.664	0.996
0.1 (Bottom)	9.143	0.284	1.124	0.869

Table 100: Results of z-test for $Sr_4Al_{14}O_{25}$: Eu^{2+}, Dy^{3+} doped LCPV devices at 0.6 suns.

Doped optical coupling (w/w %)	$\bar{x}$ (%)	SE (%)	z	P ($\mu > \mu_{control}$)
0.0	8.295	0.258	-	-
0.25	8.158	0.253	-0.378	0.353
0.5	8.597	0.267	0.813	0.792
1.0	8.312	0.258	0.046	0.518
2.0	8.278	0.257	-0.046	0.482
Doped concentrator (w/w %)	**$\bar{x}$ (%)**	**SE (%)**	**Z**	**P ($\mu > \mu_{control}$)**
0.1 (Homogenous)	8.040	0.250	-0.711	0.239
0.1 (Top)	9.537	0.296	3.163	0.999
0.1 (Bottom)	9.133	0.284	2.188	0.986

Table 101: Results of z-test for $Sr_4Al_{14}O_{25}$: Eu^{2+}, Dy^{3+} doped LCPV devices at 0.4 suns.

Doped optical coupling (w/w %)	$\bar{x}$ (%)	SE (%)	z	P ($\mu > \mu_{control}$)
0.0	9.102	0.283	-	-
0.25	9.126	0.283	0.059	0.524
0.5	9.780	0.304	1.633	0.949
1.0	10.182	0.316	2.545	0.995
2.0	9.708	0.302	1.465	0.929
Doped concentrator (w/w %)	**$\bar{x}$ (%)**	**SE (%)**	**z**	**P ($\mu > \mu_{control}$)**
0.1 (Homogenous)	9.356	0.291	0.625	0.734
0.1 (Top)	9.330	0.290	0.563	0.713
0.1 (Bottom)	9.107	0.283	0.013	0.505

Table 102: Results of z-test for $NaYF_4$: Er^{3+}, Yb^{3+} doped LCPV devices at 1 sun.

Doped optical coupling (w/w %)	$\bar{x}$ (%)	SE (%)	z	P ($\mu > \mu_{control}$)
0.0	8.730	0.271	-	-
0.25	8.820	0.274	0.232	0.592
0.5	9.567	0.297	2.081	0.981
1.0	9.965	0.310	3.000	0.999
2.0	9.507	0.295	1.938	0.974
Doped concentrator (w/w %)	**$\bar{x}$ (%)**	**SE (%)**	**z**	**P ($\mu > \mu_{control}$)**
0.1 (Homogenous)	9.438	0.293	1.773	0.962
0.1 (Top)	9.340	0.290	1.535	0.938
0.1 (Bottom)	9.245	0.287	1.303	0.904

Table 103: Results of z-test for $NaYF_4$: Er^{3+}, Yb^{3+} doped LCPV devices at 0.8 suns.

Doped optical coupling (w/w %)	$\bar{x}$ (%)	SE (%)	z	P ($\mu > \mu_{control}$)
0.0	8.703	0.270	-	-
0.25	8.807	0.274	0.270	0.606
0.5	9.544	0.296	2.098	0.982
1.0	9.938	0.309	3.011	0.999
2.0	9.532	0.296	2.068	0.981
Doped concentrator (w/w %)	**$\bar{x}$ (%)**	**SE (%)**	**z**	**P ($\mu > \mu_{control}$)**
0.1 (Homogenous)	9.285	0.288	1.473	0.930
0.1 (Top)	9.278	0.288	1.457	0.927
0.1 (Bottom)	9.103	0.283	1.024	0.847

Table 104: Results of z-test for $NaYF_4$: Er^{3+}, Yb^{3+} doped LCPV devices at 0.6 suns.

Doped optical coupling (w/w %)	$\bar{x}$ (%)	SE (%)	z	P ($\mu > \mu_{control}$)
0.0	8.295	0.258	-	-
0.25	8.499	0.264	0.553	0.710
0.5	9.255	0.287	2.487	0.994
1.0	9.644	0.300	3.415	>0.999
2.0	9.252	0.287	2.479	0.993
Doped concentrator (w/w %)	**$\bar{x}$ (%)**	**SE (%)**	**z**	**P ($\mu > \mu_{control}$)**
0.1 (Homogenous)	8.906	0.277	1.616	0.947
0.1 (Top)	8.798	0.273	1.338	0.910
0.1 (Bottom)	8.647	0.269	0.945	0.828

Table 105: Results of z-test for $NaYF_4$: Er^{3+}, Yb^{3+} doped LCPV devices at 0.4 suns.

Doped optical coupling (w/w %)	$\bar{x}$ (%)	SE (%)	z	P ($\mu > \mu_{control}$)
0.0	15.515	0.367	-	-
0.25	15.951	0.378	0.827	0.796
0.5	15.573	0.369	0.112	0.545
1.0	15.699	0.372	0.353	0.638
2.0	15.587	0.369	0.138	0.555

Table 106: Results of z-test for $Sr_4Al_{14}O_{25}$: Eu^{2+}, Dy^{3+} doped Sylgard PV cells at 1 sun.

Doped optical coupling (w/w %)	$\bar{x}$ (%)	SE (%)	z	P ($\mu > \mu_{control}$)
0.0	15.809	0.374	-	-
0.25	16.285	0.385	0.885	0.912
0.5	16.087	0.381	0.520	0.698
1.0	16.056	0.380	0.462	0.678
2.0	16.059	0.380	0.468	0.680

Table 107: Results of z-test for $Sr_4Al_{14}O_{25}$: Eu^{2+}, Dy^{3+} doped Sylgard PV cells at 0.8 suns.

Doped optical coupling (w/w %)	$\bar{x}$ (%)	SE (%)	z	P ($\mu > \mu_{control}$)
0.0	15.715	0.372	-	-
0.25	16.100	0.381	0.723	0.765
0.5	15.947	0.377	0.438	0.669
1.0	15.759	0.373	0.084	0.533
2.0	15.829	0.375	0.217	0.586

Table 108: Results of z-test for $Sr_4Al_{14}O_{25}$: Eu^{2+}, Dy^{3+} doped Sylgard PV cells at 0.6 suns.

Doped optical coupling (w/w %)	$\bar{x}$ (%)	SE (%)	z	P ($\mu > \mu_{control}$)
0.0	15.197	0.360	-	-
0.25	15.504	0.367	0.598	0.725
0.5	15.305	0.362	0.212	0.584
1.0	14.951	0.354	-0.487	0.313
2.0	15.235	0.361	0.075	0.530

Table 109: Results of z-test for $Sr_4Al_{14}O_{25}$: Eu^{2+}, Dy^{3+} doped Sylgard PV cells at 0.4 suns.

Doped optical coupling (w/w %)	$\bar{x}$ (%)	SE (%)	z	P ($\mu > \mu_{control}$)
0.0	15.515	0.367	-	-
0.25	15.761	0.373	0.471	0.681
0.5	15.748	0.373	0.445	0.672
1.0	16.283	0.385	1.442	0.925
2.0	15.887	0.376	0.707	0.760

Table 110: Results of z-test for $NaYF_4$: Er^{3+}, Yb^{3+} doped Sylgard PV cells at 1 sun.

Doped optical coupling (w/w %)	$\bar{x}$ (%)	SE (%)	z	P ($\mu > \mu_{control}$)
0.0	15.809	0.374	-	-
0.25	16.131	0.382	0.602	0.726
0.5	15.952	0.378	0.269	0.606
1.0	16.350	0.387	1.004	0.842
2.0	15.905	0.377	0.181	0.572

Table 111: Results of z-test for $NaYF_4$: Er^{3+}, Yb^{3+} doped Sylgard PV cells at 0.8 suns.

Doped optical coupling (w/w %)	$\bar{x}$ (%)	SE (%)	z	P ($\mu > \mu_{control}$)
0.0	15.715	0.372	-	-
0.25	15.734	0.372	0.037	0.515
0.5	15.593	0.369	-0.233	0.408
1.0	15.863	0.375	0.280	0.610
2.0	15.549	0.368	-0.316	0.376

Table 112: Results of z-test for $NaYF_4$: Er^{3+}, Yb^{3+} doped Sylgard PV cells at 0.6 suns.

Doped optical coupling (w/w %)	$\bar{x}$ (%)	SE (%)	z	P ($\mu > \mu_{control}$)
0.0	15.197	0.360	-	-
0.25	15.189	0.360	-0.015	0.494
0.5	14.892	0.353	-0.606	0.272
1.0	15.512	0.367	0.613	0.730
2.0	14.997	0.355	-0.396	0.346

Table 113: Results of z-test for $NaYF_4$: Er^{3+}, Yb^{3+} doped Sylgard PV cells at 0.4 suns.

From this statistical test, it is seen the implications for the LCPV devices are largely similar to what was commented in 6.3.1; the highest performing champion device categories are also usually the ones with a 95% or 99% confidence of their true mean being greater than the control. However, it can also be said this test is harsher as much less of the total device data sets reach these levels over all irradiance levels; using the t-test 32 measurement samples have a confidence level of >95% and 22 of more than 99%, whereas for the z-test these figures are just 17 and 9. This is down to the SE under this model being larger in most cases than the sample standard deviations.

Likewise, the PV cells feel the effect of this and because the SE scales linearly with PCE, by demonstrating no measurements with a confidence level above 95%, although the best two devices, 0.25% w/w for $Sr_4Al_{14}O_{25}$: Eu^{2+}, Dy^{3+} and 1% w/w doped optical coupling $NaYF_4$: Er^{3+}, Yb^{3+}, almost did with P ($\mu > \mu_{control}$) of 0.912 and 0.925 respectively. Thus, it may be concluded that 6.3.1 is the better method as it is based on real statistical observations rather than the assumed

population standard deviation which might itself be an overestimate (perhaps due to assumptions like $V_{OC} = V_{MP}$ and the concentrators not having such un-uniform optical properties as suggested by a relatively small sample of UV-Vis measurements compared to the total number of concentrators used).

6.3.3 DSSC variation in device efficiency

Such a rigorous analysis is not provided for the DSSC investigation due to the smaller sample size (of two, rather than three) diluting its meaning. However for completeness, the sample mean, range (difference between maximum and minimum PCE), sample standard deviation (range divided by 2 for all except the control device for which a total of 6 copies were made) and SE (using the very crude estimate that $s = \sigma$) are provided for the PCEs of the screen printed DSSCs in Tables 114 and 115. Further graphical presentations with SE as the error bars are shown in Figures 150 and 151 in which the same notation as used in chapter 5 is utilised to abbreviate the device names: (DB for the doctor bladed on TiO2, SC for the spin coated TiO2-rare earth mixture, DC x µl for the drop casting by x µl of the TiO2-rare earth mixture and DB CE for the doctor bladed counter electrode.

Device Category	$\bar{x}$ (%)	s (%)	SE (%)	Range (%)
Control	3.017	0.856	0.605	2.405
Doctor bladed on TiO_2	2.925	0.294	0.208	0.587
Spin coated TiO_2 mixture	3.140	0.449	0.317	0.897
Drop cast TiO_2 mixture (25 µl)	4.487	0.092	0.065	0.183
Drop cast TiO_2 mixture (50 µl)	3.413	0.391	0.276	0.782
Drop cast TiO_2 mixture (100 µl)	2.372	1.131	0.799	2.261
Drop cast TiO_2 mixture (200 µl)	2.452	0.675	0.477	1.350
Doctor bladed counter electrode	3.242	1.598	1.130	3.196

Table 114: Variation in the PCE of the $Sr_4Al_{14}O_{25}$: Eu^{2+}, Dy^{3+} doped screen printed DSSCs.

Device Category	$\bar{x}$ (%)	s (%)	SE (%)	Range (%)
Control	3.017	0.856	0.605	2.405
Doctor bladed on TiO_2	1.679	0.464	0.328	0.927
Spin coated TiO_2 mixture	3.697	0.004	0.003	0.008
Drop cast TiO_2 mixture (25 µl)	4.817	0.002	0.001	0.004
Drop cast TiO_2 mixture (50 µl)	4.813	0.491	0.347	0.981
Drop cast TiO_2 mixture (100 µl)	1.799	1.000	0.707	1.999
Drop cast TiO_2 mixture (200 µl)	3.151	0.064	0.045	0.128
Doctor bladed counter electrode	4.318	1.316	0.930	2.631

Table 115: Variation in the PCE of the $NaYF_4$: Er^{3+}, Yb^{3+} doped screen printed DSSCs.

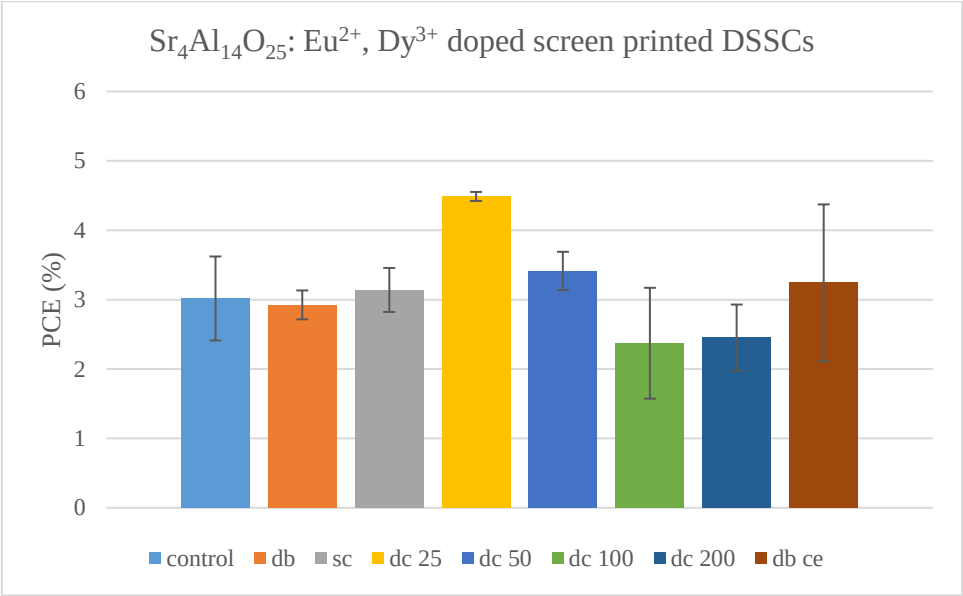

Figure 150: Graph of the sample mean PCEs of the $Sr_4Al_{14}O_{25}$: Eu^{2+}, Dy^{3+} doped screen printed DSSCs with their SE bars displayed.

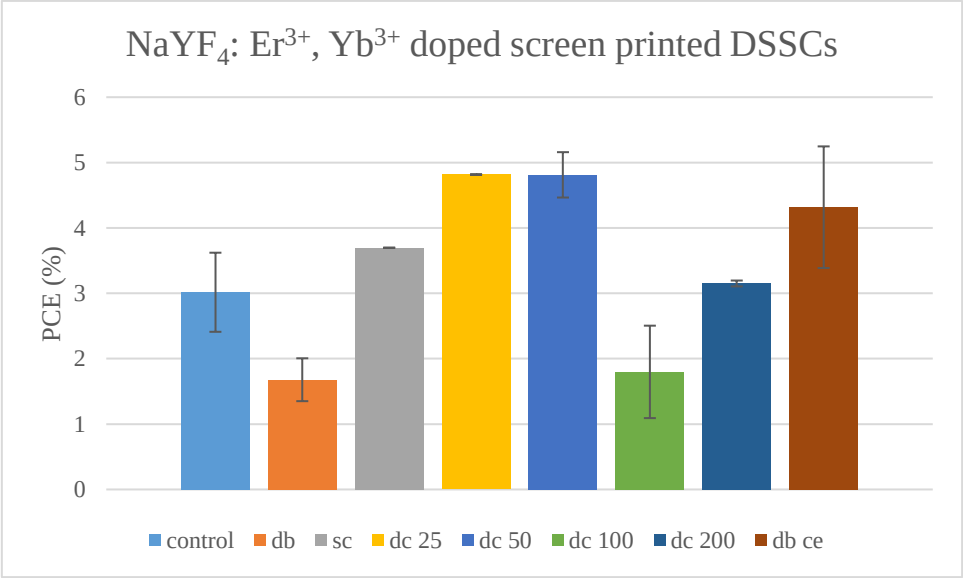

Figure 151: Graph of the sample mean PCEs of the $NaYF_4$: Er^{3+}, Yb^{3+} doped screen printed DSSCs with their SE bars displayed.

It can be seen in some instances the standard error is small, particularly for the spin coated and 25 µl drop casted devices, however, in a few occasions it is much larger (~1%) indicating possible, unavoidable inconsistencies in their fabrication process. The fact the thinner films have a lower standard error could mean the dispensing of less fluid causes a more reproducible, uniform thin film to form. As a result, the low standard error and thus relatively high average PCE of the spin coated TiO_2-rare earth mixture for both materials give it more viability as an option. Nevertheless, if the means are taken as opposed to the champion device PCE, the conclusions from chapter 5 mostly still hold. Although considering the

sample mean, $Sr_4Al_{14}O_{25}$: Eu^{2+}, Dy^{3+} 25 µl drop casted is now better than the doctor bladed counter electrode. In addition, another new observation would be that there is much less difference between the 25 µl and 50 µl drop casted layers for the $NaYF_4$: Er^{3+}, Yb^{3+} doped devices with the former now having a slightly higher PCE of 0.004%. The $NaYF_4$: Er^{3+}, Yb^{3+} doctor bladed counter electrode also has a very large range and standard deviation. The reasons for the doctor bladed CE of both materials leading to irregular efficiencies could be cause for further study, since both the films appeared visually identical, but their I-V curves were wildly different between samples and time of measurements, indicating a potential hysteresis effect. Finally, it is more difficult to quantify DSSC uncertainties but they can stem from the same characterisation equipment factors in 6.3.2 as well as human error in the fabrication process (e.g. the force or direction of applying the squeegee and dropping solutions slightly off-centre onto the substrate which can affect film quality).

6.4 Optical Models

Simple optical models will be deployed in two cases to develop the theoretical underpinning of this work and build a clearer picture of the reasons for enhanced electrical performance from first principles. Firstly, the thin film coating on silicon PV cells in the absence of concentrators will be studied using an existing model. Then with the aid of MATLAB®, a simple ray 2D trace argument will be constructed in order to attempt to justify the results observed in the LCPV modules.

6.4.1 Thin Film Layer

The physical processes and possible optical paths within a thin film of spectral conversion material coating a solar PV cell are similar to those of the LSC as shown in Figure 28 in 2.7.1. This means by considering these fundamental losses, a simple mathematical model can be made to predict the behaviour of a spectral conversion layer on a solar cell (without a concentrator). Such a model was developed by Rothemund et al in 2013 [182], specifically for LDS processes and shall be utilised here for this thesis.

The underpinning equation for this model was derived by considering the incident radiation on the LDS layer at a given wavelength which can be split into two fractions; the fraction of photons absorbed by the LDS layer, $f_{abs}\ (\lambda)$, and the

fraction transmitted directly through to the PV cell, $f_{trans}(\lambda)$, i.e. without interacting with the LDS material. These two quantities can in turn be derived from the fundamental laws of optics (given in 3.4.2) in addition to the Beer-Lambert law and are given by:

$$f_{abs}(\lambda) = (1 - \Delta R_{LDS})(1 - \exp[-\Lambda_{abs} \cdot Abs(\lambda)]) \quad (47)$$

$$f_{trans}(\lambda) = 1 - \Delta R_{LDS} - f_{abs}(\lambda) \quad (48)$$

In these expressions ΔR_{LDS} is the additional reflectance arising from the presence of the LDS particles within the host matrix (in this case Sylgard), $Abs(\lambda)$ is the absorbance as function of wavelength and Λ_{abs} is an absorbance scaling factor depending on the concentration ratio of the LDS particles and thickness of the layer containing them. For simplicity, it can be assumed that $\Delta R_{LDS} \approx 0$ which modifies the above equations to:

$$f_{abs}(\lambda) = (1 - \exp[-\Lambda_{abs} \cdot Abs(\lambda)]) \quad (49)$$

$$f_{trans}(\lambda) = 1 - f_{abs}(\lambda) \quad (50)$$

Two further factors then determine the effectiveness of the LDS layer, the emission spectral matching (ESM) and the LDS efficiency (η_{LDS}). The ESM is essentially another scaling factor that determines the average EQE of the PV cell resulting from the LDS emission across all wavelengths incident on it, and is given by:

$$ESM = \frac{\int_{\lambda_{min}}^{\lambda_{max}} PL(\lambda')EQE_{ref}(\lambda')d\lambda'}{\int_{\lambda_{min}}^{\lambda_{max}} PL(\lambda')d\lambda'} \quad (51)$$

In this expression $EQE_{ref}(\lambda)$ is the EQE of the bare cell without an LDS layer and the full derivation for ESM is given as an appendix in Rothemund's original work [182]. On the other hand, η_{LDS} is the fraction of the radiation absorbed by the LDS layer which reaches the PV cell below. In Rothemund's model this quantity depends on the iPLQY of the LDS material (denoted instead by η_{PL}) and fractional optical losses via the escape cone of spectrally converted emission (L_{esc}), self-absorption of the emission (L_{reabs}) and other sources including via the sides of the layer and reflection at the interfaces (L_{other}). These terms combine to give the η_{LDS} as follows:

$$\eta_{LDS} = \eta_{PL}(1 - L_{esc})(1 - L_{reabs})(1 - L_{other}) \quad (52)$$

Finally, these aforementioned quantities complete the terms for the underpinning equation of this model and can be combined to give a formula for the predicted EQE of the PV cell coated by an LDS layer, $EQE_{LDS}(\lambda)$ given by:

$$EQE_{LDS}(\lambda) = f_{abs}(\lambda)\eta_{LDS}ESM + f_{trans}(\lambda)EQE_{ref}(\lambda) \qquad (53)$$

This concise expression is highly useful to describe the behaviour of the system because it only requires two unknown parameters, Λ_{abs} and η_{LDS} (EQE_{ref} (λ), *Abs (λ)* and ESM are able to be known from separate experimental data) and can be applied to any solar cell technology given its bare EQE. The unknown parameters can be solved by setting up an optimisation problem in which Λ_{abs} and η_{PL} are varied to give a resulting EQE_{LDS} (λ) or EQE_{model} which can then be compared to the EQE measurements obtained earlier with the Bentham PVE300 from the LDS layer-PV cell experiment (EQE_{expt}). Ideally, when a perfect solution is found the values of EQE_{model} and EQE_{expt} should be the identical for all λ. However, this is beyond the level of accuracy for a model such as this one (due to the simplified assumptions and non-continuous input variables), so instead it shall be aimed to find the values of Λ_{abs} and η_{LDS} which produce an EQE_{model} profile that closest resembles EQE_{expt}. With a more mathematically rigorous approach, the sum of squared errors of prediction (SSE) can be calculated for different values of Λ_{abs} and η_{LDS} at each discrete data point λ_i (with n data points in total). The SSE is given by:

$$SSE = \sum_{i=1}^{i=n} (EQE_{model}(\lambda_i) - EQE_{expt}(\lambda_i))^2 \qquad (54)$$

Its value is a quantitative measure of the discrepancy between observed and predicted data points, and the smaller the SSE, the better the fit. To begin building a model for this work using the equation for EQE_{model}(λ), the inputs for EQE_{ref} (λ) and *Abs (λ)* were taken as those obtained in prior experiments. For EQE_{ref} (λ) an average of the bare EQEs recorded for the cells used in the TiO_2 coating experiments in chapter 3 was used. Similarly, for *Abs(λ)*, the data for the transmittance of the rare earth doped Sylgard thin films obtained from the Perkin Elmer Lambda 1050 was utilised (after using the relation in 3.4.2 to convert from transmittance to absorbance). Next, with the *PL(λ)* profiles for the most prominent emission profiles from 3.3.3, the ESM for each rare earth compound can be easily

calculated using a modified version of the ESM formula in which the integral for a continuous *PL(λ)* function becomes a sum over the discrete *PL(λ_i)* values in the denominator and the *PL(λ_i)* values multiplied by EQE_{ref} (λ_i) data points in the numerator. This yields ESM values of 0.80 for $Sr_4Al_{14}O_{25}$: Eu^{2+}, Dy^{3+} and 0.85 for $NaYF_4$: Er^{3+}, Yb^{3+}.

Now that all inputs for the underpinning equation have been determined, a program in an Excel spreadsheet can be constructed that allows an instantaneous output of $EQE_{model}(\lambda)$ and SSE when the values of the cells containing Λ_{abs} and η_{LDS} are changed. In order to find the optimal Λ_{abs} and η_{LDS} values, a rigorous trial and error method is used in which the calculated SSEs are noted for a large combination of Λ_{abs} and η_{LDS} inputs; when SSE is minimised, the solution is found. To ease the problem, there are some physical constraints on the value of η_{LDS} such that it must be between 0 and 1 for a pure LDS process. It must also be such that the $Sr_4Al_{14}O_{25}$: Eu^{2+}, Dy^{3+} photoluminescence is an LDS process as the emission wavelength possesses too high an energy to produce two photons from ~ 400 nm excitation. Likewise although $NaYF_4$: Er^{3+}, Yb^{3+} is a DC material, the 660 nm emission again can only be produced at a maximum of one per absorbed photon from the same energy argument (the other emitted photon will be of lower energy, but as seen from photoluminescent spectroscopy is of much weaker intensity so is omitted in this model). Conversely, Λ_{abs} is an arbitrary scaling factor with no immediate physical upper or lower limits to its size. However, a cursory study of the underpinning formula shows that because Λ_{abs} is in a negative exponent then it will lead to two cases in its extreme cases. In the limit $\Lambda_{abs} \rightarrow 0$, the equation for LDS simply becomes:

$$EQE_{LDS}(\lambda) = EQE_{ref}(\lambda) \qquad (55)$$

Whereas in the limit $\Lambda_{abs} \rightarrow \infty$, the equation simplifies to:

$$EQE_{LDS}(\lambda) = \eta_{LDS} ESM \qquad (56)$$

It was first proposed to produce a model that would fit the experimental data (EQE_{expt}) obtained for the Sylgard doped with 0.5% $Sr_4Al_{14}O_{25}$: Eu^{2+}, Dy^{3+} coated PV device studied in 3.7.3. In initial tests using η_{LDS} = 0.80 and Λ_{abs} = 1 (a sensible starting point because of the absorbance values being of order 10^{-1} and the behaviour of Λ_{abs} at large and small values), it was found the EQE_{model} produced data points that were too small in the region 300-500 nm, where

improvements are expected and experimentally observed. Hence, Λ_{abs} was increased incrementally in integer steps, to Λ_{abs} = 20. It was then noted that at higher values of Λ_{abs} (> 14), the EQE_{model} predictions were too high in the 300-400 nm region and too low in the 400-600 nm section. To compensate for this, the η_{LDS} values were then increased to yield larger predicted EQE values for λ > 400 nm. Through fine tuning Λ_{abs} to account for the higher spectral conversion efficiency, a minimal SSE of 0.00139 was found for Λ_{abs} = 5.5 and η_{LDS} = 1.

A similar procedure was repeated to obtain realistic EQE_{model} spectra for the 0.25%, 1% and 2% doped $Sr_4Al_{14}O_{25}$: Eu^{2+}, Dy^{3+} Sylgard coated devices and all the $NaYF_4$: Er^{3+}, Yb^{3+} in Sylgard layer containing PV cells, while using their appropriate experimental data from chapter 3 as inputs for the model. These results are summarised in Table 116 and the Figures 152-159 which show a graph of the spectra of the bare solar cell compared to the experimental data and that predicted by the model (from 300-600 nm to clearly show the changes). Finally, an R^2 value was calculated for each data set to quantitatively evaluate the goodness of fit (generally, the closer its value to unity, the better the experimental data is predicted by the model).

$$R^2 = 1 - \frac{SSE}{SST} \qquad (57)$$

In which SST is the total sum of squares given by:

$$SST = \sum_{i=1}^{i=n} (EQE_{expt}(\lambda_i) - \overline{EQE_{expt}})^2 \qquad (58)$$

And $\overline{EQE_{expt}}$ is the mean value of measured EQE data (EQE_{expt}), calculated as:

$$\overline{EQE_{expt}} = \frac{1}{n} \sum_{i=1}^{i=n} EQE_{expt}(\lambda_i) \qquad (59)$$

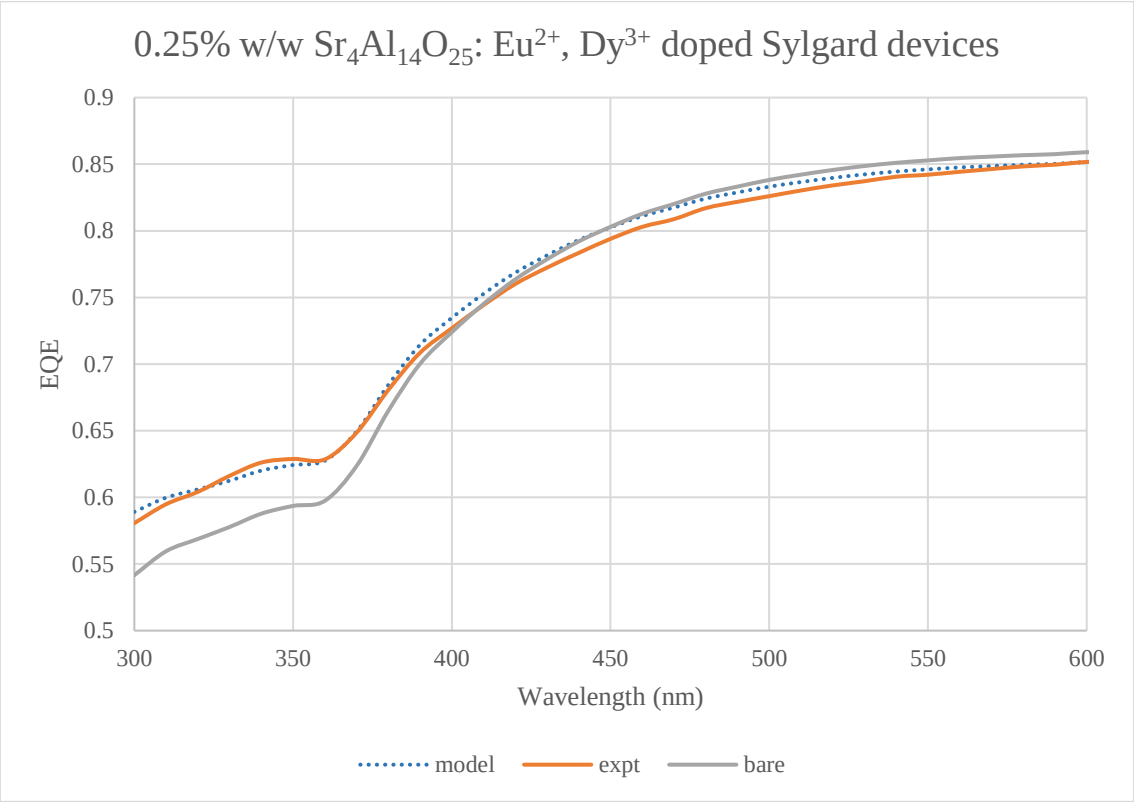

Figure 152: The EQE profile for 0.25% w/w doped $Sr_4Al_{14}O_{25}$: Eu^{2+}, Dy^{3+} Sylgard PV cells predicted by the model compared to the bare and experimentally measured EQE.

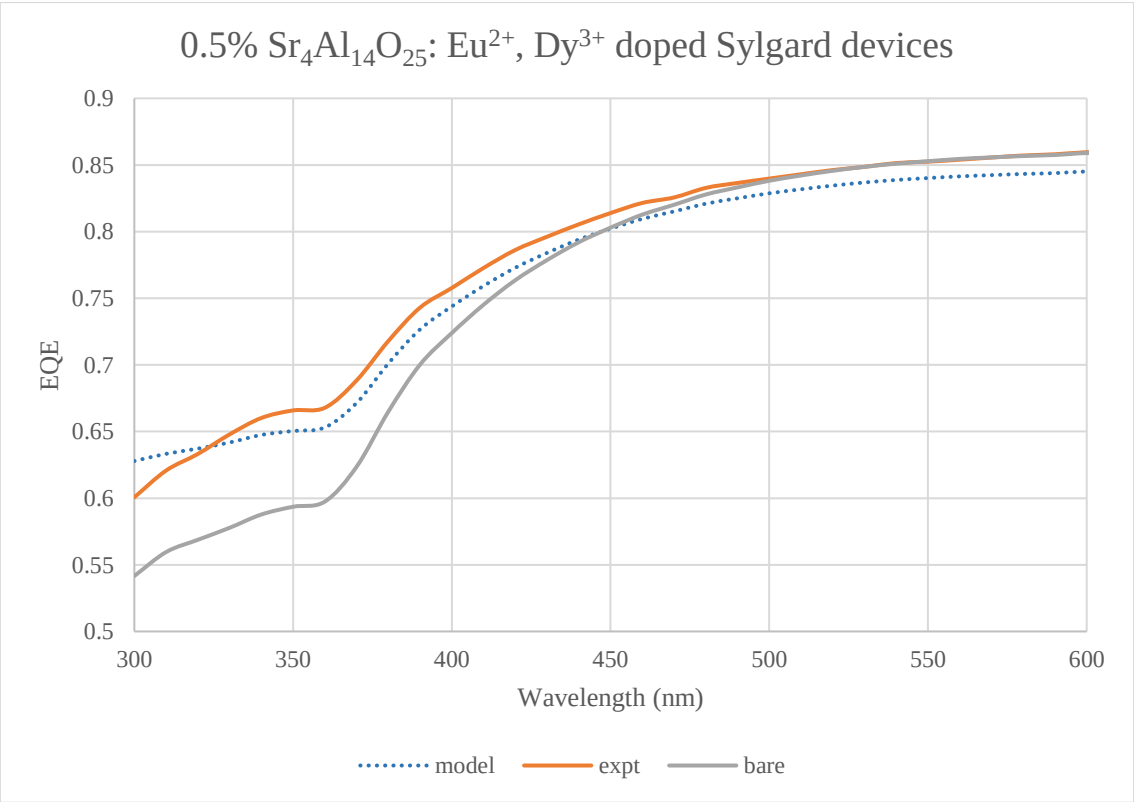

Figure 153: The EQE profile for 0.5% w/w doped $Sr_4Al_{14}O_{25}$: Eu^{2+}, Dy^{3+} Sylgard PV cells predicted by the model compared to the bare and experimentally measured EQE.

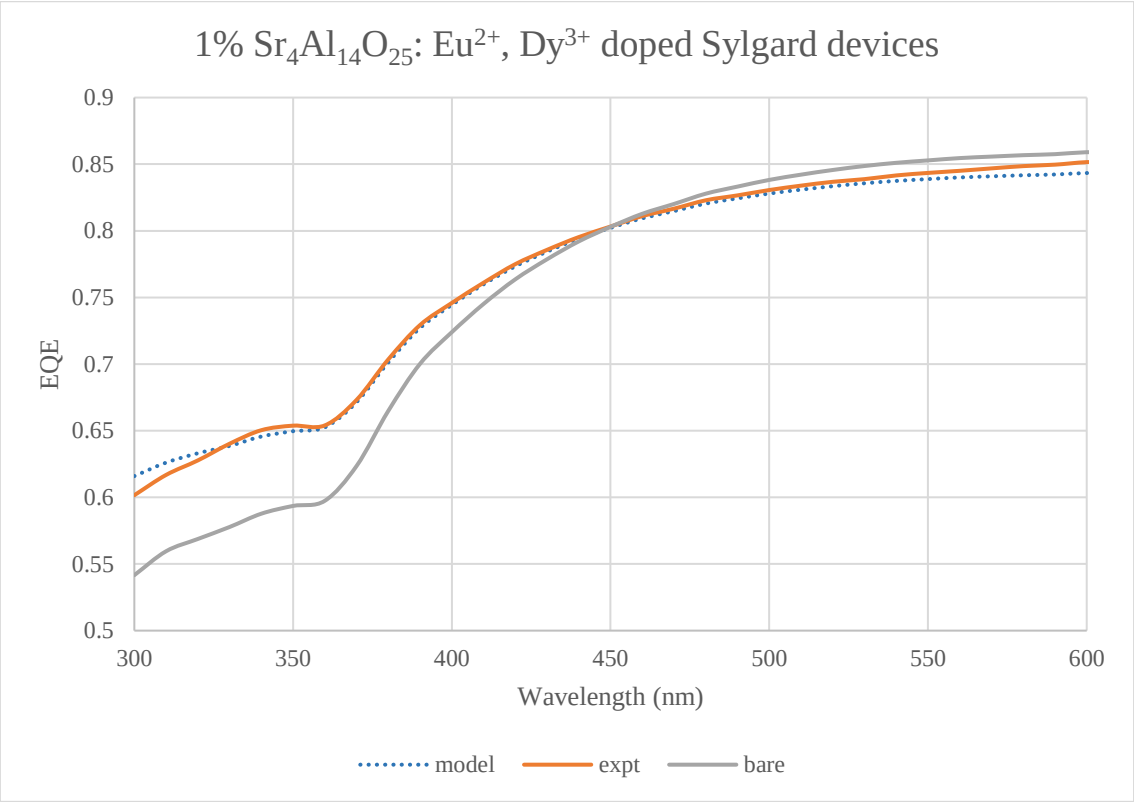

Figure 154: The EQE profile for 1% w/w doped $Sr_4Al_{14}O_{25}$: Eu^{2+}, Dy^{3+} Sylgard PV cells predicted by the model compared to the bare and experimentally measured EQE.

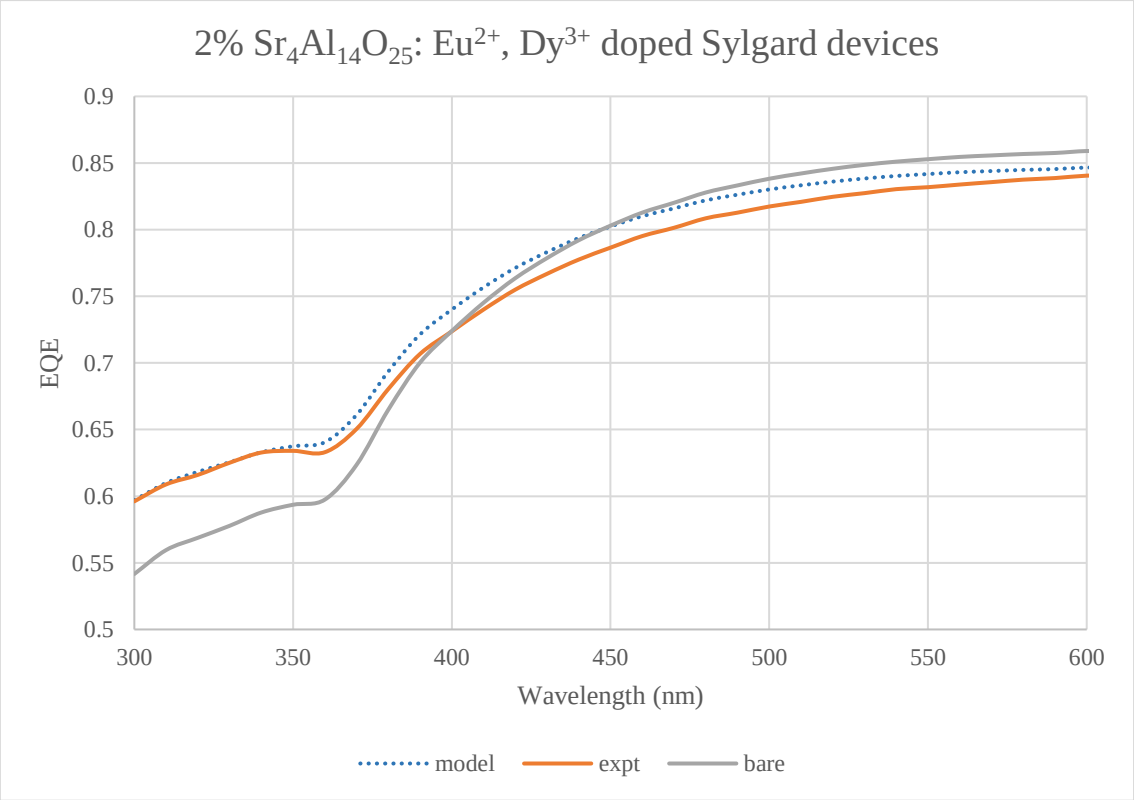

Figure 155: The EQE profile for 2% w/w doped $Sr_4Al_{14}O_{25}$: Eu^{2+}, Dy^{3+} Sylgard PV cells predicted by the model compared to the bare and experimentally measured EQE.

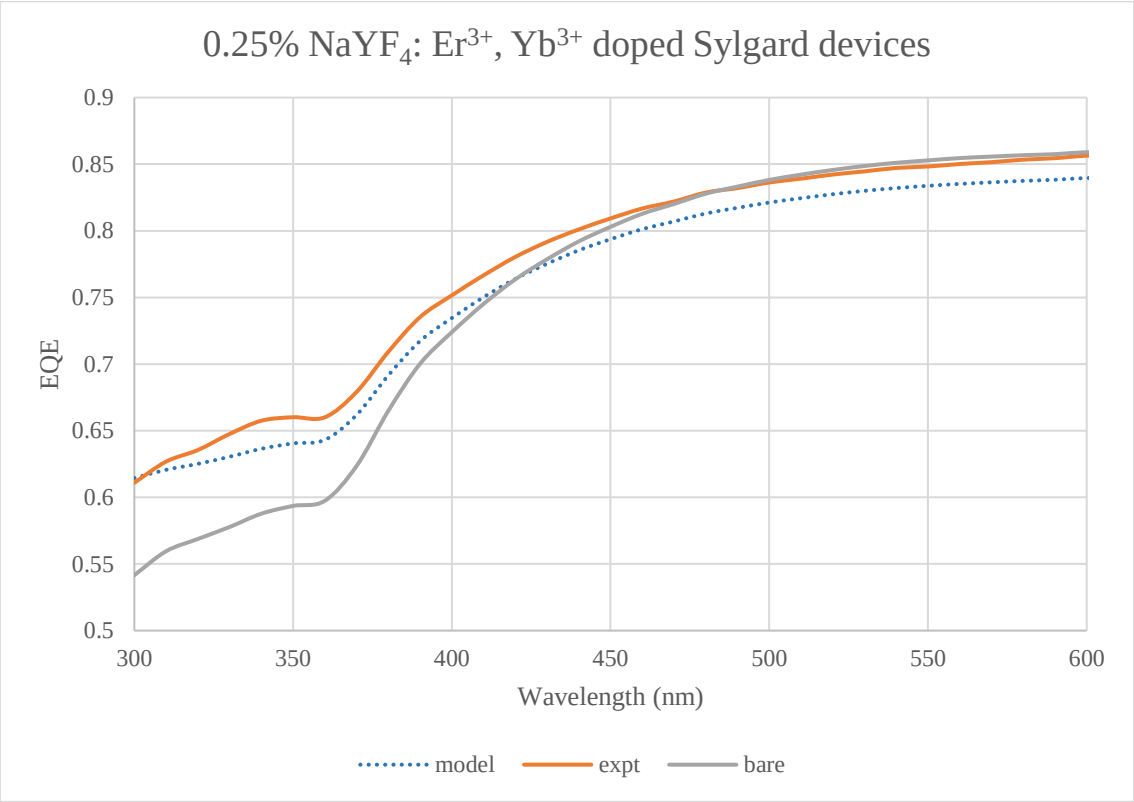

Figure 156: The EQE profile for 0.25% w/w doped $NaYF_4$: Er^{3+}, Yb^{3+} Sylgard PV cells predicted by the model compared to the bare and experimentally measured EQE.

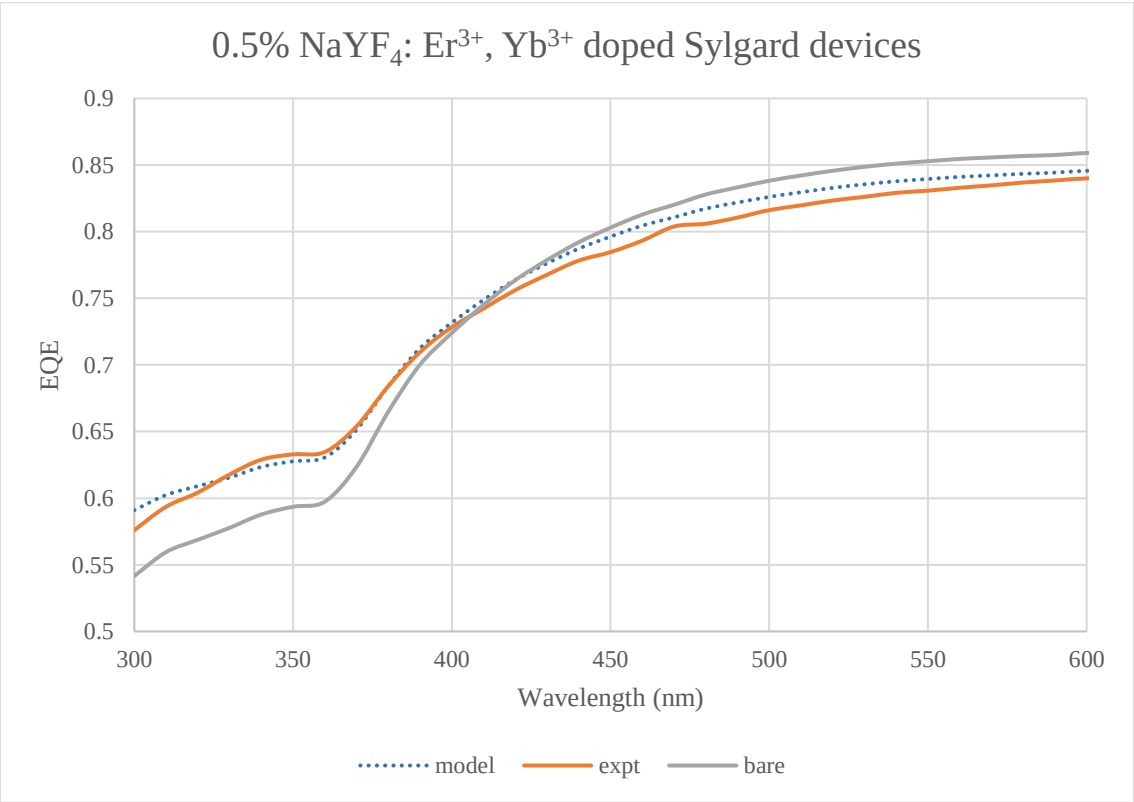

Figure 157: The EQE profile for 0.5% w/w doped $NaYF_4$: Er^{3+}, Yb^{3+} Sylgard PV cells predicted by the model compared to the bare and experimentally measured EQE.

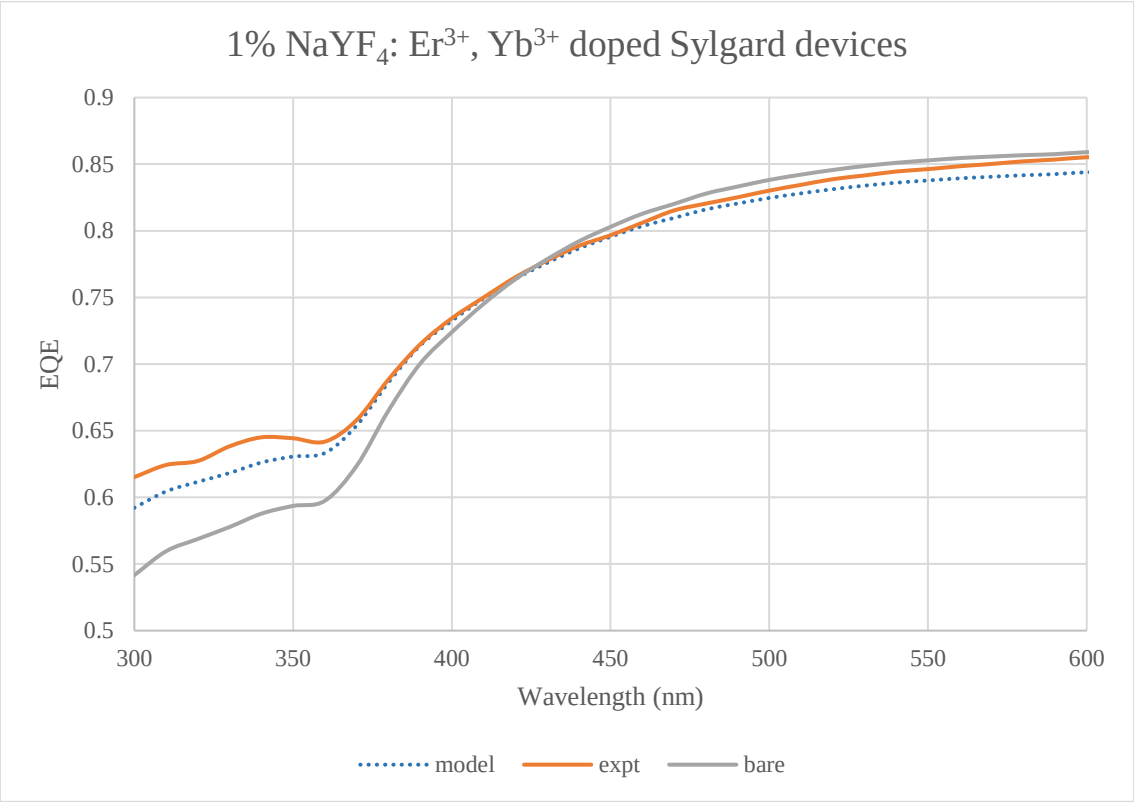

Figure 158: The EQE profile for 1% w/w doped $NaYF_4$: Er^{3+}, Yb^{3+} Sylgard PV cells predicted by the model compared to the bare and experimentally measured EQE.

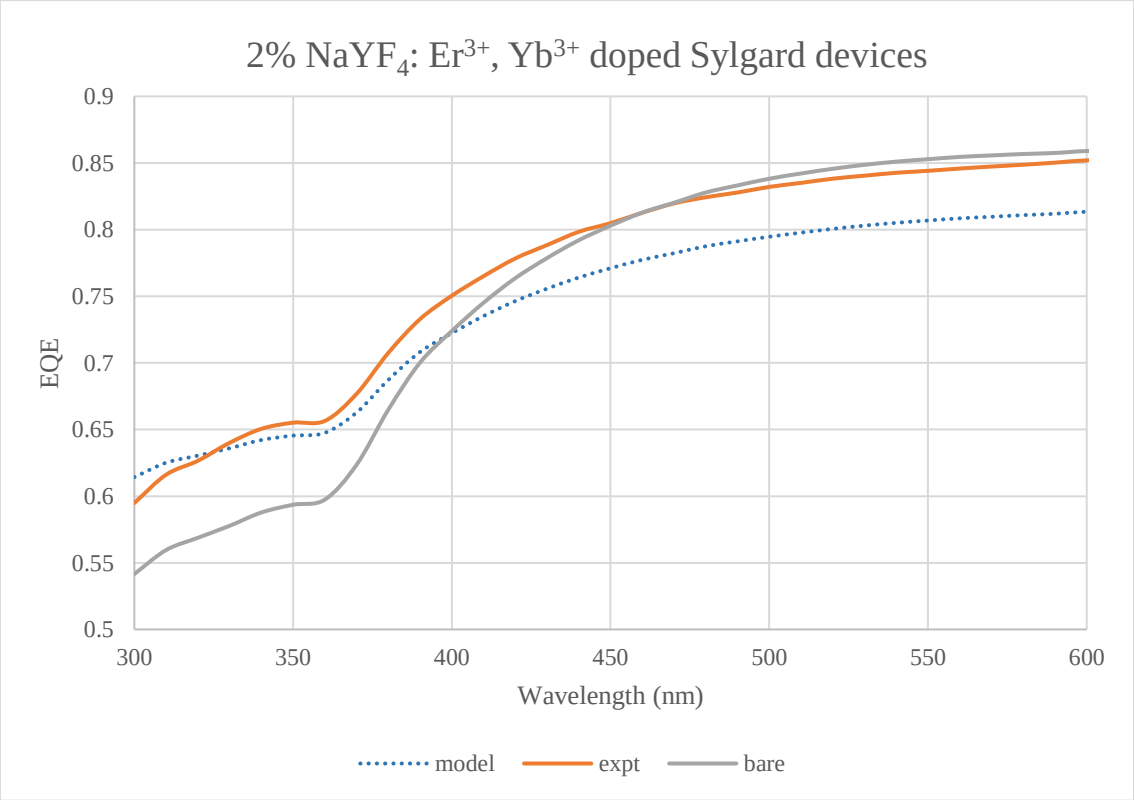

Figure 159: The EQE profile for 2% w/w doped $NaYF_4$: Er^{3+}, Yb^{3+} Sylgard PV cells predicted by the model compared to the bare and experimentally measured EQE.

Sylgard doping	Λ_{abs}	η_{LDS}	SSE ($\times 10^{-3}$)	R^2
0.25% $Sr_4Al_{14}O_{25}$: Eu^{2+}, Dy^{3+}	2.75	1	1.39	0.996
0.5% $Sr_4Al_{14}O_{25}$: Eu^{2+}, Dy^{3+}	5.5	1	8.01	0.970
1% $Sr_4Al_{14}O_{25}$: Eu^{2+}, Dy^{3+}	2	1	1.93	0.992
2% $Sr_4Al_{14}O_{25}$: Eu^{2+}, Dy^{3+}	1	1	5.08	0.982
0.25% $NaYF_4$: Er^{3+}, Yb^{3+}	6	0.9	11.87	0.959
0.5% $NaYF_4$: Er^{3+}, Yb^{3+}	3	0.9	2.21	0.993
1% $NaYF_4$: Er^{3+}, Yb^{3+}	2	0.9	5.75	0.983
2% $NaYF_4$: Er^{3+}, Yb^{3+}	2	0.9	49.84	0.800

Table 116: The derived model parameters and goodness of fit for each concentration of rare earth compound for $Sr_4Al_{14}O_{25}$: Eu^{2+}, $Dy^{3+}$and $NaYF_4$: Er^{3+}, Yb^{3+} doped Sylgard devices.

On observation of the sets of curves, the model predictions are reasonably good fits for the experimental data. The lowest SSE and highest R^2 are obtained for the 0.25% doped $Sr_4Al_{14}O_{25}$: Eu^{2+}, Dy^{3+} device while all other Sylgard doping levels have small SSEs <0.01 and $R^2 > 0.95$, except for the 0.25% and 2% doped $NaYF_4$: Er^{3+}, Yb^{3+} layers (both the result of an underestimated EQE at wavelengths > 450 nm). The Λ_{abs} values have a small range from 1-6 and tend to decrease almost linearly with increasing particle concentration (apart from the 0.25% $Sr_4Al_{14}O_{25}$: Eu^{2+}, Dy^{3+} and 2% doped $NaYF_4$: Er^{3+}, Yb^{3+} layers). This would be a problem, as Λ_{abs} would be expected to increase linearly with particle concentration, were it not for the fact that different *Abs(λ)* spectra were used for each doping level (based on their earlier transmittance spectra), so this scaling is allowed. Although given this, it might be predicted for their Λ_{abs} values all to be equal since the particle concentration is already factored into *Abs(λ)*. The discrepancy could be due to the neglection of reflectance and scattering in the derivation of *Abs(λ)*.

Conversely, the η_{LDS} values do stay constant for each doping level within the same material (1 for $Sr_4Al_{14}O_{25}$: Eu^{2+}, Dy^{3+} and 0.9 for $NaYF_4$: Er^{3+}, Yb^{3+}). This implies they do not vary with particle concentration. For simplicity this parameter was not varied by wavelength, but this is something a more complex model could account for. Furthermore, the omitting of the L_{esc}, L_{reabs} and L_{other} terms (by assuming they are all close to zero) means that η_{LDS} can be thought of as the iPLQY. Thus, the model also predicts $Sr_4Al_{14}O_{25}$: Eu^{2+}, Dy^{3+} to have a higher iPLQY than $NaYF_4$: Er^{3+}, Yb^{3+} which is consistent with the literature [179, 267]; the former's was quoted at 80.4% and the latter's at 64% (neglecting 980 nm emission). L_{reabs} will be small for these materials as there is little overlap in their excitation and emission profiles, although according to [182], for an embedding

material with a refractive index of ~1.5 like Sylgard it is expected that $L_{esc} \approx 0.12$ as a minimum, but neglecting these losses did lead to a much better fit with the observed EQE data. Moreover, in reality it is likely that ΔR_{LDS} would not equal zero and could actually be negative, so the expected increase in EQE from this aspect could compensate for the omission of escape cone losses and high predicted iPLQYs in this model.

With the EQE data, both from the model and PVE300 measurements, it is also possible calculate the J_{SC} (and compare with the control to quantify enhancements) for all coated PV cell doping levels by using a modified version of an earlier formula (Equation 9 in chapter 1). This is done by changing the integral into discrete intervals and summing over the range of wavelengths, multiplying by the wavelength interval, Δλ (in this case 10 nm), as per the equation below.

$$J_{SC} = \Delta\lambda e \sum_{n=0}^{n=80} \varphi(\lambda = 300 + 10n) EQE(\lambda = 300 + 10n) \tag{60}$$

Note that since EQE_{LDS} was only defined from 300-800 nm, where the *Abs(λ)* was factored into the equation, from 800-1100 nm the bare cell EQE_{ref} data points are used in its J_{SC} calculation and from working in S.I. units, the outputs will be in A/m^2, so can be divided by 10 to be given in the more scale appropriate mA/cm^2. All that remains is to know the numerical values for φ(λ), the photon flux, under AM 1.5 G conditions. These can be calculated from ASTM G173-03 (available as a spreadsheet from [349]) simply by dividing the spectral irradiance at a given wavelength by the energy of the photon at that wavelength.

$$\varphi(\lambda) = \frac{AM1.5G\ (\lambda)}{\left(\frac{hc}{\lambda}\right)} \tag{61}$$

From these two equations, each coated silicon PV cell's J_{SC} can be predicted from the EQE data for both the model (Mod. J_{SC}) and from the real earlier IPCE measurements (EQE J_{SC}) in Figures 84 and 85 in chapter 3. These are shown in Tables 117 and 118 along with the relative change in J_{SC} compared to the control and data from characterisation under the solar simulator (Expt. J_{SC}). Evidentially

it can be remarked that the EQE J_{SC} and Mod. J_{SC} calculated data are lower than that recorded under the solar simulator by ~4mA/cm^2. This could be down to the EQE not being independent of the photon flux (i.e. if the laser used in the Bentham PVE300 is less intense than the solar simulator) and a small contribution to J_{SC} from photons of wavelength >1100 nm and <300 nm which are not measured by the IPCE characterisation. Finally, the relative J_{SC} enhancements for each set of predictions and measurements are plotted against doping level for the two rare earth compounds in Figures 160 and 161. For the IPCE measurement calculated data, there is a good correlation with the experimental data from the solar simulator, demonstrating consistency between the two procedures (although the large deviation for 0.5% doped $Sr_4Al_{14}O_{25}$: Eu^{2+}, Dy^{3+} is unexpected and could be the result of an outlier measurement).

Disappointingly though, the predicted ΔJ_{SC} from the Rothemund model data is slightly negative, so PCE enhancements would not be expected to take place if the model completely explained cell behaviour. This might be surprising since there were significant EQE increases of up to 6% in the 300-400 nm region and except for the 2% doped $NaYF_4$: Er^{3+}, Yb^{3+}, there was always a good fit with the IPCE characterisation data and the EQE did not seem to decrease substantially at higher wavelengths. However, the reason for the smaller J_{SC} summed over AM 1.5 G is because the photon flux goes up a lot with increasing wavelength throughout the visible part of the spectrum (both due to the shape of the irradiance spectrum and inverse proportionality of photon wavelength to energy), so a small reduction in EQE at these parts of the spectrum becomes more noticeable in its contribution to the overall J_{SC} under simulated sunlight. Despite this flaw, one positive is that the Rothemund model comes close to predicting the best performing doping concentrations, since the $NaYF_4$: Er^{3+}, Yb^{3+} peaks in ΔJ_{SC} close to 1% w/w and at 0.25% w/w for $Sr_4Al_{14}O_{25}$: Eu^{2+}, Dy^{3+}, which are also doping ratios that performed well in terms of ΔPCE under solar simulator characterisation. To conclude the model provided a good prediction of the rare earth doped Sylgard coated silicon PV cell's EQE profiles but failed to accurately predict J_{SC} enhancements because it overestimates how much the EQE will decline at visible wavelengths, perhaps due to the fact that $\Delta R_{LDS} \neq 0$ or an unconsidered 980 nm emission contribution element from $NaYF_4$: Er^{3+}, Yb^{3+}.

Doping (w/w %)	Expt. J_{SC} (mA/cm^2)	Expt. Δ J_{SC} (%)	EQE J_{SC} (mA/cm^2)	EQE Δ J_{SC} (%)	Mod. J_{SC} (mA/cm^2)	Mod. Δ J_{SC} (%)
0.0	36.330	-	31.959	-	32.225	-
0.25	36.721	+1.08	32.233	+0.86	32.133	-0.29
0.5	37.552	+3.36	32.089	+0.41	32.042	-0.57
1.0	36.768	+1.21	32.274	+0.99	32.009	-0.67
2.0	36.982	+1.79	31.696	-0.82	32.046	-0.56

Table 117: Predicted J_{SC} data for the $Sr_4Al_{14}O_{25}$: Eu^{2+}, Dy^{3+} doped Sylgard layers on PV cells (from the optical model and IPCE measurements) compared to that observed under the solar simulator.

Doping (w/w %)	Expt. J_{SC} (mA/cm^2)	Expt. Δ J_{SC} (%)	EQE J_{SC} (mA/cm^2)	EQE Δ J_{SC} (%)	Mod. J_{SC} (mA/cm^2)	Mod. Δ J_{SC} (%)
0.0	36.330	-	31.959	-	32.225	-
0.25	36.794	+1.28	32.525	+1.77	31.881	-1.07
0.5	36.544	+0.59	31.917	-0.13	31.992	-0.72
1.0	36.968	+1.76	32.512	+1.73	31.961	-0.82
2.0	37.017	+1.89	32.264	+0.95	31.276	-2.95

Table 118: Predicted J_{SC} data for the $NaYF_4$: Er^{3+}, Yb^{3+} doped Sylgard layers on PV cells (from the optical model and IPCE measurements) compared to that observed under the solar simulator.

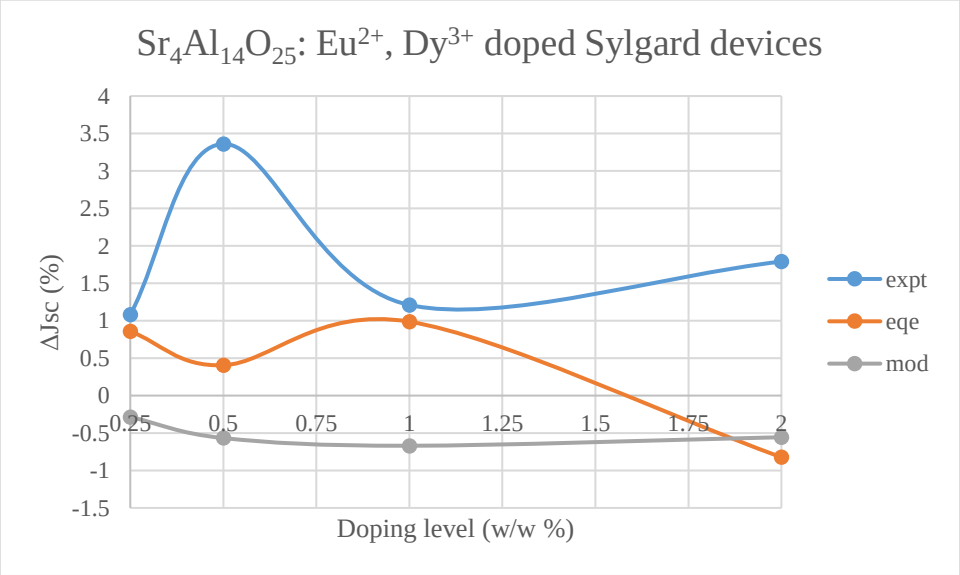

Figure 160: Relative J_{SC} gains for the $Sr_4Al_{14}O_{25}$: Eu^{2+}, Dy^{3+} doped Sylgard layers on PV cells (from the optical model and IPCE measurements) compared to that observed under the solar simulator.

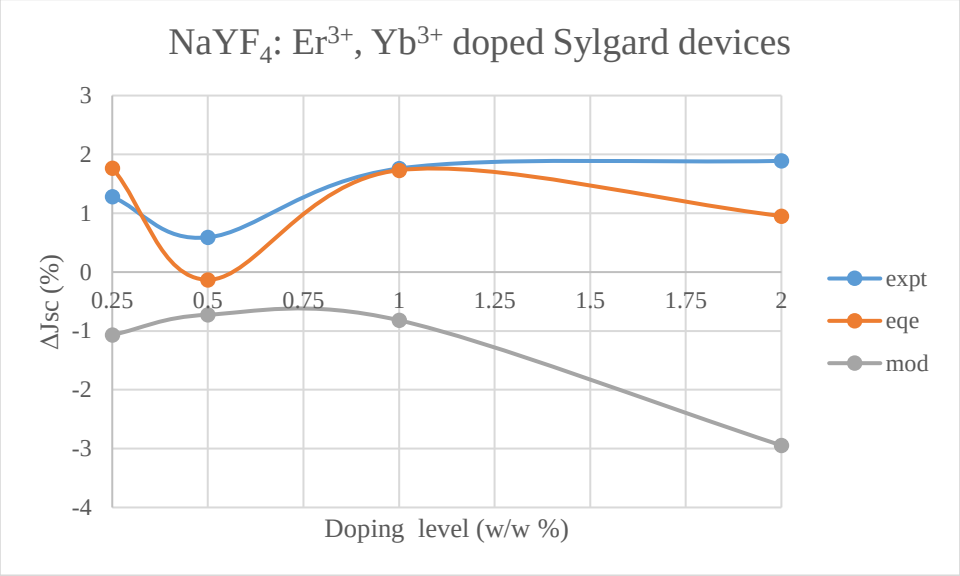

Figure 161: Relative J_{SC} gains for the $NaYF_4$: Er^{3+}, Yb^{3+} doped Sylgard layers on PV cells (from the optical model and IPCE measurements) compared to that observed under the solar simulator.

6.4.2 Concentrator 2D Ray Trace

Having successfully used an existing model to describe the EQE behaviour for the non-concentrating PV cell coatings, it was then of importance to develop a similar mathematical model to justify the results obtained from the LCPV devices. As SEH concentrators are a novel technology, there was no existing model in the literature, so one had to be constructed from first principles. In building this model, six assumptions were made. Firstly, for simplicity, the system would be analysed in 2D only. This greatly reduces the complexity of tracing the paths of internal rays. Secondly, only the side largest side of the concentrator, that with its entry aperture being the major axis of the eclipse (3 cm) will have its 2D cross section studied (as it will dominate the total percentage of incoming rays). Thirdly, surface reflectance is assumed to be 0 and the same for all wavelengths. Fourthly, only 1 total internal reflection event per ray is considered (i.e. no secondary total internal reflection of rays). Fifthly, the transmittance is initially assumed to be 100% at all wavelengths (as the concentrators are largely visibly transparent and <400 nm makes up a small portion of the incident photon flux). And finally, the refractive index of the concentrator was assumed to be a constant of 1.5 across all wavelengths. The optical coupling was also assumed to have an identical refractive index, so there would be no loss at the interface between the base of the concentrator and the solar cell.

All angles of incidence measured in Chapter 4 were considered. However, due to refraction at the top surface of the concentrator, the incident angle within the optic (θ_r) would differ from that of the incident ray (θ_i). These refracted angles of incidence can be calculated from Snell's law (in which n_i = 1, the refractive index of air, and n_r = 1.5, the refractive index of the concentrator medium), and are shown for all considered values of θ_i in Table 119.

$$n_i \sin\theta_i = n_r \sin\theta_r \qquad (62)$$

Angle of incidence (θ_i)	Refracted angle of incidence (θ_r)
0	0
10	6.65
20	13.18
30	19.47
40	25.37
50	30.71
60	35.26
70	38.79
80	41.04

Table 119: Refracted angle of incidence (θ_r) for a ray entering the concentrator at angle of incidence (θ_i) to the normal.

Recalling from chapter 1 and the operation of luminescent solar concentrators, total internal reflection (TIR) occurs when the angle of an incident ray at the interface between two media is greater than the critical angle, θ_c. Therefore, the critical angle for the concentrator and air boundary (within the concentrator) is 41.8°. This means all light rays travelling in the medium which hit an air interface at an incident angle greater than 41.8° are reflected at an angle equal to the one at which the surface was struck. For linear surfaces the calculation to determine the path of the total internal reflected ray would be trivial, but the SEH shape is somewhat more complex even in 2D. To calculate the route of the rays which undergo TIR after entering the concentrator, the angle of the surface normal at the relevant point must be known. The incident and reflected angles of the ray can then be defined relative to this normal as in TIR at linear interfaces. In order to find the normal, first the equation of the concentrator must be derived, before applying differentiation to yield the gradient of the tangent and its angle of elevation (which can then be converted into a normal by taking its negative reciprocal or adding 90°). As a starting point, the 2D cross section of the concentrator to be studied can be assumed to be a hyperbola with intersections at the points shown in Figure 162 below.

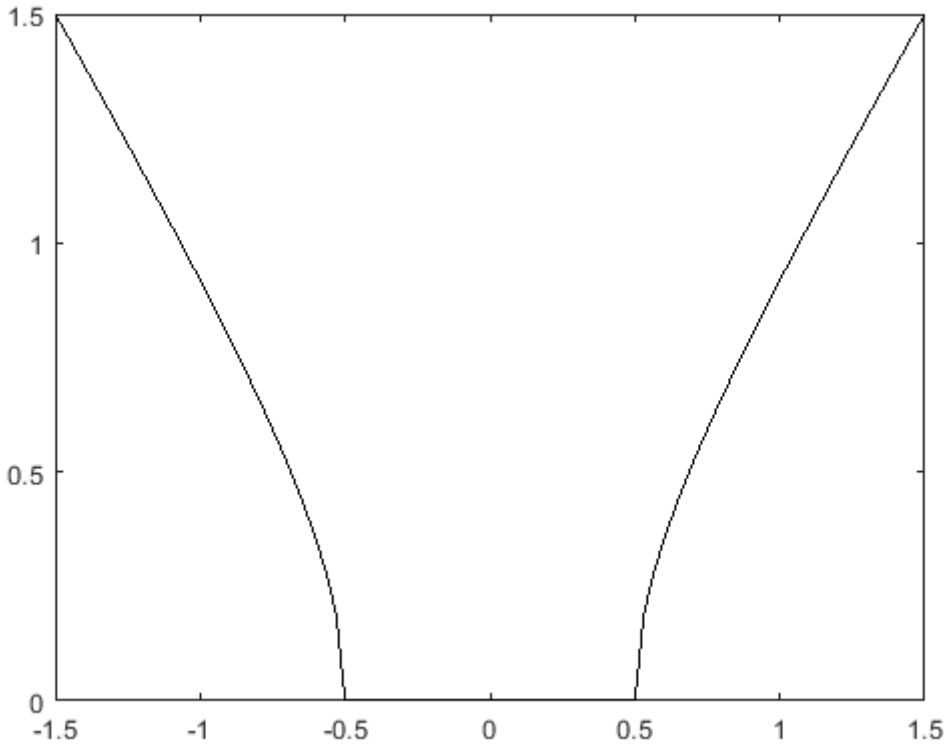

Figure 162: Cross-section plot of the SEH concentrator studied in this thesis from the face-on perspective to its largest side.

To plot this, the general equation of a hyperbola as seen below, was used to determine the values of the constants *a* and *b*, and an equation for the SEH's 2D profile given its intersection points.

$$\frac{x^2}{a^2} - \frac{y^2}{b^2} = 1 \qquad (63)$$

Finding *a* from this relation is trivial since the x-axis intercepts are always (-*a*, 0) and (*a*, 0) so a = 0.5. Then by substitution of a known co-ordinate point and some algebra, it can easily be shown that *b* = 4√2/3. Thus, the equation of this hyperbola (where 32/9 is given to 2 decimal places) is:

$$\frac{x^2}{0.25} - \frac{y^2}{3.56} = 1 \qquad (64)$$

From differential calculus, the derivative of the function (*dy/dx*) gives the formula for the gradient of the tangent at the point *x* on the curve. By rearranging the above equation, it can be shown:

$$\frac{dy}{dx} = \frac{9x}{8\sqrt{\frac{9}{32}(4x^2-1)}} = \frac{9x}{8y} \qquad (65)$$

This means the gradient of the tangent at the point (*x, y*) is (*9x/8y*). If an angle of the tangent from the horizontal, φ, is also desired it can then be given by:

$$\varphi = \arctan\left(\frac{9x}{8y}\right) \qquad (66)$$

The angle of the surface normal is then simply equal to $\varphi + 90°$. Now that the angle of the surface normal at any co-ordinate on the hyperbola is known, the rays and their paths can be traced. This is achieved by calculating the difference in angle ($\Delta\theta$) between the incident ray (θ_r) and the surface normal, checking it is greater than θ_c, and if so multiplying this difference by 2 and plotting a straight line originating at the point (*x, y*) that travels at θ_{TIR}, the resulting angle subtracted from the initial incident angle. Mathematically this is given by:

$$\theta_{TIR} = 90° + \theta_r + 2\varphi \qquad (67)$$

A code was generated in MATLAB and used to perform these calculations for 59 incident rays entering at co-ordinates (-1.5 + 0.05n, 1.5) for n = 1 to 59 for all the values of θ_r given in the earlier table and resulting images were plotted in graph form (with the red lines corresponding to the incident refracted rays and the blue lines to the rays after undergoing TIR). The points of intersection between the straight line and the hyperbola and/or y-axis were found by solving a quadratic equation (with some small modifications to formulae made depending if the x-coordinate of intersection was positive or negative). Starting with the $\theta_i = 0$ case, and in order of ascending θ_i, these ray traces are shown in the following Figures 163-171.

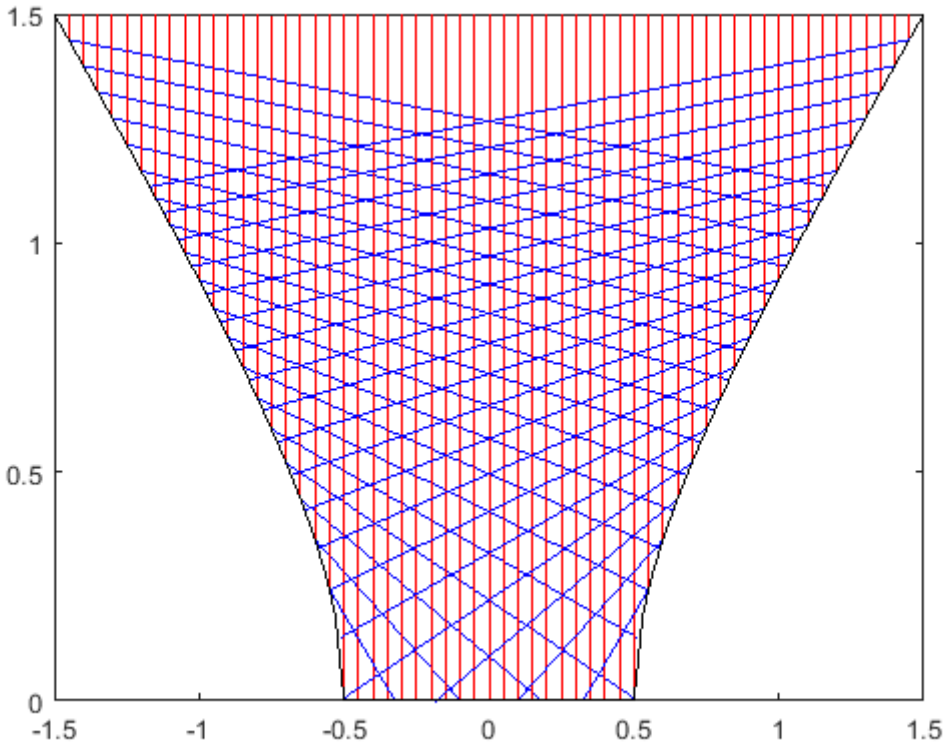

Figure 163: Ray trace for 0° angle of incidence.

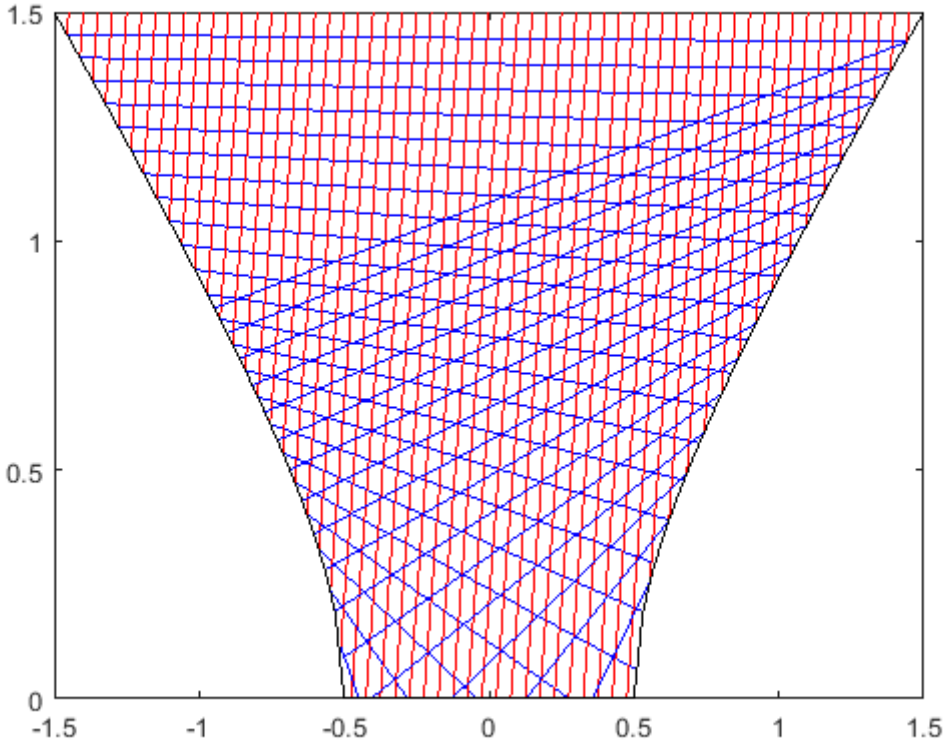

Figure 164: Ray trace for 10° angle of incidence.

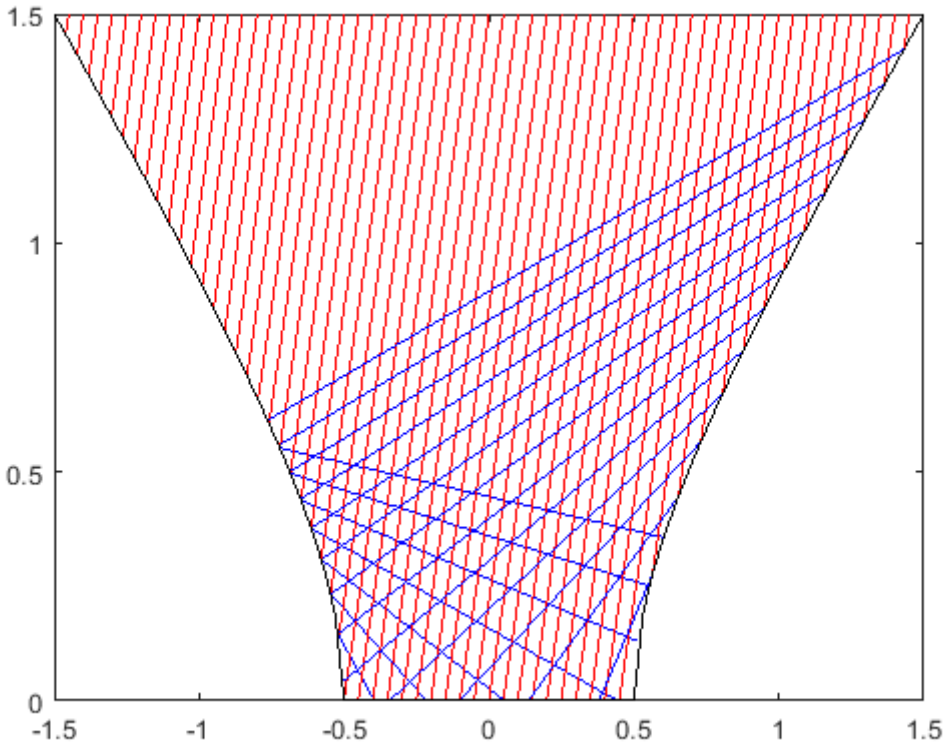

Figure 165: Ray trace for 20° angle of incidence.

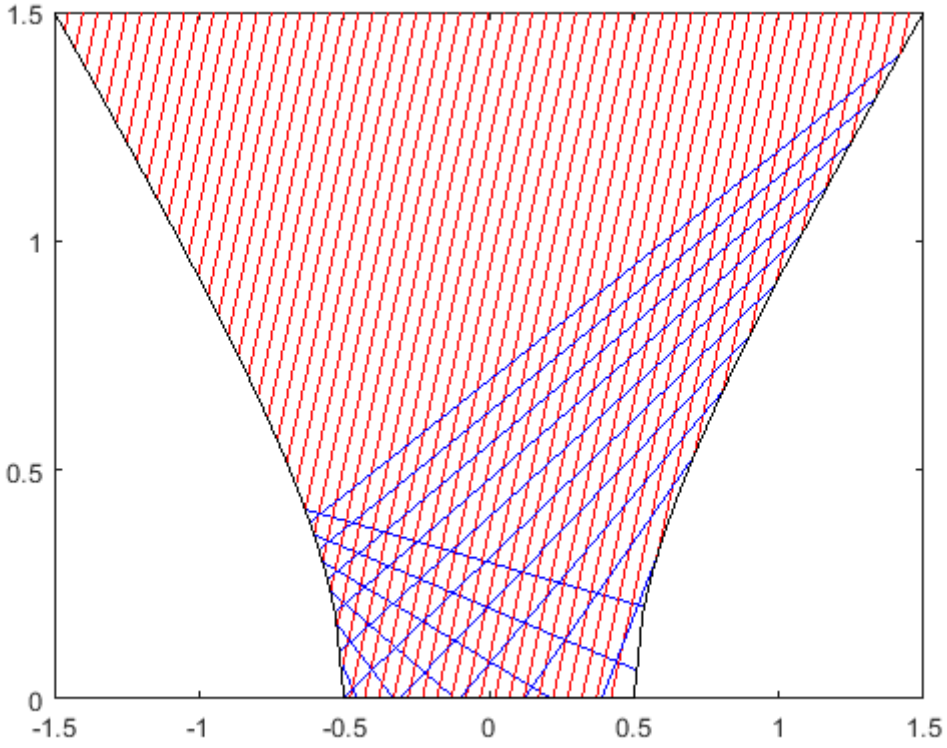

Figure 166: Ray trace for 30° angle of incidence.

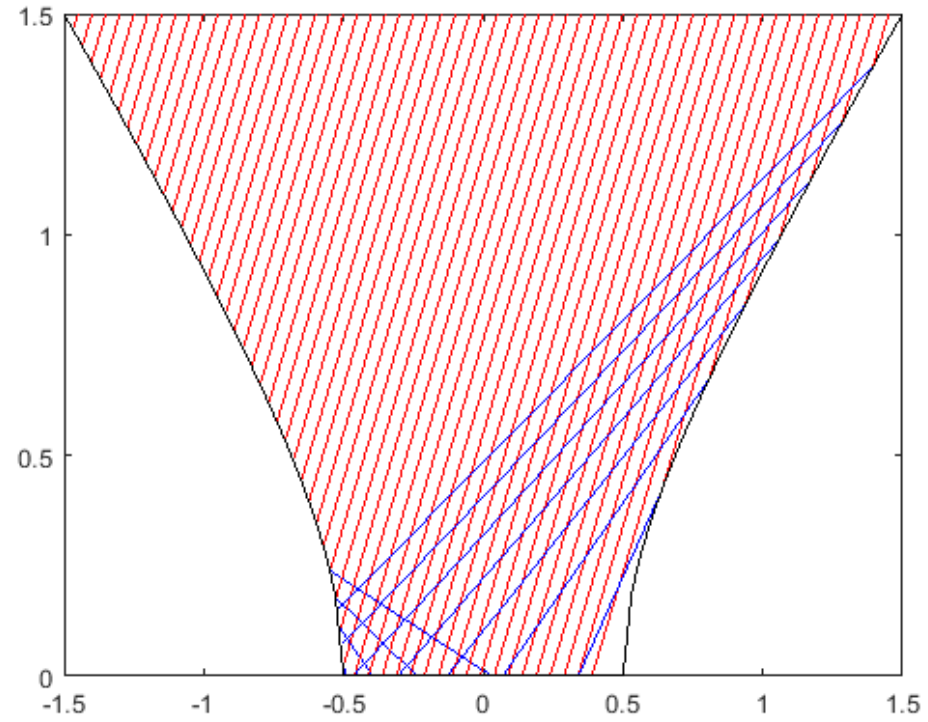

Figure 167: Ray trace for 40° angle of incidence.

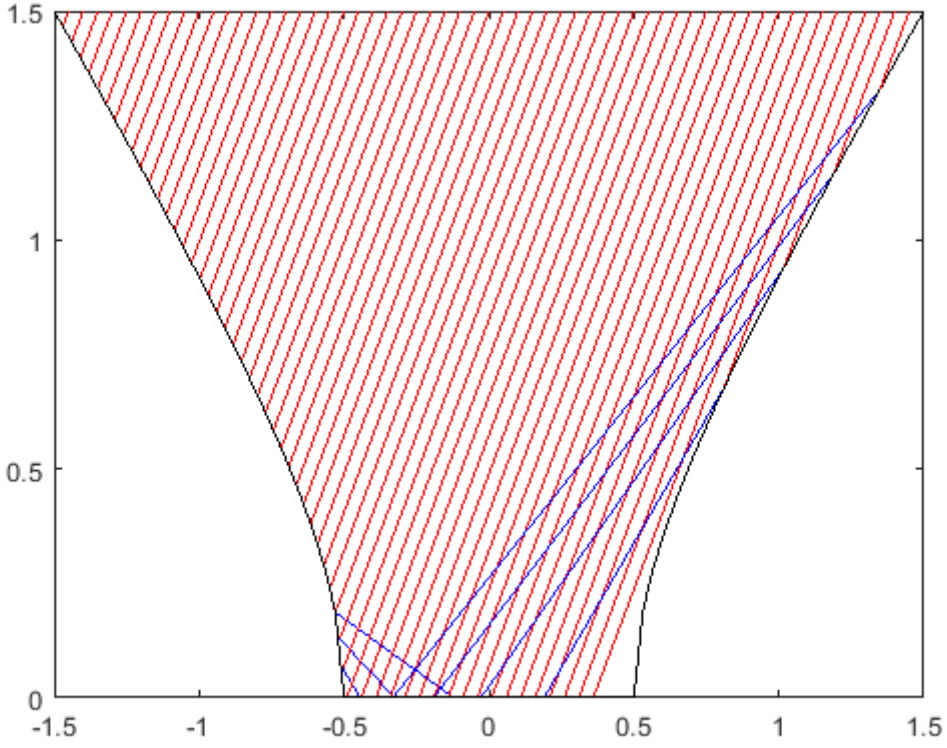

Figure 168: Ray trace for 50° angle of incidence.

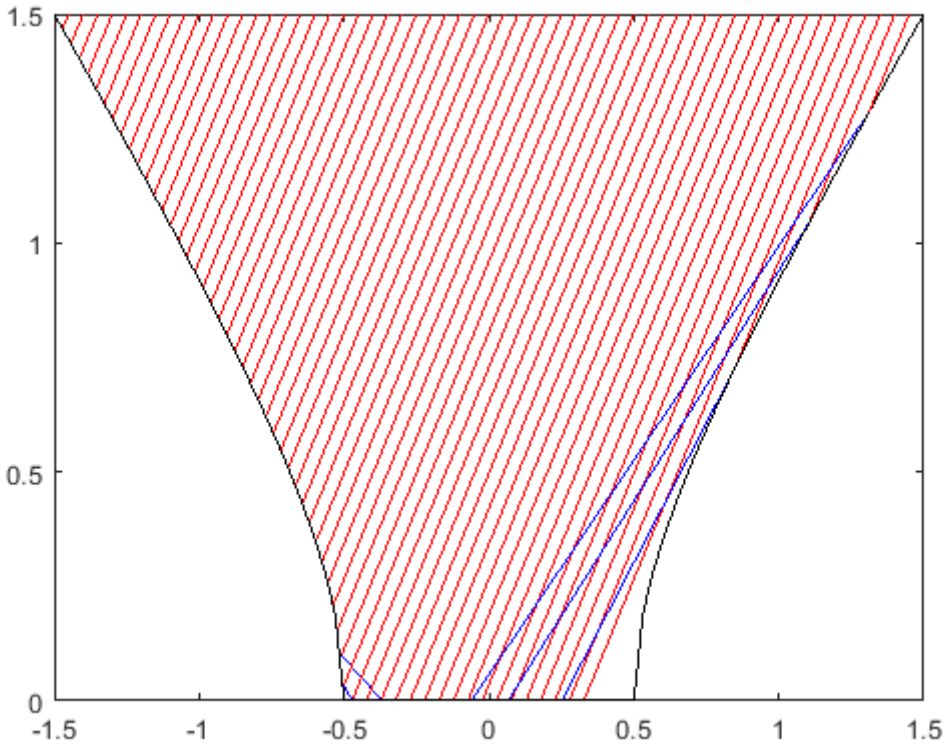

Figure 169: Ray trace for 60° angle of incidence.

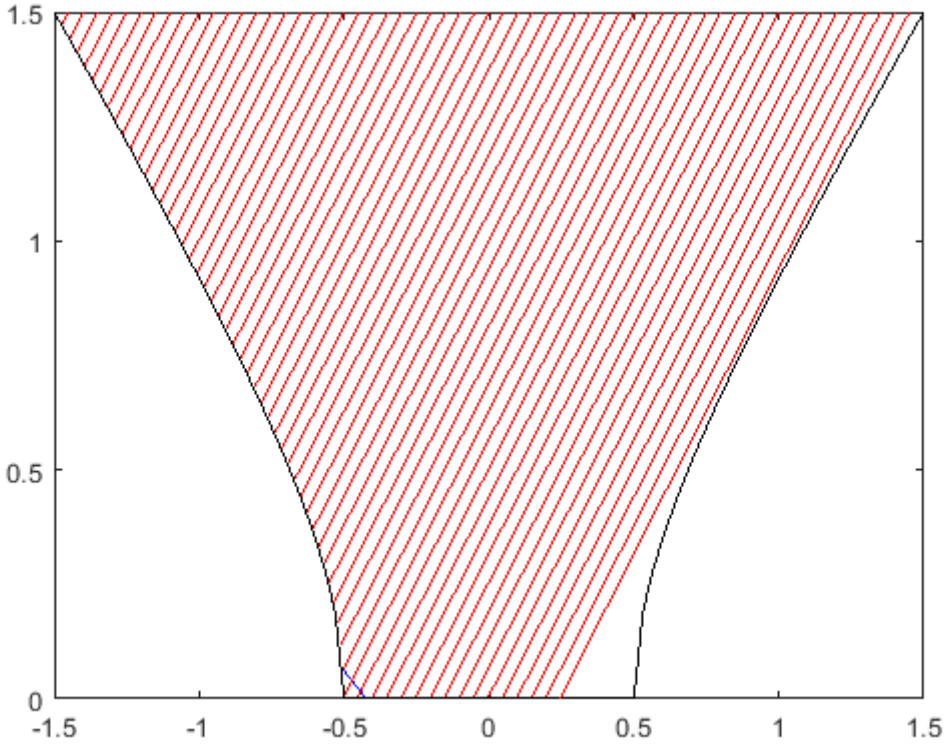

Figure 170: Ray trace for 70° angle of incidence.

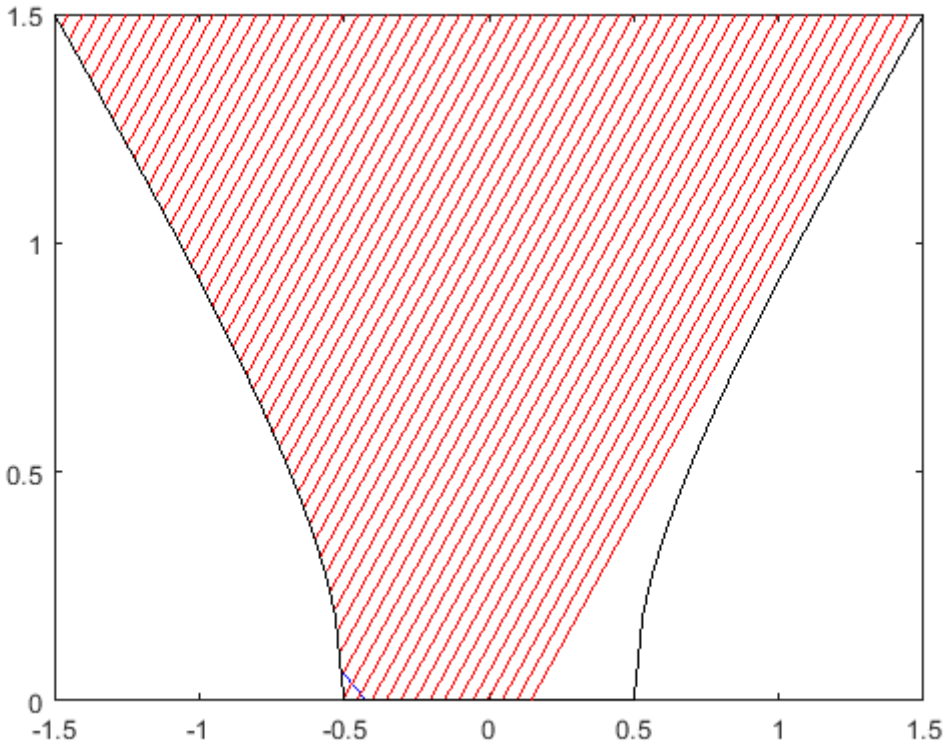

Figure 171: Ray trace for 80° angle of incidence.

Following the production of these graphical models, the estimated optical efficiency can then be calculated by counting the number of rays which reach the base of the concentrator and dividing by the total number of incident rays, 59. These are given in Table 120 and compared to earlier work by [39] for an SEH concentrator of the same profile using a much more advanced 3D model and software.

Angle of incidence (θ_i)	Rays that reach base	Optical efficiency (%)	Sellami et al. (%)
0	29	49	52
10	28	47	51
20	28	47	49
30	28	47	44
40	27	46	43
50	25	42	40
60	22	37	33
70	17	29	27
80	15	25	22

Table 120: Optical efficiency for the SEH concentrator from the 2D model at different angles of incidence compared to earlier work by Sellami et al [39].

Given this model's simplicity and many assumptions (especially the lack of reflectance and transmittance considerations), the optical efficiency predictions obtained here fit fairly well with the previous work. In addition, the calculated optical efficiency can be used to determine a theoretical J_{SC} at the different angles of incidence and compare against the experimental values obtained in 4.6. This is done by using the relation in which $J_{SC\ conc}$ is the J_{SC} with the concentrator, η_{opt} the calculated optical efficiency in the above table, G the geometric concentration ratio (which in 3D is 3.534 but 3 in this case because of the 2D approach) and $J_{SC\ no\ conc}$ the J_{SC} of the un-doped Sylgard coated cell without a concentrator as measured in chapter 3 at 36.33 mA/cm^2.

$$J_{SC\ conc} = \eta_{opt}\, G\, J_{SC\ no\ conc} \qquad (68)$$

Provided η_{opt} G is greater than 1, the J_{SC} of the LCPV cell will increase, which it does for a wide range of incident angles (up to 40°) as shown by the modelled J_{SC} outputs for each angle of incidence in Table 121. This wide acceptance of incoming light highlights the concentrator design's practical applications. Figure 172 gives a graphical comparison of the model to the experimentally observed data. At high angles (60-80°) they correlate very well, align reasonably from (20-50°) but show growing deviations at smaller angles (especially at 0° where the experimentally measured value is over 30% greater than that from the model). The differences could stem from an over-simplified model, i.e. one that neglects secondary TIR rays which could contribute to a relatively larger portion of light reaching the cell at near normal illumination conditions.

Angle of incidence (θ_i)	Model J_{SC} (mA/cm^2)	Expt. J_{SC} (mA/cm^2)
0	53.571	71.970
10	50.938	59.612
20	48.605	54.509
30	44.794	49.991
40	38.208	40.759
50	29.685	32.389
60	20.320	20.205
70	10.741	12.434
80	4.812	4.880

Table 121: The J_{SC} predicted by the ray trace model and as measured experimentally for the un-doped LCPV modules under 1 sun of light at varying angles of incidence.

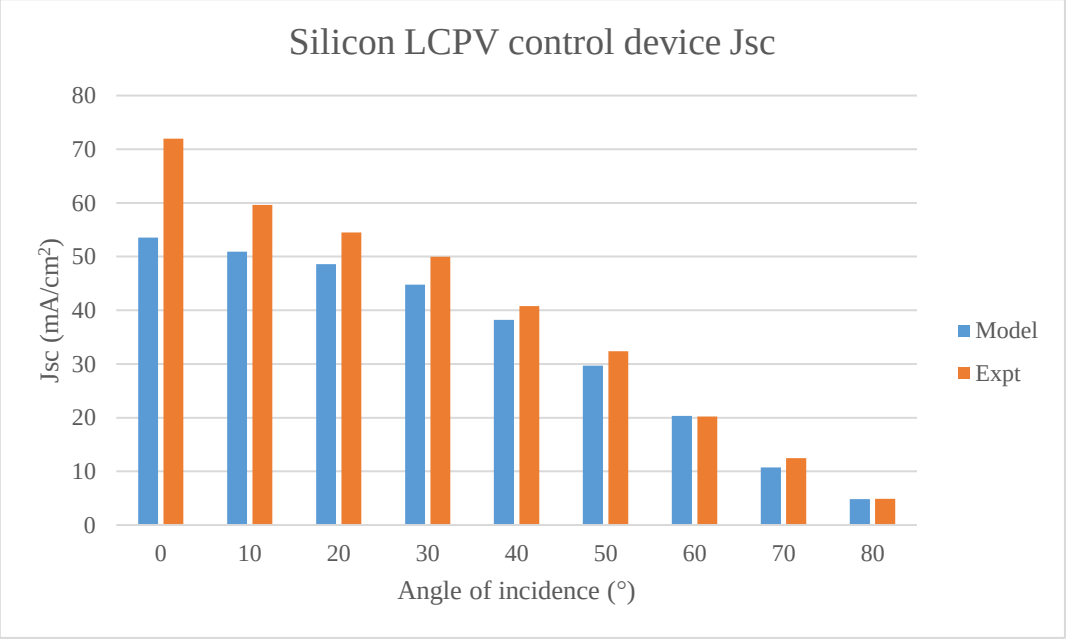

Figure 172: Graphical representation of the J_{SC} predicted by the ray trace model and as measured experimentally for the un-doped LCPV modules under 1 sun of light at varying angles of incidence.

Nevertheless, this approach has yielded reasonable estimates for the optical efficiency and electrical performance characteristics of the LCPV modules without any rare earth doped compound particles. However, ideally it should be possible to emulate this behaviour as well using a similar method and the 2D model presented so far provides a useful basis for this going forward (justified by its predicted optical efficiencies). Therefore, the model was further developed (under the same assumptions) by dividing the concentrator into 5 horizontal slices and placing the rare earth doped particles as discrete points (at vertical intervals of 0.3 and horizontal intervals of 0.15), treating these as 'absorption/emission centres' for which any passing ray, the nearest neighbour particle would describe its optical behaviour. The distribution of these points is given in Figure 173. For modelling the homogenous concentrator, they would all be used, whereas for the top and bottom doped concentrators, only the y = 1.35 or y = 0.15 points would be used respectively.

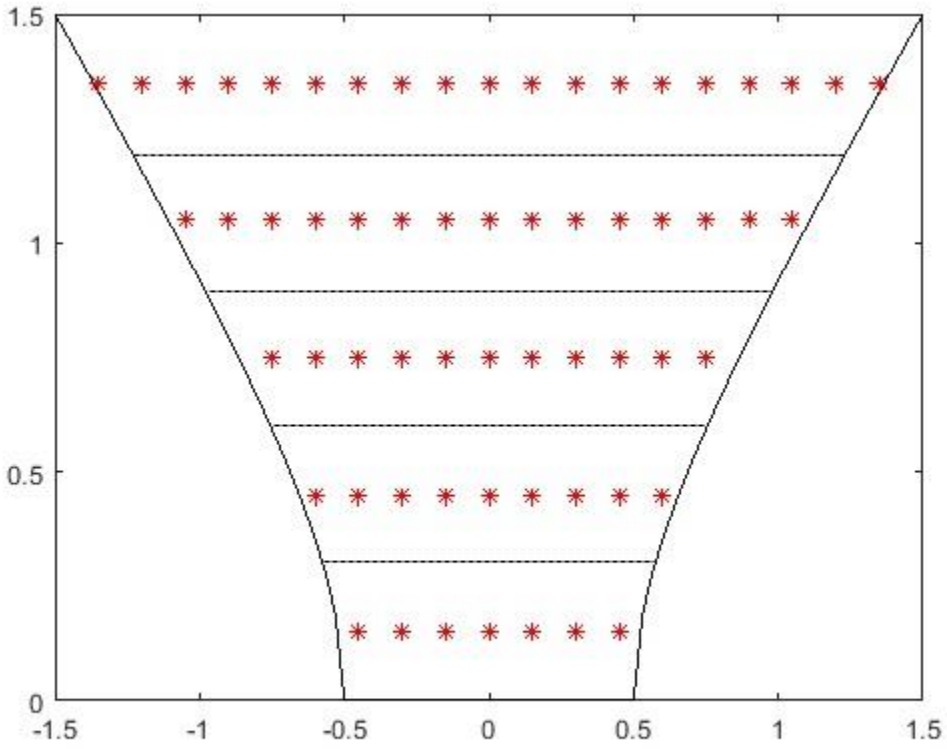

Figure 173: The positions of the absorption-emission centres within 5 horizontal slices that form the basis of the doped SEH concentrator model.

Using this geometrical layout, it was then necessary to calculate the probabilities for rays emitted from the respective point to reach the base of the concentrator and hence solar cell. This could happen both directly after the ray is emitted or following one TIR event. To calculate the probably of directly reaching the base of the concentrator, trigonometry, including the cosine and sine rule, was used to determine the angles of the triangle ABC where B is the co-ordinate of the emission event and A and C are (-0.5, 0) and (0.5, 0) respectively. The angle at point B divided by 360 would yield the probability of a randomly emitted ray of light reaching the base of the concentrator directly without the need for TIR. Due to the symmetry of the system, these calculations only need to be carried out for one horizontal half of the concentrator (i.e. for $x \geq 0$). These values are presented as percentages in Table 122.

x / y	0.15	0.45	0.75	1.05	1.35
0	40.72%	26.67%	18.72%	14.15%	11.29%
0.15	39.94%	25.88%	18.31%	13.94%	11.18%
0.30	37.93%	23.50%	17.16%	13.36%	10.85%
0.45	28.48%	19.72%	15.42%	12.46%	10.35%
0.60	-	13.67%	13.38%	11.36%	9.71%
0.75	-	-	10.34%	9.45%	8.97%
0.90	-	-	-	8.32%	7.67%
1.05	-	-	-	6.16%	6.46%
1.20	-	-	-	-	5.05%
1.35	-	-	-	-	4.09%

Table 122: Probability of emission that originates at the co-ordinate in the table directly reaching the solar cell at the exit aperture of the SEH concentrator.

Next it was necessary to calculate the percentage of emission from a particle that would reach the base after a single TIR event. These were calculated by an additional set of ray traces performed in MATLAB that plotted straight lines through each emission centre at inclinations from 0° to 180° in intervals of 1° to cover all possible directions of spectrally converted radiation. Then as before, if these rays hit the sides of the concentrator at an angle greater than θ_c, they were reflected by that angle and a new line plotted. Finally, from observation, the amount of these TIR rays reaching the base of the concentrator could be counted and divided by 360 to give a probability of an emitted photon arriving at the exit aperture via TIR following an absorption event. These values are shown for each particle co-ordinate in Table 123 and the overall probabilities of emission reaching the solar cell directly or via TIR (whose elements are the sum of the elements in Table 122 and 123) are shown in Table 124.

x / y	0.15	0.45	0.75	1.05	1.35
0	0%	0%	2.78%	3.33%	3.33%
0.15	0%	0.56%	3.06%	3.06%	3.61%
0.30	0%	2.78%	3.33%	3.06%	3.06%
0.45	5.56%	5.00%	3.61%	3.06%	2.78%
0.60	-	6.67%	3.89%	3.06%	2.78%
0.75	-	-	4.72%	3.33%	2.22%
0.90	-	-	-	3.33%	2.50%
1.05	-	-	-	4.72%	2.78%
1.20	-	-	-	-	2.50%
1.35	-	-	-	-	3.89%

Table 123: Probability of emission that originates at the co-ordinate in the table indirectly reaching the solar cell at the exit aperture of the SEH concentrator via one TIR event.

x / y	0.15	0.45	0.75	1.05	1.35
0	40.72%	26.67%	21.50%	17.48%	14.62%
0.15	39.94%	25.88%	21.37%	17.00%	14.79%
0.3	37.93%	23.50%	20.49%	16.42%	13.91%
0.45	34.04%	19.72%	19.03%	15.52%	13.13%
0.6	-	13.67%	17.27%	14.42%	12.49%
0.75	-	-	15.06%	12.78%	11.19%
0.9	-	-	-	11.65%	10.17%
1.05	-	-	-	10.88%	9.24%
1.2	-	-	-	-	7.55%
1.35	-	-	-	-	7.98%

Table 124: Total probability of emission that originates at the co-ordinate in the table reaching the solar cell at the exit aperture of the SEH concentrator directly or via one TIR event.

This data could then be used to calculate the fraction of light that reaches the solar cell for different doping configurations of concentrator, and hence build a model to predict their optical efficiency and photovoltaic performance behaviour. Moreover, some additional assumptions were added: no-reabsorption of emitted radiation, no change in reflectance or refractive index from the addition of particles, each emission event takes place at the closest co-ordinate in Table 124 to the midpoint of the path of the ray through the doped portion of the concentrator and the iPLQYs for each material are those derived in 6.4.1 (100% for $Sr_4Al_{14}O_{25}$: Eu^{2+}, Dy^{3+} and 90% for $NaYF_4$: Er^{3+}, Yb^{3+}), meaning for $NaYF_4$: Er^{3+}, Yb^{3+} emission an additional factor of 0.9 must be multiplied to the values in Table 124, and, finally, only the case of normally incident rays is considered.

As an initial trial model, the ideal case of 100% absorbance by $Sr_4Al_{14}O_{25}$: Eu^{2+}, Dy^{3+} (due to its higher iPLQY) at an arbitrary excitation wavelength was considered since this would be the optimal scenario for a LDS material (high absorbance in the area of low EQE and high emission in the area of high EQE). The rays were traced as per the instructions of this model, to give an output probability of the initial ray reaching the exit aperture P_{reach}, from entry co-ordinates of x = 0 to x = 1.45 in intervals of 0.05. These outputs are displayed graphically in Figure 174. Again, due to the symmetry of the problem, these calculations only needed to be carried out for one side of the concentrator.

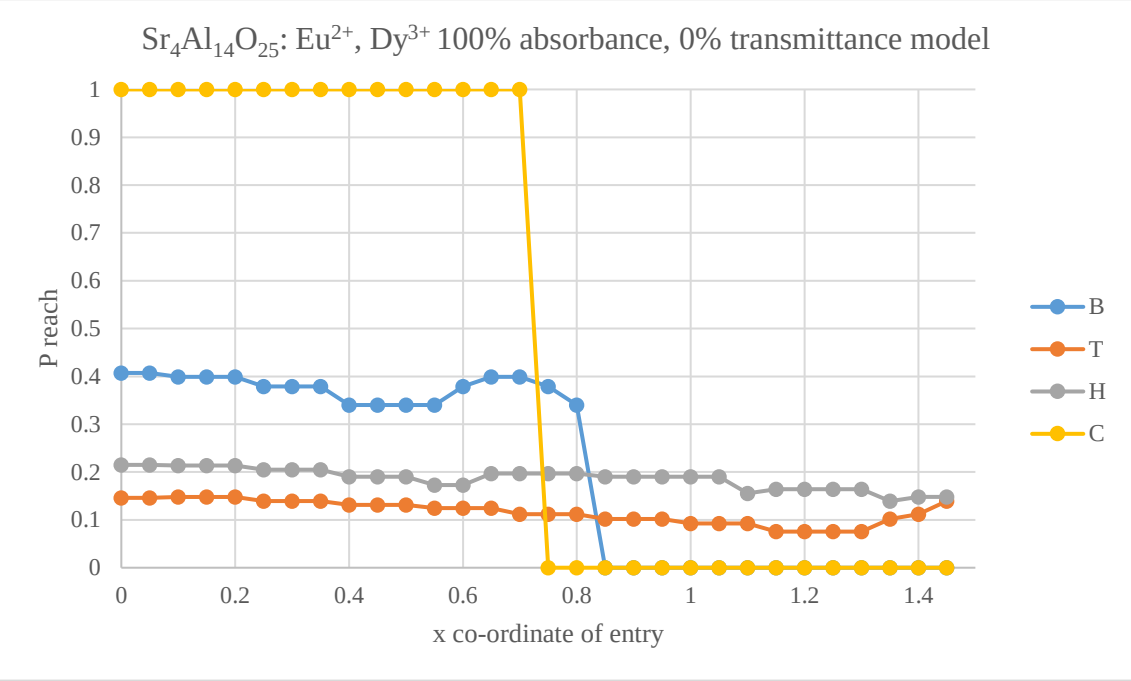

Figure 174: Probabilities of a ray of arbitrary λ_{em} entering at the x co-ordinate reaching the exit aperture for the control (un-doped), homogenously doped, top doped and bottom doped $Sr_4Al_{14}O_{25}$: Eu^{2+}, Dy^{3+} SEH concentrators.

Following the same procedure as before (considering η_{opt} as the fraction of incidents rays reaching the exit aperture), the following formula and above graph could be used to determine the optical efficiencies for each concentrator at the excitation wavelength, which are shown in Table 125.

$$\eta_{opt} = \frac{1}{59}\left(P_{reach}\,(x=0) + 2\sum_{n=1}^{n=29} P_{reach}(x=0.05n)\right) \tag{69}$$

Concentrator type	η_{opt} (%)
Control (un-doped)	49.15
Base doped	21.04
Top doped	11.60
Homogenously doped	18.58

Table 125: Predicted optical efficiencies of the control (un-doped), homogenously doped, top doped and bottom doped SEH concentrators.

In this instance, and perhaps unsurprisingly given the higher probability values for its emission reaching the solar cell, of the three doped concentrators, the bottom doped concentrator had the highest optical efficiency. Although the top and homogenously doped performed better for close to the edge rays, it could not compensate for their poor performance to light entering through the centre of the concentrator. However, the data is also telling and unfortunate in that it shows

the control concentrator has the highest optical efficiency (still while 100% absorption takes place). Even considering the difference in EQE between the absorption and emission wavelength, the bottom doped concentrator cannot increase cell performance in these conditions. To prove this, J_{SC} enhancements can be calculated by considering the photon flux at the base of the concentrator. For spectrally converted radiation, the photon flux at the emitted wavelength $\varphi'(\lambda_{em})$ is determined by the following equation, where $\varphi(\lambda_{abs})$ is the absorption wavelength photon flux under AM 1.5 G (given by the relation in 6.4.1), G = 3 and η_{opt} = 0.2104.

$$\varphi'(\lambda_{em}) = \eta_{opt} G \varphi(\lambda_{abs}) \quad (70)$$

This value can be then be used to determine $\Delta J_{SC}(\lambda_{em})$ with the following relation (as before $\Delta\lambda$ = 10 nm and e is the fundamental charge):

$$\Delta J_{SC}(\lambda_{em}) = e\Delta\lambda\varphi'(\lambda_{em}) EQE_{ref}(\lambda_{em}) \quad (71)$$

Next this can be compared to the ΔJ_{SC} from the lost transmittance at λ_{abs} given for 100% absorbance by:

$$\Delta J_{SC}(\lambda_{abs}) = -0.4915 * e\Delta\lambda\varphi(\lambda_{abs}) EQE_{ref}(\lambda_{abs}) \quad (72)$$

So for example, considering $Sr_4Al_{14}O_{25}$: Eu^{2+}, Dy^{3+} base doped concentrators, if λ_{abs} = 400 nm (where EQE_{ref} = 0.7329) and λ_{em} = 500 nm (EQE_{ref} = 0.8382), the J_{SC} enhancement from 500 nm emission (+0.18mA/cm^2) will be less than the J_{SC} decrement from decreased 400 nm transmittance which is 0% from the 100% absorbance of the rare earth compound (-0.38 mA/cm^2), resulting in a net curtailment in device performance of -0.20 mA/cm^2. In fact, a condition for net enhancement can be derived such that the EQE of the bare cell in the region of the spectral conversion emission must be greater than that in the region of absorption by more than a factor of the optical efficiency of the plain concentrator divided by that of the doped concentrator.

$$\frac{EQE_{ref}(\lambda_{em})}{EQE_{ref}(\lambda_{abs})} > \frac{\eta_{opt\ un-doped}}{\eta_{opt\ doped}} \quad (73)$$

Therefore, it can be seen that in this model, the coupled solar cell would have to have an EQE in the absorption range at least 42.8% relatively lower than in the emission part of the spectrum in order to increase J_{SC} under this model. As a

corollary, in an alternate LSC design with this same reference silicon cell and rare earth compound, the η_{opt} of the doped concentrator would have to be 86.4% that of the un-doped concentrator for performance to theoretically improve.

To build on and improve this model, one as yet neglected factor will now be considered; the absorption coefficients of the materials in the concentrator (including the polyurethane medium) and wavelength dependent optical efficiencies. This more complex model will use at its core the Beer-Lambert law of absorption in a similar vein to the Rothemund model and introduce absorption coefficients of the un-doped concentrator (α_{conc}), $Sr_4Al_{14}O_{25}$: Eu^{2+}, Dy^{3+} doped concentrator (α_{SrAl}) and $NaYF_4$: Er^{3+}, Yb^{3+} doped concentrator (α_{NaY}). For simplicity, their values were only considered at 400 nm and 410 nm and these coefficients (shown in Table 126) were calculated from the transmittance spectra in 4.3 by a simple formula rearrangement and assuming a path length of 1.5 cm (the height of the concentrator as the beam was sent through its centre). All other wavelengths (420 nm and above) were considered to be transparent to doped and un-doped concentrators as before. This assumption is semi-empirically justified as the concentrators, both doped and un-doped, displayed a near constant transmittance above 420 nm where for simplicity they are assumed to be 100% transparent. The absorption coefficients are also assumed to be constant over the same 10 nm interval as like the EQE, α_{conc}, α_{SrAl} and α_{NaY} are constant between 400-410 nm with the value for 400 nm and the same for 410-420 nm with the value for 410 nm.

Material absorption coefficient (cm^{-1}) / wavelength (nm)	400	410
Un-doped concentrator, α_{conc}	2.01	0.57
$Sr_4Al_{14}O_{25}$: Eu^{2+}, Dy^{3+} doped concentrator, α_{SrAl}	2.46	1.11
$NaYF_4$: Er^{3+}, Yb^{3+} doped concentrator, α_{NaY}	2.37	0.83

Table 126: Calculated absorption coefficients for the un-doped concentrator, $Sr_4Al_{14}O_{25}$: Eu^{2+}, Dy^{3+} doped concentrator and $NaYF_4$: Er^{3+}, Yb^{3+} doped concentrator at 400 and 410 nm.

With this information, probability-based calculations for the optical efficiency were constructed for each of the four concentrator types: the un-doped control, base doped, top doped and homogeneously doped. The latter three would need

to be evaluated twice, once for each rare earth doped compound. Moreover, they would all need to be done twice for each wavelength (400 nm and 410 nm). Additionally, this time the calculations had two components for the probability of photons reaching the base; the probability from spectral conversion events ($P_{reach\ SC}$) and the probability from transmitted photons ($P_{reach\ trans}$). These had to be carried out ray by ray along each path originating from the x co-ordinates of entry between 0 and 1.45.

First, analysing the plain concentrator, the simplest scenario as there are no spectral conversion materials, it is found $P_{reach\ SC} = 0$ for all x and $P_{reach\ trans}$ (at wavelength λ = 400 or 410 nm) is given by:

$$P_{reach\ trans}(x, \lambda) = \exp(-\alpha_{conc}(\lambda) L_{conc}) \quad (74)$$

Here L_{conc} refers to the path length of the ray through the concentrator medium before it reaches the exit aperture. Trivially, $L_{conc} = 1.5$ for x values between 0 and 0.5 and can be measured for the x = 0.55-0.7 rays, while clearly, $P_{reach\ trans} = 0$ for $x > 0.7$.

Next, considering the top and bottom doped concentrators, $P_{reach\ SC}$ was determined by the following equation, yielding the probability each ray would reach the base via interaction with the rare earth compound.

$$P_{reach\ SC}(x, \lambda) = P_{trans\ conc}\ (\lambda) P_{abs\ RE}\ (\lambda) \eta_{PL}\ P_{reach\ em} \quad (75)$$

As in 6.4.1, η_{PL} refers to the iPLQY of the rare earth compound, taken as 1 for $Sr_4Al_{14}O_{25}$: Eu^{2+}, Dy^{3+} and 0.9 for $NaYF_4$: Er^{3+}, Yb^{3+}. $P_{reach\ em}$ is the probability that the absorbed and emitted radiation reaches the base of the concentrator. It is given simply by the value in Table 124 for the co-ordinate that is the nearest neighbour to the midpoint of the ray in that layer. $P_{trans\ conc}$ is the probability that the ray will be transmitted through the concentrator medium before arriving at the doped region. For the top doped concentrator, $P_{trans\ conc}$ always equals unity whereas for the base doped concentrator, it's given by $\exp(-\alpha_{conc}(\lambda) L_{conc})$ where L_{conc} is the path length of the ray before it reaches the y = 0.3 boundary. Finally, $P_{abs\ RE}$ is the probability that the ray is absorbed by the rare earth doped region. It is given by:

$$P_{abs\ RE}(\lambda) = 1 - \exp(-\alpha_{RE}(\lambda) L_{RE}) \quad (77)$$

In this expression L_{RE} is the path length of the ray through the doped layer. For the top and bottom doped concentrators, these calculations were trivial for x = 0 to x = 0.5 with L_{RE} = 0.3 for both categories and L_{conc} = 1.2 for the bottom doped concentrator. Higher x co-ordinates needed more attention to detail though, by carefully measuring the path length through each material sector and locating the corresponding midpoint from which the variable $P_{reach\ em}$ would be based. It should also be noted unlike $P_{reach\ trans}$, $P_{reach\ SC}$ can have contributions from x > 0.7. $P_{reach\ trans}$ for the top and bottom doped concentrators is given by the below expression, with path lengths through each material found using the same logic and only considering rays that reach the exit aperture; it is evident that $P_{reach\ trans}$ will be the same for x=0 to x=0.5 for the top and bottom doped concentrators.

$$P_{reach\ trans}(x,\lambda) = \exp(-\alpha_{RE}(\lambda)L_{RE} - \alpha_{conc}(\lambda)L_{conc}) \quad (78)$$

Finally, for the homogenously doped concentrator, a new approach was used that took account for absorption being able to occur in five slices. A modified version of the earlier equation for $P_{reach\ SC}$ was used (like the top doped concentrators, $P_{trans\ conc}$ = 1) but $P_{abs\ RE}$ was modified as such (for descending layers 1-5, with $\alpha = \alpha_{RE}$ and L_n the optical path of the ray through the nth layer).

$$P_{abs\ RE} = P_{abs\ layer\ 1} + P_{abs\ layer\ 2} + P_{abs\ layer\ 3} + P_{abs\ layer\ 4} + P_{abs\ layer\ 5} \quad (79)$$

Using conditional probabilities, the absorption probability for each layer is given by the following:

$$P_{abs\ layer\ 1} = (1 - e^{-\alpha L_1}) \quad (80)$$

$$P_{abs\ layer\ 2} = e^{-\alpha L_1}(1 - e^{-\alpha L_2}) \quad (81)$$

$$P_{abs\ layer\ 3} = e^{-\alpha(L_1+L_2)}(1 - e^{-\alpha L_3}) \quad (82)$$

$$P_{abs\ layer\ 4} = e^{-\alpha(L_1+L_2+L_3)}(1 - e^{-\alpha L_4}) \quad (83)$$

$$P_{abs\ layer\ 5} = e^{-\alpha(L_1+L_2+L_3+L_4)}(1 - e^{-\alpha L_5}) \quad (84)$$

After an absorption event in a given layer, its probability of reaching the solar cell is just given by the $P_{reach\ em}$ value of the co-ordinate closest to the mid-point of the ray path in that layer multiplied by η_{PL}. Therefore, the probability of an incident ray reaching the solar cell via spectral conversion from a given layer is:

$$P_{reach\ SC\ layer\ n}(x,\lambda) = \eta_{PL} P_{abs\ RE\ layer\ n}\ P_{reach\ em} \quad (85)$$

Lastly, these can be summed over all layers to give the total probability that an incident ray will arrive at the exit aperture of the SEH concentrator.

$$P_{reach\ SC}\ (x,\lambda) = \sum_{n=1}^{n=5} P_{reach\ SC\ layer\ n}$$

(86)

Fortunately, $P_{reach\ trans}$ for the homogenously doped concentrator was much simpler to calculate (since it is not of importance where the light is absorbed) and is given by:

$$P_{reach\ trans}(x,\lambda) = \exp(-\alpha_{RE}(\lambda)L_{RE}) \quad (87)$$

With the derived equations, it is now possible to run these calculations for the relevant values of x and the resultant probabilities are shown for all concentrator configurations and both wavelengths in Figures 175-178. Furthermore, the probabilities could be summed (in the way denoted by the two equations below, taking account of the symmetry) to give the spectral conversion component of the optical efficiency ($\eta_{opt\ SC}$) of the concentrator (i.e. the fraction of the excitation wavelength radiation at the entrance of the concentrator reaching the base of the concentrator with a higher wavelength) and the transmitted radiation component of the optical efficiency ($\eta_{opt\ trans}$) for each wavelength.

$$\eta_{opt\ sc} = \frac{1}{59}\left(P_{reach\ SC}(x=0) + 2\sum_{n=1}^{n=29} P_{reach\ SC}(x=0.05n)\right)$$

(88)

$$\eta_{opt\ trans} = \frac{1}{59}\left(P_{reach\ trans}(x=0) + 2\sum_{n=1}^{n=29} P_{reach\ trans}(x=0.05n)\right)$$

(89)

Excitingly, these optical efficiencies could then be used to determine photon fluxes and effects on doped concentrator LCPV device J_{SC} relative to the control. Again, this was done in two components, for the spectrally converted and transmitted radiation. For spectrally converted radiation with λ_{abs} = 400 nm and 410 nm, and λ_{em} = 500 for $Sr_4Al_{14}O_{25}$: Eu^{2+}, Dy^{3+} and 660 nm for $NaYF_4$: Er^{3+}, Yb^{3+}, these are calculated by:

$$\varphi'(\lambda_{em}) = \eta_{opt\ SC} G \varphi(\lambda_{abs}) \quad (90)$$

$$\Delta J_{SC\ SC}(\lambda_{abs}) = e \Delta\lambda \varphi'(\lambda_{em}) EQE_{ref}(\lambda_{em}) \quad (91)$$

In the above relation, because both materials are transparent at λ_{em}, the J_{SC} contribution from $\varphi(\lambda)$ at that wavelength is the same for control and doped devices in this model so does not need to be calculated. While for transmitted radiation, to know the change in J_{SC} does require comparison to the un-doped control concentrator as the absorption coefficients vary, and is yielded from the evaluation of:

$$\varphi'_{doped}(\lambda_{abs}) = \eta_{opt\ trans\ doped} G \varphi(\lambda_{abs}) \quad (92)$$

$$\varphi'_{un-doped}(\lambda_{abs}) = \eta_{opt\ trans\ un-doped} G \varphi(\lambda_{abs}) \quad (93)$$

$$\Delta J_{SC\ trans}(\lambda_{abs}) = e \Delta\lambda EQE_{ref}(\lambda_{abs}) \left(\varphi'_{doped}(\lambda_{abs}) - \varphi'_{un-doped}(\lambda_{abs}) \right) \quad (94)$$

The total ΔJ_{SC} for each material is then given by:

$$\Delta J_{SC} = \Delta J_{SC\ SC}\ (\lambda_{abs} = 400) + \Delta J_{SC\ trans}\ (\lambda_{abs} = 400)$$
$$+ \Delta J_{SC\ SC}\ (\lambda_{abs} = 410) + \Delta J_{SC\ trans}\ (\lambda_{abs} = 410) \quad (95)$$

So, if $\Delta J_{SC\ SC} + \Delta J_{SC\ trans} > 0$, over the aggregate of both wavelengths, then the J_{SC} of the LCPV device will increase through the use of that concentrator type. The results of these calculations are given at each wavelength in Tables 127-130 and the overall effect on LCPV device J_{SC} in Tables 131 and 132. Furthermore, this model's predicted relative J_{SC} enhancements are compared to data observed under the solar simulator and displayed graphically in Figures 179-180.

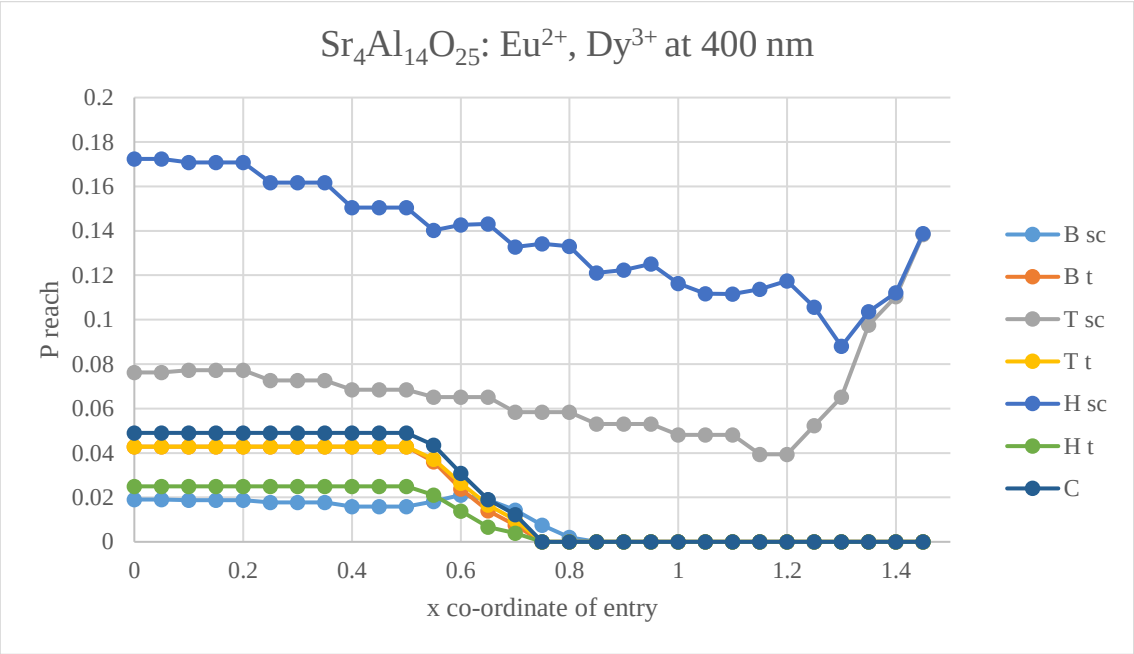

Figure 175: Probabilities of a 400 nm ray entering at the x co-ordinate reaching the exit aperture for the control (un-doped), homogenously doped, top doped and bottom doped $Sr_4Al_{14}O_{25}$: Eu^{2+}, Dy^{3+} SEH concentrators.

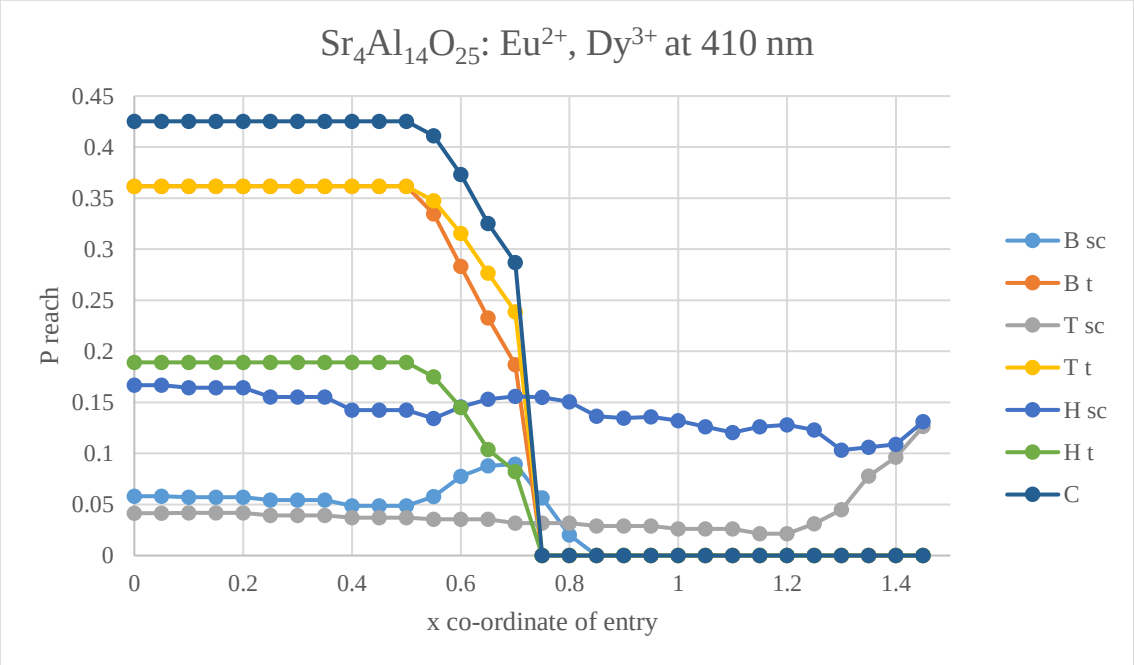

Figure 176: Probabilities of a 410 nm ray entering at the x co-ordinate reaching the exit aperture for the control (un-doped), homogenously doped, top doped and bottom doped $Sr_4Al_{14}O_{25}$: Eu^{2+}, Dy^{3+} SEH concentrators.

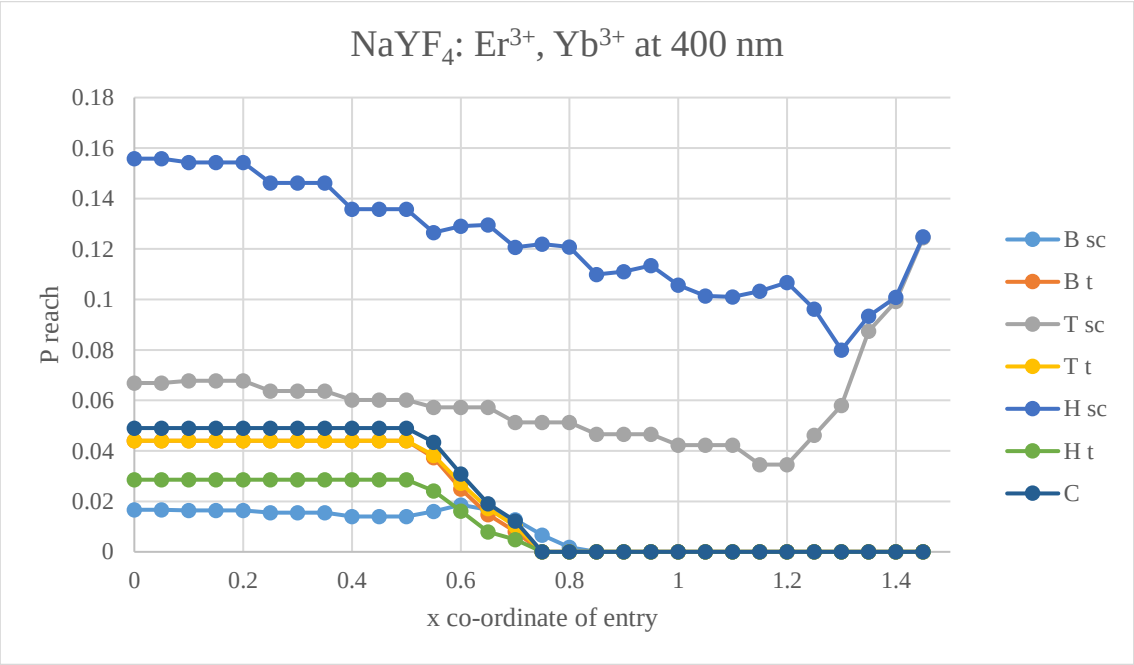

Figure 177: Probabilities of a 400 nm ray entering at the x co-ordinate reaching the exit aperture for the control (un-doped), homogenously doped, top doped and bottom doped $NaYF_4$: Er^{3+}, Yb^{3+} SEH concentrators.

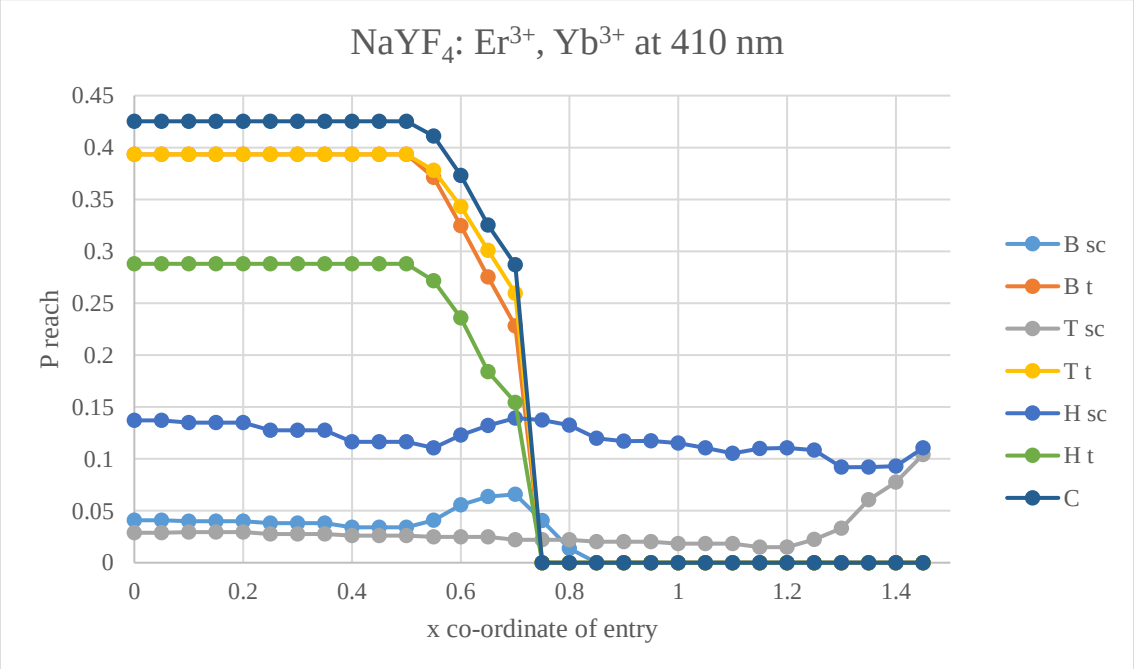

Figure 178: Probabilities of a 410 nm ray entering at the x co-ordinate reaching the exit aperture for the control (un-doped), homogenously doped, top doped and bottom doped $NaYF_4$: Er^{3+}, Yb^{3+} SEH concentrators.

Concentrator type	$\eta_{opt\ SC}$ (%)	$\eta_{opt\ trans}$ (%)	$\Delta J_{SC\ SC}$ (mA/cm^2)	$\Delta J_{SC\ trans}$ (mA/cm^2)
Control	-	2.10	-	-
Bottom	0.91	1.80	+0.008	-0.002
Top	6.74	1.83	+0.061	-0.002
Homogenous	13.63	1.04	+0.123	-0.008

Table 127: Optical efficiency components and effect on J_{SC} for the control (un-doped), bottom doped, top doped and homogenously doped $Sr_4Al_{14}O_{25}$: Eu^{2+}, Dy^{3+} *concentrators at 400 nm irradiance.*

Concentrator type	$\eta_{opt\ SC}$ (%)	$\eta_{opt\ trans}$ (%)	$\Delta J_{SC\ SC}$ (mA/cm^2)	$\Delta J_{SC\ trans}$ (mA/cm^2)
Control	-	19.87	-	-
Bottom	3.24	16.39	+0.028	-0.027
Top	4.08	16.87	+0.035	-0.023
Homogenous	14.05	8.45	+0.122	-0.088

Table 128: Optical efficiency components and effect on J_{SC} for the control (un-doped), bottom doped, top doped and homogenously doped $Sr_4Al_{14}O_{25}$: Eu^{2+}, Dy^{3+} *concentrators at 410 nm irradiance.*

Concentrator type	$\eta_{opt\ SC}$ (%)	$\eta_{opt\ trans}$ (%)	$\Delta J_{SC\ SC}$ (mA/cm^2)	$\Delta J_{SC\ trans}$ (mA/cm^2)
Control	-	2.10	-	-
Bottom	0.80	1.86	+0.007	-0.002
Top	5.94	1.88	+0.055	-0.002
Homogenous	12.34	1.20	+0.114	-0.007

Table 129: Optical efficiency components and effect on J_{SC} for the control (un-doped), bottom doped, top doped and homogenously doped $NaYF_4$: Er^{3+}, Yb^{3+} concentrators at 400 nm irradiance.

Concentrator type	$\eta_{opt\ SC}$ (%)	$\eta_{opt\ trans}$ (%)	$\Delta J_{SC\ SC}$ (mA/cm^2)	$\Delta J_{SC\ trans}$ (mA/cm^2)
Control	-	19.87	-	-
Bottom	2.30	18.07	+0.020	-0.014
Top	2.97	18.35	+0.026	-0.012
Homogenous	11.93	13.12	+0.106	-0.052

Table 130: Optical efficiency components and effect on J_{SC} for the control (un-doped), bottom doped, top doped and homogenously doped $NaYF_4$: Er^{3+}, Yb^{3+} concentrators at 410 nm irradiance.

Concentrator type	Expt. J_{SC} (mA/cm^2)	Expt. ΔJ_{SC} (%)	Mod. J_{SC} (mA/cm^2)	Mod. ΔJ_{SC} (%)
Control	71.970	-	45.686	-
Bottom	75.243	+4.55	45.693	+0.02
Top	75.168	+4.44	45.757	+0.16
Homogenous	69.976	-2.77	45.835	+0.33

Table 131: Total predicted effect on J_{SC} for the bottom doped, top doped and homogeneously doped $Sr_4Al_{14}O_{25}$: Eu^{2+}, Dy^{3+} concentrators compared to the control alongside the experimentally observed J_{SC} data.

Concentrator type	Expt. J_{SC} (mA/cm^2)	Expt. Δ J_{SC} (%)	Mod. J_{SC} (mA/cm^2)	Mod. Δ J_{SC} (%)
Control	71.970	-	45.686	-
Bottom	70.049	-2.67	45.698	+0.03
Top	72.296	+0.45	45.754	+0.15
Homogenous	73.454	+2.06	45.847	+0.35

Table 132: Total predicted effect on J_{SC} for the bottom doped, top doped and homogeneously doped $NaYF_4$: Er^{3+}, Yb^{3+} concentrators compared to the control alongside the experimentally observed J_{SC} data.

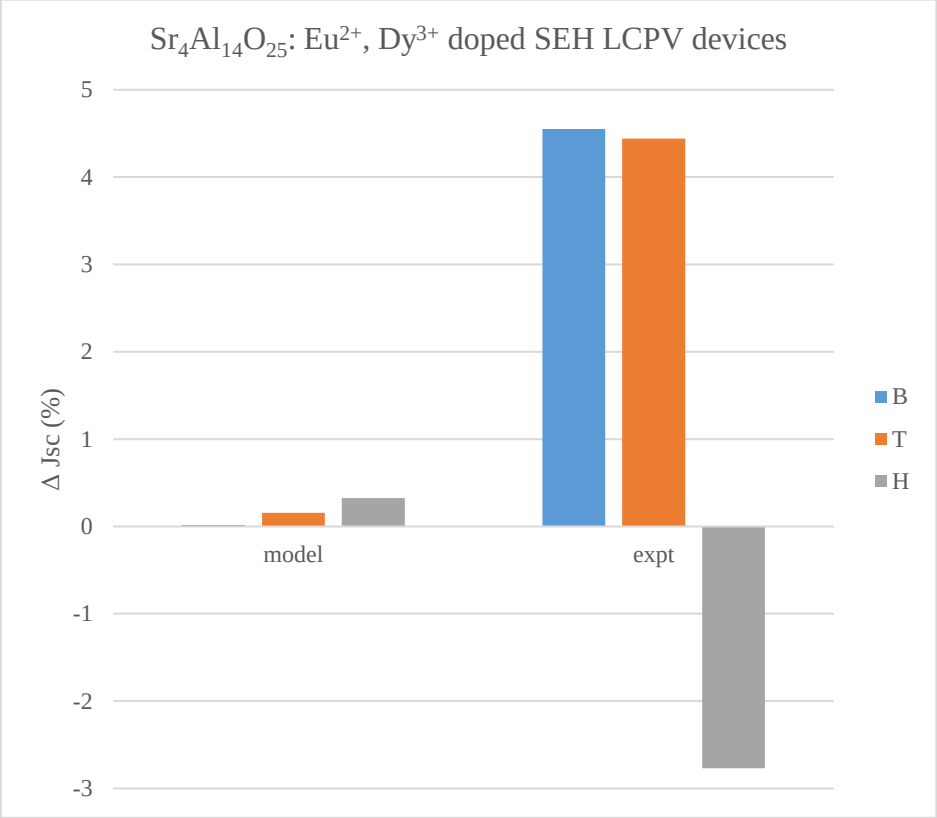

Figure 179: Predicted and observed relative J_{SC} gains for the bottom, top and homogenously doped $Sr_4Al_{14}O_{25}$: Eu^{2+}, Dy^{3+} concentrators against the un-doped concentrators.

Firstly, and most importantly, the model showed J_{SC} and by extension PCE, can increase as a result of spectral conversion in SEH concentrators due to the application of rare earth compounds (the first time this has been reported). The scale of this enhancement was calculated to be up to 0.16 mA/cm^2 for the $NaYF_4$: Er^{3+}, Yb^{3+} doped concentrators and 0.15 mA/cm^2 for the $Sr_4Al_{14}O_{25}$: Eu^{2+}, Dy^{3+} doped concentrators, relative increases of 0.35% and 0.33% respectively, both hypothesised for the homogenously doped configuration.

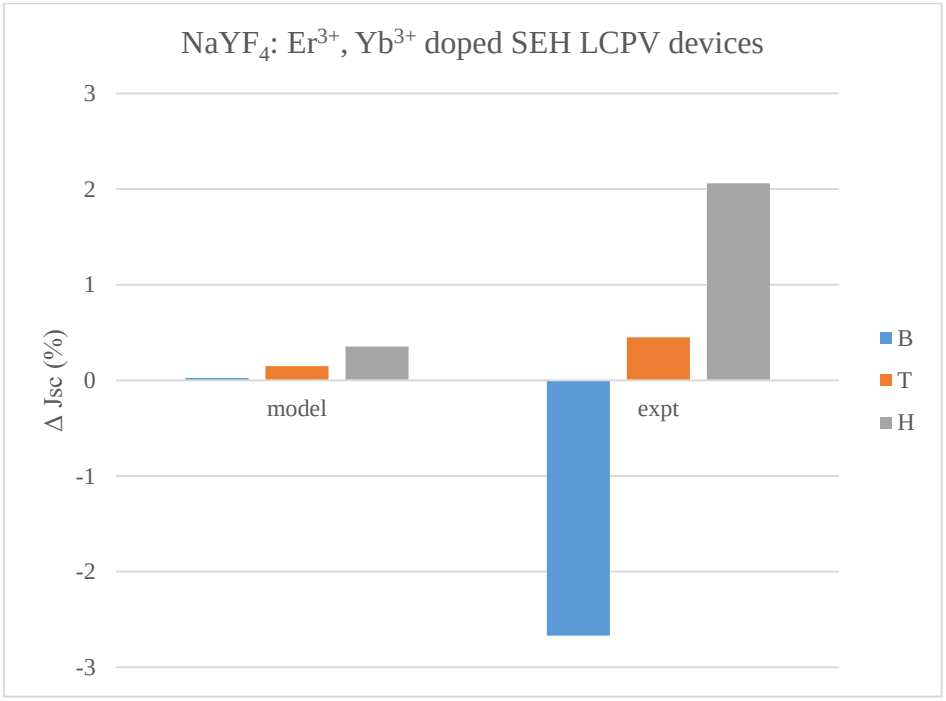

Figure 180: Predicted and observed relative J_{SC} gains for the bottom, top and homogenously doped $NaYF_4$: Er^{3+}, Yb^{3+} concentrators against the un-doped concentrators.

It is seen from the predictions of this model that when the difference in transmittances of the materials are considered, the 400 nm excited spectral conversion contributes more to the ΔJ_{SC} than the process at 410 nm for all configurations except bottom doped $NaYF_4$: Er^{3+}, Yb^{3+}. This is due to the absorption coefficient of the concentrator medium being relatively much smaller compared to that of the rare earth compounds at 410 nm than at 400 nm. The homogenously and top doped concentrators are able to utilise 400 nm and 410 nm photons fairly well, but the bottom doped concentrator cannot, as not many of those photons are able penetrate ~1.2 cm of un-doped concentrator. This leads to a juxtaposition with the 100% absorbance-0% transmittance scenario, in that the bottom doped concentrator now performs by far the poorest, following the introduction of absorption coefficients. The top doped performs significantly better but still suffers from a low probability of its emission reaching the exit aperture. This means the homogenously doped concentrator becomes, theoretically, the strongest candidate for enhancing J_{SC} with predicted rises roughly double that of the top doped configuration, due to the combination of its good absorption probability (because of longer optical paths) and emission occurring at lower y co-ordinates.

Comparing the two rare earth compounds, $NaYF_4$: Er^{3+}, Yb^{3+} slightly outperforms $Sr_4Al_{14}O_{25}$: Eu^{2+}, Dy^{3+} but the difference is very small. The reason for this is primarily due to the lower transmittance of $NaYF_4$: Er^{3+}, Yb^{3+} at the 410 nm absorption wavelength, which means less of these photons are hampered from reaching the solar cell; for the homogenously doped concentrators at 410 nm, $\Delta J_{SC\ trans}$ is -0.05 mA/cm^2 for $NaYF_4$: Er^{3+}, Yb^{3+} but -0.09 mA/cm^2 for $Sr_4Al_{14}O_{25}$: Eu^{2+}, Dy^{3+} which more than makes up for the lower $\Delta J_{SC\ SC}$ for $NaYF_4$: Er^{3+}, Yb^{3+} because of its slightly lower absorption coefficient. This variable and the lower iPLQY are also partially compensated for by $NaYF_4$: Er^{3+}, Yb^{3+} producing a respectable $\Delta J_{SC\ SC}$ due to its lower α_{RE} leading to more emission taking place at lower y coordinates than $Sr_4Al_{14}O_{25}$: Eu^{2+}, Dy^{3+}, where probabilities of emission reaching the cell are higher.

From contrasting the resulting relative change in J_{SC} predictions with measured data from chapter 4, it is clear that the model has underestimated enhancements by an order of magnitude (two orders of magnitude in the case of the $Sr_4Al_{14}O_{25}$: Eu^{2+}, Dy^{3+} bottom doped concentrator). However, this does not mean the model was a futile exercise. The results were significant for $NaYF_4$: Er^{3+}, Yb^{3+} as they predicted the same order of ascending ΔJ_{SC} as the experimental data: bottom, top, homogenous. This further supports the findings of 6.3.1, in which through the statistical analysis, $NaYF_4$: Er^{3+}, Yb^{3+} doped concentrators had a high confidence level of truly increasing PCE. Every device that saw J_{SC} rise in reality, also had its predicted J_{SC} increase, albeit by a smaller amount. Unfortunately the corollary was not true, since all doping regimes were expected to produce J_{SC} enhancements but in the real measurements at 1 sun, bottom doped $NaYF_4$: Er^{3+}, Yb^{3+} and homogenously doped $Sr_4Al_{14}O_{25}$: Eu^{2+}, Dy^{3+} concentrator devices saw their J_{SC} fall (the latter discrepancy could be due to neglecting absorption at higher wavelengths, which is more pronounced for this material). The lower enhancements could also be, like with 6.4.1, the EQE_{ref} being underestimated due to the heterogeneous light intensities between its determination and AM 1.5 G.

Another flaw is apparent from the IPCE measurements for the LCPV devices which do show EQE enhancements at ~450 nm that are not permitted by this model. This suggests other avenues through which the performance was increasing, such as enhanced anti-reflective properties. To elucidate this point,

consider the equation for the reflectance (R) at the boundary between two media under normal irradiance conditions, where n_0 is the refractive index of the material from which the light is travelling, and n_m that of what it is travelling into [350].

$$R = \frac{(n_0 - n_m)^2}{(n_0 + n_m)^2} \quad (96)$$

Given the refractive index for Crystal Clear 200 is 1.50, this means ~4% of the light is reflected at the boundary when light enters from air. However, if the refractive index were to reduce slightly upon the addition of a rare earth doped compound (to ~1.4), then for the top doped concentrator, the optical loss at the air boundary would reduce to 2.8%, followed by another 0.1% loss at the doped-un-doped interface. This could result in a potential ΔJ_{SC} of approximately +1.1% from reduced reflective losses. Likewise, consider Sylgard 184, which actually has a refractive index of 1.41 at visible wavelengths. If this refractive index were to increase slightly (e.g. to 1.55) upon the addition of rare earth compound, it would reduce the reflection loss between the coating-silicon cell interface (which has a refractive index of 4.68 at 450 nm) from 28.8% to 25.2%. For non-concentrating PV, when the air-coating boundary is factored in too, the higher refractive index doped Sylgard gives a greater fraction of incident 450 nm photons entering the solar cell, 71.4% vs 69.1% for the un-doped coating. Then, in LCPV devices, the un-doped concentrator medium having a refractive index of 1.5 could also act as a secondary anti-reflective layer, further increasing the 450 nm flux inside the silicon to 71.8% of the incident intensity (without even considering optical concentration); perhaps, a partial reason for the better performance of doped optical couplings whilst situated under an SEH concentrator. In addition, the refractive index of silicon falls with increasing wavelength, so this would explain why the spectral response is greater in the blue part of the spectrum. These as yet unconsidered aspects could, through further experimental characterisation and theoretical calculations, yield exciting prospects for the design and application of rare earth compound containing LCPV modules.

6.5 Conclusion

In conclusion this chapter was a worthwhile endeavour to reinforce the mathematical foundations of the findings of this thesis. Excitingly, cost per watt compared to the control device was shown to decrease for silicon PV, silicon LCPV and DSSCs by up to 2.5%, 8.1% and 39.6% respectively. The powers per

area of the laboratory scale devices were then calculated to give wider context to the implications of efficiency enhancement via rare earth compound addition.

Then, the t and z tests showed a high level of confidence that rare earth compound doping truly did improve efficiency at a population level, as many devices that were the highest performing in chapter 4 showed levels of confidence above 99% that their sample mean was higher than that of the control group. However, for the coated PV cells featured in chapter 3, the statistical tests were less convincing with only two samples showing a confidence level above 95%. Although this does support the notion that these methods are more effective in LCPV than non-concentrating PV.

The Rothemund optical model was deployed well to accurately predict the EQE profile of the rare earth doped Sylgard coated PV cells with low SSEs (~10^{-3}) and high R^2 (>0.96) values derived for most concentration levels. Despite this, it did not predict an overall J_{SC} increase, potentially due to overestimating the decrease in EQE at higher wavelengths. Finally, the originally developed 2D ray trace model for the rare earth compound doped concentrators did predict enhanced performance (ΔJ_{SC} up to +0.35% relative to the control) and in the correct order of configurations for the $NaYF_4$: Er^{3+}, Yb^{3+} containing optics, but the predictions were not as great as what was observed experimentally (~4% increase in J_{SC}). The shortcomings of both models owe to their simplicity and neglected effects, chiefly changes in reflectance from the addition of rare earth compounds.

Chapter 7. Conclusions and Future Outlook

7.1 Chapter Summaries

Each chapter has presented some key ideas and findings which may be summarised as follows.

Chapter 1 conveyed the motivation for this work and current status of solar PV technology, which are presented along with the principles of how a single junction cell generates electricity and how modifying the incident spectrum could be a viable approach to increase device performance.

In chapter 2, the existing literature on spectral conversion is critically analysed and catalogued for a range of historical and state-of-the-art studies on various solar cell technologies, including silicon, thin-film and emerging PV; a maximum relative PCE enhancement of 70% was reported through simultaneous UC and DC in rare earth compounds for DSSCs (although in this case and many others, it was the dual functional nature of particles that was responsible for such a large increase compared to the control device). It was also seen that the use of nanoscale phenomena such as plasmonic resonance, photonic crystals and dye ligands can particularly aid the UC process efficiency for further developments. On the other hand, LDS has achieved considerable advances and demonstrates more immediate potential through LSCs. Finally, the cost aspects of spectral conversion and knowledge gaps were looked at, essentially concluding that small improvements in efficiency at a low change in the fabrication cost were the best way forward.

After introducing the materials and characterisation methods to form the basis of investigations in the first part of chapter 3, results from preliminary studies on coating silicon PV cells are presented. Adding the two rare earth compounds ($Sr_4Al_{14}O_{25}$: Eu^{2+}, Dy^{3+} and $NaYF_4$: Er^{3+}, Yb^{3+}) in Sylgard in concentrations of 0.25% to 2% w/w and coating the cells via drop casting was found to be most effective method; relative improvements in the PCE of up to 4.9% and 5.4% were attained for the 1% w/w doped $NaYF_4$: Er^{3+}, Yb^{3+} and 0.5% w/w $Sr_4Al_{14}O_{25}$: Eu^{2+}, Dy^{3+} layers respectively. It was also noted that at slightly lower irradiance (0.8 suns), the enhancements were more pronounced, before being less so at 0.4 and 0.6 suns.

Then in chapter 4, a similar investigation was conducted but using SEH concentrators with BIPV applications to increase the light flux on the silicon PV cells via an optical coupling. Furthermore, the concentrators themselves were doped with the same rare earth doped compounds (at 0.1% w/w either homogenously throughout the concentrator, or at its top or bottom), a major innovation of this thesis. At 1 sun, it was found the greatest PCE enhancements were observed for the top and bottom $Sr_4Al_{14}O_{25}$: Eu^{2+}, Dy^{3+} doped SEH concentrators and the 1% w/w doped $NaYF_4$: Er^{3+}, Yb^{3+} optical coupling, which were 5.7%, 5.3% and 11.1% respectively. The relative PCE gains were again more pronounced at lower irradiances and the doped optical couplings showed a greater relative rise in performance than their analogues without SEH concentrators (up to 16.1% greater at 0.4 suns for 0.5% w/w doped $NaYF_4$: Er^{3+}, Yb^{3+} Sylgard). Finally, in this chapter, the effect of a varied angle of incidence was studied, and it was found the rare earth doped concentrators could still achieve PCE gains under these conditions, particularly at 60° and 80°, where the relative rises were greatest.

Next in chapter 5, the focus was shifted from silicon-based devices to the emerging PV technology of DSSCs. Firstly, the operating principles of a DSSC were discussed before different methods were described (by drawing from the literature) and attempted to best incorporate the rare earth compound powders into a layer. Following characterisation, it was the 18NR-AO TiO_2/rare earth compound mixtures (drop casted at 25 or 50 µl) and counter electrode coated devices that exhibited the greatest enhancements in performance; maximum PCEs of 5.30% and 4.32% were recorded for the $NaYF_4$: Er^{3+}, Yb^{3+} (50 µl drop casted) and $Sr_4Al_{14}O_{25}$: Eu^{2+}, Dy^{3+} (doctor bladed counter electrode) devices compared to 3.46% for un-doped control. Although IPCE measurements were inconclusive to prove whether spectral conversion was the dominant phenomenon causing the superior behaviour, since EQE for the doped devices was not higher in the excitation wavelengths but instead across the visible spectrum. The same SEH concentrators were then shown to increase the power output of a control DSSC by up to 36.3% for the 0.1% bottom doped $Sr_4Al_{14}O_{25}$: Eu^{2+}, Dy^{3+} concentrator (despite its sub-optimal design for the photoactive area) and the key results from a collaborative study are presented which used new materials (porphyrin dye, carbon coated counter electrode, and Y_2O_3: Yb^{3+}, Tm^{3+},

Ho^{3+} or Y_2O_3: Yb^{3+}, Ho^{3+}). The latter devices achieved higher PCE (by 10.3% relative with the addition of Y_2O_3: Yb^{3+}, Tm^{3+}, Ho^{3+}) and remarkably improved stability in performance over 90 days due to decreased dye photo-degradation (the Y_2O_3: Yb^{3+}, Tm^{3+}, Ho^{3+} kept 40% of its initial PCE compared to just 5% for the control).

Lastly in chapter 6, a basic cost analysis from the price paid for the laboratory materials was conducted to show that cost per watt can be lowered by this approach in silicon PV, silicon LCPV and DSSCs. A statistical analysis was then carried out to analyse the raw PCE data of all the cells which made up an identically produced batch. Through a Welch's t-test from the sample standard deviations and z-test using an estimated population standard deviation by considering the sources of uncertainty, confidence levels of the findings in chapter 3 and 4 were presented, and broadly agreed with. As a final exercise, two models were used (one prior developed by Rothemund et al [182] and one built from first principles) to justify the findings of the J_{SC} enhancements of the coated PV cells and doped concentrator LCPV devices respectively. The former gave a well fitted EQE profile but did not predict J_{SC} to increase, while the doped concentrators were predicted to lead to relative J_{SC} enhancements of up to 0.35% for homogenous doping of $NaYF_4$: Er^{3+}, Yb^{3+} (an underestimate compared to observed data). Thus, it is concluded spectral conversion may not be the dominant process but part of a package of optical behaviours (including anti-reflective properties) to be further explored and that would explain the superior PV and LCPV performances observed.

7.2 Future Outlook

As a final thought exercise, it is necessary to recognise the limitations of this work and recognise the future potential of this approach, in order to aid subsequent studies and leave a meaningful imprint on the field of solar PV knowledge.

Two of the main limitations were the small sample size and fabrication process imperfections of the devices due to practical constraints. Using the maximum values rather than a mean, to draw the initial conclusions in chapters 3 and 4, could potentially have amplified outliers. Although in spite of this, and as shown through the chapter 6 statistical analysis, the results are still strongly indicative of

increased performance through the methods employed in this work. However, a larger repeated study would give even more confidence to this approach.

As well as a larger number of cells, another issue to explore that goes beyond of the scope of this work, would be the long term stability of these modules since a higher performance after initial device fabrication is admirable, but to be impactful would need to be maintained over the system's working lifetime (typically 20 years for silicon PV). This lifetime analysis could be done with accelerated light exposure using powerful LEDs [272]. Alternatively, a shorter term stability investigation could consist of a collection of substantially sized rare earth compound containing LCPV arrays with their power outputs monitored over one or more years to give annual generation yields, which would also answer important questions about how these systems perform under real sunlight conditions as compared to an indoor solar simulator. A further aspect that was not considered is temperature (important to be kept low for cell performance). If less UV photons are being absorbed, then less thermalisation will occur, so there could be a secondary beneficial effect on device temperature.

In addition, it might be of interest to construct LCPV modules with other types of cells. The ones provided by NAREC were mono-crystalline silicon which is falling in its status as the preferred wafer-based PV technology, so the use of multi-crystalline cells with their lower costs and rising market share might be more appropriate for future studies. Additionally, multi-crystalline silicon displays a poorer response in the UV and blue regions of the spectrum, so would stand to gain more from LDS or DC of high of energy photons [351]. It was seen in chapter 2 that thin-film cells such as CdTe suffer from the same low EQE at these wavelengths, so could also stand to benefit from these rare earth compounds.

With regards to emerging PV technologies, having successfully incorporated these materials with DSSCs, it would be logical to apply them to other types of cell, particularly PSCs due to their higher efficiency and them having a similar mesoporous TiO_2 structure for one of their layers, so a similar mixing technique could be used. Although in the long term, it seems solid state DSSCs will have more potential for commercialisation than the liquid electrolyte devices featured in this thesis, so spectral conversion studies on the former category would be a worthy endeavour, especially on modules with flexible substrates and coming in a range of colours, two exciting properties for potential BIPV applications. Like

with the silicon modules, stability tests could be carried out and annual power output measured in real conditions for solid state DSSCs; spectral conversion could be particularly effective in this aspect since it could reduce the amount of UV light entering the system and degrading the cell (as shown by the 5.7 results). This could be alternatively achieved by coating the front electrode in ball milled $Sr_4Al_{14}O_{25}$: Eu^{2+}, Dy^{3+} and opting for a single crystal approach, although internal doping was chosen to be explored in chapter 5 because of higher efficiencies attained in the literature this way. On the other hand, the cell could be upside down, if the doctor bladed counter electrode can have a sufficiently high transparency, to act as a UV filter from that side. In addition, tandem emerging PV-silicon PV modules are expected to become more widespread, so spectral conversion could aid their performance too.

Concerning the concentrators, there is scope to use this method for different dimensions of the SEH. For example, the University of Exeter group has access to prototypes with higher geometric concentration ratios than the value of 3.5 used in this work. These higher concentrating optics might find better practical applications, since they further reduce the area of cells required for the same power output, an important challenge in BIPV. In addition, concentrators with a smaller exit aperture (equal to that of the active area of the DSSC) can be combined with the emerging PV for more rigorous investigations on their effect on performance when spectral conversion materials are present.

The experiment could also be repeated with different types of 3D static concentrators such as the ones presented in 1.2.2 (e.g. compare she with CPC) or by using different optical media (i.e. replace either or both of Crystal Clear and Sylgard with alternatives presented in chapter 2 such as PMMA or even a biopolymer for added sustainability benefits). The optimal doping ratio could be further probed for the PV coating and optical couplings with smaller intervals in the range of 0.25% to 2% w/w, although it is unlikely necessary to go outside these upper and lower limits due to the best performing devices typically having a 0.5% or 1% concentration of the rare earth compound. However, variation in doping ratio was something that was not examined for the SEH concentrators in which the level was kept constant at 0.1% w/w (except the order of magnitude higher 1% w/w concentrators that were not suitably transparent on observation), so this could be further varied to, for example, 0.05% and 0.2% such that the

absorption coefficients change which may lead to further PCE enhancements for the PV cells below. More geometric doping designs could also be applied to the concentrators (e.g. thinner doped layers or a bottom and top doped design). DSSCs also had their rare earth compound content predominantly varied by amount dispensed (not weight percentage), so this could be a focus of follow up investigations, as well as dual region doping (e.g. at the counter electrode and mesoporous layer simultaneously).

A more advanced model in 3D rather than 2D that takes account of reflection, geometric scattering and more physical properties (e.g. the change in refractive index from the addition of impurities to the concentrator medium and accounts for scattering) would be a way to build the theoretical understanding and resolve the paradox of how the model in 6.4.2 predicts lower efficiencies in doped concentrators at illumination wavelengths of 420 nm and above, yet results from 4.4 show the contrary to be true. Also, the DSSCs were not considered in any model, so could be explored theoretically (both in terms of light collection and charge transport).

Although other spectral conversion materials were excluded on grounds of cost or complexity to produce, comparing their performance to $Sr_4Al_{14}O_{25}$: Eu^{2+}, Dy^{3+} and $NaYF_4$: Er^{3+}, Yb^{3+} whilst in the same configurations together with a cost-benefit analysis would be a useful exercise. Particular recommendations would be for the widely used Lumogen dyes and for an in situ synthesised $NaYF_4$: Er^{3+}, Yb^{3+} that demonstrates a stronger UC emission upon 980 nm illumination. In this latter activity, the state-of-the-art nanoscale phenomena could also be utilised, although the use of, for example, gold nanoparticles to achieve this could considerably increase fabrication costs, which is aimed to be avoided in this work.

7.3 Concluding Remarks

In this chapter thus far, the key results and findings of each chapter have been presented while limitations of the investigations conducted and suggestions for areas of focus in futures studies have been discussed.

The novelty of this work is highlighted by the following:

- First time $Sr_4Al_{14}O_{25}$: Eu^{2+}, Dy^{3+} has been applied to silicon PV cells
- First time SEH concentrators have been doped with rare earth compounds

- Comparison between performance of doped layer on PV cell with and without concentrator
- Evaluation of rare earth doped concentrators at a range of angles of incidence
- First time $Sr_4Al_{14}O_{25}$: Eu^{2+}, Dy^{3+} has been applied to DSSCs
- First time placement of a spectral conversion layer at the counter electrode
- Cost analysis provided for these materials and implications for a commercial sized system
- Originally developed a 2D ray trace model for spectral conversion within SEH concentrators

It is hoped that this thesis will serve as a useful leaf in the much larger tree of PV science and add impetus towards the drive for more efficient, low-cost LCPV and BIPV modules. Finally, it must be considered if the primary objective set out in chapter 1 (and repeated below) has been met.

- Develop a cost-effective method for incorporating spectral conversion materials into established and emerging types of solar PV cells and technologies with the aim to increase efficiency and electrical power output.

The PCE has been enhanced for silicon based LCPV and DSSCs by up to 11.1% and 53.4% respectively, while analysis showed their costs per W_p fell by 8.1% and 39.6% through these materials and methods. So therefore, in this regard, it has certainly been successful in achieving the objective and surpassing the 5% PCE enhancement targeted in 1.5.7. Although to be self-critical, it is debatable how much these enhancements were entirely due to spectral conversion. On the one hand, the recorded EQE data for silicon devices (with greater EQE at 400-450 nm) and 2D ray tracing model showed J_{SC} (and by extension PCE) to increase through the LDS and DC of high energy photons. However, the Rothemund model predicted a small decrease in J_{SC} and the EQE measurements for DSSC samples displayed increased spectral response across the whole visible spectrum not just the region of rare earth compound excitation. Likewise, even the SEH concentrator-silicon LCPV model proved it apparent that spectral conversion alone cannot increase the device performance at wavelengths above 410 nm (contrary to the observed data). There are two possibilities for these inconsistencies. Firstly, that these discrepancies are due to experimental flaws

(e.g. small sample size and human error in fabrication) along with an oversimplified model. Or secondly, that these rare earth compounds actually can increase performance across a substantial range of visible wavelengths through other means (scattering, anti-reflective properties etc.). It could be argued that the exact mechanism is not the primary concern, i.e. the increased power output at a lower cost per W_p is the key desirable regardless of what is causing it and the dual functionality is an additional boon to performance. Although, as material scientists and physicists, a pure theory is a beautiful thing to appreciate and grow collective understanding, so should be the focus of follow up work. In addition, a model accounting for spectral dependence should be developed to formulate the long-term stability of such devices. This would include spectral variation due to the continuous solar position, influencing meteorological information and effects of the particulates in the atmosphere, all based on local data, to study the LCPV system behaviour in detail.

To conclude, while not the panacea it first appears, spectral conversion has been shown to be a viable option for enhancing the performance of LCPV, for both silicon and DSSC modules and merits further study that notes the recommendations made in 7.2.

Bibliography

[1] UNFCC. "The Paris Agreement." https://unfccc.int/process-and-meetings/the-paris-agreement/the-paris-agreement (accessed 10 Sept 2018).

[2] UK Government. https://www.gov.uk/government/news/uk-becomes-first-major-economy-to-pass-net-zero-emissions-law (accessed 1 Oct 2019).

[3] Reuters. "Norway brings forward carbon neutrality goal to 2030." https://www.reuters.com/article/us-norway-climatechange/norway-brings-forward-carbon-neutrality-goal-to-2030-idUSKCN0YT1KM (accessed 2 Oct 2019).

[4] C. Shearer, R. Fofrich, and S. J. Davis, "Future CO2 emissions and electricity generation from proposed coal-fired power plants in India," *Earth's Future,* vol. 5, no. 4, pp. 408-416, 2017, doi: 10.1002/2017ef000542.

[5] USEPA. "Global Greenhouse Gas Emissions Data." https://www.epa.gov/ghgemissions/global-greenhouse-gas-emissions-data#Trends (accessed 12 Sept 2018).

[6] Centre for Energy and Climate Solutions. "Global Emissions." https://www.c2es.org/content/international-emissions/ (accessed 12 Sept 2018).

[7] M. Perez and R. Perez, "Update 2015–a fundamental look at supply side energy reserves for the planet," *IEA-SHCP-Newsletter,* vol. 62, pp. 4-6, 2015.

[8] R. Pandy, "Electrochemical Synthesis and characterization of Copper Indium Gallium Selenide (CIGS) absorber layer for solar cells," MTech, Department of Metallurgical and Materials Engineering, National Institute of Technology Rourkela, Odisha, India, 2015.

[9] PVTECH. "Bids in 300MW Saudi solar tender breach two cents." https://www.pv-tech.org/news/technical-bids-for-300mw-of-solar-in-saudi-arabia-already-breach-2-cents (accessed 13 Sept 2018).

[10] FISE. "Levelized Cost of Electricity Renewable Energy Technologies." https://www.ise.fraunhofer.de/content/dam/ise/en/documents/publications/studies/EN2018_Fraunhofer-ISE_LCOE_Renewable_Energy_Technologies.pdf (accessed 13 Sept 2018).

[11] E. Becquerel, "Mémoire sur les effets électriques produits sous l'influence des rayons solaires," *Comptes Rendus,* vol. 9, pp. 561-567, 1839.

[12] N. Bloomberg. "Clean Energy Investment Exceeded $300 Billion Once Again in 2018." https://about.bnef.com/blog/clean-energy-investment-exceeded-300-billion-2018/ (accessed 1 Feb 2019).

[13] EPVIA. "Global Market Outlook for Photovoltaics 2014-2018." https://www.webcitation.org/6QGSvAF7w (accessed 1 Feb 2019).

[14] BP. "Statistical Review of World Energy – all data, 1965-2017." https://www.bp.com/en/global/corporate/energy-economics/statistical-review-of-world-energy.html (accessed 1 Feb 2019).

[15] M. Ram *et al.*, "Global Energy System based on 100% Renewable Energy – Power, Heat, Transport and Desalination Sectors," Lappeenranta University of Technology and Energy Watch Group, Berlin, Germany, 2019.

[16] Economist. "Pricing sunshine." https://www.economist.com/graphic-detail/2012/12/28/pricing-sunshine (accessed 2 Feb 2019).

[17] D. M. Powell, M. T. Winkler, H. J. Choi, C. B. Simmons, D. B. Needleman, and T. Buonassisi, "Crystalline silicon photovoltaics: a cost analysis framework for determining technology pathways to reach baseload electricity costs," *Energy & Environmental Science,* 10.1039/C2EE03489A vol. 5, no. 3, pp. 5874-5883, 2012, doi: 10.1039/C2EE03489A.

[18] L. C. Andreani, A. Bozzola, P. Kowalczewski, M. Liscidini, and L. Redorici, "Silicon solar cells: toward the efficiency limits," *Advances in Physics: X,* vol. 4, no. 1, p. 1548305, 2019/01/01 2019, doi: 10.1080/23746149.2018.1548305.

[19] M. Raugei, S. Bargigli, and S. Ulgiati, "Life cycle assessment and energy pay-back time of advanced photovoltaic modules: CdTe and CIS compared to poly-Si," *Energy (Oxford),* vol. 32, no. 8, pp. 1310-1318, 2007, doi: DOI:101016/jenergy200610003.
[20] Y. Tawada, M. Kondo, H. Okamoto, and Y. Hamakawa, "Window Effects of Hydrogenated Amorphous Silicon Carbide in a p-i-n a-Si Solar Cell," *Japanese Journal of Applied Physics,* vol. 21, pp. 297-303, 1982.
[21] S. Yang, W. Fu, Z. Zhang, H. Chen, and C.-Z. Li, "Recent advances in perovskite solar cells: efficiency, stability and lead-free perovskite," *Journal of Materials Chemistry A,* 10.1039/C7TA00366H vol. 5, no. 23, pp. 11462-11482, 2017, doi: 10.1039/C7TA00366H.
[22] NREL. "Best Research-Cell Efficiency Chart." https://www.nrel.gov/pv/cell-efficiency.html (accessed 20 Oct 2019).
[23] Oxford PV. "Oxford PV perovskite solar cell achieves 28% efficiency." https://www.oxfordpv.com/news/oxford-pv-perovskite-solar-cell-achieves-28-efficiency (accessed 15 Oct 2019).
[24] PV Magazine. "Oxford PV, Oxford University target 37% efficient perovskite solar cells." https://www.pv-magazine.com/2018/09/26/oxford-pv-oxford-university-target-37-efficient-perovskite-solar-cells/ (accessed 13 Feb 2019).
[25] PV EnergyTrend. "PV spot prices." https://www.energytrend.com/pricequotes.html (accessed 15 Feb 2020).
[26] Alibaba. "A grade low price flexible amorphous silicone solar panel price per watt made in China." https://www.alibaba.com/product-detail/A-grade-low-price-flexible-amorphous_60299950049.html?spm=a2700.7724857.normalList.2.54c06e33H4DTz0 (accessed 13 Feb 2020).
[27] Free Clean Solar. "125W solar panel MiaSole MS125GG CIGS." http://www.freecleansolar.com/125W-solar-panel-MiaSole-MS125GG-CIGS-p/ms125gg.htm (accessed 13 Feb 2020).
[28] Inverse. "Solar Energy: Adding selenium can increase power and cut costs for solar panels." https://www.inverse.com/article/55820-a-key-solar-panel-defect-has-been-solved-and-that-may-mean-big-price-drops (accessed 13 Feb 2020).
[29] J. Day, S. Senthilarasu, and T. K. Mallick, "Improving spectral modification for applications in solar cells: A review," *Renewable Energy,* vol. 132, pp. 186-205, 2019/03/01/ 2019, doi: https://doi.org/10.1016/j.renene.2018.07.101.
[30] Next Big Future. "Commercial Perovskite solar cells at 10 cents per watt could soon bring lower cost energy." https://www.nextbigfuture.com/2018/02/commercial-perovskite-solar-cells-at-10-cents-per-watt-could-soon-bring-lower-cost-energy.html (accessed 13 Feb 2020).
[31] CHEOPS. "Cost of Ownership calculation of perovskite PV technology." https://www.cheops-project.eu/2019/05/23/cost-of-ownership-calculation-of-perovskite-pv-technology/ (accessed 15 Oct 2019).
[32] Solartron Energy Systems Inc. "HCPV Solar Parabolic Solar Concentrator Technology." https://www.solartronenergy.com/hcpv-solar/ (accessed 13 Feb 2020).
[33] S. Kurtz, "Opportunities and Challenges for Development of a Mature Concentrating Photovoltaic Power Industry," NREL, Golden, Colorado, 2012.
[34] K. Shanks, S. Senthilarasu, and T. K. Mallick, "Optics for concentrating photovoltaics: Trends, limits and opportunities for materials and design," *Renewable and Sustainable Energy Reviews,* vol. 60, pp. 394-407, 2016/07/01/ 2016, doi: https://doi.org/10.1016/j.rser.2016.01.089.
[35] M. G. Debije and P. P. C. Verbunt, "Solar Concentrators: Thirty Years of Luminescent Solar Concentrator Research: Solar Energy for the Built

Environment (Adv. Energy Mater. 1/2012)," *Advanced Energy Materials,* vol. 2, no. 1, pp. 1-1, 2012/01/01 2012, doi: 10.1002/aenm.201290003.
[36] E. Mokri and M. Emziane, "Concentrator photovoltaic technologies and market: a critical review," presented at the World Renewable Energy Congress 2011, Linköping, Sweden., 8-13 May 2011.
[37] M. Wiesenfarth, I. Anton, and A. W. Bett, "Challenges in the design of concentrator photovoltaic (CPV) modules to achieve highest efficiencies," *Applied Physics Reviews,* vol. 5, no. 4, p. 041601, 2018/12/01 2018, doi: 10.1063/1.5046752.
[38] P. G. Green, "Optical Properties of Luminescent Solar Concentrators," PhD, Department of Physics and Astronomy, University of Sheffield, Sheffield, UK, 2014.
[39] N. Sellami, T. K. Mallick, and D. A. McNeil, "Optical characterisation of 3-D static solar concentrator," *Energy Conversion and Management,* vol. 64, pp. 579-586, 2012/12/01/ 2012, doi: https://doi.org/10.1016/j.enconman.2012.05.028.
[40] FISE and NREL, "Current Status of Concentrator Photovoltaic (CPV) Technology," Freiburg, Germany, 2017.
[41] L. Micheli, K. S. Reddy, and T. K. Mallick, "Plate Micro-fins in Natural Convection: An Opportunity for Passive Concentrating Photovoltaic Cooling," *Energy Procedia,* vol. 82, pp. 301-308, 2015/12/01/ 2015, doi: https://doi.org/10.1016/j.egypro.2015.12.037.
[42] UNEP. "Global Status Report 2018." https://www.unenvironment.org/resources/report/global-status-report-2018 (accessed 3 Feb 2019).
[43] F. J. W. Osseweijer, L. B. P. van den Hurk, E. J. H. M. Teunissen, and W. G. J. H. M. van Sark, "A comparative review of building integrated photovoltaics ecosystems in selected European countries," *Renewable and Sustainable Energy Reviews,* vol. 90, pp. 1027-1040, 2018/07/01/ 2018, doi: https://doi.org/10.1016/j.rser.2018.03.001.
[44] C. Ballif, L.-E. Perret-Aebi, S. Lufkin, and E. Rey, "Integrated thinking for photovoltaics in buildings," *Nature Energy,* vol. 3, no. 6, pp. 438-442, 2018/06/01 2018, doi: 10.1038/s41560-018-0176-2.
[45] Treehugger. "Building Integrated Solar Power Tiles Now Available With SunRun Solar-As-Service Program." https://www.treehugger.com/renewable-energy/building-integrated-solar-power-tiles-now-available-with-sunrun-solar-as-service-program.html (accessed 14 Mar 2019).
[46] LAMILUX. "Glass-integrated Photovoltaics - Pure Aesthetics " https://www.lamilux.co.uk/daylight-systems/photovoltaics/glazing-integrated-photovoltaics.html (accessed 15 Mar 2019).
[47] AZURE. "Solar Squared by Build Solar." https://www.azuremagazine.com/product-guide/solar-squared-build-solar/ (accessed 20 Mar 2019).
[48] SEAC, "BIPV REPORT 2013. State of the art in Building Integrated Photovoltaics.," 2013.
[49] MKS. Newport. https://www.newport.com/t/introduction-to-solar-radiation (accessed 4 Feb 2019).
[50] H. W. Wu, A. Emadi, G. de Graaf, J. Leijtens, and R. F. Wolffenbuttel, "Design and Fabrication of an Albedo Insensitive Analog Sun Sensor," *Procedia Engineering,* vol. 25, pp. 527-530, 2011/01/01/ 2011, doi: https://doi.org/10.1016/j.proeng.2011.12.131.
[51] OPI. "Fundamentals of Semiconductor physics." http://www.optique-ingenieur.org/en/courses/OPI_ang_M05_C02/co/Contenu_02.html (accessed 30 Jan 2019).
[52] J. C. Goldschmidt *et al.*, "Experimental analysis of upconversion with both coherent monochromatic irradiation and broad spectrum illumination," *Solar Energy Materials and Solar Cells,* vol. 95, no. 7, pp. 1960-1963, 2011/07/01/ 2011, doi: https://doi.org/10.1016/j.solmat.2011.01.019.

[53] S. Fischer, "Upconversion of Sub-Band-Gap Photons for Silicon Solar Cells," Doctor of Natural Sciences, Department of Microsystems Engineering, University of Freiburg, Freiburg, Germany, 2014.
[54] B. S. Richards, A. Ivaturi, S. K. W. MacDougall, and J. Marques-Hueso, *Up- and down-conversion materials for photovoltaic devices* (SPIE Photonics Europe). SPIE, 2012.
[55] Solar Love. "How Solar Cells Work — Components & Operation of Solar Cells." https://solarlove.org/how-solar-cells-work-components-operation-of-solar-cells/ (accessed 14 Sept 2018.
[56] G. N. Lewis, "A New Principle of Equilibrium," (in eng), *Proc Natl Acad Sci U S A,* vol. 11, no. 3, pp. 179-183, 1925, doi: 10.1073/pnas.11.3.179.
[57] W. Shockley and H. J. Queisser, "Detailed Balance Limit of Efficiency of p-n Junction Solar Cells," *Journal of Applied Physics,* vol. 32, no. 3, pp. 510-519, 1961, doi: 10.1063/1.1736034.
[58] D. Kim. "Donghum Kim's Research Page." http://www.donghunkim.com/research.html (accessed 10 Feb 2019).
[59] PV Education. "IV Curve." https://www.pveducation.org/pvcdrom/solar-cell-operation/iv-curve (accessed 7 Feb 2019).
[60] PV Education. "Quantum Efficiency." https://www.pveducation.org/pvcdrom/solar-cell-operation/quantum-efficiency (accessed 7 Feb 2019).
[61] PV Education. "Spectral Response." https://www.pveducation.org/pvcdrom/solar-cell-operation/spectral-response (accessed 7 Feb 2019).
[62] S. Sharma, "Performance Enhancement of Building-Integrated Concentrator Photovoltaic System Using Phase Change Materials," PhD, University of Exeter, Exeter, UK, 2017.
[63] Solar Power World. "What is PERC? Why should you care?" https://www.solarpowerworldonline.com/2016/07/what-is-perc-why-should-you-care/ (accessed 10 Jan 2019).
[64] Meyer Burger. "Heterojunction Technology: The Solar Cell of the Future." https://www.meyerburger.com/user_upload/dashboard_news_bundle/2eac5e97a268041cdcd1485668e3184c2ecd487b.pdf (accessed 10 Jan 2019).
[65] D. J. Aiken, "High performance anti-reflection coatings for broadband multi-junction solar cells," *Solar Energy Materials and Solar Cells,* vol. 64, no. 4, pp. 393-404, 2000/11/01/ 2000, doi: https://doi.org/10.1016/S0927-0248(00)00253-1.
[66] M. Gu *et al.*, "Nanoplasmonics: a frontier of photovoltaic solar cells," in *Nanophotonics* vol. 1, ed, 2012, p. 235.
[67] R. Rawat, R. Lamba, and S. C. Kaushik, "Thermodynamic study of solar photovoltaic energy conversion: An overview," *Renewable and Sustainable Energy Reviews,* vol. 71, pp. 630-638, 2017/05/01/ 2017, doi: https://doi.org/10.1016/j.rser.2016.12.089.
[68] A. D. Vos, "Detailed balance limit of the efficiency of tandem solar cells," *Journal of Physics D: Applied Physics,* vol. 13, no. 5, pp. 839-846, 1980/05/14 1980, doi: 10.1088/0022-3727/13/5/018.
[69] A. Belghachi, "Theoretical Calculation of the Efficiency Limit for Solar Cells," in *Solar Cells - New Approaches and Reviews*, L. A. Kosyachenko Ed. London, UK: Intech, 2015, ch. 2, pp. 48-76.
[70] O. E. Semonin *et al.*, "Peak External Photocurrent Quantum Efficiency Exceeding 100% via MEG in a Quantum Dot Solar Cell," *Science,* vol. 334, no. 6062, p. 1530, 2011, doi: 10.1126/science.1209845.
[71] Q. Shao, A. A. Balandin, A. I. Fedoseyev, and M. Turowski, "Intermediate-band solar cells based on quantum dot supracrystals," *Applied Physics Letters,* vol. 91, no. 16, p. 163503, 2007, doi: 10.1063/1.2799172.

[72] M. Wolf, "Limitations and Possibilities for Improvement of Photovoltaic Solar Energy Converters: Part I: Considerations for Earth's Surface Operation," *Proceedings of the IRE,* vol. 48, no. 7, pp. 1246-1263, 1960, doi: 10.1109/JRPROC.1960.287647.
[73] N. Bloembergen, "Solid State Infrared Quantum Counters," *Physical Review Letters,* vol. 2, no. 3, pp. 84-85, 02/01/ 1959, doi: 10.1103/PhysRevLett.2.84.
[74] T. Trupke, M. A. Green, and P. Würfel, "Improving solar cell efficiencies by up-conversion of sub-band-gap light," *Journal of Applied Physics,* vol. 92, no. 7, pp. 4117-4122, 2002, doi: 10.1063/1.1505677.
[75] X. Huang, S. Han, W. Huang, and X. Liu, "Enhancing solar cell efficiency: the search for luminescent materials as spectral converters," *Chemical Society Reviews,* 10.1039/C2CS35288E vol. 42, no. 1, pp. 173-201, 2013, doi: 10.1039/C2CS35288E.
[76] F. Wang *et al.*, "Tuning upconversion through energy migration in core–shell nanoparticles," *Nature Materials,* Article vol. 10, p. 968, 10/23/online 2011, doi: 10.1038/nmat3149 https://www.nature.com/articles/nmat3149#supplementary-information.
[77] Y. Y. Cheng *et al.*, "Increased upconversion performance for thin film solar cells: a trimolecular composition," *Chemical Science,* 10.1039/C5SC03215F vol. 7, no. 1, pp. 559-568, 2016, doi: 10.1039/C5SC03215F.
[78] A. J. Nozik, "Quantum dot solar cells," *Physica E: Low-dimensional Systems and Nanostructures,* vol. 14, no. 1, pp. 115-120, 2002/04/01/ 2002, doi: https://doi.org/10.1016/S1386-9477(02)00374-0.
[79] Y. Shang, S. Hao, C. Yang, and G. Chen, "Enhancing Solar Cell Efficiency Using Photon Upconversion Materials," (in eng), *Nanomaterials (Basel),* vol. 5, no. 4, pp. 1782-1809, 2015, doi: 10.3390/nano5041782.
[80] J. Wang, T. Ming, Z. Jin, J. Wang, L.-D. Sun, and C.-H. Yan, "Photon energy upconversion through thermal radiation with the power efficiency reaching 16%," *Nature Communications,* Article vol. 5, p. 5669, 11/28/online 2014, doi: 10.1038/ncomms6669

https://www.nature.com/articles/ncomms6669#supplementary-information.
[81] T. Trupke, M. A. Green, and P. Würfel, "Improving solar cell efficiencies by down-conversion of high-energy photons," *Journal of Applied Physics,* vol. 92, no. 3, pp. 1668-1674, 2002, doi: 10.1063/1.1492021.
[82] M. Alkiswani, "Spectrum conversion in solar cells industry," Master Thesis, Department of Renewable Energy, Halmstad University, Halmstad, Sweden, 2015.
[83] W. G. J. H. M. v. Sark, A. Meijerink, and R. E. I. Schropp, "Solar Spectrum Conversion for Photovoltaics Using Nanoparticles," in *Third Generation Photovoltaics*, V. Fthenakis Ed. London: InTech, 2012.
[84] U. Rau, F. Einsele, and G. C. Glaeser, "Efficiency limits of photovoltaic fluorescent collectors," *Applied Physics Letters,* vol. 87, no. 17, p. 171101, 2005, doi: 10.1063/1.2112196.
[85] A. Shalav, B. S. Richards, and M. A. Green, "Luminescent layers for enhanced silicon solar cell performance: Up-conversion," *Solar Energy Materials and Solar Cells,* vol. 91, no. 9, pp. 829-842, 2007/05/23/ 2007, doi: https://doi.org/10.1016/j.solmat.2007.02.007.
[86] G. H. Dieke, "Spectra and Energy Levels of Rare Earth Ions in Crystals," *American Journal of Physics,* vol. 38, no. 3, pp. 399-400, 1970, doi: 10.1119/1.1976350.
[87] F. Auzel, "Upconversion and Anti-Stokes Processes with f and d Ions in Solids," *Chemical Reviews,* vol. 104, no. 1, pp. 139-174, 2004/01/01 2004, doi: 10.1021/cr020357g.
[88] Hyper Physics. "Term Symbols." http://hyperphysics.phy-astr.gsu.edu/hbase/Atomic/Term.html (accessed 15 Feb 2019).

[89] G. E. Arnaoutakis, J. Marques-Hueso, A. Ivaturi, K. W. Krämer, T. K. Mallick, and B. S. Richards, "Enhancement of Upconversion for Photovoltaics with β-NaYF4:Er3+ and Concentrating Integrated Optics," in *Renewable Energy and the Environment*, Tucson, Arizona, 2013/11/03 2013: Optical Society of America, in OSA Technical Digest (online), p. PT3C.4, doi: 10.1364/PV.2013.PT3C.4. [Online]. Available: http://www.osapublishing.org/abstract.cfm?URI=PV-2013-PT3C.4

[90] L.-D. Sun, H. Dong, P.-Z. Zhang, and C.-H. Yan, "Upconversion of Rare Earth Nanomaterials," *Annual Review of Physical Chemistry,* vol. 66, no. 1, pp. 619-642, 2015, doi: 10.1146/annurev-physchem-040214-121344.

[91] L. Tian *et al.*, "The Upconversion Luminescence of Er(3+)/Yb(3+)/Nd(3+) Triply-Doped β-$NaYF_4$ Nanocrystals under 808-nm Excitation," (in eng), *Materials (Basel),* vol. 7, no. 11, pp. 7289-7303, 2014, doi: 10.3390/ma7117289.

[92] W. G. van Sark, J. de Wild, J. K. Rath, A. Meijerink, and R. E. Schropp, "Upconversion in solar cells," *Nanoscale Research Letters,* journal article vol. 8, no. 1, p. 81, February 15 2013, doi: 10.1186/1556-276x-8-81.

[93] W. Yang, X. Li, D. Chi, H. Zhang, and X. Liu, "Lanthanide-doped upconversion materials: emerging applications for photovoltaics and photocatalysis," *Nanotechnology,* vol. 25, no. 48, p. 482001, 2014/11/14 2014, doi: 10.1088/0957-4484/25/48/482001.

[94] H. Rodríguez-Rodríguez, M. H. Imanieh, F. Lahoz, and I. R. Martín, "Analysis of the upconversion process in Tm3+ doped glasses for enhancement of the photocurrent in silicon solar cells," *Solar Energy Materials and Solar Cells,* vol. 144, pp. 29-32, 2016/01/01/ 2016, doi: https://doi.org/10.1016/j.solmat.2015.08.017.

[95] F. Lahoz, C. Pérez-Rodríguez, S. E. Hernández, I. R. Martín, V. Lavín, and U. R. Rodríguez-Mendoza, "Upconversion mechanisms in rare-earth doped glasses to improve the efficiency of silicon solar cells," *Solar Energy Materials and Solar Cells,* vol. 95, no. 7, pp. 1671-1677, 2011/07/01/ 2011, doi: https://doi.org/10.1016/j.solmat.2011.01.027.

[96] D. L. Dexter, "Possibility of Luminescent Quantum Yields Greater than Unity," *Physical Review,* vol. 108, no. 3, pp. 630-633, 11/01/ 1957, doi: 10.1103/PhysRev.108.630.

[97] R. T. Wegh, H. Donker, K. D. Oskam, and A. Meijerink, "Visible Quantum Cutting in LiGdF₄:Eu³⁺ Through Downconversion," *Science,* vol. 283, no. 5402, p. 663, 1999, doi: 10.1126/science.283.5402.663.

[98] M. B. de la Mora, O. Amelines-Sarria, B. M. Monroy, C. D. Hernández-Pérez, and J. E. Lugo, "Materials for downconversion in solar cells: Perspectives and challenges," *Solar Energy Materials and Solar Cells,* vol. 165, pp. 59-71, 2017/06/01/ 2017, doi: https://doi.org/10.1016/j.solmat.2017.02.016.

[99] Y. Tai, G. Zheng, H. Wang, and J. Bai, "Broadband down-conversion based near infrared quantum cutting in Eu2+–Yb3+ co-doped SrAl2O4 for crystalline silicon solar cells," *Journal of Solid State Chemistry,* vol. 226, pp. 250-254, 2015/03/01/ 2015, doi: https://doi.org/10.1016/j.jssc.2015.02.020.

[100] T. S. Atabaev, Y.-H. Hwang, and H. K. Kim, "Color-tunable properties of Eu- and Dy-codoped Y2O3 phosphor particles," *Nanoscale Research Letters*, vol. 7, no. 1, pp. 556, 2012, doi: 10.1186/1556-276X-7-556

[101] J. Zhou *et al.*, "Intense infrared emission of Er^{3+} in $Ca_8Mg(SiO_4)_4Cl_2$ phosphor from energy transfer of Eu^{2+} by broadband down-conversion." *Optics Express,* vol. 18, no. 21, pp. 21663-21668, 2010, doi: https://doi.org/10.1364/OE.18.021663

[102] M. J. Keevers and M. A. Green, "Efficiency improvements of silicon solar cells by the impurity photovoltaic effect," *Journal of Applied Physics,* vol. 75, no. 8, pp. 4022-4031, 1994, doi: 10.1063/1.356025.

[103] P. Gibart, F. Auzel, J.-C. Guillaume, and K. Zahraman, "Below Band-Gap IR Response of Substrate-Free GaAs Solar Cells Using Two-Photon Up-

Conversion," *Japanese Journal of Applied Physics,* vol. 35, no. Part 1, No. 8, pp. 4401-4402, 1996/08/15 1996, doi: 10.1143/jjap.35.4401.
[104] B. S. Richards, "Enhancing the performance of silicon solar cells via the application of passive luminescence conversion layers," *Solar Energy Materials and Solar Cells,* vol. 90, no. 15, pp. 2329-2337, 2006/09/22/ 2006, doi: https://doi.org/10.1016/j.solmat.2006.03.035.
[105] H. J. Hovel, R. T. Hodgson, and J. M. Woodall, "The effect of fluorescent wavelength shifting on solar cell spectral response," *Solar Energy Materials,* vol. 2, no. 1, pp. 19-29, 1979/09/01/ 1979, doi: https://doi.org/10.1016/0165-1633(79)90027-3.
[106] W. H. Weber and J. Lambe, "Luminescent greenhouse collector for solar radiation," *Appl. Opt.,* vol. 15, no. 10, pp. 2299-2300, 1976/10/01 1976, doi: 10.1364/AO.15.002299.
[107] B. Ahrens *et al.*, "Neodymium-doped fluorochlorozirconate glasses as an upconversion model system for high efficiency solar cells," *physica status solidi (a),* vol. 205, no. 12, pp. 2822-2830, 2008, doi: 10.1002/pssa.200880452.
[108] S. Fischer *et al.*, "Enhancement of silicon solar cell efficiency by upconversion: Optical and electrical characterization," *Journal of Applied Physics,* vol. 108, no. 4, p. 044912, 2010, doi: 10.1063/1.3478742.
[109] B. R. Judd, "Optical Absorption Intensities of Rare-Earth Ions," *Physical Review,* vol. 127, no. 3, pp. 750-761, 1962.
[110] C. B. Layne, W. H. Lowdermilk, and M. J. Weber, "Multiphonon relaxation of rare-earth ions in oxide glasses," *Physical Review B,* vol. 16, no. 1, pp. 10-20, 07/01/ 1977, doi: 10.1103/PhysRevB.16.10.
[111] F. S. Ermeneux *et al.*, "Multiphonon relaxation in ${\mathrm{YVO}}_{4}$ single crystals," *Physical Review B,* vol. 61, no. 6, pp. 3915-3921, 02/01/ 2000, doi: 10.1103/PhysRevB.61.3915.
[112] S. Wang and H. Zhang, "Foundations of Up-conversion Nanoparticles," in *Phosphors, Up Conversion Nano Particles, Quantum Dots and Their Applications: Volume 2*, R.-S. Liu Ed. Singapore: Springer Singapore, 2016, pp. 215-236.
[113] J.-G. Li, X. Wang, W. Liu, Q. Zhu, X. Li, and X. Sun, "(La0.97RE0.01Yb0.02)2O2S Nanophosphors Converted from Layered Hydroxyl Sulfate and Investigation of Upconversion Photoluminescence (RE=Ho, Er)," *Nanoscale Research Letters,* journal article vol. 12, no. 1, p. 508, August 24 2017, doi: 10.1186/s11671-017-2277-4.
[114] J. F. Suyver, J. Grimm, M. K. van Veen, D. Biner, K. W. Krämer, and H. U. Güdel, "Upconversion spectroscopy and properties of NaYF4 doped with Er3+, Tm3+ and/or Yb3+," *Journal of Luminescence,* vol. 117, no. 1, pp. 1-12, 2006/03/01/ 2006, doi: https://doi.org/10.1016/j.jlumin.2005.03.011.
[115] K. W. Krämer, D. Biner, G. Frei, H. U. Güdel, M. P. Hehlen, and S. R. Lüthi, "Hexagonal Sodium Yttrium Fluoride Based Green and Blue Emitting Upconversion Phosphors," *Chemistry of Materials,* vol. 16, no. 7, pp. 1244-1251, 2004/04/01 2004, doi: 10.1021/cm031124o.
[116] S. K. W. MacDougall, A. Ivaturi, J. Marques-Hueso, K. W. Krämer, and B. S. Richards, "Ultra-high photoluminescent quantum yield of β-NaYF4: 10% Er3+ via broadband excitation of upconversion for photovoltaic devices," *Opt. Express,* vol. 20, no. S6, pp. A879-A887, 2012/11/05 2012, doi: 10.1364/OE.20.00A879.
[117] S. Ivanova and F. Pellé, "Strong 1.53 μm to NIR-VIS-UV upconversion in Er-doped fluoride glass for high-efficiency solar cells," *J. Opt. Soc. Am. B,* vol. 26, no. 10, pp. 1930-1938, 2009/10/01 2009, doi: 10.1364/JOSAB.26.001930.
[118] S. Fischer, E. Favilla, M. Tonelli, and J. C. Goldschmidt, "Record efficient upconverter solar cell devices with optimized bifacial silicon solar cells and monocrystalline BaY2F8:30% Er3+ upconverter," *Solar Energy Materials and Solar Cells,* vol. 136, pp. 127-134, 2015/05/01/ 2015, doi: https://doi.org/10.1016/j.solmat.2014.12.023.

[119] R. Martín-Rodríguez *et al.*, "Highly Efficient IR to NIR Upconversion in Gd2O2S: Er3+ for Photovoltaic Applications," *Chemistry of Materials,* vol. 25, no. 9, pp. 1912-1921, 2013/05/14 2013, doi: 10.1021/cm4005745.
[120] K. K. Markose, R. Anjana, A. Antony, and M. K. Jayaraj, "Synthesis of Yb3+/Er3+ co-doped Y2O3, YOF and YF3 UC phosphors and their application in solar cell for sub-bandgap photon harvesting," *Journal of Luminescence,* vol. 204, pp. 448-456, 2018/12/01/ 2018, doi: https://doi.org/10.1016/j.jlumin.2018.08.005.
[121] C. Wei *et al.*, "Quantum Yields over 80% Achieved in Luminescent Europium Complexes by Employing Diphenylphosphoryl Tridentate Ligands," *Inorganic Chemistry,* vol. 57, no. 13, pp. 7512-7515, 2018/07/02 2018, doi: 10.1021/acs.inorgchem.8b01028.
[122] H. Ahmed, S. J. McCormack, and J. Doran, "External Quantum Efficiency Improvement with Luminescent Downshifting Layers: Experimental and Modelling," *International Journal of Spectroscopy,* vol. Volume 2016, p. Article ID 8543475, 2016.
[123] F. Vetrone, R. Naccache, V. Mahalingam, C. G. Morgan, and J. A. Capobianco, "The Active-Core/Active-Shell Approach: A Strategy to Enhance the Upconversion Luminescence in Lanthanide-Doped Nanoparticles," *Advanced Functional Materials,* vol. 19, no. 18, pp. 2924-2929, 2009, doi: 10.1002/adfm.200900234.
[124] A. Ivaturi *et al.*, "Optimizing infrared to near infrared upconversion quantum yield of β-NaYF4:Er3+ in fluoropolymer matrix for photovoltaic devices," *Journal of Applied Physics,* vol. 114, no. 1, p. 013505, 2013, doi: 10.1063/1.4812578.
[125] V. K. Tikhomirov *et al.*, "Optimizing Er/Yb ratio and content in Er–Yb co-doped glass-ceramics for enhancement of the up- and down-conversion luminescence," *Solar Energy Materials and Solar Cells,* vol. 100, pp. 209-215, 2012/05/01/ 2012, doi: https://doi.org/10.1016/j.solmat.2012.01.019.
[126] S. Y. Kim, Y.-H. Won, and H. S. Jang, "A Strategy to enhance Eu3+ emission from LiYF4:Eu nanophosphors and green-to-orange multicolor tunable, transparent nanophosphor-polymer composites," *Scientific Reports,* Article vol. 5, p. 7866, 01/19/online 2015, doi: 10.1038/srep07866

https://www.nature.com/articles/srep07866#supplementary-information.
[127] S. Fischer, B. Fröhlich, K. W. Krämer, and J. C. Goldschmidt, "Relation between Excitation Power Density and Er3+ Doping Yielding the Highest Absolute Upconversion Quantum Yield," *The Journal of Physical Chemistry C,* vol. 118, no. 51, pp. 30106-30114, 2014/12/26 2014, doi: 10.1021/jp510209x.
[128] S. F. Lim, W. S. Ryu, and R. H. Austin, "Particle size dependence of the dynamic photophysical properties of NaYF4:Yb, Er nanocrystals," *Opt. Express,* vol. 18, no. 3, pp. 2309-2316, 2010/02/01 2010, doi: 10.1364/OE.18.002309.
[129] D. Li, Q. Shao, Y. Dong, and J. Jiang, "Phase-, shape- and size-controlled synthesis of NaYF4:Yb3+,Er3+ nanoparticles using rare-earth acetate precursors," *Journal of Rare Earths,* vol. 32, no. 11, pp. 1032-1036, 2014/11/01/ 2014, doi: https://doi.org/10.1016/S1002-0721(14)60179-4.
[130] Y. Noh, M. Choi, K. Kim, and O. Song, "Properties of Working Electrodes with Nano YBO3:Eu3+ Phosphor in a Dye Sensitized Solar Cell," *J. Korean Ceram. Soc,* vol. 53, no. 2, pp. 253-257, 3 2016, doi: 10.4191/kcers.2016.53.2.253.
[131] X. Chen *et al.*, "Size-dependent downconversion near-infrared emission of NaYF4:Yb3+,Er3+ nanoparticles," *Journal of Materials Chemistry C,* 10.1039/C7TC00267J vol. 5, no. 9, pp. 2451-2458, 2017, doi: 10.1039/C7TC00267J.
[132] D. Ross *et al.*, "The Impact of Luminescent Down Shifting on the Performance of CdTe Photovoltaics: Impact of the Module Vintage," *IEEE Journal of Photovoltaics,* vol. 4, no. 1, pp. 457-464, 2014, doi: 10.1109/JPHOTOV.2013.2282896.
[133] L. Dumont *et al.*, "SiNx:Tb3+–Yb3+, an efficient down-conversion layer compatible with a silicon solar cell process," *Solar Energy Materials and Solar*

Cells, vol. 145, pp. 84-92, 2016/02/01/ 2016, doi: https://doi.org/10.1016/j.solmat.2015.09.031.
[134] A. Boccolini, J. Marques-Hueso, and B. S. Richards, "Self-absorption in upconverter luminescent layers: impact on quantum yield measurements and on designing optimized photovoltaic devices," *Optics Letters,* vol. 39, no. 10, pp. 2904-2907, 2014/05/15 2014, doi: 10.1364/OL.39.002904.
[135] B. Lipovšek *et al.*, "Optical Model for Simulation and Optimization of Luminescent down-shifting Layers in Photovoltaics," *Energy Procedia,* vol. 84, pp. 3-7, 2015/12/01/ 2015, doi: https://doi.org/10.1016/j.egypro.2015.12.288.
[136] S. Fischer, B. Fröhlich, H. Steinkemper, K. W. Krämer, and J. C. Goldschmidt, "Absolute upconversion quantum yield of β-NaYF4 doped with Er3+ and external quantum efficiency of upconverter solar cell devices under broad-band excitation considering spectral mismatch corrections," *Solar Energy Materials and Solar Cells,* vol. 122, pp. 197-207, 2014/03/01/ 2014, doi: https://doi.org/10.1016/j.solmat.2013.12.001.
[137] S. Fischer *et al.*, "Upconversion solar cell measurements under real sunlight," *Optical Materials,* vol. 84, pp. 389-395, 2018/10/01/ 2018, doi: https://doi.org/10.1016/j.optmat.2018.05.072.
[138] Y.-C. Chen and T.-M. Chen, "Improvement of conversion efficiency of silicon solar cells using up-conversion molybdate La2Mo2O9:Yb, R (R=Er, Ho) phosphors," *Journal of Rare Earths,* vol. 29, no. 8, pp. 723-726, 2011/08/01/ 2011, doi: https://doi.org/10.1016/S1002-0721(10)60530-3.
[139] J. de Wild, A. Meijerink, J. K. Rath, W. G. J. H. M. van Sark, and R. E. I. Schropp, "Towards upconversion for amorphous silicon solar cells," *Solar Energy Materials and Solar Cells,* vol. 94, no. 11, pp. 1919-1922, 2010/11/01/ 2010, doi: https://doi.org/10.1016/j.solmat.2010.06.006.
[140] B. Qu *et al.*, "Improved performance of a-Si:H solar cell by using up-conversion phosphors," *Journal of Alloys and Compounds,* vol. 658, pp. 848-853, 2016/02/15/ 2016, doi: https://doi.org/10.1016/j.jallcom.2015.11.024.
[141] Z. Chen *et al.*, "Highly efficient up-conversion luminescence in BaCl2:Er3+phosphors via simultaneous multiwavelength excitation," *Applied Physics Express,* vol. 8, no. 3, p. 032301, 2015/02/05 2015, doi: 10.7567/apex.8.032301.
[142] Z. Chen *et al.*, "BaCl2:Er3+—A High Efficient Upconversion Phosphor for Broadband Near-Infrared Photoresponsive Devices," *Journal of the American Ceramic Society,* vol. 98, no. 8, pp. 2508-2513, 2015, doi: 10.1111/jace.13558.
[143] H. Jia *et al.*, "Upconversion Luminescence from Ln3+(Ho3+,Pr3+) Ion-Doped BaCl2 Particles via NIR Light of Sun Excitation," *The Journal of Physical Chemistry C,* vol. 122, no. 17, pp. 9606-9610, 2018/05/03 2018, doi: 10.1021/acs.jpcc.8b02434.
[144] Z. Chen *et al.*, "Improved Up-Conversion Luminescence from Er3+:LaF3 Nanocrystals Embedded in Oxyfluoride Glass Ceramics via Simultaneous Triwavelength Excitation," *The Journal of Physical Chemistry C,* vol. 119, no. 42, pp. 24056-24061, 2015/10/22 2015, doi: 10.1021/acs.jpcc.5b08103.
[145] J. C. Goldschmidt *et al.*, "Advanced upconverter systems with spectral and geometric concentration for high upconversion efficiencies," in *2008 Conference on Optoelectronic and Microelectronic Materials and Devices*, 28 July-1 Aug. 2008 2008, pp. 307-311, doi: 10.1109/COMMAD.2008.4802153.
[146] S. Fischer *et al.*, "Upconverter silicon solar cell devices for efficient utilization of sub-band-gap photons under concentrated solar radiation," *IEEE Journal of Photovoltaics,* vol. 4, pp. 183-189, 2014.
[147] G. E. Arnaoutakis, J. Marques-Hueso, T. K. Mallick, and B. S. Richards, "Coupling of sunlight into optical fibres and spectral dependence for solar energy applications," *Solar Energy,* vol. 93, pp. 235-243, 2013/07/01/ 2013, doi: https://doi.org/10.1016/j.solener.2013.04.008.

[148] G. E. Arnaoutakis *et al.*, "Enhanced up-conversion for photovoltaics via concentrating integrated optics," *Opt. Express,* vol. 22, no. S2, pp. A452-A464, 2014/03/10 2014, doi: 10.1364/OE.22.00A452.
[149] G. E. Arnaoutakis *et al.*, "Enhanced energy conversion of up-conversion solar cells by the integration of compound parabolic concentrating optics," *Solar Energy Materials and Solar Cells,* vol. 140, pp. 217-223, 2015/09/01/ 2015, doi: https://doi.org/10.1016/j.solmat.2015.04.020.
[150] S. V. Boriskina and G. Chen, "Exceeding the solar cell Shockley–Queisser limit via thermal up-conversion of low-energy photons," *Optics Communications,* vol. 314, pp. 71-78, 2014/03/01/ 2014, doi: https://doi.org/10.1016/j.optcom.2013.10.042.
[151] Z. Chen *et al.*, "Up-conversion luminescence from single vanadate through blackbody radiation harvesting broadband near-infrared photons for photovoltaic cells," *Journal of Alloys and Compounds,* vol. 663, pp. 204-210, 2016/04/05/ 2016, doi: https://doi.org/10.1016/j.jallcom.2015.12.136.
[152] Z.-S. Wang, H. Kawauchi, T. Kashima, and H. Arakawa, *Significant influence of TiO2 photoelectrode morphology on the energy conversion efficiency of N719 dye-sensitized solar cell*. 2004, pp. 1381-1389.
[153] G.-B. Shan and G. P. Demopoulos, "Near-Infrared Sunlight Harvesting in Dye-Sensitized Solar Cells Via the Insertion of an Upconverter-TiO2 Nanocomposite Layer," *Advanced Materials,* vol. 22, no. 39, pp. 4373-4377, 2010, doi: 10.1002/adma.201001816.
[154] G. Xie *et al.*, "Application of upconversion luminescence in dye-sensitized solar cells," *Chinese Science Bulletin,* vol. 56, no. 1, pp. 96-101, 2011/01/01 2011, doi: 10.1007/s11434-010-4115-2.
[155] P. Ramasamy and J. Kim, "Combined plasmonic and upconversion rear reflectors for efficient dye-sensitized solar cells," *Chemical Communications,* 10.1039/C3CC47290F vol. 50, no. 7, pp. 879-881, 2014, doi: 10.1039/C3CC47290F.
[156] G. Han, M. Wang, D. Li, J. Bai, and G. Diao, "Novel upconversion Er, Yb-CeO2 hollow spheres as scattering layer materials for efficient dye-sensitized solar cells," *Solar Energy Materials and Solar Cells,* vol. 160, pp. 54-59, 2017/02/01/ 2017, doi: https://doi.org/10.1016/j.solmat.2016.10.021.
[157] S. Günes, H. Neugebauer, and N. S. Sariciftci, "Conjugated Polymer-Based Organic Solar Cells," *Chemical Reviews,* vol. 107, no. 4, pp. 1324-1338, 2007/04/01 2007, doi: 10.1021/cr050149z.
[158] H.-Q. Wang, T. Stubhan, A. Osvet, I. Litzov, and C. J. Brabec, "Up-conversion semiconducting MoO3:Yb/Er nanocomposites as buffer layer in organic solar cells," *Solar Energy Materials and Solar Cells,* vol. 105, pp. 196-201, 2012/10/01/ 2012, doi: https://doi.org/10.1016/j.solmat.2012.06.005.
[159] A. A. D. Adikaari *et al.*, "Near infrared up-conversion in organic photovoltaic devices using an efficient Yb3+:Ho3+ Co-doped Ln2BaZnO5 (Ln = Y, Gd) phosphor," *Journal of Applied Physics,* vol. 111, no. 9, p. 094502, 2012, doi: 10.1063/1.4704687.
[160] W. Chen *et al.*, "Sub-bandgap photon harvesting for organic solar cells via integrating up-conversion nanophosphors," *Organic Electronics,* vol. 19, pp. 113-119, 2015/04/01/ 2015, doi: https://doi.org/10.1016/j.orgel.2015.01.036.
[161] F. Wang *et al.*, "Enhancing light harvesting and charge transport in organic solar cells via integrating lanthanide-doped upconversation materials," *Journal of Physics D: Applied Physics,* vol. 51, no. 26, p. 265105, 2018/06/11 2018, doi: 10.1088/1361-6463/aac568.
[162] J. Zhao, S. Ji, and H. Guo, "Triplet–triplet annihilation based upconversion: from triplet sensitizers and triplet acceptors to upconversion quantum yields," *RSC Advances,* 10.1039/C1RA00469G vol. 1, no. 6, pp. 937-950, 2011, doi: 10.1039/C1RA00469G.
[163] T. F. Schulze *et al.*, "Efficiency Enhancement of Organic and Thin-Film Silicon Solar Cells with Photochemical Upconversion," *The Journal of Physical*

Chemistry C, vol. 116, no. 43, pp. 22794-22801, 2012/11/01 2012, doi: 10.1021/jp309636m.

[164] I. Robel, V. Subramanian, M. Kuno, and P. V. Kamat, "Quantum Dot Solar Cells. Harvesting Light Energy with CdSe Nanocrystals Molecularly Linked to Mesoscopic TiO2 Films," *Journal of the American Chemical Society,* vol. 128, no. 7, pp. 2385-2393, 2006/02/01 2006, doi: 10.1021/ja056494n.

[165] K. Wang, J. Jiang, S. Wan, and J. Zhai, "Upconversion enhancement of lanthanide-doped NaYF4 for quantum dot-sensitized solar cells," *Electrochimica Acta,* vol. 155, pp. 357-363, 2015/02/10/ 2015, doi: https://doi.org/10.1016/j.electacta.2014.11.131.

[166] D. Ramachari *et al.*, "Synthesis of co-doped Yb3+-Er3+:ZrO2 upconversion nanoparticles and their applications in enhanced photovoltaic properties of quantum dot sensitized solar cells," *Journal of Alloys and Compounds,* vol. 698, pp. 433-441, 2017/03/25/ 2017, doi: https://doi.org/10.1016/j.jallcom.2016.12.026.

[167] Y. Sun *et al.*, "Upconverting nanophosphor incorporated photoanodes for improved photoelectric performances of quantum dot sensitized solar cells," *Materials Research Letters,* vol. 6, no. 6, pp. 314-320, 2018/06/03 2018, doi: 10.1080/21663831.2018.1447521.

[168] A. Mei *et al.*, "A hole-conductor–free, fully printable mesoscopic perovskite solar cell with high stability," *Science,* vol. 345, no. 6194, p. 295, 2014, doi: 10.1126/science.1254763.

[169] PV Magazine. "Oxford PV raises $41m to commercialize perovskite tech." https://www.pv-magazine.com/2019/03/20/oxford-pv-raises-41m-to-commercialize-perovskite-tech/ (accessed 10 Apr 2019).

[170] X. Chen *et al.*, "Highly Efficient LiYF4:Yb3+, Er3+ Upconversion Single Crystal under Solar Cell Spectrum Excitation and Photovoltaic Application," *ACS Applied Materials & Interfaces,* vol. 8, no. 14, pp. 9071-9079, 2016/04/13 2016, doi: 10.1021/acsami.5b12528.

[171] M. He *et al.*, "Monodisperse Dual-Functional Upconversion Nanoparticles Enabled Near-Infrared Organolead Halide Perovskite Solar Cells," *Angewandte Chemie International Edition,* vol. 55, no. 13, pp. 4280-4284, 2016, doi: 10.1002/anie.201600702.

[172] J. Roh, H. Yu, and J. Jang, "Hexagonal β-NaYF4:Yb3+, Er3+ Nanoprism-Incorporated Upconverting Layer in Perovskite Solar Cells for Near-Infrared Sunlight Harvesting," *ACS Applied Materials & Interfaces,* vol. 8, no. 31, pp. 19847-19852, 2016/08/10 2016, doi: 10.1021/acsami.6b04760.

[173] X. Wang *et al.*, "Enhanced Photovoltaic Performance of Perovskite Solar Cells Based on Er-Yb Co-doped TiO2 Nanorod Arrays," *Electrochimica Acta,* vol. 245, pp. 839-845, 2017/08/10/ 2017, doi: https://doi.org/10.1016/j.electacta.2017.06.032.

[174] G. Gao and L. Wondraczek, "Near-infrared down-conversion in Mn2+–Yb3+ co-doped Zn2GeO4," *Journal of Materials Chemistry C,* 10.1039/C3TC00803G vol. 1, no. 10, pp. 1952-1958, 2013, doi: 10.1039/C3TC00803G.

[175] S. González-Pérez *et al.*, "Luminescent polymeric film containing an Eu(III) complex acting as UV protector and down-converter for Si-based solar cells and modules," *Surface and Coatings Technology,* vol. 271, pp. 106-111, 2015/06/15/ 2015, doi: https://doi.org/10.1016/j.surfcoat.2014.12.074.

[176] L. d. A. Florêncio, L. A. Gómez-Malagón, B. C. Lima, A. S. L. Gomes, J. A. M. Garcia, and L. R. P. Kassab, "Efficiency enhancement in solar cells using photon down-conversion in Tb/Yb-doped tellurite glass," *Solar Energy Materials and Solar Cells,* vol. 157, pp. 468-475, 2016/12/01/ 2016, doi: https://doi.org/10.1016/j.solmat.2016.07.024.

[177] L. Li, C. Lou, H. Cao, H. Diao, and S. K. Karunakaran, "Enhancing concentrator monocrystalline Si solar cells by down conversion Ce3+-Yb3+ co-doped YAG phosphors," *Applied Physics Letters,* vol. 113, no. 10, p. 101905, 2018, doi: 10.1063/1.5043221.

[178] N. Yao *et al.*, "Efficiency enhancement in dye-sensitized solar cells with down conversion material ZnO: Eu3+, Dy3+," *Journal of Power Sources,* vol. 267, pp. 405-410, 2014/12/01/ 2014, doi: https://doi.org/10.1016/j.jpowsour.2014.05.135.
[179] H. Sun, L. Pan, G. Zhu, X. Piao, L. Zhang, and Z. Sun, "Long afterglow Sr4Al14O25:Eu,Dy phosphors as both scattering and down converting layer for CdS quantum dot-sensitized solar cells," *Dalton Transactions,* 10.1039/C4DT01276C vol. 43, no. 40, pp. 14936-14941, 2014, doi: 10.1039/C4DT01276C.
[180] X. Hou, T. Xuan, H. Sun, X. Chen, H. Li, and L. Pan, "High-performance perovskite solar cells by incorporating a ZnGa2O4:Eu3+ nanophosphor in the mesoporous TiO2 layer," *Solar Energy Materials and Solar Cells,* vol. 149, pp. 121-127, 2016/05/01/ 2016, doi: https://doi.org/10.1016/j.solmat.2016.01.021.
[181] J. Jia, J. Dong, J. Lin, Z. Lan, L. Fan, and J. Wu, "Improved photovoltaic performance of perovskite solar cells by utilizing down-conversion NaYF4:Eu3+ nanophosphors," *Journal of Materials Chemistry C,* 10.1039/C8TC05864D vol. 7, no. 4, pp. 937-942, 2019, doi: 10.1039/C8TC05864D.
[182] R. Rothemund, "Optical modelling of the external quantum efficiency of solar cells with luminescent down-shifting layers," *Solar Energy Materials and Solar Cells,* vol. 120, pp. 616-621, 2014/01/01/ 2014, doi: https://doi.org/10.1016/j.solmat.2013.10.004.
[183] W.-B. Hung and T.-M. Chen, "Efficiency enhancement of silicon solar cells through a downshifting and antireflective oxysulfide phosphor layer," *Solar Energy Materials and Solar Cells,* vol. 133, pp. 39-47, 2015/02/01/ 2015, doi: https://doi.org/10.1016/j.solmat.2014.11.011.
[184] W.-J. Ho, Y.-T. Shen, Y.-J. Deng, C.-W. Yeh, and R.-S. Sue, "Performance enhancement of planar silicon solar cells through utilization of two luminescent down-shifting Eu-doped phosphor species," *Thin Solid Films,* vol. 618, pp. 141-145, 2016/11/01/ 2016, doi: https://doi.org/10.1016/j.tsf.2016.03.063.
[185] O. Maalej, J. Merigeon, B. Boulard, and M. Girtan, "Visible to near-infrared down-shifting in Tm3+ doped fluoride glasses for solar cells efficiency enhancement," *Optical Materials,* vol. 60, pp. 235-239, 2016/10/01/ 2016, doi: https://doi.org/10.1016/j.optmat.2016.07.047.
[186] T. Uekert *et al.*, "Nanostructured organosilicon luminophores in highly efficient luminescent down-shifting layers for thin film photovoltaics," *Solar Energy Materials and Solar Cells,* vol. 155, pp. 1-8, 2016/10/01/ 2016, doi: https://doi.org/10.1016/j.solmat.2016.04.019.
[187] S. D. Hodgson, W. S. M. Brooks, A. J. Clayton, G. Kartopu, V. Barrioz, and S. J. C. Irvine, "The impact of quantum dot concentration on the optical properties of QD/PMMA luminescent down-shifting films applied to CdTe photovoltaic devices," *Nano Energy,* vol. 4, pp. 1-6, 2014/03/01/ 2014, doi: https://doi.org/10.1016/j.nanoen.2013.12.004.
[188] P. Song, C. Zhang, and P. Zhu, "Eu3+-Mn2+-doped bi-functional glasses with solar photon downshifting: Application to CdS/CdTe solar cells," *Journal of Alloys and Compounds,* vol. 661, pp. 14-19, 2016/03/15/ 2016, doi: https://doi.org/10.1016/j.jallcom.2015.11.168.
[189] P. P. C. Verbunt and M. Debije, *Progress in Luminescent Solar Concentrator Research: Solar Energy for the Built Environment*. 2011.
[190] C. Wang, H. Abdul-Rahman, and S. P. Rao, "A new design of luminescent solar concentrator and its trial run," *International Journal of Energy Research,* vol. 34, no. 15, pp. 1372-1385, 2010, doi: 10.1002/er.1681.
[191] M. D. Hughes, D.-A. Borca-Tasciuc, and D. A. Kaminski, "Highly efficient luminescent solar concentrators employing commercially available luminescent phosphors," *Solar Energy Materials and Solar Cells,* vol. 171, pp. 293-301, 2017/11/01/ 2017, doi: https://doi.org/10.1016/j.solmat.2017.06.018.
[192] C. Tummeltshammer, A. Taylor, A. J. Kenyon, and I. Papakonstantinou, "Losses in luminescent solar concentrators unveiled," *Solar Energy Materials and Solar*

Cells, vol. 144, pp. 40-47, 2016/01/01/ 2016, doi: https://doi.org/10.1016/j.solmat.2015.08.008.

[193] W. G. J. H. M. v. Sark, Z. Krumer, C. D. M. Donegá, and R. E. I. Schropp, "Luminescent Solar Concentrators: The route to 10% efficiency," in *2014 IEEE 40th Photovoltaic Specialist Conference (PVSC)*, 8-13 June 2014 2014, pp. 2276-2279, doi: 10.1109/PVSC.2014.6925380.

[194] B. S. Richard and A. Shalav, "The role of polymers in the luminescence conversion of sunlight for enhanced solar cell performance," *Synthetic Metals,* vol. 154, no. 1, pp. 61-64, 2005/09/22/ 2005, doi: https://doi.org/10.1016/j.synthmet.2005.07.021.

[195] J. Zhang *et al.*, "Optimization of large-size glass laminated luminescent solar concentrators," *Solar Energy,* vol. 117, pp. 260-267, 2015/07/01/ 2015, doi: https://doi.org/10.1016/j.solener.2015.05.004.

[196] M. Zettl, O. Mayer, E. Klampaftis, and B. S. Richards, "Investigation of Host Polymers for Luminescent Solar Concentrators," *Energy Technology,* vol. 5, no. 7, pp. 1037-1044, 2017, doi: 10.1002/ente.201600498.

[197] F. I. Chowdhury, C. Dick, L. Meng, S. M. Mahpeykar, B. Ahvazi, and X. Wang, "Cellulose nanocrystals as host matrix and waveguide materials for recyclable luminescent solar concentrators," *RSC Advances,* 10.1039/C7RA04344A vol. 7, no. 51, pp. 32436-32441, 2017, doi: 10.1039/C7RA04344A.

[198] C.-H. Chou, M.-H. Hsu, and F.-C. Chen, "Flexible luminescent waveguiding photovoltaics exhibiting strong scattering effects from the dye aggregation," *Nano Energy,* vol. 15, pp. 729-736, 2015/07/01/ 2015, doi: https://doi.org/10.1016/j.nanoen.2015.06.001.

[199] A. Jones, O. Moudam, N. Robertson, B. Rowan, L. Wilson, and B. Richards, *Visible and Near-InfraRed Emitting Lanthanide Complexes for Luminescent Solar Concentrators*. 2009.

[200] F. Meinardi *et al.*, "Highly efficient luminescent solar concentrators based on earth-abundant indirect-bandgap silicon quantum dots," *Nature Photonics,* Article vol. 11, p. 177, 02/20/online 2017, doi: 10.1038/nphoton.2017.5

https://www.nature.com/articles/nphoton.2017.5#supplementary-information.

[201] Y. Zhou *et al.*, "Colloidal carbon dots based highly stable luminescent solar concentrators," *Nano Energy,* vol. 44, pp. 378-387, 2018/02/01/ 2018, doi: https://doi.org/10.1016/j.nanoen.2017.12.017.

[202] J. Roncali and F. Garnier, "Photon-transport properties of luminescent solar concentrators: analysis and optimization," *Appl. Opt.,* vol. 23, no. 16, pp. 2809-2817, 1984/08/15 1984, doi: 10.1364/AO.23.002809.

[203] M. Kennedy *et al.*, "Luminescent Solar Concentrators: A Comparison of Thermodynamic Modelling and Ray-Trace Modelling Predictions," in *23rd European Photovoltaic Solar Energy Conference and Exhibition*, Valencia, Spain, 1-5 September 2008, pp. 334-337.

[204] M. K. Assadi *et al.*, "Enhancing the efficiency of luminescent solar concentrators (LSCs)," *Applied Physics A,* journal article vol. 122, no. 9, p. 821, August 12 2016, doi: 10.1007/s00339-016-0359-2.

[205] K. Wu, H. Li, and V. I. Klimov, "Tandem luminescent solar concentrators based on engineered quantum dots," *Nature Photonics,* vol. 12, no. 2, pp. 105-110, 2018/02/01 2018, doi: 10.1038/s41566-017-0070-7.

[206] T. Dienel, C. Bauer, I. Dolamic, and D. Brühwiler, "Spectral-based analysis of thin film luminescent solar concentrators," *Solar Energy,* vol. 84, no. 8, pp. 1366-1369, 2010/08/01/ 2010, doi: https://doi.org/10.1016/j.solener.2010.04.015.

[207] S. Chandra, S. J. McCormack, M. Kennedy, and J. Doran, "Quantum dot solar concentrator: Optical transportation and doping concentration optimization," *Solar Energy,* vol. 115, pp. 552-561, 2015/05/01/ 2015, doi: https://doi.org/10.1016/j.solener.2015.01.048.

[208] J. Videira, E. Bilotti, and A. J. Chatten, *Cylindrical array luminescent solar concentrators: Performance boosts by geometric effects*. 2016, p. A1188.

[209] E.-H. Banaei and A. F. Abouraddy, "Design of a polymer optical fiber luminescent solar concentrator," *Progress in Photovoltaics: Research and Applications,* vol. 23, no. 4, pp. 403-416, 2015, doi: 10.1002/pip.2435.
[210] M. Gajic, F. Lisi, N. Kirkwood, T. A. Smith, P. Mulvaney, and G. Rosengarten, "Circular luminescent solar concentrators," *Solar Energy,* vol. 150, pp. 30-37, 2017/07/01/ 2017, doi: https://doi.org/10.1016/j.solener.2017.04.034.
[211] M. D. Hughes, C. Maher, D.-A. Borca-Tasciuc, D. Polanco, and D. Kaminski, "Performance comparison of wedge-shaped and planar luminescent solar concentrators," *Renewable Energy,* vol. 52, pp. 266-272, 2013/04/01/ 2013, doi: https://doi.org/10.1016/j.renene.2012.10.034.
[212] K. R. McIntosh, N. Yamada, and B. S. Richards, "Theoretical comparison of cylindrical and square-planar luminescent solar concentrators," *Applied Physics B,* journal article vol. 88, no. 2, pp. 285-290, July 01 2007, doi: 10.1007/s00340-007-2705-8.
[213] R. Bose, "Raytrace simulations and experimental studies of luminescent solar concentrators," PhD Physics, Imperial College London, London, UK, 2014.
[214] X. Sheng *et al.*, "Doubling the Power Output of Bifacial Thin-Film GaAs Solar Cells by Embedding Them in Luminescent Waveguides," *Advanced Energy Materials,* vol. 3, no. 8, pp. 991-996, 2013, doi: 10.1002/aenm.201201064.
[215] J. C. Goldschmidt *et al.*, "Increasing the efficiency of fluorescent concentrator systems," *Solar Energy Materials and Solar Cells,* vol. 93, no. 2, pp. 176-182, 2009/02/01/ 2009, doi: https://doi.org/10.1016/j.solmat.2008.09.048.
[216] M. Peng *et al.*, "Integration of fiber dye-sensitized solar cells with luminescent solar concentrators for high power output," *Journal of Materials Chemistry A,* 10.1039/C3TA14284A vol. 2, no. 4, pp. 926-932, 2014, doi: 10.1039/C3TA14284A.
[217] T. S. Parel, L. Danos, and T. Markvart, "Application of concentrating luminescent down-shifting structures to CdS/CdTe solar cells with poor short wavelength response," *Solar Energy Materials and Solar Cells,* vol. 140, pp. 306-311, 2015/09/01/ 2015, doi: https://doi.org/10.1016/j.solmat.2015.04.026.
[218] L. J. Brennan, F. Purcell-Milton, B. McKenna, Trystan M. Watson, Y. K. Gun'ko, and R. C. Evans, "Large area quantum dot luminescent solar concentrators for use with dye-sensitised solar cells," *Journal of Materials Chemistry A,* 10.1039/C7TA04731B vol. 6, no. 6, pp. 2671-2680, 2018, doi: 10.1039/C7TA04731B.
[219] L. H. Slooff *et al.*, "A luminescent solar concentrator with 7.1% power conversion efficiency," *physica status solidi (RRL) – Rapid Research Letters,* vol. 2, no. 6, pp. 257-259, 2008, doi: 10.1002/pssr.200802186.
[220] Y. Zhang *et al.*, "Polymethylmethacrylate-based luminescent solar concentrators with bottom-mounted solar cells," *Energy Conversion and Management,* vol. 95, pp. 187-192, 2015/05/01/ 2015, doi: https://doi.org/10.1016/j.enconman.2015.02.043.
[221] B. D. Markman, R. R. Ranade, and N. C. Giebink, "Nonimaging optics in luminescent solar concentration," *Opt. Express,* vol. 20, no. S5, pp. A622-A629, 2012/09/10 2012, doi: 10.1364/OE.20.00A622.
[222] n-techResearch, "BIPV Technologies and Markets 2017-2024," 2017. [Online]. Available: https://www.ntechresearch.com/market-reports/building-integrated-photovoltaics-reports-2017-2024/.
[223] Polysolar, "Building Integrated Transparent Photovoltaic Glass," 2018. [Online]. Available: http://www.polysolar.co.uk/.
[224] Buildsolar, "Solar Squared - a clean energy solution for buildings," 2018. [Online]. Available: https://www.buildsolar.co.uk/.
[225] Philips, "Luminescent Solar Concentrator," 2015. [Online]. Available: http://www.lighting.philips.com/main/ip/licensing/luminescent-solar-concentrator.
[226] M. Kanellis, M. M. de Jong, L. Slooff, and M. G. Debije, "The solar noise barrier project: 1. Effect of incident light orientation on the performance of a large-scale

luminescent solar concentrator noise barrier," *Renewable Energy,* vol. 103, pp. 647-652, 2017/04/01/ 2017, doi: https://doi.org/10.1016/j.renene.2016.10.078.
[227] F. Meinardi, F. Bruni, and S. Brovelli, *Luminescent solar concentrators for building-integrated photovoltaics*. 2017, p. 17072.
[228] E. P. J. Merkx, O. M. ten Kate, and E. van der Kolk, "Rapid optimization of large-scale luminescent solar concentrators: evaluation for adoption in the built environment," *Opt. Express,* vol. 25, no. 12, pp. A547-A563, 2017/06/12 2017, doi: 10.1364/OE.25.00A547.
[229] S. Tsoi, "Structured luminescent solar energy concentrators : a new route towards inexpensive photovoltaic energy," PhD, Chemical Engineering and Chemistry, Technische Universiteit Eindhoven, Eidhoven, Netherlands, 2012.
[230] A. Kerrouche, D. A. Hardy, D. Ross, and B. S. Richards, "Luminescent solar concentrators: From experimental validation of 3D ray-tracing simulations to coloured stained-glass windows for BIPV," *Solar Energy Materials and Solar Cells,* vol. 122, pp. 99-106, 2014/03/01/ 2014, doi: https://doi.org/10.1016/j.solmat.2013.11.026.
[231] W. van Sark *et al.*, "The “Electric Mondrian” as a Luminescent Solar Concentrator Demonstrator Case Study," *Solar RRL,* vol. 1, no. 3-4, p. 1600015, 2017, doi: 10.1002/solr.201600015.
[232] F. M. Vossen, M. P. J. Aarts, and M. G. Debije, "Visual performance of red luminescent solar concentrating windows in an office environment," *Energy and Buildings,* vol. 113, pp. 123-132, 2016/02/01/ 2016, doi: https://doi.org/10.1016/j.enbuild.2015.12.022.
[233] F. Meinardi *et al.*, "Highly efficient large-area colourless luminescent solar concentrators using heavy-metal-free colloidal quantum dots," *Nature Nanotechnology,* Article vol. 10, p. 878, 08/24/online 2015, doi: 10.1038/nnano.2015.178

https://www.nature.com/articles/nnano.2015.178#supplementary-information.
[234] C. Yang and R. R. Lunt, "Limits of Visibly Transparent Luminescent Solar Concentrators," *Advanced Optical Materials,* vol. 5, no. 8, p. 1600851, 2017, doi: 10.1002/adom.201600851.
[235] K. Kapsis, "Modelling, Design and Experimental Study of Semi-Transparent Photovoltaic Windows for Commercial Building Applications," PhD Thesis, Engineering and Computer Science, Concordia University, Montréal, Canada, 2016.
[236] N. Aste *et al.*, "Design and performance monitoring of a LSC smart window," in *2017 6th International Conference on Clean Electrical Power (ICCEP)*, 27-29 June 2017 2017, pp. 179-183, doi: 10.1109/ICCEP.2017.8004812.
[237] A. Reinders, M. G. Debije, and A. Rosemann, "Measured Efficiency of a Luminescent Solar Concentrator PV Module Called Leaf Roof," *IEEE Journal of Photovoltaics,* vol. 7, no. 6, pp. 1663-1666, 2017, doi: 10.1109/JPHOTOV.2017.2751513.
[238] C. Corrado *et al.*, "Power generation study of luminescent solar concentrator greenhouse," *Journal of Renewable and Sustainable Energy,* vol. 8, no. 4, p. 043502, 2016, doi: 10.1063/1.4958735.
[239] B. Vishwanathan *et al.*, "A comparison of performance of flat and bent photovoltaic luminescent solar concentrators," *Solar Energy,* vol. 112, pp. 120-127, 2015/02/01/ 2015, doi: https://doi.org/10.1016/j.solener.2014.12.001.
[240] A. C. Pan, C. del Cañizo, E. Cánovas, N. M. Santos, J. P. Leitão, and A. Luque, "Enhancement of up-conversion efficiency by combining rare earth-doped phosphors with PbS quantum dots," *Solar Energy Materials and Solar Cells,* vol. 94, no. 11, pp. 1923-1926, 2010/11/01/ 2010, doi: https://doi.org/10.1016/j.solmat.2010.06.028.
[241] A. C. Pan, I. Zanesco, and A. Moehlecke, "Industrial Bifacial Silicon Solar Cells with Up-converter and PbS Quantum Dots," *Energy Procedia,* vol. 44, pp. 160-166, 2014/01/01/ 2014, doi: https://doi.org/10.1016/j.egypro.2013.12.023.

[242] J. D. Joannopoulos, S. G. Johnson, J. N. Winn, and R. D. Meade, *Photonic Crystals: Molding the Flow of Light*, 2nd Edition ed. Princeton, USA: Princeton University Press, 2008.
[243] J. Marques-Hueso, R. Peretti, R. Abargues, B. S. Richards, C. Seassal, and J. P. Martínez-Pastor, "Photonic Crystal-Driven Spectral Concentration for Upconversion Photovoltaics," *Advanced Optical Materials,* vol. 3, no. 4, pp. 568-574, 2015, doi: 10.1002/adom.201400402.
[244] K. Q. Le and S. John, "Synergistic plasmonic and photonic crystal light-trapping: Architectures for optical up-conversion in thin-film solar cells," *Opt. Express,* vol. 22, no. S1, pp. A1-A12, 2014/01/13 2014, doi: 10.1364/OE.22.0000A1.
[245] W. Zou, C. Visser, J. A. Maduro, M. S. Pshenichnikov, and J. C. Hummelen, "Broadband dye-sensitized upconversion of near-infrared light," *Nature Photonics,* Article vol. 6, p. 560, 07/15/online 2012, doi: 10.1038/nphoton.2012.158

https://www.nature.com/articles/nphoton.2012.158#supplementary-information.
[246] X. Huang, "Broadband dye-sensitized upconversion: A promising new platform for future solar upconverter design," *Journal of Alloys and Compounds,* vol. 690, pp. 356-359, 2017/01/05/ 2017, doi: https://doi.org/10.1016/j.jallcom.2016.08.142.
[247] W. Shao *et al.*, "Lanthanide-Doped Fluoride Core/Multishell Nanoparticles for Broadband Upconversion of Infrared Light," *Advanced Optical Materials,* vol. 3, no. 4, pp. 575-582, 2015, doi: 10.1002/adom.201400404.
[248] Y. Zhang, Y. Shi, Z. Qin, M. Song, and W. Qin, "Synthesis of Small Ce3+-Er3+-Yb3+ Tri-Doped BaLuF5 Active-Core-Active-Shell-Active-Shell Nanoparticles with Strong Down Conversion Luminescence at 1.5 μm," *Nanomaterials,* vol. 8, no. 8, p. 615, 2018. [Online]. Available: https://www.mdpi.com/2079-4991/8/8/615.
[249] H. P. Paudel *et al.*, "Enhancement of Near-Infrared-to-Visible Upconversion Luminescence Using Engineered Plasmonic Gold Surfaces," *The Journal of Physical Chemistry C,* vol. 115, no. 39, pp. 19028-19036, 2011/10/06 2011, doi: 10.1021/jp206053f.
[250] A. C. Atre, A. García-Etxarri, H. Alaeian, and J. A. Dionne, "Toward high-efficiency solar upconversion with plasmonic nanostructures," *Journal of Optics,* vol. 14, no. 2, p. 024008, 2012/01/12 2012, doi: 10.1088/2040-8978/14/2/024008.
[251] Y. Liu, Y. Xia, Y. Jiang, M. Zhang, W. Sun, and X.-Z. Zhao, "Coupling effects of Au-decorated core-shell β-NaYF4:Er/Yb@SiO2 microprisms in dye-sensitized solar cells: plasmon resonance versus upconversion," *Electrochimica Acta,* vol. 180, pp. 394-400, 2015/10/20/ 2015, doi: https://doi.org/10.1016/j.electacta.2015.08.144.
[252] M. Luoshan *et al.*, "Surface plasmon resonance enhanced multi-shell-modified upconversion NaYF4:Yb3+, Er3+@SiO2@Au@TiO2 crystallites for dye-sensitized solar cells," *Journal of Power Sources,* vol. 307, pp. 468-473, 2016/03/01/ 2016, doi: https://doi.org/10.1016/j.jpowsour.2016.01.028.
[253] H. Ahmed, J. Doran, and S. J. McCormack, "Increased short-circuit current density and external quantum efficiency of silicon and dye sensitised solar cells through plasmonic luminescent down-shifting layers," *Solar Energy,* vol. 126, pp. 146-155, 2016/03/01/ 2016, doi: https://doi.org/10.1016/j.solener.2016.01.003.
[254] J. A. M. Garcia, L. Bontempo, L. A. Gomez-Malagon, and L. R. P. Kassab, "Efficiency boost in Si-based solar cells using tellurite glass cover layer doped with Eu3+ and silver nanoparticles," *Optical Materials,* vol. 88, pp. 155-160, 2019/02/01/ 2019, doi: https://doi.org/10.1016/j.optmat.2018.11.028.
[255] H. Liu *et al.*, "Scattering enhanced quantum dots based luminescent solar concentrators by silica microparticles," *Solar Energy Materials and Solar Cells,* vol. 179, pp. 380-385, 2018/06/01/ 2018, doi: https://doi.org/10.1016/j.solmat.2018.01.029.

[256] S. M. El-Bashir, F. M. Barakat, and M. S. AlSalhi, "Double layered plasmonic thin-film luminescent solar concentrators based on polycarbonate supports," *Renewable Energy,* vol. 63, pp. 642-649, 2014/03/01/ 2014, doi: https://doi.org/10.1016/j.renene.2013.10.014.
[257] N. D. Bronstein *et al.*, "Quantum Dot Luminescent Concentrator Cavity Exhibiting 30-fold Concentration," *ACS Photonics,* vol. 2, no. 11, pp. 1576-1583, 2015/11/18 2015, doi: 10.1021/acsphotonics.5b00334.
[258] M. Rüdiger *et al.*, "Bifacial n-type silicon solar cells for upconversion applications," *Solar Energy Materials and Solar Cells,* vol. 128, pp. 57-68, 2014/09/01/ 2014, doi: https://doi.org/10.1016/j.solmat.2014.05.014.
[259] W.-J. Ho, C.-Y. Wei, J.-J. Liu, W.-C. Lin, and C.-H. Ho, "Performance characterization of planar silicon solar cells using NIR up-conversion layer comprising YF3:Yb3+/Er3+ phosphors," *Vacuum,* vol. 166, pp. 1-5, 2019/08/01/ 2019, doi: https://doi.org/10.1016/j.vacuum.2019.04.046.
[260] N. Yao *et al.*, "Enhanced light harvesting of dye-sensitized solar cells with up/down conversion materials," *Electrochimica Acta,* vol. 154, pp. 273-277, 2015/02/01/ 2015, doi: https://doi.org/10.1016/j.electacta.2014.12.095.
[261] P. Song, C. Zhang, and P. Zhu, "Enhanced solar photons harvesting of a-SiC:H solar cells with ZBLA fluoride glasses containing rare earth ions," *Journal of Alloys and Compounds,* pp. 65-69, 2016, doi: DOI:101016/jjallcom201603288.
[262] S.-J. Ha, J.-H. Kang, D. H. Choi, S. K. Nam, E. Reichmanis, and J. H. Moon, "Upconversion-Assisted Dual-Band Luminescent Solar Concentrator Coupled for High Power Conversion Efficiency Photovoltaic Systems," *ACS Photonics,* vol. 5, no. 9, pp. 3621-3627, 2018/09/19 2018, doi: 10.1021/acsphotonics.8b00498.
[263] K.-T. Lee *et al.*, "Simultaneous Enhancement of Upconversion and Downshifting Luminescence via Plasmonic Structure," *Nano Letters,* vol. 15, no. 4, pp. 2491-2497, 2015/04/08 2015, doi: 10.1021/nl5049803.
[264] P. A. Loiko, N. M. Khaidukov, J. Méndez-Ramos, E. V. Vilejshikova, N. A. Skoptsov, and K. V. Yumashev, "Up- and down-conversion emissions from Er3+ doped K2YF5 and K2YbF5 crystals," *Journal of Luminescence,* vol. 170, pp. 1-7, 2016/02/01/ 2016, doi: https://doi.org/10.1016/j.jlumin.2015.10.016.
[265] A. Bahadur, R. S. Yadav, R. V. Yadav, and S. B. Rai, "Multimodal emissions from Tb3+/Yb3+ co-doped lithium borate glass: Upconversion, downshifting and quantum cutting," *Journal of Solid State Chemistry,* vol. 246, pp. 81-86, 2017/02/01/ 2017, doi: https://doi.org/10.1016/j.jssc.2016.11.004.
[266] Y. Wang, H. Zhang, S. Qu, and C. Su, "Downconversion and upconversion emissions of GdPO4:Yb3+/Tb3+ and its potential applications in solar cells," *Journal of Alloys and Compounds,* vol. 677, pp. 266-270, 2016/08/25/ 2016, doi: https://doi.org/10.1016/j.jallcom.2016.03.242.
[267] L. Aarts, B. M. v. d. Ende, and A. Meijerink, "Downconversion for solar cells in NaYF4:Er,Yb," *Journal of Applied Physics,* vol. 106, no. 2, p. 023522, 2009, doi: 10.1063/1.3177257.
[268] T. V. Gavrilović, D. J. Jovanović, V. Lojpur, and M. D. Dramićanin, "Multifunctional Eu3+- and Er3+/Yb3+-doped GdVO4 nanoparticles synthesized by reverse micelle method," *Scientific Reports,* Article vol. 4, p. 4209, 02/27/online 2014, doi: 10.1038/srep04209.
[269] EPHOCELL. "Smart light collecting system for the efficiency enhancement of solar cells." https://cordis.europa.eu/project/rcn/90161/reporting/en (accessed 10 Mar 2019).
[270] A. Le Donne, M. Acciarri, D. Narducci, S. Marchionna, and S. Binetti, "Encapsulating Eu3+ complex doped layers to improve Si-based solar cell efficiency," *Progress in Photovoltaics: Research and Applications,* vol. 17, no. 8, pp. 519-525, 2009, doi: 10.1002/pip.902.
[271] T. F. Schulze and T. W. Schmidt, "Photochemical upconversion: present status and prospects for its application to solar energy conversion," *Energy & Environmental Science,* 10.1039/C4EE02481H vol. 8, no. 1, pp. 103-125, 2015, doi: 10.1039/C4EE02481H.

[272] B. R. Sutherland, "Cost Competitive Luminescent Solar Concentrators," *Joule,* vol. 2, no. 2, pp. 203-204, 2018/02/21/ 2018, doi: https://doi.org/10.1016/j.joule.2018.02.004.
[273] D. Kumar *et al.*, "Recent advances in enhanced luminescence upconversion of lanthanide-doped NaYF4 phosphors," *Physica B: Condensed Matter,* vol. 535, pp. 278-286, 2018/04/15/ 2018, doi: https://doi.org/10.1016/j.physb.2017.08.003.
[274] G. B. Nair, A. Kumar, H. C. Swart, and S. J. Dhoble, "Facile precipitation synthesis of green-emitting BaY2F8:Yb3+, Ho3+ upconverting phosphor," *Ceramics International,* vol. 45, no. 11, pp. 14205-14213, 2019/08/01/ 2019, doi: https://doi.org/10.1016/j.ceramint.2019.04.127.
[275] E. Favilla *et al.*, "Comparative analysis of upconversion efficiencies in fluoride materials for photovoltaic application," *Solar Energy Materials and Solar Cells,* vol. 157, pp. 415-421, 2016/12/01/ 2016, doi: https://doi.org/10.1016/j.solmat.2016.05.005.
[276] R. Lesyuk, V. Marinov, E. K. Hobbie, A. Elbaradei, I. Tarnavchyk, and Y. Bobitski, "Toward cadmium-free spectral down-shifting converters for photovoltaic applications," *Solar Energy Materials and Solar Cells,* vol. 151, pp. 52-59, 2016/07/01/ 2016, doi: https://doi.org/10.1016/j.solmat.2016.02.021.
[277] H. Shpaisman, O. Niitsoo, I. Lubomirsky, and D. Cahen, "Can up- and down-conversion and multi-exciton generation improve photovoltaics?," *Solar Energy Materials and Solar Cells,* vol. 92, no. 12, pp. 1541-1546, 2008/12/01/ 2008, doi: https://doi.org/10.1016/j.solmat.2008.08.006.
[278] Sigma Aldrich. "Sodium yttrium fluoride, ytterbium and erbium doped " https://www.sigmaaldrich.com/catalog/product/aldrich/756555?lang=en&region=GB (accessed 10 May 2019).
[279] Sigma Aldrich. "Rare earth doped upconversion nanoparticles." https://www.sigmaaldrich.com/catalog/product/aldrich/900556?lang=en&region=GB (accessed 10 May 2019).
[280] B. Richards and E. Klampaftis, *Luminescent Encapsulation Layers for Mutlicrystalline Silicon PV Modules*. 2011, pp. 104-109.
[281] Sigma Aldrich. "CdSe/ZnS core-shell type quantum dots." https://www.sigmaaldrich.com/catalog/product/aldrich/748099?lang=en&region=GB (accessed 10 May 2019).
[282] I. Bite *et al.*, "Novel method of phosphorescent strontium aluminate coating preparation on aluminum," *Materials & Design,* vol. 160, pp. 794-802, 2018/12/15/ 2018, doi: https://doi.org/10.1016/j.matdes.2018.10.021.
[283] M. J. Weber, *Handbook of Optical Materials*, 1st Edition ed. Boca Raton, USA: CRC Press, 2002.
[284] F. Sima, C. Ristoscu, L. Duta, O. Gallet, K. Anselme, and I. N. Mihailescu, "3 - Laser thin films deposition and characterization for biomedical applications," in *Laser Surface Modification of Biomaterials*, R. Vilar Ed.: Woodhead Publishing, 2016, pp. 77-125.
[285] M. Eckert, "Max von Laue and the discovery of X-ray diffraction in 1912," *Annalen der Physik,* vol. 524, no. 5, pp. A83-A85, 2012, doi: 10.1002/andp.201200724.
[286] Hyper Physics. "Bragg's Law." http://hyperphysics.phy-astr.gsu.edu/hbase/quantum/bragg.html (accessed 15 Mar 2019).
[287] NPTEL. "Catalyst characterization -XRD analysis: Working principle and Instrumentation. ." https://nptel.ac.in/courses/103103026/module2/lec12/2.html (accessed 15 Feb 2019).
[288] V. Sharma, A. Das, V. Kumar, O. M. Ntwaeaborwa, and H. C. Swart, "Potential of Sr4Al14O25: Eu2+,Dy3+ inorganic oxide-based nanophosphor in Latent fingermark detection," *Journal of Materials Science,* journal article vol. 49, no. 5, pp. 2225-2234, March 01 2014, doi: 10.1007/s10853-013-7916-2.
[289] S. Wu, Y. Ning, and S. Zhang, "Hydrothermal Synthesis of :Yb, Er Nanocrystals with Upconversion Fluorescence Using Tetraethylene Pentamine as Chelating Ligand," *Journal of Nanomaterials,* vol. 2012, p. 8, 2012, Art no. 369605, doi: 10.1155/2012/369605.

[290] University of Liverpool. "Introduction to Electron Microscopes." http://www.materials.ac.uk/elearning/matter/introductiontoelectronmicroscopes/sem/everhart.html (accessed 15 Mar 2019).
[291] Thermo Fisher Scientific. "Sputter coating for SEM: how this sample preparation technique assists your imaging." https://blog.phenom-world.com/sputter-coating-sem (accessed 15 Mar 2019).
[292] EdinburghInstruments. "FS5 Spectrofluorometer." https://www.edinst.com/products/fs5-spectrofluorometer/ (accessed 12 June 2019.
[293] Ossila. "Spin Coating: A Guide to Theory and Techniques." https://www.ossila.com/pages/spin-coating (accessed 3 Apr 2019).
[294] University of Louisville. "Spin Coating Theory." https://louisville.edu/micronano/files/documents/standard-operating-procedures/SpinCoatingInfo.pdf (accessed 17 Feb 2019.
[295] Perkin Elmer. "LAMBDA 1050 UV/Vis Spectrophotometer." https://www.perkinelmer.com/product/lambda-1050-uv-vis-nir-spectrophotometer-l1050 (accessed 13 Apr 2019).
[296] EMS. "Sylgard™ 184 - Technical Data Sheets." https://www.emsdiasum.com/microscopy/technical/datasheet/24236-10.aspx (accessed 13 Apr 2019).
[297] N. Rahimi, R. A. Pax, and E. M. Gray, "Review of functional titanium oxides. I: TiO2 and its modifications," *Progress in Solid State Chemistry,* vol. 44, no. 3, pp. 86-105, 2016/09/01/ 2016, doi: https://doi.org/10.1016/j.progsolidstchem.2016.07.002.
[298] B. S. Richards, S. F. Rowlands, C. B. Honsberg, and J. E. Cotter, "TiO2 DLAR coatings for planar silicon solar cells," *Progress in Photovoltaics: Research and Applications,* vol. 11, no. 1, pp. 27-32, 2003, doi: 10.1002/pip.474.
[299] Y. Zhu, L. Zhang, C. Gao, and L. Cao, "The synthesis of nanosized TiO2 powder using a sol-gel method with TiCl4 as a precursor," *Journal of Materials Science,* journal article vol. 35, no. 16, pp. 4049-4054, August 01 2000, doi: 10.1023/a:1004882120249.
[300] G. Puccetti and R. M. Leblanc, "Hydrolysis/Condensation Reactions at the Sol−Gel/Air Interface: Pure Titania Alkoxide Exposed to Air−Water Molecules," *The Journal of Physical Chemistry B,* vol. 102, no. 45, pp. 9002-9005, 1998/11/01 1998, doi: 10.1021/jp981931o.
[301] Retsch. High Energy Ball Mills: Grinding and Particle Sizing on a Nanoscale. *The Sample – Customer Magazine*.
[302] NAREC. *PV Technology Centre. . A cross section of LGBC technology.* . (2009).
[303] J. Montes-Romero, M. Piliougine, J. V. Muñoz, E. F. Fernández, and J. De la Casa, "Photovoltaic Device Performance Evaluation Using an Open-Hardware System and Standard Calibrated Laboratory Instruments," *Energies,* vol. 10, no. 11, p. 1869, 2017. [Online]. Available: https://www.mdpi.com/1996-1073/10/11/1869.
[304] M. Shah, S. Pandey, and M. Marathe, "Comparative Study of Two Different Make of PV I-V Tracers," *International Journal Of Electrical, Electronics And Data Communication,* vol. 4, no. 10, pp. 62-64, 2016.
[305] N. Sellami, "Design and characterisation of a novel translucent solar concentrator," PhD Thesis, School of Engineering and Physical Sciences, Heriot-Watt University, Edinburgh, UK, 2013.
[306] B. O'Regan and M. Grätzel, "A low-cost, high-efficiency solar cell based on dye-sensitized colloidal TiO2 films," *Nature,* vol. 353, no. 6346, pp. 737-740, 1991/10/01 1991, doi: 10.1038/353737a0.
[307] R.-T. Chen and C.-F. Liao, "Evaluation and Optimization to Recycle Used TiO2 Photoelectrode for Dye-Sensitized Solar Cells," *International Journal of Photoenergy,* vol. 2014, p. 7, 2014, Art no. 650945, doi: 10.1155/2014/650945.
[308] K. Hara and H. Arakawa, "Dye-Sensitized Solar Cells," in *Handbook of Photovoltaic Science and Engineering*, A. Luque and S. Hegedus Eds., 2005.

[309] J. Kwon *et al.*, "Two-terminal DSSC/silicon tandem solar cells exceeding 18% efficiency," *Energy & Environmental Science,* 10.1039/C6EE02296K vol. 9, no. 12, pp. 3657-3665, 2016, doi: 10.1039/C6EE02296K.
[310] K. Sharma, V. Sharma, and S. S. Sharma, "Dye-Sensitized Solar Cells: Fundamentals and Current Status," *Nanoscale Research Letters,* vol. 13, no. 1, p. 381, 2018/11/28 2018, doi: 10.1186/s11671-018-2760-6.
[311] Y. Tachibana, J. E. Moser, M. Grätzel, D. R. Klug, and J. R. Durrant, "Subpicosecond Interfacial Charge Separation in Dye-Sensitized Nanocrystalline Titanium Dioxide Films," *The Journal of Physical Chemistry,* vol. 100, no. 51, pp. 20056-20062, 1996/01/01 1996, doi: 10.1021/jp962227f.
[312] H. Choi *et al.*, "The effect of TiCl4-treated TiO2 compact layer on the performance of dye-sensitized solar cell," *Current Applied Physics,* vol. 12, no. 3, pp. 737-741, 2012/05/01/ 2012, doi: https://doi.org/10.1016/j.cap.2011.10.011.
[313] M. K. Nazeeruddin *et al.*, "Conversion of light to electricity by cis-X2bis(2,2'-bipyridyl-4,4'-dicarboxylate)ruthenium(II) charge-transfer sensitizers (X = Cl-, Br-, I-, CN-, and SCN-) on nanocrystalline titanium dioxide electrodes," *Journal of the American Chemical Society,* vol. 115, no. 14, pp. 6382-6390, 1993/07/01 1993, doi: 10.1021/ja00067a063.
[314] A. K. Baranwal, T. Shiki, Y. Ogomi, S. S. Pandey, T. Ma, and S. Hayase, "Tandem dye-sensitized solar cells with a back-contact bottom electrode without a transparent conductive oxide layer," *RSC Advances,* 10.1039/C4RA07539K vol. 4, no. 88, pp. 47735-47742, 2014, doi: 10.1039/C4RA07539K.
[315] T. V. S. S. P. Sashank, B. Manikanta, and A. Pasula, "Fabrication and Experimental Investigation on Dye Sensitized Solar Cells Using Titanium Dioxide Nano Particles," *Materials Today: Proceedings,* vol. 4, no. 2, Part A, pp. 3918-3925, 2017/01/01/ 2017, doi: https://doi.org/10.1016/j.matpr.2017.02.291.
[316] S. Ito *et al.*, "Fabrication of screen-printing pastes from TiO2 powders for dye-sensitised solar cells," *Progress in Photovoltaics: Research and Applications,* vol. 15, no. 7, pp. 603-612, 2007, doi: 10.1002/pip.768.
[317] Y. Xu, L.-S. Qiang, Y.-L. Yang, L.-G. Wei, P. Wang, and R.-Q. Fan, "Enhanced performance of ruthenium dye-sensitized solar cell by employing an organic co-adsorbent of N,N'-bis((pyridin-2-yl)(methyl) methylene)-o-phenylenediamine," *Chinese Chemical Letters,* vol. 27, no. 1, pp. 127-134, 2016/01/01/ 2016, doi: https://doi.org/10.1016/j.cclet.2015.06.010.
[318] S. Ito, K. Takahashi, S.-i. Yusa, M. Saito, and T. Shigetomi, "Ultradurable Dye-Sensitized Solar Cells under 120°C Using Cross-Linkage Dye and Ionic-Liquid Electrolyte," *International Journal of Photoenergy,* vol. 2013, p. 9, 2013, Art no. 501868, doi: 10.1155/2013/501868.
[319] H. J. Snaith, "Estimating the Maximum Attainable Efficiency in Dye-Sensitized Solar Cells," *Advanced Functional Materials,* vol. 20, no. 1, pp. 13-19, 2010, doi: 10.1002/adfm.200901476.
[320] A. Mohamed and Y. Selim, "Factors Affect Dye Sensitized Solar Cells performance," *2017,* dye-sensitized solar cells; DSSC performance; dye; Factors improve DSSC efficiency vol. 3, no. 1, p. 4, 2017-03-18 2017, doi: 10.21622/resd.2017.03.1.083.
[321] S. Castro-Hermosa *et al.*, "Stability issues pertaining large area perovskite and dye-sensitized solar cells and modules," *Journal of Physics D: Applied Physics,* vol. 50, no. 3, p. 033001, 2016/12/08 2016, doi: 10.1088/1361-6463/50/3/033001.
[322] M. Wang *et al.*, "Efficient and Stable Solid-State Dye-Sensitized Solar Cells Based on a High-Molar-Extinction-Coefficient Sensitizer," *Small,* vol. 6, no. 2, pp. 319-324, 2010, doi: 10.1002/smll.200901317.
[323] A. Lennert, K. Wagner, R. Yunis, J. M. Pringle, D. M. Guldi, and D. L. Officer, "Efficient and Stable Solid-State Dye-Sensitized Solar Cells by the Combination of Phosphonium Organic Ionic Plastic Crystals with Silica," *ACS Applied Materials & Interfaces,* vol. 10, no. 38, pp. 32271-32280, 2018/09/26 2018, doi: 10.1021/acsami.8b12334.

[324] V. K. Narra *et al.*, "D–π–A system based on zinc porphyrin dyes for dye-sensitized solar cells: Combined experimental and DFT–TDDFT study," *Polyhedron,* vol. 100, pp. 313-320, 2015/11/04/ 2015, doi: https://doi.org/10.1016/j.poly.2015.08.035.
[325] S. Wang. "How to UV Ozone Cleaning." https://chem.uiowa.edu/sites/chem.uiowa.edu/files/people/shaw/Scarlett-How%20to%20UV-OZONE%20Sep_15th.pdf (accessed 30 July 2019).
[326] F. Nurosyid, L. Furqoni, A. Supriyanto, and R. Suryana, "Effect of screen printing type on transparent TiO2 layer as the working electrode of dye sensitized solar cell (DSSC) for solar windows applications," *Journal of Physics: Conference Series,* vol. 776, p. 012011, 2016/11 2016, doi: 10.1088/1742-6596/776/1/012011.
[327] A. Usami, "Theoretical study of application of multiple scattering of light to a dye-sensitized nanocrystalline photoelectrichemical cell," *Chemical Physics Letters,* vol. 277, no. 1, pp. 105-108, 1997/10/03/ 1997, doi: https://doi.org/10.1016/S0009-2614(97)00878-6.
[328] S. Senthilarasu, T. A. N. Peiris, J. García-Cañadas, and K. G. U. Wijayantha, "Preparation of Nanocrystalline TiO2 Electrodes for Flexible Dye-Sensitized Solar Cells: Influence of Mechanical Compression," *The Journal of Physical Chemistry C,* vol. 116, no. 36, pp. 19053-19061, 2012/09/13 2012, doi: 10.1021/jp301638p.
[329] Z. Hosseini, N. Taghavinia, and E. Wei-Guang Diau, "Luminescent Spectral Conversion to Improve the Performance of Dye-Sensitized Solar Cells," *ChemPhysChem,* vol. 18, no. 23, pp. 3292-3308, 2017, doi: 10.1002/cphc.201700920.
[330] X. Wei-Wei, D. Song-Yuan, H. Lin-Hua, L. Lin-Yun, and W. Kong-Jia, "Influence of Yb-Doped Nanoporous TiO2Films on Photovoltaic Performance of Dye-Sensitized Solar Cells," *Chinese Physics Letters,* vol. 23, no. 8, pp. 2288-2291, 2006/07/21 2006, doi: 10.1088/0256-307x/23/8/089.
[331] J. Wu *et al.*, "Counter electrodes in dye-sensitized solar cells," *Chemical Society Reviews,* 10.1039/C6CS00752J vol. 46, no. 19, pp. 5975-6023, 2017, doi: 10.1039/C6CS00752J.
[332] P. Selvaraj *et al.*, "Enhancing the efficiency of transparent dye-sensitized solar cells using concentrated light," *Solar Energy Materials and Solar Cells,* vol. 175, pp. 29-34, 2018/02/01/ 2018, doi: https://doi.org/10.1016/j.solmat.2017.10.006.
[333] T. Higashino and H. Imahori, "Porphyrins as excellent dyes for dye-sensitized solar cells: recent developments and insights," *Dalton Transactions,* 10.1039/C4DT02756F vol. 44, no. 2, pp. 448-463, 2015, doi: 10.1039/C4DT02756F.
[334] N. V. Krishna *et al.*, "Donor-π–Acceptor Based Stable Porphyrin Sensitizers for Dye-Sensitized Solar Cells: Effect of π-Conjugated Spacers," *The Journal of Physical Chemistry C,* vol. 121, no. 12, pp. 6464-6477, 2017/03/30 2017, doi: 10.1021/acs.jpcc.6b12869.
[335] A. Pandey and V. K. Rai, "Colour emission tunability in Ho3+–Tm3+–Yb3+ co-doped Y2O3 upconverted phosphor," *Applied Physics B,* journal article vol. 109, no. 4, pp. 611-616, December 01 2012, doi: 10.1007/s00340-012-5224-1.
[336] V. Lojpur, M. Nikolic, L. Mancic, O. Milosevic, and M. D. Dramicanin, "Y2O3:Yb,Tm and Y2O3:Yb,Ho powders for low-temperature thermometry based on up-conversion fluorescence," *Ceramics International,* vol. 39, no. 2, pp. 1129-1134, 2013/03/01/ 2013, doi: https://doi.org/10.1016/j.ceramint.2012.07.036.
[337] R. J. Yang and P. X. W. Zou, "Building integrated photovoltaics (BIPV): costs, benefits, risks, barriers and improvement strategy," *International Journal of Construction Management,* vol. 16, no. 1, pp. 39-53, 2016/01/02 2016, doi: 10.1080/15623599.2015.1117709.
[338] G. Calogero, A. Bartolotta, G. Di Marco, A. Di Carlo, and F. Bonaccorso, "Vegetable-based dye-sensitized solar cells," *Chemical Society Reviews,*

10.1039/C4CS00309H vol. 44, no. 10, pp. 3244-3294, 2015, doi: 10.1039/C4CS00309H.
[339] PhotonicUniverse. "300W MONOCRYSTALLINE SOLAR PANEL WITH 1M CABLE." https://www.photonicuniverse.com/en/catalog/full/473-300W-monocrystalline-solar-panel-with-1m-cable.html (accessed 15 Aug, 2019).
[340] H. M. Lee and J. H. Yoon, "Power performance analysis of a transparent DSSC BIPV window based on 2 year measurement data in a full-scale mock-up," *Applied Energy,* vol. 225, pp. 1013-1021, 2018/09/01/ 2018, doi: https://doi.org/10.1016/j.apenergy.2018.04.086.
[341] S. G. Hashmi *et al.*, "Dye-sensitized solar cells with inkjet-printed dyes," *Energy & Environmental Science,* 10.1039/C6EE00826G vol. 9, no. 7, pp. 2453-2462, 2016, doi: 10.1039/C6EE00826G.
[342] UoMaryland. "Random vs Systematic Error." https://www.physics.umd.edu/courses/Phys276/Hill/Information/Notes/ErrorAnalysis.html (accessed 15 June, 2019).
[343] G. D. Ruxton, "The unequal variance t-test is an underused alternative to Student's t-test and the Mann–Whitney U test," *Behavioral Ecology,* vol. 17, no. 4, pp. 688-690, 2006, doi: 10.1093/beheco/ark016.
[344] B. K. Moser and G. R. Stevens, "Homogeneity of Variance in the Two-Sample Means Test," *The American Statistician,* vol. 46, no. 1, pp. 19-21, 1992/02/01 1992, doi: 10.1080/00031305.1992.10475839.
[345] C. D. H. Mellinger, Thomas A., *Quantitative Research Methods in Translation and Interpreting Studies*. Abingdon, Oxon, UK: Routledge, 2017.
[346] J. Stangroom. "P Value from T Score Calculator." https://www.socscistatistics.com/pvalues/tdistribution.aspx (accessed 17 April 2019).
[347] "P Value from Z Score Calculator." https://www.socscistatistics.com/pvalues/normaldistribution.aspx (accessed 24 April 2019).
[348] H. Castrup, "Estimating and Combining Uncertainties " in *8th Annual ITEA Instrumentation Workshop*, Lancaster, CA, USA, 5 May 2004.
[349] RReDC. "Reference Solar Spectral Irradiance: ASTM G-173." https://rredc.nrel.gov/solar//spectra/am1.5/ASTMG173/ASTMG173.html (accessed 17 Jun, 2018).
[350] K.-C. Kim, "Effective graded refractive-index anti-reflection coating for high refractive-index polymer ophthalmic lenses," *Materials Letters,* vol. 160, pp. 158-161, 2015/12/01/ 2015, doi: https://doi.org/10.1016/j.matlet.2015.07.108.
[351] E. Klampaftis, D. Ross, K. R. McIntosh, and B. S. Richards, "Enhancing the performance of solar cells via luminescent down-shifting of the incident spectrum: A review," *Solar Energy Materials and Solar Cells,* vol. 93, no. 8, pp. 1182-1194, 2009/08/01/ 2009, doi: https://doi.org/10.1016/j.solmat.2009.02.020.